IIUM ENGINEERING JOURNAL

Copyright Notice

IIUM ENGINEERING JOURNAL

AIMS & SCOPE OF IIUMENGINEERING JOURNAL

The **IIUM Engineering Journal**, published biannually (January and July), is a carefully refereed international publication of International Islamic University Malaysia (IIUM). Contributions of high technical merit within the span of engineering disciplines; covering the main areas of engineering: Electrical and Computer Engineering; Mechanical and Manufacturing Engineering; Automation and Mechatronics Engineering; Material and Chemical Engineering; Environmental and Civil Engineering; Biotechnology and Bioengineering; Engineering Mathematics and Physics; and Computer Science and Information Technology are considered for publication in this journal. Contributions from other areas of Engineering and Applied Science are also welcomed. The IIUM Engineering Journal publishes contributions under *Regular papers and Invited review papers*. It also welcomes contributions that address solutions to the specific challenges of the developing world and address science and technology issues from an Islamic and multidisciplinary perspective.

REFEREES' NETWORK

All papers submitted to IIUM Engineering Journal will be subjected to a rigorous reviewing process through a worldwide network of specialized and competent referees. Each accepted paper should have at least two positive referees' assessments.

SUBMISSION OF A MANUSCRIPT

A manuscript should be submitted online to the IIUM-Engineering Journal website at http://journals.iium.edu.my/ejournal. Further correspondence on the status of the paper could be done through the journal website.

INTERNATIONAL ADVISORY COMMITTEE

Table of Contents

MATERIALS AND MANUFACTURING ENGINEERING

MECHANICAL AND AEROSPACE ENGINEERING

MECHATRONICS AND AUTOMATION ENGINEERING

CONSOLIDATION INTEGRATED BUOYANCY EQUATION FOR SOFT GROUND IMPROVED WITH LIGHTWEIGHT POLYURETHANE FOAM

DIANA CHE LAT[1*], ISMACAHYADI BAGUS MOHAMED JAIS[2],
NAZRI ALI[3], NOR ZURAIRAHETTY MOHD YUNUS[3], NOR HIBATUL WAFI NOR
ZARIN[4] AND ATIQAH NAJWA ZAINUDDIN[1]

[1]Faculty of Civil Engineering, Universiti Teknologi MARA (UiTM) Johor,
Pasir Gudang Campus, 81750, Masai, Johor
[2]Faculty of Civil Engineering, Universiti Teknologi MARA (UiTM) Selangor,
Shah Alam Campus, 40450, Shah Alam, Selangor
[3]School of Civil Engineering, Faculty of Engineering, Universiti Teknologi Malaysia,
81310 Johor Bahru, Johor
[4]Cawangan Kejuruteraan Cerun, JKR Malaysia, Jalan Sultan Salahuddin,
50582 Kuala Lumpur

*Corresponding author: dianacl@uitm.edu.my

ABSTRACT: Consolidation settlement occurs when a saturated soil is subjected to an increase in overburden pressure that causes a volume change in the soil. When a lightweight material is used as a ground improvement, the stress is reduced as the soft soil is partially removed and replaced by the lightweight material. In addition, the improved ground with lightweight material has a potential to uplift due to the buoyancy of lightweight material. The uplift force reduces the stress imposed on the underlying soil as it acts in the upward direction, thus further reducing the consolidation settlement. This study is executed to produce an alternative equation for consolidation settlement incorporating the buoyancy effect for lightweight polyurethane (PU) foam as a ground improvement method. A Rowe Cell consolidation laboratory test was conducted on untreated marine clay soil as well as on improved marine clay with different thicknesses of lightweight PU foam. Validation of the laboratory test results was done by finite element analysis, PLAXIS 2D. The thickness of PU foam governs the buoyancy and the hydrostatic pressure of water displaced by PU foam, which is incorporated in the alternative equation. The alternative consolidation settlement equation is applicable for ground improved with lightweight polyurethane foam and found to be more economical and practical as the buoyancy is taken into account in the equation.

ABSTRAK: Mendapan pengukuhan berlaku apabila tanah tepu mengalami peningkatan tekanan beban yang menyebabkan perubahan isipadu tanah. Apabila bahan ringan digunakan sebagai penambahbaikan tanah, tekanan akan berkurang kerana sebahagian tanah lembut dikeluarkan dan diganti dengan bahan ringan. Selain itu, tanah yang diperbaiki dengan bahan ringan berpotensi untuk terangkat ke atas keranan daya apung bahan ringan. Daya angkat bahan ringan mengurangkan tekanan yang dikenakan ke atas tanah kerana daya bertindak ke arah atas, dan seterusnya megurangkan mendapan pengukuhan. Kajian ini dijalankan untuk menghasilkan persamaan alternatif bagi mendapan pengukuhan dan digabungkan dengan kesan daya apung untuk busa poliuretena ringan (PU) sebagai kaedah penambahbaikan tanah. Ujian makmal mendapan pengukuhan menggunakan peralatan Rowe Cell dilakukan pada tanah liat marin yang asal serta yang diperbaiki dengan ketebalan busa PU ringan yang berbeza.

Pengesahan hasil ujian makmal dilakukan dengan analisis elemen terhingga, PLAXIS 2D. Ketebalan busa PU mempengaruhi daya apung dan tekanan hidrostatik bagi kedalaman air yang disesarkan oleh busa PU dan digabungkan dalam persamaan alternatif. Persamaan alternatif mendapan pengukuhan tersebut boleh digunapakai untuk pembaikan tanah menggunakan bahan ringan busa poliuretena dan didapati menjimatkan kos dan praktikal kerana keapungan diambilkira didalam persamaan tersebut.

KEYWORDS: *soft ground; consolidation settlement; buoyancy; polyurethane; lightweight*

1. INTRODUCTION

Construction on soft clay causes consolidation settlement of the soil due to increased overburden load and low permeability of clay soil. In order to reduce the overburden load, lightweight materials are proposed as a ground improvement for soft clay. Some of the lightweight fill materials such as foamglass, sawdust and bark residue, foamed concrete, lightweight clay aggregate, shredded tires, floating bamboo and plastic bags [1,2] have been investigated as a ground improvement method. Low et al. [3] proposed a new floating foundation system, namely a lightweight concrete infill buoyant system whereby plastic bags, used tires, and tubes were used as a lightweight material for foundation construction whilst bamboo and bakau were used to encapsulate the waste materials and form a composite floating foundation. On top of that, lightweight foams are also currently in demand due their ability to enable fast construction work with less manpower as the foam can be pre-fabricated in the factory.

This study focuses on lightweight foam, namely polyurethane (PU) foam, as a ground improvement method. In 1937, Dr. Otto Bayer was the first person to produce and investigate polyurethane [4]. Polyurethane is a class of polymers with a mix of polyol (-OH) and isocyanate (-NCO) that react during polymerization of polyurethane [5-8]. Nowadays, PU foams are recognized as one of the most crucial classes of polymers that transform the quality of human life [9]. It was predicted that the worldwide consumption of PU will be over 79 billion USD in 2021 [10]. As the demand increases, the sustainable production of PU foam is very crucial. Polyol can be produced from bio-based oil and crude glycerol [11-13] whilst isocyanate can be produced from non-isocyanate material (NIPU), which is non-petroleum based [14-17].

When this lightweight material is used as a ground improvement method on saturated soil, buoyancy of the material may cause uplift. Excessive uplift may damage the structure founded on it [18]. The buoyancy is an upward force exerted by a fluid that acts on an immersed object. Over two millennia ago, Archimedes of Syracuse [19] developed the Archimedes' principle, which states that "any object, wholly or partially immersed in a fluid, is buoyed up by a force equal to the weight of the fluid displaced by the object." The buoyancy acting on an underground structure in either shallow or deep foundation was measured and compared with Archimedes' principle [20-22]. Frydelund and Aaboer [23] had reported on a few failure cases of embankment, which was founded on lightweight geofoam due to buoyancy. In 1987, the first lightweight geofoam, namely expanded polystyrene foam (EPS) fill built-in Norway, floated off during an unpredicted rainfall season and rising flood waters. In Thailand, the unexpected water level washed away a road filled with EPS. The geofoam experienced uplift during flooding as the weight of earthfill overlying the foam was inadequate. Various methods have been proposed to prevent the effect of hydrostatic uplift pressure, such as providing adequate load overlying the foam, proper drainage underneath the foam and installation of ground anchors [24].

Consolidation settlement occurs when a saturated soil is subjected to an increase in overburden pressure that causes a soil volume change. The consolidation settlement reduces as the saturated soil is partially removed and replaced with the lightweight PU foam. In addition, the PU foam that is immersed in water as well as in saturated soil, produces a buoyant force that acts in an upward direction that might further reduce the consolidation settlement of the soil. Therefore, the consolidation settlement considering the effect of buoyancy for the ground improved with PU foam is investigated in this study.

2. METHODOLOGY

The consolidation settlement test for untreated and treated soil samples with different thickness of PU foam was executed utilizing Rowe Cell. The Rowe Cell was developed at Manchester University, UK by Professor Rowe [25]. The detailed description of the principles and practice of Rowe Cell testing are given in Head [26]. In the Rowe Cell, the test sample is loaded hydraulically by water pressure acting on a flexible diaphragm. Drainage of the sample can be controlled and pore water pressure is measured [27]. The advantages of Rowe Cell over Oedometer test includes minimum vibration effects, measurable pore water pressure, as well as the execution of the saturation process [26]. Rowe Cell differs from Oedometer as the load is applied continuously instead of incrementally. Cell pressure, back pressure, and pore water pressure drainage line are attached on top and bottom part of the Rowe Cell apparatus as shown in Fig. 1.
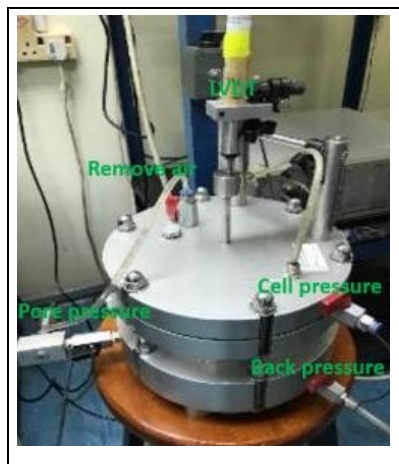
Fig.1: Rowe Cell apparatus.

2.1 Rowe Cell Consolidation Test on Saturated Marine Clay with PU Foam Partial Replacement

The test procedure for Rowe Cell consolidation test on saturated clay is as shown in Fig. 2. Prior to the testing, the calibration of the Rowe Cell apparatus was performed according to BS1377-Part 6:1990 [28] and Head [26]. For sample preparation, one kilogram of oven dried soil sample was mixed with distilled water at 1.4 times the liquid limit to form a slurry before placing it into the Rowe Cell mould. The PU foam is produced by mixing polyol and isocyanate until it reacts, expands and hardens to form PU. Next, the sample of soil is placed inside the mould followed by the replacement of PU foam on the soil sample. It was followed by the placement of the top cell which was attached to LVDT, load cell, and cell pressure. Back pressure and pore pressure were attached to the bottom cell. The determination of consolidation and buoyancy behaviour of the clay soil improved with PU foam were carried out on a few samples of PU foam.

Partial replacement of the soft clay with PU foam was done at shallow depth. Thus, in this laboratory test, the thickness of soft clay was 25 mm whilst the thicknesses of PU foam were 5 mm, 10 mm, 15 mm and 20 mm which were equivalent to 20%, 40%, 60% and 80% of PU foam to initial soft clay thickness respectively. In general, there were two phases during the consolidation integrated buoyancy test: the saturation and consolidation phases. The saturation process was carried out by applying cell pressure and back pressure alternately until Skempton's degree of saturation value, β equalled or exceeded 0.95.

During the consolidation process, the samples were tested in 150 mm diameter mould of Rowe Cell with the effective overburden pressure of 10, 20, 50, 100, 200 and 400 kPa. The test procedures are described in detail in BS1377-Part 6:1990b for step-loading test using Rowe Cell [28]. All samples for four (4) different polyurethane foam thicknesses and untreated soil samples were tested and the data recorded using Data System 7.2 (DS7) software by ELE International.
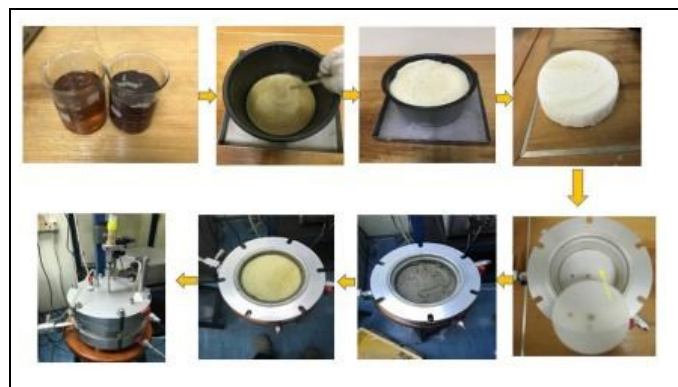
Fig. 2: Procedure of Rowe Cell consolidation test.

2.2 The Validation of Rowe Cell Test with Finite Element Model PLAXIS 2D

The validation of Rowe Cell laboratory test results was done with finite element model of PLAXIS 2D [29]. The finite element replicates the condition of PU foam construction at a shallow depth of road/walkway foundation and the typical cross-section is as shown in Fig. 3. The material model used in the finite element analysis was a plane strain with 15 nodes with a standard fixities boundary. Under long structure, the strain in the longitudinal direction will be zero (except at each end), therefore, strain takes places only in the plane of cross-section producing plane strain with effective volumetric modulus, K' subject to effective Young's Modulus, E' and Poisson's ratio, *v*' as in Eq. (1):

$$K' = E'/[2(1+v')(1-2v')] \tag{1}$$

The soft clay was in undrained condition as it is the most critical condition that the saturated clay experienced during and after construction due to very low permeability of the soil. However, the shear strength parameter input in soft-soil creep model in PLAXIS only allowed the use of effective shear strength parameter as the water is not supposed to resist any shear stress. The finite element model of the existing condition of the site before ground improvement is as shown in Fig. 4 whilst Fig. 5 shows the finite element model of the site after ground improvement with PU foam partial replacement at shallow depth of soft clay. Table 1 shows the details of subsoil and PU properties used in the finite element model whilst Fig. 6 shows the detailed cross-section for the ground improved with 1 m thickness of PU foam as an example. The effective shear strength parameters of the clay

were obtained from the consolidated undrained (CU) triaxial strength test whilst the properties of PU foam were obtained from the unconfined compressive strength test. The finite element model for the existing condition consisted of 2.5 m thick soft clay, followed by a hard layer of about 10 m thick. A layer of PU foam was used as a ground improvement method varying in thickness from 0.5 m, 1 m, 1.5 m and 2 m, which was equivalent to 20%, 40%, 60% and 80% of initial soft clay thickness, respectively. This was equivalent to the thickness of PU foam used in Rowe Cell consolidation test, as shown in Table 2. The geotextile separator shown in Figs. 4 and 5 functioned as a separator between soft clay and PU foam which did not contribute any strength, therefore, it was not modelled in PLAXIS. The FEM analysis was executed for 5 years which is equivalent to 90% degree of consolidation based on the coefficient of consolidation, C_v obtained for the clay sample.
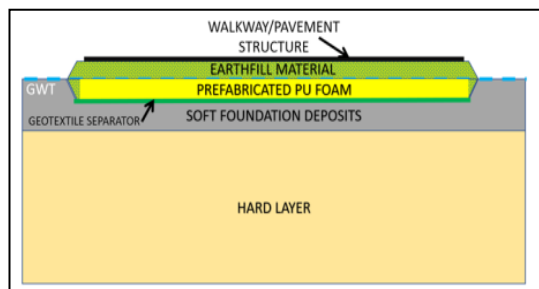
Fig. 3: Typical cross-section of PU foam construction at shallow depth of road foundation.
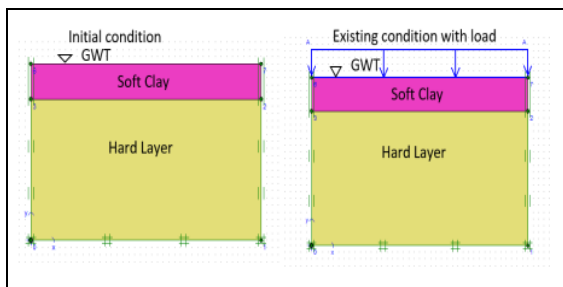
Fig. 4: Cross-section of existing site in finite element model.
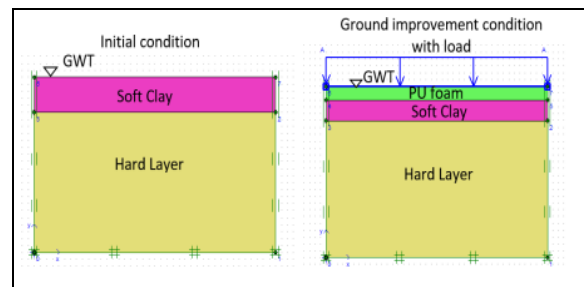
Fig. 5: Cross-section of the site after ground improvement with PU foam partial replacement at shallow depth of soft clay.

Table 1: Properties of soil and PU

		Soft clay			**Hard layer**	**PU**
Type	Unit	Undrained			Drained	Non-porous
Model		Soft Soil Creep			Mohr Coulomb	Linear Elastic
γ_{unsat}	[kN/m³]	10			18	3
γ_{sat}	[kN/m³]	16			20	-
k_x	[m/day]	1.45E10^{-5}			0.010	-
k_y	[m/day]	1.45E10^{-5}			0.010	-
E_{ref}	[kN/m²]	-			50000	30000
ν	[-]	0.495			0.3	0.3
c'_{ref}	[kN/m²]	5	3	2	5	-
ϕ'	[°]	23	22	18	30	-
$\lambda*$		0.093				
$\kappa*$		0.041				
$\mu*$		0.0046				
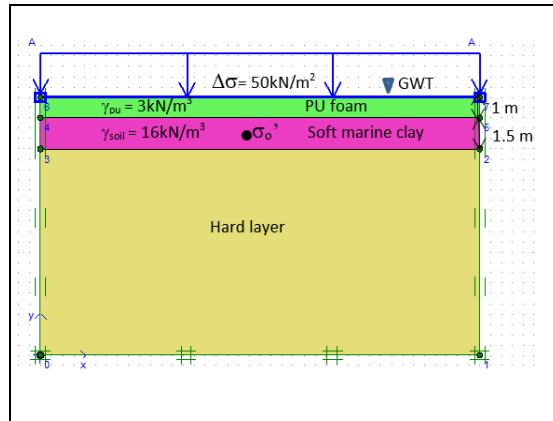
Fig. 6: Cross-section of improved ground with subsoil properties.

Table 2: The details of PU foam thickness in FEM analysis and Rowe Cell laboratory test

% PU foam to initial soft clay thickness	PU foam thickness in Rowe Cell lab (mm) (initial soft clay thickness = 25 mm)	PU foam thickness in FEM (m) (initial soft clay thickness = 2.5 m)
20%	5	0.5
40%	10	1
60%	15	1.5
80%	20	2.0

3. RESULTS AND DISCUSSION

The condition of the PU foam before and after Rowe Cell test is shown in Fig. 7. The PU foam did not show any distress or crack after the consolidation process, indicating that it was highly resistant to compression. Therefore, PU foam is currently one of the best alternative ground improvement methods for soft soil because of its many advantages [30-32]. The design of PU foam as a ground improvement takes into account the effect of buoyancy in the consolidation process. Thus, the current consolidation settlement equation was modified to integrate the buoyancy effect of the PU foam. The buoyant force, Fb acts in the opposite direction to the overburden load pressure (P) as shown in Fig. 8. Therefore, a buoyant force is able to reduce the consolidation settlement of the soft ground due to the increased load.

Fig. 7: Conditions of PU foam before and after Rowe Cell consolidation test.
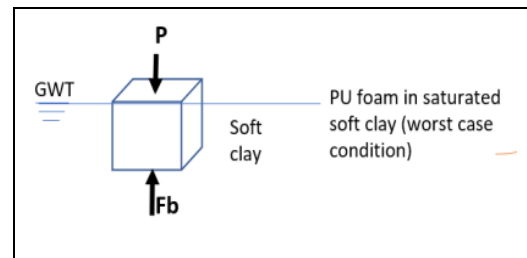
Fig. 8: Buoyant force acting on PU foam at shallow depth of soft clay.

From the Rowe Cell laboratory consolidation test as well as the finite element model, the compressibility index of the soil improvements with PU foam, Cc_{pu} for different thickness of PU foam were obtained. Existing consolidation settlement as in Eq. (2) is used to calculate the existing ground as well as improved ground based on the Cc_{pu}

obtained. However, the consolidation settlement equation based on the compressibility index, Cc, of existing soft clay is more practical instead of Cc_{pu}, therefore, Eq. (2) was modified to produce an alternative equation that incorporated the buoyant force, Fb, and hydrostatic pressure at the PU foam area, Uh_{pu}, as in Eq. (3). Since PU foam is a lightweight material, the buoyant force is introduced by the weight of water that is displaced by the PU foam, Fb, as in Eq. (4) and this is in line with Archimedes' principle [19] and equivalent to the hydrostatic pressure at the PU foam area Uh_{pu}. The buoyant force acts in the opposite direction to the overburden load, and as the PU foam thickness increases, the buoyant force increases as more water is displaced by the PU foam in the saturated soil. Therefore, a buoyant force is able to reduce the consolidation settlement of soft ground, δ.

$$\delta_{PU} = \frac{C_c pu.H}{1+e_0} \log \left[\frac{\sigma'_0 + \sigma pu + \Delta\sigma}{\sigma'_0 + \sigma pu} \right] \tag{2}$$

The initial effective stress in the alternative equation of consolidation settlement integrated buoyancy for the ground improved with PU foam as in Eq. (3) refers to the effective stress of the soft clay soil, σ_o', the stress from PU foam σ_{pu} and the hydrostatic pressure at PU foam, Uh_{pu}. The increase in the effective stress refers to the applied load pressure, Δσ and the buoyant force, Fb, which acts in the opposite direction of the applied load pressure, Δσ. Fig. 9 shows an example of the improved ground condition with the detailed parameters for elaboration on the alternative equation. The alternative equation applicable for normally consolidated soil with an overconsolidated ratio OCR value of 1.
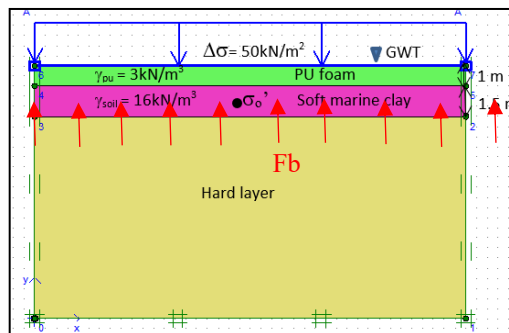
Fig. 9: Example of improved ground condition with detailed parameters for elaboration of the alternative equation.

$$\delta = \frac{C_c H}{1+e_0} \log \left[\frac{\sigma'_0 + \sigma pu + Uhpu + \Delta\sigma - Fb}{\sigma'_0 + \sigma pu + Uhpu} \right]$$

$$\delta = \frac{C_c H}{1+e_0} \log \left[\frac{\sigma'_0 + \sigma pu + \Delta\sigma}{\sigma'_0 + \sigma pu + Uhpu} \right] \tag{3}$$

where:

C_c = compression index for marine clay soil

H (m)= drainage path length

e_o = initial void ratio

σ_o' (kPa)= initial effective stress

σ_{pu} (kPa)= stress from PU foam

Δσ (kPa) = the increase of overburden stress

F_b (kN) = buoyant force per square meter area = weight of water displaced by PU foam (Uh_{pu})

$$F_b = Uh_{pu} = \gamma_w.T_{pu} \qquad (4)$$

Figure 10 shows the relationship between load pressure and settlement for the ground improved with PU foam with 20% PU foam thickness to initial soft clay. The comparisons are made between the results of Rowe Cell consolidation laboratory test (%PU-Lab), finite element model (%PU-FEM), consolidation settlement integrated buoyancy equation (%PU new eq) and existing consolidation settlement equation (%PU ex eq). All the results show good agreement with each other with the difference tolerance less than 20% except for the existing consolidation equation whereby the settlement value is overpredicted and the tolerance is more than 20%. The results are also compared with the untreated soil sample based on Rowe Cell consolidation laboratory test and finite element model in the same graph. For untreated soil samples, the settlement value obtained from Rowe Cell laboratory test (Soil only-Lab) is very close to the finite element analysis results (Soil only-FEM). The settlement reduces with the ground improvement of 20% PU foam to initial soft clay thickness. A similar trend occurs for other thicknesses of PU foam of 40%, 50%, 60% and 80% as shown in Figs. 11 to 14.
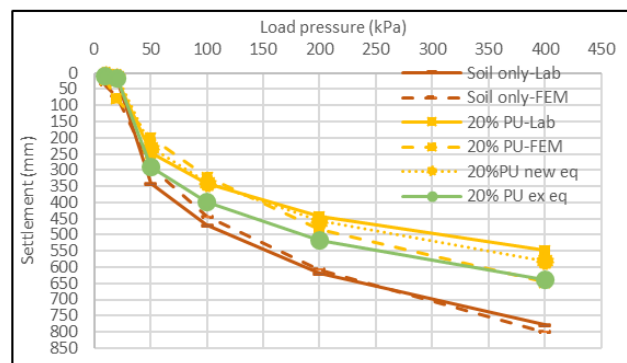
Fig. 10: Load pressure and settlement relationship for untreated and improved soil sample (20% PU foam to initial soft clay depth)
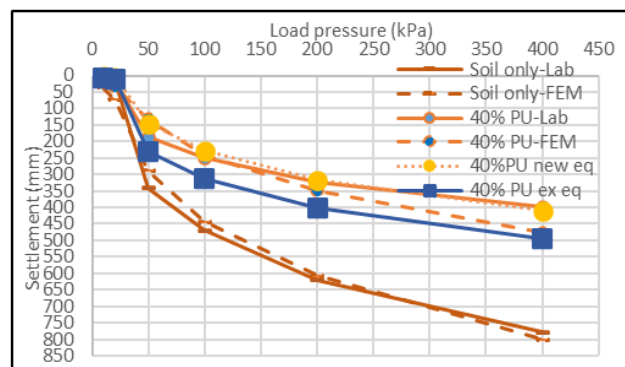
Fig. 11: Load pressure and settlement relationship for untreated and improved soil sample (40% PU foam to initial soft clay depth).
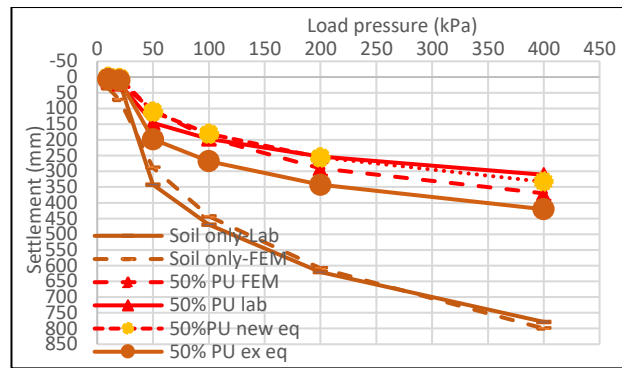
Fig. 12: Load pressure and settlement relationship for untreated and
improved soil sample (50% PU foam to initial soft clay depth).
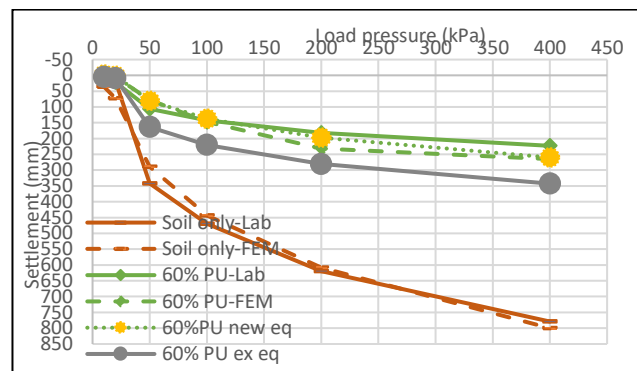
Fig. 13: Load pressure and settlement relationship for untreated and
improved soil sample (60% PU foam to initial soft clay depth).
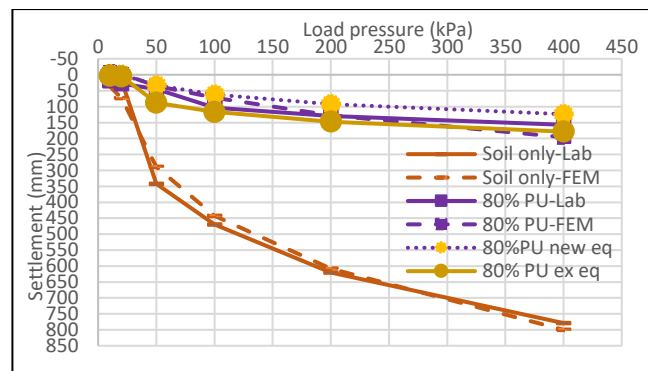
Fig. 14: Load pressure and settlement relationship for untreated and
improved soil sample (80% PU foam to initial soft clay depth).

All the samples of improved soil with PU foam indicate that the settlement value is overpredicted by the existing consolidation settlement equation. The existing equation does not take into consideration the buoyancy effect of the PU foam to the consolidation settlement of the ground. Therefore, an alternative equation of consolidation settlement integrated buoyancy should be applied for improved ground with PU foam to avoid overprediction of settlement value thus more conservative and might increase the construction cost. Figure 15 shows the combination of load pressure vs consolidation settlement for the soil improved with different thickness of PU foam ranging from 20% to 80% of PU foam to initial soft clay thickness as well as the untreated soil sample. The trend shows that the consolidation settlement reduces with the increase in PU foam

thickness. With the increase in PU foam thickness, the overburden pressure decreases as the lightweight PU foam has partially replaced the soft soil and the upward buoyant force increases as well, thus the settlement reduces.
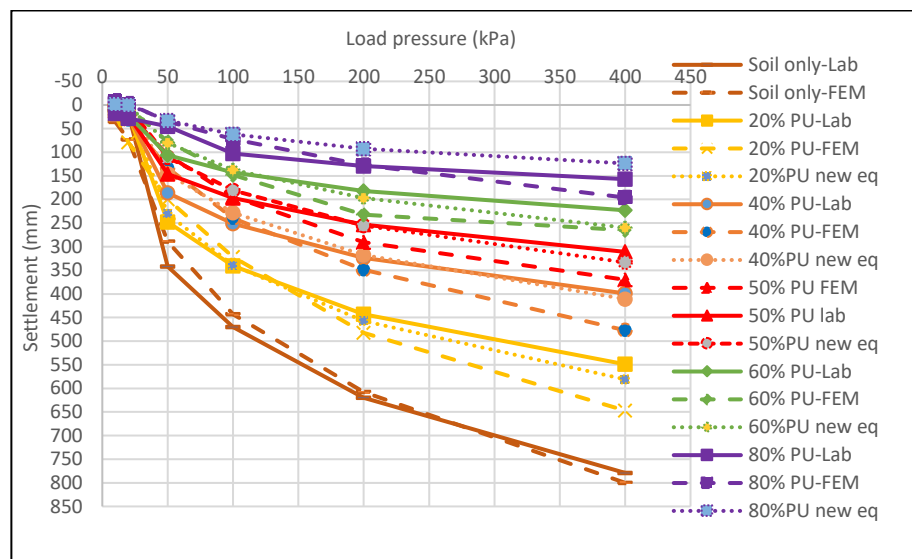
Fig. 15: Load pressure and settlement relationship for untreated and improved soil sample with different thickness of PU foam to initial soft clay depth.

4. CONCLUSION

The design of lightweight PU foam as a ground improvement method should take into account the effect of buoyancy in the consolidation process. This is due to the density of PU foam which is lower than water as well as the saturated soil which has the tendency of uplift due to buoyancy. Based on the results of Rowe Cell consolidation laboratory test as well as the finite element model, PLAXIS, the existing consolidation settlement equation was modified to integrate the buoyancy effect of the PU foam as a ground improvement. The buoyant force that is introduced by PU foam, Fb, equivalent to the weight of water displaced by PU foam is in line with Archimedes' principle and acts in the opposite direction of the overburden load pressure. The consolidation settlement value of the improved soil samples was overpredicted by the existing consolidation settlement equation as the buoyancy effect of the PU foam to the consolidation settlement of the ground was not accounted for. Therefore, an alternative equation of consolidation settlement integrated buoyancy might be applied for the ground improved with PU foam in order to avoid overprediction of consolidation settlement value; which is more conservative and increases the construction cost.

REFERENCES

[1] Ibrahim A, Huat BB, Asadi A, Nahazanan H. (2014) Foundation and embankment construction in peat: An overview. Electronic Journals of Geotechnical Engineering, 19: 10079-10094.

[2] Zhang J, Zhai JF, Wang XM. (2014) Instrumented full scale test and numerical analysis to investigate performance of bamboo pile-mattress system as soil reinforcement for coastal embankment on soft clay. Applied Mechanics and Materials, 501: 2132-2137.

[3] Low KS, Tioh NH, Ng SC. (2013) Lightweight concrete infill buoyant platform and the method thereof. World Inventor Award Festival, 2013

[4] Howard GT. (2012) Polyurethane biodegradation. Environmental Science and Engineering 2012. Springer-Verlag Berlin Heidelberg. https://doi.org/10.1007/978-3-642-23789-8_14

[5] Bayer O. (1947) Polyurethanes. Mod Plast, 24:149–152.

[6] Buzzi O, Fityus S, Sasaki Y, Sloan S. (2008).. Structure and properties of expanding polyurethane foam in the context of foundation remediation in expansive soil. Mechanics of Materials, 40: 1012-1021.

[7] Buzzi O, Fityus S, Sasaki Y, Sloan S. (2010) Use of expanding polyurethane resin to remediate expansive soil foundation. Canadian Geotechnical Journal, 47: 623-634.

[8] Badri K. (2012). Biobased polyurethane from palm kernel oil based polyol. License InTech 2012

[9] Ionescu M. (2005) Chemistry and technology of polyols for polyurethanes, Rapra Technology Limited, Shawbury, UK, ISBN 1859574912

[10] Polyurethane global market size forecast 2021. https://www.statista.com/statistics/ 720449/global-polyurethane-market-size-forecast/ accessed on 25 September 2019

[11] Zeltins V, Yakushin V, Cabulis U, Kirpluks M. (2017) Crude tall oil as raw material for rigid polyurethane foams with low water absorption. Solid State Phenom, 267: 17–22.

[12] Athawale VD, Nimbalkar RV. (2011) Polyurethane dispersions based on sardine fish oil, soybean oil, and their interesterification products. J. Dispers. Sci. Technol, 32: 1014–1022.

[13] Pawar MS, Kadam AS, Dawane BS, Yemul OS. (2016) Synthesis and characterization of rigid polyurethane foams from algae oil using biobased chain extenders. Polym. Bull, 73: 727–741.

[14] Figovsky OL. (2000) Hybrid non-isocyanate polyurethane network polymers and composites formed therefrom. U.S. Patent, 6:120,905.

[15] Guan J, Song Y, Lin Y, Yin X, Zuo M, Zhao Y, Tao X, Zheng Q. (2011) Progress in study of non-isocyanate polyurethane. Ind. Eng. Chem. Res, 50: 6517–6527.

[16] Li Z, Zhao Y, Yan S, Wang X, Kang M, Wang J, Xiang H. (2008) Catalytic synthesis of carbonated soybean oil. Catal. Lett, 123: 246–251.

[17] Tamami GWSS .(2004). Using tetrabutylammonium bromide catalyst. U.S. Patent 20040230009 A1.

[18] Rathod MA, Upadhyaya DS, Panchal SL. (2014) Preventation of hydrostatic uplift pressure underneath of basement floor slab in high water table area. International Journal of Futuristic Trends in Engineering and Technology, 1(03): 72-75.

[19] Heath TL. (1897) The worlds of Archimedes. Edited in Modern Notation with Introductory chapters, Cambridge University Press, 257

[20] Song LH, Liu Y, Mei GX, Zai JM. (2008) Experimental study on buoyancy effect on deep foundation in clay. Hydrogeology & Engineering Geology, 35(6): 80–84.

[21] Song L, Kang X, and Mei G. (2017) Buoyancy force on shallow foundations in clayey soil: an experimental investigation based on the Half Interval Search, Ocean Engineering, 129: 637–641.

[22] Ni P, Kang X, SongL, Mei G, Zhao Y. (2019) Model tests of buoyant force on underground structures. Journal of Testing and Evaluation, 47(2): 1216–1235.

[23] Frydelund TE, Aaboer R. (2002) Lightweight filling materials for road construction. EPS Geofoam 3rd International Conference 2002, Salt Lake City

[24] Stephen S. (2016) Pressure reduction on wide culverts with EPS geofoam backfill. Dissertations-ALL. 548. https://surface.syr.edu/etd/548

[25] Rowe PW, Barden L. (1966) A new consolidation cell. Géotechnique, 16(2): 162-170. https://doi.org/10.1680/geot.1966.16.2.162

[26] Head KH (1985). Manual of soil laboratory testing, 3: Effective stress tests pp.1129-1225

[27] Premchitt J, Ho KS, Evans NC. (1995) Conventional and CRS Rowe cell consolidation test on some Hong Kong clays.

[28] BS1377-Part 6:1990: Consolidation and permeability tests in hydraulic cells and with pore pressure measurement.

[29] Brinkgreve RBJ (2002). Plaxis 2D Version 8, Material Models Manual

[30] Saleh S, Ahmad K, Mohd Yunus N. (2020) Evaluating the toxicity of polyurethane during marine clay stabilisation. Environ Sci Pollut Res, 27: 21252–21259. https://doi.org/10.1007/s11356-020-08549-y

[31] Al-Atroush ME, Sebaey TA. (2021) Stabilization of expansive soil using hydrophobic polyurethane foam: A review. Transportation Geotechnics, 27:100494. https://doi.org/10.1016/j.trgeo.2020.100494

[32] Abdurahman MN, Kasbi Basri AZ, Kassim A (2021). Assessment of physical and mechanical properties of polyurethane as ground improvement material for peat. Neutron, 20(2): 149–156. https://doi.org/10.29138/neutron.v21i1.99

POTENTIAL VOLUMIZING EFFECT OF THE POST-MORPH LIME FILLER IN ATTENUATING CONCRETE CARBONATION

**MUHAMAD HASIF HUSSIN[1], MOHD HAZIMAN WAN IBRAHIM[1*],
NOR HAZURINA OTHMAN[2], MOHAMMED YAHYA MOHAMMED AL-FASIH[3],
AND MOHD FADZIL ARSHAD[4]**

[1]*Jamilus Research Center, Faculty of Civil Engineering and Built Environment,
Universiti Tun Hussein Onn Malaysia, Batu Pahat, Johor, Malaysia*
[2]*Departtment of Civil Engineering, Faculty of Civil Engineering and Built Environment,
Universiti Tun Hussein Onn Malaysia, Batu Pahat, Johor, Malaysia*
[3]*School of Civil Engineering, Faculty of Engineering, Universiti Teknologi Malaysia,
Skudai, Johor, Malaysia*
[4]*Faculty of Civil Engineering, Universiti Teknologi MARA (UiTM),
Shah Alam, Selangor, Malaysia*

*Corresponding author haziman@uthm.edu.my

ABSTRACT: A study on the crystallography of the lime that comes from mussel shell has been conducted to determine the packing density of the material. The experimental analysis encompasses of concrete samples preparation with lime replacement at 5%, 7.5% and 10% by cement weight. The samples were carbonised naturally over a period of six months and subjected to the phenolphthalein test at 60, 90, 120 and 180 days. It has been found that lime originating from the mussel shell is of both the aragonitic and calcitic crystal types. Both crystal polymorphs of aragonite and calcite are denser than the typical normal concrete by 27.8% and 18.3% respectively. This suggest a volumizing effect that is beneficial to reduce carbonation penetration into the capillarity of the concrete. Results from the carbonation test indicate that concrete containing mussel shell lime ash showed up to 51% lower carbonation coefficient and significantly lower intensity of capillarity as shown via FESEM.

ABSTRAK: Kajian mengenai kristalografi kapur yang didapati daripada kulit kupang telah dijalankan bagi menentukan kepadatan bahan tersebut. Analisis eksperimen merangkumi penyediaan sampel-sampel konkrit yang mengandungi gantian kapur pada 5%, 7.5% dan 10% daripada berat simen. Sampel-sampel telah dikarbonatkan secara alami selama enam bulan dan menjalani ujian fenolftalin pada usia 60, 90, 120 dan 180 hari. Kajian telah mendapati bahawa kulit kupang terdiri daripada kapur-kapur berjenis aragonit dan kalsit. Kedua-dua polimorf kapur aragonit dan kalsit adalah 27.8% dan 18.3% lebih tumpat berbanding konkrit biasa. Hal ini berpotensi menjadi bahan penumpat yang bagus untuk mengurangkan serapan pengkarbonatan ke dalam kapilari konkrit. Keputusan ujian pengkarbonatan menunjukkan konkrit yang mengandungi abu kapur kulit kupang mempunyai pekali pengkarbonatan sehingga 51% lebih rendah dan mempunyai kerendahan kapilariti yang signifikan seperti yang ditunjukkan melalui FESEM.

KEYWORDS: *mussel shell ash; natural carbonation; calcium carbonate crystal*

1. INTRODUCTION

Concrete carbonation leads to the precipitation of lime (calcium carbonate) in the pores and this can either be advantageous or problematic, depending on the involved situation. In practice, some civil engineering structures such as mass concrete and girders take advantage of the carbonation process through the densifying property of the lime which can reduce the porosity of concrete. Several researchers such as Sideris [1], Phung et al. [2] and Rezvani [3] have indicated the pro-filler attribute of using lime in concretes.

Carbonation is notoriously known to cause serviceability issue in reinforced concretes. When the embedded steel reinforcement corrodes due to carbonation of concrete, the steel expanded in volume which causes the concrete cover to spall. This can expose the embedded steel and deeper part of the concrete to various other chemical and physical attacks apart from the costly repair. According to Ekolu [4], global corrosion related damage cost is at about 3-4% of the global gross domestic product (GDP). These 3-4% out of the GDP figure is accumulative of various industries and not limited to construction alone. However, Shibata [5] highlighted that buildings and infrastructures sectors had contributed a staggering 38% out of the global 3-4% figure which summed up to one trillion US dollars.

Many research and methods were imposed to counter concrete carbonation ever since and this include but not limited to increasing concrete cover (most common) in the range of 25-30 mm as suggested by Benitez [6] and Nakai [7], using well known substances such as fly ash [8-21], slag [12,13,20,22-24], lime [1,8-10,16,20,25-35] and even using commercial rust inhibitor [36,37]. It has been found that by using cover depth of 25-30 mm, the concrete service life increased significantly. However, there are also several case studies that have been conducted [38,39] which indicated that over-reliance on concrete cover thickness will not suffice. Possan [38] study indicated that the mean carbonation depth of the thirty-five years old concrete structure is 33.0 ± 6.6 mm. Whereas, Oliveira and Nogueira [39] study indicated mean carbonation depths for the thirty-one years old concrete structure varied from 54.01-104.83 mm. These are already beyond the limit of the suggested thickness in the previous studies. Since the typical and minimum design life of common concrete structures is fifty-years old and can go a maximum of one-hundred years if it is civil engineering structures such as in [38] and [39], the covers indeed underperformed in both cases. Thicker concrete cover requires more material, more space allocations and needless to say, bigger budget. None of these are ideal when it comes to modern projects with complex structural twist in the design that may limit available space for extra cover thickness and the typical demand for "minimum cost, maximum output".

Fly ash is a very common material used in the industry to carter for special needs in terms of engineering aspect. Unfortunately, carbonation studies incorporating fly ash [8, 11,12-14,18-21] at various percentages indicated a trend that is prone to anti-filler effect when it comes to concrete carbonation. About only twenty-two percent of the studies indicated increased in carbonation resistance [10,12,15,16], sixty-seven percent indicated decreased in carbonation resistance [8,11,12-14,18-21] and eleven percent indicated as unresponsive variable [9,17]. The issue with fly ash is that it increases the concrete porosity and this is verified through the extended x-ray (XRAM) and Mercury Intrusion Porosimetry (MIP) methods as discussed in [18]. Concrete containing slags showed no better improvement in terms of carbonation resistance either. A study [12] reported that the carbonation resistance of slag concrete is even lower than the fly ash concrete. Another study [23] indicated that significant impairment towards carbonation resistance can already be observed at replacement percentage as low as 10%.

Research on concrete containing lime however, showed a more promising outcome with more results that are supportive towards the improvement of carbonation resistance emerged [1,25,27,28,31,33,35]. Even so, just as fly ash, there seems little direct correlations between the amounts of replacement with the pro- or anti-filler effect. This is true since some studies [1,25,31] indicated that high replacements (50% and more) are required to achieve the filling effect, while others [27,28,35] indicated the otherwise. Even in the studies that showed anti-filler effect [8,10,16,20,26,29,30,32,34], the replacement percentage has little to do with the outcome. This has led this study to believe that given a proper treatment, lime has a potential to be used as filler even at lower dosage. The aforementioned studies utilized the lime in its final form which is calcium carbonate. Calcium carbonate is inert filler and possess little to no hydration property such as the cement. Hence, the potential filling effect is limited by the position at which these inert filler particles reside within the concrete. If more of it happened to reside within the capillary chambers, than filler affect may be observed. Conversely, if more of these inert particles reside within the gel itself or stuck in the aggregate pores, than the filling effect would have been wasted. Hence, the occurrence of the Dispersion Paradox phenomenon described in [27].

It is the continuous hydration of the cement that makes the concrete increase in strength overtime due to the gel growth and densification that will ultimately filling the void within the binder matrix. This gel growth phenomenon inspired this study to emulate it in other form and this is where this study differs in the method of lime utilization and is explained later in this section. Rust inhibitors that depend on cathodic/anodic/cathodic-anodic reactions can protect the steel bar from corrosion but not without sacrifice on cost and additional subject matter expert employment. This is because there are many types of corrosion inhibitors that can be browsed through the market such as organic, inorganic, combination of organic-inorganic, water-based and coating which all have their respective purposes and correct methods of applications. On top of that, research on corrosion inhibitors generally focus on eliminating chloride elements and hydrochloric acid [37]. As to whether or not the inhibition mechanisms work similarly in carbonation rich environment is unknown. The use of rust inhibitor focusses on projects with special requirements such as underground and offshore structures exposed to aggressive chloride environment [37] and certainly not for all-purpose use for just any projects. This is shown in a series of test conducted by [36] which indicated that at given circumstances, calcium nitrate based inhibitors failed to perform its task but alkanolamine based inhibitor did success. Hence, rust inhibitor may not be an option for many projects.

In light of the highlighted issues along with other out of scope factors, sustainability has become the spotlight for contingency plans throughout the world. In Malaysia, Ministry of Energy, Green Technology and Water, has outlined the 2017 national Green-Technology Policy [40] that encourages people to consume more on the renewable natural resources as an alternative to the non-renewable natural resources apart from emphasizing construction and building sustainability. This is where the wasted mussel shells fit in the research design of this study.

The chemistry of concrete carbonation relies on the diffusion of carbon dioxide gas into the hardened binder. To inhibit corrosion due to carbonation, method to isolate the chemical interaction has to be devised and this can be achieved by applying the pro-filler principle of the lime in the aforementioned studies. In this study, a counter-intuitive approach designed to use the carbonation itself to inhibit the carbonation process is proposed. This design is called as the self-suffocation method in which the lime in its designed intermediate form shall hinder the carbon dioxide flux as the carbonation process proceeds.

Lime has a much higher mass unit than the quicklime or slaked lime. In atomic scale, higher mass unit is normally associated with higher atomic radii. This study postulates that the resulting higher atomic radii imposes a volumizing effect. Since the carbon dioxide flux proceeds via the capillarity matrix, there is a maximum 80% probability that this volumizing effect happens within [41]. This research named the material of interest as the Post-morph Lime Filler (PLF). The idea behind the naming of "Post-morph" comes from the expected behavior of the quicklime and slaked lime upon carbonation. The lime crystals will only morphed once the concrete is exposed to carbonation. Contrary to many other researchers that incorporate the lime during concrete mixing, this research incorporates the quicklime instead. The term "Post-morph" indicates that the actual lime will only be autogenously deposited after the exposure. The amount of deposition strictly dependent of the degree of carbonation. By designing the mechanism of interaction in this way, the natural carbonation process is fully taken advantage of.

2. MATERIAL PREPARATION AND METHODS

The mussel shell sample were obtained from the Danga River. The shells were washed using tap water and manually soaked with a brush to remove stubborn impurities. The cleaned shells were then air dried for a few days before being oven dried at 105°C for 24 hours to remove pore humidity. The shells were then isothermally heated at 1000°C for 1 hour to remove carbon dioxide from the calcium carbonate. The calcined shells were left to cool for several hours to the room temperature before being subjected to milling process for 1 hour. The milled calcined shell was sifted to pass the 63 µm aperture and the samples were then considered ready for experimentations. However, some experimentations did used some samples that were not calcined.

Mix design was prepared using the Department of Environment method (DOE) [42] with a target 28th day mean strength of 35MPa (standard deviation, s of 3.05). Concretes were made from Tasek (Malaysia) brand CEM1 OPC (grade 42.5), crushed granites with 20 mm maximum size, crushed quarry sand (33.3% passing the 600 µm mesh) and tap water. Mixing was done using a rotary mixer with feeding sequence of water, cement+PLF mixture, sand and finally granites. Mixing time followed recommendation from [43]. Table 1 shows the mix design for the control and the PLF concretes.

Table 1: Concrete mix design

Cube size	100 x 100 x 100 mm		
Characteristic strength	30 MPa		
Target mean strength (28th day)	35 MPa		
Margin	Within 1.64s		
	s = 3.05 MPa		
w/c	0.6		
Replacement groups	Control	PLF5	PLF7.5	PLF10
Cement (kg/m³)	360	342	333	324
PLF (kg/m³)	0	18	27	36
Water (kg/m³)	216		
Sand (kg/m³)	967		
Granite (kg/m³)	857		
Conditioning	Plastic sheathing for 6 and 27 days at room temperature and humidity.		

2.1 Methods

The beginning part of the study focused more on the fundamental and metallurgic analyses which includes particle dispersion, mineralogy and crystallography. Then the focusing shifted to the study of the effect of aforementioned fundamentals in civil engineering aspect which includes carbonation and microstructure analysis.

2.1.1 Particle Dispersion

Two groups of materials were given focus for particle size distribution analysis and they were the OPC and the PLF itself. The test was conducted using CILAS1180 laser diffraction machine at room temperature of 25 ºC and a mean relative humidity of 65±3%. Distilled water was used as dispersing agent and 5-10 grams of samples were prepared for each group.

2.1.2 Chemical and Mineralogical Analyses

Three materials were tested for either their chemical or mineralogical or both compositions. They are the OPC, un-calcined mussel shell, and calcined mussel shell (including PLF). All the tested samples were in powdered form and sieved to pass the 63 μm aperture. XRD analysis was carried out using the Bruker D8 diffractometer, scanned between 10º – 90º Bragg angle with step of 0.02º and X-ray wavelength (λ) of 1.5406 angstrom (Å). The chemical and minerals were determined using the Evaluation (EVA) software and some match analyses were doubly verified using Crystallographic Open Database (COD).

The XY coordinates of the obtained diffractograms were used to perform computerized Gaussian fitting. This is a specialize technique applied to only the un-calcined mussel shell diffractogram in this study to perform the crystallite size measurement. Gaussian fitting was conducted to execute measurements of the Full Width at Half Maximum (FWHM) of the selected peaks with the most pronounced intensity. The components of the FWHM were obtained from Snyder and Jenkins [44]. The obtained components of the FWHM are transferred into a spreadsheet software to perform the necessary crystallite size measurement using the Scherer's equation shown in the Eq. (1) below where d is the diameter of the crystallite measured in Angstrom (Å), K is the correction factor which is typically taken as 1 for spherical shape assumption, λ is the wavelength of the x-ray measured in Angstrom (Å), B is the FWHM converted in radians and $\cos(\varTheta_B)$ is the cosine of the angle of B measured also in radians.

$$d = \frac{K\,\lambda}{B\,\cos(\theta_B)} \tag{1}$$

The crystallite sizes were used to give a rough estimation of the crystal packing efficiency by comparing the median particle size (D_{50}) obtained via the particle size distribution (PSD) analysis, and the amount of crystallite needed to match the longest span (median diameter) of the particle. This was done using Eq. (2).

$$Amount\ of\ crystallite = \frac{D_{50}}{d_m} \tag{2}$$

Further justifications were made by using 2-dimensional draws of the involved crystal systems in the un-calcined mussel shell. Modelling of any crystal structure was made using the Visualization for Electronic and Structural Analysis (VESTA) software version 3.4.7.

2.1.3 Carbonation

Method for testing concrete carbonation was adapted from three standards which are the BS EN 14630 (Determination of carbonation depth in hardened concrete by the phenolphthalein method) [45], the BS EN 13295 (Determination of resistance to carbonation) [46] and the BS EN 12390 – 10 (Determination of the carbonation resistance at atmospheric levels of carbon dioxide) [47]. The exposure was conducted for 6 months at intervals of 60, 90, 120 and 180 days.

Four groups of concrete were assigned and they were the control group, and concretes containing 5% (PLF5), 7.5% (PLF7.5) and 10% (PLF10) replacements. This test was performed in a natural environment (exposed to ambient air but sheltered from rain). The exposure to the environmental carbon dioxide (CO_2) at 0.0552% (552 ppm) begun after the 27th day of curing in the plastic wrap.

Three environmental parameters were recorded on daily basis which are the concentration of the carbon dioxide gas, relative humidity and ambient temperature. In the three aforementioned standards for the carbonation testing, the carbon dioxide gas concentration is to be recorded three times a day, whereas the ambient relative humidity value has to be recorded at least once a day for as long as the carbonating testing proceeds.

The carbonation depth of each and every carbonated face were taken in the form of mean average. The test was carried out by pressing the concrete cube in between two metal bars using a hydraulic compression machines and carbonation depth was measured using a digital Vernier caliper. The depth of the natural carbonation follows the square root of time function as stated by [47] and was used in this study to obtain the carbonation coefficient. The square root of time function is shown in Eq. (3) where D: depth of carbonation in millimeter, k: carbonation coefficient in (mm/√year), and t is time in years.

$$D = \frac{k}{\sqrt{t}} \tag{3}$$

2.1.4 FESEM and EDX

The analyses were performed using the Jeol JSM 7600F. All samples were coated with Aurum (Au)/gold to enhance conductivity. The 2-dimensional SEM image of the interest topography was subjected to a specialized contouring technique that caused it to become 3-dimensional. This is done to give the actual in-depth view of the topography through a more sophisticated approach. Any other 3-dimensional objects such as the representation of particle grains were also made possible through graphical enhancement. The capillarity network of the concretes were compared to observe the volumizing effect of the PLF at high level magnifications. Elemental mapping was also made possible through the complementary EDX.

3. RESULTS AND DISCUSSION

This subtopic contains the outcomes of the conducted analyses. Note that the diffractogram from mineralogical analyses of the tested materials are compiled in a single diffractogram for easier comparison.

3.1 Particle Dispersion

Laser diffraction indicated that the prepared mussel shell ash particle dispersion resembles to that of the OPC's (Fig. 1). The median particle diameter (D_{50}) of the PLF is 19.69 μm which is approximately 23% larger than the OPC's. The typical median average

(D_{50}) size of the OPC can be as low as 10-15 µm [48] and may go as high as 10-20 µm [49]. The tested OPC and PLF average sizes are tally with the statements in [48] and [49]. However, it is important to also note that in order to achieve a good PLF particle dispersion amongst the OPC's, median size (D_{50}) may not be as important as concentration. Ideally, the incorporation of PLF into the cement through replacement, will naturally increases and decreases certain range of available particle sizes. Since it is impossible to know which exact particle size were omitted and which were included, it has become an uncertainty. Hence, analysis should focus more on the entire sets of size through the dispersion curve rather than a single number like the D_{50}.

The tested particle dispersion of cement containing 5%, 7.5% and 10% PLF exhibited overlapping curves with each other within the upper limit (OPC) and lower limit (PLF) curves. Hence, they are not included due to repetition of considerably identical patterns but suffice to say that the incorporation of the PLF into the cement at 10% maximum did not alter the original OPC particle dispersion significantly. This suggest that within 10% dosage, the PLF particle can be in homogeny (disperse properly) with the OPC particle. Hence, maximizing the filler effect across the binder region of the concrete.
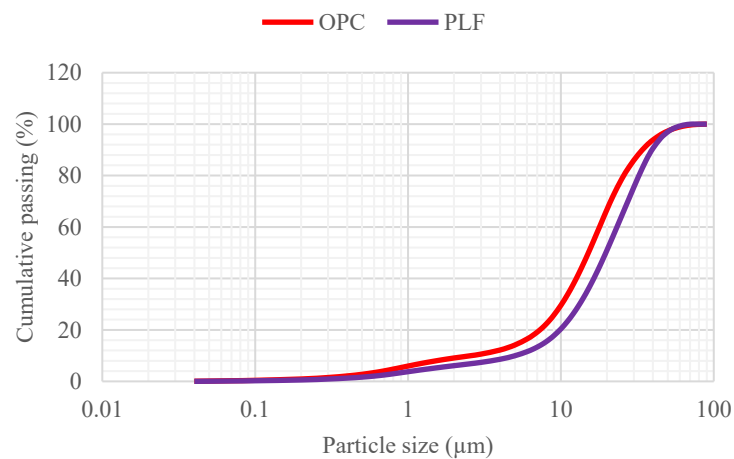
Fig. 1: Particle distribution curve of OPC and PLF.

3.2 Ordinary Portland Cement Mineralogy

Estimations that have been made through the matching of these signatures in EVA and COD give out the percentage of Bogue compositions as 59% for tricalcium silicate, 25.9% for dicalcium silicate, 1.6% tricalcium aluminate, 9.7% calcium aluminoferrite and 3.8% gypsum. The estimated amount of tri- and di- calcium silicates and calcium aluminoferrite are in a good agreement with the values reported by Santhakumar [50] which stated that the amount of the tricalcium silicate in OPC should varies in the range of 30-50%. Whereas, dicalcium silicate varies in the range of 20-45%. Calcium aluminoferrite should varies in the range of 6-10%. However, the calcium aluminate content in the tested OPC was found to be below average with the typically reported range of 8-12%. The gypsum amount is within the tolerated zone of 2-4%.

3.3 Mussel Shell (un-calcined form) Mineralogy

Diffraction pattern (*refer Fig. 8 at later page*) of the un-calcined mussel shell powder indicates that it contains largely calcium carbonate with orthorhombic crystal system. Orthorhombic profile in calcium carbonate compound is characteristic to aragonite polymorph which is highly anticipated in the shell of carbonate secreting organisms such as

the mollusk [51]. There are some traces of rhombohedral system which is characteristic to calcium carbonate of the calcite polymorph. According to Boggs [51], calcite is the most stable form of calcium carbonate which may take some amount of time to transform from the original aragonite arrangement.

The diffractogram peaks (Fig. 8) indicate that the tested sample are highly crystalline in regards to the very slim full-width at half maximum (FWHM) intensity [52]. Slim FWHM is also an indication of large crystallites [52]. Even with very slim FWHM, it is still considered a polymeric (crystal-amorphous) system nonetheless since perfect crystal would be impossible to obtain from the nature, but with a stressed minimum degree of amorphousness. As such, crystallite size measurement through the Scherer equation is made possible and shown in Table 2 whereas Fig. 2 shows the schematic diagram of the crystallites in a single particle grain of the micron size (drawn not to scale). Based on Fig. 2(a), one particle grain of mussel shell powder has a median diameter (D_{50}) of 19.69 μm as determined through the Cilas 1180 Particle Size Analyzer (PSA). A single particle grain contains hundreds if not, thousands of crystallites that are nano in size as shown in Fig. 2(b). This study believes that the amount of these nano crystallites present in a known grain diameter, can be taken advantage of for an indirect and qualitative density measurement.

(a) 1 mussel shell particle grain D_{50} = 19.69 μm

(b) Magnified to nano scale

1 unit crystallite = 10th nm
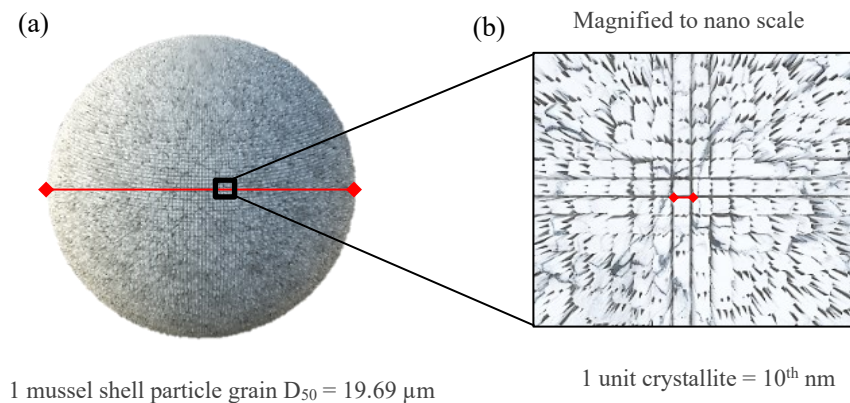
Fig. 2: Schematic diagram (a) particle grain (b) crystallites.

Based on Table 2, the mean sizes of the aragonitic and calcitic crystallites are 44.56 nm and 37.54 nm respectively. Some minor amount of peaks cannot be analyzed due to poor Gaussian fitting and skipped. Nevertheless, the data indicated that the present aragonitic crystallite in the tested sample is 18.7% smaller than the calcitic crystallite. By using this information, and considering two mussel shell particle grains, one is composed of pure aragonite, while the other is composed of pure calcite, a qualitative estimation of the crystal packing efficiency can be made. Using equation (2), the amount of crystallite that exist along the longest path of the particle can be predicted. Figure 3 shows the calculation of the diameter and crystallite packing.

Based on Fig. 3(a), if one mussel shell particle of 19.69 μm in diameter is made up of entirely aragonite crystal, there would be approximately 525 unit of aragonitic crystallite along the red line shown in Fig. 3(a). Likewise, if the same particle is made up of entirely calcite crystal instead, there would be approximately 442 unit of calcitic crystallite along the red line shown in Fig. 3(b). This indicates that for a fixed 2-dimension, aragonitic crystallite can be packed much more than the calcitic crystallite. In simple words, aragonite crystal can be denser than the calcite crystal. This is tally with the reported density values

of both crystals which happened to be at 2.94 g/cm^3 for aragonite [53] and 2.72 g/cm^3 for calcite [52].

Table 2: Components of the Scherer equation for crystallite size measurement of the mussel shell sample

Peak	Poly-morph	FWHM	2-Theta	Theta	FWHM(rad)	Theta (rad)	d (Å)	d (nm)	d (µm)
1	Ara	0.14886	26.21726	13.10863	0.002598097	0.22878875	547.9539	54.7954	0.0548
2	Ara	0.15146	27.23282	13.61641	0.002643476	0.23765119	539.6825	53.9683	0.0540
3	Cal	0.13587	31.10151	15.55076	0.002371379	0.27141188	606.9149	60.6915	0.0607
4	Ara	0.16921	33.11591	16.55796	0.002953272	0.28899083	489.8041	48.9804	0.0490
5	Ara	0.21286	36.09764	18.04882	0.003715108	0.31501134	392.532	39.2532	0.0393
6	Cal	0.19361	37.87276	18.93638	0.003379132	0.33050218	433.8019	43.3802	0.0434
7	Ara	0.31042	38.56152	19.28076	0.005417851	0.33651274	271.1277	27.1128	0.0271
10	Cal	0.19877	42.91974	21.45987	0.003469191	0.37454539	429.4441	42.9444	0.0429
11	Ara	0.2348	45.86098	22.93049	0.004098033	0.40021255	367.3733	36.7373	0.0367
12	Cal	0.27871	48.39646	24.19823	0.004864407	0.42233879	312.496	31.2496	0.0312
13	Ara	0.25499	50.23365	25.11683	0.004450415	0.43837129	344.0885	34.4089	0.0344
14	Ara	0.25583	52.42184	26.21092	0.004465076	0.45746685	346.1201	34.6120	0.0346
15	Ara	0.27972	52.9827	26.49135	0.004882035	0.46236128	317.3275	31.7327	0.0317
16	Ara	0.32815	66.02007	33.01004	0.005727298	0.5761338	288.6959	28.8696	0.0289
17	Ara	0.42884	69.00089	34.50045	0.00748467	0.60214636	224.7855	22.4786	0.0225
Mean calcite crystallite size (d$_m$)								44.56	0.04456
Mean aragonite crystallite size (d$_m$)								37.54	0.03754
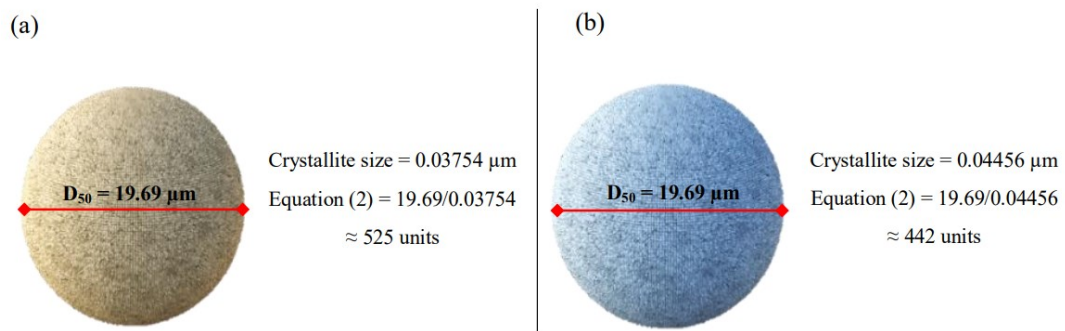
Fig. 3: Mussel shell crystallites unit measurements (a) only an aragonite particle composition, (b) only a calcite particle composition.

Comparing the density of these crystals with the density of a hardened normal concrete which typically stood at 2.3 g/cm^3 (converted from 2300 kg/m^3), it can be said that the packing of both crystals is higher than the concrete (27.8% and 18.3% higher respectively). This finding suggests that both type of these calcium carbonate polymorphs (aragonite and calcite) potentially possess densifying attribute when used in concrete.

In the view of this study, in regards to the packing efficiency of the said crystal systems, the densely packed aragonitic crystallite is due to the basis arrangement itself which revealed to be orthorhombic system through the XRD analysis. According to Wahab [54], orthorhombic system has a higher degree of freedom along the lattice axes such that a ≠ b ≠

c. Considering crystal habit phenomenon during the formation of the aragonite itself, the crystallite can arrange themselves in every axes with multiple combinations of number a, b and c while maintaining the orthorhombic profile since a, b and c do not strictly need to be the same. Hence, the crystal can easily pack themselves. Contrary to the rhombohedral (hexagonal) arrangement of the calcite in which $a = b \neq c$. Two axes have to have equal dimension which result to a limited (rigid) possible crystal arrangement during the formation of the calcite. This is shown in the software-generated and -modified crystals of aragonite and calcite based on the models of Antao and Hassan [55] and Graf [56] respectively. The crystals with polyhedral views are plotted over their own respective 3x2 lattices in Fig. 4. Within the same lattice size, it can be seen that the arrangement of the calcite (Fig. 4(b)) is more geometric and rigidly spaced compared to the aragonite structure (Fig. 4(a)). On the contrary, the packing of aragonite crystals can be seen denser than the calcite crystals. This further validates previous discussions by this study.

(a) Tight arrangement	(b) Less-tight arrangement
Aragonite (orthorhombic)	Calcite (rhombohedral)
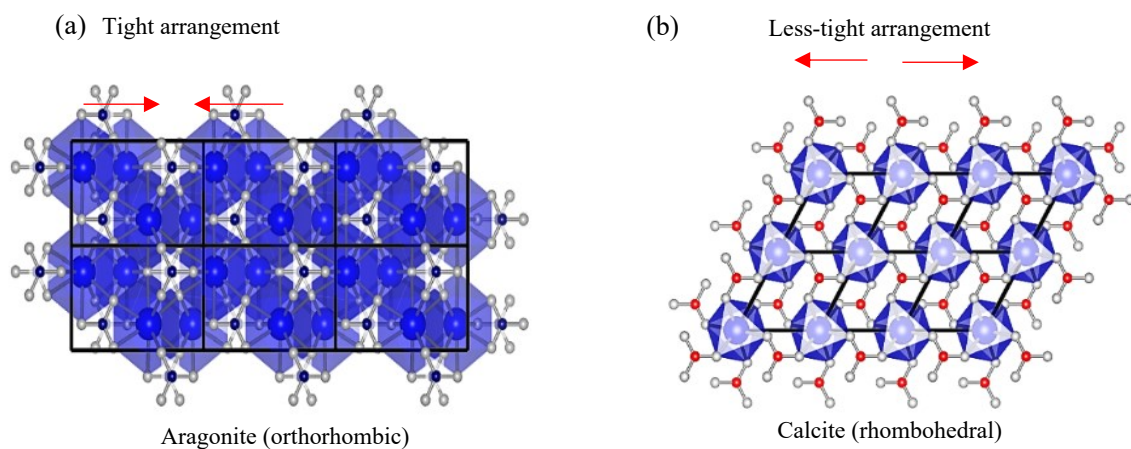
Fig. 4: Crystal structural arrangements (a) aragonite and (b) calcite.

According to Moore [57] and Haldar [58], calcite polymorph arrangement is thermodynamically stable at atmospheric level of pressure and temperature compared to aragonite. This means that it stays on being calcitic as long as not being subjected to geological event that leads to immense pressurization, water movement and temperature rise. It is due to this stability as well that cause calcite to become practically insoluble in water compared to aragonite. In the view of this study, by taking advantage of this calcite attribute, combined with proper adjustment to the degree of densification through dosage control, outward migration of the lime from concrete capillarity due to fluid movement can be hindered. Fluid movement, especially rain penetration can potentially migrate or wash off filler material at surface level. Thus, reducing its efficacy. This however, requires further studies and development.

Figure 5 shows the image of the shell magnified through the electron microscope at x5.0k zoom. The 2-dimensional image (Fig. 5(a)) has been processed into 3-dimensional figure (Fig. 5(b)) using a specialized technique to have a real and in-depth view of the topographic profile of the un-calcined shell. Local chemical constituents that are present have also been determined through the complementary energy-dispersive equipment. Based on Fig. 5(a), the topographic profile of the un-calcined mussel shell is revealed to be plates of flaky shape. The plates are more pronounced in the rendered 3-dimensional image (Fig. 5(b)). The plates are multi-layered which suggest the multi-stages of shell development throughout the life-span of the mussel. The platy profile is tally with the previous discussion

that indicates the presence of orthorhombic crystal system that is characteristic to the aragonite polymorph of the calcium carbonate.

(a)   2-dimensional topography   (b)   3-dimensional topography
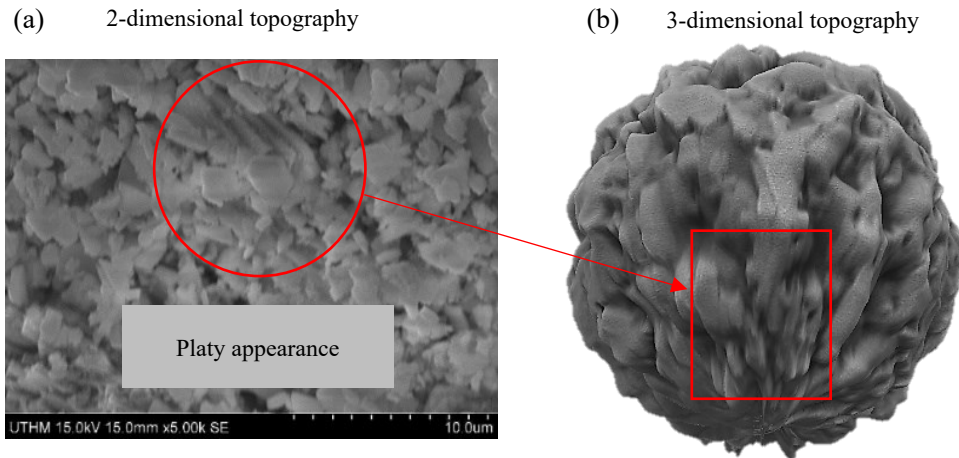
Fig. 5: Topographic profiles of the un-calcined mussel shell (a) 2-dimensional topography (b) 3-dimensional topography.

The platy profile of the un-calcined shell can also be observed in the findings from the previous studies [51,54,59,60]. The redundant proves in several studies signal the agreement of the presence of orthorhombic crystal system mentioned in this article that is characteristic to the aragonite polymorph of the calcium carbonate [61]. Orthorhombic system is basically an overextended version of a cubic system over two sides which resulted to a rectangular shape and if sufficiently thin, may assume platy appearance. Despite the known petrological knowledge that the existence of aragonite polymorph in normal environment is rare [57], these studies indicated that it is indeed possible via bio-mineralization process by these carbonate secreting organisms such as mussels and oysters. Whatever differences in the outcome of research that focus on the utilization of the un-calcined versus calcined shell husk in concrete may owed to this crystallographic variety. Hence, the significance of this piece of information. Since studies on concrete filler through crystallography point of view is largely insufficient, this particular finding may spark more attention.

3.4 Mussel Shell (Calcined Form) Mineralogy

Diffraction pattern of the calcined mussel shell sample indicated 90.61% match as calcium oxide profile and 76.1% match as calcium hydroxide profile as determined from the Crystallography Open Database (COD). Analysis has estimated the proportions of the compound as 93.6% CaO and 6.4% $Ca(OH)_2$. This study suspect that the minuscule presence of the calcium hydroxide is due to the hydration of the calcined mussel shell ash when it is exposed to the environmental humidity during the experimentation. No traces of calcium carbonate can be seen and this signify the effectiveness of the calcining method practiced in this study.

In regards to the exposure time during the experimentation, logically the calcium oxide should react with the environmental carbon dioxide to produce calcium carbonate as mentioned by Santhakumar [50]. Still, no traces of calcium carbonate due to this phenomenon has been detected either. This finding suggest that the rate of hydration is faster than the rate of carbonation. It has been further theorized by this study that the level of carbon dioxide concentration (0.0552%) versus the level of relative humidity concentration (>60%) may have a direct influence in the speed of reaction between the two.

The calcined mussel shell which is technically calcium oxide, is the first intermediate product formed during the high temperature treatment. This is followed by the second intermediate product which is the calcium hydroxide formed during the concrete mixing activity when the intermixed cement-calcined mussel shell ash reacts with the added water. This is verified through the live-image during hydration that was captured using a digital camera that was attached to an optical microscope which showed the characteristic hexagonal morphology of the calcium hydroxide (Fig. 6(a) and (b)). This is also observed under SEM microscopy (Fig. 7) and has been also crossed verified with other study [62].
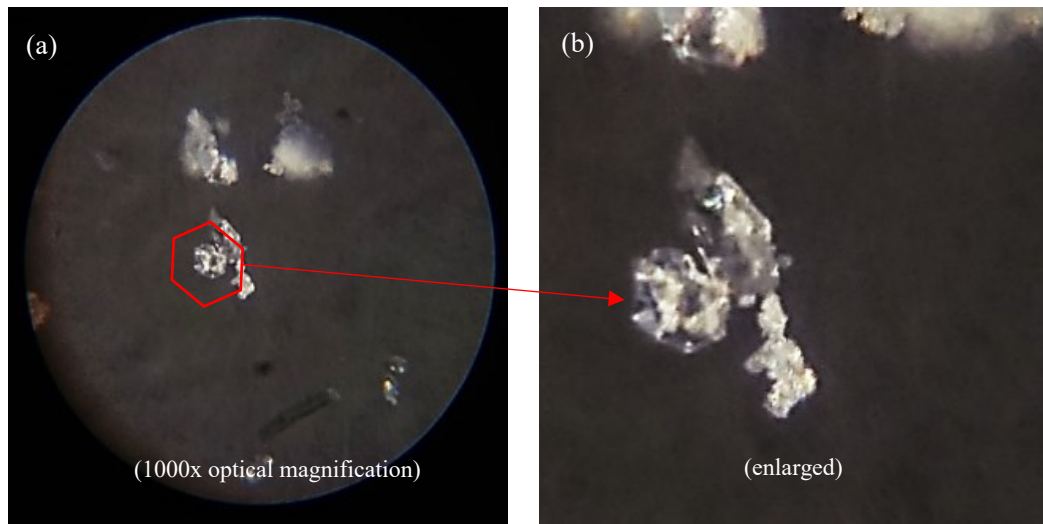
Fig. 6: Micrograph of the calcium hydroxide crystal exposed to visible spectrum wavelength (a) at 1000x (b) enlarged (zoom-in).
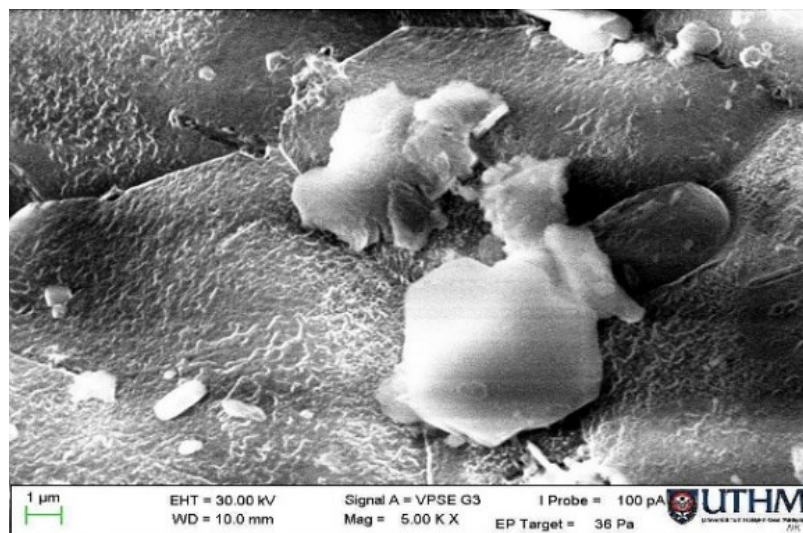
Fig. 7: SEM image of calcium hydroxide crystal exposed to X-ray spectrum wavelength.

Figure 8 summarized the diffractograms of the mussel shell at different stages. Based on Fig. 8, the last stage (Post-morphing) was tested at 180 days and it was found that a large portion of the calcium hydrate (CH) remained un-carbonated. There are two hypothetical statements that may be associated with this phenomenon. First, based on the evidence from the microstructure analysis, calcium carbonate appears to engulf the surrounding area where it has grown. This may create a layer of canopy or a blanket that shielded the underneath

and deeper CH from reacting with the carbon dioxide gas at surface level. More evidence linking to the blanket appearance of lime is portrayed in several other literatures [63,64]. Second, the degree of carbonation may simply has not reach a substantial level to convert a major amount of CH. It is also interesting to note that lime that was originally of the aragonitic system turned out to be calcitic after calcination and re-carbonation for 180 days. This is tally with the statement by Boggs [51]. However, this study is yet to fully understand the cause of this event but suffice to say, that the polymorph of these two crystals may change under certain circumstances even though they were once come from the same material. Hence, the importance of conducting more future studies on this particular subject.
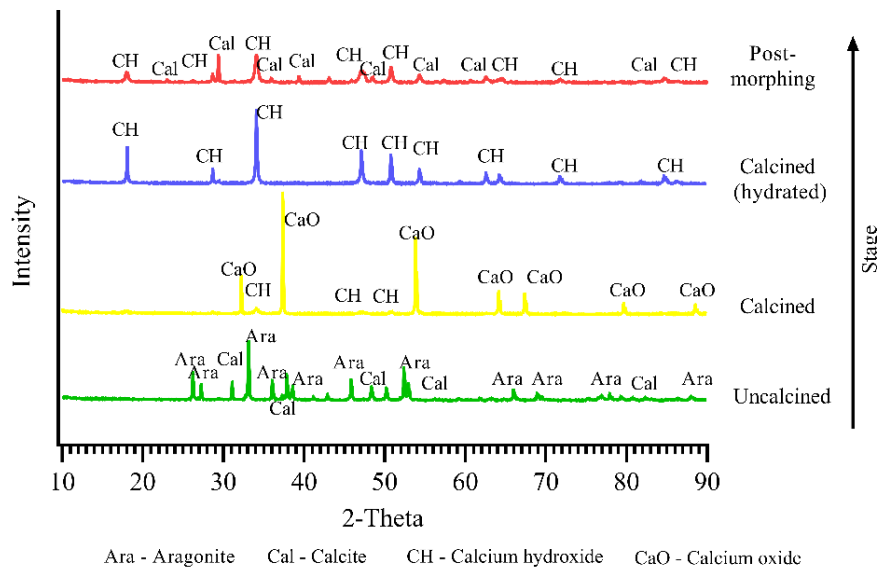
Fig. 8: Summary of mussel shell chemical and mineralogical analyses at different stages.

3.5 Carbonation

The obtained (actual) data are paired against theoretical (calculated) data using the model described in [65]. They are found to correlate positively and are in high agreement (R^2 approaching 0.9 and above). However, replacement percentage of PLF is inversely proportional to the correlation agreement value. This outcome suggests that, at a sufficiently high amount of replacement, the commonly used carbonation estimation model may no longer be valid. As for the scope of this study, it can be seen that 10% replacement exhibit a signal of downtrend in the R^2 where the value is marginally reaching 0.9 (Fig. 9(d)). This signify the limit of replacement where the model described in Neville [65] may stay true. It was found that the average carbonation depths of concrete containing the PLF are lower than the control concrete. Although, control concrete group in itself performed well below the typical carbonation coefficient range of 3-4 mm/√year. The carbonation coefficient of the control concrete is at 2.92 mm/√year and this indicates a performance of better than average. The presence of the PLF improved the performance even more with a descending carbonation coefficient pattern across all experimental concrete samples. The carbonation coefficients of the PLF5, PLF7.5 and PLF10 are 1.83, 1.79 and 1.43 mm/√year respectively. Based on the coefficients, PLF10 concrete indicated the highest improvement which is up to a maximum of 51% lower carbonation coefficient compared to the control concrete. Figure 9 shows the correlational measurements of the actual and calculated data.
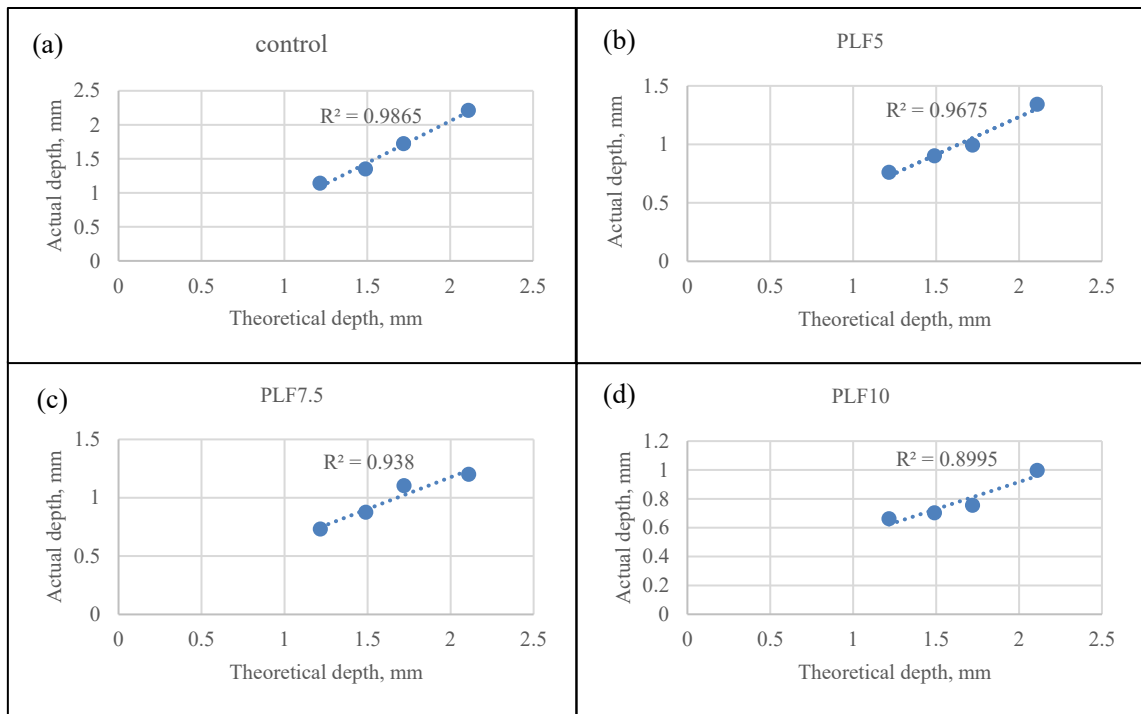
Fig. 9: Correlative measurement of the actual and theoretical data
(a) control sample (b) at 5% of PLF (c) at 7.5% of PLF and (d) at 10% of PLF.

Incorporation of cementitious material greater than 5% interrupts the original requirement of CEM1 OPC which does not allow for such matter. Higher replacement than 5% will results to the reclassification into different cement class. Even so, if this limitation is to be considered, 5% incorporation of PLF already improves the carbonation coefficient by as much as 37% which is rather significant. Within the scope of this study, it seems possible to push replacement level beyond 5% limitation. Palm [66] showed that it is possible to incorporate high lime material (up to 50% replacement) while still keeping the carbonation performance on par with the control concrete. However, Palm [66] method required a proper water to cementitious ratio adjustment to achieve that. This is probably due to the different water demand for proper hydration when the cement is replaced at such a higher percentage. In the point of academicals arguments, it is indeed possible. However, practical engineering knowledge may not allow for such a high replacement due to the need of balancing for other admixtures such as plasticizer, accelerator and water proofing. Hence, the method practiced in this study (lower replacement but better performance) has better advantage in terms of allocating rooms for other cementitious materials that are synonym in most civil engineering projects.

3.6 FESEM and EDX

Concrete samples containing PLF which were exposed to natural carbonation for 180 days with a mean CO_2 level of 552 ppm (global CO_2 baseline is 400 ppm) at a humidity of 60-75% and daily temperature of 28-34 ºC, indicate lesser porosity compared to the control specimen. Figure 10 shows the FESEM image of the control and PLF5 concretes at a similar magnification of 2000x. The red lines are the capillarity of the concrete. The more of these line present, the more intense the capillary networks which are responsible for the overall porosity of the binder matrix. Only locations with deep fall were marked. Shallow falls were not considered as discontinuity since they may have just been variations in surface elevation. Concrete containing 5% (Fig. 10(b)) showed significantly lower discontinuity compared to

the control concrete (Fig. 10(a)) which may explain the lower carbonation depth in the phenolphthalein test, hence lower carbonation coefficient.

This study is confident that this phenomenon is contributed by the post-morphing of the PLF during exposure. Point-by-point surface elemental analysis of the specimen containing 5% PLF indicated the presence of all elements that make up the calcium carbonate which are calcium (Fig. 10(c)), carbon (Fig. 10(d)) and oxygen (Fig. 10(e)). No other unknown elements nor elements that are not indigenous to the original composition of a hardened concrete were detected except for aurum (Au) which is technically the gold coating, hence excluded.
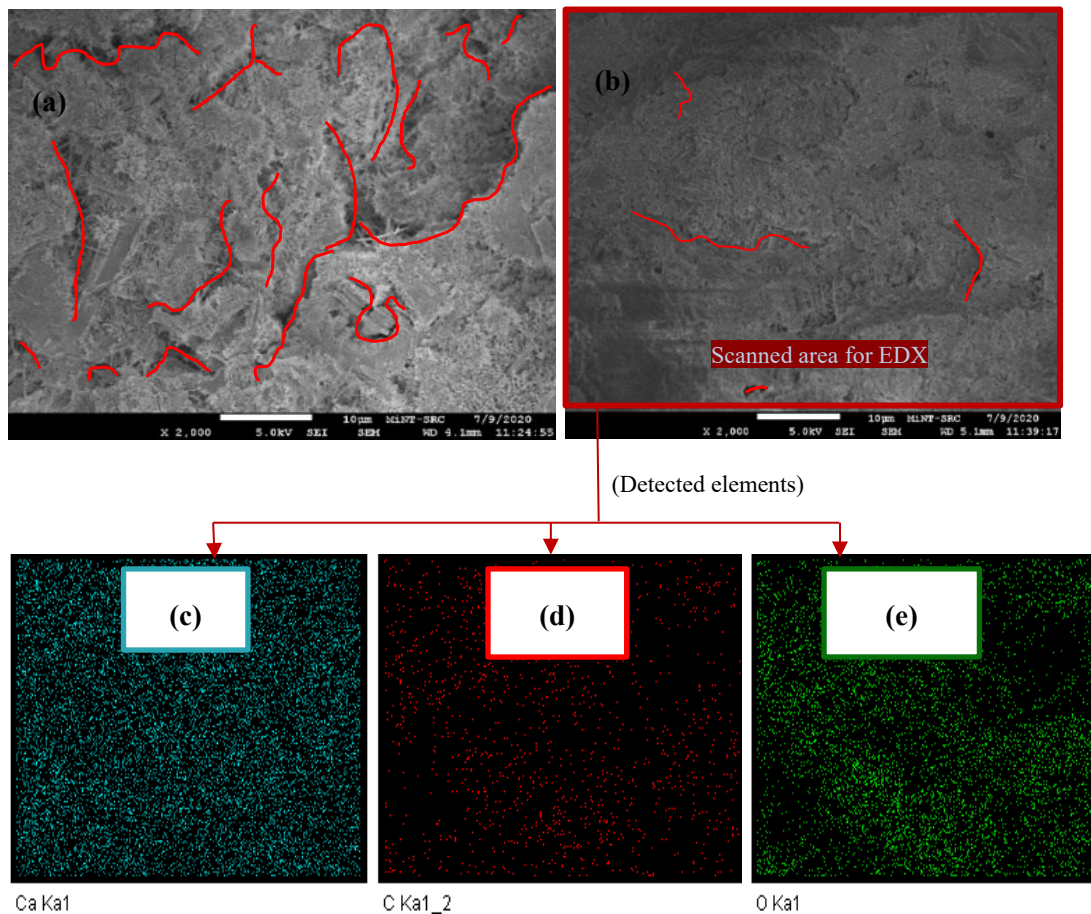
Fig. 10: Intensity of capillarity (a) control sample (b) sample with 5% PLF and surface elemental mapping (c) Calcium (d) Carbon (e) Oxygen.

In Fig. 11(a), it can be seen that at 8000x magnification, discontinuity, pores and typical hardened concrete products (CSH, ettringite, etc.) can clearly be seen. However, this is not the case for the PLF concretes especially for the PLF7.5 (Fig. 11(b)) and PLF10 (Fig. 11(c)) in which the typical products were not seen at the same level of magnification of 8000x. They are all concealed by the post-morphing of the lime. This is again verified by the EDX and the morphological images of the lime are identical across several other literatures such as those depicted by Chang [67] and Hamester [63]. Note that the flakes of lime in for PLF7.5 (Fig. 11(b)) is thinner than PLF10 (Fig. 11(c)). This is probably due to the lower concentration of the PLF. At lower concentration, the amount of carbonate minerals may not be sufficient to form the 3-dimensional structure vividly. If a sufficiently high concentration of carbonate mineral is present, the geometric arrangement of $a = b \neq c$ stated

in [51] becomes more pronounced such as in PLF10 (Fig. 11(c)) and hence, emanating cuboidal and "boxy" features across the surface.
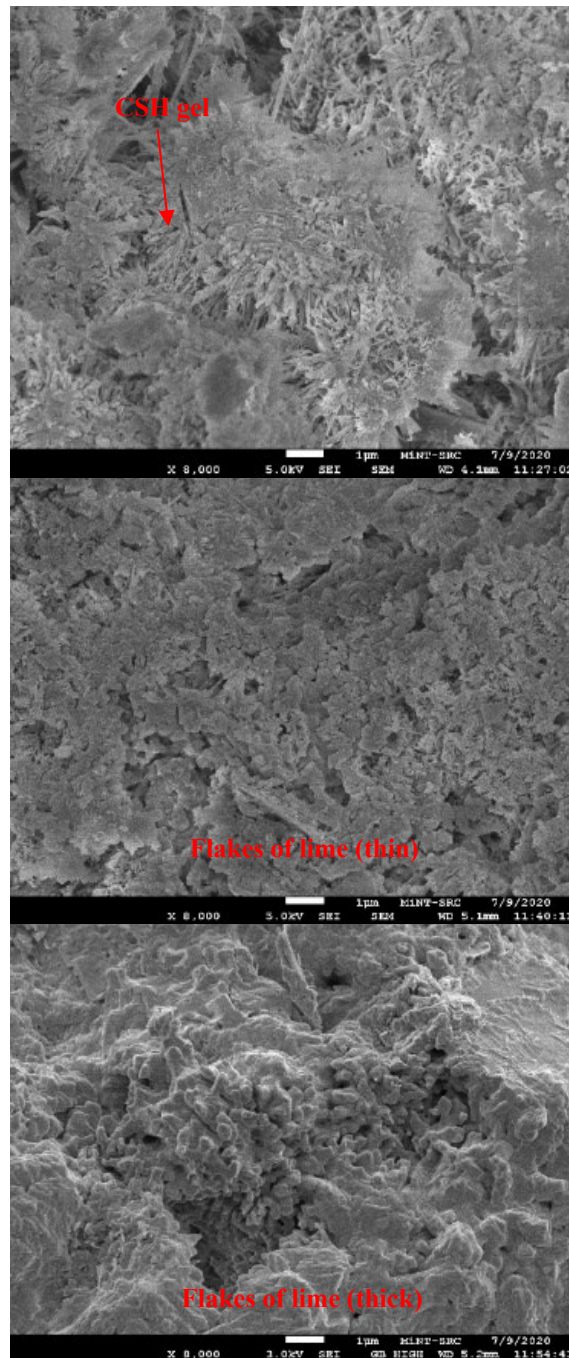
Fig. 11: PLF's filler effect that enclosed (blanket) the concrete surface (a) control sample (b) sample with 7.5% PLF and (c) sample with 10%PLF.

4. CONCLUSIONS

Based on the conducted experiments, several conclusions can be deduced;

- Mussel shells are composed of aragonitic calcium carbonate in which the crystal system may change to calcitic under certain condition.

- Both aragonitic and calcitic calcium carbonate are denser (27.8% and 18.3% respectively) than concrete, hence their high potential as filler materials.

- Aragonite is denser than calcite due to its close-pack crystal arrangement.

- Concrete containing up to 10% PLF showed significantly lowered carbonation coefficient (up to 51%) and lower intensity of capillarity.

- FESEM analysis provided an incontrovertible evidence that the mussel shell ash (PLF) has clogged up the experimental concrete pores which was not found within the control sample.

ACKNOWLEDGEMENT

REFERENCES

[1]   Sideris KK, Anagnostopoulos NS. (2013) Durability of normal strength self-compacting concretes and their impact on service life of reinforced concrete structures. Construction and Building Materials, 41: 491–497. https://doi.org/10.1016/j.conbuildmat.2012.12.042

[2]   Phung QT, Maes N, Jacques D, Bruneel E, Van Driessche I, Ye G, De Schutter G. (2015) Effect of limestone fillers on microstructure and permeability due to carbonation of cement pastes under controlled CO_2 pressure conditions. Construction and Building Materials, 82: 376–390. https://doi.org/10.1016/j.conbuildmat.2015.02.093

[3]   Rezvani M, Proske T. (2017) Influence of chemical-mineralogical properties of limestone on the shrinkage behaviour of cement paste and concrete made of limestone-rich cements. Construction and Building Materials, 157: 818–828. https://doi.org/10.1016/j.conbuildmat.2017.09.101

[4]   Ekolu SO. (2016) A review on effects of curing, sheltering, and CO_2 concentration upon natural carbonation of concrete. Construction and Building Materials, 127: 306–320. https://doi.org/10.1016/j.conbuildmat.2016.09.056

[5]   Shibata T. (2002) Cost of corrosion in Japan. Corrosion Science & Technology, 31(2): 97-102.

[6]   Benítez P, Rodrigues F, Talukdar S, Gavilán S, Varum H, Spacone E. (2019) Analysis of correlation between real degradation data and a carbonation model for concrete structures. Cement and Concrete Composites, 95: 247–259. https://doi.org/10.1016/j.cemconcomp.2018.09.019

[7]   Nakai A, Imamoto K, Kiyohara C, Sato S, Tanaka A, Niwano K, Amemiya S. (2013) Influence of Finishing Materials on Carbonation Suprression of Concrete in Existing Structure. RILEM International Workshop on Performance-Based Specification and Control of Conrete Durability, 377-384.

[8]   Lollini F, Redaelli E, Bertolini L. (2016) A study on the applicability of the efficiency factor of supplementary cementitious materials to durability properties. Construction and Building Materials, 120: 284–292. https://doi.org/10.1016/j.conbuildmat.2016.05.031

[9]   Bogas JA, Real S, Ferrer B. (2016) Biphasic carbonation behaviour of structural lightweight aggregate concrete produced with different types of binder. Cement and Concrete Composites, 71: 110–121.
      https://doi.org/10.1016/j.cemconcomp.2016.05.006

[10] Mohammed MK, Dawson AR, Thom NH. (2014) Carbonation of filler typed self-compacting concrete and its impact on the microstructure by utilization of 100% CO_2 accelerating techniques. Construction and Building Materials, 50: 508–516. https://doi.org/10.1016/j.conbuildmat.2013.09.052

[11] Singh N, Singh SP. (2016) Carbonation resistance and microstructural analysis of Low and High Volume Fly Ash Self Compacting Concrete containing Recycled Concrete Aggregates. Construction and Building Materials, 127: 828–842. https://doi.org/10.1016/j.conbuildmat.2016.10.067

[12] Shah V, Bishnoi S. (2018) Carbonation resistance of cements containing supplementary cementitious materials and its relation to various parameters of concrete. Construction and Building Materials, 178: 219–232. https://doi.org/10.1016/j.conbuildmat.2018.05.162

[13] Li Z, Li S. (2018) Carbonation resistance of fly ash and blast furnace slag based geopolymer concrete. Construction and Building Materials, 163: 668–680. https://doi.org/10.1016/j.conbuildmat.2017.12.127

[14] Marques PF, Chastre C, Nunes Â. (2013) Carbonation service life modelling of RC structures for concrete with Portland and blended cements. Cement and Concrete Composites, 37(1): 171–184. https://doi.org/10.1016/j.cemconcomp.2012.10.007

[15] Tekin I, Yasin Durgun M, Gencel O, Bilir T, Brostow W, Hagg Lobland HE. (2017) Concretes with synthetic aggregates for sustainability. Construction and Building Materials, 133: 425–432. https://doi.org/10.1016/j.conbuildmat.2016.12.110

[16] Proske T, Hainer S, Rezvani M, Graubner CA. (2014) Eco-friendly concretes with reduced water and cement content - Mix design principles and application in practice. Construction and Building Materials, 67(part C): 413–421. https://doi.org/10.1016/j.conbuildmat.2013.12.066

[17] Harilal M, Rathish VR, Anandkumar B, George RP, Mohammed MSHS, Philip J, Amarendra G. (2019) High performance green concrete (HPGC) with improved strength and chloride ion penetration resistance by synergistic action of fly ash, nanoparticles and corrosion inhibitor. Construction and Building Materials, 198: 299–312. https://doi.org/10.1016/j.conbuildmat.2018.11.266

[18] Cui D, Banthia N, Wang Q, Sun W. (2019) Investigation on porosity of partly carbonated paste specimens blended with fly ash through dual CT scans. Construction and Building Materials, 196, 692–702. https://doi.org/10.1016/j.conbuildmat.2018.11.156

[19] Esquinas AR, Ledesma EF, Otero R, Jiménez JR, Fernández JM. (2018) Mechanical behaviour of self-compacting concrete made with non-conforming fly ash from coal-fired power plants. Construction and Building Materials, 182: 385–398. https://doi.org/10.1016/j.conbuildmat.2018.06.094

[20] Bucher R, Diederich P, Escadeillas G, Cyr M. (2017) Service life of metakaolin-based concrete exposed to carbonation: Comparison with blended cement containing fly ash, blast furnace slag and limestone filler. Cement and Concrete Research, 99: 18–29. https://doi.org/10.1016/j.cemconres.2017.04.013

[21] Carević V, Ignjatović I, Dragaš J. (2019) Model for practical carbonation depth prediction for high volume fly ash concrete and recycled aggregate concrete. Construction and Building Materials, 213: 194–208. https://doi.org/10.1016/j.conbuildmat.2019.03.267

[22] Younsi A, Turcry P, Aït-Mokhtar A, Staquet S. (2013) Accelerated carbonation of concrete with high content of mineral additions: Effect of interactions between hydration and drying. Cement and Concrete Research, 43(1): 25–33. https://doi.org/10.1016/j.cemconres.2012.10.008

[23] Yagüe A, Valls S, Vázquez E, Albareda F. (2005) Durability of concrete with addition of dry sludge from waste water treatment plants. Cement and Concrete Research, 35(6): 1064–1073. https://doi.org/10.1016/j.cemconres.2004.07.043

[24] Sideris KK, Tassos C, Chatzopoulos A, Manita P. (2018) Mechanical characteristics and durability of self compacting concretes produced with ladle furnace slag. Construction and Building Materials, 170: 660–667. https://doi.org/10.1016/j.conbuildmat.2018.03.091

[25] Palm S, Proske T, Rezvani M, Hainer S, Müller C, Graubner CA. (2016) Cements with a high limestone content - Mechanical properties, durability and ecological characteristics of the concrete. Construction and Building Materials, 119: 308–318. https://doi.org/10.1016/j.conbuildmat.2016.05.009

[26] El-Hassan H, Shao Y. (2015) Early carbonation curing of concrete masonry units with Portland limestone cement. Cement and Concrete Composites, 62: 168–177. https://doi.org/10.1016/j.cemconcomp.2015.07.004

[27] Hussin MH, Othman NH, Wan Ibrahim MH. (2019) Carbonation of concrete containing mussel (Perna viridis) shell ash. Journal of Engineering, Design and Technology, 17(5): 904–928.   https://doi.org/10.1108/JEDT-12-2018-0228

[28] Phung QT, Maes N, Jacques D, Bruneel E, Van Driessche I, Ye G, De Schutter G. (2015) Effect of limestone fillers on microstructure and permeability due to carbonation of cement pastes under controlled CO2 pressure conditions. Construction and Building Materials, 82: 376–390. https://doi.org/10.1016/j.conbuildmat.2015.02.093

[29] Lollini F, Redaelli E, Bertolini L. (2014) Effects of portland cement replacement with limestone on the properties of hardened concrete. Cement and Concrete Composites, 46: 32–40. https://doi.org/10.1016/j.cemconcomp.2013.10.016

[30] Río O, Nguyen VD, Nguyen K. (2015) Exploring the potential of the functionally graded SCCC for developing sustainable concrete solutions. Journal of Advanced Concrete Technology, 13(3): 193–204. https://doi.org/10.3151/jact.13.193

[31] Rezvani M, Proske T. (2017) Influence of chemical-mineralogical properties of limestone on the shrinkage behaviour of cement paste and concrete made of limestone-rich cements. Construction and Building Materials, 157: 818–828. https://doi.org/10.1016/j.conbuildmat.2017.09.101

[32] Courard L, Michel F. (2014). Limestone fillers cement based composites: Effects of blast furnace slags on fresh and hardened properties. Construction and Building Materials, 51: 439–445. https://doi.org/10.1016/j.conbuildmat.2013.10.076

[33] Valcuende, M., & Parra, C. (2010). Natural carbonation of self-compacting concretes. Construction and Building Materials, 24(5), 848–853. https://doi.org/10.1016/j.conbuildmat.2009.10.021

[34] Meddah MS, Lmbachiya MC, Dhir RK. (2014) Potential use of binary and composite limestone cements in concrete production. Construction and Building Materials, 58: 193–205. https://doi.org/10.1016/j.conbuildmat.2013.12.012

[35] Tsivilis S, Batis G, Chaniotakis E, Grigoriadis G, Theodossis D. (2000) Properties and behavior of limestone cement concrete and mortar. Cement and Concrete Research, 30(10): 1679–1683. https://doi.org/10.1016/S0008-8846(00)00372-0

[36] Dhouibi L, Triki E, Raharinaivo A. (2002) The application of electrochemical impedance spectroscopy to determine the long-term effectiveness of corrosion inhibitors for steel in concrete. Cement and Concrete Composites, 24(1): 35–43. https://doi.org/10.1016/S0958-9465(01)00062-2

[37] Dariva CG, Galio AF. (2014) Corrosion inhibitors–principles, mechanisms and applications. Developments in corrosion protection, 16: 365-378. http://dx.doi.org/10.5772/57255

[38] Possan E, Thomaz WA, Aleandri GA, Felix EF, dos Santos ACP. (2017) CO2 uptake potential due to concrete carbonation: A case study. Case Studies in Construction Materials, 6: 147–161.

[39] Oliveira TV, Nogueira AA. (2016) Analysis of development of carbonation and surface wear of the concrete: a case study in Ship Lock 1 of the transposition system of Tucuruí dam. Journal of Building Pathology and Rehabilitation, 1(1): 1–8. https://doi.org/10.1007/s41024-016-0019-0

[40] Ministry of Energy, Green Technology and Water (2017), Green Technology Masterplan Malaysia 2017-2030. Malaysia. https://doi.org/ISBN NO. 978-967-5893-09-4

[41] Hussin MH. (2018) Keupayaan kadar pengkarbonatan konkrit campuran abu kulit kupang sebagai bahan gantian separa simen. Master thesis, Universiti Tun Hussein Onn Malaysia, Department of Civil Engineering.

[42] Teychenné DC, Franklin RE, Erntroy HC. (1997).Design of normal concrete mixes. Building Research Establishment Ltd, 331(1): 46.

[43] Shalon R, Reinitz RC. (1958) Mixing time of concrete: technological and economic aspects. Building Research Station.

[44] Jenkins R, Snyder RL. (1996) Introduction to X-ray Powder Diffractometry. In Introduction to X-ray Powder Diffractometry. John Wiley. https://doi.org/10.1002/9781118520994.

[45] British Standards Institution. Determination of Carbonation Depth in Hardened Concrete by the Phenolphthalein Method. London, BS EN 14630. 2006

[46] British Standards Institution. Determination of Resistance to Carbonation. London, BS EN 13295. 2004

[47] British Standards Institution. Determination of the Carbonation Resistance at Atmospheric Levels of Carbon Dioxide. London, BS EN 12390 – 10. 2017

[48] Mehta PK, Monteiro PJM. (2006) Third Edition Prentice- Hall, Inc., Englewood Cliffs, NJ. In Concrete: microstructure, properties, and materials.

[49] Khankhaje E, Hussin MW, Mirza J, Rafieizonooz M, Salim MR, Siong HC, Warid MNM. (2016) On blended cement and geopolymer concretes containing palm oil fuel ash. Materials and Design, 89: 385–398. https://doi.org/10.1016/j.matdes.2015.09.140

[50] Santhakumar AR. (2007) Concrete technology. Oxford University Press.

[51] Boggs S. (2009) Petrology of sedimentary rocks, second edition. In Petrology of Sedimentary Rocks, Second Edition (2nd ed., Vol. 9780521897167). Cambridge University Press. https://doi.org/10.1017/CBO9780511626487.

[52] Waseda Y, Muramatsu A. (2004) Morphology control of materials and nanoparticles: advanced materials processing and characterization. Berlin. Springer-Verlag.

[53] Klein and Dutrov (2008). The 23rd Edition of the Manual of Mineral Science (23rd ed.). Hoboken, NJ. Wiley J.

[54] Wahab MA. (2009) Essentials of Crystallography. Oxford. Alpha Science International.

[55] Antao SM, Hassan I. (2010) Temperature dependence of the structural parameters in the transformation of aragonite to calcite, as determined from in situ synchrotron powder X-ray-diffraction data. Canadian Mineralogist, 48(5): 1225–1236. https://doi.org/10.3749/canmin.48.5.1225

[56] Graf DL. (1961) Crystallographic tables for the rhombohedral carbonates. American Mineralogist, 46: 1283–1316.

[57] Haldar SK. (2020) Introduction to Mineralogy and Petrology (2nd ed.). Elsevier. https://doi.org/10.1016/C2012-0-03337-6

[58] Moore CH. (2001) Developments in Sedimentology. Elsevier.

[59] Buasri A, Chaiyut N, Loryuenyong V, Worawanitchaphong P, Trongyong S. (2013) Calcium oxide derived from waste shells of mussel, cockle, and scallop as the heterogeneous catalyst for biodiesel production. The Scientific World Journal, 2013. https://doi.org/10.1155/2013/460923

[60] Hossain A, Bhattacharyya SR, Aditya G. (2015) Biosorption of cadmium by waste shell dust of fresh water mussel lamellidens marginalis: Implications for metal bioremediation. ACS Sustainable Chemistry and Engineering. https://doi.org/10.1021/sc500635e

[61] Monneron-Gyurits M, Joussein E, Soubrand M, Fondanèche P, Rossignol S. (2018) Valorization of mussel and oyster shells toward metakaolin-based alkaline activated material. Applied Clay Science, 162: 15–26. https://doi.org/10.1016/j.clay.2018.05.027

[62] Rochelle CA, Czernichowski-Lauriol I, Milodowski AE. (2004) The impact of chemical reactions on CO2 storage in geological formations: A brief review. Geological Society, London, Special Publications, 233(1): 87-106.

[63] Hamester MRR, Balzer PS, Becker D. (2012) Characterization of calcium carbonate obtained from oyster and mussel shells and incorporation in polypropylene. Materials Research, 15(2): 204–208. https://doi.org/10.1590/S1516-14392012005000014

[64] Hossain MZ. (2013) Waste Shell Husks Concrete: Durability, Permeability and Mechanical Properties. Journal of Building Construction and Planning Research, 01(03): 61–66. https://doi.org/10.4236/jbcpr.2013.13009

[65] Neville AM. (2011) Properties of concrete (5th ed.). England. Longman.

[66] Palm S, Proske T, Rezvani M, Hainer S, Müller C, Graubner CA. (2016) Cements with a high limestone content - Mechanical properties, durability and ecological characteristics of the concrete. Construction and Building Materials, 119: 308–318. https://doi.org/10.1016/j.conbuildmat.2016.05.009

[67] Chang JJ, Yeih W, Huang R, Chi JM. (2003) Mechanical properties of carbonated concrete. Journal of the Chinese Institute of Engineers, Transactions of the Chinese Institute of Engineers,Series A/Chung-Kuo Kung Ch'eng Hsuch K'an, 26(4): 513–522. https://doi.org/10.1080/02533839.2003.9670804

CRITICAL SUCCESS FACTORS FOR BUILDING INFORMATION MODELLING (BIM) IMPLEMENTATION FOR POWER PLANT PROJECTS IN MALAYSIA

MOHD AZRUL AZIZ[1], CHEE FUI WONG[2*], NUZUL AZAM HARON[3], AIDI HIZAMI ALES[3], RAJA AHMAD AZMEER RAJA AHMAD EFFENDI[4] AND OOI KUAN TAN[2]

[1]*TNB Power Generation Sdn Bhd, PJX HM Shah Tower, Jalan Persiaran Barat, 46500, Petaling Jaya, Selangor, Malaysia*
[2]*Department of Civil Engineering, Lee Kong Chien Faculty of Engineering and Science, Universiti Tunku Abdul Rahman, 43000, Kajang, Selangor, Malaysia*
[3]*Department of Civil Engineering, Faculty of Engineering, Universiti Putra Malaysia, 43400, Seri Kembangan, Selangor, Malaysia;*
[4]*Department of Industrial Design, Faculty of Design and Architectural, Universiti Putra Malaysia, 43400, Seri Kembangan, Selangor, Malaysia*

*Corresponding author: cfwong@utar.edu.my

ABSTRACT: Building Information Modelling (BIM) has become increasingly important for the construction industry in Malaysia. BIM implementation process requires proper strategic planning and considerations from many aspects.Malaysian government has realised the importance of BIM as an emerging technology to transform the construction industry in Malaysia,and thus has classified BIM as one of the twelve main technology in CIDB "Construction 4.0 Strategic Plan 2021-2025". BIM implementation offer significant benefits to the power generation sector in Malaysia Thisstudy was conducted using the quantitaive research method in which questionnaires survey were distributed to the clients' representatives in the Malaysian power sector. This study has identified the 13 critical success factors to be considered by clients for BIM implementation in power plant projects in Malaysia. The success factors were classified based on the four (4) main fields or factors namely management, people, process and technology. The study findings show that management support is the most important success factor for the power plant projects while other success factors such as people, process and technology were also identified and discussed.

ABSTRAK: Model Pembangunan Maklumat (BIM) merupakan sebuah konsep penting bagi industri pembinaan di Malaysia. Proses pelaksanaan BIM memerlukan perancangan strategik dan pertimbangan wajar dari pelbagai aspek. Kerajaan Malaysia sedar akan kepentingan BIM sebagai teknologi pemangkin dalam transformasi industri pembinaan Malaysia di mana BIM telah disenaraikan sebagai salah satu daripada 12 teknologi utama dalam CIDB "Plan Strategik 4.0 Pembangunan 2021-2025". Pelaksanaan BIM memberi faedah ketara kepada sektor jana kuasa di Malaysia. Kajian ini dibuat menggunakan kaedah kuantitatif melalui kaji selidik ke atas wakil klien dalam sektor tenaga Malaysia. Kajian ini telah mengenal pasti 13 faktor kejayaan kritikal yang perlu dipertimbangkan oleh klien bagi menghasilkan projek loji jana kuasa di Malaysia. Faktor kejayan ini telah diklasifikasi berdasarkan 4 bidang utama seperti pengurusan, pekerja, proses dan teknologi. Dapatan kajian menunjukkan bahawa sokongan daripada pihak pengurusan

merupakan faktor utama bagi kejayaan sesebuah projek jana kuasa, di samping faktor-faktor lain seperti pekerja, proses dan teknologi juga telah dikenal pasti dan dibincangkan.

1.   INTRODUCTION

The construction industry is a vital part of the economy, environment, and society. The construction activities affect the quality of human life. Other industries especially the economic related industries are connected to the construction industry since all industries require buildings or other built assets. In Malaysia, construction industry contributed almost 5% to the national Gross Domestic Product (GDP) and 9% to employment in 2016, with more than 100 other industries depended on construction for their growth [1]. Based on recent report produced by Bank Negara Malaysia [2], the construction sector registered slightly higher growth at 0.5% for the second (2nd) quarter of the year 2019 which contributed mainly by residential and special trade sub-sectors to become 4.9% of the national GDP. As reported by World Economic Forum 2016 [3], the construction industry is the largest raw material consumer globally with 50% of steel production and more than three billion tons of raw materials. The industry contributes 6% of total global GDP. Therefore, any improvement in productivity as well as successful adoption of modern innovative will contribute major impact to the industry.

Electric energy produced by the power plants is very essential for economic growth and development of any country. Among the major power plants standings on the globe are and the hydroelectric power plants and the thermal power plants which converts heat intro electric energy such as the conventional steam power plant, diesel power plant, gas turbine power plant, and nuclear power plant [4]. Another source for electric energy comes from renewable energy which naturally reloaded by nature such as solar, wind, small hydropower, biomass, geothermal and tidal energy [5]. According to the BP Statistical Review of World Energy (2019) [6], energy consumption grew at a rate of 2.9% in 2018, almost double its 10-year average of 1.5% per year, and the fastest since 2010.

In relation to IR 4.0 and innovation, power plants that approach innovative digitalization strategy will gain significant competitive advantage as well as sustaining operational efficiency throughout the plant's lifecycle [7]. In this perspective, Building Information Modelling (BIM) is specified as the key platform of digital technology to be adopted. Based on the evaluation and estimation from industry experts on the case study of BIM application at a gas turbine power plant; potential cost saving in design, engineering and construction is estimated at 10% to 20%, while in operation phase is estimated at 8% to 13% [8].

Building Information Modelling (BIM) is the key enabler for technology innovations in the construction industry. By adopting BIM, project's lifecycle costs can be reduced by almost 20% and BIM can significantly improve completion time, quality, and safety [9]. Instead of recording information in drawings, as conventional practice by the industry players, BIM stores, maintains and exchanges information through comprehensive digital representations in the building information models. This methodology intensely improves the coordination of the design activities, the integration of simulations, the setup and control of the construction process, as well as the handover of building information for the operator or end user. Furthermore, by reducing the manual data entry, difficulty and error-prone work can be avoided, thus increase the productivity and quality of the construction projects [10].

BIM as part of ICT was recognized as vital in improving the construction industry in Malaysia. However, the implementation process requires proper strategic planning and considerations from many aspects [11]. Beside construction sector, BIM implementation can benefit the power generation sector in Malaysia. However, since there is no report and research related to the BIM adoption in the power plant projects in Malaysia, it is anticipated that BIM was only applied during design and construction stage by the international contractors or consultants and does not benefit the local clients throughout the projects' lifecycle. Therefore, it is crucial to identify the current level of BIM implementation in power plant projects in Malaysia, the benefits that BIM can offer to projects' stakeholders especially the clients, and the success factors to be considered by the clients,

This research focused on the clients' perspective of Malaysian conventional power plants which comprise the coal-fired power plants, gas turbine power plants, co-generation power plants, and hydroelectric power plants. Additionally, the assessed power plant projects were constructed between year 2010 to 2019 throughout Peninsular Malaysia, Sabah and Sarawak, when BIM implementation was relevant. This research is primarily interested in assessing the benefits that BIM can offer throughout the lifecycle the power plant projects and factors to be considered for successful BIM implementation in power plant projects in Malaysia.

2. BUILDING INFORMATION MODELLING FOR POWER PLANT PROJECTS IN MALAYSIA

2.1 Power Plants in Malaysia

Based on data retrieved from Malaysian Energy Commission in 2017, there were 61 existing power plants excluding 13 new power plant projects that were under construction or negotiation throughout Malaysia [12,13]. This 2017 research only concentrated on the clients' perspective of Malaysian conventional power plants which comprise coal-fired power plants, gas turbine power plants, and hydroelectric power plants. The research excludes renewable energy power plants such as solar and wind power plants. Therefore, focus then given to conventional power plant projects that has been constructed between year 2014 to 2025 in Peninsular Malaysia, Sabah, and Sarawak, as BIM implementation is relevant throughout that duration. As shown in Table 1 there are 23 projects that were completed, or still ongoing construction, or in negotiation phase within that duration.

2.2 BIM Implementation in the Construction of Electrical Power Plants

There are two types of power plants in Malaysia which are thermal power plants and hydroelectric plants. Thermal power plants generate electricity from coal, natural gas, biomass and fuel oil, while hydropower plants transform water-heads into electric energy through water turbine [14]. According to survey by Royal Institute of Chartered Surveyor in 2013 [15], BIM is suitable for larger and more complex buildings such as power plant, thus benefited in term of design consistency and visualization, cost estimations, clash detection, implementation of lean construction or improved stakeholder collaboration. Basically, BIM model is created by incorporating structures, equipment, instruments, piping and electrical facilities mainly for space management by the designers or contractors [16]. Boston Consulting Group in 2016, reported that based on case study of BIM application at a gas turbine power plant; potential cost saving in design, engineering and construction is estimated at 10% to 20% while in operation phase is estimated at 8% to 13% [17].

Table 1: List of power plant projects in Malaysia from 2014 until 2025 [18].

Year Completed	Details		Type / Fuel	Capacity (MW)	Status
2014	SPR Energy Kimanis, Sabah	SPR Energy (M) Sdn Bhd	Gas	100	Commissioned
	Kimanis Power, Sabah	KImanis Power Sdn Bhd (KPSB)	Gas	300	Commissioned
2015	TNB Janamanjung (Unit 4), Manjung, Perak	TNB Janamanjung Sdn Bhd	Coal	1,010	Commissioned
	Hulu Terengganu HEP, Terengganu	TNB	Hydro	250	Commissioned
2016	Ulu Jerai HEP, Pahang	TNB	Hydro	372	Commissioned
	Hulu Terengganu (Tembat), Terengganu	TNB	Hydro	15	Commissioned
	TNB Prai, Prai Penang	TNB Prai Sdn Bhd	Gas	1,071	Commissioned
	TNB Connaught Bridge, Klang, Selangor	TNB Connaught Bridge Sdn Bhd	Gas	375	Commissioned
	Tanjung Bin Energy, Kukup, Johor	Malakoff Corporation Berhad	Coal	1,000	Commissioned
2017	Pengerang Co-Gen Pangerang, Johor	PETRONAS	Gas	600	400 MW commissioned & 200 MW in construction
	TNB Manjung Five, Manjung Perak	TNB Manjung Five Sdn Bhd	Coal	1,000	Commissioned
2019	Jimah East Power, Mukim Jimah, Negeri Sembilan	Jimah East Power Sdn Bhd	Coal	2,000	Ongoing construction
2020	Southern Power Generation, Pasir Gudang, Johor	Southern Power Generation Sdn Bhd	Gas	1,440	Ongoing construction
	Upper Padas, HEP, Sabah	SESB	Hydro	192	Negotiation Phase
2021	Erda Energy, Alor Gajah, Melaka	Erda Energy Sdn Bhd	Gas	2,422	Ongoing construction
	Tanjung Kidurong, Bintulu, Sarawak	SEB	Gas	842	Ongoing construction
	Tekai, HEP Jerantut, Pahang	TNB	Hydro	168	Negotiation phase
2022	Nenggiri HEP, Gua Musang, Kelantan	TNB	Hydro	300	Negotiation phase
2023	Tadmax Indah Sdn Bhd, Pulau Indah, Selangor	Tadmax Indah Sdn Bhd	Gas	1,200	Negotiation phase
	Lebir HEP, Gua Musang, Kelantan	TNB	Hydro	274	Negotiation phase
2024	THB Power Gurun, Kedah	THB Power Sdn Bhd	Gas	1,200	Negotiation phase
	Telom, HEP, Kuala Lipis, Pahang	TNB	Hydro	132	Negotiation phase
2025	Baleh, HEP, Sarawak	SEB	Hydro	1,285	Ongoing construction
	TOTAL CAPACITY (MW)			**17,548**	

Compared to normal building projects which usually use Autodesk Revit and Autodesk Naviswork for BIM modelling, power plant projects require special BIM software for power plant design and modelling. Among the popular software in market for the plant design is E3D (Aveva), PDS and Smart3D (Intergraph), Bentley Plant Wise and Autodesk Plant 3D. According to Gerber & Rice (2010), [16] the hydro powerplant project "Hunan Hydro & Power Design Institute" which was developed by Hanjiang Yakou Shipping Hub was selected as the winner for the 'Going Digital Advancements in Power Generation' category in year 2019. The BIM model for this project was developed using Bentley's Open Buildings Designer software that helped complete design works within 45 days and helped collaborative environment to eliminate errors and material shortages, thus reduced on-site change orders by 80%. Overall, the Bentley software helped the team to complete the task three months ahead of work schedule [19].

In Malaysia, Construction Industry Development Board (CIDB) has defined BIM as modelling technology and associated set of processes to produce, communicate, analyse and use as digital information models throughout the construction project life cycle. BIM is an intelligent three-dimension (3D) model-based process that gives the architecture, engineering, and construction professionals an insight and tools to plan more efficiently, design, construct and manage buildings and infrastructure [20].

Malaysian government has realised the importance of BIM as an emerging technology to transform the construction industry in Malaysia where BIM has been classified as one of the twelve main technologies in CIDB "Construction 4.0 Strategic Plan 2021-2025". The Construction Industry Transformation Programme 2016 -2020 (CITP 2016-2020) was introduced to transform the Malaysian construction industry into one that is highly productive, sustainable and world-class by 2020. Under CIDB productivity strategic thrust, a key initiative is to roll out technological advantage across project life cycle by using advanced technologies such as BIM. The CITP 2016-2020 has outlined BIM as an emerging technology that will improve the construction productivity. The Ministry of Works of Malaysia through the Public Works Department 's (JKR) Strategic Plan 2021-2025 has set the adoption of the mechanism to reach 50% by 2021 and 80% by 2025 [21].

The benefits that the power plant clients from the Malaysian industry perspective during planning and design stages can gain from BIM implementation are better understanding via model visualization in 3D, quicker approvals of project at early stages, upfront involvement of key stakeholders for earlier feedback, intelligent transfer of information between stakeholders, and improved efficiency for design production. Meanwhile, during construction stage, the benefits would be improved coordination between client-consultant-contractor, improved communication between all stakeholders, reduce construction errors and waste, effective and accurate project time planning and sequencing, produce accurate quantity and cost estimate, and improved safety, quality and risk identification.

3. RESEARCH METHOD

3.1 Project Sampling and Research Method

This research is conducted using quantitative methods with questionnaire survey distributed amongst the clients' representatives in Malaysian power sector. The clients' engineers or technical representatives of the identified power plant projects were to answer closed ended questions in order to gain a thorough understanding on the BIM implementation over Malaysian power plant projects.

The respondents for this quantitative study are the four personnel that are involved in the BIM implementation of twenty-three (23) projects, namely BIM coordinator, civil engineer, mechanical engineer, and electrical or control & instrumentation (C&I) engineer. Therefore, by multiplying with 23 projects, the total number of respondents, the client's representative for BIM implementation in the Malaysian power plant projects perspective, is 92. Subsequently by referring to formula as indicated below [22], a sample size of 42 was obtained at 90% confidence level which gives score, Z of 1.65; sample proportion of 50%; and margin error of 10%.

$$n = N \times \frac{\frac{Z^2 \times p(1-p)}{e^2}}{[N-1+\left(\frac{Z^2 \times p(1-p)}{e^2 N}\right)]} = 92 \times \frac{\frac{1.65^2 \times 0.5(1-0.5)}{0.1^2}}{[92-1+\left(\frac{1.65^2 \times 0.5(1-0.5)}{0.1^2 \times 92}\right)]} = 40 \qquad (1)$$

where;

N = Population size,

Z = Critical value of the normal distribution at the required confidence level,

p = Sample proportion,

e = Margin of error

The study by Roscoe [23], indicated that the appropriate sample size for a study must be ranged between 30 to 500. More than 30 respondents were deemed as the best population for sampling in this study context and followed the rules of thumb in determining the sample size [23] [24]. Therefore, the sample size of 42 has met the requirement of sampling design and 1was adopted for the purpose of this study.

Questionnaire data were collected using various methods such as personal questionnaire, mail questionnaires, and electronic questionnaires. This method made the questionnaire easily accessible and made compiling data effortless [25]. The questions were generated from the literature review and distributed to the relevant personnel using online platforms such as email, WhatsApp and LinkedIn. The four sections of the structured questionnaire consist of the respondent's details, respondent's background, benefits of BIM, and success factors for BIM implementation using content-based and close-ended questions. The questionnaire used was checked for validity and reliability before distribution. The quantitative data was then coded and analysed using descriptive statistics such as percentages and mean and standard deviation. Statistical Package for Social Sciences (SPSS version 23.0) were employed to aid in the coding, entry and analysis of the data obtained through questionnaires.

The reliability analysis using Cronbach's alpha coefficient was conducted in this study to examine the validity of the data on the benefits of BIM to clients and the Pareto analysis was used to determine the critical success factors for BIM implementation for power plants projects in Malaysia. According to [26], reliability analysis refers to the stability and consistency of items in the study. Additionally [27], stated that reliability is the extent to which results are consistent over time and representative of the total population of the study. In this study the reliability of all variables was examined by Cronbach's alpha score.

The Pareto analysis which was founded by Vilfredo Pareto in the late 1940s was adopted fort his research. Pareto analysis is a formal technique useful with many possible courses of action are competing for attention. In essence, the problem-solver estimates the benefit delivered 115 by each action while it is common to refer to Pareto as "80/20" rule under the assumption that in all situations, 20% of cause determine 80% of problems.

4. RESULTS AND DISCUSSION

4.1 Research Respondents

The aim of this research was to examine the benefits of Building Information Modelling (BIM) to power plant projects' clients throughout the project lifecycle and to determine the critical success factors for BIM implementation of power plants projects in Malaysia.

This research collected 42 questionnaires responses from the conventional power plant projects stakeholders that include the Tenaga National Berhad (TNB), Sarawak Energy Berhad (SEB), Southern Power Generation (SPG), Sabah Electricity Sdn Bhd (SESB), TNB Prai Sdn Bhd, TNB Manjung Five Sdn Bhd, Jimah East Power Sdn Bhd (JEP), Petronas, Kimanis Power Sdn Bhd (KPSB), TNB Janamanjung Sdn. Bhd. and TNB Connaught Bridge Sdn. Bhd. Table 2 summarises the respondents' organisation. The respondents 'designation and years of service in the organisation were tabulated in Table 3 and Table 4. Table 5 shows the summary of the involvement of the respondents in power plant projects. The result indicates that majority of the respondents were involved in one or two power plant projects, 40.5% or 17 respondents were involved in only one project, 42.9% or 18 respondents were already involved in two power plant projects. Additionally, five respondents (11.9%) were involved in three projects, and only two respondents (4.8%) were involved in all four types of power plant projects which are covered in this study, namely gas fired power plant, coal-fired power plant, co-generation power plant and hydroelectric power plant.

Table 2: Respondent's organisation

Name of Organisation	n	%
Tenaga Nasional Berhad	22	52.4
Sarawak Energy Berhad	4	9.5
Southern Power Generation	3	7.1
Sabah Electricity Sdn Bhd	2	4.8
TNB Prai Sdn Bhd	2	4.8
TNB Manjung Five Sdn Bhd	2	4.8
Jimah East Power Sdn Bhd	2	4.8
Petronas	2	4.8
Kimanis Power Sdn Bhd	1	2.4
TNB Janamanjung Sdn. Bhd.	1	2.4
TNB Connaught Bridge Sdn Bhd	1	2.4
TOTAL	**42**	**100**

Table 3: Respondent's designation

Designation	n	%
Engineer	16	38.1
Senior Engineer	15	35.7
Manager	5	11.9
Executive	4	9.5
Senior Manager	2	4.8
TOTAL	42	100

Table 4: Respondent's year of organisation

Years in Organisation	n	%
1-5 years	13	31.0
6-10 years	13	31.0
11-15 years	12	28.6
16-20 years	2	4.8
More than 20 years	2	4.8
TOTAL	42	100

Table 5: Respondent's involvement in power plant project

Involvement of Power Plant Project	n	%
1 Type of Power Plant Project Only	17	40.5
2 Type of Power Plant Projects	18	42.9
3 Type of Power Plant Projects	5	11.9
All 4 Type of Power Plant Projects	2	4.8
TOTAL	42	100

4.2 Reliability Analysis

Table 6 indicates the reliability analysis of critical success factors for BIM implementation along the lifecycle of power plants projects in Malaysia. The value of Cronbach's alpha for management, people, process and technology were recorded at 0.946, 0.893, 0.914 and 0.948 respectively. All items of the reliability analysis were considered acceptable since the value is greater than 0.60 [24].

Table 6: Reliability analysis for critical success factors for BIM implementation throughout the lifecycle of power plants projects in Malaysia

Variables	Cronbach's alpha
Management	0.946
People	0.893
Process	0.914
Technology	0.948

4.3 Benefits of BIM Implementation

BIM practices have been very beneficial in achieving project success. The finding for this quantitative study was formulated using Likert Scale approach and the respondents were asked to rate what their opinion on the listed BIM benefits based on their knowledge or experience in applying BIM in their power plant projects. These responses were assessed through ranking based on Average Index (Ai) values presented in Table 7.

4.4 Critical Success Factors for BIM Implementation

The critical success factors for BIM implementation were assessed through the questionnaires using Likert Scale approach. The respondent's opinion on the listed critical success factors for BIM implementation based on their knowledge or experience in applying BIM in their power plants projects were assess and ranked using the Average Index (AI) values and presented in Table 8.

Table 7: Benefits of BIM Implementation (Overall)

No	Benefits of BIM	AI	Standard Deviation	Rank
1.	Construction Stage- Improved coordination between client-consultant-contractor	4.2432	0.95468	1
2.	Planning and Design Stage- Better understanding via model visualization in 3D	4.2432	0.89460	2
3.	Facility Management Stage- Allow for future updates of current asset information	4.1351	0.85512	3
4.	Facility Management Stage- Provide a single source of information for project handover	4.1081	0.96563	4
5.	Construction Stage- Reduce construction errors and waste	4.1081	01.10010	5
6.	Construction Stage- Produce accurate quantity and cost estimate	4.0541	0.94122	6
7.	Planning and Design Stage- Improved efficiency for design production	4.0541	0.97028	7
8.	Planning and Design Stage-Quicker approvals of project at early stages	4.0541	0.99850	8
9.	Construction Stage- Improved communication between all stakeholders	4.0541	1.02594	9
10.	Facility Management Stage- Better information for the whole lifecycle of asset management	4.0270	1.04047	10
11.	Planning and Design Stage- Intelligent transfer of information between stakeholders	4.0000	1.10554	11
12.	Facility Management Stage- Enhanced evaluation on maintenance approach of plant	3.9730	0.89711	12
13.	Construction Stage- Effective and accurate project time planning and sequencing	3.9730	1.21304	13
14.	Planning and Design Stage- Upfront involvement of key stakeholders for earlier feedback	3.9730	0.98563	14
15.	Construction Stage- Improved safety, quality and risk identification	3.8378	1.01416	15

Table 8: Critical success factors for BIM implementation (overall)

No	Critical Success Factors for BIM Implementation	AI	Standard Deviation	Rank
1	Management- High commitment and continuous support	4.2703	0.87078	1
2	Technology- Relevant software available for BIM application	4.2162	0.88616	2
3	Technology- Central repository system to house project information	4.1892	0.84452	3
4	Process- Comprehensive client's requirements	4.1892	0.87679	4
5	People- Change of mindset and awareness	4.1892	0.87679	5
6	People- Adequate education and trainings	4.1622	0.89795	6
7	Management- Clear business plan, vision and mission	4.1622	0.86646	7
8	Technology- Stable and fast internet network system	4.1351	0.94757	8
9	Technology- Appropriate hardware i.e. high-end computers	4.1351	0.91779	9
10	Process- Systematic approach throughout project	4.0811	0.95389	10
11	People- Well defined roles and responsibilities	4.0811	0.89376	11
12	Technology- Other tools and equipment i.e. drone for reality modeling	4.0000	0.97183	12
13	Process- Agreed deliverables for asset lifecycle	4.0000	0.91287	13

The result shown in Fig. 1 was employed to focus on the top portion of the critical success factors for BIM implementation throughout the lifecycle of power plant projects in Malaysia. From the Pareto chart, 8 out of 13 factors of BIM implementation were selected to be included in the concept map and "Management – High commitment and continuous support" stated the highest percentage among the critical factor with 7.9% followed by "Technology- Relevant software available for BIM application" (7.9%), "-Technology- Central repository system to house project information" (7.8%), "Process- Comprehensive client's requirements" (7.8%), "People- Change of mindset and awareness" (7.7%), "People- Adequate education and trainings" (7.7%), "Management- Clear business plan, vision and mission" (7.6%), and "Technology- Stable and fast internet network system" that indicated 7.6%.
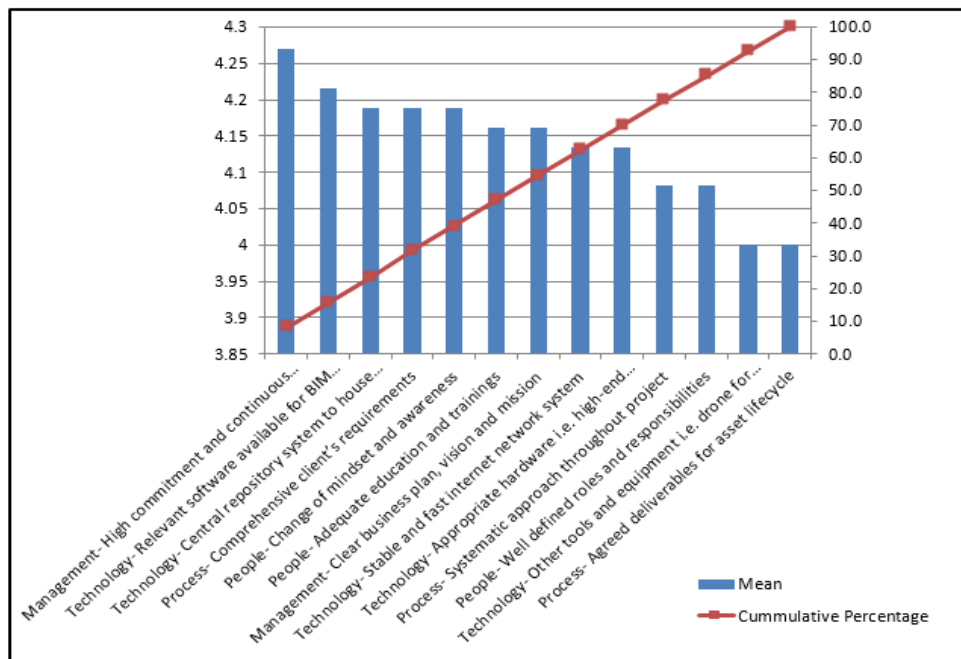
Fig. 1: Pareto analysis of critical success factors for BIM implementation throughout the lifecycle of power plant projects in Malaysia.

5. CONCLUSION

This research has identified the benefits of Building Information Modelling (BIM) to power plant projects' clients throughout the project lifecycle and has identified 13 critical success factors that need to be considered for BIM implementation in Malaysia. This research has identified the most important benefit of BIM for power plant projects is the improved coordination between client, consultant and contractor during the construction stage. Other benefits identified include better 3D visualisation during planning and design stage as well as smooth updates of asset information and single source handover project information during the facilities management stage. This research has also identified the most critical success factor for BIM implementation of power plant projects in Malaysia as the commitment and continuous management support. Besides that, the power plants project stakeholders consider relevant software availability, central repository system, comprehensive client's requirements and the change of mindset as the critical success factors for BIM adoption for power plant projects in Malaysia.

REFERENCES

[1]   Ipsos (2017) Reference Document & Financial Report: It's Time for Simplicity.

[2]   Bank Negara Malaysia (2019) Outlook and Policy in 2019. Bank Negara Malaysia

[3]   World Economic Forum (2016) Shaping the Future of Construction. A Breakthrough in Mindset and Technology.

[4]   Raja, A. K., & Srivastava, A. P. (2006). Power plant engineering. New Age International.

[5]   Ellabban O, Haitham AR, Blaabjerg F. (2014) Renewable energy resources: Status, prospects, and their enabling technology. Renewable and Sustainable Energy Reviews, 39: 748-764. DOI: 10.1016/j.rser.2014.07.113

[6]   BP (2019) BP Statistical Review of World Energy

[7]   ABB (2017) Digitalization and power generation Evolve, adapt, and thrive during the Energy and Fourth Industrial Revolutions, ABB White Paper.
      https://library.e.abb.com/public/5b1f31f8444f41a7922b200207e47177/Digitalization%20and% 20power%20generation_WP.pdf

[8]   CIDB (2008) Malaysian construction industry outlook, presentation by Business Development, Sector of CIDB, in Master Builders Journal (3rd Quarter), 2008, 8-14.

[9]   CIDB (2009) Construction Economic Indicators. Kuala Lumpur: Construction Industry Development Board of Malaysia

[10] Borrmann, A., König, M., Koch, C., & Beetz, J. (2018). Building information modeling: Why? what? how? In Building information modeling (pp. 1-24). Springer, Cham.

[11] Haron NA, Raja Soh RPZA, Harun AN. (2017) Implementation of Building Information Modelling (BIM) in Malaysia: A review. Pertanika Journal of Science & Technology, 25(3): 661-674.

[12] Energy Commission (2017) Energy Malaysia, Volume 12, Energy Commission, Malaysia.

[13] Energy Commission (2017) Performance and Statistical Information on Electricity Supply Industry in Malaysia, Energy Commission.

[14] Shamsudin MSN, Rahman MN, Wahid MA. (2016) Power Generation Sources in Malaysia: Status and Prospects for Sustainable Development. Journal of Advanced Review on Scientific Research, 25(1): 11-28.

[15] Royal Institution of Chartered Surveyors (2014) International BIM implementation guide.
      https://www.rics.org/globalassets/rics-website/media/upholding-professional-standards/sector-standards/construction/international-bim-implementation-guide-1st-edition-rics.pdf

[16] Gerber BB, Rice S. (2015) The Perceived Value of Building Information Modeling in the U.S. Building Industry. Journal of Information Technology in Construction, 15: 185-201.

[17] Boston Consulting Group (2016) Digital in Engineering and Construction. The Transformative Power of Building Information Modeling.

[18] Energy Commission (2018) Malaysia_Energy_Statistics_Handbook, Energy Commission, Malaysia. http://www.sciencedirect.com/science/article/pii/S1364032114005656

[19] Bentley (2019) BIM Projects in China Using Bentley's Open Applications Are Setting a Higher Bar in Manufacturing and Power Generation. Bentley Systems. https://www.bentley.com/en/about-us/news/2019/october/21/901-ai-bim-projects-china

[20] CIDB Malaysia (2017) Malaysia Building Information Modeling Report 2016.

[21] CIDB (2015) Construction Industry Transformation Programme 2016-2020: Driving Construction Excellence together. CIDB (ISBN: 978-967-5317-96-5)

[22] Arya, R., Antonisamy, B., & Kumar, S. (2012). Sample size estimation in prevalence studies. The Indian Journal of Pediatrics, 79(11), 1482-1488.
      https://link.springer.com/article/10.1007/s12098-012-0763-3

[23] Roscoe JT. (1975) Fundamental Research Statistics for the Behavioral Sciences. (2nd Edition). New York: Holt, Rinehart, and Winston.

[24] Sekaran. (2003) Research methods for business (4th edition). New York, USA: John Wiley & Sons, vol. 65. https://doi.org/10.1017/CBO9781107415324.004

[25] Millar M, Dillman DA. (2012) Encouraging Survey Response via Smartphones. Survey Practice 5(3). https://doi.org/10.29115/SP-2012-0018

[26] Sekaran U, Bougie R. (2013) Research methods for business: a skill-building approach (6th ed.). Chichester, West Sussex: John Wiley & Sons, Inc.

[27] Joppe, M. (2000). The research process. Retrieved February 2000.
https://www.academia.edu/930161/The_research_process?pop_sutd=true

PERFORMANCE ANALYSIS ON DYNAMIC WIRELESS CHARGING FOR ELECTRIC VEHICLE USING FERRITE CORE

SITI HAJAR YUSOFF*, AMIRA AZIERA ABDULLAH, NADIA NAZIEHA NANDA
AND AHMED SAMIR ABED BADAWI

*Department of Electrical and Computer Engineering, Faculty of Engineering,
International Islamic University Malaysia,
Jalan Gombak, 53100 Kuala Lumpur, Malaysia*

*Corresponding author: sitiyusoff@iium.edu.my

ABSTRACT: The technology of dynamic Wireless Power Transfer (WPT) has been accepted in the Electric Vehicle (EV) industry. Recently, for a stationary EV charging system, the existence of a ferrite core improves power efficiency. However, for dynamic wireless charging, the output power fluctuates when the EV moves. Two main obstacles that must be dealt with is air-gaps and misalignment between the coils. This paper investigates clear design guidelines for fabrication of an efficient Resonant Inductive Power Transfer (RIPT) system for the EV battery charging application using a ferrite core. Two different geometry shapes of ferrite core, U and I cores, will be investigated and tested using simulation and experimental work. The proposed design was simulated in JMAG 14.0, and the prototype was tested in the laboratory. The expected output analysis from these two techniques was that the power efficiency of the ferrite pair should first be calculated. From the analysis and experimental results, it is seen that the pair of ferrite cores that used a U shape at the primary and secondary side provides the most efficient coupling in larger air-gap RIPT application with 94.69% on simulation JMAG 14.0 and 89.7% from conducting an experiment.

ABSTRAK: Teknologi Alih Kuasa Wayarles (WPT) dinamik telah diterima pakai dalam Kenderaan Elektrik (EV). Baru-baru ini, kewujudan teras ferit dalam sistem pengecasan pegun EV dapat meningkatkan kecekapan kuasa. Namun, kuasa pengecasan ini akan berubah apabila EV bergerak bagi sistem pengecasan wayarles secara dinamik. Dua halangan utama yang harus ditangani adalah ketidakjajaran dan jarak antara dua gegelung. Kajian ini merupakan garis panduan yang jelas mengenai rekaan fabrikasi dan kecekapan sistem Alih Kuasa Induktif Resonan (RIPT) bagi aplikasi pengecasan bateri EV menggunakan teras ferit. Dua bentuk geometri teras ferit, iaitu teras U dan I telah dikaji dan diuji menggunakan simulasi dan eksperimen. Rekaan ini telah disimulasi menggunakan JMAG 14.0 dan prototaip diuji di dalam makmal. Kedua-dua teknik ini diharapkan dapat menghasilkan kecekapan kuasa yang sama. Dapatan kajian menunjukkan kedua-dua teras ferit pada sisi primer dan sekunder berbentuk U mempunyai gandingan paling efisien bagi jarak paling besar antara 2 gegelung menggunakan aplikasi RIPT dengan 94.69% simulasi JMAG 14.0 dan 89.7% secara eksperimen.

1. INTRODUCTION

An Electric Vehicle (EV) is an automobile vehicle that operates entirely on electricity without the emission of gases typical of conventional cars. The working principle is straightforward and plays a role in preventing environmental degradation. EVs can be associated with the use of an electric motor for propulsion and powering by electricity, either by plug-in, battery, or solar panel sources. This vehicle is not a new concept but was instead developed in the mid-18th century. However, during the 20th century, EVs became obsolete because of their limited driving range and high price compared to gasoline-powered vehicles. It is expected that by 2050, the number of vehicles on the road is expected to reach up to 2.5 billion [1].

Regarding the future transport significance, EVs are considered the likely replacement for internal combustion engine-driven vehicles. EVs can reduce carbon discharges by reducing CO_2 emissions, air pollution, and reliance on imported fuel [2]. The government of Malaysia also encourages electric cars by providing a total EV tax exemption [3]. Due to this, EV technology has captured the world's attention. Many researchers have realized the significance of EV; thus, intense studies have been reported on this technology.

EVs have rechargeable batteries onboard, as shown in Fig. 1. The power source no longer uses oil or gas and eliminates emissions since EVs are 100% electrical transportation. Instead, their source of power comes from a battery pack. This battery pack is charged using a wireless power transfer method. The primary transmitter coil acts as a transmitter to transmit the power from a primary to a secondary. The vehicle's pick-up coil acts as the receiver, also known as the secondary, in order to charge the battery pack. Referring to Fig. 1, the fully charged battery pack acts as the energy source to drive the traction motor inside the vehicle. As with gas emission transports, the battery pack of an EV needs to be recharged first.
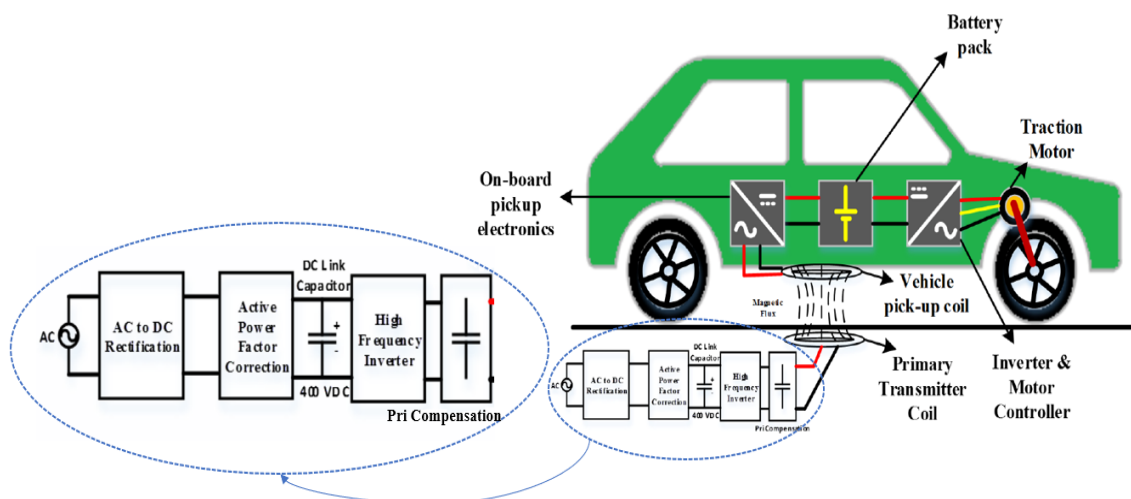
Fig. 1: Electric Vehicle (EV) System Model [4].

Battery recharging for EV can be done in three different ways, as stated by [5]:

1) static charging;

2) quasi-dynamic charging;

3) dynamic charging.

Contactless charging or wireless charging is a new technology for EV power transfer. Charging is done using a wireless power transmitter and receiver to supply continuous power to the EV. A few years back, EVs only used Static Wireless Charging (SWC), where the vehicle needed to stay in the charging area throughout the recharge time. The problem or limitation in this technology is that the vehicle can only be charged when parked or in stationary modes such as parked in car parks and garages, or waiting at traffic lights [6]. The significant issues in public acceptance of EV correlate to its high battery cost and limited driving range.

The lithium-ion battery is widely used as the primary power source for the EV's drivetrain due to its high specific energy (100-265 W/kg) and specific power density (250-340 W/kg) compared to other battery technologies. Despite its superior characteristics, such a battery still adds considerable weight and size to the vehicle. For example, Nissan Leaf's 24 kWh battery pack weighs around 200 kg. In addition to high weight and size, the estimated price for an EV is about double that of its gasoline counterparts, with nearly half of the cost going toward the battery alone [7]. The limited driving range is an even more significant obstacle to the market penetration than the vehicles' higher cost. For example, gasoline vehicles can go over 500 km before refueling, which takes about 2-3 minutes at a filling station located every few kilometers.

On the other hand, most EVs can only go about 100-200 km before requiring another round of recharging that can last from about 30 minutes to more than 12 hours [8]. Besides this, charging stations are not as readily available as fuel stations. These limitations of static charging EVs has awakened researcher interest in a new dynamic charging method. The power transmission coil concept is used by the WPT method to transfer electric power from the primary grid source to energize the EV [9]. For a dynamic WPT, the vehicle needs to be charged while moving. Thus, the significant problem of high-power loss is encountered. This high-power loss is due to significant air gaps and misalignment between the primary and secondary pads [10]. When the loss is significant, the efficiency of power transfer is low.

Much research has been done to mitigate the mentioned problem [11,12]. However, none have come out with the optimal solutions and high-power efficiency. The other problem related to power loss is also due to low magnetic flux density. As the air-gap increases or misalignment occurs between the primary and secondary pad, the magnetic flux density is also reduced. Magnetic flux density is proportionally related to the induced current, thus directly affecting the power produced. As a result, low power transfer is due to having low magnetic flux density in primary and secondary coils. Some researchers have suggested including a ferrite core inside the primary and secondary coils. However, the design of the ferrite core is still an open issue. Adding an unsuitable ferrite core design can lead to unwanted additional weight and an increase in the manufacturing cost. That is why, even today, these problems are still in open research.

The research in this paper builds upon the improvements of previous research on novel ferrite cores [13] in wireless charging for EV applications. In this paper, Inductive Wireless Power Transfer (IWPT) uses coils embedded in the roadway and the vehicles. The IPT system consists of a pair of loosely coupled coils as transmitter and receiver. When the current flows through the coils, the magnetic field will be generated and thus will provide a wireless power transfer [14]. Figure 2 shows the Inductive Wireless Power Transfer System.
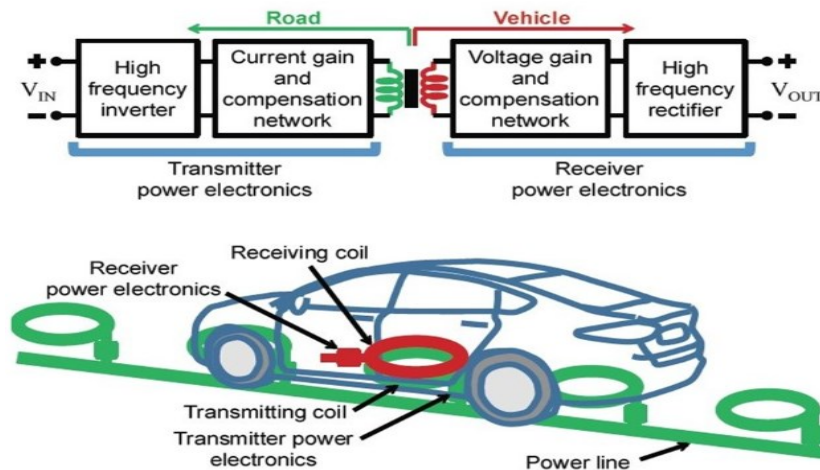
Fig. 2: Inductive WPT system [15].

2. METHODOLOGY

This section will discuss the proposed methodology used in designing the wireless charging system. Figure 3 shows the steps involved: calculation of coil parameters, identification of core shape, experimentation, and evaluation of results obtained. Next, subsection 2.1 will discuss the process of design and simulation using JMAG Designer 14.0. Finally, subsection 2.2 is the preparation of experimental work. In this study, the U and I ferrite core characteristics were investigated using two techniques. The first technique used a simulation on JMAG Designer 14.0. The simulation work was crucial for obtaining magnetic flux density for each pair of ferrite cores. Six designs of ferrite core, as shown in Table 1, were run in this simulation. In addition, air-gaps of 1 cm and 2 cm with no misalignment was tested on all pairs of the ferrite cores.

Fig. 3: Steps for designing inductive charging coupler.

The second technique used in this paper conducted an experiment to obtain the results from the prototype. The experiment was conducted in the university laboratory. From the simulation and experiment analyses, the power efficiency results were compared to each other in order to select the combination of ferrite cores that gave greatest power transfer. The calculation of parameters was first calculated, as discussed in [16]. In this paper, the power required for the EV was ratioed down to 16.7 W. In an actual application, 36 kW of power would be required. Table 2 shows the parameters used in this study. Table 2 lists the primary and secondary voltages, primary and secondary currents, load resistor, primary and secondary inductances, mutual inductance, and primary and secondary capacitors.

Figure 4 shows the flowcharts for the a) first and b) second technique, for simulation in JMAG Designer 14.0 and experimental work. By using the JMAG software, the magnetic flux of each ferrite pair was measured. For the U ferrite core's shape, there are three possible ways to wind the copper coil around the U core. Therefore, this study focused on winding the copper coil around the U core. Table 3 shows the winding method around the U shape. The three different winding methods were examined only for the U shape, while the coil was simply wound at the central limb for the I core.

Next, the final part of this study experimented on six pairs of ferrite cores. The experiment varied the air-gap from 1 cm with 0 cm to 5 cm misalignment. Section 3 will show the performance evaluation of each pair.

Table 1: Six pair of ferrite core
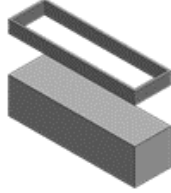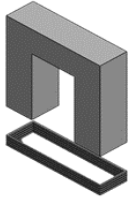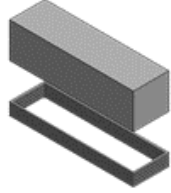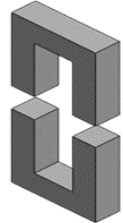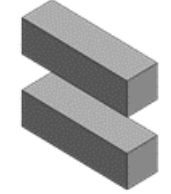
Secondary side
Primary side

Pair 1: Primary U ferrite core and secondary coil

Secondary side
Primary side

Pair 4: Primary I ferrite core and secondary coil

Secondary side
Primary side

Pair 2: Primary coil and secondary U ferrite core

Secondary side
Primary side

Pair 5: Primary coil and secondary I ferrite core

Secondary side
Primary side

Pair 3: Primary and secondary U ferrite core

Secondary side
Primary side

Pair 6: Primary and secondary I ferrite core

Table 2: Calculated parameters for WPT system

Parameters	Values
$V_{p,rms}$	12 V
$V_{s,rms}$	5 V
$I_{P,rms}$	1.39 A
$I_{s,rms}$	3.33 A
R_L	1.5 Ω
L_P	330.72 μH
L_s	36.65 μH
M	22.0 μH
C_p	113.3 nF
C_s	1022.4 nF
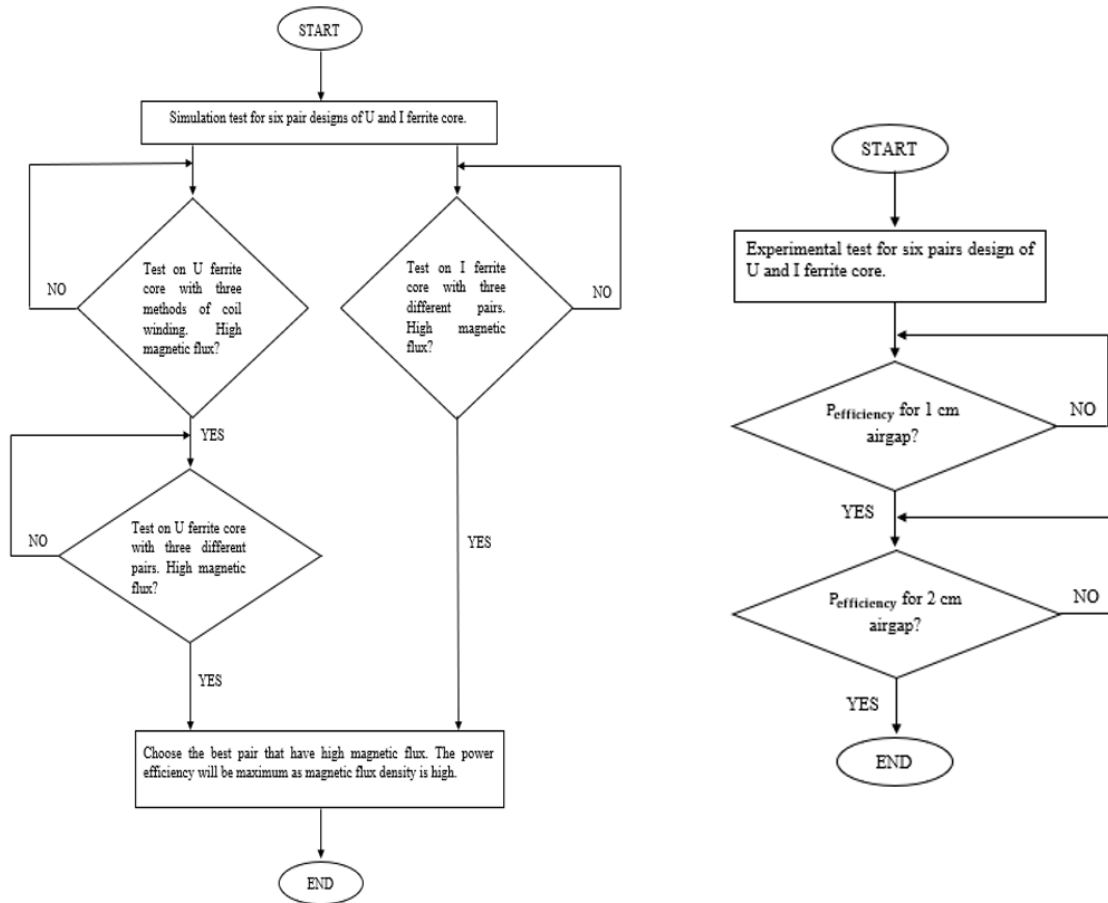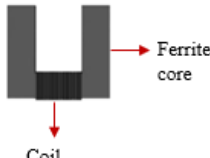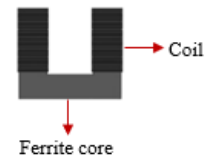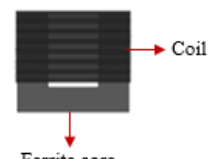
Fig. 4: Flowchart of a) first technique b) second technique.

Table 3: Winding method for U shape

No.	Winding Method for U shape	Illustration
1	**Central winding:** The copper coil is winding at the center of the U ferrite core.	
2	**Edge separate winding:** The copper coil is winding separately at two edges of the U ferrite core.	
3	**Edge together winding:** The copper coil is winding in one direction only at the edge of the U ferrite core.	

2.1   Simulation Using JMAG 14.0

Table 4 displays the geometry editor for six ferrite core pairs created in JMAG 14.0 before running the simulation.

The blue, red, and yellow colors in all figures are indicated as follows:

1. The blue color indicates ferrite core at primary side

2. Red color is the secondary side.

3. Yellow color indicates the winding of the copper coil.

Table 4: Simulation using JMAG Designer 14.0
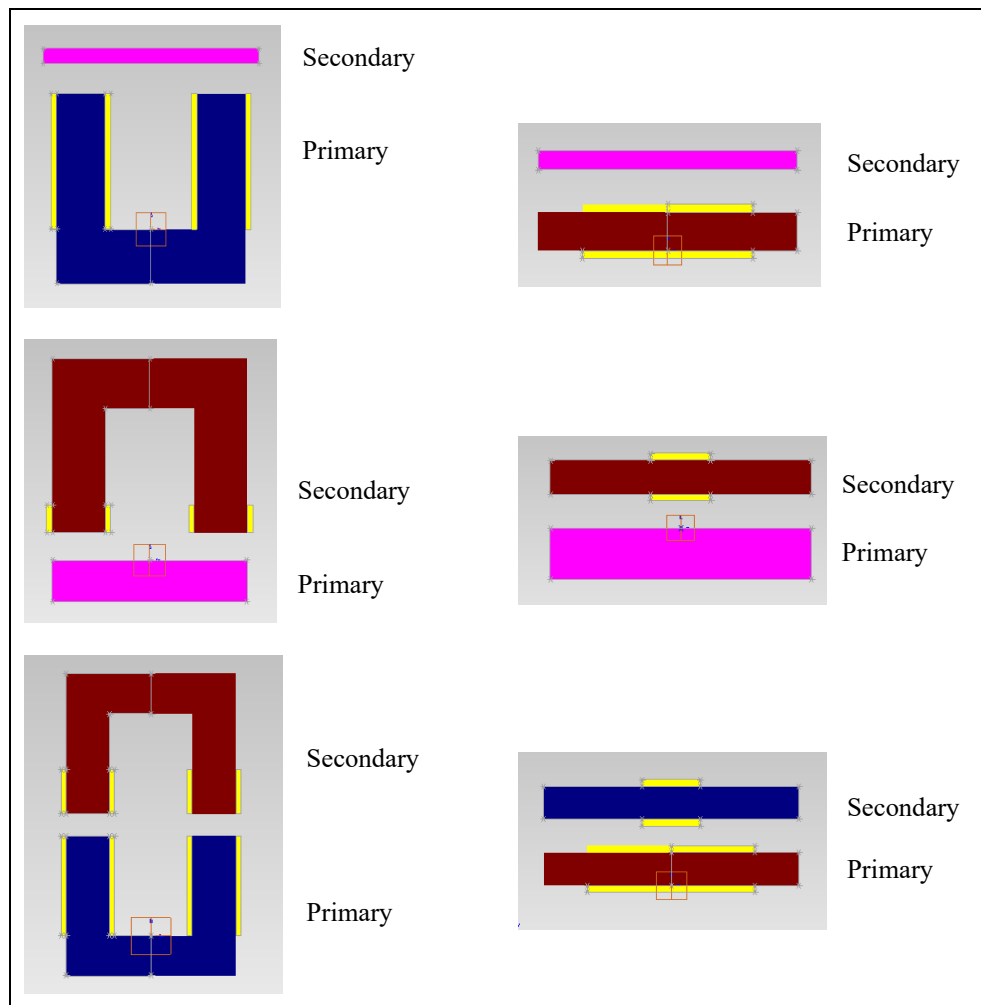
2.2 Experimental Setup

The wireless power transfer circuit was constructed before conducting the experiment. Transmitter and receiver circuits were constructed using fritzing software. Figure 5 shows the construction of the transmitter (primary circuit), while Fig. 6 shows the receiver (secondary circuit).

3. RESULTS

This section contains two subsections to evaluate the obtained results. Subsection 3.1 will discuss the simulation results from running the design in JMAG Designer. In this subsection, two main parts to run the simulation in JMAG designer software will be discussed. The first part is crucial for the U ferrite core to identify the most suitable method to wind the copper coil around the U ferrite core. This part is crucial because the U shape's

geometric design creates many possibilities to wind the coil, unlike the I ferrite core. Therefore, three different methods were investigated to choose the best winding to create high magnetic flux. After a few tests, the best coil winding was identified: method 2, edge separate winding. Then, the six pairs of ferrite cores listed in Table 1 were simulated using this software. Finally, among the six pairs, one pair was selected as the best ferrite core pair for the WPT system. The selection mainly focused on the highest magnetic flux produced.
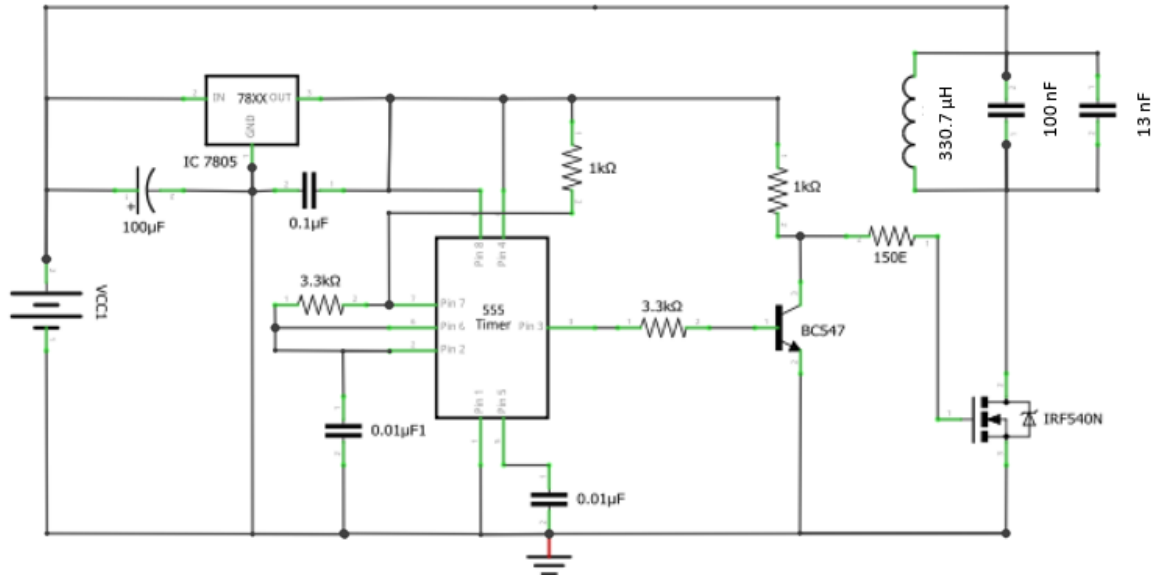
Fig. 5: Transmitter or Primary Circuit.
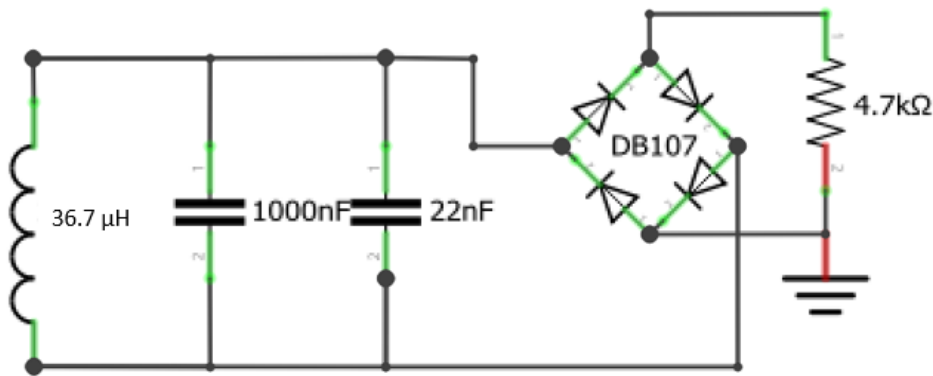
Fig. 6: Receiver or Secondary Circuit.

3.1 Simulation Using JMAG 14.0 Software

Table 5 shows the magnetic flux density of six pairs of the ferrite cores. The simulation of the JMAG designer provided a color region to indicate the strongest or weakest areas around the coil, U, and I ferrite cores. For all results of the three pairs, the color scale regions are shown together, with the strongest point identified. Note that all the simulation pairs are at a 1 cm air-gap.

Table 5: Magnetic flux density for six pairs of ferrite core

Pair 1	**Pair 4**
Pair 2	**Pair 5**
Pair 3	**Pair 6**
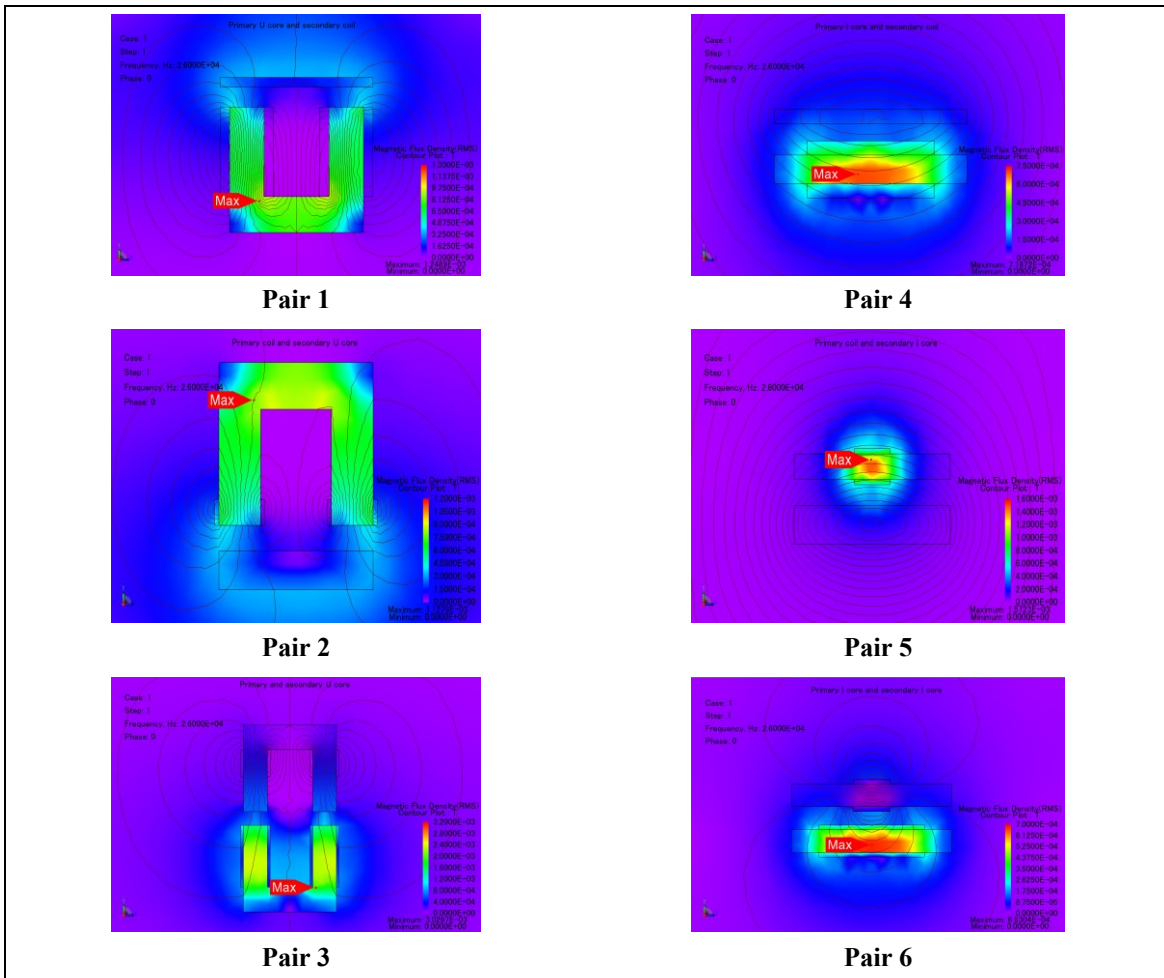
All six proposed design pairs in this study have been simulated using JMAG Designer. The magnetic flux obtained for each pair is shown in Fig. 7. Overall, as the air-gap between primary and transmitter increased, lower magnetic flux was produced. This result is because more flux leakages are created as the distance between the two sides increases. Thus, the best pair with high magnetic flux is pair 3, in which the U ferrite core is located at the primary and secondary sides.
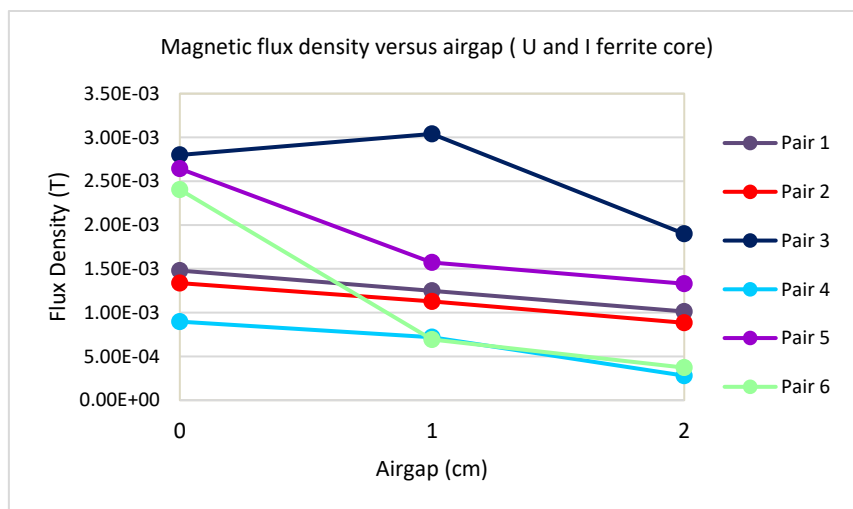
Fig. 7: Magnetic flux density for six coil pair designs.

The electric power efficiency was calculated and plotted for all six pair designs, as shown in Fig. 8. In this simulation result, a pair of U ferrite cores at both the primary and secondary sides, known as pair 3, offered the best power efficiency among the other pairs, followed by pair 5. At 0 cm air-gap, the power of efficiency of this pair was 90.3 %. By increasing the air-gap to 1 cm, the power efficiency was about 94.69 %. However, if the air-gap was increased to 2 cm, the power efficiency dropped to a level similar to the other pairs.

Meanwhile, pair 6 showed good performance when there was no air-gap. Surprisingly, it showed rapid drops when the air-gap increased to 1 cm and slowly fell at the 2 cm air-gap. The performance of power efficiency pair 1 and pair 2 was almost the same throughout the air-gap. The lowest efficiency pair was the primary I ferrite core and secondary coil, known as pair 4. The power efficiency was consistently below 60 % in every air-gap. Comparing the graph of magnetic flux versus air-gap from the Fig. 7 and power efficiency versus air-gap in Fig. 8, shows that the relationship between magnetic flux and power produced is directly proportional. Therefore, a pair design must have a high magnetic flux density to serve maximum power transfer.
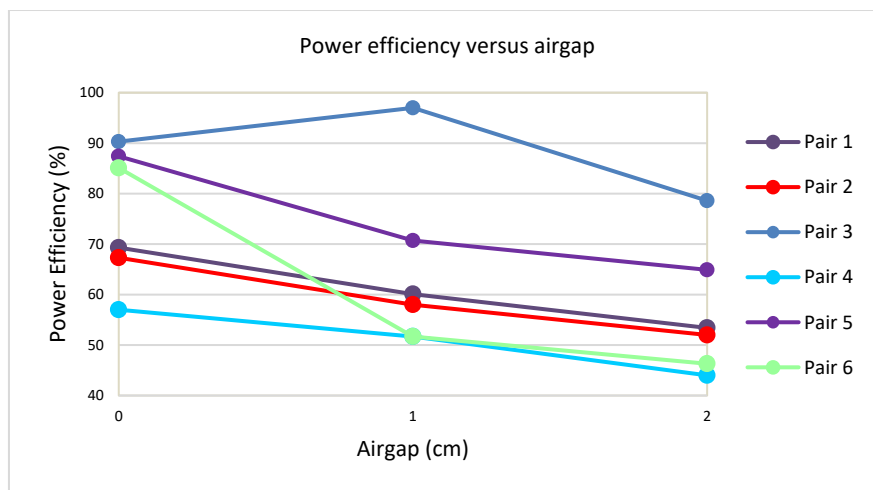
Fig. 8: Power efficiency with varies air-gap for six coil pair.

3.2 Experimental Results

This section evaluated the collected results for all pairs of U and I ferrite cores. The main case was the performance of all tested pairs while varying the misalignment at a 1 cm air-gap. In this experiment, a mini prototype was built to test the proposed designs in this study. Even though the standard air-gap for a real EV is 8 cm until 10 cm, an air-gap of 1 cm was used in this experiment as a starting development for the EV charging system. Figure 9 shows the percentage of power transfer versus misalignment between the primary and secondary sides. The highest power transfer delivered was from pair 3 (the U ferrite core at the primary and secondary side) with 94.69%, followed by pair 5 at 89.7%. As shown in Table 1, these two pairs use ferrite cores at both sides, primary and secondary. Therefore, it shows that the existence of a ferrite core in the system improves the power transfer. Then, pairs 1 and 6 have the same amount of power transfer at 15 mm misalignment with 51% of power transfer. While pairs 2 and 4 have an equal amount of power delivered, which is 49.7% at 10 mm misalignment. Overall, the power transfer delivered showed a constant decrease from 0 mm to 50 mm misalignment. As the distance between primary and secondary increased, more flux leakage occurred and reduced the power obtained at the primary side.
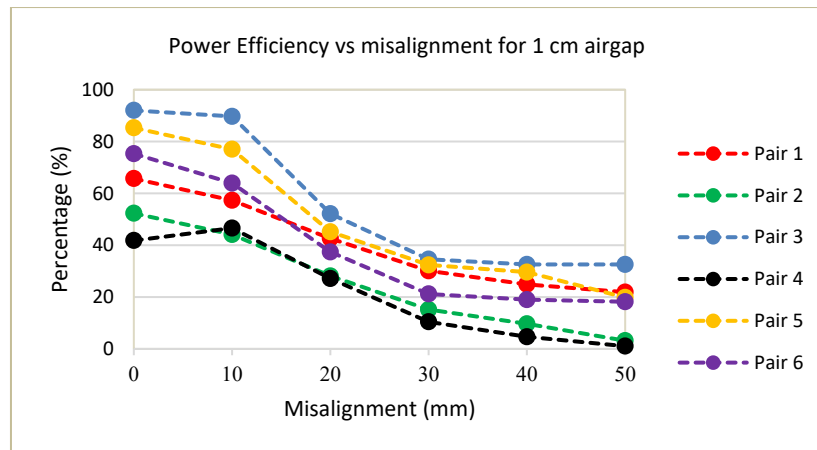
Fig. 9: Power efficiency at 1 cm air-gap.

Figure 10 shows the final prototype of this project. The experiment was conducted in the laboratory with the equipment provided. A 1 V DC voltage was supplied to the primary circuit and transferred to the secondary circuit. The figure below labels the power supply and oscilloscope to calculate the power obtained, and the primary and secondary sides of the system. As discussed previously, the best pair of ferrite cores is pair 3. As shown in Fig. 10, the proposed design of pair 3 is a U ferrite core at both the primary and secondary sides.
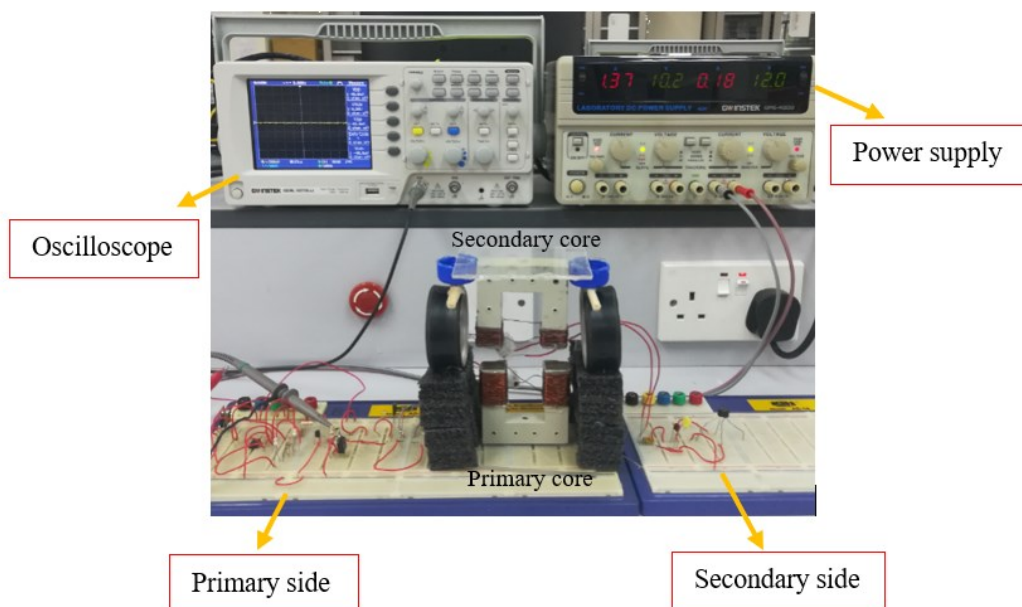
Fig. 10: Pair 3, best pair of U ferrite core.

To conclude, the best pair design was pair 3, which is the primary and secondary U ferrite core. The U ferrite core can reduce the leakage of magnetic flux and experience high magnetic flux density, as shown in Fig. 7. The magnetic flux density for this pair is the highest among all the pairs, which is 3.00E-03 T. Since this pair had a high magnetic flux density, the power transfer efficiency was also high. Figure 9 shows that pair 3 with high magnetic flux density also had high power transfer, which was 94.69 %. Therefore, the U shaped ferrite core is excellent for a wireless charging system because of its better magnetic flux distribution and reduced flux leakage. The design of the U ferrite core can reduce the flux leakage by feeding back the magnetic fluxes into the core and to the secondary side

[17]. Therefore, it is proven that the pair design of U ferrite cores at the primary and secondary sides was the best design that gave high magnetic flux and led to the maximum power efficiency of WPT, as mentioned by Pathipati et al. [13]. The extension of this research is that there is a pair where the ferrite core is not at both sides simultaneously. Previous research by Pathipati et al. [13], who also investigated the ferrite core, proposed that all the designs have a ferrite core in both the primary and secondary sides. Instead of using a ferrite core at both sides, this thesis investigated a different pair if one of the sides was a copper coil and the other was a ferrite core. Running the JMAG Designer and experiment test showed the lower power efficiency pair was pair 4, the primary I ferrite core and the secondary coil. This result was due to high magnetic flux and power transfer leakage occurring without the ferrite core at the secondary side.

Here, table 6 lists the comparison of power transfer obtained from these two techniques. The first technique was to obtain the magnetic flux density produced between the primary and secondary sides by running JMAG designer 14.0. The second technique was by experimenting with obtaining power transfer for each pair of the ferrite cores. In both techniques, pair 3 showed a high performance compared to other pairs. The different power efficiency from the experiment and JMAG Designer software was about 4.99 %. This slight difference in power efficiency was due to equipment limitations, inductance values, and other factors that led to the error.

Table 6: Power efficiency of pair 3 in simulation and experiment test

Method	JMAG Designer	Experiment
$P_{efficiency}$ (%)	94.69	89.7

Static wireless charging allows the recharging process to take place once the vehicles is located above the charging plate and must be static. Dynamic wireless charging is better suited to recharging the battery pack while in motion. However, the biggest elements that must be tolerated with the dynamic wireless charging system is air-gap and misalignment. Even though many studies show the effectiveness of a wireless pad design using ferrite cores, they rarely proposed an effective method to solve the problems by varying the geometric shape of the ferrites. The misalignment between the primary and secondary coils has an impact on the dynamic charging system performance. Among them are the power fluctuation from the transmitter to the receiver coils if the EV is moving. This power fluctuation also means that the coupling coefficient changed with motion. Meanwhile, for static charging, even with misalignment, the power fluctuation did not occur as the EV stayed in one place during the charging process. Therefore, the coupling coefficient stayed constant until the EV was fully charged.

4. CONCLUSION

In this paper, a prototype of a wireless charging system for EVs was developed. Before conducting the experiment, a literature review and simulation work were first carried out. Then, six pairs of ferrite cores were proposed in this study to select which pair showed better delivered power. The observation showed that the reduction of power transfer was caused by increasing the distance between the primary and secondary sides. The performance of the system in this study was that it can produce 1.8 W of delivered power. Although the prototype's performance was prolonged to charge the real EV charging system, this paper has proven that power can be transferred from one medium to another wirelessly using the inductive coupling principle.

ACKNOWLEDGEMENT

REFERENCES

[1]   Kumar PP, Abd Halim A. (2018) Electric-based national car proposal being developed. The Malaysian Reserve, https://themalaysianreserve.com/2018/07/26/electric-based-national-car-proposal-being-developed/

[2]   Tian Y, Li D, Tian J, Xia B. (2016) A Comparative Study of State-of-Charge Estimation Algorithms for Lithium-Ion Batteries in Wireless Charging Electric Vehicles. IEEE PELS Workshop on Emerging Technologies: Wireless Power, WoW 2016, no. 2016, pp. 186–190. doi: 10.1109/WoW.2016.7772089

[3]   Zaini SA, Yusoff SH, Abdullah AA, Khan S, Abd Rahman F, Nanda NN. (2020) Investigation of Magnetic Properties for Different Coil Sizes of Dynamic Wireless Charging Pads for Electric Vehicle (EV). IIUM Engineering Journal, 21(1): 23–32.
doi: https://doi.org/10.31436/iiumej.v21i1.1108

[4]   Pathipati V. K., Azeez N. A., Aditya K., Williamson S. S., Dohmeier and Botting N. C. (2016) Performance Analysis of a High-efficiency Multi-winding Wireless EV Charging System Using U-U and U-I Core Geometries, 2016 IEEE Transportation Electrification Conference and Expo (ITEC): pp. 1-8. doi: 10.1109/ITEC.2016.7520243.

[5]   Ahmad A, Alam MS, Chabaan R. (2017) A Comprehensive Review of Wireless Charging Technologies for Electric Vehicles. IEEE Transactions on Transportation Electrification, 4(1): 38–63. doi: 10.1109/TTE.2017.2771619.

[6]   Panchal C, Stegen S, Lu J. (2018) Review of Static and Dynamic Wireless Electric Vehicle Charging System. International Journal Engineering Science and Technology, 21(5): 922-937. doi: 10.1016/j.jestch.2018.06.015

[7]   Aditya K, Williamson S. (2019) Design Guidelines to Avoid Bifurcation in a Series-Series Compensated Inductive Power Transfer System. IEEE Transactions on Industrial Electronics, 66(5): 3973–3982. doi: 10.1109/TIE.2018.2851953

[8]   How long does it takes to charge an electric car? (2016) Pod Point, 2016. https://pod-point.com/guides/driver/how-long-to-charge-an-electric-car

[9]   Nanda NN, Yusoff SH, Toha SF, Hasbullah NF, Roszaidie NAS. (2020) A Brief Review: Basic Coil Designs for Inductive Power Transfer. Indonesian Journal of Electrical Engineering and Computer Science, 20(3):1703–1716.
doi: 10.11591/ijeecs.v20.i3.pp1703-1716.

[10]   National Academy of Engineering (2018) Frontiers of Engineering: Reports on Leading-Edge Engineering from the 2017 Symposium, The National Academies Press, , Washington, DC. 37-46. https://doi.org/10.17226/24906.

[11]   Varikkottil S, Febin Daya JL. (2019) Estimation of Optimal Operating Frequency for Wireless EV Charging System under Misalignment. Electronics (Switzerland), 8(3) :342.
https://doi.org/10.3390/electronics8030342.

[12]   Kalwar KA. (2017) A Design Method for Developing a High Misalignment Tolerant Wireless Charging System for Electric Vehicles. Journal of the International Measurement Confederation (Measurement). doi: https://doi.org/10.1016/j.measurement. 2017.12.013

[13]   Pathipati VK, Azeez NA, Aditya K, Williamson SS, Dohmeier N, Botting C. (2016) Performance Analysis of a High-efficiency Multi-winding Wireless EV Charging System Using U-U and U-I Core Geometries. IEEE Transportation Electrification Conference and Expo, ITEC 2016. doi: 10.1109/ITEC.2016.7520243.

[14] Wan Noor Nadira Wan Fauzi, Mohamad Syafiq Mazli, Sheroz Khan, Khairil Azhar Adnan, Ezzidin Hassan Aboadla, Majdee Tohtayong, Mashkuri Yaacob (2018) Beaming of Inductive Field with an Asymmetric Four-Coil Resonator for Wireless Power Transfer, 2018 7th International Conference on Computer and Communication Engineering (ICCCE). 301-305. https://doi.org/10.1109/ICCCE.2018.8539312.

[15] Patrick P. Mercier, Anantha P. Chandrakasan (2015) Ultra-Low-Power Short-Range Radios, Springer, Cham. 343-375. https://doi.org/10.1007/978-3-319-14714-7

[16] Aditya K, Sood VK, Williamson SS. (2017) Magnetic Characterization of Unsymmetrical Coil Pairs using Archimedean Spirals for Wider Misalignment Tolerance in IPT Systems. IEEE Transactions on Transportation Electrification, 3(2): 454–463.
doi: 10.1109/TTE.2017.2673847.

[17] Panchal C., Lu J. and Stegen S. (2013) Investigation of magnetic flux distribution of EV wireless charging systems, 2013 Asia-Pacific Symposium on Electromagnetic Compatibility (APEMC). 1-4. doi: 10.1109/APEMC.2013.7360652.

DESIGN AND ANALYSIS OF A MICROSTRIP PATCH ANTENNA AT 7.5 GHZ FOR X-BAND VSAT APPLICATION

Sarah Yasmin Mohamad[1*], Noralya Fatin Muzamil[1], Norun Farihah Abdul Malek[1], S.M.A. Motakabber[1], Rafidah Abd Malik[2] and Nurain Izzati Shuhaimi[3]

[1]*Department of Electrical and Computer Engineering, Faculty of Engineering, International Islamic University Malaysia, Jalan Gombak, 53100 Kuala Lumpur, Malaysia.*
[2]*Department of Instrumentation & Electronics Technology, The Science & Technology Research Institute for Defence (STRIDE) Malaysia.*
[3]*Faculty of Electrical Engineering, Universiti Teknologi MARA, 40450 Shah Alam, Selangor Darul Ehsan, Malaysia.*

Corresponding author: smohamad@iium.edu.my

ABSTRACT: In this paper, a microstrip patch antenna is designed to be used for X-band VSAT application at 7.5 GHz. The antenna is proposed to replace the massive and commonly used parabolic reflector antennas (46.0 inch × 29.3 inch × 13.5 inch (116.84 cm × 74.42 cm × 34.29 cm) with weight of 66.2 kg) in terms of portability due to its compact and lightweight features, with overall dimensions of 19.00 mm × 30.55 mm. The 7.5 GHz frequency is chosen based on the X-band frequency used in Malaysia, as reported by STRIDE. The microstrip patch antenna is first designed and simulated using CST Microwave Studio (CST MWS) and exhibits a good return loss (S_{11}) of -42.09 dB, a bandwidth of 399 MHz, directivity of 7.63 dB and gain of 7.18 dB. The antenna is then fabricated using RT/duroid ® High Frequency 5880 substrate with a dielectric constant of ε_r = 2.2, loss tangent of δ = 0.0009 and thickness of t = 1.574 mm. Next, the return loss and radiation pattern measurements are carried out to confirm the simulated results. The measurement of the antenna prototype provides a return loss S_{11} of -30.53 dB, bandwidth of 455 MHz, directivity of 5.51 dB and gain of 3.88 dB.

ABSTRAK: Di dalam kajian ini, antena jalurmikro dicadangkan untuk tujuan aplikasi jalur-X VSAT pada 7.5 GHz. Antena jalurmikro ini dicadangkan untuk menggantikan antena reflektor parabola yang besar dan biasa digunakan (46.0 inci × 29.3 inci × 13.5 inci (116.84cm × 74.42cm × 34.29cm) dengan berat 66.2kg), kerana cirinya yang mudah alih dengan fizikalnya yang kecil dan ringan, dan dimensi keseluruhan 19.00 mm × 30.55 mm. Frekuensi 7.5 GHz dipilih berdasarkan frekuensi jalur-X yang digunakan di Malaysia, seperti yang dilaporkan oleh STRIDE. Antena jalurmikro ini direka dan disimulasi menggunakan perisian CST Studio Gelombang Mikro (CST MWS) dan menghasilkan kehilangan pulangan yang baik S_{11} -42.09 dB, lebar jalur 399 MHz, keterarahan 7.63 dB dan gandaan 7.18 dB. Antena jalurmikro ini kemudiannya direalisasikan dengan menggunakan substrat RT / duroid ® Frekuensi Tinggi 5880 dengan pemalar dielektrik ε_r = 2.2, tangen kehilangan δ = 0.0009 dan ketebalan t = 1.574 mm. Seterusnya, pengukuran kehilangan pulangan dan corak radiasi dilakukan untuk mengesahkan keputusan simulasi. Pengukuran prototaip antena jalurmikro menunjukkan kehilangan pulangan S_{11} -30.53 dB, lebar jalur 455 MHz, keterarahan 5.51 dB dan gandaan 3.88 dB.

KEYWORDS: *microstrip patch antenna; VSAT application; X-band communication*

1. INTRODUCTION

As technology evolves at a very fast pace, antennas have become extremely important in the world of communication technology. Antennas play a major role in transmitting and/or receiving electromagnetic waves with respect to their specific direction and properties for the intended application [1]. There are various forms of antennas available in the market for instances wires, apertures, arrays, parabolic reflectors, lenses, and microstrip patches. The microstrip patch antenna is one of the most used antennas nowadays due to its excellent properties such as having a low profile and lightweight structure, having low cost, ease of fabrication and ease of integration with circuits [1]. A compact and lightweight antenna is always opted for VSAT, very small aperture terminal [2,3], satellite applications so that it can be easily carried around or accommodated on moving stations, especially for military communication services [4,5].

Generally, the frequency of military communication lies in the X-band range of 8-12 GHz [6-10]. However, according to the Science & Technology Research Institute for Defence (STRIDE), the range of X-band frequency used in Malaysia started at 7 GHz [11]. The common antennas used for this specific application are array and parabolic reflectors. The common dimensions of the parabolic reflectors that were used for X-band operation can reach up to 116.84 cm × 74.42 cm × 34.29 cm, with a load of 66.2 kg [11]. Also, this already omits the positioned case that can reach an additional load of 40 kg, which is compulsory to be used together with the parabolic reflectors. The evolution of military technologies nowadays requires an antenna that is not hefty, portable, and easy to carry around or accommodate on moving stations [4,5]. Hence, a microstrip patch antenna is proposed in this paper to fulfil this requirement where it can provide the advantages of having a lightweight, low profile and compact structure compared to the parabolic reflectors which are more massive, bulkier, and difficult to use on a moving vehicle. The microstrip patch antenna is designed to be working at 7.5 GHz which lies in the frequency range of X-band services in Malaysia [11].

2. DESIGN OF THE MICROSTRIP PATCH ANTENNA

The theoretical dimensions of the microstrip patch antenna proposed in this paper are determined using equations (1) to (5);

$$Patch\ Width = \frac{v_o}{2f_r}\sqrt{\frac{2}{\varepsilon_r+1}} \tag{1}$$

$$Patch\ Length = L_{eff} - 2\Delta L \tag{2}$$

$$L_{eff} = \frac{c}{2f_r\sqrt{\varepsilon_{eff}}} \tag{3}$$

$$\Delta L = \frac{(\varepsilon_{eff}+0.3)\left(\frac{w}{h}+0.264\right)}{(\varepsilon_{eff}-0.258)\left(\frac{w}{h}+0.8\right)} \tag{4}$$

$$\varepsilon_{eff} = \frac{\varepsilon_r+1}{2} + \frac{\varepsilon_r-1}{2}\left(\frac{1}{\sqrt{1+\frac{12h}{w}}}\right) \tag{5}$$

By using equations (1) to (5), the length, *L* and the width, *W* of the 7.5 GHz rectangular microstrip antenna is calculated to be *L* = 12.5 mm and *W* = 15.8 mm. Nevertheless, these equations are just the basic step to determine the initial dimension of the antenna for use at 7.5 GHz, and the performance results may slightly differ from the target research's demand. Thus, a huge number of recent studies and designs are referred in order to support the finding

of the optimum dimensions. Moreover, the antenna is designed using RT/duroid ® High Frequency 5880 substrate with a dielectric constant of ε_r = 2.2, loss tangent of δ = 0.0009 and thickness of t = 1.574 mm. The substrate is chosen due to its exceptional dielectric constant uniformity over a wide frequency range [12]. Fig. 1(a) and Table 1 depict the final dimensions of the proposed antenna.

The antenna is then manually fabricated. First, the CST file is converted into a Gerber File as the layout for the board, followed by printing out the layout with the exact dimensions. The board (substrate RT/duroid ® High Frequency 5880) is cut according to the exact dimension before the copper for the interior layers was printed on top of the board. Finally, the etching process is carried out to completely remove the unwanted copper. The performance of the fabricated antenna is measured to confirm the simulated results. The fabricated antenna can be seen in Fig. 1(b).
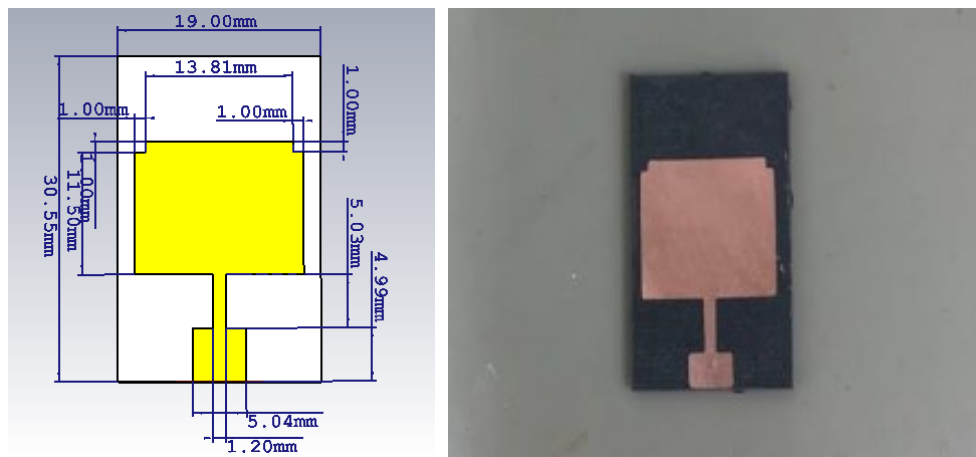
Fig. 1: (a) The front view of the microstrip patch antenna with dimensions, and (b) the front view of the fabricated antenna.

Table 1: The parameters and values of the microstrip patch antenna.

Parameters	Values
Patch width	13.81 mm
Patch length	12.54 mm
Transformer width	1.20 mm
Transformer length	5.03 mm
Feeding width	5.04 mm
Feeding length	4.99 mm
Patch thickness	0.035 mm
Dielectric and ground plane width	19.00 mm
Dielectric and ground plane length	30.55 mm
Dielectric thickness	1.575 mm
Ground plane thickness	0.35 mm

3.   SIMULATED AND MEASURED RESULTS

The simulated and measured results of the antenna performances are presented and discussed in this section. Figure 2 shows the simulated and measured return loss of the proposed antenna. In Fig. 2(a), it can be observed that the microstrip patch antenna is resonating at the targeted frequency of 7.5 GHz with return loss, S_{11} = -42.09 dB, which proved that the designed antenna is well-matched to the 50 ohm reference impedance. Figure

2(b) shows the measurement result of the return loss of the antenna prototype using the Vector Network Analyzer, as shown in Fig. 3(a). The measurement result depicts a return loss of S_{11} = -30.53 dB which differs slightly from the simulated result, but still shows a very good transmission from the antenna.
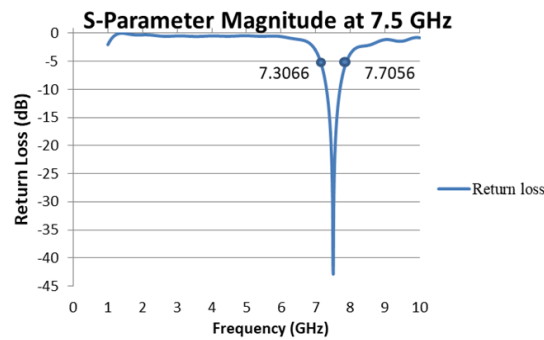
(a)
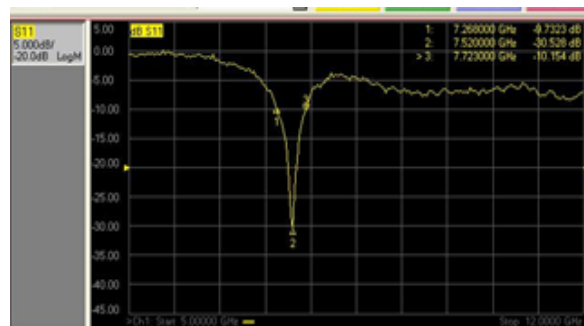
(b)

Fig. 2: The (a) simulated and (b) measured return loss S_{11} of the microstrip patch antenna.

From these results, the bandwidth of the antenna can also be observed. The simulated result in Fig. 2(a) depicts a bandwidth of BW = 399 MHz, while the measured result in Fig. 2(b) depicts a bandwidth of BW = 455 MHz. These bandwidth results are calculated based on equation (6);

$$Bandwidth = F_H - F_L \qquad\qquad (6)$$

where: F_H = higher frequency at S_{11} at -10 dB

F_L = lower frequency at S_{11} at -10 dB

(a)   (b)

Fig. 3: The measurement of the microstrip patch antenna prototype with (a) Vector Network Analyzer and in (b) Anechoic chamber.

Figure 4 and 5 show the simulated and measured 3D far field radiation pattern of the microstrip patch antenna. Moreover, Fig. 6 and Fig. 7 show the simulated and measured polar far field radiation pattern (in E-plane and H-plane) of the microstrip patch antenna. The antenna's radiation pattern is measured in an anechoic chamber, as shown in Fig. 3(b).

It can be seen from Fig. 4 to Fig. 7 that the antenna exhibits a directive pattern in the 2D and 3D view. From the simulation, it is observed that the directivity and gain of the antenna at the intended frequency of 7.5 GHz are 7.63 dB and 7.18 dB, respectively. However, the directivity and gain for the measured antenna prototype are 5.51 dB and 3.88 dB, respectively. It is believed that the gain between the simulation results and measurement results varies due to the mismatch of impedance matching and also due the losses that occur during the measurement.

(a)   (b)   (c)
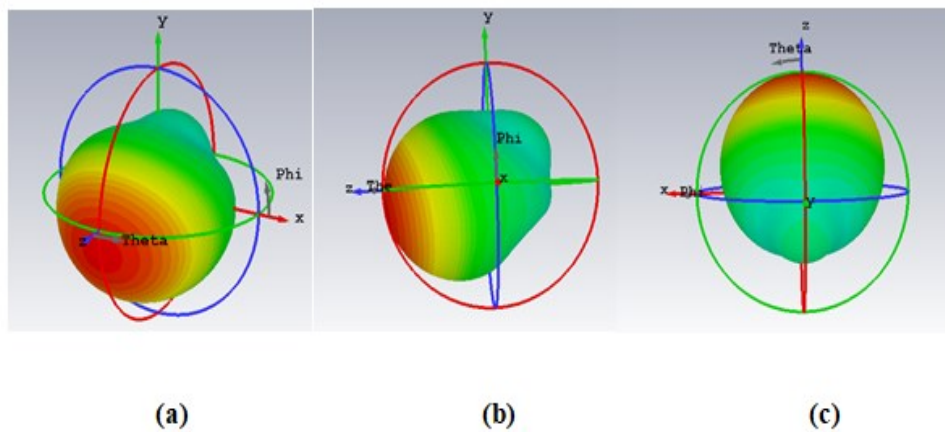
Fig. 4: The simulated 3D far field radiation pattern in (a) isometric, (b) y-axis and (c) x-axis view of the microstrip patch antenna at 7.5 GHz.

(a)   (b)   (c)
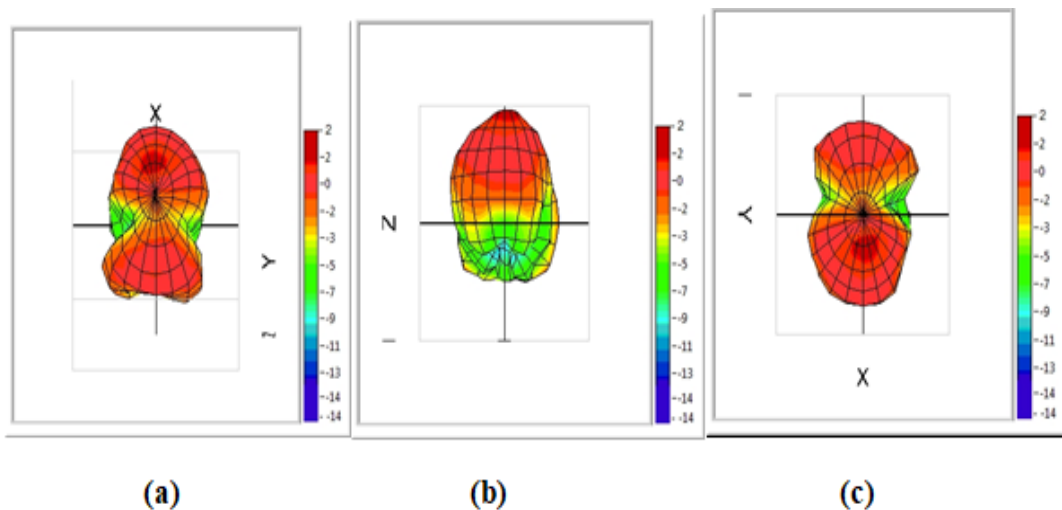
Fig. 5: The measured 3D farfield radiation pattern from (a) below, (b) front and (c) top view of the microstrip patch antenna at 7.5 GHz.

Finally, Table 2 summarizes the overall performances (simulated and measured) of the microstrip patch antenna in terms of return loss, bandwidth, directivity, gain, and main lobe direction.
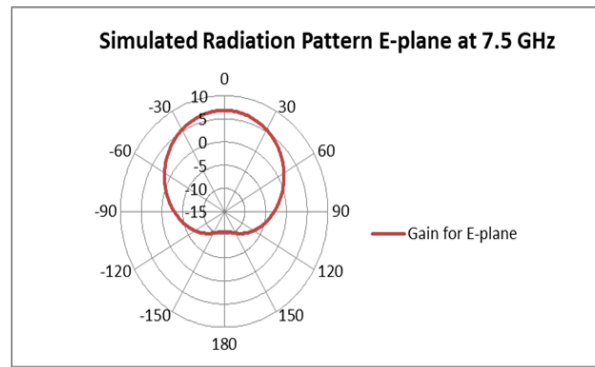
(a)
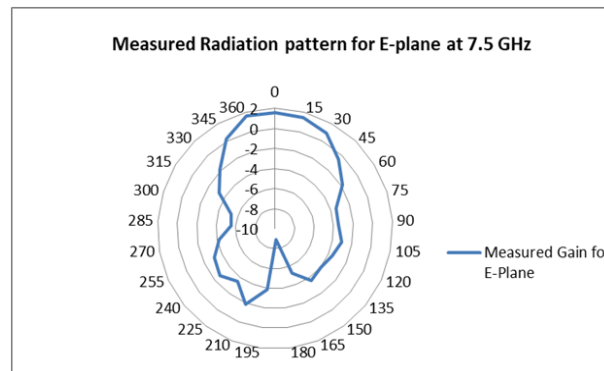
(b)

Fig. 6: The (a) simulated and (b) measured polar far field radiation pattern for E-plane of the microstrip patch antenna at 7.5 GHz.
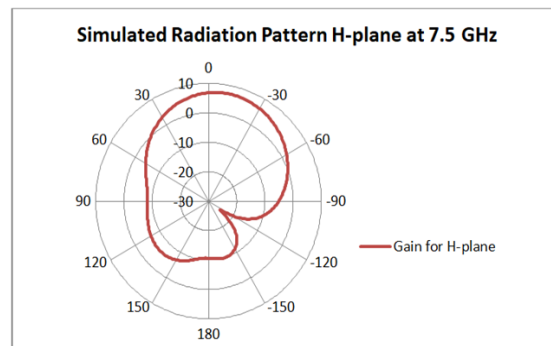
(a)
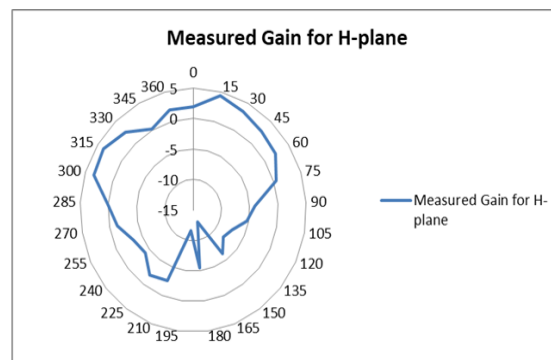
(b)

Fig. 7: The (a) simulated and (b) measured polar far field radiation pattern for H-plane of the microstrip patch antenna at 7.5 GHz.

Table 2: The overall performance (simulated and measured) of the microstrip patch antenna at 7.5 GHz, in terms of return loss, bandwidth, directivity, gain and main lobe direction

Antenna performances	Simulation	Measurement
Return loss (dB)	-42.09	-30.53
Bandwidth (MHz)	399	455
Directivity (dB)	7.18	3.88
Gain (dB)	7.63	5.51
Main lobe direction (degree)	11.0	15.0

4. CONCLUSION

A microstrip patch antenna for X-band VSAT application at 7.5 GHz has been designed, simulated, and tested. The antenna has a compact and lightweight structure with an overall dimension of 19.00 mm × 30.55 mm. The antenna depicted a good simulated performance with a return loss of -42.09 dB, bandwidth of 399 MHz, directivity of 7.18 dB. and gain of 7.63 dB. The prototype of the antenna is then tested where the return loss S_{11} measurement is performed using a Vector Network Analyzer, while the radiation pattern measurement is carried out in an anechoic chamber. The antenna prototype exhibits a measured return loss S_{11} of -30.53 dB, bandwidth of 455 MHz, directivity of 3.88 dB, and gain of 5.51 dB. The proposed antenna can be a good replacement and a solution for the massive and bulkier parabolic reflector antenna for X-band VSAT application at 7.5 GHz and will also be suitable for use on a moving vehicle or station.

REFERENCES

[1] Balanis CA. (2016) Antenna Theory - Analysis and Design. Hoboken, John Wiley & Sons, Inc.
[2] Madiawati H, Suryana J. (2016) Design and implementation of mobile antenna VSAT with microstrip array based at Ku Band Frequency. In Proceedings of the 10th International Conference on Telecommunication Systems Services and Applications (TSSA), pp. 1-5.
[3] Asci Y, Curuk E, Yegin K, Ozdemir C. (2016) Improved splash-plate feed parabolic reflector antenna for Ka-Band VSAT applications. In Proceedings of the 46th European Microwave Conference (EuMC), pp. 1283-1286.
[4] Ruslan AA, Mohamad SY, Badron K, Ismail AF, Abdul Malek NF, Mohd Isa FN. (2020) Study of microstrip patch array antenna for side lobe suppression in the X-band region using uniform, binomial and tschebyscheff excitation methods. IIUM Engineering Journal, 21(1): 61-72.
[5] Mohamed N, Mohamad SY, Abdul Malek NF, Mohd Isa FN. (2019) A compact and lightweight microstrip antenna array with Wilkinson power divider for X-band application at 9.5 GHz. In Proceedings of the IEEE Asia-Pacific Conference on Applied Electromagnetics (APACE); pp. 1-5.
[6] ESA-Satellite frequency bands. Available: https://www.esa.int/Applications/ Telecommunications _Integrated_Applications/Satellite_frequency_bands.
[7] Ishtaique-ul Huque MT, Hosain MK, Islam S, Chowdhury A. (2011) Design and performance analysis of microstrip array antennas with optimum parameters for X-band applications. International Journal of Advanced Computer Science and Applications, 2(4): 81-87.
[8] Samsuzzaman M, Islam MT. (2014) Inverted S-shaped compact antenna for X-band applications. Scientific World Journal: 11.
[9] Singh V, Mishra B, Singh R. (2015) A compact and wide band microstrip patch antenna for X-band applications. In Proceedings of the 2nd International Conference on Advances in Computing and Communication Engineering, pp. 296-300.

[10] Ahmad Mustafa AM, Mohamad SY, Abdul Malek NF, Mohd Isa FN and Rafiqul IM. (2018) A wideband circularly-polarized spiral antenna for cubesat application. Journal of Telecommunication, Electronic and Computer Engineering, 10(1-8): 17-20.

[11] Model 1098 Fly Away Integrated Terminal System (2017) Operations and Maintenance Manual, AVL Technologies, 900-085-001-D.

[12] RT/duroid 5870 and 5880 Data Sheet – Rogers Corporation. Available: https://rogerscorp.com/-/media/project/rogerscorp/documents/advanced-connectivity-solutions/english/data-sheets/rt-duroid-5870---5880-data-sheet.pdf

Hidayat et al.

WAVELET DETAIL COEFFICIENT AS A NOVEL WAVELET-MFCC FEATURES IN TEXT-DEPENDENT SPEAKER RECOGNITION SYSTEM

SYAHRONI HIDAYAT[1,2]*, MUHAMMAD TAJUDDIN[3], SITI AGRIPPINA ALODIA YUSUF[2], JIHADIL QUDSI[4] AND NENET NATASUDIAN JAYA[5]

[1]Department of Agricultural Engineering, University of Mataram, Mataram City, Indonesia
[2]Research and Development, Sekawan Institute, Mataram City, Indonesia
[3]Department of Computer Science, Universitas Bumigora, Mataram City, Indonesia
[4]Department of Medical Record, Politeknik Medica Farma Husada, Mataram City, Indonesia
[5]Depaertment of Management, Universitas Mahasaraswati Mataram, Mataram City, Indonesia

*Corresponding author: syahronihidayat@unram.ac.id

ABSTRACT: Speaker recognition is the process of recognizing a speaker from his speech. This can be used in many aspects of life, such as taking access remotely to a personal device, securing access to voice control, and doing a forensic investigation. In speaker recognition, extracting features from the speech is the most critical process. The features are used to represent the speech as unique features to distinguish speech samples from one another. In this research, we proposed the use of a combination of Wavelet and Mel Frequency Cepstral Coefficient (MFCC), Wavelet-MFCC, as feature extraction methods, and Hidden Markov Model (HMM) as classification. The speech signal is first extracted using Wavelet into one level of decomposition, then only the sub-band detail coefficient is used as the feature for further extraction using MFCC. The modeled system was applied in 300 speech datasets of 30 speakers uttering "HADIR" in the Indonesian language. K-fold cross-validation is implemented with five folds. As much as 80% of the data were trained for each fold, while the rest was used as testing data. Based on the testing, the system's accuracy using the combination of Wavelet-MFCC obtained is 96.67%.

ABSTRAK: Pengecaman penutur adalah proses mengenali penutur dari ucapannya yang dapat digunakan dalam banyak aspek kehidupan, seperti mengambil akses dari jauh ke peranti peribadi, mendapat kawalan ke atas akses suara, dan melakukan penyelidikan forensik. Ciri-ciri khas dari ucapan merupakan proses paling kritikal dalam pengecaman penutur. Ciri-ciri ini digunakan bagi mengenali ciri unik yang terdapat pada sesebuah ucapan dalam membezakan satu sama lain. Penyelidikan ini mencadangkan penggunaan kombinasi Wavelet dan Mel Frekuensi Pekali Cepstral (MFCC), Wavelet-MFCC, sebagai kaedah ekstrak ciri-ciri penutur, dan Model Markov Tersembunyi (HMM) sebagai pengelasan. Isyarat penuturan pada awalnya diekstrak menggunakan Wavelet menjadi satu tahap penguraian, kemudian hanya pekali perincian sub-jalur digunakan bagi pengekstrakan ciri-ciri berikutnya menggunakan MFCC. Model ini diterapkan kepada 300 kumpulan data ucapan daripada 30 penutur yang mengucapkan kata "HADIR" dalam bahasa Indonesia. Pengesahan silang K-lipat dilaksanakan dengan 5 lipatan. Sebanyak 80% data telah dilatih bagi setiap lipatan, sementara selebihnya digunakan sebagai data ujian. Berdasarkan ujian ini, ketepatan sistem yang menggunakan kombinasi Wavelet-MFCC memperolehi 96.67%.

1. INTRODUCTION

Speaker recognition is the process of recognizing the speaker from his speech by comparing the sound biometrics of the words he has spoken with his pronunciation model, which has previously been used as a reference and stored in a database [1]. Speaker recognition can be used in many aspects; this technology is expected to make daily life easier by accessing personal devices remotely. As a biometric tool, speaker recognition also can be applied in secure access voice control, information structuring, customizing services, and forensic investigation. As a non-invasive biometric, speech can be collected without the knowledge of the speaker [2]. The speaker recognition system first appeared in 1962, in an article published by Nature entitled Voiceprint Identification. The research claimed had developed a method for identifying an individual with high success rates. The research developed a visual representation of speech called a spectrogram. However, the first successful implementation in speaker recognition was a text-dependent system developed in 1977, using Euclidean distance as a verification decision. In the last several years, many researchers have been interested in this field and made significant improvements to it [3], especially in feature extraction and classification.

In speaker recognition, feature extraction is a necessary process that can affect the performance of the system recognition. These features are used to represent and describe the signal. Each speaker has a unique vocal characteristic; this leads to two different features: morphological and behavioral features. Morphological features are determined by the length of the vocal tract and the size of vocal folds. At the same time, the behavioral features are determined by education, background, parental influence, personality type, place of birth, and language [1]. There are a few properties of good features, such as the ease of measurement and extraction, robustness, uniqueness, and independence between one feature and another.

Several feature extraction techniques are commonly used in speaker recognition, such as the Mel Frequency Cepstral Coefficient (MFCC), Gammatone Frequency Cepstral Coefficient (GFCC), Wavelet, and the combination of Wavelet-MFCC. Each of the methods has its advantages and disadvantages. Feature extraction using MFCC is found in [4], the research employed MFCC to extract the features. MFCC is an excellent features extractor; it can form features to mimic human hearing [5]. Although it was said that MFCC is the best feature extractor, especially in distant-talking speaker recognition [1], in the matter of robustness towards noise, GFCC is better [6]. Ayoub et al. [7] employed GFCC as a features extractor in speaker identification system over VoIP network. The Discrete Wavelet Transformation (DWT) has also become popular and is employed in a variety of applications. The extension version of DWT, Wavelet Packet Transform (WPT), has superior presentation to DWT; it gives more flexibility in decomposition since WPT decomposes both details and approximations [8]. It is stated that the features extracted using a wavelet give equal accuracy to MFCC. Aside from that, many previous kinds of research claim that extracting features using wavelet yielded better results compared to MFCC [9]. WPT was employed to extract features on TIMIT and TALUNG databases [10]. However, it is shown that in the speaker recognition system, MFCC is commonly used as a feature extractor and can be combined with another new method such as DNN [1].

Several previous types of research have combined Wavelet and MFCC, forming MFCC based on wavelet to overcome the noisy environment. Application of both, in combination integrates the merits of both methods. MFCC can represent the speech spectrum in a compact form and is based on the model of human auditory perception, but

the FFT process can cause the loss of information [5,11]. Meanwhile, the wavelet can map the signal into the time and frequency domain; thus, no information is lost in this process [9]. MFCC was combined with 3 level decomposition of DWT to extract signal uttering digits 0-9 in the Indian language [12]. WPT-MFCC was combined employing all of the sub-band obtained from WPT to find the MFCC [13]. MFCC was combined with Wavelet sub-band coefficient (SBC) in an isolated word for speaker recognition [14]. The combination of Wavelet-MFCC yielded better results than conventional MFCC and GMM [15].

The modeling and decision making in speaker recognition also vary, starting from the widely used HMM [4,16], vector quantization (VQ) [9], SVM [14], the classical technique Gaussian Mixture Model (GMM) [10,12,13], and ANN [17,18]. However, from the decision-making model, HMM is more suitable for modeling speaker features, especially in text-dependent speaker recognition systems, where there are two types of HMM, Ergodic and left-right [19].

Much previous research that employed Wavelet-MFCC as feature extraction either used approximated sub-band coefficient [9], or a combination of approximated and detailed sub-band of the sub-band [12,17]. There are three aims in this research. First, we determine the best sub-band coefficient as an input for another feature extraction using MFCC. Second, we determine the best wavelet family in Wavelet-MFCC feature extraction method. We also try to find the influence of gender in the recognition system. Then, we compare the proposed method with other feature extractions such as conventional MFCC, MFCC + delta, and MFCC + delta-delta. As for the decision-making, we employed HMM.

2. RELATED WORKS

As the algorithm evolves for speaker recognition, one of the best algorithms is Mel Frequency Cepstral Coefficient (MFCC) [20]. Many previous researchers have used this algorithm to extract features from a sound signal. MFCC was employed as a feature extractor in the NTT database, and the Japanese Newspaper Article Sentences (JNAS) database and Vector Quantization (VQ) were used as a recognizer [21]. The obtained result shows excellent accuracy, which is 98.75%.

It is said that GFCC works better than MFCC to extract features from noisy signals and shows an encouraging result. [7] studied and evaluated the performance of the method in text-independent over VoIP networks and obtained high identification rates. [10] applied WPT to extract features in two public databases, TALUNG and TIMIT. The research proposed a new method based on a multilayer neural network to reduce the dimension of wavelet packet features. The recognition rate obtained was 94% in the TALUNG database. WPT was also applied in speaker identification for security systems based on the energy of speaker utterance and achieved a 96.6% of recognition rate [11].

The hybrid features were based on Wavelet-MFCC [12]. The features were extracted in ten isolated Hindi digits using 3 level decomposition of Wavelet, then extracted using MFCC on every sub-band. The methods yielded 100% average performance. Adam et al. [22] proposed an improved feature extraction method called Wavelet Cepstral Coefficient (WCC) for isolated speech recognition in the English alphabet. The research replaced the DFT with DWT in order to obtain the merit of the wavelet transform. The coefficient from DWT is then used as a feature vector to calculate the log power spectrum and DCT.

3. METHODOLOGY

In this research, generally, the proposed method consists of four steps: collecting database, preprocessing, feature extraction, and speech recognition. Figure 1 shows the steps of the proposed method.
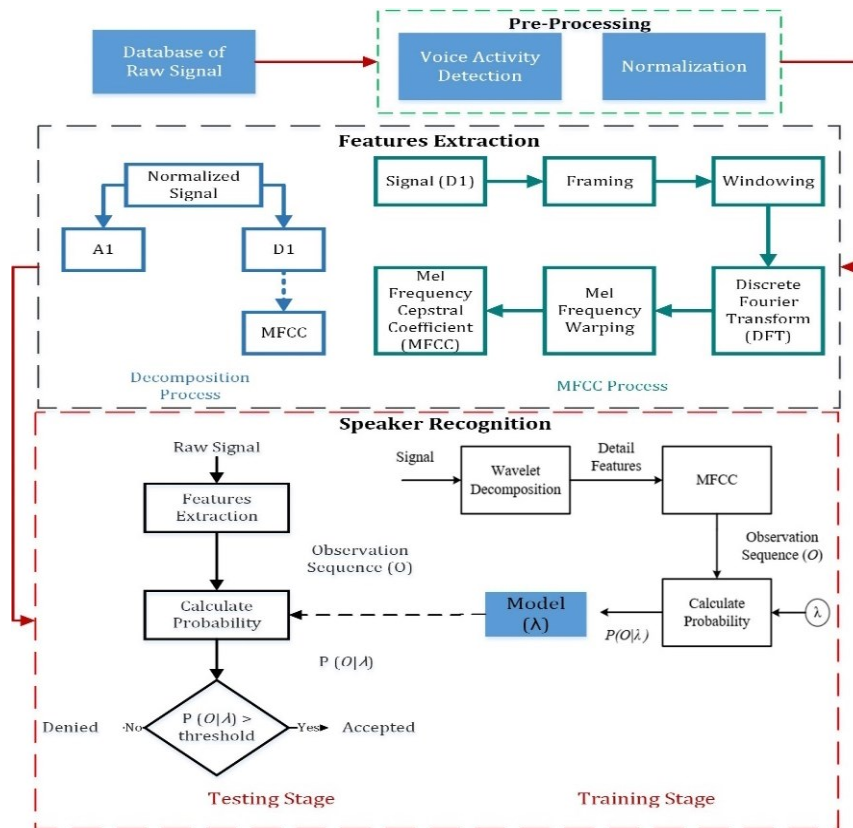
Fig. 1: Proposed method.

3.1 Database

The database used in this research was created with the help of 30 volunteers consisting of 20 male and 10 female adults. All of the speakers were native Indonesian speakers and asked to utter the word "HADIR" in Indonesian, which in English means "PRESENT," and repeat the word ten times. The total dataset obtained was 300 datasets. In accordance with collecting the sound database, this research used a smartphone integrated with a microphone and used Audacity software. There were two settings done in recording; the first was an environmental setting, and the second was the recording properties setting in Audacity software. In the environmental setting, the recording was taken indoors to reduce the noise, and the recorder was placed 0.5 meters from the speaker; the Audacity setting was shown in the following table.

Table 1: Recording properties

No.	Variable	Value
1	Recording channel	Mono
2	Frequency Sampling	8096
3	Bits per Sample	16-bit PCM
4	Format	*.wav

3.2 Preprocessing

The aim of preprocessing is to enhance the quality of the signal. There were three steps in the preprocessing stage that consisted of noise reduction, voice activity detection, and signal normalization. In the first step, we applied a pre-emphasis filter to reduce the noise. Pre-emphasis is also able to emphasize the high frequency in the signal. Generally, the coefficient used in pre-emphasis oscillates between 0.9-0.97. In this research, we used $\alpha = 0.97$. Therefore, the following Eq. (1) is used to calculate pre-emphasis, where y[n] is the output, x[n] is the input signal n, and x[n-1] is the previous signal.

$$y[n] = x[n] - \alpha * x[n-1] \tag{1}$$

The next step was applying the voice activity detection algorithm. By applying this algorithm, the silent sound in the signal was removed [23]. This algorithm was developed by [23], and this algorithm uses the value of energy E as a threshold to distinguish the silent sound in the signal. The energy of the signal can be calculated using Eq. (2).

$$E = \frac{1}{N}\sum_{n=1}^{N}|x(n)|^2 \tag{2}$$

The last step of preprocessing was signal normalization, S_{norm}. Signal normalization aims to obtain the same magnitude value. By doing this, the maximum magnitude value is ±1. Eq. (3) was used to obtain the normalized signal. S_{norm} is the normalized signal, and $max|S|$ is the maximum value of the signal.

$$Snorm = \frac{S}{max\ |S|} \tag{3}$$

3.3 Feature Extraction

Feature extraction is a process to extract features from the signal. The extracted features must be unique and have high variability, among other features. In this step, two different methods were combined, wavelet and MFCC. The goal of this combination was to take advantage of both methods.

For wavelet feature extraction, this research applied Discrete Wavelet Transformation (DWT). Wavelet transformation is suitable for analyzing stationary and non-stationary signals since it can localize the signal in the time-frequency domain and has multi-resolution characteristics [12]. The signal then decomposed into one level decomposition. The decomposition itself was a convolution and decimation process of a signal by a factor of two [24], the result was two sub-bands for each level, sub-band A1, also known as approximation coefficient, obtained from low pass filter (LPF) g[n] and sub-band D, known as detail coefficient, obtained from high pass filter (HPF) h[n]. One Level decomposition is shown in Fig. 2.
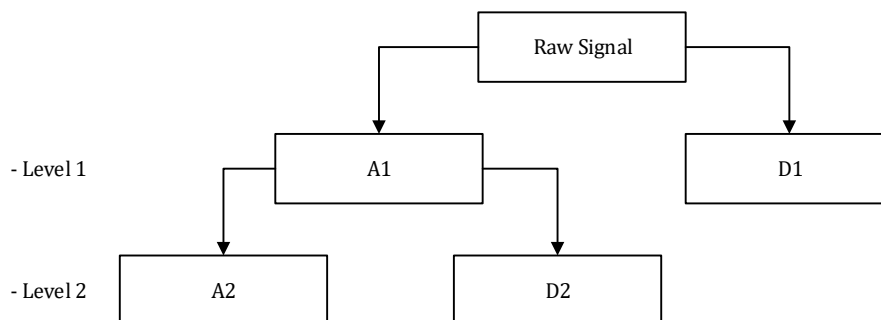
Fig. 2: DWT with two levels of decomposition.

The implementation of LPF and HPF shown in Eq. (4) and (5) respectively.

$$A[n] = \sum_{k=-\infty}^{\infty} s[k]g[2n-k] \tag{4}$$

$$D[n] = \sum_{k=-\infty}^{\infty} s[k]h[2n-k] \tag{5}$$

Then, the signal detail coefficient (D1) was used as a feature vector for further extraction using MFCC. The process of feature extraction using MFCC is shown in Fig. 3.
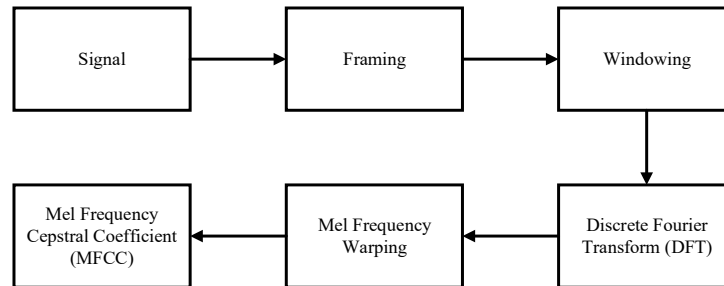
Fig. 3: MFCC feature extraction.

One of the most used and popular algorithms for speaker recognition is MFCC, which is also known for representing the information of the speaker's vocal tract [25]. Extracting features using MFCC consists of several steps: framing, windowing, discrete Fourier transform (DFT), Mel frequency warping, and Mel frequency cepstral coefficient.

The framing step, also called signal segmentation, is a process to divide the signal into equal sizes of frames; hence, the voice signal was the non-stationary signal. This process assumed the signal as a stationary signal for a short duration. The frame size used in this research was N = 0.025 seconds, with the overlap M = 0.01 second. Figure 4 shows how framing works. The framing process caused discontinuity in the framed signal; thus, the windowing function was applied to remove it. We used Hamming window function to eliminate the discontinuity. In terms of calculating the Hamming window, Eq. (6) was used.

$$w(n) = 0.54 - 0.46 \cos\left(\frac{2\pi n}{N}\right) \tag{6}$$

where $0 \leq n \leq N$ and N is frame length.
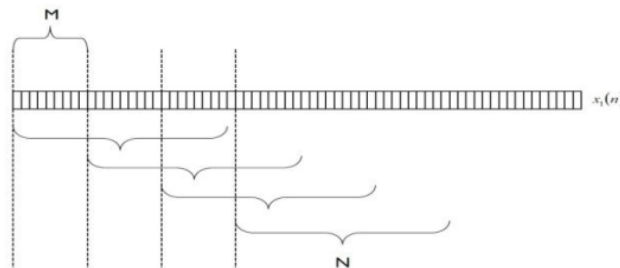
Fig. 4: Framing step.

Transforming the signal from the time domain into the frequency domain was the next step. The process was applied using discrete Fourier transformation. We used a total of 512 FFT points. The algorithm is shown in Eq. (7).

$$X[k] = \sum_{n=0}^{N-1} x[n]e^{-j2\pi nk/N} \tag{7}$$

where $X[k]$ is the result of DFT and $x[n]$ is the n-th discrete signal.

After transforming the signal using DFT, the next step was warping the signal using a triangle filter. This process is called Mel frequency warping. This was applied because the signal sound was different from the perception of human hearing, where signal sound did not have frequencies on a linear scale. Regarding the Mel frequency value, *mel(f)* and triangle filter $H_m[k]$ were used. The following Eq. shows how to calculate *mel(f)* and $H_m[K]$, respectively.

$$mel(f) = 1125 \ln \left(1 + \frac{f_{hz}}{700}\right) \tag{8}$$

$$H_m[k] = \begin{cases} 0 & k < f[m-1] \\ \frac{(k-f[m-1])}{(f[m]-f[m-1])} & f[m-1] \le k \le f[m] \\ \frac{(f[m+1]-k)}{(f\{m+1\}-f[m])} & f[m] \le k \le f[m+1] \\ 0 & k > f[m+1 \end{cases} \tag{9}$$

We applied a 26-triangle filter, which means we obtained 26 coefficients, but for features, we used the first 13 coefficients as MFCC. The first aim of this research was to determine the best wavelet coefficient as a feature when combined with MFCC. To achieve this, we decomposed the signal into levels 1 and 2 using Haar. The second aim was to determine the best wavelet family when combining with MFCC; hence, we employed all wavelet families, decomposed the signal into one level decomposition, and combined only the detailed coefficient channel with MFCC. Figure 5 shows the process of feature extraction using the combination of wavelet-MFCC.
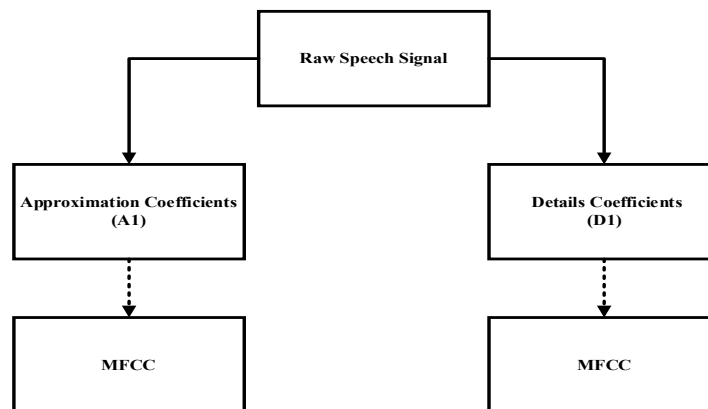
Fig. 5: Wavelet-MFCC feature extraction process.

3.4 Speaker Recognition System

There are various algorithms for speaker recognition, the most used and proven to have excellent performance is Hidden Markov Model (HMM). HMM works by modeling a stochastic process defined by a set of states and several mixtures per state [26]. HMM can solve two characteristics of problems; the first is state-based characteristics, which include the hidden state and the observation state. In the second, there were two types of data consisting of the observation-state sequence and hidden-state sequence [4]. HMM has two types, Ergodic and left-right. The left-right HMM was used to model the speech signal because the speech cannot be repeated to the previous state. Moreover, generally, the observation probability distribution of HMM is modeled by Gaussian Mixture Model (GMM) [19]. The following elements model an HMM:

$$\lambda = (A, B, \pi) \tag{10}$$

A is state transition probability defined as Eq. (11), π is prior probability state distribution defined as Eq. (12), and B is observation probability distribution defined as Eq. (13). This definition represents the left-right type of HMM.

$$A = \{a_{ij}\} \tag{11}$$

Where, $a_{ij} = 0$ for $j < i$, and $j > i + 1$. $a_{NN} = 1$, $a_{Nj} = 0$, for $j < N$.

$$\pi = \{\pi_i\} \tag{12}$$

Where, $\pi_i = 1$ for $I = 1$, and $\pi_i = 0$ for $I \neq 0$.

$$B = b_j(k) \tag{13}$$

Generally, the HMM observation probability distribution is defined as Gaussian Mixture Model (GMM). However, in practice, this model gives problems in computation. Therefore, the Euclidean distance probability approach can be the alternative solution [19]. It is defined as Eq. (14) and Eq. (15):

$$d(O_t, \mu_j) = \sqrt{\sum_{k=1}^{M} \left(\frac{1}{1+d(O_t, \mu_j)}\right)^2} \tag{14}$$

$$d(O_t, \mu_j) = \sqrt{\sum_{k=1}^{M} (O_{tk} - \mu_{jk})^2} \tag{15}$$

The built model of the recognition system is shown in Fig. 6. The signal was first decomposed into one level using wavelet, and then the sub-band detail coefficient was used as a feature for further extraction using MFCC. The probability of the DWT-MFCC features then calculated probability to be used as a model. In this research, the speaker recognition system used is shown in Fig. 7.
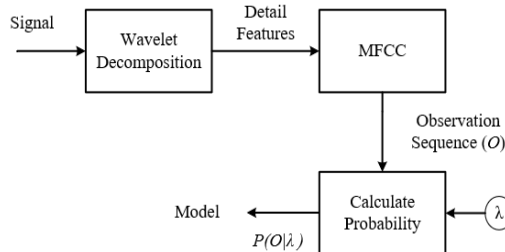
Fig. 6: Speaker recognition system for the training phase.
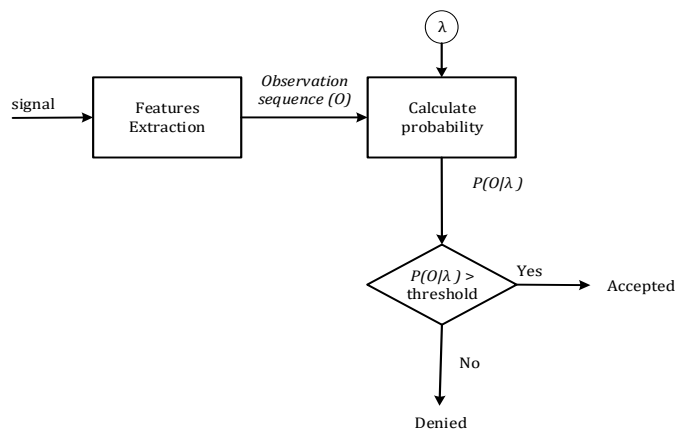
Fig. 7: Speaker recognition system for testing phase.

The features of the signal were extracted using the proposed method. The extracted features were then called the observation sequence (O), and fed into the Viterbi algorithm to measure the probability towards lambda (λ). The Viterbi algorithm was employed to find the most likely sequence of hidden states, and the result was an observed sequence. Lambda is a probability sequence obtained from the training model. The model was then compared to the observation sequence to obtain the classification result.

3.5 Evaluation and Validation

The accuracy of the classification result was evaluated using Eq. (16) [2,27]:

$$Accuracy = \frac{NSRC}{TNS} \times 100 \qquad (15)$$

$NSRC$ is the number of speakers recognized correctly and TNS is the total number of speakers.

The K-fold validation method was applied to keep the variation of accuracy low; this method divided the dataset into K datasets. The first dataset was used as a testing dataset, while the second and third K were used as training datasets. Furthermore, the process was repeated, where the second dataset used as testing datasets, the first, third K were used as training datasets. The process was repeated until K times, and the total accuracy is the number of accuracies divided by K. In this research, the number of folds used is 5; thus, in each process, the testing dataset was 20% of the total dataset [28].

4. RESULTS AND ANALYSIS

This research proposed a feature extraction algorithm for speaker recognition based on the combination of wavelet-MFCC. We used 300 sound signals obtained from 30 male and female adult volunteers uttering the word "HADIR" in Indonesian, and each volunteer repeated the word ten times. Each signal was then preprocessed to enhance the quality by applying pre-emphasis and normalization.

4.1 Determining the Best Wavelet Coefficient

To obtain the result for the first aim, we employed one- and two-level decomposition using the Wavelet Haar family on both levels of decomposition. The coefficients A1, D1, and a combination of coefficients A1 and D1 were used as features. The next step was extracting those coefficients using MFCC, 13 first coefficients were then used as features. The recognition process was modeled using HMM. We obtained accuracy, as shown in Table 2.

Table 2: Accuracy result

Coefficient	Accuracy (%)	
	Level 1	Level 2
A	92	90
D	95	78
A+D	95	85

The highest accuracy was obtained on the one-level decomposition using coefficient D and the combination of A + D, where the accuracy was 95%. Nevertheless, increasing the decomposition level reduced the accuracy of the system recognition, where the highest accuracy obtained was 90%. Hence, it is not necessary to increase the decomposition level

as it reduces accuracy. Moreover, the use of the sub-band detail coefficient yielded the best accuracy.

4.2 Determining Best Wavelet Family

Once we figured out the best coefficient, we employed all wavelet families and decomposed the signal into one level decomposition. This allowed us to determine the best wavelet family. The one-level decomposition yielded two sub-bands, approximation and detail. The next step was finding the MFCC of the detail coefficient obtained from the previous step. This way, we obtained wavelet-MFCC features. In order to determine the best family wavelet type when combined with MFCC, we employed all family wavelet types. Then, in the recognition step, we employed HMM to build the model; we evaluated its accuracy using the k-fold cross-validation method described above. The recognition results are shown in Table 3.

Table 3: Recognition result of Wavelet-MFCC for each of wavelet family

Type	Acc (%)	Type	Acc (%)	Type	Acc (%)	Type	Acc (%)	Type	Acc (%)
bior 1.1	96.33	coif7	92.33	db11	94.33	db32	92.00	symlet16	93.33
bior 1.3	94.67	coif8	94.33	db12	93.67	db33	93.00	symlet17	93.67
bior 1.5	94.67	coif9	93.00	db13	93.33	db34	91.33	symlet18	93.00
bior 2.2	94.33	coif10	91.67	db14	93.67	db35	91.00	symlet19	92.67
bior 2.4	93.33	coif11	91.33	db15	92.33	db36	91.00	symlet20	94.33
bior 2.6	93.00	coif12	94.00	db16	93.00	db37	93.00	rbio1.1	96.33
bior 2.8	94.33	coif13	90.33	db17	92.67	db38	93.00	rbio1.3	94.67
bior 3.1	94.00	coif14	92.00	db18	92.33	symlet2	95.33	rbio1.5	92.67
bior 3.3	93.67	coif15	93.00	db19	93.00	symlet3	92.67	rbio2.2	95.33
bior 3.5	93.33	coif16	92.00	db20	91.67	symlet4	93.67	rbio2.4	94.00
bior 3.7	94.00	coif17	91.00	db21	91.67	symlet5	92.67	rbio2.6	92.67
bior 3.9	93.67	**db1**(haar)	**96.67**	db22	91.33	symlet6	93.67	rbio2.8	94.00
bior 4.4	93.33	db2	95.33	db23	92.33	symlet7	93.00	rbio3.1	95.33
bior 5.5	93.33	db3	93.67	db24	90.33	symlet8	92.33	rbio3.3	93.33
bior 6.8	94.00	db4	94.33	db25	93.33	symlet9	93.33	rbio3.5	93.00
coif1	95.00	db5	93.67	db26	91.33	symlet10	94.33	rbio3.7	94.67
coif2	93.33	db6	93.67	db27	91.67	symlet11	91.67	rbio3.9	93.00
coif3	92.00	db7	94.67	db28	91.33	symlet12	93.00	rbio4.4	93.67
coif4	92.67	db8	94.00	db29	92.00	symlet13	93.33	rbio5.5	92.67
coif5	95.00	db9	94.33	db30	91.33	symlet14	93.00	rbio6.8	94.00
coif6	93.33	db10	93.33	db31	92.33	symlet15	92.67	dmey	94.33

exp (added terms): bior – Wavelet Biorthogonal, coif – Wavelet Coiflet, db – Wavelet Daubechies, sym – Wavelet Symlet, rbio – Wavelet Reverse biorthogonal, dmey – Wavelet Dmeyer

4.3 Gender Influence in Speaker Recognition

In this research, we also experimented to find out the influence of the speaker's gender in the recognition system, and there were two focuses on evaluating the influence of gender. First was the influence of gender on each of the wavelet families as a coefficient detail. Second was the influence of gender on each of extracting method, such as MFCC, MFCC + delta, and MFCC + delta-delta.

In the first condition, as shown in Table 4, we obtained better average accuracy for female speakers than the male speakers for each wavelet family. The obtained average accuracy was about 96% for females and about 92% for male speakers. The low accuracy of male speakers was due to the large gap between each wavelet family's highest and lowest accuracy. The obtained gap was up to 8%. While on the female speaker, the gap

between the highest and lowest accuracy was up to 5%, where the highest accuracy was 98.17%, and the lowest was 93.00%.

Table 4: Gender influence the wavelet families

Wavelet Family	Average Accuracy (%)					
	Male	Female	Max Male	Min Male	Max Female	Min Female
Daubechies	90.89	95.76	95.61	87.44	98.17	93.83
Coiflet	91.19	95.11	93.50	88.00	98.17	93.17
Symlet	91.49	95.80	93.50	90.22	98.17	93.00
Biorthogonal	92.41	96.41	95.06	90.78	98.17	93.83
Rbiorhogonal	92.24	96.58	95.11	90.22	98.17	94.83
Dmeyer	92.89	96.50	92.89	92.89	96.50	96.50
Average	91.85	96.03	94.28	89.93	97.89	94.19

Nevertheless, from each wavelet family, it can be said that the best accuracy was obtained using Wavelet Daubechies. The obtained result is shown in Table 3, and Table 4 stated that Wavelet Daubechies is the best wavelet family to combine with the proposed method to create Wavelet-MFCC feature extraction.

In the second condition, based on the testing result in Table 5, we obtained the highest average accuracy using the proposed method in male speaker recognition, where the average accuracy was 95.61%. However, for female speaker recognition, there was no difference between the methods; the average accuracy was varied for each of the methods. The accuracy of male and female speakers was influenced by the acoustical characteristic, fundamental frequency or F0, formant frequency, vocal tract length, and vocal fold. The obtained result was in line with the previous research by [29], [30].

Table 5: Gender influence accuracy

Method	Accuracy (%)	
	Male	Female
Proposed Method (db1- MFCC)	95.61	98.17
MFCC	94.00	99.00
MFCC + Delta	94.50	99.00
MFCC + Delta-Delta	93.00	98.00

In the previous research, the recognition of male speakers gives better accuracy than for the female speakers. It was believed that the result was influenced by the F0 of females being higher than males [31]. In males, F0 was around 110 Hz in the range of 100-146 Hz, while in females, around 200 Hz in the range of 188-221 Hz.

4.4 Comparison of other Features Extraction Method

Table 6 shows the comparison of the proposed method compared to conventional MFCC, MFCC + delta, and MFCC + delta-delta.

Table 6: Comparison of Features Extraction Method

Methods	Accuracy (%)
Proposed Method (db1 - MFCC)	96.67
MFCC	95.67
MFCC + Delta	96.00
MFCC + Delta-Delta	94.67

In this research, we proposed using a detail coefficient as a feature in the combination of wavelet-MFCC feature extraction for speaker recognition. The voice that we heard was obtained from the combination of voice sound, resonance, and articulation. The voice sound was the output of the vocal fold vibration; the voice sound was amplified and modified by the vocal tract resonator. The vocal tract resonator includes the throat, mouth cavity, and nasal passage. This resonator makes the sound that distinguishes individual persons. Whereas articulation is the modified process to produce recognizable words.

The resonator can distinguish each person because the produced sound has different variability frequencies. In male and female sounds, the variability lies in high frequency. Specifically, the speaker's identity lies in the area where the formant frequency is higher [32]. The higher frequency is generally analogized as noise, but in the case of sound, the noise component plays an essential role in perceiving sound quality. This noise component is usually modeled as white noise, where the spectrum is not flat and portrays the different shapes of spectral [33]. It is affected by the glottal opening, flow rate, and the shape of the vocal tract. The interaction among spectral shape, the relative level of harmonic, and noise energy in the sound source influence the perception of the quality of the sound. Hence, it can be concluded that the use of wavelet decomposition separates the voice sound and resonance where the voice sound lies in the approximation coefficient, whereas the resonance, which is the speaker identity, lies in the detail coefficient.

5. CONCLUSION

In this research, we employed wavelet-MFCC to extract the features from the sound signal and HMM for recognition. There were several aims in this research. First, determining the best sub-band coefficient. According to the experiment result, the best sub-band was sub-band detail in one level decomposition, where the accuracy was 95%. Once we found out the best sub-band, the second aim was to determine the best wavelet family combined with MFCC. From 105 types of wavelet families, we obtained the best wavelet family, Daubechies order 1 (Haar), where the accuracy was 96.67%. Although the gender type of the speaker also influenced the type of wavelet family, we experimented to find the best wavelet family for recognition of each gender. Based on the result, we concluded that the wavelet Daubechies was the best wavelet family to extract the features on both genders. Therefore, it can be said that from the obtained result, wavelet Daubechies was the best wavelet coefficient to combine with MFCC. Then, we compared the proposed method to other methods such as conventional MFCC, MFCC + delta, and MFCC + delta-delta. From the comparison, we obtained that the best method for feature extraction was the combination of db1 – MFCC.

For future research, the proposed method needs to be evaluated using more speaker datasets and in noisy environments so the system's robustness can be seen. In addition, the proposed method needs to be investigated in the speaker-independent recognition system, emotion, gender, and speech recognition. Finally, real-time speaker recognition for the proposed method also needs to investigated further.

ACKNOWLEDGEMENT

REFERENCES

[1] Tirumala SS, Shahamiri SR, Garhwal AS, Wang R. (2017) Speaker identification features extraction methods: A systematic review. Expert Systems with Applications, 90:250-271. doi:10.1016/j.eswa.2017.08.015

[2] Alsulaiman M, Mahmood A, Muhammad G. (2017) Speaker recognition based on Arabic phonemes. Speech Communication, 86:42-51. doi:10.1016/j.specom.2016.11.004

[3] Shaver, Clark D. and Acken, John M. (2016) A Brief Review of Speaker Recognition Technology. Electrical and Computer Engineering Faculty Publications and Presentations. 350. http://pdxscholar.library.pdx.edu/ece_fac/350

[4] Wei, Y. (2020). Adaptive Speaker Recognition Based on Hidden Markov Model Parameter Optimization. IEEE Access, 8: 34942-34948. doi:10.1109/ACCESS.2020.2972511

[5] Huang, Xuedong and Acero, Alex, Hon H-W. (2001) Spoken Language Processing: A Guide to Theory, Algorithm, and System Development. Upper Saddle River, NJ, United States.

[6] Zhao X, Wang Y, Wang D. Robust. (2014) Speaker Identification in Noisy and Reverberant Conditions. ICASSP, IEEE Int Conf Acoust Speech Signal Process – Proc, 22(4):3997-4001. doi:10.1109/ICASSP.2014.6854352

[7] Ayoub B, Jamal K, Arsalane Z. (2016) Gammatone frequency cepstral coefficients for speaker identification over VoIP networks. 2016 Int Conf Inf Technol Organ Dev IT4OD. doi:10.1109/IT4OD.2016.7479293

[8] Daqrouq K, Al Azzawi KY. (2012) Average framing linear prediction coding with wavelet transform for text-independent speaker identification system. Comput Electr Eng, 38(6):1467-1479. doi:10.1016/j.compeleceng.2012.04.014

[9] Amelia F, Gunawan D. (2019) DWT-MFCC Method for Speaker Recognition System with Noise. 7th Int Conf Smart Comput Commun ICSCC 2019, pp.1-5. doi:10.1109/ICSCC.2019.8843660

[10] Lung SY. (2007) Efficient text independent speaker recognition with wavelet feature selection based multilayered neural network using supervised learning algorithm. Pattern Recognit, 40(12):3616-3620. doi:10.1016/j.patcog.2007.05.010

[11] Wu J Da, Lin BF. (2009) Speaker identification using discrete wavelet packet transform technique with irregular decomposition. Expert Syst Appl, 36(2 PART 2):3136-3143. doi:10.1016/j.eswa.2008.01.038

[12] Kumar P, Chandra M. (2011) Hybrid of wavelet and MFCC features for speaker verification. Proc 2011 World Congr Inf Commun Technol WICT 2011, pp. 1150-1154. doi:10.1109/WICT.2011.6141410

[13] Turner C, Joseph AA. (2015) Wavelet Packet and Mel-Frequency Cepstral Coefficients-Based Feature Extraction Method for Speaker Identification. Procedia Comput Sci, 61:416-421. doi:10.1016/j.procs.2015.09.177

[14] Kishore KVK, Sharrefaunnisa S, Venkatramaphanikumar S. (2015). An efficient text dependent speaker recognition using fusion of MFCC and SBC. 1st Int Conf Futur Trends Comput Anal Knowl Manag ABLAZE 2015, (Ablaze):18-22. doi:10.1109/ABLAZE.2015.7154960

[15] Rathor S, Jadon RS. (2017) Text indpendent speaker recognition using wavelet cepstral coefficient and butter worth filter. 8th Int Conf Comput Commun Netw Technol ICCCN, pp.1-5. doi:10.1109/ICCCNT.2017.8204079

[16] Badrit N, Tadjt ABC, Gargourt C, Ramachandrant K. (2002) On the use of wavelet and Fourier transforms for speaker verification. The 2002 45th Midwest Symposium on Circuits and Systems, 2002. MWSCAS-2002., Tulsa, OK, USA, pp. III-344. doi: 10.1109/MWSCAS.2002.1187043

[17] Adam TB, Salam MS, Gunawan TS. (2013) Wavelet based cepstral coefficients for neural network speech recognition. IEEE ICSIPA 2013 - IEEE Int Conf Signal Image Process Appl, pp.447-451. doi:10.1109/ICSIPA.2013.6708048

[18] Rozario MS, Thomas A, Mathew D. (2019) Performance Comparison of Multiple Speech Features for Speaker Recognition using Artifical Neural Network. 9th International Conference on Advances in Computing and Communication (ICACC), Kochi, India, pp. 234-239. doi: 10.1109/ICACC48162.2019.8986182 19.

[19] Hidayat S. Hidayat R. Adji TB. (2016) Speech Recognition of Kv-Patterned Indonesian Syllable Using Mfcc, Wavelet and Hmm. Kursor, 8(2):67. doi:10.28961/kursor.v8i2.63

[20] Sharma G, Umapathy K, Krishnan S. (2020) Trends in audio signal feature extraction methods. Appl Acoust. 158:107020. doi:10.1016/j.apacoust.2019.107020

[21] Sunitha C, Chandra E. (2015) Speaker recognition using MFCC and improved weighted vector quantization algorithm. International Journal of Engineering and Technology, 7(5):1685-1692.

[22] Adam TB, Salam MS, Gunawan TS. (2013) Wavelet Cepstral Coefficients for Isolated Speech Recognition. TELKOMNIKA, 11(5):2731-2738. doi:10.11591/telkomnika.v11i5.2510

[23] Hidayat S, Hasanah U, Rizal AA. (2016) Algoritma Penghapus Derau / Silence Dan Penentuan Endpoint Dengan Nilai Ambang Terbobot Untuk Sinyal Suara. In: Seminar Nasional APTIKOM (SEMNASTIKOM), pp.320-323.

[24] Sekkate S, Khalil M, Adib A. (2018) Fusing wavelet and short-term features for speaker identification in noisy environment. Int Conf Intell Syst Comput Vision, ISCV 2018. May:1-8. doi:10.1109/ISACV.2018.8354030

[25] Jahangir, R. Teh, YW. Memon, NA. Mujtaba, G. Zareei, M. Ishtiaq, U. AKhtar, MZ. Ali, I. (2020) Text-independent Speaker Identification through Feature Fusion and Deep Neural Network. IEEE Access, 8: 32187-32202. doi:10.1109/ACCESS.2020.2973541

[26] El-henawy IM, Khedr WI, Elkomy OM, Abdalla AMI. (2014) Recognition of phonetic Arabic figures via wavelet based Mel Frequency Cepstrum using HMMs. HBRC J, 10(1):49-54. doi:10.1016/j.hbrcj.2013.09.003

[27] Maurya A, Kumar D, Agarwal RK. (2018) Speaker Recognition for Hindi Speech Signal using MFCC-GMM Approach. Procedia Comput Sci, 125:880-887. doi:10.1016/j.procs.2017.12.112

[28] Picard RR, Cook RD. (1984). Cross-Validation of Regression Models. J Am Stat Assoc, 79(387):575-583. doi:10.2307/2288403

[29] Li L, Zheng TF. (2015) Gender-dependent feature extraction for speaker recognition. In IEEE China Summit and International Conference on Signal and Information Processing, ChinaSIP 2015 - Proceedings, pp 509-513. doi:10.1109/ChinaSIP.2015.7230455

[30] Kanervisto A, Vestman V, Sahidullah M, Hautamaki V, Kinnunen T. (2017) Effects of gender information in text-independent and text-dependent speaker verification. ICASSP, IEEE Int Conf Acoust Speech Signal Process - Proc., pp. 5360-5364. doi:10.1109/ICASSP.2017.7953180

[31] Titze IR. (1989) Physiologic and acoustic differences between male and female voices. J Acoust Soc Am, 85:1699-1707. doi:https://doi.org/10.1121/1.397959

[32] Lee Y, Keating P, Kreiman J. (2019) Acoustic voice variation within and between speakers. J Acoust Soc Am, 146(3):1568-1579. doi:10.1121/1.5125134

[33] Zhang Z. (2016) Mechanics of human voice production and control. J Acoust Soc Am, 140(4):2614-2635. doi:10.1121/1.4964509

IN-IDRIS: MODIFICATION OF IDRIS STEMMING ALGORITHM FOR INDONESIAN TEXT

FEBIARTY WULAN SUCI, NUR HAYATIN* AND YUDA MUNARKO

Department of Informatics, Engineering Faculty,
University of Muhammadiyah Malang, Malang, Indonesia

*Corresponding author: noorhayatin@umm.ac.id

ABSTRACT: Stemming has an important role in text processing. Stemming of each language is different and strongly affected by the type of text language. Besides that, each language has different rules in the use of words with an *affix*. A large number of the words used in the Indonesian language are formed by combining root words with *affixes* and other combining forms. One of the problems in Indonesian stemming is having different types of *affixes*, and also having some *prefixes* that changes according to the first letters of the root words. Implementing Idris stemmer for Indonesian text is of interest because Indonesia and Malaysia have the same language root. However, the results do not always produce the actual word, because the Idris algorithm first removes the prefix according to Rule 2. This elimination directly affected the Idris stemmer result when implemented to Indonesian text. In this study, we focus on a modified Idris stemmer (from Malay) to IN-Indris with Indonesia context. In order to test the proposed modification to the original algorithm, Indonesian online novels excerpts are used to measure the performance of IN-Idris. A test was conducted to compare the proposed algorithm with other *stemmers*. From the experiment result, IN-Idris had an accuracy of approximately 82.81%. There was an increased accuracy up to 5.25% when compared to Idris accuracy. Moreover, the proposed stemmer is also running faster than Idris with a gap of speed of around 0.25 seconds.

ABSTRAK: Stemming mempunyai peranan penting dalam pemprosesan teks. Stem setiap bahasa adalah berbeza dan sangat dipengaruhi oleh jenis bahasa teks. Selain itu, setiap bahasa mempunyai peraturan yang berbeza dalam penggunaan kata dengan awalan. Sebilangan besar kata-kata yang digunakan dalam bahasa Indonesia dibentuk dengan menggabungkan kata akar dengan afiks dan bentuk gabungan lain. Salah satu masalah dalam bahasa Indonesia adalah mempunyai pelbagai jenis awalan, dan juga mempunyai beberapa awalan yang berubah sesuai dengan huruf pertama kata dasar. Menerapkan stemder Idris untuk teks Indonesia adalah minat kerana Indonesia dan Malaysia mempunyai akar bahasa yang sama. Namun, hasilnya tidak selalu menghasilkan kata yang sebenarnya, kerana algoritma Idris pertama kali menghapus awalan menurut Peraturan 2. Penghapusan ini secara langsung mempengaruhi hasil batang Idris ketika diterapkan ke teks Indonesia. Dalam kajian ini, kami memfokuskan pada stemmer Idris yang diubahsuai (dari bahasa Melayu) ke IN-Indris dengan konteks Indonesia. Untuk menguji cadangan pengubahsuaian pada algoritma asli, petikan novel dalam talian Indonesia digunakan untuk mengukur prestasi IN-Idris. Ujian dilakukan untuk membandingkan algoritma yang dicadangkan dengan stemmer lain. Dari hasil eksperimen, IN-Idris mempunyai ketepatan sekitar 82,81%, ada peningkatan ketepatan hingga 5,25% dibandingkan dengan ketepatan Idris. Selain itu, stemmer yang dicadangkan juga berjalan lebih cepat daripada Idris dengan jurang kelajuan sekitar 0.25 saat.

1. INTRODUCTION

Finding the root words of derivative words is still a challenge, especially for text processing. Stemming is a process to transform derivative words into root words. Stemming methods are widely applied in Natural Language Processing (NLP) and also text mining especially when involved in extracting information that is used to find new information from various written sources [1], such as sentiment analysis [2]. Stemmer, an algorithm for stemming, has an important role in text processing because the results of stemming are used to extract features in the text. For the text mining area, stemmer is important in the initial stage, which has a function to convert unstructured text into structured representative formats that can then be processed by machines [3]. Implementing stemmer for text processing has proven to improve the performance of text pre-processing [4]. It also has an impact on instance classification results using Indonesian Quran translation [5], and reduces the different forms of a word into a root word [6].

Stemming of each language is different, and it is strongly influenced by the type of text language. Moreover, each language has different rules in the use of words with *affixes* [7]. However, for some languages stemming can be achieved by applying the appropriate morphological rules [8]. Indonesian used Bahasa Indonesia as a formal language. In the Indonesian text, words are formed from morphological rules [9]. A large number of the words used in the Indonesian language are formed by combining root words with *affixes* and other combining forms [10]. Indonesian has stemming problems that are specific to the language. One of the problems is having different types of *affix*, another is having some *prefixes* that change according to the first letters of the root words. For example, the *prefix* "*me-*" becomes "*mem-*" when attached to a root word starting with the letter "*b-*" as in "*mem-buat*" (to make, in English), but it becomes "*meny-*" when attached to a root word starting with the letter "*s-*" as in "*meny-*[s]*impan*" (to store, in English) [11].

In Indonesian text processing, some researchers used a stemming algorithm such as Nazief and Adriani (N&A) [12], Confix Stripping Algorithm (CS) [13], and Enhanced Confix Stripping (ECS) [14], which are developed for Indonesian text. However, several researchers also implemented *stemmers* from other languages such as Idris stemmer (for Malay language) [15], and Potter stemmer (for English) [16]. In this study, we focus on Idris stemmer. This is interesting because Indonesian and Malay have the same language root. Malay has similarities with the Indonesian language, so the Idris algorithm can also be used to process Indonesian texts [17].

Earlier research compared the processing time and accuracy of the Nazief and Adriani (N&A) stemmer with the Idris stemmer [8]. The research applied to Indonesian text to know which algorithm was better. For the evaluation, the researcher used five story texts to compare the stemming result. The result presented that the N&A stemmer obtained a 97% accuracy with a processing time of approximately 0.03 seconds per word, while the Idris stemmer reached an accuracy of 91% but needed around 0.02 seconds per word for processing. Another research focused on analysing stemmer strength in Indonesian text documents based on the parameters of the *icf* and *wc* values, and also analysed the level of accuracy and speed based on word results. As a result, Idris stemmer was accurate and succeeded in producing root words from Indonesian text, but it still had shortcomings namely, increasing the possibility of *overstemming*. The results of stemming are not appropriate because the Idris algorithm first removes the *prefix* according to Rule 2. Elimination directly refers to the Rule 2 effect on the results of stemming, where the

algorithm does not always result in the actual word. Moreover, other experiments [8] have proven that the Idris algorithm has an advantage in the speed of the stemming process but the level of accuracy is still low.

To obtain a better level of accuracy and faster process for the stemming, this study proposed to modify the Idris algorithm with Indonesian text. We measured the accuracy and the speed of the stemming process as a result of the modification of the Idris algorithm. The modified algorithm is called IN-IDRIS.

2.   RELATED WORK

2.1   Indonesian Stemmers Algorithm

The Nazief and Adriani (N&A) stemmer [12] is based on morphological rules that are interlinked and grouped, then encapsulate the allowed part of the word and do not include *affixes* such as *prefixes*, *suffixes*, and *confixes* to get the root of a word. The performance of this algorithm is based on three parts, they are grouping *affixes*, usage rules and the establishment of limits, and use of the dictionary. The dictionary becomes an important part because it is used to check whether a word has met its stem or not. Before the *affix* removal process, several things must be considered in the uses of this algorithm, such as *inflexion suffixes*, derivation *suffixes*, derivation *prefixes*, and *prefix* disallowed *suffixes* [18]. The performance of the N&A approach is the most complex approach.

Confix Stripping (CS) algorithm is an Indonesian stemmer [6] that was developed based on improvement from the Nazief & Adriani algorithm. CS stemmer added an additional stemming step called *LoopPengembalianAkhiran* (final return loop). This algorithm was done by adding some *prefix* rules and modifying *prefix* rules, particularly adding rule precedence. From comparing performance results, it is shown that the CS algorithm has better performance than the N&A stemmer [13]. The development of the CS stemmer is the Enhanced Confix stripping (ECS) [14]. From the experiment, the result showed that the ECS stemmer succeeded in increasing the accuracy from the modification of the ECS stemmer using a non-deterministic method that was able to identify the possibilities of root words that can be formed in a single word through the candidate list [19].

An Indonesian stemmer based on the dictionary is the VEGA stemmer. This algorithm used rule sets to determine whether an *affix* can be removed from a word. The rules are accessed in the order they are presented in the code. When one rule fails, the algorithm proceeds to the next. A major shortcoming of the VEGA approach is the absence of a lookup stage where words are only compared to a dictionary of known root words. Stemming continues as long as the word contains *affix* letters, often leading to *overstemming*. Moreover, the algorithm does not cater to cases where recoding is required. Finally, the reliance on strict rules necessitates that the rules be correct and complete, and prevents ad hoc restoration of *affix* combinations [20].

2.2 Idris Stemmer Algorithm

The Idris stemmer is developed by Idris et al. that is designed for the Malay language. The Malay language has similarities with the Indonesian language [16], so this algorithm is also applicable to Indonesian texts. This algorithm has two dictionaries (general and local dictionaries) in determining stemming results [17]; where the local dictionary contained a list of root words in the Malay history vocabularies. This algorithm implements only two patterns of the rules which are *prefix* and *suffix* rules. By using only two patterns of *affixes* that are *prefix* and *suffix*, it can reduce the numbers of the rule sets.

Idris algorithm first checks the words against *prefix* rules then checks the words against the *suffix* rules. If not, many errors such as *overstemming* can occur [15]. Idris algorithm adopts Arifin and Setiono's assumption that each Indonesian word has two *prefixes* and three *suffixes* [21].

Idris algorithm applied a different recoding scheme and progressive stemming. The algorithm checks the dictionary after each step, stopping and returning the stemmed word if it is found. The scheme works as follows: first, after checking for the word in the dictionary, the algorithm tests if the *prefix* of the word matches a *prefix* that may require recoding; second, if recoding is required, it is performed and the resultant word is searched for in the dictionary, while if recoding is not required, the *prefix* is removed as usual and the word is checked in the dictionary; third, having removed a *prefix*, *suffix* removal is attempted and, if it succeeds, the word is checked in the dictionary; and, last, the algorithm returns to the second step with the partially stemmed word. There are two variants of this algorithm: the first changes *prefix* and then performs recoding, while the second does the reverse [22]. The Idris algorithm description is referred to in Table 1.

Table 1: The description of Idris algorithm

ALGORITHM 1: Idris Algorithm
1. Check the word in the dictionary. If the word is found, then the word is considered as the root word and exit. Otherwise, proceed to the next step.
2. Check the word in the *prefix* rules. If the word matches the *prefix* rules, check the *prefix* pattern and the first letter of the stem word. Otherwise, go to step 7.
3. If the *prefix* pattern matches the pattern in Rule 2, then apply Rule 2 to the word. Otherwise, remove the *prefix* and go to step 6.
4. Check the *prefix* of the word, adjust the pattern in Rule 2. If it matches the fourth rule, then check the stem word in the dictionary and proceed to the next step. Otherwise, remove the *prefix* and go to step 6.
5. If the word is not in the dictionary, then return to step 4, otherwise, remove the *prefix* and proceed to the next step.
6. Check the word in the dictionary. If the word found, then the word is considered as the root word and exit. Otherwise, proceed to the next step.
7. Check the words in the *suffix* rules. If it matches with the *suffix* rules, then remove

Prefixes usually give rise to spelling variations and exceptions in the root word. Errors may occur during the *stemming* process where the stemmed word is not complete. The Idris algorithm has another rule called Rule 2 where it can be applied to the *prefix* removal only [15]. The rule is if the word *stemming* is not complete, checking the first letter of the word and if the word starts with a vowel, then:

1. Add *t* after removing *men-* or *pen-*

2. Add *k* after removing *meng-* or *peng-*

3. Add *s* after removing the *meny-* or *peny-*

4. Add *f* or *p* after removing *mem-* or *pem-*

3. MODIFICATION OF IDRIS ALGORITHM

In this section, we explain the proposed modification of the Idris algorithm, called IN-Idris. From the results of experiments and analysis of the Idris stemmer, there are some

examples of words that are not appropriate. For example, the word "*memasukkan*" (to enter, in English) found the root word "*pasuk*". The word is in the dictionary and the algorithm will consider it as the root word, but the word "*pasuk*" is not meant, and the actual root word is "*masuk*" (enter, in English).

The results of stemming are not appropriate because the Idris algorithm first removes the *prefix* according to Rule 2. In the example, after removing the *prefix* "*mem-*" the word "*asuk*" is obtained, so the fourth rule in Rule 2 after removing the prefix "*mem-*" then add the letter *p*, then it becomes the word "*pasuk*". Elimination directly refers to the Rule 2 effect on the results of stemming, where the algorithm does not always result in the actual word.

The process occurs because at the 2nd stage, the algorithm only checks whether or not the words are in accordance with the *prefix* rules and Rule 2 patterns without *prefix* removal and if at the 3rd stage if the checked words are in accordance with Rule 2, the algorithm immediately applied the rule to the word. After analysing the results of stemming, the next step is to make improvements by changing the process from stages 2 and 3. The proposed improvements are as follows:

1. In step 2 the algorithm will first check the word in the *prefix* rule, if appropriate then the *prefix* will immediately be removed.

2. In step 3 if checking the *prefix* rule is not appropriate, the algorithm will check the *prefix* pattern in Rule 2 and the first letter of the input word. If it is in accordance with Rule 2, the algorithm will apply the rule to the word.

The modification of the Idris algorithm is described in Table 2 below:

Table 2: The description of IN-Idris algorithm

ALGORITHM 2: IN-Idris Algorithm
1. Check the word in the dictionary. If the word is in the dictionary, then the word is considered as the root word and exit. Otherwise, proceed to the next step.
2. Check the word in the *prefix* rule. If the word matches the prefix rules, then remove the *prefix* and go to step 6. Otherwise, proceed to the next step.
3. Check the *prefix* pattern and the first letter of the word to be stemmed. If the *prefix* pattern matches Rule 2, then apply Rule 2 to the word. Otherwise, remove the *prefix* and go to step 6.
4. Check the *prefix* of the word, adjust the pattern in Rule 2. If it matches the fourth rule, then check the stem word in the dictionary and proceed to the next step. Otherwise, remove the *prefix* and go to step 6.
5. If the word is not found in the dictionary, then return to step 4, otherwise, remove the *prefix* and proceed to the next step.
6. Check the word in the dictionary. If the word found, then the word is considered as the root word and exit. Otherwise, proceed to the next step.
7. Check the words in the *suffix* rules. If it matches with the *suffix* rules, then remove the *suffix* and go to step 1. Otherwise, just go to step 1.

From Fig.1 we can see the step-by-step of the proposed algorithm depicted through the flowchart. The processes with grey colour use the modified rule from Idris stemmer.
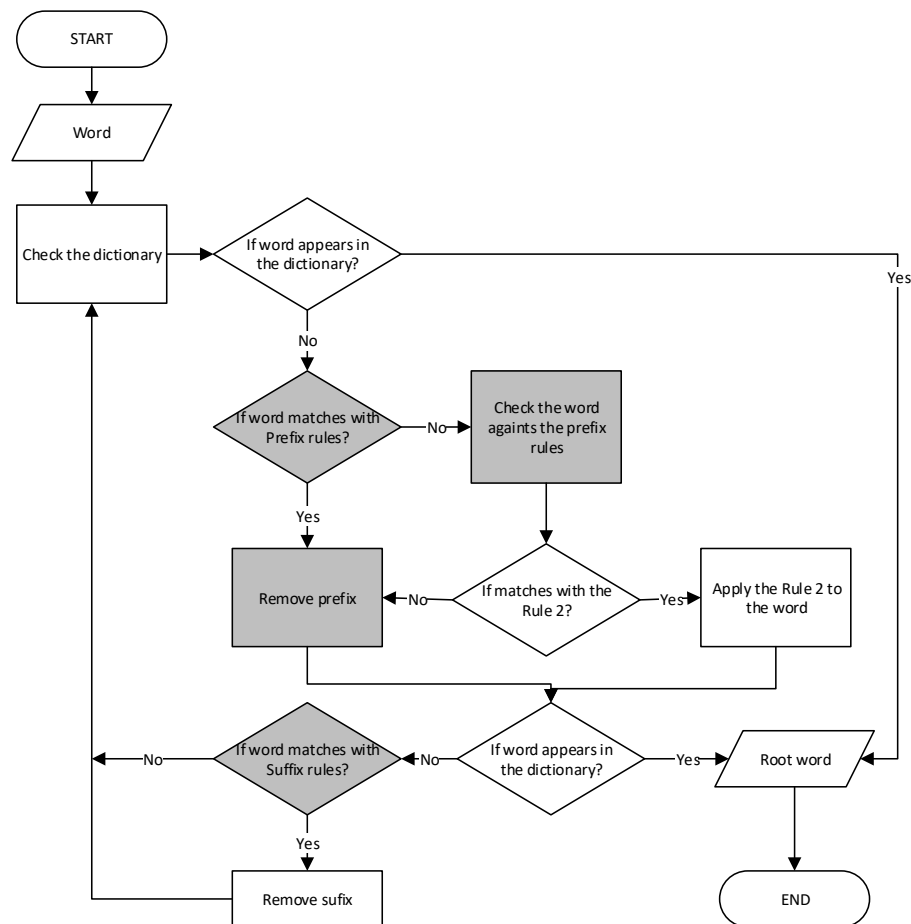
Fig. 1: The flowchart of modified Idris algorithm (IN-Idris).

4. EXPERIMENT AND EVALUATION

4.1 Dataset

For the experiment process, this study used a dataset retrieved from Indonesian online novel excerpts to measure the performance of the proposed algorithm. The novel data were sourced from research by Permatasi [6] which have a total of 6 novels, and there were 4 novels from our collection so that there is a total of 10 novels to be used. Novel excerpt data represented as a document so that a total of the document is 10 documents for the evaluation process. Novel excerpt data used was the only content without using the title of the novel. The dataset needs to go through the *preprocessing* stage so that it can be processed to the next stage. Meanwhile, the dictionary of root words is used based on Kamus Besar Bahasa Indonesia (The Big Indonesian Dictionary, in English). Kamus Besar Bahasa Indonesia (KBBI) is the most complete Indonesian dictionary which is popularly used as a reference in Indonesian text processing.

4.2 Evaluation Scenarios

The research evaluation was done by comparing the *stemming* results of the modification of the Idris algorithm (IN-Idris) and other *stemming* algorithms (original Idris, N&A, ECS). In this experiment, we analysed the accuracy and the speed of every stemmer. Testing scenarios that were carried out tested 10 Indonesian novels excerpts. Generated output was in the form of stemming root words, followed by counting the number of true and false stemming results from each algorithm. Several steps were used,

including case folding, tokenization, eliminating *stopwords*, and *stemming*. Case folding is the process of changing all letters to lowercase and removing punctuation, numbers, and certain symbols [9]. After that, the tokenization process is breaking a stream of text up into phrases, word, symbols, or other elements [23]. Then, the words taken from tokenizing results will be processed to eliminate the unimportant words that are included in the *stopwords* list. Furthermore, each document content will be stemmed. The *stemming* process is then carried out to process the *affix* words into root words.

The results will be assessed to produce the number of both true words and wrong words; so that the accuracy value of both *stemmers* can be calculated. This evaluation also measured the speed of processing time during changing the root word from the stem word of the document. Eq. (1) [8] is used to calculate the accuracy value of *stemming* result from each document d_i where i =1 to 10. Furthermore, t represented the total of true words from d_i while w is the total of the wrong words from d_i and the word total is represented by n.

$$Accuracy = \left(\frac{t-w}{n}\right) x 100\% \qquad (1)$$

4.3 Experiment Results and Discussion

The first experiment compared the *stemming* result of the Idris and the IN-Idris stemmer. The testing results are shown in Table 3, which describes the experimental results for every document tested. The table also presents the number of words contained in each document, the number of true and wrong words, and also the speed and accuracy value of both *stemmers*. For both Idris and IN-Idris *stemmers*, the maximum accuracy resulted from document 2, which changed from 83.13% to 87.95%. On the other hand, the minimum accuracy was produced in document 7 *stemming* results with around 69.49% for the IN-Idris and 67.01% for the Idris *stemmer*.

Table 3: Comparison accuracy and speed of both Idris and IN-Idris Stemmer

Doc	Number of words	Idris				IN-Idris			
		True Word	Wrong Word	Speed (s)	Accuracy (%)	True Word	Wrong Word	Speed (s)	Accuracy (%)
1	239	97	27	3.40	78.23	106	17	3.32	86.18
2	261	120	28	3.62	81.08	127	21	3.02	85.81
3	323	138	28	3.79	**83.13**	146	20	3.80	**87.95**
4	511	188	46	**5.28**	80.34	192	42	**5.96**	82.05
5	608	233	79	7.96	74.68	257	55	8.81	82.37
6	2224	912	230	**42.16**	79.86	967	173	**47.17**	84.82
7	1361	522	257	25.56	**67.01**	539	237	18.52	**69.46**
8	1210	415	137	14.71	75.18	443	109	13.59	80.25
9	794	361	91	12.95	79.87	384	65	12.90	85.52
10	997	366	114	18.61	76.25	400	78	18.40	83.68
Average				13.80	77.56			13.55	82.81

On the other hand, in terms of speed, *stemming* based on IN-Idris needed around 13.55 seconds. However, this is faster than processing root words with the Idris *stemmer* which has an average time of around 13.80 seconds. In general, based on the researcher's experiment (shown in Table 3), it could be concluded that documents that have under 600 words just need under 9 seconds for *stemming*. Meanwhile, if the number of the words is

under 1300, it will take under 25 seconds to process. Furthermore, for the documents that have over 2000 words, over 47 seconds are required.

Figures 2 and 3 show the accuracy and speed comparison from both *stemmers* represented in a graph. Based on Fig. 2, in general, it showed that the accuracy value produced by IN-Idris was higher than the Idris *stemmer* result. The average value of accuracy from the IN-Idris *stemmer* was approximately 82.81% while *stemming* using the Idris algorithm showed an accuracy of just 77.56%. IN-Idris performance dominated for whole documents tested and reached an accuracy of over eight in ten.

Generally, IN-Idris presented a faster speed than Idris in stem word processing (shown in Figure 3). However, Idris showed good speed when processing documents 4, 5, and 6. In terms of accuracy, IN-Idris was better than Idris when processing those documents. The average speed of the proposed algorithm reached approximately 13.55 seconds while Idris needed 13.80 seconds on average for *stemming*. As a result, the speed gap between the IN-Idris and the Idris *stemmers* is around 0.25 seconds.
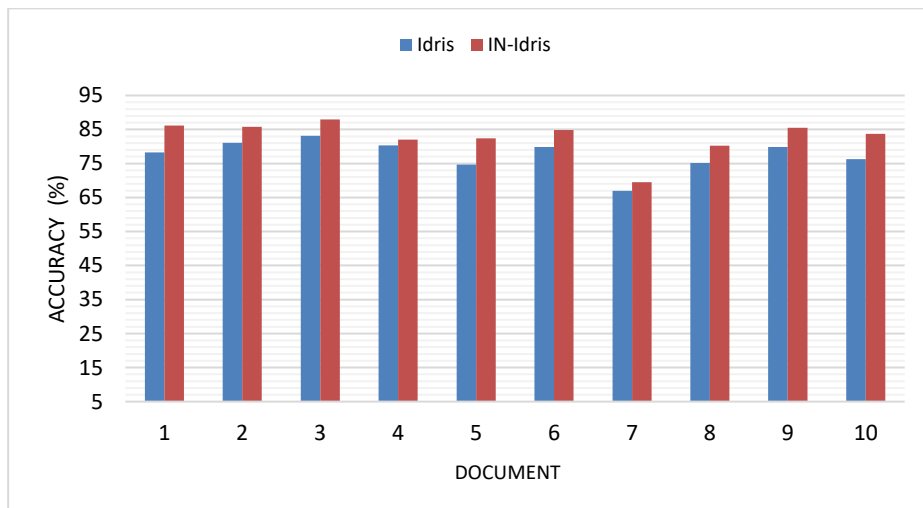
Fig. 2: The graph visualization of accuracy comparison between
Idris and IN-Idris *stemming*.
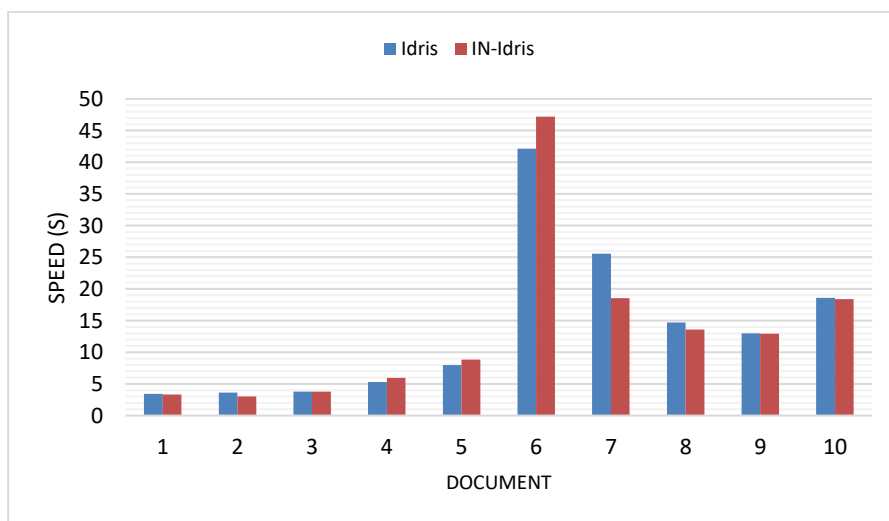
Fig. 3: The graph visualization of speed between Idris and IN-Idris *stemming*.

Table 4 shows the sample text of the *stemming* result from the Idris and the IN-Idris *stemmers*. The table contained: stem words (the original word taken from the novel collections), the root word for ground truth (the word which is used as a reference for evaluation), and the *stemming* result from both stemmers. The *stemming* result columns present which stem words were successfully changed to their root word and also show which were unsuccessful. There are some cases where IN-Idris was more powerful than Idris, as proven from cases no. 1, 2, 4, 5, 6, 7, 9, and 10. However, for case no. 3 both algorithms could not work properly. Some cases have shown that the Idris *stemmer* affected character's reduction, such as root word "pendek" changed to be "dek", and the root word "tetes" changed to be "tes".

Table 4: Sample text from *Stemming* result

Case no.	Stem Word	Root Word Ground truth	In English	Stemming Result	
				IDRIS	IN-IDRIS
1	*memusnahkan*	*musnah*	destroyed	*memusnahkan*	*musnah*
2	*percayai*	*percaya*	believe	*percayai*	*percaya*
3	*kelahiranmu*	*lahir*	born	*kelahiranmu*	*kelahiranmu*
4	*menyeramkan*	*seram*	scary	*menyeramkan*	*seram*
5	*menyakitkan*	*sakit*	sick	*menyakitkan*	*sakit*
6	*mengerikan*	*ngeri*	horrified	*gerik*	*ngeri*
7	*pendekku*	*pendek*	short	*dek*	*pendek*
8	*terulur*	*ulur*	stretch out	*ulut*	*ulut*
9	*tetesan*	*tetes*	drops	*tes*	*tetes*
10	*menuruni*	*turun*	down	*urun*	*turun*

In a further experiment, we compared the result of the IN-Idris *stemmer* with two other algorithms (N&A and ECS) in addition to the previous Idris result. Table 3 presented the accuracy and speed of those four *stemmer* results when tested using 10 documents selected. From the table, the accuracy of ECS *stemmer* in both upper and lower accuracy is around 90.37% and 80.36% respectively. On the other hand, the result of N&A *stemmer* has a maximum accuracy of 89.86%, and the minimum accuracy is just 73.78%. Meanwhile, the accuracy of both Idris and IN-Idris have been described and presented in the previous table. Overall, the accuracy results showed significant performance over eight in ten.

In terms of speed, Table 5 described that the fastest time needed by the ECS *stemmer* is approximately 2.41 seconds while the longest time is around 30.50 second. This result is not much different from the N&A result that has a speed in maximum and minimum around 36.68 seconds and 2.51 seconds, respectively. Meanwhile, Idris has around 42.16 seconds as its lowest speed and around 3.40 seconds as its fastest speed. On the other hand, IN-Idris has the fastest and longest speeds, approximately 3.02 seconds and 47.17 seconds, respectively.

In Fig. 4, the graph presented a comparison of the accuracy of the four *stemming* algorithms. Overall, the accuracy results showed significant performance over eight in ten. Whereas Idris produced lower accuracy, which just reached 77.56% inaccuracy, and the ECS *stemmer* has the highest accuracy of 85.92%. Meanwhile, the proposed *stemmer,* IN-Idris, signified accuracy in 82.81%, which is lower than both the ECS and N&A *stemmers*, but the accuracy gap was small with just around 3%.

Table 5: Comparison accuracy and speed result between Idris and IN-Idris *Stemmer*

Doc	N&A		ECS		Idris		IN-Idris	
	Speed (s)	Accuracy (%)	Speed (s)	Accuracy (%)	Speed (s)	Accuracy (%)	Speed (s)	Accuracy (%)
1	2.51	89.43	2.73	90.37	3.40	78.23	3.32	86.18
2	3.19	89.86	3.14	87.73	3.62	81.08	**3.02**	85.81
3	4.37	88.55	3.55	85.75	3.79	83.13	3.80	87.95
4	5.87	86.32	2.41	82.58	5.28	80.34	5.96	82.05
5	7.35	84.94	6.71	87.66	7.96	74.68	8.81	82.37
6	36.68	86.93	30.50	88.46	42.16	79.86	47.17	84.82
7	21.66	73.78	13.73	87.00	25.56	67.01	18.52	69.46
8	19.45	86.59	9.59	85.49	14.71	75.18	13.59	80.25
9	12.65	86.49	12.98	85.61	12.95	79.87	12.90	85.52
10	11.97	87.45	16.62	80.36	18.61	76.25	18.40	83.68
Average	**12.57**	**85.61**	**10.20**	**85.92**	**13.80**	**77.56**	**13.55**	**82.81**
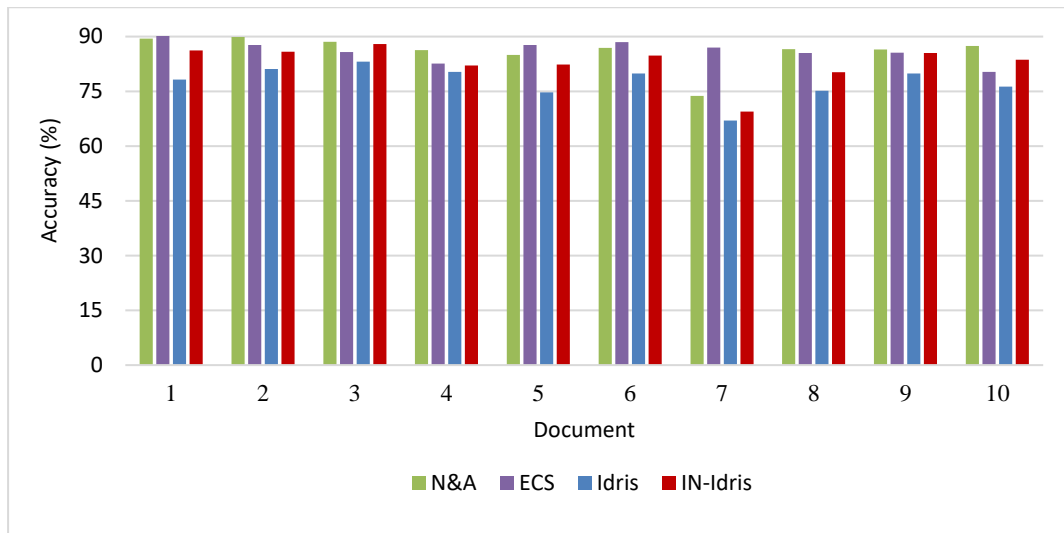
Fig. 4: The graph visualization of accurate comparison results for both stemmers.
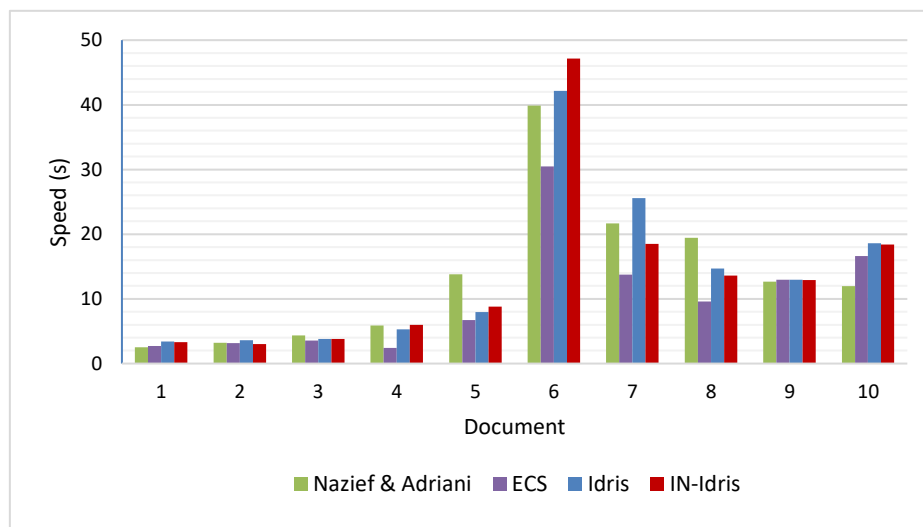
Fig. 5. The graph visualization of accurate comparison results for both stemmers.

Figure 5 depicts a comparison of the *stemming* speed of the four algorithms. *Stemming* processed by ECS was the fastest, with just 10.20 seconds, and the longest *stemming* needed approximately 13.80 seconds when it was processed through the Idris *stemmer*. On the other hand, the proposed method IN-Idris has a duration time of around 13.55 seconds to transform words into their root. This result is proof that IN-Idris needs extra time than N&A and ECS in *stemming*. However, there is one instance when IN-Idris finished *stemming* faster than the others, it is shown for document 2, where just needed 3.02 seconds.

Based on the experiment, the accuracy value is affected by the true word total produced for each document of *stemming* results. The higher the number of true words, the higher accuracy produced. However, the smaller the number of true words, the smaller the resulting accuracy. Furthermore, the result of the *stemming* accuracy for each document is different for each *stemmer*. It can be caused by the different rules implemented in each algorithm, which can be called a *stemmer* characteristic.

On the other hand, in terms of speed, the ECS *stemmer* is faster than the Idris algorithm. That result is a refutation for the previous research [6] which was conducted to test the accuracy of the Idris and ECS *stemmers* implemented in Indonesian text documents. That research has claimed that Idris has an excellent performance in speed. We concluded that the speed processing in *stemming* related to the number of words contained in each document, where the time needed to do the *stemming* process is relatively based on the tool or programming language used [24].

It was found that the Idris algorithm had a low accuracy value caused by an *affix* cutting error in the *stemming* process that affected the results. The error was related to the application of the *prefix* removal first rule on the Idris *stemming*. This caused root words that had the same letters as a *prefix* to be discarded, and it caused un-matching and errors in the final result. This error could be corrected by IN-Idris that obtained good *stemming* results with an increased accuracy until 5.25% from the Idris *stemmer*. However, in the modification of the Idris algorithm, IN-Idris still had a deficiency that caused words to fail in *stemming*. There is a shortcoming that IN-Idris could not handle, such as the *affix* "*se-ku*" on the word "*sebelahku*" (next to me, in English) whereas with the Idris algorithm, the word "*sebelahku*" was changed to "*belah*".

The challenge to develop a good *stemming* algorithm for future work is how a *stemmer* can be able to handle some problems including deletion error particularly occurring due to typing errors and mistakes in place names, people's names, and also foreign languages. The most powerful *stemmer* is the ECS algorithm, and some of its rules can be adopted to improve IN-Idris performance. However, the ECS *stemmer* applied the *suffix* deletion rule first and checked the dictionary every time it removed the *affix*. This can lead to word *overstemming* because the *affix* removal process was carried out as much as possible according to the applied rules, thus affecting the accuracy results. Besides that, there is need for further development that can modify a combination of *prefix* and *suffix* rules to produce a better-*stemming* performance.

5. CONCLUSION AND FUTURE WORK

IN-Idris is a new *stemmer* for Indonesian text that was inspired from and improved upon the Idris Malay *stemmer*. Based on the experiment, the researchers found that the Idris algorithm has a low accuracy value caused by affix cutting errors on the *stemming* process which affected the results. This error could be corrected by IN-Idris so that it can

Suci et al.

obtain good *stemming* results with an increased accuracy until 5.25% from Idris *stemmer*. IN-Idris performance dominated for all documents tested, and overall the accuracy results showed significant performance of over eight in ten. In terms of speed, IN-Idris presented a faster speed than Idris in stem word processing. Finally, we conclude that the accuracy value is affected by the total of true words produced for each *stemming* result document. The higher the true words, the higher accuracy produced. However, the smaller the true words, the smaller the accuracy that resulted.

REFERENCES

[1]   Vijayarani DS, Ilamathi, MJ., Nithya M. (2015) Preprocessing techniques for text mining - An overview. J. Computer Science & Communication Networks, 5(1): 7-16.
[2]   Buntoro G, Arifin R, Syaifuddiin G, Selamat A, Krejcar O, Hamido F. (2021) The Implementation of the machine learning algorithm for the sentiment analysis of Indonesia's 2019 Presidential election. IIUM Engineering Journal, 22(1): 78-92.
[3]   Nassirtoussia AK, Aghabozorgia S, Wah TY, David CLN. (2014) Text mining for market prediction: A systematic review. Expert Systems with Applications, 7653-7670.
[4]   Rizki AS, Tjahyanto A, Trialih R. (2019) Comparison of stemming algorithms on Indonesian text processing. Telkomnika, 17(1): 95-102.
[5]   Utomo FS, Suryana N, Sanusi Azmi, M. (2020) Stemming Impact analysis on Indonesia Quran translation and their tafsir classification for ontology instances. IIUM Engineering Journal, 21(1): 33-50.
[6]   Permatasari N. (2016) Analisis Perbandingan algoritma Idris dan algoritma enhanced confix stripping (ECS) stemmer pada dokumen teks bahasa Indonesia. Universitas Komputer Indonesia. https://repository.unikom.ac.id/130/
[7]   Titin W, Kerami J, Arief S. (2017) Determining Term on text document clustering using algorithm of enhanced confix stripping stemming. International Journal of Computer Applications, 157(9): 8-13.
[8]   Prasidhatama A, Suryaningrum KM. (2018) Perbandingan algoritma Nazief & Adriani dengan algoritma Idris Untuk pencarian kata dasar. Jurnal Teknologi & Manajemen Informatika, 4(1): 1-4.
[9]   Prihatini PM, Putra ID, Giriantari IAD, & Sudarma M. (2017) Stemming Algorithm for Indonesian Digital News Text Processing. International Journal of Engineering and Emerging Technology, 2(2): 1-7.
[10]   Mena VV, Saputri K. (2018) Contrastive analysis between English and Indonesian prefixes and suffixes in the descriptive texts of student's textbooks. English Community Journal, 2(1): 175-182.
[11]   Jelita A. (2007) Effective Techniques for Indonesian Text Retrieval. Melbourne: RMIT University.
[12]   Adriani M, Asian J, Nazief B, Tahaghoghi SMM, & Williiams HE. (2007) Stemming Indonesian: A confix-stripping approach. ACM Transactions on Asian Language Information Processing (TALIP), 6(4): 1-33.
[13]   Widayanto H & Huda AF. (2017) Comparison Nazief Adriani and CS stemmer algorithm for stemm real data. In e-Proceeding of Engineering, 4(3): 5215. Bandung, Indonesia.
[14]   Arifin AZ, Mahendra IPAK, & Ciptaningtyas HT. (2009) Enhanced Confix stripping stemmer and ants algorithm for classifying news document in Indonesian language. in International Conference on Information & Communication Technology and Systems. In The International Conference on Information & Communication Technology and Systems, 5:149-158. Surabaya, Indonesia.
[15]   Idris N, Mustapha SS. (2001) Stemming For Term Conflation In Malay Texts.
[16]   Porter, M. F. (1980). An algorithm for suffix stripping. Program1, 14(3): 130-137.
[17]   Paramitha ES. (2012) Analisis dan implementasi stemming menggunakan algoritma Idris pada dokumen teks berbahasa indonesia. Telkom University, Indonesia.

[18] Mardiana T, Adji TB, Hidayah I. (2016) Stemming Influence on Similarity Detection of Abstract Written in Indonesia. Telkomnika, 14(1): 219-227.

[19] Rifai W, Winarko E. (2019) Modification of Stemming algorithm using a non deterministic approach to Indonesian text. Indonesian Journal of Computing and Cybernetics Systems, 13(4): 379-388.

[20] Vega VB. (2001) Information retrieval for the Indonesian language. Master's thesis, National University of Singapore.

[21] Arifin AZ & Setiono AN. (2002) Klasifikasi dokumen berita kejadian berbahasa Indonesia dengan algoritma single pass clustering. In Prosiding Seminar on Intelligent Technology and its Applications (SITIA). Teknik Elektro, Institut Teknologi Sepuluh Nopember Surabaya.

[22] Asian J, Williams HE, & Tahaghoghi SMM. (2005) Stemming Indonesian. In Proceedings of the Twenty-eighth Australasian conference on Computer Science, 38: 307-314. Australia.

[23] Winarti T, Kerami J, Arief S. (2014) Tokenization and Filtering process in rapidminer. International Journal of Applied Information Systems, 7(2): 16-18.

[24] Zaman B. (2014) Modifikasi algoritma Porter untuk stemming pada kata bahasa Indonesia. In Seminar Nasional Teknologi Informasi dan Komunikasi (SENTIKA 2014), 543-550. Surabaya, Indonesia.

BOTNET DETECTION USING INDEPENDENT COMPONENT ANALYSIS

WAN NUR HIDAYAH IBRAHIM[1,2], MOHD SYAHID ANUAR[5], ALI SELAMAT[1,3,4*] AND ONDREJ KREJCAR[4]

[1]*School of Computing, Faculty of Engineering, Universiti Teknologi Malaysia, Media and Game Innovation Centre of Excellence (MaGICX), Universiti Teknologi Malaysia, 81310 Johor Baharu, Johor, Malaysia*
[2]*Jabatan Teknologi Maklumat dan Komunikasi (JTMK), Politeknik Sultan Idris Shah, 45200 Sg Lang, Selangor, Malaysia*
[3]*Malaysia Japan International Institute of Technology (MJIIT), Universiti Teknologi Malaysia, Jalan Sultan Yahya Petra, 54100 Kuala Lumpur, Malaysia*
[4]*Center for Basic and Applied Research, Faculty of Informatics and Management, University of Hradec Kralove, Rokitanskeho 62, 500 03 Hradec Kralove, Czech Republic*
[5]*Razak Faculty of Technology and Informatics, Universiti Teknologi Malaysia, Jalan Sultan Yahya Petra, 54100 Kuala Lumpur, Malaysia*

Corresponding author: aselamat@utm.my

ABSTRACT: Botnet is a significant cyber threat that continues to evolve. Botmasters continue to improve the security framework strategy for botnets to go undetected. Newer botnet source code runs attack detection every second, and each attack demonstrates the difficulty and robustness of monitoring the botnet. In the conventional network botnet detection model that uses signature-analysis, the patterns of a botnet concealment strategy such as encryption & polymorphic and the shift in structure from centralized to decentralized peer-to-peer structure, generate challenges. Behavior analysis seems to be a promising approach for solving these problems because it does not rely on analyzing the network traffic payload. Other than that, to predict novel types of botnet, a detection model should be developed. This study focuses on using flow-based behavior analysis to detect novel botnets, necessary due to the difficulties of detecting existing patterns in a botnet that continues to modify the signature in concealment strategy. This study also recommends introducing Independent Component Analysis (ICA) and data pre-processing standardization to increase data quality before classification. With and without ICA implementation, we compared the percentage of significant features. Through the experiment, we found that the results produced from ICA show significant improvements. The highest F-score was 83% for Neris bot. The average F-score for a novel botnet sample was 74%. Through the feature importance test, the feature importance increased from 22% to 27%, and the training model false positive rate also decreased from 1.8% to 1.7%.

ABSTRAK: Botnet merupakan ancaman siber yang sentiasa berevolusi. Pemilik bot sentiasa memperbaharui strategi keselamatan bagi botnet agar tidak dapat dikesan. Setiap saat, kod-kod sumber baru botnet telah dikesan dan setiap serangan dilihat menunjukkan tahap kesukaran dan ketahanan dalam mengesan bot. Model pengesanan rangkaian botnet konvensional telah menggunakan analisis berdasarkan tanda pengenalan bagi mengatasi halangan besar dalam mengesan corak botnet tersembunyi seperti teknik penyulitan dan teknik polimorfik. Masalah ini lebih bertumpu pada perubahan struktur berpusat kepada struktur bukan berpusat seperti rangkaian rakan ke rakan (P2P). Analisis tingkah laku ini

seperti sesuai bagi menyelesaikan masalah-masalah tersebut kerana ianya tidak bergantung kepada analisis rangkaian beban muatan trafik. Selain itu, bagi menjangka botnet baru, model pengesanan harus dibangunkan. Kajian ini bertumpu kepada penggunaan analisa tingkah-laku berdasarkan aliran bagi mengesan botnet baru yang sukar dikesan pada corak pengenalan botnet sedia-ada yang sentiasa berubah dan menggunakan strategi tersembunyi. Kajian ini juga mencadangkan penggunakan Analisis Komponen Bebas (ICA) dan pra-pemprosesan data yang standard bagi meningkatkan kualiti data sebelum pengelasan. Peratusan ciri-ciri penting telah dibandingkan dengan dan tanpa menggunakan ICA. Dapatan kajian melalui eksperimen menunjukkan dengan penggunaan ICA, keputusan adalah jauh lebih baik. Skor F tertinggi ialah 83% bagi bot Neris. Purata skor F bagi sampel botnet baru adalah 74%. Melalui ujian kepentingan ciri, kepentingan ciri meningkat dari 22% kepada 27%, dan kadar positif model latihan palsu juga berkurangan dari 1.8% kepada 1.7%.

KEYWORDS: *botnet detection; flow-based; machine learning; independent component analysis; traffic analysis*

1. INTRODUCTION

A botnet is a collection of computers infected by malicious software (malware) that a botmaster manages. All Internet-of-Things (IoTs) devices, such as closed-circuit television cameras (CCTV), web cameras, computers, and mobile devices, can be infected devices. The vulnerabilities and the computing resources of these infected devices are exploited where they operate remotely as servants following the instructions given by their botmaster. The main aim of assigning a botnet is to launch an assault on the victim. However, the number of bots depends on the frequency of the attacks. Therefore, the most significant factor contributing to the frequency of the attacks is the number of bots in botnet environments [1], [2].

They can execute major attacks on victims, such as DDOS or email spam, because of the large number of bots, rendering victims unable to function for hours or days. For example, in the Mirai incident of 2016, the vast and unlimited number of bots produced a massive impact assault [3]. In the Mirai incident of 2016, the attacks were identified from 600,000 Internet-of-things (IoT) devices [4]. At that moment, Mirai attacks were noteworthy since the bots used Internet-of-things (IoT) devices, not just computers or laptops. Consider the result if 600,000 devices concurrently sent a ping to a specific website, leading to that website being overwhelmed, inaccessible, and its services slowed down.

The botnet detection model has become a hot topic among researchers due to the history of botnet attacks and their impact on the industry. The arms race never ends between the botmasters and the researchers trying to beat each one. Every group continues to develop its abilities, and this can be seen through the botnet revolution. Botnet evolves or mutates every day after the source code has been released to the public [5]. It can be seen in the Mirai botnet and the Mirai version. Two months after the release of the Mirai source code to the public, the bots multiplied with variant complexity, from 213,000 to 493,000, twice. They show the statistics of various botnet attacks on Securelist websites, and 39.35 percent of new botnet found in 2018 is based on the Kaspersky Lab Botnet Monitoring project compared to 2017 botnet attacks [6]. Subsection 1.1 briefly clarifies why the botnet relies heavily on the Rallying stage or C&C stage Command & Control server. The importance of preventing the server from being identified by the security system also explains the botnet structure's revolution. The botnet framework revolution switches from centralized to a decentralized. Centralized botnet, such as IRC and HTTP, via the primary server, call the Command & Control server. Decentralized botnet, such as Peer-to-peer (P2P), are more advanced since the bots themselves can act as servers. P2P is designed to hide the C&C server, as stated in [7], [8].

The botnet's strength lies in its capacity to elude security systems and carry out large-scale attacks thanks to various tactics such as packet data concealment and encrypted packet data [9]. A botnet can hide from the protection system and imitate the regular traffic flow where normal traffic is usually more random [10], it then waits for stage and imbalanced class distribution. The P2P technique is also a part of the concealment strategy to mask the C&C server [7], [8].

The botnet is now becoming a profitable business, according to [8], where the botmaster provides the service for any cyber-attacks. However, the current capability leading the business of these services must monitor the bots, advise of subsequent attacks, lengthen the duration of the attacks, and avoid monitoring its identity.

1.1 Botnet Life-Cycle and Structure

It is necessary to understand the life cycle of the botnet when designing a behavior-based analysis of the botnet detection model since the choice of related features of this model depends on it. Other than that, identification must also be carried out before the attacks occur and it is too late [11]. As below, the botnet life-cycle can be divided into four main stages: -

- Phase I: Injection (I)
- Phase II: Command & Control (C&C)
- Phase III: Attack
- Phase IV: Release

The first stage is injection or replication. This stage can be achieved in several ways on the network, such as exchanging folders, visiting malicious websites, or adding emails. The bot herder increases the number of bots at this level. The Command & Control stage or 'Rallying' stage is the second stage. The infected devices already behave like bots in this process. The bots keep updating the devices' status, and if necessary, the bot herder submits a new source code [12]. The revised source code and the vulnerability report are designed to ensure the bots are undetected and robust [13]. The third stage is the attack phase, where all bots are targeted at attacking specific victims. The botmaster gives an attack launch order, and the bots simultaneously launch the attack based on the command. The Release Period is the last stage. The release stage is where the botmaster removes fingerprints, substitutes new systems for identified bots, and does not leave a digital footprint behind. Often the botmaster distributes the source code to hinder government investigations. During this process, learning from the previous attack, the functionality of the bot system is also enhanced [14].

We concentrate on botnet activity in the process of Command & Control or Rallying for our study. The infected system continues to attempt to connect to the C&C server to send reports of the infected devices. The system also receives updated source code to keep hiding from protection [8]. Based on a Kaspersky Lab study [15], monitoring DDOS attacks is the correct time to detect botnet to intercept the command from the Command & Control.

1.2 Motivation and Contribution

Our inspiration is the potential and consequences of a botnet (a botnet attack), to discover its method before the attack is launched. However, our critical general incentive to build a model that can predict a novel botnet is due to the continuous evolution of the botnet. The technological motivation for using behavior-based patterns and flow-based functionality is due to the shortcomings in detecting the new forms of botnets in the signature-based detection model. Other than that, we were motivated by the research from [16] that combined Principal Component Analysis (PCA) for clustering with k-means.
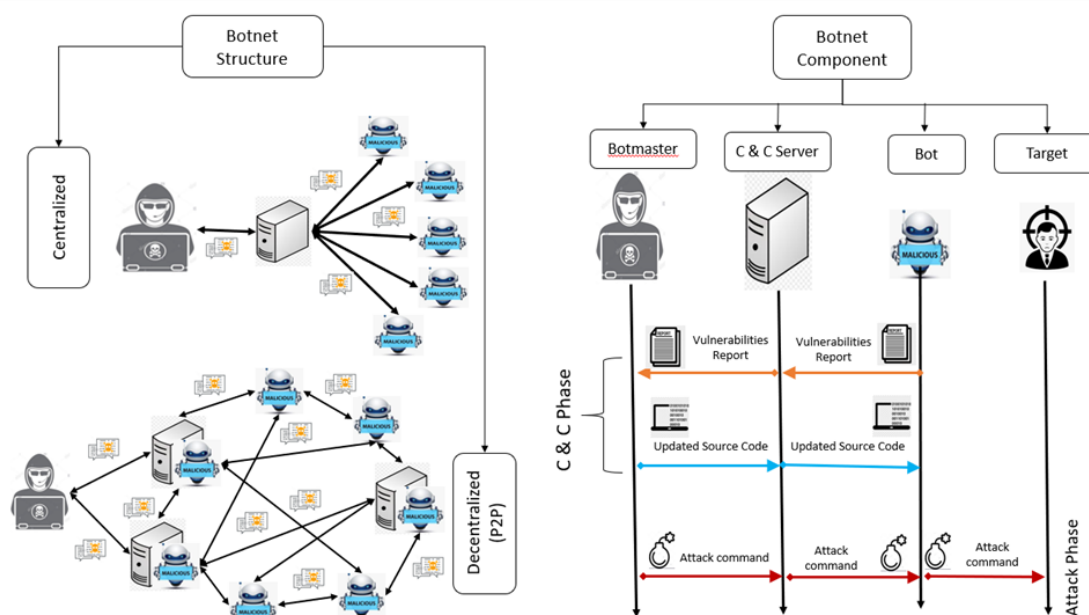
Fig. 1: The botnet structure and botnet component.

In statistics, principal component analysis is a technique used to describe a data set in terms of new uncorrelated variables ("components"). The components are ordered by the amount of original variance they describe, so the technology helps reduce the dimensionality of a data set. In comparison, Independent Component Analysis (ICA) is a machine learning technique used to distinguish independent sources from a mixed input. Unlike principal component analysis, which focuses on maximizing data point variance, independent component analysis emphasizes independence or independent components. Since we are using aggregation for pre-processing data, the vital information might be lost, resulting in decreased performance, so we agreed to use ICA. The explanation about ICA is in subsection 0. The significant contributions to this analysis are: -

- This method can detect network packets even in concealment strategies such as obfuscation, code encryption, oligomorphic strategy, polymorphic strategy, and metamorphic.

- This method used the CTU-13 botnet benchmark dataset that consists of centralized and decentralized structures. It proves that our framework can detect both structures.

- The evaluation of this framework used the different types of botnets, proving that our framework can detect novel botnets.

- Our result shows the average 74% f-score that tests on five types of novel botnets.

- The performance of the framework is compared with other researchers that used the same source of data.

2. RELATED WORKS

The latest developments in the concealment technique of packet data in network traffic make the signature-based or content-based inefficient in detecting new forms of botnets. For example, Singh et al. [17] suggested that the signature time-to-time was revamped by the botnet and significantly modified. These changes in behavior caused signature-based analysis output to drop on the new release botnet because signature-based analysis relied heavily on the bot's

signature. In addition, many concealing tactics are used to mask packet data content in network traffic, including obfuscation, code encryption, oligomorphic approach, polymorphic strategy, and metamorphic strategy [18].

Patsakis et al. [8] raised many concerns about DNS queries that have been used to conceal the botnet on the encrypted channel. Although AsSadhan et al. [17], claimed that packet data contents should be shielded to safeguard the identity of the private information of the individual or user, where only the header of the packets can be released to the public. This author also concentrated on analyzing traffic, exchanging packets, and providing a framework for lightweight security. But their work is considered DNS and is only for the DGA botnet. A model was also developed by this author using the actions of the botnet when interacting with others, but the time interval used for this study is 31-49 minutes.

Two common approaches, 1) payload-based and 2) traffic-based can be classified into machine learning models to detect network operations. The payload-based approach trains models based on characteristics derived from the payload/data portion of the packets transmitted over the network, as the name implies. The disadvantages of such models are the resource-intensive challenge (where features for each packet need to be evaluated), privacy problems, and encrypted information where features cannot be extracted [18,19]. By analyzing the communication packet headers or Netflow information, the traffic-based approach aims to mitigate some of the model's drawbacks. While privacy remains an issue with such an approach (such as individual IP addresses in features), this can be mitigated by aggregating time window records.

2.1 Behavior-based and Flow-based Features

What is behavior-based? What are the differences between behavior-based and signature-based? Behavior-based and signature-based are in contrast to each other. In computing, all objects have attributes that can be used to develop a custom signature. Signature-based analysis refers to detecting attacks by searching for specific patterns, like byte sequences in network traffic or known malicious instruction sequences used by malware [22]. This terminology is derived from anti-virus software, which refers to these detected patterns as signatures.

Although behavior-based analysis is an analysis that does not directly analyze the data like signature-based, there are some advantages of behavior-based analysis compared to signature-based analysis. For example, it is more secure or effective in detecting new and novel forms of malware threat. In addition, it can detect a single instance of malware that targets a person or organization. It can also identify what the malware does when files are opened in a specific environment and obtains comprehensive malware information. However, according to Resende and Drummond [21], most research defines behavior-based analysis with anomaly-based detection, but anomaly detection can also be done using signature-based analysis. So, it means that anomaly-based cannot be defined as behavior-based analysis in malware detection.

The definition of behavior-based Resende and Drummond [21] is the most accurate to our definition. Resende and Drummond [21] define behavior-based analysis in Network Intrusion Detection Systems as detection techniques that are not evaluated or referred directly to the source, destination, and payload of packets. It is an analysis that assesses the behavior of an object. Behavior-based detection can be performed by using API call logs [24], network flow (NetFlow) [10], and is also a hybrid between API call and Netflow [25]. A flow is a collection of packets that come from the same source and destination. Flow-based botnet detection techniques employ statistics of all packet headers in a flow (flow record). Because the flow-

based approach only catches packet header information, it can reduce the computational complexity [24-26] and be processed very quickly.

Flow-based features are the characteristics chosen to illustrate the network flow pattern or connection to distinguish either the usual network or a botnet network. Flow-based characteristics also relate to packet data information, such as total packets per second, bytes per packet, total packet bytes, and the number of packets [29]. The description of flow-based functionality is shown in Table 1 and consists of the features, the time window, and the data tools derived from published work. Thus, when designing our characteristics and the time window, Table 1 became our crucial guide.

The feature selection process was interpreted in the same concept as used in aggregation. As mentioned in Gezer et al. [40], one of the challenges in machine learning is feature selection because feature selection needs a good understanding of the domain knowledge. Not all features in the data are relevant to building the model (Resende and Drummond [21]). On the other hand, aggregation is a process of transforming the data based on a specific theory, and it enables the extraction of sufficient data for analysis. Based on [30], aggregation is a part of the data mining technique in machine learning for efficient knowledge discovery about network flows.

2.2 Independent Component Analysis

Independent Component Analysis (ICA) is a source separation technique in signal processing. According to [31], in their survey, ICA and PCA are among the popular methods used to select essential network features. PCA extracts and reduces the dimension of features, while ICA separates the noise to enhance and maximize each feature's data pattern [32]. The authors in [33] claim that principal component analysis (PCA) is a technique for reducing features by identifying the relevant feature set. The implementations of ICA and PCA clustering algorithm in feature selection has been reported [16]. It is a semi-supervised model where the author combined unsupervised and supervised techniques.

In ICA, the mutual connection between features is minimized by maximizing the non-Gaussianity. Research from Palmieri et al. [34] is the most similar to our approach. The author used ICA in Network Anomaly Detection from the University of Naples, Italy's network traffic. On the other hand, we try to find the implementation of ICA in detecting botnet, and we only found an article from Mao et al. [35] where this author used ICA in detecting spamming botnet.

We can summaries that behavior-based analysis that used the flow-based features can solve the issues of concealment botnet, but it produces high false alarm (false positive rate). High false alarm in machine learning occurs due to the unclear separation between classes that also come from the unclear pattern produce by the data. Although some attempts have been made to address this issue, it still puts limitations on ICA implementation.

3. PROPOSED FRAMEWORK AND PRE-EVALUATION RESULT

In order to reach the objective, this study proposed a new framework as shown in Fig. . The proposed framework starts with selecting the network traffic dataset and pre-processing the dataset. This study highlighted the pre-processing phases where the data is provided to produce a high-performance during classification.

Table 1: Summary of behavior-based analysis in previous works

Author	Features	Time Window (seconds)	Data resources
Ehsan and Hamid [36]	Group duration time, Number of Receive Packets, Number of Send packets, Distance from the previous group	Group duration time	Kelihos, CVUT Malware Capture Facility Project
Stevanovic and Pedersen [37]	* Basic conversation features: Port number, layer 7 protocol, duration (last pkt - first pkts), the total number of packets, total number of bytes, mean of the number of bytes per packet & Std of the number of bytes per packet * Time-based-based features: number of packets & bytes per second, mean & std of packets inter-arrival time * Bidirectional features: a ratio of number of packets & bytes in and out, a ratio of inter-arrival times in and out * TCP specific features: such as percentage TCP SYN packets, percentages of TCP SYN-ACK packets, percentages of TCP ACK & percentages of TCP ACK PUSH packets	300 s	Combination of the dataset: - • ISCX, ISOT • Contagio • Honeyjar • Malware Capture Facility Project (MCFP)
Fernandez Maimo et al. [38]	* Number of flows, number of incoming flows, number of outgoing flows; * % of incoming and outgoing flows over the total * % of symmetric and asymmetric incoming over the total * Sum, maximum, minimum, mean, and variance of IP, packets per incoming outgoing, and totals flows	20 - 30 s	CTU-13
Debashi and Vickers [39]	Array 1:(Src Addr), Dst Port, Packet Count Algorithm 2: Dst Addr, Dst Port, Packet count. Array 2: Dst Addr, Src addr list, Src Addr count, Dst Port List, Dst Port Count	60 s	ISOT
Gezer et al. [40]	* Total forward & backward volume * Max forward & backward packet length * Min, Max, Mean before idle and before active. * Max backward inter-arrival time	600 s	capture own network data
Garg et al. [41]	Send Syn, Recv ACK, Recv Rst, Send pkts, Recv pkts, ICMP unr, Send len, Recv Len	120 s	Combination of P2P botnet

3.1 Input: Data Source and Data Distribution

For this study, the following vital data are extracted from the botnet benchmark dataset CTU-13 [42] from the website of the Stratosphere Research Laboratory. This dataset consists of 13 files with several types of botnets in different protocols and different structures. Since this framework aims to detect novel botnet, this dataset is divided into two sets, training and testing, for building the model and evaluating the dataset, as shown in Table 2. The model is evaluated with data from the evaluating dataset separated from data for building the model. The separation of this data ensures that the model is derived and tested using a different set of data, as explained in Step 2: Dividing Dataset in Section 3.2.

Table 2: The distribution of bot in training and evaluating dataset

Data File No	Duration (hrs)	Bot Name	No of Bots	Training Dataset	Evaluating Dataset
1	6.15	Neris	1		√
2	4.12		1		√
3	66.85	Rbot	1	√	
4	4.12		1	√	
5	11.63	Virut	1	√	
6	2.18	Menti	1		√
7	0.38	Sogou	1	√	
8	19.5	Murlo	1		√
9	5.18	Neris	10		√
10	4.75	Rbot	10	√	
11	0.26		3	√	
12	1.21	Nsis.ay	3	√	
13	16.36	Virut	1	√	

Table 2 summarizes the distribution of data based on the Data File No. In the third column are the names of bots in the dataset. The explanation of the bot name, bot category, and structure are given in Table 3. It is essential to have both structures (centralized and decentralized) in this research. As a result, our data source selection appears reasonable in terms of independent structure and bot reliability. Columns 5 and 6 in Table 2 show the separation of training and evaluating data for the novel bot.

Table 3: The description of the bot based on the name

	Bot Name	Bot Category	Structure
1	Neris	IRC	Centralized
2	Rbot	IRC	
3	Virut	HTTP	
4	Menti	IRC	
5	Soguo	HTTP	
6	Murlo	IRC	
7	Nsis.ay	P2P	Decentralized

3.2 Data Pre-processing

Pre-processing data is the phase in which the data is prepared before being incorporated into the algorithm to construct the prediction model. Since we used behavior-based analysis, the information needed to go through several steps. A behavior-based analysis is not a straightforward extraction process but rather a tool for analyzing the raw data. There are several vital components or measures that we have grouped into the pre-processing data

module, such as Labeling, Cleaning, Dividing Dataset, Feature Selection, Aggregation, and Data Quality Process Implementation.
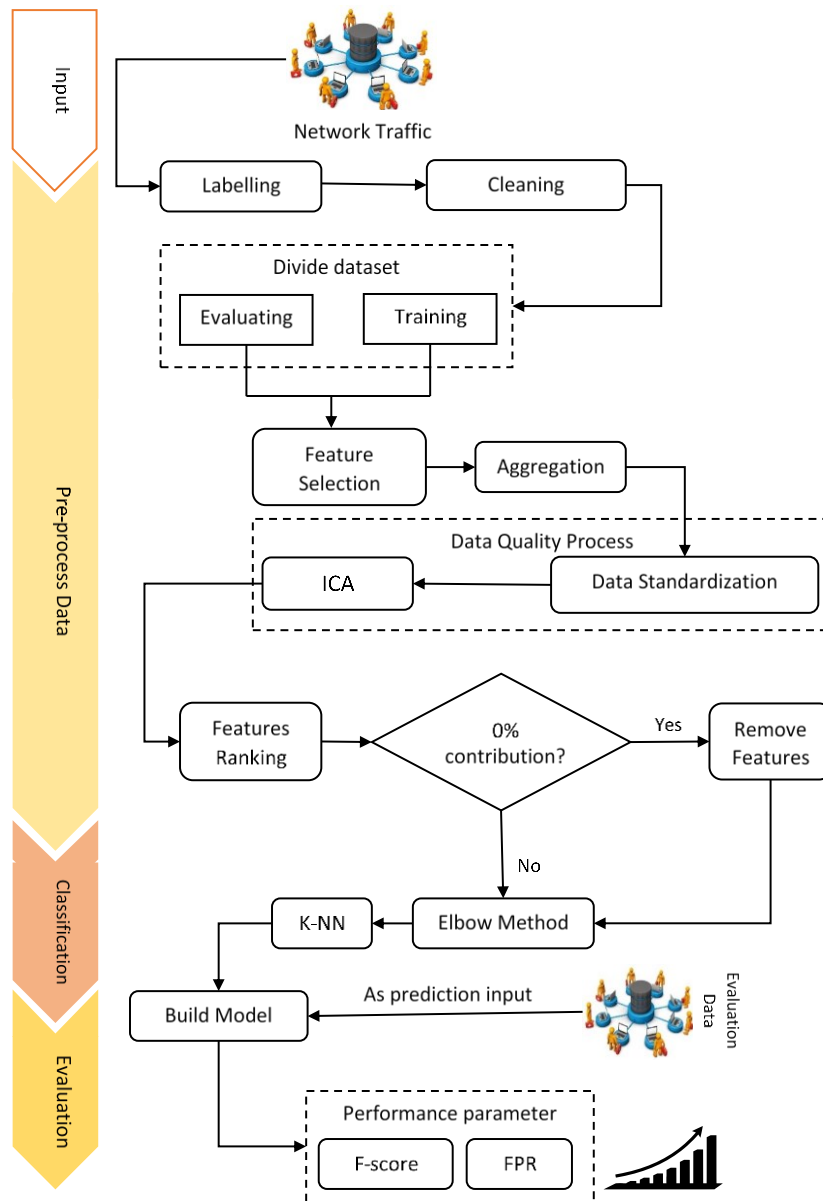
Fig. 2: The proposed framework for pre-processing flow-based features.

3.2.1 Step 1: Labeling and Cleaning

The first step was re-labeling the dataset. Although the CTU-13 dataset is supervised, the dataset contains labels but those labels are in string/text, not in numbers. There are 74 types of descriptive labels in CTU13, as we have shown in Appendix A, but basically, the label is based on 3 types of labels: 'Normal', 'Botnet', and 'Background'. Due to that, we re-labeled the CTU-13 as stated in (1) below. Once the labeling was completed, we removed the uncertain data in Label = 2 for the cleaning process.

$$Label = \begin{cases} 0 & \text{if the label state is "Normal"} \\ 1 & \text{if the label state is "botnet"} \\ 2 & \text{if the label state is "background"} \end{cases} \tag{1}$$

3.2.2 Step 2: Dividing Dataset

After the cleaning process, the data was split into two main data sets: Creating Model Data and Analysing Data. This separation aimed to ensure that the construction model evaluation is performed on a novel botnet. The model was based on Constructing Model Data, divided into 70-30 ratios of training and testing data.
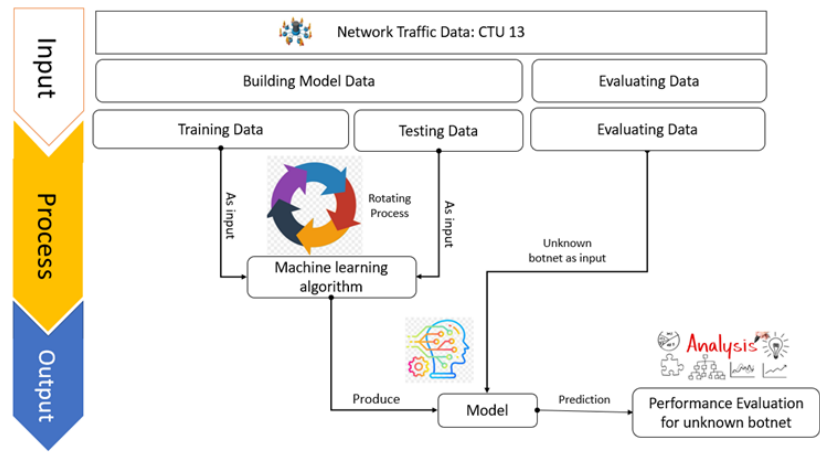
Fig. 1: Process of dividing dataset for novel botnet.

3.2.3 Step 3: Features Selection and Aggregation

Once the dataset division was completed, the dataset was ready for the following process: selecting the features and aggregating them in a specific time interval. We aimed to build the fastest detection, so for this research we chose a short time interval (1 sec) for aggregation.

Feature selection is a process of selecting specific variables/features/attributes in the data. The purpose of this process was to reduce the complexity and processing time. We chose the features based on the theory of communication. This theory is between botmaster and its bots during the C&C stage in the botnet life-cycle for this research. As mentioned in the bot life-cycle in subsection 1.1: Botnet Life-Cycle & Structure, during the C&C phase, bots and botmaster keep communicating. This communication pattern is different from the regular communication pattern, where a typical communication pattern is usually more random. In contrast, a bot's communication pattern is more uniform with the same amount of transferring data to multiple destinations. The features that we used for this research are shown in Table 4.

Table 4: Data type for features in the dataset

No	Feature	Data Types	Calculation
1	Destination Address	Categorical data	$n(x)$
2	Destination port	Categorical data	$n(x)$
3	Packet data	Continuous data	Min, Max, Median, std deviation, $n(x)$
4	Time	Categorical data	Δt

The data are aggregated or grouped in two parameters: time interval (t) and source address (Sip), as shown in Eq. (2). We used the aggregation technique to calculate the occurrence number of the communication within the time interval that represented the bot's behavior in a particular given time.

$$[Sip, t] = \{X_0, \ X_1, \ldots\ldots, X_n\} \tag{2}$$

Since the data in the NetFlow is in continuous type and categorical data type, the aggregation of these two types of data is different, as shown in Eq. (3). If the data was continuous, we implemented the statistical technique such as minimum, maximum, median, standard deviation, and specific number, n(x). But if the data type was categorical data, we implemented only the total distinct number, n(x), where the total distinct number (n(x)) that define as the frequency of unique elements in the set can be described as shown in Eq. (4).

$$f(x) = \begin{cases} Min, Max, Median, std\ deviation, n(x) & if\ data\ is\ continuous\ number \\ Total\ Distint\ Number, n(x) & if\ data\ is\ categorical\ number \end{cases} \tag{3}$$

$$n(x) = \{X_i, X_j, \ldots\ldots, X_n | X_i \neq X_j, i \neq j, \ i \geq 0, j = 1, \ldots\ldots, n\} \tag{4}$$

While for time, this data is used, whereas the aggregation or rounding process is shown in Eq. (1). Time is also used in calculating the Different Time (Δt) between the last time, tn and the start time, t1 in 1 second (time interval) duration. The equation for Different Time (Δt) is shown in Eqs. (5) and (6).

$$f(t) = \{t_1, t_2, \ldots\ldots\ldots, t_n\} \tag{5}$$

$$\Delta t = t_n - t_1 \tag{6}$$

3.2.4 Step 4: Data Quality Process

This process is the point where the most interesting things occur. This process improves the quality of the data and features, improving the performance of detecting novel botnets. Therefore, we label it as Data Quality Process to be represented as the objective of this combination process. This process utilized a two-step approach of standardization and Independent Component Analysis (ICA). Specifically, we used this theory because the classifier we chose was related to a distance-based classifier.

A) Standardization

Standardization is a re-scaling process for the distribution of the dataset to obtain the mean of the data equal to 0, and the standard deviation equal to 1. In other words, standardization is a process of centering the data. Standardizing a data set for a wide range of machine learning estimators is a common need. However, it could be harmful if the individual features do not look more or less like standard normally distributed data (e.g., Gaussian with 0 mean and unit variance). Therefore, test x is calculated as the standard value of:

$$z = {(x - \mu)}/{s} \tag{7}$$

where μ is the mean of the training samples or zero if, with mean= False, s is the standard deviation of the training samples or with std= False, respectively.

Centering and scaling occurred on each feature independently by computing the relevant statistics on the samples in the training set. Mean and standard deviation were then stored in a transform to be used on later data.

B) Independent Component Analysis

For this research, we used FastICA from *sklearn*. decomposition package in python, as shown in Algorithm 1 below. As the name FastICA implies, it is the short version of ICA. FastICA rotates the data until the data looks non-Gaussian in every axis. By making the

mean equal to zero and normalization the variance in all directions, the algorithm can rotate the data in any direction. The process of normalizing the variance is called the whitening process. As shown in Algorithm 1, the python code to implement ICA is through the whitening process. The whitening process is the decorrelation to ensure that all features are treated equally before the Algorithm of ICA run.

After the centering process (mean equal to zero) and the whitening process (normalization of variance), the data ran the ICA algorithm. The main goal of ICA is to find the unmixing vector of W, where W is the inverse of A, X is the input data, and A is the mixing signal. The equation is shown in Eqs. (8) to (10):

$$X = A\,S \tag{8}$$

$$S = A^{-1}X \tag{9}$$

$$S = W\,X \tag{10}$$

C) Features Importance Ranking

We evaluated our feature selection through Features Importance Ranking calculated using Extra Tree Classifier, as shown in Algorithm 2. Extra Trees Classifier for features importance in *Scikit*.learn module is based on impurity-based importance where it calculated the importance of training data without reflecting the prediction ability.

From the feature's importance ranking in Fig. **2**, we can see the percentage of the highest contribute features. For example, the 1st feature increased from 22.75% to 27.74% and the lowest contributing feature, the 9th feature, increased from 1.8% to 4.31%. Since no feature had a 0% contribution, the removal process was not executed.

```
Feature ranking:
1. feature 1 (0.227549)
2. feature 2 (0.226752)
3. feature 8 (0.168363)
4. feature 0 (0.106055)
5. feature 3 (0.089665)
6. feature 6 (0.072501)
7. feature 5 (0.047629)
8. feature 4 (0.043459)
9. feature 7 (0.018028)
```

```
Feature ranking:
1. feature 0 (0.277363)
2. feature 7 (0.193162)
3. feature 6 (0.192068)
4. feature 1 (0.070917)
5. feature 5 (0.066546)
6. feature 3 (0.053179)
7. feature 4 (0.052309)
8. feature 2 (0.051360)
9. feature 8 (0.043096)
```


a) original features

b) feature ranking with ICA
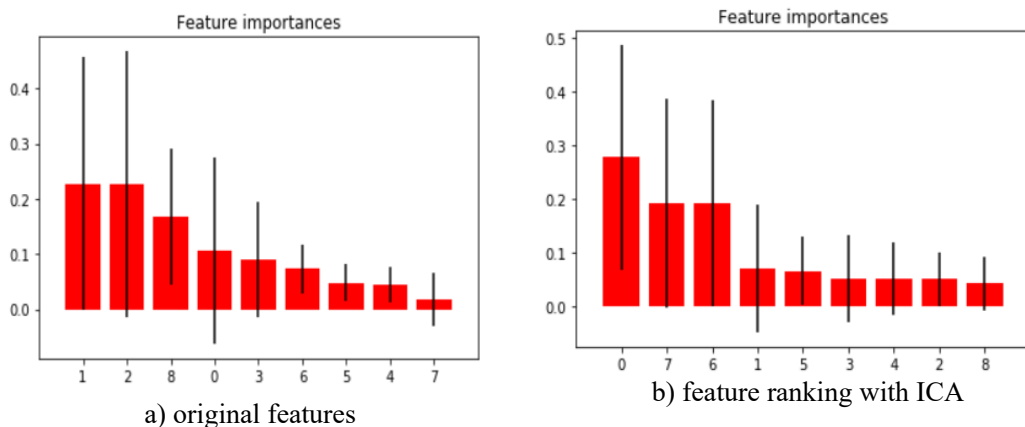
Fig. 2: The comparison of features ranking with and without ICA.
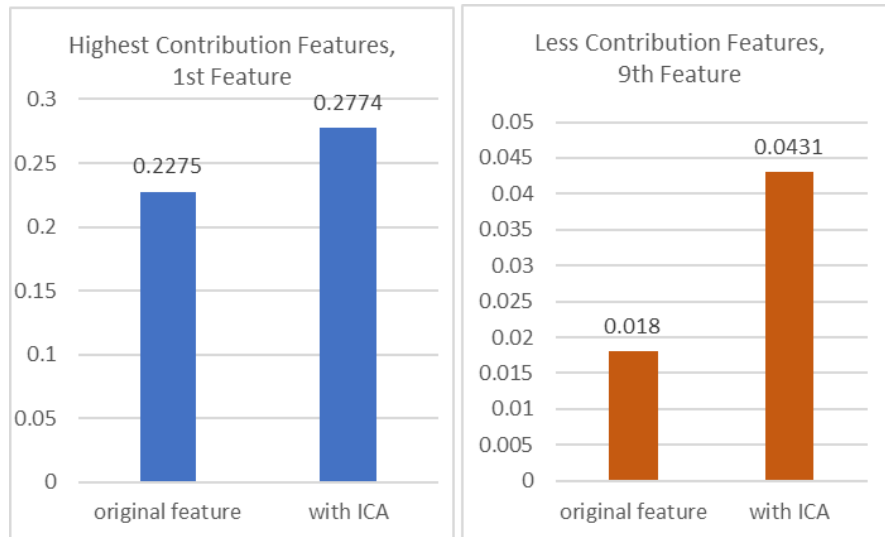
Fig. 3: Percentage differences in the highest and lowest ranking features.

3.3 Building Model using Classification

Once the data completed pre-processing, we moved to the classification process. The classifier that we chose is K-Nearest Neighbor (K-NN). K - Nearest Neighbor (KNN) is one of the most straightforward classification machines that stores all available cases and classifies new cases based on a similarity measure [2,41]. The idea behind KNN is that if a sample belongs to a specific class in the space of several similar samples (k), the sample is also in the category. Thus, techniques based on Nearest-Neighbor classify samples based on the similarity of the population. KNN falls into the algorithm family of supervised learning. Informally, this means that a labeled data set consisting of training observations (x, y) is provided, and the relationship between x and y wants to be captured. More formally, our objective was to learn a function h:X→Y to predict the corresponding y output confidently with an unseen observation x. First, we needed to determine the k-value of the number of groups (cluster) to use K-NN. For this research, we used Elbow Method to determine the k value.

3.3.1 Determine k-value (Elbow Method)

Elbow method ran the k-NN algorithm several times and calculated the WSS error for different values of k. To find the optimal value of k, we used the elbow method that derives from the Within-cluster Sum of Squared (WSS). The Elbow method is a heuristic approach in determining the number of clusters for k-means or k-NN. The equation of WSS is described by Eq. (11):

$$WSS = \sum_{k=1}^{k} \sum_{X_i \in C_k} (X_i - \mu_k)^2 \tag{11}$$

where;
Ck = cluster of k
μk = the mean value of the data that point to the cluster
Xi = an observation to the Ck

The optimal value of k is at the elbow curve, or the distortion point that starts decreasing linearly, as described in Fig. 6. Although the value of k = 2 looks like there is a curve/ distortion from k= 2 until the k = 4, the decrease is still significant and not linear. Due to that, for this research, the k-value was k = 4.
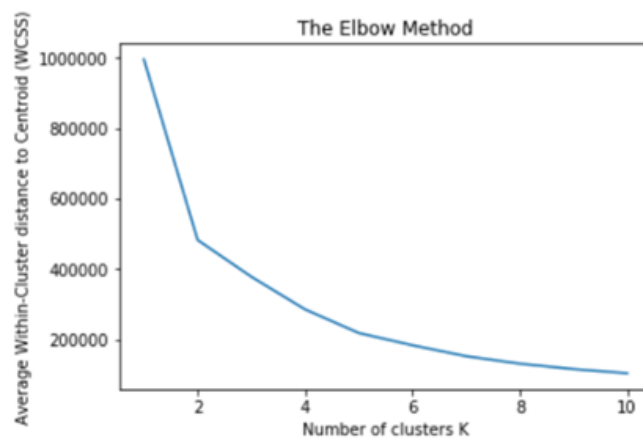
Fig. 4: The Elbow method.

3.3.2 Building the Model

Once we have determined the k-value for K-NN, we started training and building the machine learning model. The Building Model Data was divided into training data and testing data with a 70:30 ratio, as explained in Section 3.2. During the building model process, once the model was built, the prediction of the Evaluation Data was ready to start. We tested it file-by-file to evaluate how well the model could predict a particular bot.

4. EVALUATION

We evaluated the performance of our techniques based on the Confusion Matrix in terms of accuracy, precision, recall, f-score, false-negative rate (FNR), and false-positive rate (FPR). A confusion matrix is the most widely used method to evaluate a machine-learning model's performance. The distribution of the results can be seen clearly by creating a confusion matrix from the model. The confusion matrix consisted of a two-dimensional table with the class "actual" and "cluster/projection" in a single-dimension structure and evaluated only two (2) classes. The other dimension was rated as "Botnet" positive and "Human" negative. Thus, the cases were classified into four fractions: False Positive (FP), False Negative (FN), True Positive (TP), and True Negative (TN), as shown in Table 5.

Table 5: The Confusion Matrix for this article

		Prediction (Cluster)	
		Normal	**Botnet**
Actual (Label)	**Normal**	TN	FP
	Botnet	FN	TP

When the data is in the state "True", either TP or TN, it shows that the classifier predicted it in the correct class. In the "False" state, there was an incorrect prediction class. For example, when the data was in a False Negative state, it means that the classifier Falsely predicted as Negative (Normal) where the data was positive (botnet), while the Positive and Negative indicate Botnet or Normal class.

Table 6: The explanation of Confusion Matrix's fraction used in this article

Fraction	Module 2
True Positive (TP)	TP is counted when the model **CORRECT**ly predicted the botnet traffic/IP
True Negative (TN)	TN is counted when the model **CORRECT**ly predicted the normal (Negative) traffic/IP
False Positive (FP)	FP is counted when the model **INCORRECT**ly predicted the normal (Negative) traffic as the **BOTNET** (Positive) traffic/IP
False Negative (FN)	FN is counted when the model **INCORRECT**ly predicted the botnet (Positive) as the normal (**NEGATIVE**) traffic/IP

The Confusion Matrix can generate several performance evaluation parameters, but for this research, we focused on accuracy, precision, recall, f-score, false-negative rate (FNR), and false-positive rate (FPR). These parameters were chosen to make a comparison with other researcher's results that used the same dataset. The overall performance was from the Accuracy, but we preferred to compare the overall performance using the f-score.

4.1 Performance Parameter

4.1.1 Accuracy

Accuracy is often used to measure the overall performance of the machine learning classifier because it is a parameter that measures how often the algorithm correctly classifies a data point. Accuracy is the number of correctly predicted data points from all data points where it can be described in the Eq. (12) below:-

$$Accuracy = \frac{\sum total\ correct\ prediction}{\sum data} = \frac{TP+TN}{TP+TN+FN+FP} \tag{12}$$

4.1.2 Precision

The 'Precision' parameter is the count of data classified as a botnet (positive) that are genuinely botnet. Precision also can be described as in equation (13):-

$$Precision = \frac{Positive\ prediction\ that\ truly\ positive}{\sum Total\ positive\ prediction} = \frac{TP}{TP+FP} \tag{13}$$

4.1.3 Recall

A recall is also known as Sensitivity, where it is the fraction of actual positives that are identified correctly. Recall also can be described as the ability of a model to find the relevant cases.

$$Recall\ (TPR) = \frac{Positive\ prediction\ that\ truly\ positive}{All\ botnet\ data} = \frac{TP}{TP+FN} \tag{14}$$

4.1.4 F-score

F1 score is the harmonic combination of recall and precision. F1 score is the equal weight.

$$F_{score} = 2 * \frac{Precision*Recall}{Precision+Recall} \tag{15}$$

5.   RESULTS AND DISCUSSION

The evaluation for the framework was conducted in 2 parts; one was when building the model and the other one was the prediction of novel data using the Evaluating Data.

5.1 Building Model

This section summarizes the findings during the Model Building. The performance of the flow-based features and K-NN framework was compared to the performance of the same framework but with additional ICA during pre-processing. Both performance evaluations are shown in Table 7.

Table 7: The performance comparison of the training model with and without ICA

	Accuracy	Precision	Recall	F1-score	FNR	FPR
without ICA	0.9689	0.9831	0.958	0.9704	0.0419	0.01875
with ICA	0.969	0.9846	0.9568	0.9705	0.0431	0.0169

This result was evaluated on the testing data split from the Building Model Data illustrated in Fig. 3. Table 7 lists the parameters used in the evaluation. From the results in Table 7, if we compare the Accuracy and F-score, there are tiny increments, but the False Positive Rate (FPR) decreased from 1.88% to 1.69%.

5.2 Prediction Novel Bots

CTU-13, the benchmark botnet dataset, is also used by several researchers to evaluate their prediction model's performance. So, we compared the result from another article that used the same data source and the same evaluation parameter. There were 5 files in Evaluating Data that were separated before the building model process. The data is described in Table 8.

Table 8: The data number and the botnet type in Evaluating Data

Data Number	Bot Name
data 1	
data 2	Neris
data 6	Menti
data 8	Murlo
data 9	Neris

Table 9: Performance differences between models with and without ICA against novel botnet

K-NN Model	Data Number	Accuracy	F1-score	FPR
without ICA	data 1	0.6708	0.6895	0.2187
	data 2	0.7583	0.784	0.0679
	data 6	0.7032	0.6041	0.1826
	data 8	0.7658	0.2871	0.1547
	data 9	0.5067	0.6436	0.1891
with ICA	data 1	0.7912	0.8298	0.278
	data 2	0.6734	0.6958	0.1262
	data 6	0.7767	0.7673	0.2995
	data 8	0.8005	0.5859	0.2244
	data 9	0.7134	0.8222	0.3309

Based on Table 9, the model with ICA showed a better F score than the Model Without ICA. But, the model without ICA showed the lowest FPR compared to the other model. Thus, the yellow box in Table 9 indicates the best value, either the highest F score or the lowest FPR. Since we were focused on the F-score for comparison, we extracted it to Table 10.

Table 10: The F score for both models (with and without ICA)

	data 1	data 2	data 6	data 8	data 9
without ICA	0.6895	0.784	0.6041	0.2871	0.6436
with ICA	0.8298	0.6958	0.7673	0.5859	0.8222

Table 10 shows that 4 files from 5 novel botnet files had the highest F-score using the K-NN model with ICA. Only one file, File No 2, showed the opposite result. Due to that, we agree that the K-NN Model with ICA performed better than the K-NN Model without ICA. The result for the K-NN Model with ICA was compared to other researcher's results. The results were directly compared with previously reported findings on a novel botnet prediction model that used the same data sources. Table 11 summarizes the comparison result and lists the parameters used in every previous article.

Table 11: Performance model comparison between previous researchers

Parameter	Data No/ researcher	Garcia, S., Zunino, A., & Campo, M. (2014)[42]	Garcia, S. (2015). [44]	Kozik, R. (2018) [45]	Wang, J. & Paschalidis, I.C. (2017)[46]	Fernandez Maimo et al. [38]	wnh ibrahim et al.
Recall	1	0.4	1	0.077	0.91	0.91	0.8357
	2	0.3	0.88	0.046	0.55	0.95	0.5687
	6	0	0	0.12	0.95	1	0.8836
	8	0.1	0	0.044	0.76	0.26	0.9424
	9	0.1	0.38	0.08	0.38	0.99	0.7171
Precision	1	0.5	0.87	0.86	0.73	0.68	0.824
	2	0.6	0.96	0.8	0.65	0.88	0.8961
	6	0.4	-1	0.69	0.7	0.92	0.6781
	8	0.2	0	0.6	0.4	0.47	0.4251
	9	0.4	0.72	0.73	0.95	0.89	0.9635
F1 Score	1	0.48	0.93	0.14	0.81	0.77	0.8298
	2	0.41	0.92	0.088	0.59	0.92	0.6958
	6	0.04	0	0.21	0.8	0.96	0.7673
	8	0.14	-1	0.082	0.53	0.33	0.5859
	9	0.25	0.5	0.14	0.54	0.94	0.8222

Based on Table 11, in the F-Score parameter, our technique defeated other results for Data number 8 (red font). However, three out of five novel botnet files hade the highest f-score from Fernandez Maimo et al. [31]. To measure the overall performance, we calculated the average for each parameter. The average of each data (Data from File 1,2,6,8,9) and parameter (Precision, Recall, and F Score) from Table 11 are illustrated in Fig. 7. These plots show that our method proposed here outperformed the other approaches except Fernandez Maimo et al. [31].

Since the Fernandez Maimo et al. [31] techniques outperformed the overall evaluation, we compared the different approaches they used. For example, Fernandez Maimo et al. [31] also used flow-based features, but they considered the features from dual-direction, incoming, and outgoing traffic. Their approach resembled our technique in that both methods focused on concealment network traffic and used statistical analysis to aggregate the data.
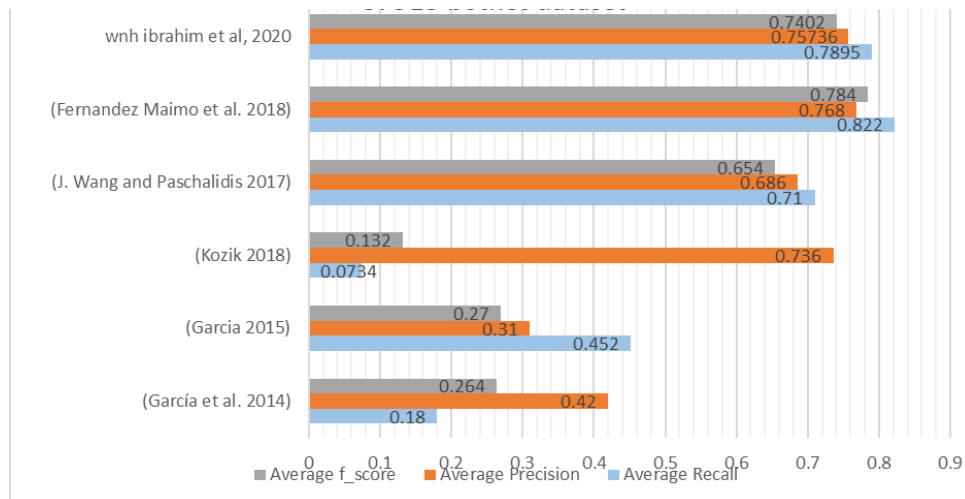
Fig. 5: The performance comparison among other researchers on botnet classification.

6. CONCLUSION

This paper proposes the framework for novel botnet detection that implements data standardization and Independent Component Analysis (ICA) during flow-based features pre-processing data. The strength of our framework is that we used flow-based features that have the benefits of detecting traffic from the concealment network. Other than that, the complexity and processing time can also be minimized by flow-based features compared to content-based ones. Also, for aggregation, for the quick detection method, we used the shortest time interval. Our approach can be applied to botnet concealment and new/novel forms of a botnet.

The use of data standardization and Independent Component Analysis (ICA) improves key rating attributes and classification outcomes. However, the overall result is still not the best relative to other previous approaches. Nevertheless, it generated an improved result using Data Standardization and Independent Component Analysis (ICA). We can also assume that behavior analysis caused some noise to the pattern.

Future directions are connected to enhancing the collection of functionalities. Further developments are expected to lead to a deeper understanding of the nature of the selection of functions.

ACKNOWLEDGEMENT

REFERENCES

[1] Ibrahim, W.N.H., Selamat, A., Anuar, S., & Krejcar, O. (2019). Clustering botnet behavior using K-means with uncertain data, Frontiers in Artificial Intelligence and Applications vol. 318. pp.244–257.

[2] Liang, X. & Znati, T. (2019). On the performance of intelligent techniques for intensive and stealthy DDos detection, Computer Networks vol. 164. p.106906.

[3] Gross, G. (2016). Detecting and destroying botnets, Network Security vol. 2016, no. 3. pp.7–10.

[4] WHITE OPS. (2018). Retrieved June 1, 2020, https://www.whiteops.com/blog/9-of-the-most-notable-botnets.

[5] Kolias, C., Kambourakis, G., Stavrou, A., & Voas, J. (2017). DDoS in the IoT: Mirai and other botnets, Computer vol. 50, no. 7. pp.80–84.

[6] Eremin, A. (2019). Retrieved June 1, 2020, https://securelist.com/bots-and-botnets-in-2018/90091/.

[7] Khan, R.U., Zhang, X., Kumar, R., Sharif, A., Golilarz, N.A., & Alazab, M. (2019). An adaptive multi-layer botnet detection technique using machine learning classifiers, Applied Sciences (Switzerland) vol. 9, no. 11. p.2375.

[8] Patsakis, C., Casino, F., & Katos, V. (2020). Encrypted and covert DNS queries for botnets: Challenges and countermeasures, Computers & Security vol. 88. p.101614.

[9] Bezerra, V.H., da Costa, V.G.T., Barbon Junior, S., Miani, R.S., & Zarpelão, B.B. (2019). IoTDS: A one-class classification approach to detect botnets in internet of things devices, Sensors (Switzerland) vol. 19, no. 14. p.3188.

[10] Wang, Y.-H., Li, Z.-N., Xu, J.-W., Yu, P., Chen, T., & Ma, X.-X. (2020). Predicted Robustness as {QoS} for Deep Neural Network Models, Journal of Computer Science and Technology vol. 35, no. 5. pp.999–1015.

[11] Prasad, K.M., Reddy, A.R.M., & Rao, K.V. (2020). BARTD: Bio-inspired anomaly based real time detection of under rated App-DDoS attack on web, Journal of King Saud University - Computer and Information Sciences vol. 32, no. 1. pp.73–87.

[12] Su, S.C., Chen, Y.R., Tsai, S.C., & Lin, Y.B. (2018). Detecting P2P Botnet in Software Defined Networks, Security and Communication Networks vol. 2018. pp.1–13.

[13] Mahmoud, M., Nir, M., & Matrawy, A. (2015). A Survey on botnet architectures, detection and defences, International Journal of Network Security vol. 17, no. 3. pp.272–289.

[14] Mathur, L., Raheja, M., & Ahlawat, P. (2018). Botnet Detection via mining of network traffic flow, Procedia Computer Science vol. 132. pp.1668–1677.

[15] Kupreev, O., Badovskaya, E., & Gutnikov, A. (2019). Retrieved June 1, 2020, https://securelist.com/ddos-report-q3-2019/94958/.

[16] Aamir, M. & Zaidi, S.M.A. (2019). Clustering based semi-supervised machine learning for DDoS attack classification, Journal of King Saud University - Computer and Information Sciences.

[17] Singh, M., Singh, M., & Kaur, S. (2019a). Detecting bot-infected machines using DNS fingerprinting, Digital Investigation vol. 28. pp.14–33.

[18] Bazrafshan, Z., Hashemi, H., Fard, S.M.H., & Hamzeh, A. (2013). A survey on heuristic malware detection techniques, IKT 2013 - 2013 5th Conference on Information and Knowledge Technology no. May. pp.113–120.

[19] AsSadhan, B., Bashaiwth, A., Al-Muhtadi, J., & Alshebeili, S. (2018). Analysis of P2P, IRC and HTTP traffic for botnets detection, Peer-to-Peer Networking and Applications vol. 11, no. 5. pp.848–861.

[20] Alauthaman, M., Aslam, N., Zhang, L., Alasem, R., & Hossain, M.A. (2018). A P2P Botnet detection scheme based on decision tree and adaptive multilayer neural networks, Neural Computing and Applications vol. 29, no. 11. pp.991–1004.

[21] Santana, D., Suthaharan, S., & Mohanty, S. (2018). What we learn from learning - Understanding capabilities and limitations of machine learning in botnet attacks.

[22] Rauf, M.A.A.A., Asraf, S.M.H., & Idrus, S.Z.S. (2020). Malware Behaviour Analysis and Classification via Windows DLL and System Call, Journal of Physics: Conference Series vol. 1529, no. 2.

[23] Resende, P.A.A. & Drummond, A.C. (2018). A survey of random forest based methods for intrusion detection systems, ACM Computing Surveys vol. 51, no. 3. pp.1–36.

[24] Tobiyama, S., Yamaguchi, Y., Shimada, H., Ikuse, T., & Yagi, T. (2016). Malware Detection with Deep Neural Network Using Process Behavior, Proceedings - International Computer Software and Applications Conference vol. 2. pp.577–582.

[25] Muhtadi, A.F. & Almaarif, A. (2020). Analysis of Malware Impact on Network Traffic using Behavior-based Detection Technique, International Journal of Advances in Data and Information Systems vol. 1, no. 1. pp.17–25.

[26] Apruzzese, G. & Colajanni, M. (November 2018). Evading botnet detectors based on flows and random forest with adversarial samples. Paper presented at NCA 2018 - 2018 IEEE 17th International Symposium on Network Computing and Applications.

[27] Beigi, E.B., Jazi, H.H., Stakhanova, N., & Ghorbani, A.A. (2014). Towards effective feature selection in machine learning-based botnet detection approaches, 2014 IEEE Conference on Communications and Network Security, CNS 2014 pp.247–255.

[28] Cabeza, L.F., Solé, C., Castell, A., Oró, E., & Gil, A. (2016). Unsupervised Network Intrusion Detection Systems for Zero-Day Fast- Spreading Attacks and Botnets Payam, International Journal of Digital Content Technology and its Applications(JDCTA) vol. 10, no. 2.

[29] Singh, M., Singh, M., & Kaur, S. (2019b). Detecting bot-infected machines using DNS fingerprinting, Digital Investigation vol. 28. pp.14–33.

[30] Malik, R. & Alankar, B. (2019). Botnet and Botnet Detection Techniques, International Journal of Computer Applications vol. 178, no. 17. pp.8–11.

[31] Koroniotis, N., Moustafa, N., Sitnikova, E., & Turnbull, B. (2019). Towards the development of realistic botnet dataset in the Internet of Things for network forensic analytics: Bot-IoT dataset, Future Generation Computer Systems vol. 100. pp.779–796.

[32] Huda, S., Abawajy, J., Al-Rubaie, B., Pan, L., & Hassan, M.M. (2019). Automatic extraction and integration of behavioural indicators of malware for protection of cyber–physical networks, Future Generation Computer Systems vol. 101. pp.1247–1258.

[33] Bou-Harb, E., Debbabi, M., & Assi, C. (2014). On fingerprinting probing activities, Computers and Security vol. 43, no. January 2012. pp.35–48.

[34] Palmieri, F., Fiore, U., & Castiglione, A. (2014). A distributed approach to network anomaly detection based on independent component analysis, Concurrency and Computation: Practice and Experience vol. 26, no. 5. pp.1113–1129.

[35] Mao, C.-H., Lin, C.-C., Pan, J.-Y. (Tim), Chang, K.-C., Faloutsos, C., & Lee, H.-M. (2012). EigenBot: Foiling spamming botnets with matrix algebra. Paper presented at Proceedings of the ACM SIGKDD Workshop on Intelligence and Security Informatics - ISI-KDD '12, New York, New York, USA.

[36] Ehsan, K. & Hamid, reza shahriari. (2018). BotRevealer: Behavioral Detection of Botnets based on Botnet Life-cycle, International Journal of Information Security vol. 10, no. 1. pp.55–61.

[37] Stevanovic, M. & Pedersen, J.M. (2015). On the use of machine learning for identifying botnet network traffic, Journal of Cyber Security and Mobility vol. 4, nos. 2–3. pp.1–32.

[38] Fernandez Maimo, L., Perales Gomez, A.L., Garcia Clemente, F.J., Gil Perez, M., & Martinez Perez, G. (2018). A Self-Adaptive Deep Learning-Based System for Anomaly Detection in 5G Networks, IEEE Access vol. 6. pp.7700–7712.

[39] Debashi, M. & Vickers, P. (2018). Sonification of Network Traffic for Detecting and Learning about Botnet Behavior, IEEE Access vol. 6. pp.33826–33839.

[40]   Gezer, A., Warner, G., Wilson, C., & Shrestha, P. (2019). A flow-based approach for Trickbot banking trojan detection, Computers and Security vol. 84. pp.179–192.

[41]   Garg, S., Peddoju, S.K., & Sarje, A.K. (2016). Scalable P2P bot detection system based on network data stream, Peer-to-Peer Networking and Applications vol. 9, no. 6. pp.1209–1225.

[42]   Garcia, S., Zunino, A., & Campo, M. (2014). "Identifying, Modeling and Detecting Botnet Behaviors in the Network".

[43]   Han, W., Xue, J., Wang, Y., Liu, Z., & Kong, Z. (2019). MalInsight: A systematic profiling based malware detection framework, Journal of Network and Computer Applications vol. 125, no. October 2018. pp.236–250.

[44]   Garcia, S. (2015). Modelling the Network Behaviour of Malware To Block Malicious Patterns . The Stratosphere Project : a Behavioural Ips, Virus Bulletin no. September. pp.1–8.

[45]   Kozik, R. (2018). Distributing extreme learning machines with Apache Spark for NetFlow-based malware activity detection, Pattern Recognition Letters vol. 101. pp.14–20.

[46]   Wang, J. & Paschalidis, I.C. (2017). Botnet Detection Based on Anomaly and Community Detection, IEEE Transactions on Control of Network Systems vol. 4, no. 2. pp.392–404.

COLOR IMAGE RETRIEVAL BASED ON FUZZY NEURAL NETWORKS AND SWARM INTELLIGENCE TECHNIQUES

BAYDAA IBRAHEEM KHALEEL

Computer Science Department, College of Computer Science & Mathematics,
University of Mosul, Mosul, Iraq

*Corresponding author: baydaaibraheem@uomosul.edu.iq

ABSTRACT:Image retrieval is an important system for retrieving similar images by searching and browsing in a large database. The image retrieval system can be a reliable tool for people to optimize the use of image accumulation, and finding efficient methods to retrieve images is very important. Recent decades have marked increased research interest in field image retrieval. To retrieve the images, an important set of features is used. In this work, a combination of methods was used to examine all the images and detect images in a database according to a query image. Linear Discriminant Analysis (LDA) was used for feature extraction of the images into the dataset. The images in the database were processed by extracting their important and robust features and storing them in the feature store. Likewise, the strong features were extracted for specific query images. By using some Meta Heuristic algorithms such as Cuckoo Search (CS), Ant Colony Optimization (ACO), and using an artificial neural network such as single-layer Perceptron Neural Network (PNN), similarity was evaluated. It also proposed a new two method by hybridized PNN and CS with fuzzy logic to produce a new method called Fuzzy Single Layer Perceptron Neural Network (FPNN), and Fuzzy Cuckoo Search to examine the similarity between features for query images and features for images in the database. The efficiency of the system methods was evaluated by calculating the precision recall value of the results. The proposed method of FCS outperformed other methods such as PNN, ACO, CS, and FPNN in terms of precision and image recall.

ABSTRAK: Imej dapatan semula adalah sistem penting bagi mendapatkan imej serupa melalui carian imej dan melayari pangkalan besar data. Sistem dapatan semula imej ini boleh dijadikan alat boleh percaya untuk orang mengoptimum penggunaan pengumpulan imej, dan kaedah pencarian yang berkesan bagi mendapatkan imej adalah sangat penting. Beberapa dekad yang lalu telah menunjukan banyak penyelidikan dalam bidang imej dapatan semula. Bagi mendapatkan imej-imej ini, ciri-ciri set penting telah digunakan. Kajian ini menggunakan beberapa kaedah bagi memeriksa semua imej dan mengesan imej dalam pangkalan data berdasarkan imej carian. Kami menggunakan Analisis Diskriminan Linear (LDA) bagi mengekstrak ciri imej ke dalam set data. Imej-imej dalam pangkalan data diproses dengan mengekstrak ciri-ciri penting dan berkesan daripadanya dan menyimpannya dalam simpanan ciri. Begitu juga, ciri-ciri penting ini diekstrak bagi imej carian tertentu. Persamaan dinilai melalui beberapa algoritma Meta Heuristik seperti Carian Cuckoo (CS), Pengoptimuman Koloni Semut (ACO), dan menggunakan lapisan tunggal rangkaian neural buatan seperti Rangkaian Neural Perseptron (PNN). Dua cadangan baru dengan kombinasi hibrid PNN dan CS bersama logik kabur bagi menghasilkan kaedah baru yang disebut Lapisan Tunggal Kabur Rangkaian Neural Perseptron (FPNN), dan Carian Cuckoo Kabur bagi mengkaji persamaan antara ciri carian imej dan imej pangkalan data. Nilai kecekapan kaedah sistem dinilai dengan mengira

ketepatan mengingat pada dapatan hasil. Kaedah FCS yang dicadangkan ini mengatasi kaedah lain seperti (PNN), (ACO), (CS) dan (FPNN) dari segi ketepatan dan ingatan imej.

KEYWORDS:*image retrieval; linear discriminant analysis (LDA); cuckoo search (CS); ant colony optimization (ACO); neural network*

1. INTRODUCTION

We are witnessing an era of great development in the fields of information techniques, Internet, and services for web. People can take pictures anywhere, anytime, using mobile smart phones or digital cameras. This has led to a significant increase in the use of image groups and digital media. To obtain integrated and rapid capabilities of the current technology and to facilitate dealing with large image groups, there must be effective capabilities and rapid mechanisms for user-driven image searching through huge image datasets. Therefore, efficient and fast methods of retrieving images must be used. Here, some artificial intelligence techniques are used. Image retrieval methods are used in important areas such as security, criminal investigation, and medical imaging [1, 2]. Feature extraction refers to the study of dimensionality reduction methods that describe the data. Its purpose is to reduce computational costs by using fewer features to represent data, without degrading discriminatory ability. Feature extraction is the process of using a subset of the original feature areas [3]. Artificial neural networks are a branch of artificial intelligence techniques that are computational structures that can be trained on to learn models from examples. Optimal solutions can be reached using the training group that tests the relationship between inputs and outputs and the method of learning, and networks that learn through supervision do local improvement [4]. Swarm intelligence is also one of the branches of artificial intelligence technology that depends on social behaviour. Its behaviour is inspired by nature, and the swarm has a great tolerance, so the failure of one factor does not stop the performance of the whole system. Swarm intelligence has enormous applications in many areas such as image processing, robotics, and telecommunications [5].

In this work, the linear discriminant analysis (LDA) algorithm was used for dimensionality reduction and to extract important features from the image datasets and query images. Meta Heuristic algorithms were used, such as algorithms of CS and ACO. Single layer perceptron neural network was also used and then the fuzzy membership function with single layer perceptron and CS were combined to produce a new method called fuzzy single layer perceptron neural network (FPNN). Fuzzy Cuckoo Search (FCS) found similar images and place them in one class, i.e. to create several classes of the input images group, each class contained similar images, and to find similarities between the query images and the group of images in the image database being used.

2. PREVIOUS WORKS

The use of ACO algorithm to retrieve images from 120 images with an accuracy of 91.6% for the image retrieval system has been reported [1]. Ramandeep and Ashok used the Cuckoo Search Engine for content based image retrieval. They compared Cuckoo search to neural networks, which took more iterations [6]. Arvind et al.presented a feed-forward neural network to recall and retrieve images and, due to its highly efficient and accurate classification capability, they obtained a retrieval precision equal to 88% and recall rate equal to 78% [4]. Pathareand Kimmatkar[7]implemented a system that was a mixture of a color-feature based recovery, Firefly, and SVM for region-based image retrieval (RBIR). The accuracy result gained in the retrieval of the RBIR images equalled to 95% and TPR

was equal to 65%. Kurchaniya and Johari[8] extracted edge and texture information of images using IEHD and RLBP respectively, and they used PSO to measure similarities between images. All images in the databases used gave a better result in terms of accuracy and recall, where the system was implemented on three types of database. They reached accuracy rates equal to 84.60% for LI database, 85.62% for WANG, and 85.20% for Caltech-101databases. Nie proposed a network model based on the particle swarm optimization algorithm and then established a mathematical model based on swarm intelligence for a Use Content-based image retrieval [9].

3. LINEAR DISCRIMINANT ANALYSIS (LDA)

The goal of the Linear Discriminant Analysis technique is to project the original data matrix onto a lower dimensional space. The LDA method has been developed in order to transform features into space with fewer dimensions, and this increases the variance between classes and reduces the variance within the class. This helps to obtain the highest separation between classes. Consider a group of N image samples $\{x_1, x_2, \ldots x_n\}$, where image space takes up n-dimensional. Assume C classes $\{C_1, C_2, \ldots C_c\}$ and each image belongs to one of these classes. There are N_i samples in a class. Then,

$$C_i(i = 1,2,3,....,c), \mu_i = \frac{1}{N}\sum_{i=1}^{N} x_i \tag{1}$$

is the mean of the samples in class C_i, and the between-class scatter matrix S_B is defined as

$$S_B = \frac{1}{N}\sum_{i=1}^{c} N_i(\mu_i - \mu)(\mu_i - \mu)^T \tag{2}$$

The within-class matrix S_w is defined as

$$S_\omega = \frac{1}{N}\sum_{i=1}^{c}\sum_{x_k \in c_i} (x_i - \mu_i)(x_i - \mu_i)^T \tag{3}$$

$$W_{op} = \arg m \times w \left|\frac{W^T S_B W}{W^T S_\omega W}\right| = [\omega_1 \omega_2 \omega_3 \ \omega_4 ....\omega_j] \tag{4}$$

where $\{W_i | i = 1,2,3,\ldots\ldots j\}$ denote generalized eigenvector sets S_B and S_w that correspond to (m) largest generalized Eigen values $\{\lambda_i = 1,2,3,\ldots\ldots j\}$ or their mean [3,10].

$$S_B \omega_i = \lambda_i S_\omega \omega_i , i = 1,2,3,..., j \tag{5}$$

4. ANT COLONY OPTIMIZATION

Meta-heuristic algorithms based on the principles of artificial intelligence are most used in image processing, in the fields of engineering and informatics [5,11]. An ant colony's algorithm is a meta-heuristic algorithm that belongs to the intelligence of swarms and is based on the behavior of ants. Ants, by their nature, are able to find the shortest path from the source of the food to the nest. To do this, the ant places a chemical on the ground as a guide for others to find food. The path selection for later ants depends on the density of the chemical, and therefore the behaviour of the ants stimulates the emergence of an algorithm consisting of a group of intelligent ants (artificial ants) as a group of simple agents that work with each other to solve problems by exchanging information via chemicals (pheromones) that act as a distributed memory to the linked ants. Therefore, this algorithm representing system ants is applied to a number of complex optimization problems. From the ants' foraging behaviour, the idea of the algorithm came about as follows [12]:

A group of ants begin to leave the cell randomly in multiple directions. This process occurs the first time only, but subsequently the ants choose a specific path after testing each path.

- An ant secretes a certain percentage of pheromone as it passes and that pheromone is used to know the path the ant has passed.

- When finding the food source, the ant takes a sufficient amount of it, then returns to the cell, and chooses a specific path where it chooses the path that has the largest amount of pheromone. When the ant returns, the same amount of pheromone is released.

- When the ant leaves the cell again, it tests the amount of pheromone in all paths and chooses the path with the largest amount of pheromone.

- In each determined time period, the pheromone amount is updated, because the pheromone concentration will disappear over time.

It has been observed that the shortest path is always the one that contains the largest pheromone amount. Therefore, this is the path through which all ants will pass. The ant algorithm is a dynamic algorithm, meaning that if a problem occurs in the shorter path, a new path ant will choose in same way. The steps of the Ant Colony Optimization algorithm are [12,13]:

1. Ant Searching Behavior as follows:

When the ant K is in cell i, it uses the heuristic function η_{ij}, and pheromone τ_{ij} to calculate the probability that it will choose cell j as the next cell according of the following equation:

$$P_{ij}^{K} = \begin{cases} \dfrac{\tau_{ij}^{\alpha} \cdot \eta_{ij}^{\beta}}{\sum_{j \in N_i^{(K)} \tau_{ij}^{\alpha} \cdot \eta_{ij}^{\beta}}} & if \ j \in N_i^{K} \\ 0 & otherwise \end{cases} \tag{6}$$

$N_i^{(K)}$ represents the group of elements that do not belong to the partial solution of the ant. K, α, β represent fixed values that determine the importance of the pheromone substance and the heuristic information respectively, the heuristic function is calculated by the equation

$$\eta_{ij} = \frac{1}{d_{ij}} \tag{7}$$

and d_{ij} represents the distance between the edge i and the edge j.

2. Track the path and update the pheromone before returning to the parent node (nest), K, an ant places $\Delta\tau^{(K)}$ from a pheromone (the aromatic substance) on the edges it visited, so the value of the pheromone τ_{ij} at the edge (i,j) that the ant has crossed is calculated as follows

$$\tau_{ij} = \tau_{ij} + \Delta\tau^{(K)} \tag{8}$$

In general, the increase in the amount of pheromone on a specific edge leads to an increase in the probability of being selected by the rest of the ants in the colony.

3. Pheromone Trail Evaporation. The pheromone begins to evaporate from all edges when K ant moves to next node, as shown in following equation

$$\tau_{ij} = (1 - p)_{\tau_{ij}} \tag{9}$$

$$\forall (i, j) \in A$$

As the $p \in (0,1)$ represent the coefficient of evaporation, A indicates the edges that an ant traversed on its way from the parent node to the destination, and generally the evaporation of the pheromone contributes to increasing the ability of the algorithm to explore different paths during the search process, and also contributes to reducing the amount of pheromone on the edges.

To update the pheromone after ants return to the main node, according to following equation

$$\tau_{ij} = (1-p)_{\tau_{ij}} + \sum_{K=1}^{N} \Delta \tau_{ij}^{K} \tag{10}$$

The goal of updating the pheromone is to increase the pheromone amount associated with promising and good paths. Therefore, the pheromones placed at the edge by the K ant are calculated as shown in the equation:

$$\Delta \tau_{ij}^{K} = \frac{R}{L_{K}} \tag{11}$$

As R represents a fixed value that works to determine the amount of increase in the amount of pheromone in a limited range, L represents the path that the ant K crosses and in general the repetition represents a complete cycle that includes the movement of ants and the evaporation of the pheromone.

In this paper, the clustering process was adopted using the Mahalanobis distance to find the similarity between the query image and the database images by calculating the distance according to the following equation:

$$dist_{ij} = (data_j - center_i)^T A_i (data_j - center_i) \tag{12}$$

where this algorithm gave satisfactory results in the process of retrieving colour images.

5. SINGLE LAYER PERCEPTRON NEURAL NETWORK

Single layer perceptron SLP consist of input layer and output layer. Each layer consists of one or more neurons (nodes), and each node in the input layer receives information from the outside world and is linked by connection weights with all nodes in the output layer. The data flows from the input layer to the output layer, and in the event of an error during learning, weights are changed. Perceptron neural network is used for resolving linearly separable data. The steps of basic perceptron algorithm as follows [4]:

Firstly, initialize weights at random W_{kj}, and for each training pair / pattern [X_i, t_i], where $X_i = x_1, x_2, \ldots, x_n$, then compute output Y, and compute error

$$E_i = t_i - f\left(\sum_k W_{ik} X_k\right) = t_i - f(net_i) \tag{13}$$

And finally use the error to update weights as follows

$$W_{ij}^{new} = W_{ij}^{old} + \Delta W_{ij} \tag{14}$$

where $\Delta W_{ij} = \alpha * e_i * E_i \tag{15}$

$\alpha$is the learning rate, and it is a small value that is greater than zero. Repeat the step until convergence [4,14].

In this paper, to improve the work of the perceptron network and accelerate the access to the optimal solution, the neural network was hybridized with fuzzy logic by adding a membership function to the equation of adjusting the weights to ensure that the ideal weights are obtained with the least time and effort. Here, a new proposed method was obtained that called it Fuzzy Single Layer Perceptron Neural Network (FPNN) as shown in equations below:

$$\Delta W_{ij} = U_i(t)\alpha * \mathrm{e}_i * \mathrm{E}_i \tag{16}$$

$$U_i = (\mu_{ik})^{f_m} \tag{17}$$

$$\mu_{ik} = \frac{\left(\dfrac{1}{D_{ik}}\right)^{\frac{1}{f_m-1}}}{\displaystyle\sum_{p=1}^{c}\left(\dfrac{1}{D_{pk}}\right)^{\frac{1}{f_m-1}}} \tag{18}$$

where$U_i$denotes the fuzzy membership function, and$D_{ik} = d(x_k, w_i)$ represents the Euclidean distance between the input data and the weights of the output cells that play an important role in computing the value of the membership function.

6. CUCKOO SEARCH

This algorithm is based on behaviour inspired from nature. A cuckoo will lay its eggs in other birds' nests so that the other birds will raise their cuckoo babies. If the other bird discovers that an egg in its nest is not its own, the unwanted and unfamiliar egg would be pushed and rejected from the nest. The cuckoo algorithm uses this principle to model a new solution as a cuckoo egg where every egg in a nest represents a unique solution. A bad solution can be replaced by a new solution in the nest. There are basic rules used in the cuckoo algorithm:

- Only one egg is placed by the cuckoo at a time, where the cuckoo randomly selects a nest and places the egg in it
- Desired nests with lots of eggs will be passed on to the next generation
- The nest of the host will be repaired. The host bird detects an egg that the cuckoo bird lays with probability p_d. In such a case, this egg will either be thrown out by the host bird or it will build a new nest elsewhere.

According to these basic rules, basic CS algorithm steps can be explained at follows:

```
Start
Objective Function    f(y) = (y₁, y₂,........., yₛ)ᵀ
Initialize a Random population of n host nest yᵢ
While (t <MaxGen)
        Get randomly a cuckoo (example i) by Lévy Flights
        Fitness function Evaluation  fᵢ
        Choose randomly a nest from n (example j) with Fitness fⱼ
        If (fⱼ≥fᵢ)
        Replace j with new solution;
        End
```

Abandon worse nests or a fraction p_d and build new nests in a new position by Lévy Flights

The best solutions – nests – are preserved

Solutions and best objective (best nest) are arranged

end While loop

stop

New solutions $y^{(i+1)}$ for cuckoos i, when found, implement Lévy flight using the following equation

$$y_i^{(t+1)} = y_i^t + \alpha \oplus Le'vy(\lambda) \tag{19}$$

where $\alpha > 0$ represent step size, we can take α as 1. $\oplus$ denotes of the entry wise multiplications. Whereas, Lévy flights mainly provide random walk, while from the Lévy distribution, its random steps are drawn into large steps, as in equation below.

$$Le'vy \sim u = t^{-\lambda}.(1\langle \lambda \leq 3) \tag{20}$$

Lévy flight provides random walking and forms random walking with step length distribution. On the current best solution, new solutions are created which help speed up local search [15,16].

In this method, the clustering principle was used in the retrieval process by using the Mahalanobis distance to find the distance between the features of the database images and the query image to calculate the similarity value between these images, and retrieve the images related to the query image with high accuracy by employing this distance within the cuckoo algorithm in the calculation of the fitness function to obtain the optimal solution, high accuracy of retrieval, and excellent results, as shown in the tables.

When developing this algorithm by adding the fuzzy membership function to the fitness function, a proposed method was obtained, called fuzzy cuckoo search algorithm (FCS), which obtained better results.

7. DESIGN OF PROPOSED SYSTEM

The system is designed to retrieve images based on some artificial intelligence techniques such as the swarm algorithms, which are represented by the Ant Colony (ACO) algorithm and the Cuckoo Search (CS) algorithm. Additionally, artificial neural networks were used such as the perceptron neural network (PNN) and the proposed methods of Fuzzy Perceptron Neural Network (FPNN) and Fuzzy Cuckoo Search (FCS) that were used to retrieve the images, as shown in Fig. 1.

These methods (PNN, ACO, CS, FPNN, and FCS) have been built to retrieve images from the datasets. In the training phase, these five methods are able to retrieve accurate and similar images with high efficiency on their own. The image retrieval system based on these five methods was designed to include two stages: the training phase and the testing phase. Initially, we used the Linear Discriminant Analysis (LDA) to extract features for all the images in the database as well as the query image. In the training phase, the features extracted from the images are entered to the ACO, CS, PNN, FPNN, and FCS in order to learn these methods, and the base knowledge is stored in these five methods through the training process. This knowledge is used in the testing phase for comparison and decision making by these methods (PNN, ACO, CS, FPNN, and FCS). The comparison involves comparing features between query images and the trained image set, where the best images with identical and similar features are retrieved.
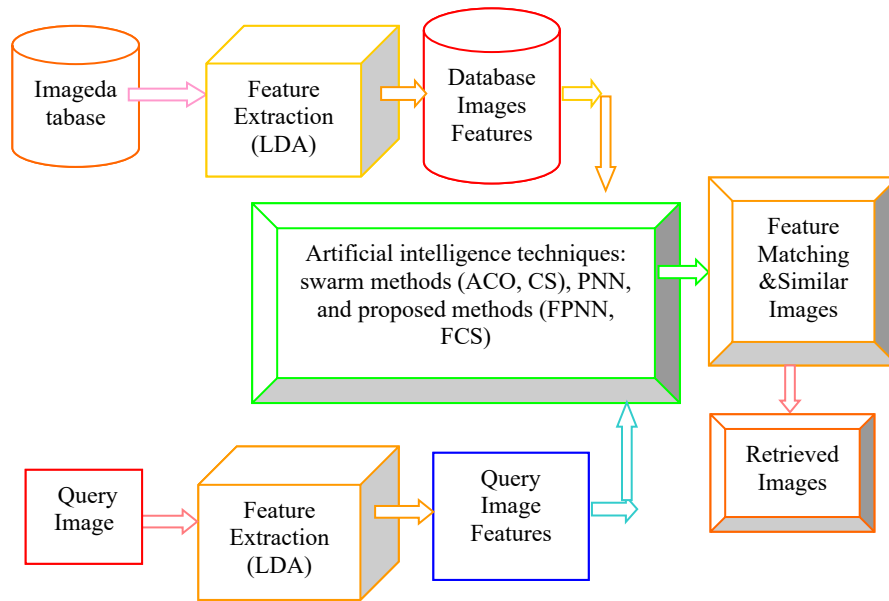
Fig. 1: System flowchart of the image retrieval.

8. EXPERIMENTAL RESULTS

In this paper, five artificial intelligent methods were used: Cuckoo Search (CS), Ant Colony optimization (ACO), and then combined Fuzzy membership function with SLP neural network and CS to produce Fuzzy single layer perceptron neural network (FPNN), and Fuzzy Cuckoo search (FCS). Linear Discriminant Analysis (LDA) was also used for feature extraction of the image database and Query image. To evaluate the performance of these methods, we used two indicators, recall and precision [17], as shown in Eq. (21), Eq. (22):

$$\mathrm{Re}\,call = \frac{\text{No. of relevant images retrieved}}{\text{Total no. of relevant image in the collection}} \times 100 \tag{21}$$

$$\mathrm{Pr}\,ecision = \frac{\text{No. of relevant images retrieved}}{\text{Total no. of images retrieved}} \times 100 \tag{22}$$

In this work we used an image dataset that contained 10 categories, each category contained different numbers of images. The image categories are shown in Table 1. The five methods PNN, ACO, CS, FPNN, and FCS were applied to this database. In the training phase, these methods obtained 10 cluster centres, according to ten image categories, these methods discovered all the data in the database completely and accurately. In the testing phase, query images for each category were entered on these methods (PNN, ACO, CS, FPNN, FCS). The distance between query image features and cluster centres for 10 categories, minus the distance equates to the similarity. These methods find the similarity and matching between the query image and the images in the stored database.

Table 1: Images dataset

Category type	Number of images	Rate%
california_Gull	61	17.23
mflowers	44	12.43
cflowers	15	4.24

rose_marron	18	5.08
nflower	15	4.24
blue_winged_warble	59	16.67
brown_pelican	56	15.82
cardinal	57	16.10
horse	10	2.82
human	19	5.37
total	354	100%

The recall rate and precision rate were calculated for all these methods. Different (Recall and Precision) rates were obtained for (PNN, ACO, CS) and FPNN methods (Table 2).While the FCS method obtained Recall rate and Precision rate equal (100%), the FCS is better than (PNN, ACO, CS) and FPNN methods. Table 3 shows the results for all methods PNN, ACO, CS, FPNN and FCS that were used in this work. This table contains query image, category type, relevant retrieved, retrieved number, recall rate, and precision rating for these methods.

From these tables, we note that the FCS method was the best as the values of recall and precision were equal to 100%, while the values of recall and precision for FPNN were equal to 97.2 and 87.83 respectively.

We notice that the order of preference of the methods was as follows: first the PNN method gave results that are not good, then the ACO method had better results, and when using the CS method, the results became better than the previous two methods. Then the PNN method was developed by hybridizing it with fuzzy logic, where very satisfactory results were obtained. From monitoring the results of the CS method, the precision values were equal to 100% and that by the FPNN hybrid method and the recall values were high compared to other methods. Therefore, the CS method was hybridized with fuzzy logic to improve its performance. The best results were obtained with this proposed method of fuzzy hybridization, where the values of recall and precision were equal to 100%. Figure 2 shows the samples of query images for all categories of database. Figures 3-7 show the number of relevant - retrieved images for all methods used in this work.

Table 2: Recall rate and precision rate for PNN, ACO, CS and FPNN methods

Category type	PNN		ACO		CS		FPNN	
	Recall rate%	Precision rate%	Recall rate%	Precision rate%	Recall rate%	Precision rate%	Recall rate%	Precision rate%
california_Gull	81.967	69.4	95.08	90.63	96.72	100	98.36	98.36
mflowers	68.18	53.57	86.36	79.16	95.45	100	97.72	100
cflowers	60	39.13	73.3	78.57	93.3	100	93.33	87.5
rose_marron	72.2	38.24	83.3	93.75	88.8	100	94.44	100
nflower	66.7	55.6	73.3	91.7	86.7	100	93.33	93.33
Blue_winged_warble	61.02	56.3	83.1	92.45	91.53	100	96.61	100
brown_pelican	85.71	64.86	91.07	80.95	94.64	100	98.21	98.21
cardinal	82.46	68.12	92.98	89.83	96.49	100	100	100
horse	80	30.77	80	57.14	90	100	100	90.90
human	57.89	30.6	73.68	60.87	94.74	100	100	100
Average	71.6127	50.659	83.217	81.505	92.837	100	97.2	87.83

Table 3: The results for PNN, ACO, CS, FPNN and FCS methods with query images, category type, relevant retrieved, retrieved number, recall rate, and precision rate

Query image	Category type	Relevant retrieved	Retrieved number	Recall rate	Precision rate	Method
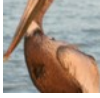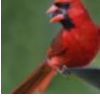
	california_Gull	50	72	81.967	69.4	PNN
		58	64	95.08	90.63	ACO
		59	59	96.72	100	CS
		60	61	98.36	98.36	FPNN
		61	61	100	100	FCS
	Mflowers	30	56	68.18	53.57	PNN
		38	48	86.36	79.16	ACO
		42	42	95.45	100	CS
		43	43	97.72	100	FPNN
		44	44	100	100	FCS
	Cflowers	9	23	60	39.13	PNN
		11	14	73.3	78.57	ACO
		14	14	93.3	100	CS
		14	16	93.33	87.5	FPNN
		15	15	100	100	FCS
	rose_marron	13	34	72.2	38.24	PNN
		15	16	83.3	93.75	ACO
		16	16	88.8	100	CS
		17	17	94.44	100	FPNN
		18	18	100	100	FCS
	Nflower	10	18	66.7	55.6	PNN
		11	12	73.3	91.7	ACO
		13	13	86.7	100	CS
		14	15	93.33	93.33	FPNN
		15	15	100	100	FCS
	blue_winged_warble	36	64	61.02	56.3	PNN
		49	53	83.1	92.45	ACO
		54	54	91.53	100	CS
		57	57	96.61	100	FPNN
		59	59	100	100	FCS
	brown_pelican	48	74	85.71	64.86	PNN
		51	63	91.07	80.95	ACO
		53	53	94.64	100	CS
		55	56	98.21	98.21	FPNN
		56	56	100	100	FCS
	Cardinal	47	69	82.46	68.12	PNN
		53	59	92.98	89.83	ACO
		55	55	96.49	100	CS
		57	57	100	100	FPNN
		57	57	100	100	FCS
	Horse	8	26	80	30.77	PNN
		8	14	80	57.14	ACO
		9	9	90	100	CS
		10	11	100	90.90	FPNN
		10	10	100	100	FCS
	Human	11	36	57.89	30.6	PNN
		14	23	73.68	60.87	ACO
		18	18	94.74	100	CS
		19	19	100	100	FPNN
		19	19	100	100	FCS

Fig.2:Query images for ten categories of image database.
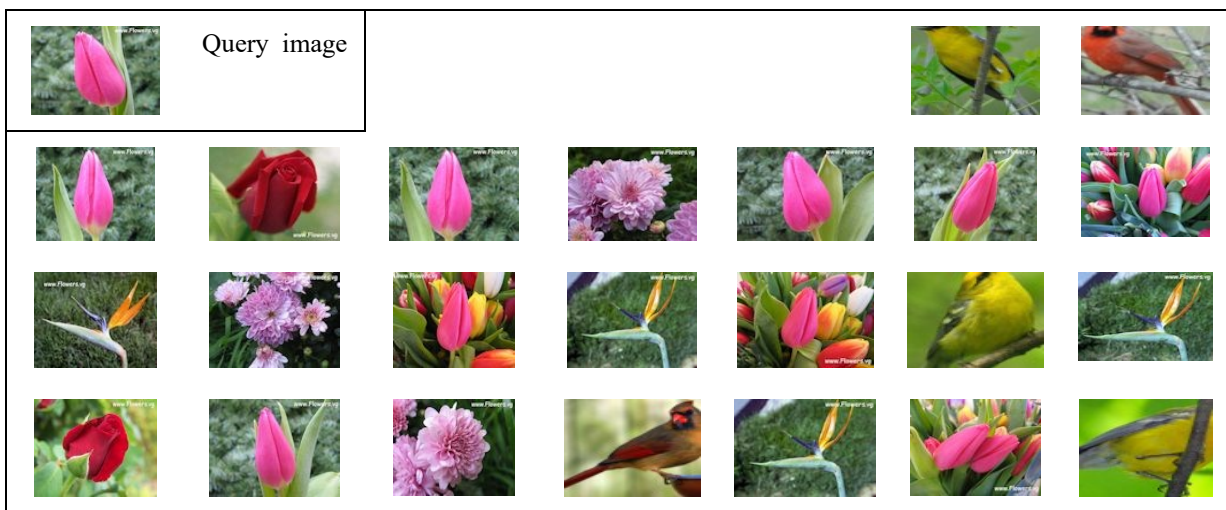
Fig. 3: Number of relevant-retrieved images = 9 for PNN method.

Fig. 4: Number of relevant-retrieved images = 11 for ACO method.

Fig. 5: Number of relevant-retrieved images = 14 for CS method.

Fig.6: Number of relevant-retrieved images =14 for FPNN method.

Fig. 7: Number of relevant-retrieved images = 15 for FCS method.

9. CONCLUSION

In this paper, we used some of artificial intelligence techniques for image retrieval. Initially, we presented Linear Discriminant Analysis (LDA) for feature extraction of images in the dataset. Then we used some swarm algorithms such as ACO and CS optimization algorithms. We also used artificial neural network such as PNN, and combined the fuzzy membership function with single layer perceptron and Cuckoo search to produce new

methods called Fuzzy Perceptron Neural Network (FPNN) and Fuzzy Cuckoo Search (FCS). These five methods were applied to an image dataset. We used two measures (recall and precision rate) for evaluating these methods. The FCS method got the best performance for image retrieval among the other methods (PNN, ACO, CS) and FPNN used in this work.

ACKNOWLEDGMENT

REFERENCES

[1]   Tessy AV. (2010) Performance enhanced optimization based image retrieval system. IJCA Special Issue on Evolutionary Computation,1: 31-34.
[2]   Hung HT, Bae MC, Shin HL. (2014) Rotation-invariant texture image retrieval using particle swarm optimization and support vector regression. Applied Soft Computing, 17: 127-139.
[3]   Santhi N, Annbuselvi K, Sivakumar S. (2018) Performance analysis of feature extraction techniques: PCA and LDA for face recognition. Int JEngRes CompSciand Eng, 5(3): 289-294.
[4]   Arvind N, Manimozhi, Jetendranath M. (2014) Content-based image retrieval system using feed-forward backpropagation neural network.Int J Comp Sci Network Security, 14(6): 70-77.
[5]   Shahbaa IK, Karam MMS. (2012) Detection of network anomaly based on hybrid intelligence techniques. AL-Rafidain J Comp Sciences and Mathematics, 9(2): 81-98.
[6]   Ramandeep K, Ashok KB. (2014) Enhanced content-based image retrieval using Cuckoo search algorithm. Int J Advanced Res Comp Sci Software Engineering, 4(9): 233-241.
[7]   Pathare RN, Kimmatkar KW. (2016) Multi-step approach for speeding-up region based image retrieval using indexing technique. Int Res J Engineering and Technology, 3(8): 323- 327.
[8]   Kurchaniya D, Johari PK. (2017) An efficient approach for image retrieval using particle swarm optimization. Int J Computer Sciences and Engineering, 5(6): 90-99.
[9]   Nie Q. (2018) Research on image network retrieval application based on swarm optimization algorithm.Advances in Intelligent Systems Research, 147: 524-529.
[10] Steven F, JoseminB. (2013) Performance analysis of PCA-based and LDA based algorithms for face recognition. Int J Signal Processing Systems, 1(1): 1-6.
[11] Shahbaa IK, Ragad WK. (2014) Selection and prioritization of test cases by using bees colony. AL-Rafidain JComputer Sciences and Mathematics, 11(1): 179-201.
[12] Hasancebi O, Carba S. (2011) Ant colony search method in practical structural optimization. Int J Optimization in Civil Engineering, 1: 91-105.
[13] FangyuC,HongweiW, ChaoQ, YongX. (2013) An ant colony optimization routing algorithm for two order pickers with congestion consideration. Computers & Industrial Engineering, 66: 77-85.
[14] Arvind N, Manimozhi I. (2013) Content-based image retrieval system using feed-forward backpropagation neural network. Int J Computer Science Engineering, 2(4): 143-151.
[15] Vennilal S, Venkatesan A. (2017) Improved color satellite image segmentation using cuckoo search algorithm.Int J Innovative Res Comp and Comm Eng, 5(4): 8229-8236.
[16] Priya V. (2018) Ant colony and Cuckoo search algorithm for document clustering. ARPN JEng Appl Sci, 13(7): 2429-2437.
[17] Yogapriya J, Saravanabhavan C, IlaV. (2017) An effective machine learning algorithm for texture based medical image retrieval system. Int Res J Pharmacy, 8(11): 201-218.

ENHANCEMENT OF STABILITY ON AUTONOMOUS WAYPOINT MISSION OF QUADROTOR USING LQR INTEGRATOR CONTROL

**OKTAF AGNI DHEWA[1], TRI KUNTORO PRIYAMBODO[2*],
ARIS NASUHA[1] AND YASIR MOHD MUSTAFAH[3]**

*[1]Department of Electronics and Informatics Engineering,
Yogyakarta State University, Yogyakarta, Indonesia
[2]Department of Computer Science and Electronics,
Universitas Gadjah Mada, Yogyakarta, Indonesia
[3]Department of Mechatronics Engineering,
International Islamic University Malaysia,
Jalan Gombak, 53100 Kuala Lumpur, Malaysia*

*Corresponding author: mastri@ugm.ac.id

ABSTRACT: The ability of the quadrotor in the waypoint trajectory tracking becomes an essential requirement in the completion of various missions nowadays. However, the magnitude of steady-state errors and multiple overshoots due to environmental disturbances leads to motion instability. These conditions make the quadrotor experience a shift and even change direction from the reference path. As a result, to minimize steady-state error and multiple overshoots, this study employs a Linear Quadratic Regulator control method with the addition of an Integrator. Comparisons between LQR without Integrator and LQR with Integrator were performed. They were implemented on a quadrotor controller to track square and zig-zag waypoint patterns. From experimental results, LQR without Integrator produce of 2 meters steady-state error and -1.04 meters undershoot average with an accuracy of 64.84 % for square pattern, along 3.19 meters steady-state error, and -1.12 meters undershoot average with an accuracy of 46.73 % for a zig-zag way. The LQR method with integrator produce of 1.06 meters steady-state error with accuracy 94.96 % without multiple-overshoot for square pattern, the 1.06 meters steady-state error, and -0.18 meters undershoot average with an accuracy of 86.49 % for the zig-zag way. The results show that the LQR control method with Integrator can minimize and improve steady-state error and multiple overshoots in quadrotor flight. The condition makes the quadrotor able to flying path waypoints with the correct system specification.

ABSTRAK: Kemampuan quadrotor dalam pengesanan lintasan waypoint menjadi syarat penting dalam menyelesaikan pelbagai misi pada masa kini. Walau bagaimanapun, besarnya ralat keadaan mantap dan banyak kelebihan kerana gangguan persekitaran menyebabkan ketidakstabilan pergerakan. Keadaan ini menjadikan quadrotor mengalami pergeseran dan bahkan mengubah arah dari jalur rujukan. Oleh itu, kajian ini menggunakan kaedah kawalan Linear Quadratic Regulator dengan penambahan integrator dalam meminimumkan ralat keadaan mantap dan banyak kelebihan. Perbandingan antara LQR tanpa Integrator dan LQR dengan Integrator dilakukan. Mereka dilaksanakan pada pengawal quadrotor untuk mengesan corak titik jalan persegi dan zig-zag. Dari hasil eksperimen, LQR tanpa Integrator menghasilkan ralat keadaan mantap 2 meter dan -1.04 meter rata-rata undur tembak dengan ketepatan 64.84% untuk corak persegi, sepanjang ralat keadaan tetap 3.19 meter, dan -1.12 meter rata-rata undur

bawah dengan ketepatan 46.73 % untuk cara zig-zag. Kaedah LQR dengan integrator menghasilkan ralat keadaan mantap 1.06 meter dengan ketepatan 94.96% tanpa tembakan berlebihan untuk corak segi empat sama, ralat keadaan mantap 1.06 meter, dan rata-rata undur tembak -0.18 meter dengan ketepatan 86.49% untuk zig-zag cara. Hasilnya menunjukkan bahawa kaedah kawalan LQR dengan Integrator dapat meminimumkan dan memperbaiki ralat keadaan mantap dan banyak overhoot dalam penerbangan quadrotor. Keadaan tersebut menjadikan quadrotor dapat terbang ke titik jalan dengan spesifikasi sistem yang betul.

KEYWORDS: *optimal control; quadrotor; stability; waypoint*

1. INTRODUCTION

Unmanned aerial vehicle (UAV) is an unmanned aircraft with comfortable and efficient use accessibility [1]. UAV has attracted the attention of invention activists in the industrial, civilian, and military fields to use UAVs as a vehicle to help complete various missions that are being developed [2]. Such as aerial surveillance, reconnaissance, aerial photography, transportation of goods, and many others [3].

Completion of these missions is not only required of UAVs to be able to maintain a stable attitude of orientation and altitude but also expected to have the ability to trace the flight path following a predetermined row of earth location coordinates or called waypoints mission. The completeness of the existing capabilities makes UAVs map an area precisely and accurately, which is also the main requirement for developing various current missions [4][5].

Along with advances in technological science, many UAVs have experienced improvements in both physical form patterns and flight systems to achieve specific mission operational targets. One of these UAVs is a quadrotor, which uses four motor actuators as a flight driver. More broadly, a quadrotor is a UAV that can take off and land vertically (VTOL) even in a limited area [6]. A quadrotor also has a constant flight speed to hover in a specific location with its stationary motion [7].

Looking deeply at the quadrotor architecture, the potential capabilities of quadrotors do not necessarily exist by themselves. It was still built through the involvement of several relatively complex system infrastructures. There is one system in all existing quadrotor system infrastructure that plays a vital role as a determining factor in the flight process. The system is a quadrotor flight control system. Without a well-managed control system, the quadrotor cannot maintain rotational or translation movements, causing the plane's crash.

As previously mentioned, quadrotor motion control is divided into two categories: controlling rotational motion and translational motion. The quadrotor motion control started from rotational movement and was followed by translational motion with rules accommodated by a particular control method to achieve a stable state. By referring to several studies conducted by [8] and [9], which focus on controlling quadrotor rotational attitudes, the vehicle can have good flight stability by applying the Linear Quadratic Regulator (LQR) control system method full state feedback. The author's research explains that the LQR method provides regulatory characteristics in the control signal by forcing the control signal to a value close to zero. LQR control makes the system able to overcome errors through a fast response. This statement was strengthened from several other studies, such as applying LQR control methods on UAV aircraft that are more effective and robust

than PID control to a stable system [10]. LQR can maintain system stability in less than 1 second, producing shallow errors [11,12].

However, referring to other research literature regarding the performance of LQR control, it indicates that this method is not good enough to accommodate the translational motion of an object with a significant average deviation that occurs when the system has reached its steady-state [13]. This statement was visualized through research conducted by [14]. The author built an autopilot control system on a quadrotor in moving to the waypoint coordinates using LQR control. In tracing the four waypoint coordinates, the research test found that the quadrotor maintained the anti-rotational motion that met the flight success standards. However, the quadrotor has quite a significant deviation of the mean translational movement of the x and y axes, which is about 2 meters from the reference of the flight path.

The process of tracing the coordinates of the Earth's location on a quadrotor requires a navigation system with data information obtained from the Global Positioning System (GPS) [15]. GPS is a prototype that provides latitude and longitude information at an earth location. Changes in the GPS reading point position converted to the displacement of the x and y axes in meters. The displacement will be used as the error reference value for the quadrotor control to the destination point [16].

The environment disturbance can influence the stability of the quadrotor in the waypoint mission. If the quadrotor has not an eligible control system, it produces more significant error ever. The larger deviation will be accompanied by the results of the steady-state error or the average deviation, which is also getting more significant. This condition causes the quadrotor to experience a shift from the proper track. Also, a steady-state error that diverges with intensity as often as possible will trigger the system to experience multiple overshoots, which result in flight conditions not only shifting but also affecting the aircraft to change direction from the trajectory traced [17].

The main focus of this study is to design by adding the compensation Integrator component to the anatomy structure LQR control method. This compensation involves past information to correct the current signal. This process makes minimize steady-state errors and multiple overshoots in the system. So, the stability of translation motion can be enhanced and managed to track the path correctly.

2. QUADROTOR DYNAMICS MODEL

The Newton-Euler equation is necessary to build a quadrotor with flight in x-configuration. This study uses an inertial North-East-Down (NED) frame of reference and a body fixed frame to fulfil this Equation. The NED frame of reference has two axes, N and E, parallel to the north and east and one D axis directed downward towards the center of the Earth, so Newton's first law will apply to this frame of reference. Another frame of reference, the body fixed frame, is indicated by the direction of the x, y, and z axes with a center point that coincides with the center of gravity on the quadrotor body [3]. The two terms of reference are shown in Fig. 1.

In control theory, the dynamic behaviour of a given system can be obtained from its states. There are six quadrotor attitudes related to rotation, namely: Euler angle $[\phi \quad \theta \quad \psi]$ (*Roll – Pitch – Yaw*) and angular velocity around each axis body-fixed frame $[p \quad q \quad r]$, for the other six states, namely: from the center of gravity (cog) position $[x \quad y \quad z]$ and linear

velocity in $[\dot{x} \quad \dot{y} \quad \dot{z}]$, relative to the body fixed frame. Therefore, the quadrotor has 12 states representing 6 degrees of freedom (DOF) [3].
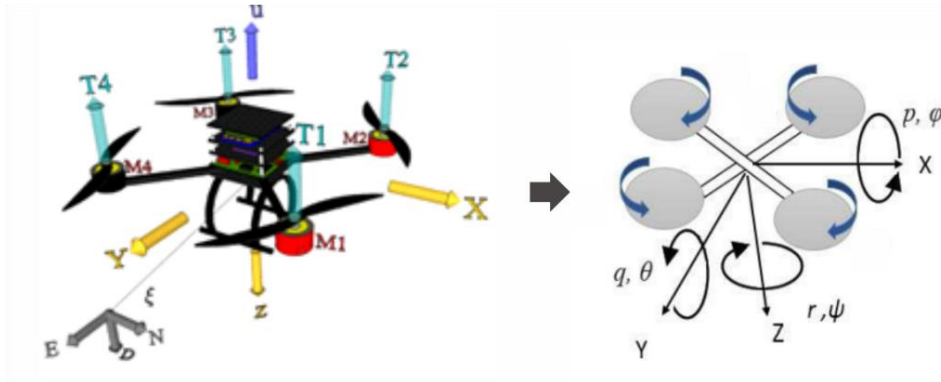
Fig. 1: NED frame of quadrotor.

Quadrotor modelling consists of 3-axis rotational movement (roll, pitch, yaw) and 3-axis translation movement of the Earth's x, y, z-axis (Earth) to the z-axis of the body. Quadrotor translation movement references used in modelling are inertial earth frame (E-frame) $[E_x \quad E_y \quad E_z]$ and inertial body frame (B-frame)) $[B_x \quad B_y \quad B_z]$.

The rotational movement ϕ (roll) is the quadrotor movement around the y-axis of the body, the rotational movement θ (pitch) is the quadrotor movement around the x-axis of the body, and the rotational movement ψ (yaw) is the quadrotor movement around the z-axis of the body.

The change in the position of the body frame coordinates to the earth frame can be determined by a rotation matrix, where the final position of the body to the earth frame can be determined if the rotation matrix is known, as in Equation (1).

$$\begin{bmatrix} x' \\ y' \\ z' \end{bmatrix} = \begin{bmatrix} x \\ y \\ z \end{bmatrix} \tag{1}$$

Determination of coordinate changes is carried out with a rotational matrix that corresponds to the rotating axis of the body frame. Like when the quadrotor body rotates on the x, y, and z-axis of the body frame, the final position of the coordinates of the body to the earth frame can be found with a rotational matrix which is sequential for each axis through Eq. (2) to Eq. (4)[3].

$$R_x(\phi) = \begin{bmatrix} 1 & 0 & 0 \\ 0 & \cos(\phi) & -\sin(\phi) \\ 0 & \sin(\phi) & \cos(\phi) \end{bmatrix} \tag{2}$$

$$R_y(\theta) = \begin{bmatrix} \cos(\theta) & 0 & \sin(\theta) \\ 0 & 1 & 0 \\ -\sin(\theta) & 0 & \cos(\theta) \end{bmatrix} \tag{3}$$

$$R_x(\phi) = \begin{bmatrix} \cos(\psi) & -\sin(\psi) & 0 \\ \sin(\psi) & \cos(\psi) & 0 \\ 0 & 0 & 1 \end{bmatrix} \tag{4}$$

The three rotational matrix equations create a relationship between body frame coordinates and earth frame coordinates. The relationship is created from the multiplication of the three rotational matrices and is shown in Eq. (5), where c is cos and s is sin.

$$R_B^E(\psi, \theta, \phi) = \begin{bmatrix} c(\psi)c(\theta) & -s(\psi)c(\phi) + c(\psi)s(\theta)s(\phi) & s(\psi)s(\phi) + c(\psi)c(\phi)s(\theta) \\ s(\psi)c(\theta) & c(\psi)s(\theta) + s(\phi)s(\theta)s(\psi) & -c(\psi)s(\phi) + s(\theta)s(\psi)c(\phi) \\ -s(\theta) & c(\theta)s(\phi) & c(\theta)c(\phi) \end{bmatrix} \qquad (5)$$

The rotation matrix on the quadrotor used is only the z coordinates of the body frame against the x, y, and z coordinates of the earth frame. The quadrotor can only move up and down along the z coordinates of the body. The movement of the quadrotor at the x and y coordinates of the earth frame is the result of changes in the orientation of the roll angle and pitch from point 00 when the quadrotor moves on the z-axis of the body [3].

Quadrotor modeling is calculated using the Newton-Euler approach, where Newton II's law also applies in the system. Newton's second law describes the relationship between the force F and the acceleration a experienced by a center of mass, with the three forces and the acceleration for each axis on the quadrotor, so the relationship is as shown in Eq. (6).

$$F = m.a \qquad (6)$$

The quadrotor has a net force determined by the lift force of the four rotors, which can be calculated through Eq. (7).

$$F_T = u_1 = \sum_{i=1}^{4} f_i \qquad (7)$$

Quadrotor movement on the x, y, and z coordinate axes of the earth frame can be modeled with the rotation matrix of Eq. (5) and Newton II's law in Equation (6). The rotation matrix in the third column of Eq. (5) with the axis used is only the z-axis of the body frame to the x, y, and z axes of the earth frame.

Based on this modeling, the translational motion on the x, y, z axes of the earth frame is described through Eq. (8) and Eq. (10).

$$F_x = F_T.B_{B_x}^{E_z} \qquad (8)$$

$$F_y = F_T.B_{B_y}^{E_z} \qquad (9)$$

$$F_z = F_T.B_{B_z}^{E_z} + m.g \qquad (10)$$

From Eqs. (8) to (10), described by the rotation matrix equation obtained by c (.) is cos, and s (.) is sin shown in Eqs. (11) to (13).

$$m.\ddot{x} = F_T\big(c(\phi)s(\theta)c(\psi) + s(\phi)s(\psi)\big) \qquad (11)$$

$$m.\ddot{y} = F_T(-c(\psi)s(\phi) + s(\theta)s(\psi)c(\phi)) \qquad (12)$$

$$m.\ddot{z} = F_T(c(\phi)c(\theta) + m.g) \qquad (13)$$

The thrust or F_T obtained from Eq. (7) will experience a change in pitch angle (θ), roll angle (ϕ), yaw angle (ψ) for translational movement on each axis of the quadrotor earth frame so that Eqs. (11) to (13) can be simplified to,

$$m.\ddot{x} = F_T.s(\theta) \qquad (14)$$

$$m.\ddot{y} = F_T(-s(\phi)) \qquad (15)$$

$$m.\ddot{z} = F_T + m.g \qquad (16)$$

This equation can be further simplified into Eqs. (17) to (19) with a slight angle approximation (close to 0°) by simulating the value of the angular acceleration sin α, and the result is close to the angle α itself.

$$\ddot{x} = \frac{F_T.\theta}{m} \tag{17}$$

$$\ddot{y} = \frac{F_T.\phi}{m} \tag{18}$$

$$\ddot{z} = \frac{F_T}{m} + g \tag{19}$$

Quadrotor rotational motion modeling can use the second Euler's law. This law describes the relationship between torque (τ) and angular acceleration (α) and the relationship between angular momentum (L) and rotational speed (ω) for each axis experienced by a center of mass, as shown in Eq. (20).

$$\tau = I.\alpha + Lx\omega \tag{20}$$

with the cross product of momentum and angular velocity, the torque can be solved through Eq. (21),

$$\tau = I.\alpha + Lx\omega \sin\beta \tag{21}$$

β is the angle formed by angular momentum and rotational speed. The angle formed in the quadrotor rotation motion is minimal and does not affect so that the angle can be ignored by giving it a zero value. From this, it makes Eq. (21) only affected by the relationship of torque, angular acceleration, and inertia as in Eqs. (22) and (23).

$$\tau = I.\alpha \tag{22}$$

$$\tau = I.\dot{\omega} \tag{23}$$

The relationship τ (torque) with lift or (thrust) is shown in Eq. (24).

$$\tau = F.r \tag{24}$$

The matrix component I (inertia) is shown in Eq. (25), and the angular acceleration and angular torque matrix are shown in Eqs. (26) and (27). In contrast, the lift or thrust matrix is shown in Eq. (28).

$$I = \begin{bmatrix} I_{xx} & 0 & 0 \\ 0 & I_{yy} & 0 \\ 0 & 0 & I_{zz} \end{bmatrix} \tag{25}$$

$$\alpha = \begin{bmatrix} \ddot{\phi} \\ \ddot{\theta} \\ \ddot{\psi} \end{bmatrix} \tag{26}$$

$$\tau = \begin{bmatrix} \tau_\phi \\ \tau_\theta \\ \tau_\psi \end{bmatrix} \tag{27}$$

$$F = \begin{bmatrix} F_\phi \\ F_\theta \\ F_\psi \end{bmatrix} \tag{28}$$

The form of roll rotation (ϕ) and pitch (θ) can be modeled into Eqs. (29) and (30).

$$I_{xx}.\ddot{\phi} = F_\phi.r \tag{29}$$

$$I_{yy}.\ddot{\theta} = F_\theta.r \tag{30}$$

where, I_{xx} is the inertia of the quadrotor on the x-axis, $\ddot{\phi}$ is the angular acceleration of the roll, r is the distance between the motor and the center of gravity of the quadrotor and τ_ϕ is the roll torque. Also, I_{yy} is the inertia of the quadrotor on the y-axis, $\ddot{\theta}$ is the

acceleration of the pitch angle, r is the distance between the motor and the center of gravity of the quadrotor and τ_θ is the pitch torque. So, the roll and pitch motion models can be simplified in Eqs. (31) and (32).

$$\ddot{\phi} = \frac{\tau_\phi}{I_{xx}} \tag{31}$$

$$\ddot{\theta} = \frac{\tau_\theta}{I_{yy}} \tag{32}$$

Then for the form of yaw rotational motion (ψ) can be shown in Eq. (33), where I_{zz} is the quadrotor inertia on the z-axis, $\ddot{\psi}$ is the yaw angular acceleration and τ_ψ is the yaw torque.
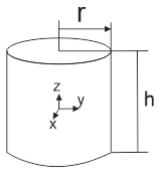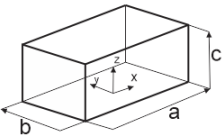
$$I_{zz}.\ddot{\psi} = \sum_{i=1}^{4} \tau_{M_i} \tag{33}$$

The yaw movement model does not use a thrust acting on the arm and motor but uses the torque resulting from the rotation of the motor at each end of the quadrotor arm so that the model can be simplified to Eq. (34).

$$\ddot{\psi} = \frac{\tau_\psi}{I_{zz}} \tag{34}$$

The quadrotor has a moment of inertia resulting from rotation on the x, y, and z axes. The Equation for the moment of inertia is adjusted to the shape of the component to be measured. There are two primary forms used to calculate the inertia of an object, namely the shape of a block or a cube and a cylinder. The equations used are in Table 1.

Table 1: Inertia equation [21]

Form	Image	Equation
Cylinder		$I_{G_{xx}} = I_{G_{yy}} = \frac{1}{12}m(3r^2 + h^2)$ $I_{G_{zz}} = \frac{1}{2}mr^2$
Solid Beams		$I_{G_{xx}} = \frac{1}{12}m(b^2 + c^2)$ $I_{G_{yy}} = \frac{1}{12}m(a^2 + c^2)$ $I_{G_{zz}} = \frac{1}{12}m(a^2 + b^2)$

3. CONTROL SYSTEM DESIGN

3.1 Linear Quadratic Regulator (LQR) Control

LQR control is an optimal control that has a robust character and can produce a minimal steady-state error. This study utilizes LQR control with full state feedback gain. LQR control block diagram is interpreted in Fig. 2.
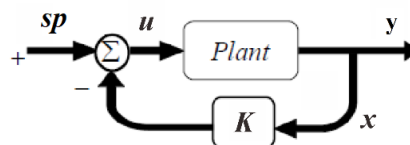
Fig. 2: LQR control diagram [18].

where sp is a reference or set point, $\boldsymbol{u}$ is control signal input, y is output signal, x is state control, and K is feedback gain. All components of LQR control are transformed in matrix dimension. The linear system equation in the LQR method is written through Eqs. (35) and (36) [19].

$$\dot{x} = Ax + Bu \tag{35}$$

$$y = Cx + Du \tag{36}$$

The cost function or index performance determines the performance of the LQR control. The best control signal performance is associated with the least possible yield weight. The formulation of the cost function is presented in Eq. (37) [19].

$$J = \int_{t^0}^{\infty} (x^T Q x + u^T R u)\, dt \tag{37}$$

Based on Eq. (37), the control signal (u) is generated from the control state's multiplication and the full state feedback gain. The control signal equation is shown in equation (38)[19].

$$u = -Kx \tag{38}$$

In the presence of Eq. (38), Eq. (35) will become Eq. (39) with the close-loop property in it.

$$\dot{x} = Ax - B(Kx) = (A - BK)x = A_c x \tag{38}$$

Also, by substituting Eq. (38) into Eq.(37), the cost function control equation will be,

$$J = \int_{t^0}^{\infty} (x^T Q x + K^T R K)x\, dt \tag{40}$$

The selection of the correct feedback value (K) will result in optimal control. The accuracy of the K value is indicated by the performance value index or cost function J which is very minimal, close to 0. The performance index (J) can be interpreted as a function of energy maintained at a small value in a closed-loop system. The performance index (J) is weighted by state $x(t)$ and the control input $u(t)$, where if J is minimized, state x (t) will go to zero for an infinite time that the closed-loop system will be stable.

The Q and R matrices are also influencing to performance of LQR control. Selecting the correct Q and R metrics will determine the best K feedback gain value for the system. The rule selection of matrics Q and R are as follows,

- The larger weight matrices Q will increase the value of gain feedback (K), making a fast response system to achieve the intermediate state cost function.
- The larger weight matrices R will decrease the value of gain feedback (K) which can slow down the steady-state (energy drive).

The optimal feedback gain K is found by deriving Eq. (40) using the Hamilton - Jacobi - Bellman method with procced as follows.

$$\frac{d}{dt}(x^T S x) = x^T (Q + K^T R K)x \tag{41}$$

$$J = \int_{0}^{\infty} \frac{d}{dt}(x^T S x)dt = x^T(0)Sx(0) \tag{42}$$

where S is the auxiliary variable matrix. From Eq. (42), it is assumed that the closed-loop system is in a stable state with J being independent of the current K which depends on S and the initial conditions. By deriving and substituting Eq. (38) into Eq. (41), then,

$$\dot{x}^T S x + x^T S \dot{x} + x^T Q x + x^T K^T R K x = 0 \tag{42}$$

$$x^T A_c{}^T S x + x^T S A_c x + x^T Q x + x^T K^T R K x = 0 \tag{43}$$

$$x^T(A_c{}^T S + SA_c + Q + K^T RK)x = 0 \tag{44}$$

$$(A - BK)^T S + S(A - BK) + Q + K^T RK = 0 \tag{45}$$

$$A^T S + SA + Q + K^T RK - K^T B^T S - SBK = 0 \tag{46}$$

Based on Eq. (46), the feedback gain K is obtained by the following Eq. (47),

$$K = R^{-1} B^T S \tag{47}$$

with Eq. (46) solved by the Algebraic Riccati Equation (ARE). The equation for solving ARE can be seen in Eqs. (48) and (49) [19].

$$A^T S + SA + Q + (R^{-1}B^T S)^T R(R^{-1}B^T S) - (R^{-1}B^T S)^T B^T S - PB(R^{-1}B^T S) = 0 \tag{48}$$

$$A^T S + SA - SBR^{-1}B^T S + Q = 0 \tag{49}$$

3.2 Integral Control

Control of a closed-loop system using only proportional control or full state feedback control will almost certainly result in a steady-state error in the response for each system input. The steady-state error that occurs is called offset. The offset unit step is shown in Fig. 3.
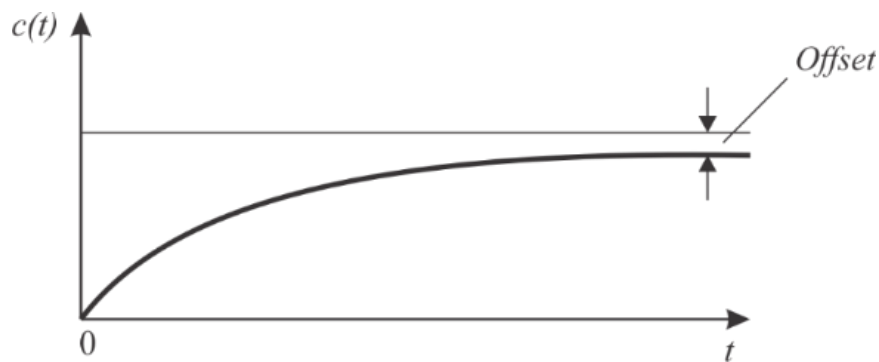
Fig. 3: Unit step response and offset [20].

The offset can be eliminated if integral control is added to the control system in controlling the system. Integral control has a functional equation described in Eq. (50)[20].

$$K_i = \int e(t)dt \tag{50}$$

3.3 LQR and Integrator Control Design on Quadrotor

A control system with a quadratic concept use12 states as states obtained from quadrotor modelling. Based on Eqs. (17), (18), (19), (31), (32), and (33) are first converted into state-space, which refers to Eqs. (35) and (36). The basic concept of changing the form of a linear representation uses a system model with various orders spelt out into first-order orders. The shape of the quadrotor model state space is shown in Eq. (51) with the output signal—the form of state-space presented in Eq. (52).

$$\begin{bmatrix} \dot{x} \\ \dot{V}_x \\ \dot{y} \\ \dot{V}_y \\ \dot{z} \\ \dot{V}_z \\ \dot{\phi} \\ \dot{\omega}_\phi \\ \dot{\theta} \\ \dot{\omega}_\theta \\ \dot{\psi} \\ \dot{\omega}_\psi \end{bmatrix} = \underbrace{\begin{bmatrix} 0 & 1 & 0 & 0 & 0 & 0 & 0 & 0 & 0 & 0 & 0 & 0 \\ 0 & 0 & 0 & 0 & 0 & 0 & 0 & 0 & 0 & -\frac{u_1}{m} & 0 & 0 & 0 \\ 0 & 0 & 0 & 1 & 0 & 0 & 0 & 0 & 0 & 0 & 0 & 0 \\ 0 & 0 & 0 & 0 & 0 & 0 & \frac{u_1}{m} & 0 & 0 & 0 & 0 & 0 \\ 0 & 0 & 0 & 0 & 0 & 1 & 0 & 0 & 0 & 0 & 0 & 0 \\ 0 & 0 & 0 & 0 & 0 & 0 & 0 & 0 & 0 & 0 & 0 & 0 \\ 0 & 0 & 0 & 0 & 0 & 0 & 0 & 1 & 0 & 0 & 0 & 0 \\ 0 & 0 & 0 & 0 & 0 & 0 & 0 & 0 & 0 & 0 & 0 & 0 \\ 0 & 0 & 0 & 0 & 0 & 0 & 0 & 0 & 0 & 1 & 0 & 0 \\ 0 & 0 & 0 & 0 & 0 & 0 & 0 & 0 & 0 & 0 & 0 & 0 \\ 0 & 0 & 0 & 0 & 0 & 0 & 0 & 0 & 0 & 0 & 0 & 1 \\ 0 & 0 & 0 & 0 & 0 & 0 & 0 & 0 & 0 & 0 & 0 & 0 \end{bmatrix}}_{A} \underbrace{\begin{bmatrix} x \\ V_x \\ y \\ V_y \\ z \\ V_z \\ \phi \\ \omega_\phi \\ \theta \\ \omega_\theta \\ \psi \\ \omega_\psi \end{bmatrix}}_{x} + \underbrace{\begin{bmatrix} 0 & 0 & 0 & 0 \\ 0 & 0 & 0 & 0 \\ 0 & 0 & 0 & 0 \\ 0 & 0 & 0 & 0 \\ 0 & 0 & 0 & 0 \\ -\frac{1}{m} & 0 & 0 & 0 \\ 0 & 0 & 0 & 0 \\ 0 & \frac{1}{I_{xx}} & 0 & 0 \\ 0 & 0 & 0 & 0 \\ 0 & 0 & \frac{1}{I_{yy}} & 0 \\ 0 & 0 & 0 & 0 \\ 0 & 0 & 0 & \frac{1}{I_{zz}} \end{bmatrix}}_{B} \underbrace{\begin{bmatrix} u_1 \\ u_2 \\ u_3 \\ u_4 \end{bmatrix}}_{u} \tag{51}$$

$$\begin{bmatrix} y_1 \\ y_2 \\ y_3 \\ y_4 \\ y_5 \\ y_6 \end{bmatrix} = \underbrace{\begin{bmatrix} 1 & 0 & 0 & 0 & 0 & 0 & 0 & 0 & 0 & 0 & 0 & 0 \\ 0 & 0 & 1 & 0 & 0 & 0 & 0 & 0 & 0 & 0 & 0 & 0 \\ 0 & 0 & 0 & 0 & 1 & 0 & 0 & 0 & 0 & 0 & 0 & 0 \\ 0 & 0 & 0 & 0 & 0 & 0 & 1 & 0 & 0 & 0 & 0 & 0 \\ 0 & 0 & 0 & 0 & 0 & 0 & 0 & 0 & 1 & 0 & 0 & 0 \\ 0 & 0 & 0 & 0 & 0 & 0 & 0 & 0 & 0 & 0 & 1 & 0 \end{bmatrix}}_{C} \underbrace{\begin{bmatrix} x \\ V_x \\ y \\ V_y \\ z \\ V_z \\ \phi \\ \omega_\phi \\ \theta \\ \omega_\theta \\ \psi \\ \omega_\psi \end{bmatrix}}_{x} + \underbrace{\begin{bmatrix} 0 & 0 & 0 & 0 \\ 0 & 0 & 0 & 0 \\ 0 & 0 & 0 & 0 \\ 0 & 0 & 0 & 0 \\ 0 & 0 & 0 & 0 \\ 0 & 0 & 0 & 0 \end{bmatrix}}_{D} \underbrace{\begin{bmatrix} u_1 \\ u_2 \\ u_3 \\ u_4 \end{bmatrix}}_{u} \tag{52}$$

where the inertia of the x, y, and z axes which are the components of Eq. (51), can be obtained by using reference Tabel 1 with Eqs. (53) to (55).

$$I_{xx} = \sum_{j=1}^{n}(I_{G_{xxj}} + m_j(y_j^2 + z_j^2)) \tag{53}$$

$$I_{yy} = \sum_{j=1}^{n}(I_{G_{yyj}} + m_j(x_j^2 + z_j^2)) \tag{54}$$

$$I_{zz} = \sum_{j=1}^{n}(I_{G_{zzj}} + m_j(x_j^2 + y_j^2)) \tag{55}$$

The LQR control method is specialized as a regulator. The problem that arises in this control system is when the user or the autonomous system wants to change the reference from the state. Changing the connection with a physical quantity of a state not equal to the input reference quantity can be done using the state reference (x_{ref}).

Reference state can help maintain the vehicle's state with a specific position, such as an altitude position or translating the x and y axes of the Earth to a particular place. The existence of a reference state will modify Eqs. (35) to (56).

$$\dot{x} = Ax + B(-K(x - x_{ref}) \tag{56}$$

Based on Eq. (47), the calculation of the control signal ($x - x_{ref}$) is an error against the desired reference, which is called an error. The error causes the system to produce a steady-state error or an offset against the reference or even more significant overshoot because the change in the value of the state changes directly, especially to maintain the translational motion of the x, y, and z axes of the vehicle to the Earth's axis. The calculation can be overcome by integrating the error and multiplied by a Gain. LQR control with a reference state is added to an Integrator component that converts Eq. (56) into Eq. (57).

$$\dot{x} = Ax + B\left(-K\left(x - x_{ref}\right) + K_i \int\left(x - x_{ref}\right)\right) \tag{57}$$

This system has an *A* matrix system with 12x12 dimensions, a *B* matrix system with 12x4 dimensions, a *C* matrix system with 6x12 dimensions, the output signal (*y*) in 6x1 dimension, and a control signal (*u*) 12x1 matrix dimension. The control diagram design that interprets quadrotor control with state reference and Integral control is shown in Fig. 4.
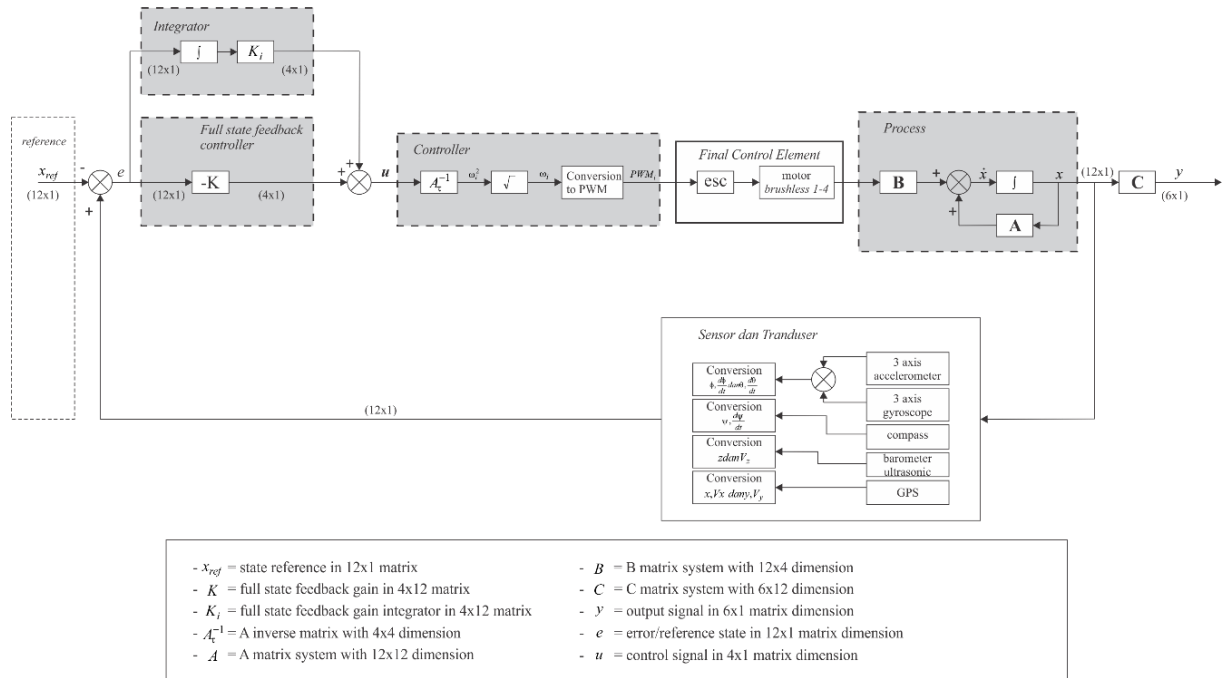
Fig. 4: LQR and Integrator control system on quadrotor.

Implementation of LQR Integrator control on quadrotor motion is based on the result of the integration of the dynamic equation. The force and torque on the quadrotor shown in Eq. (58).

$$\begin{bmatrix} F_T \\ \tau_\phi \\ \tau_\theta \\ \tau_\psi \end{bmatrix} = \begin{bmatrix} -b & -b & -b & -b \\ -lb & -lb & lb & lb \\ lb & -lb & -lb & lb \\ k & -k & k & -k \end{bmatrix} \begin{bmatrix} \omega_1^2 \\ \omega_2^2 \\ \omega_3^2 \\ \omega_4^2 \end{bmatrix} \tag{58}$$

where *b* and *k* are the coefficients of the thrust force and torque obtained from the calculation of Eqs. (59) and (60) [22].

$$b = C_T \rho A R_p{}^2 \tag{59}$$

$$k = C_q \rho A R_p{}^3 \tag{60}$$

where C_T and C_q are coefficients from propeller characteristics. ρ is the density of air, and A is the circle area of propeller and R_p is a radius of the propeller. The speed of each motor can be calculated through Eq. (61).

$$\begin{bmatrix} \omega_1^2 \\ \omega_2^2 \\ \omega_3^2 \\ \omega_4^2 \end{bmatrix} = A_z^{-1} \begin{bmatrix} F_T \\ \tau_\phi \\ \tau_\theta \\ \tau_\psi \end{bmatrix} = \begin{bmatrix} -b & -lb & lb & k \\ -b & -lb & -lb & -k \\ -b & lb & -lb & k \\ -b & lb & lb & -k \end{bmatrix} \begin{bmatrix} u_1 \\ u_2 \\ u_3 \\ u_5 \end{bmatrix} \tag{61}$$

4. QUADROTOR MOVEMENT SCENARIO ON WAYPOINT TRACKING

Waypoint tracking flights require a structured and sequenced flight scenario to complete the mission. The quadrotor flight scenario in this study developed, which is described in Fig. 5.
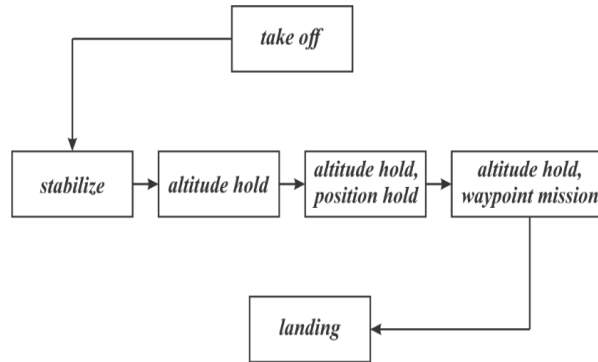
Fig. 5: Quadrotor movement scenario.

Quadrotor flying motion in tracing the waypoint trajectory is always set to move forward. This situation certainly causes the control of the x-axis translation of the quadrotor not only to utilize GPS latitude data, as well as the control of the y-axis translation of the quadrotor not only to utilize GPS longitude data. The quadrotor moves on the x-axis of the Earth. That refers to the longitude coordinates. It will rotate in front of the quadrotor, for example, 90°. The position makes the control of the quadrotor x-axis translation motion refer to latitude data. Figure 6 describes the quadrotor movement.
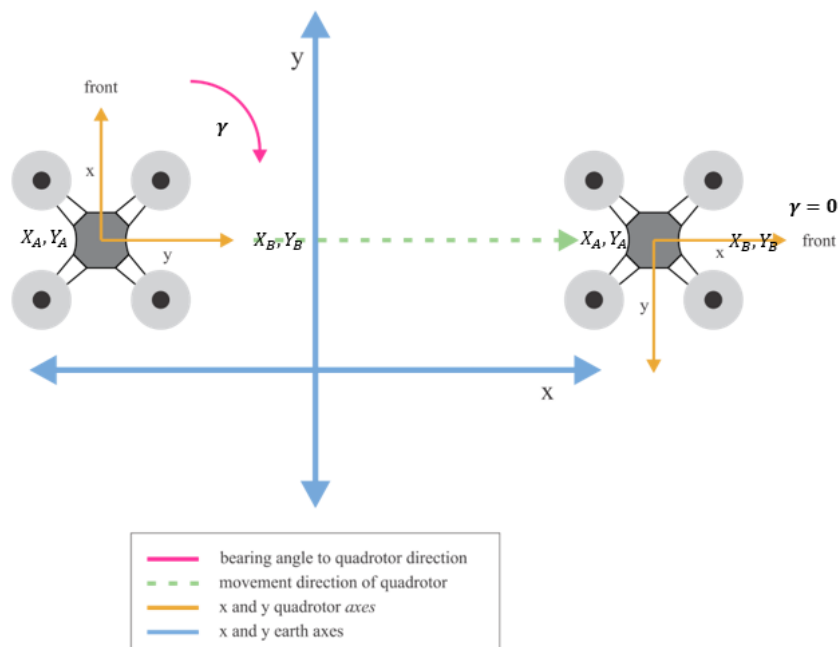
Fig. 6: Quadrotor direction to waypoint reference.

The rotation matrix concept solves the translational movement issue with the quadrotor's face. The face does not just face north, as indicated by the compass value of 0°. The rotation is centered on the z-axis and directed towards the quadrotor's x and y axes.

It is building a new axis based on the resulting angle. The new axis equation of the rotation matrix for the x and y axes is described by Eqs. (62) and (63).

$$X_A = X_B cos\gamma - Y_B sin\gamma \tag{62}$$

$$Y_A = X_B sin\gamma + Y_B cos\gamma \tag{63}$$

Another requirement for the quadrotor to constantly move forward when carrying out a search mission is adjusting the quadrotor from the current coordinate point to the intended waypoint coordinates. This adjustment is in the form of a calculation angle from two different coordinate points as the reference state yaw value. The calculated angle is called the bearing angle. The position of the angle is shown in Fig. 7 [16].
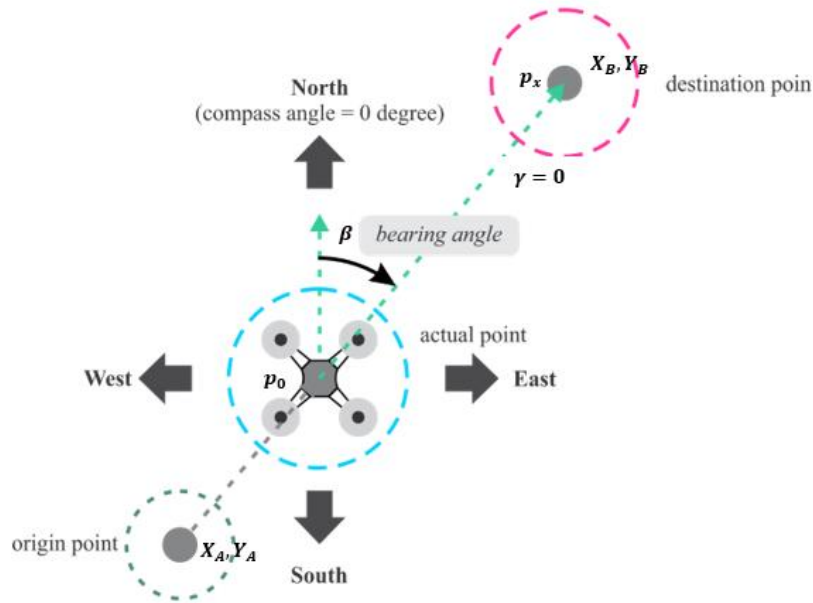
Fig. 7: Bearing angle from two difference of coordinate point location.

The bearing angle (β) is based on taking the compass angle value of 0° with the magnetic north of Earth. This angle (β) is obtained from two positions of latitude (φ) and longitude (λ) measures of the GPS coordinate frame. Two coordinate points meant are the actual point of the quadrotor in any position during flight and destination point. The actual point is represented by the longitude and latitude of GPS coordinate with p_0 symbol. On the other hand, the destination point is represented by the longitude and latitude of the following planning position coordinate with p_x symbol. Updating bearing angel can be calculated by the Haversine formula, where the first step is found longitude distance (δ_λ) between p_0 and p_x in radians units. The longitude distance can be processed as follows [16],

$$\delta_\lambda = \left(\lambda_{p_0} - \lambda_{p_x}\right) \tag{64}$$

Different longitude distance is then converted from degree to radians as follows in Eq. (65).

$$\delta_\lambda = \left(\lambda_{p_0} - \lambda_{p_x}\right) * \frac{180}{\pi} \tag{65}$$

We know if Earth has a round form with 3 Dimension perspective. So the Haversine formula should be implemented in this calculation to obtain accurate information. Therefore, Eq. (66) is described using a formula,

$$a_\lambda = \sin(\delta_\lambda) * \cos\left(\varphi_{p_x} * \frac{180}{\pi}\right) \tag{66}$$

This process also applies to latitude coordinates that can be described by Eqs. (67) and (68).

$$a_{\varphi_1} = \sin\left(\varphi_{p_0} * \frac{180}{\pi}\right) * \cos\left(\varphi_{p_x} * \frac{180}{\pi}\right) \cos(\delta_\lambda) \tag{67}$$

$$a_{\varphi_2} = \cos\left(\varphi_{p_0} * \frac{180}{\pi}\right) * \sin\left(\varphi_{p_x} * \frac{180}{\pi}\right) - a_{\varphi_1} \tag{68}$$

Based on the relation of longitude and latitude in the radians unit, the bearing angel (β) can be calculated in degree unit using Eq. (69).

$$\beta = atan2(a_\lambda, a_{\varphi_2}) \tag{69}$$

5. ARCHITECTURE SYSTEMS

5.1 Electronic Design System

Input from the quadrotor system in several sensors measuring data is the design's value, especially in the quadrotor control system. The sensors are an accelerometer and a gyroscope that produce data in the form of roll angle and pitch values from the sensor fusion process using the DMP method. Yaw angle data is obtained from the compass sensor.

The following sensors are barometer and ultrasonic, which are used to provide altitude data. The barometer sensor is used when the quadrotor flies above one meter. The pressure data is filtered and converted to altitude using the SISO Kalman filter.

Then the U-block LEA-6H module GPS sensor is used with an accuracy of up to 0.010. This sensor provides longitude and latitude data which is converted into meters. Also, this sensor acts as quadrotor control data in maintaining position and as a control in tracking the waypoint path. Like the barometer, this sensor also experiences drifting, especially for readings of the Earth's longitude, requiring data filtering first. The Kalman filter also uses the method of filtering GPS data. The hardware used in processing the algorithm in this study is an ARM Cortex-M4 microcontroller with a computational speed of 96 MHz and rated speed which can be increased through overclocking up to 120 MHz.
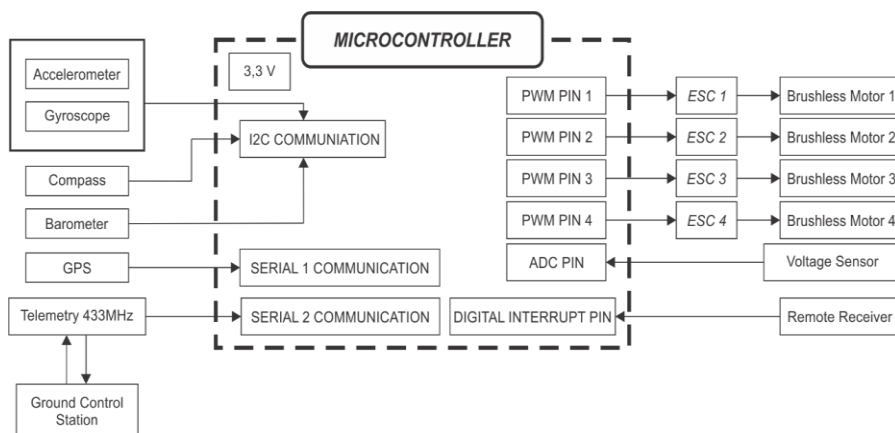
Fig. 8: Electronics architecture of quadrotor.

The last part of the electronic device system is the output part. This section is an actuator to drive the speed and direction of flight of the quadrotor. The electronic hardware used is a brushless motor with a specification of 980 kV. The engine is a three-

phase DC motor controlled using an electronic speed controller module that pulses from the microcontroller PWM port. This motor uses a propeller 10 x 4.5. The relation of the three electronic hardware is shown in Fig. 8.

5.2 Mechanical Design

This mechanical frame consists of an upper canter plate, lower center plate, and four arms attached to the sides of the canter plate. Between the upper and lower center plates, space is occupied by a battery in the form of a sized block and a telemetry module. The top center plate is used to place the microcontroller shield and the GPS buffer antenna, and the GPS module itself. Another part of the frame is the arm. It is used as the 980 kV brushless motor placement with a 10 x 5 propeller HQ-prop type and ESC. The mechanics of the aircraft spacecraft are shown in Fig. 9 and Fig. 10.

Fig. 9: Mechanics design of quadrotor in top view.
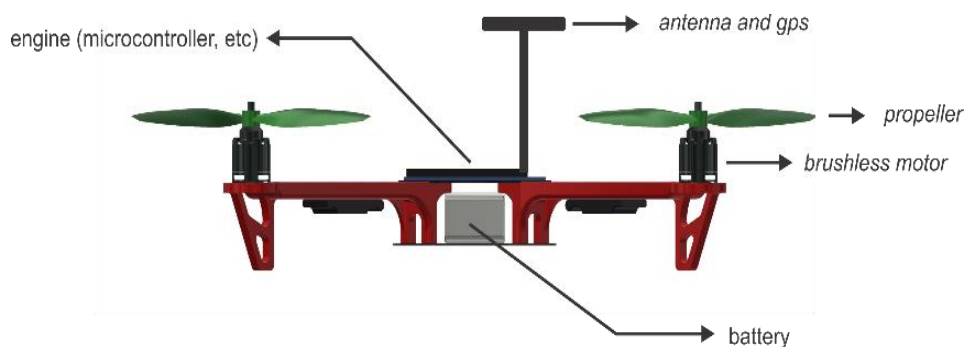
Fig. 10: Mechanics design of quadrotor inside view.

5.3 Flow Concept Programming

The main program of the Quadrotor system starts by declaring the header and several libraries used, then declarations of variables needed in the system. Furthermore, the system will enter into a setup condition, where this section is the initial condition of the sensor access, telemetry, remote reading receiver, and actuator. After the program enters the setup section, the program will enter the loop function. This function is a function that will run the program repeatedly until the system is disabled. In this function, the system will check the condition of getting flight orders or not. When the system conditions are changed into flight commands, the system will take raw data from the sensors, where the

sensor data is processed and acquired through the filtering and sensor fusion processing sub-functions. Then the program will operate the rotational motion correction function, namely flight control, by maintaining the quadrotor rotational attitude using the LQR and Integrator control system control. The flow of the main algorithm is shown in Fig. 11.
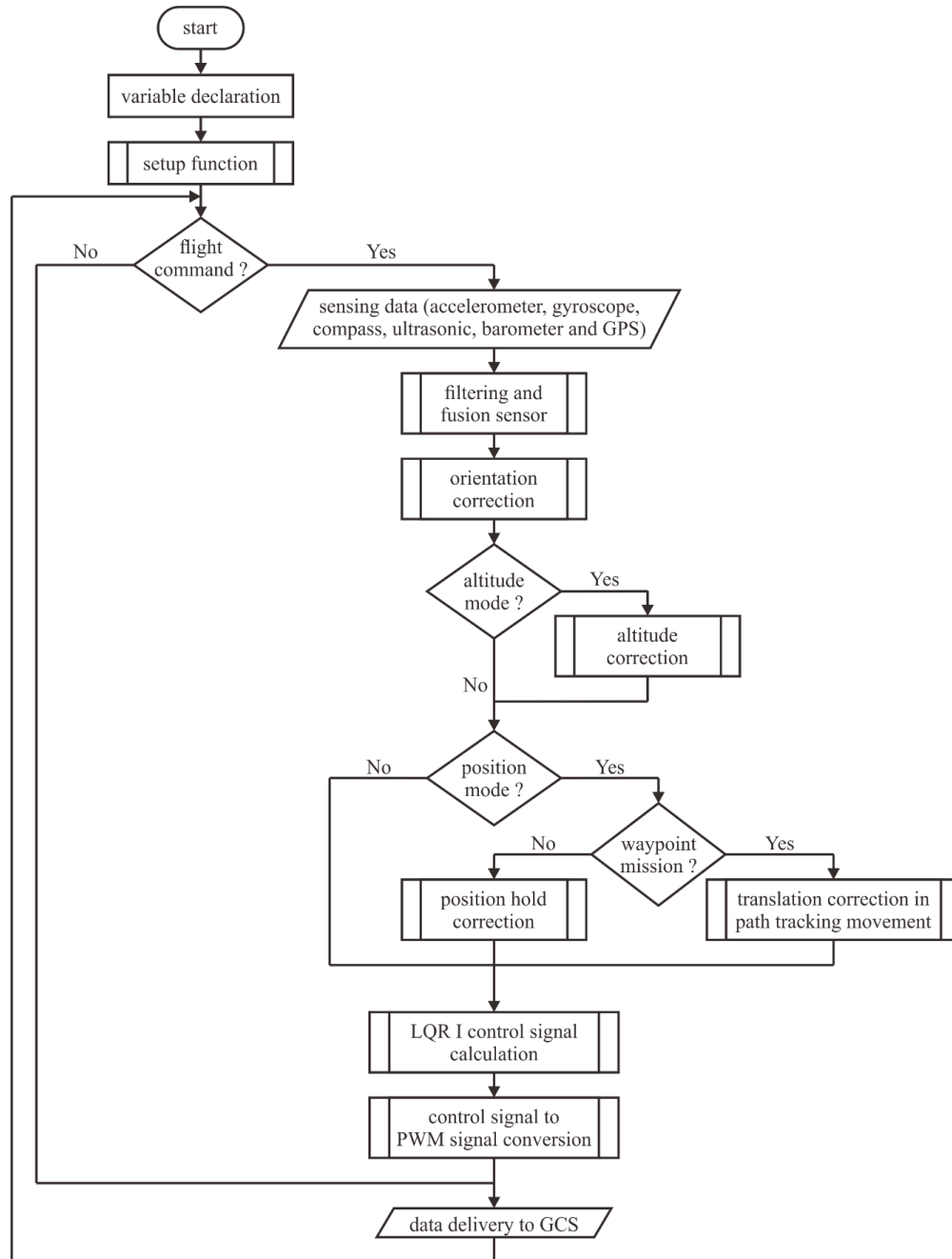
Fig. 11: Main flow diagram of a quadrotor system.

6. RESULTS AND DISCUSSION

Based on the flight scenario that has been designed, it is necessary to test and analyze the characteristics of the quadrotor. Observations were made at the point of maintaining anti-rotational motion, maintaining altitude, maintaining the anti-translational motion of the x and y axes, and defending the waypoint path. This stability test refers to the plane parameters calculated physically and mathematically, as shown in Table 2.

Table 2: Parameters of quadrotor

Parameter	Value	Unit
C_T	1.915 x 10^{-4}	-
C_Q	1.830 x 10^{-5}	-
R	1.250 x 10^{-1}	m
ρ	1.184	kg.m^3
A	4.910 x 10^{-2}	m^2
I_{xx}	1.320 x 10^{-2}	kg.m^2
I_{yy}	1.402 x 10^{-2}	kg.m^2
I_{zz}	1.237 x 10^{-2}	kg.m^2
b	1.739 x 10^{-7}	-
k	1.229 x 10^{-9}	-

Based on the experiments, it is found that the movement attitudes have increased stability with integrator control. The stability is obtained by determining the full state feedback constant value K and K_i of each quadrotor state. The constants are influenced by the weighting of the Q and R elements [23]. The greater weighting of the Q element will result in a more significant gain value K as well. The greater the gain value K, the greater the torque on the quadrotor system, making the system more responsive than giving a small gain value K [24]. The best correlation constants with Q and R quadrotor in this study are shown in Tables 3 and 4.

Table 3: Conversion matrix of Q element to gain K on quadrotor

Q	R	K
$\begin{bmatrix} 0.87 & 0 & 0 & 0 & 0 & 0 & 0 & 0 & 0 & 0 & 0 & 0 \\ 0 & 124.6 & 0 & 0 & 0 & 0 & 0 & 0 & 0 & 0 & 0 & 0 \\ 0 & 0 & 1.77 & 0 & 0 & 0 & 0 & 0 & 0 & 0 & 0 & 0 \\ 0 & 0 & 0 & 124.6 & 0 & 0 & 0 & 0 & 0 & 0 & 0 & 0 \\ 0 & 0 & 0 & 0 & 178.3 & 0 & 0 & 0 & 0 & 0 & 0 & 0 \\ 0 & 0 & 0 & 0 & 0 & 1955.9 & 0 & 0 & 0 & 0 & 0 & 0 \\ 0 & 0 & 0 & 0 & 0 & 0 & 1.73 & 0 & 0 & 0 & 0 & 0 \\ 0 & 0 & 0 & 0 & 0 & 0 & 0 & 6.89 & 0 & 0 & 0 & 0 \\ 0 & 0 & 0 & 0 & 0 & 0 & 0 & 0 & 2.95 & 0 & 0 & 0 \\ 0 & 0 & 0 & 0 & 0 & 0 & 0 & 0 & 0 & 325.5 & 0 & 0 \\ 0 & 0 & 0 & 0 & 0 & 0 & 0 & 0 & 0 & 0 & 4.81 & 0 \\ 0 & 0 & 0 & 0 & 0 & 0 & 0 & 0 & 0 & 0 & 0 & 168.6 \end{bmatrix}$	1	$\begin{bmatrix} 0 & 0 & 0 & 0 & 13.35 & 44.61 & 0 & 0 & 0 & 0 & 0 & 0 \\ 0 & 0 & 1.33 & 11.67 & 0 & 0 & 1.32 & 2.63 & 0 & 0 & 0 & 0 \\ 0.93 & 11.67 & 0 & 0 & 0 & 0 & 0 & 0 & 1.72 & 18.07 & 0 & 0 \\ 0 & 0 & 0 & 0 & 0 & 0 & 0 & 0 & 0 & 0 & 2.19 & 12.99 \end{bmatrix}$

Table 4: Integrator constant (K_i) matrix on quadrotor

K_i
$\begin{bmatrix} 0 & 0 & 0 & 0 & 0.04 & 0 & 0 & 0 & 0 & 0 & 0 & 0 \\ 0 & 0 & 0.002 & 0 & 0 & 0 & 0.0053 & 0.0008 & 0 & 0 & 0 & 0 \\ 0.004 & 0 & 0 & 0 & 0 & 0 & 0 & 0 & 0.004 & 0.0011 & 0 & 0 \\ 0 & 0 & 0 & 0 & 0 & 0 & 0 & 0 & 0 & 0 & 0 & 0.005 \end{bmatrix}$

As a starting point, the Q for each observed state is the value 1. Then the Q value approach is carried out in getting the best feedback gain system response through trial error and graphical analysis. Meanwhile, the value of R is set at 1 for all states.

The results of testing each quadrotor state that has been carried out are described in the following sub-sections.

6.1 Rotation Movement Characteristics Stability

Testing of roll, pitch, and yaw rotational motion is carried out by giving a range of 20 degrees counterclockwise deviations for state roll and pitch and 20 degrees clockwise for state yaw. The test was applied to 5 experiments with a period of 9 seconds. From the testing process, the characteristics response of each rotation is shown in Table 5 for roll response, Table 6 for pitch response and Table 7 for yaw response.

Table 5: Roll rotation stability response

Response Transient	Test 1	Test 2	Test 3	Test 4	Test 5	Average	Requirement System
Rise Time (tr) →	0.24	1.54	**0.19**	0.27	0.18	0.65	< 1 seconds
Settling time (ts) →	2	1.4	**1.5**	1.5	2.6	1.48	< 3 seconds
Overshoot →	3.22	0	**3.92**	4.38	6.8	3.66	< 9 degrees
Undershoot →	-2.11	-3.82	**0**	-2.96	-4.11	2.6	> -9 degrees
Steady State Error →	0.85	0.02	**-0.02**	0.38	0.01	0.25	± 4.5 degrees

Table 6: Pitch rotation stability response

Response Transient	Test 1	Test 2	Test 3	Test 4	Test 5	Average	Requirement System
Rise Time (tr) →	0.32	**0.48**	0.47	0.35	0.16	0.37	< 1 seconds
Settling time (ts) →	2.3	**0.9**	1.7	1,8	2.8	1.9	< 3 seconds
Overshoot →	4.72	**1.77**	4.76	2.71	4.71	3.73	< 9 degrees
Undershoot →	-2.57	**0**	0	-3.11	-4.74	2.08	> -9 degrees
Steady State Error →	0.69	**-0.46**	0.04	-0.61	0.06	-0.06	± 4.5 degrees

Table 7: Yaw rotation stability response

Response Transient	Test 1	Test 2	Test 3	Test 4	Test 5	Average	Requirement System
Rise Time (tr) →	1.45	4.71	0.84	**0.96**	0.83	1.76	< 1 seconds
Settling time (ts) →	4.6	4.90	4.7	**2.5**	4.3	4.2	< 3 seconds
Overshoot →	0	0	0	**0**	5.23	1.02	< 9 degrees
Undershoot →	-8.91	0	-8.59	**-1.28**	0	3.76	> -9 degrees
Steady State Error →	-0.88	-0.55	-1.67	**0.80**	-3.16	-1.09	± 4.5 degrees

Based on Tables 5 to 7, state roll, pitch, and yaw with LQR and Integrator control for the entire trial of five times, the quadrotor has response characteristics that meet the minimum specifications for system stability. The best response attitude results in the third test for the state roll. The third test results only have an overshoot of 3.92 degrees and no undershoot. The rise time and settling time in the third test results are among the fastest in stabilizing the system, namely 0.19 seconds and 1.5 seconds. This test also produces a minimum steady-state error of 0.02 degrees compared to other test results. While the best result for pitch is the second test and the fourth test for the yaw state. The three best responses are the results of the analysis of the flight data plots shown in Figs. 12 to 14.
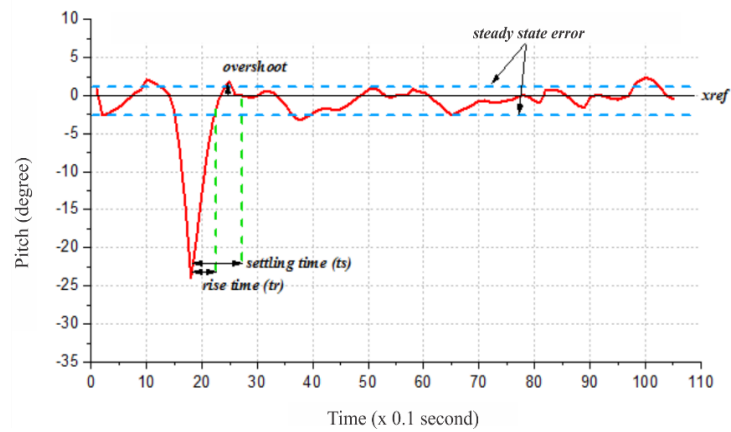
Fig. 12: Pitch angle rotation response.
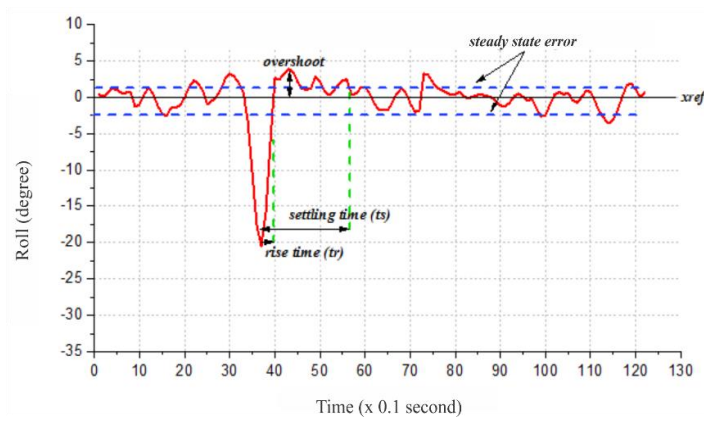
Fig. 13: Roll angle rotation response.
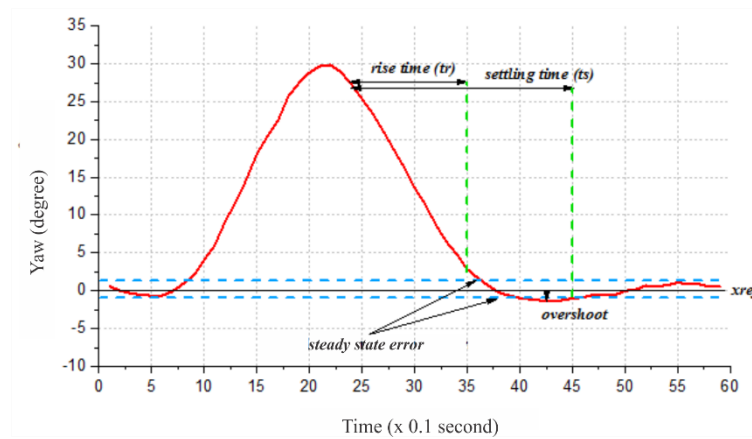
Fig. 14: Yaw angle rotation response.

Tests conducted on the three states prove that the LQR control with the addition of an Integrator can maintain the torsional stability of both roll, pitch, and yaw against disturbances that only require minimal potential energy. Besides, the short response speed of the test results indicates the need for a small cost function to stabilize the roll rotation motion [25].

On the other hand, there is a significant difference in rising time, settling time, overshooting, and undershooting the yaw state control analysis. The yaw angle data still fluctuates even though it has gone through compensation and data filtering stages.

Fluctuations occur because the magnetometer sensor's readings are influenced by the magnetic field around the sensor and the Earth's magnetic field [26]. Even so, the system is still able to accommodate a quadrotor to fly to control the yaw torque with good stability specifications.

6.2 Altitude Response Stability

Control in maintaining altitude controls the vertical axis z quadrotor translational motion associated with a thrust. This study utilizes data from the barometer and ultrasonic sensors to obtain elevation values above the ground as a controlled state.

The weighting mechanism of the Q_z and Q_{V_z} Elements in the LQR control start from a value of 1, which is then added and subtracted to get a K gain that meets the system requirements. In contrast, the Integrator Ki gain is tuned from the smallest possible value starting with one 100 of the best K LQR value. The bigger of the Integrator will provide a response strength that can cause rapid oscillation [27].

To analyze the response of the quadrotor system in altitude maintenance. The test set off altitude flight of quadrotor in 75 cm, giving some disturbance in the form of a deviation in the range of 25 cm towards the ground surface. The results of these tests are interpreted through the analysis of the response characteristics of the altitude hold motion shown in Table 8.

Table 8: Altitude hold stability response

Response Transient	Test 1	Test 2	Test 3	Test 4	Test 5	Average	Requirement System
Rise Time (tr) →	0.75	0.76	**0.83**	0.96	1.17	0.89	< 3 seconds
Settling time (ts) →	3.8	4.6	**2.7**	3.3	3.7	3.62	< 6 seconds
Overshoot →	0.07	0.03	**0.03**	0.07	0.03	0.04	<= 0.07 meters
Undershoot →	0	-0.02	**0**	0	0	0.004	>= -0.07 meters
Steady State Error →	-0.02	-0.01	**-0.02**	0.02	0.01	-0.004	± 0.0375 meters

The best characteristics of the aircraft are obtained when the third test. The resulting test only has a minimum overshoot of 0.03 degrees and no undershoot in the system. Furthermore, the system has the fastest settling time than others. This test also produces a minimum steady-state error of -0.02 degrees. The characteristic is carried out, shown by the flight data plotting, as shown in Fig. 15.
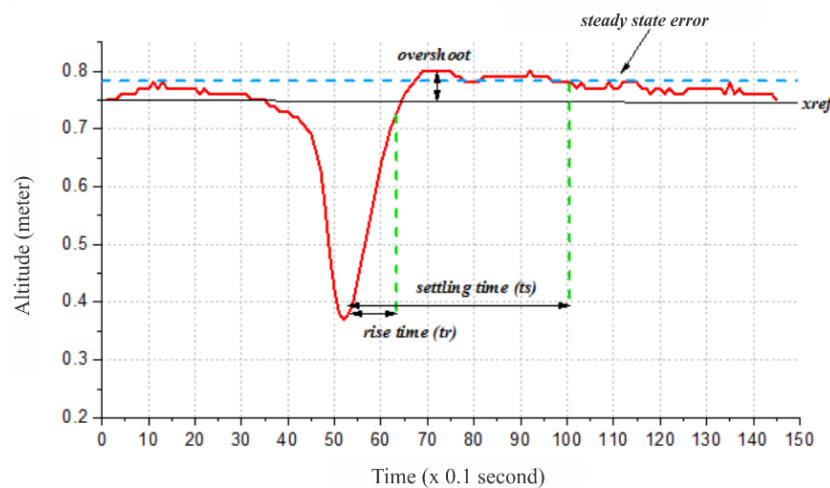
Fig. 15: Altitude hold response.

The characteristics of the quadrotor have a settling time for each test, having a relatively slow time and minimal undershoot in reaching a steady state. This condition is caused by updating the vertical translation speed state, which is longer, and using a considerable gain value so that the quadrotor will slowly hold the momentum after the overshoot occurs.

Testing is also carried out by varying the reference height to find out more characteristics. The variation in altitude is adjusted to the reference height of 1.8 m, 3.4 m, and 4.8 m by utilizing the height data from the barometer sensor. The results of the flight test are depicted in Fig. 16.

The calculation result of the steady-state error is -0.0131 m for a height of 1.8 m, -0.0283 m for a height of 3.4 m, and 0.025 m for a height of 4.8 m. A minor steady-state error generated at the lowest altitude does not mean that the system has the minimum error. The system is steady-state with the slightest inclination interval, namely the range ± 0.02 m, namely at an altitude of 4.8 m. The barometer sensor readings are accurate at higher altitudes.
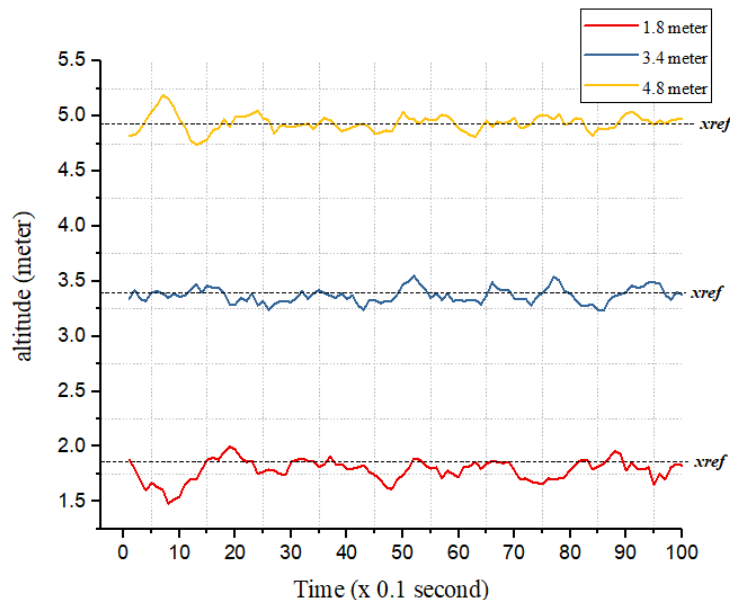
Fig. 16: Altitude hold response in different reference of high.

However, the LQR control system with the addition of the Integrator concept as compensation can be appropriately controlled by meeting the system requirements specification. The steady-state error occurs no more than 10% of the reference altitude.

6.3 Translation Movement Characteristics Stability

This test is categorized into two segments: translational motion, maintaining absolute earth coordinates, and translational motion when performing a waypoint mission.

6.3.1 Position Hold Stability

In principle, a horizontal translational motion has two controlled x and y axes. Control of horizontal quadrotor translation motion depends on the accuracy of using the Global Positioning System sensor to obtain data in the form of displacement state and x-axis translation speed from longitude data conversion and y-axis data from latitude data conversion. Referring to previous research conducted by [28], giving a tolerance limit of

2.5 m to the front, back, right, and left of the quadrotor. The quadrotor translation motion test is analyzed based on comparing the use of the LQR and LQR Integrator controls.

This part of the translational motion trial was carried out five times without getting disturbed by the current environmental conditions. Based on the five tests, the quadrotor has flight characteristics in maintaining the x-axis and y-axis positions as described in Tables 9 and 10.

Table 9: Comparison of x-axis translation stability using LQR and LQR Integrator

Control Method	Error Properties	Test 1	Test 2	Test 3	Test 4	Test 5	Average
LQR	Max. deviation (meters)	2.71	2.74	3.23	1.78	3.15	2.72
	Min. deviation (meters)	-2.63	0.40	-1.14	1.69	0.22	-0.29
	Steady state error (meters)	0.12	1.84	0.93	-0.06	1.91	0.95
LQR Integrator	Max. deviation (meters)	0.41	0.39	1.49	0.14	0.74	0.63
	Min. deviation (meters)	-1.35	-1.04	-0.12	-1.36	-1.49	-1.07
	Steady state error (meters)	0.10	-0.35	0.55	-0.72	-0.36	-0.15

Table 10: Comparison of y-axis translation stability using LQR and LQR Integrator

Control Method	Error Properties	Test 1	Test 2	Test 3	Test 4	Test 5	Average
LQR	Max. deviation (meters)	3.21	-0.03	0.14	4.09	4.96	2.47
	Min. deviation (meters)	0.80	-1.93	-2.99	0.57	0.48	-0.61
	Steady state error (meters)	2.07	-1.19	-1.36	2.45	2.10	0.82
LQR Integrator	Max. deviation (meters)	0.40	1.95	2.28	1.98	2.27	1.52
	Min. deviation (meters)	0.47	2.19	-1.96	-1.52	-1.79	-0.52
	Steady state error (meters)	-0.28	0.21	-0.51	-0.70	0.98	-0.06

The results also prove, by using the LQR control coupled with Integral. It can give a quadrotor translation motion system needed. The error calculation of a steady-state error has an average of -0.06 meters for the x-axis and -0.15 meters for the y-axis. On the other hand, the steady state error using the LQR control produces a more considerable error with an average of 0.95 for the x-axis and 0.82 for the y-axis. The accuracy and precision of the control process can be seen in Table 11.

Table 11: Comparison between LQR and LQR Integrator method in position hold stabilization of a quadrotor

Control Method	Parameter	Test 1	Test 2	Test 3	Test 4	Test 5	Average
LQR	Accuracy in %	62	90	80	66	58.67	71.33
	Precision in %	23.81	30.18	45.89	32.84	46.82	35.91
LQR Integrator	Accuracy in %	100	100	100	100	100	100
	Precision in %	45.45	35	38.62	37.93	31.54	37.71

Accuracy and precision are evidenced in Fig. 17, which compares the distribution of quadrotor data with LQR and LQR and Integrator.

(a) (b)
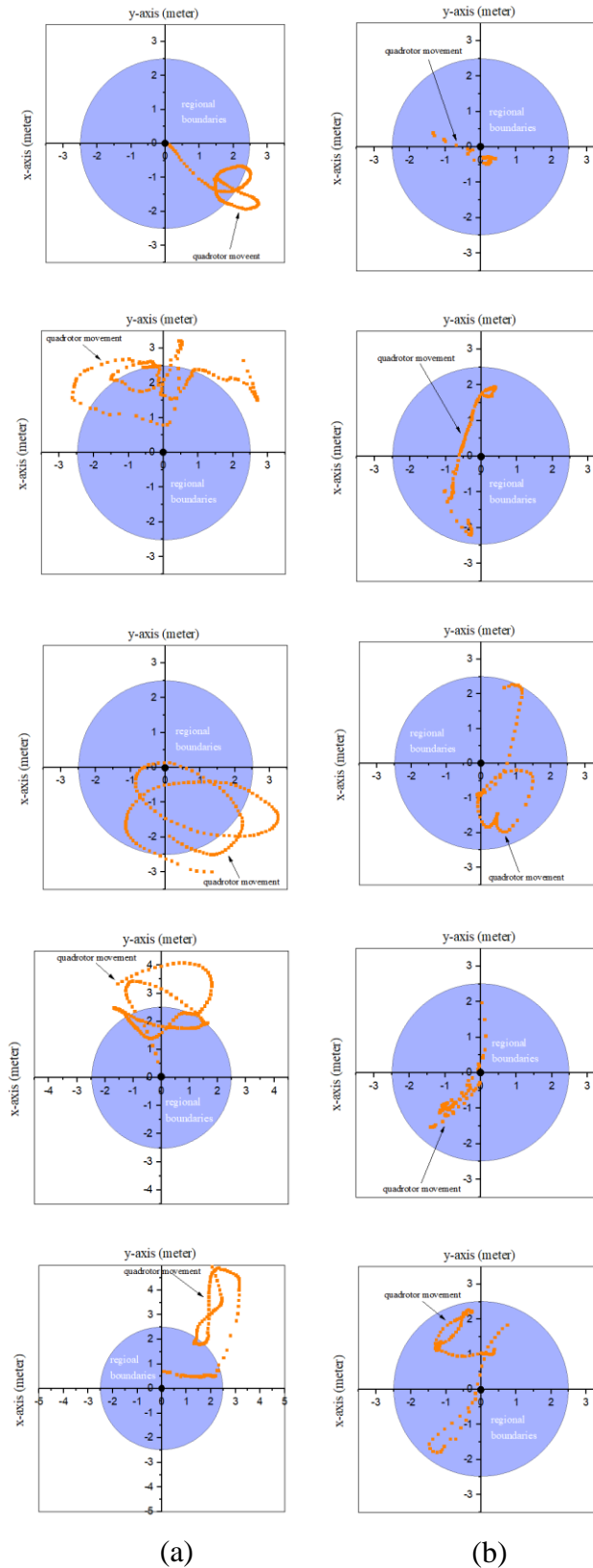
Fig. 17: Quadrotor position hold movement using (a) LQR control (b) LQR
Integrator control.

The accuracy is calculated from a division of the number data in the tolerance limit (the light blue circle) by a value of 150 and multiplied by 100%. It can be written into the following Eq. (70) form,

$$Accuracy = \frac{Number\ of\ data\ in\ limit\ tolerance}{150} x100\% \qquad (70)$$

The number 150 comes from taking flight data from the quadrotor test, where each flight is carried out for 15 seconds and produces 150 data. The calculation results prove that using LQR and Integrator control as a quadrotor control system can increase the accuracy to 100% from 71.33% accuracy of LQR control accommodation only. The LQR and Integrator control making the quadrotor system only requires less energy than the LQR control.

High accuracy does not necessarily have high precision either. The precision itself is the closeness of the difference in the value of each data distribution from a data set. In the case of anti-translational motion control, the precision given to the LQR and Integrator control on the system is not so significant, which only increases the range of 1.8% of the LQR control. The compensation of Integrator does have properties that increase the system's responsiveness. So, the quadrotor error can be reduced, but it is not meaningful with good damping properties.

Meanwhile, the precision value is obtained from the calculation step of the average of each position distance to the reference and the standard deviation, where one data is represented by two displacement data x and y with displacement references x and y equal to zero. Then the distance of a position point to the reference point can be calculated using the Pythagoras formula, such as Eq. (71):

$$range\ position\ to\ the\ reference = \sqrt{x^2 + y^2} \qquad (71)$$

The precision of each distance as a ratio of the standard deviation against the average of range postopn to the reference multiplied by 100%, as in Eq. (72),

$$Precision = \frac{deviation\ standar\ of\ rage\ position\ to\ the\ refernce}{average\ of\ range\ position\ to\ the\ reference} x100\% \qquad (72)$$

6.3.2 Translation Stability in Waypoint Mission

The control system testing on translational movement when tracing a path is applied to a different path pattern. The track pattern consists of squares and zig-zags. The box waypoint trajectory pattern is constructed by entering four different latitude and longitude coordinates, where the coordinates of the points are shown in sequence in Table 12.

Table 12: Coordinate trajectory pattern of waypoint

State Coordinate of waypoint	Square Pattern		Zig-zag Pattern	
	Latitude	Longitude	Latitude	Longitude
1	-7.751096	110.348807	-7.751096	110.348807
2	-7.750976	110.348807	-7.751096	110.348927
3	-7.750976	110.348927	-7.750976	110.348807
4	-7.751096	110.348927	-7.750976	110.348927

These coordinate points are determined based on satellite image data on one of the features provided by Google Earth by forming the path of each flight trajectory pattern as shown in Fig.18 (a, b).

(a)   (b)
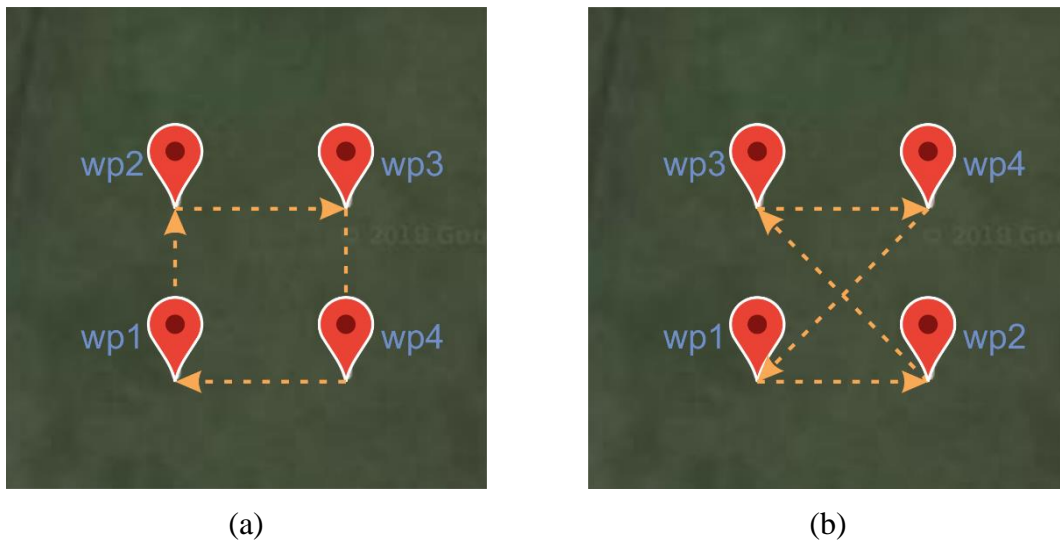
Fig. 18: Waypoint flow movement of the quadrotor in (a) square and (b) zig-zag trajectory pattern.

The basic concept of this translational motion control system analysis is carried out in the movement of the x-axis or lateral axis of the aircraft. The velocity of the quadrotor becomes one of the determining factors for the success of the quadrotor in the waypoint mission. The velocity will generate momentum in the plane, which makes it unable to defend stabilization. The correct value of velocity in a waypoint mission flight will make the quadrotor fly more accurate towards the right path [29]. Therefore, this study varies the speed of the quadrotor in each flight mission in tracing the trajectory with three-speed variations that can minimize the percentage of flight errors or errors, as explained in Table 13.

Table 13: Quadrotor flight velocity variation to the performance of trajectory error

Trajectory Pattern	Velocity ($\frac{m}{s}$)	Range (m)	% Error
Square	0.5	52	37.78
	1	52	5.04
	1.5	52	68,89
Zig-zag	0.5	62.76	37.83
	1	62.76	13.51
	1.5	62.76	66.72

The error presentation reflects the accuracy of the quadrotor to be traced in the path. The error presentation is calculated from the position based on the fault tolerance limit during the flight mission. Error calculation can be calculated using Eq. (73),

$$\% \, Error = \frac{The\ amount\ of\ quadrotor\ position\ data\ is\ out\ of\ tolerance}{Total\ of\ data\ recording\ in\ waypoint\ mission} x100\% \qquad (73)$$

From the results of data processing, it was found that the slightest error percentage in both inbox and zig-zag trajectory occurred in the quadrotor system with a flight speed of 1 m / s. In comparison, the most significant error happened when the quadrotor speed was set at 1.5 m / s with an error percentage of 68.89% for the square track pattern and 66.72%

for the zig-zag trajectory. A higher velocity than the system requirement will produce a steady-state that is out of the path tolerance limit. It happened because lateral motion control requires navigation data to run slower in correcting errors. Also, the high velocity can make overshoot component on the flight of a quadrotor. Overshoot occurs because the process of moving the quadrotor movement moves forward towards a stop condition when it enters the waypoint point to change the direction of a quadrotor. In this situation will be tremendous momentum so that the plane is likely to bounce.

The low speed of the system requirements will also affect the number of errors that occur, although not as large as the errors generated at high-speed settings. The percentage of error was 37.78% in the square track pattern and 37.83% in a zig-zag way for the velocity of 0.5 $\frac{m}{s}$. The velocity is set lower than the system requirement. It will make the aircraft character less able to correct the drift that occurs. Resulting in the quadrotor to produce track tracking movements still with errors that are high enough then the tolerance limit.

6.3.3 Comparison between LQR and LQR Integrator Control Method Performance in Square Trajectory Pattern

The quadrotor flight behavior in tracing the waypoint trajectory in a box pattern is visualized in Fig. 19 (a, b) and their characteristics as shown in Table 14.
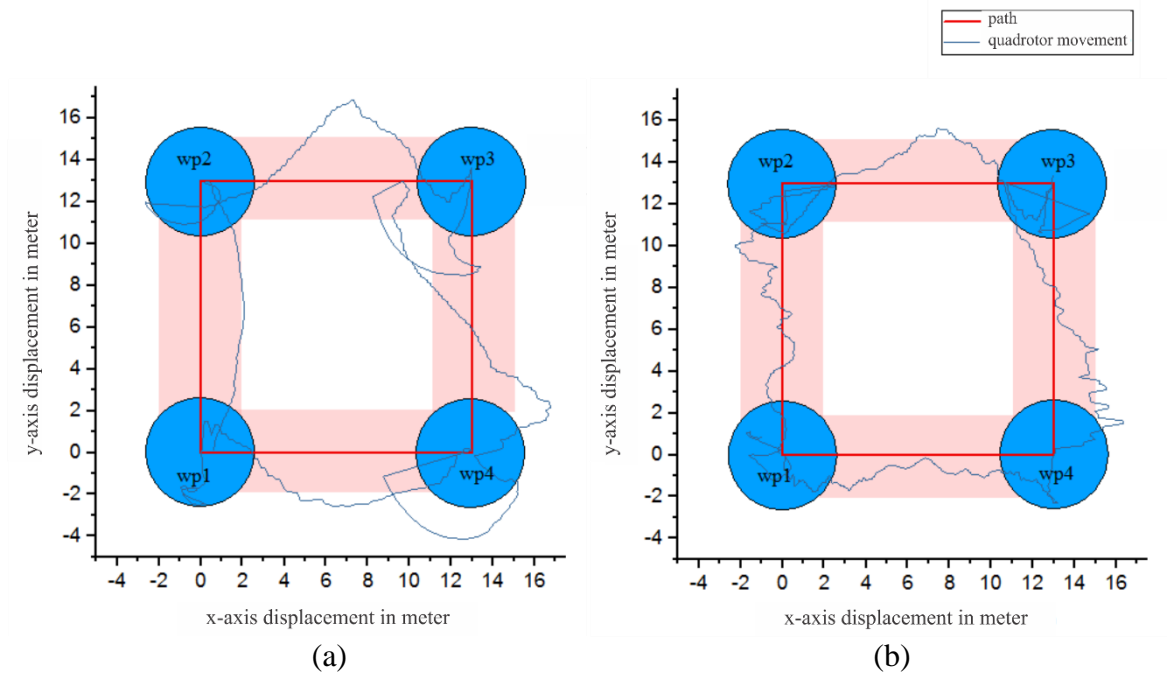
Fig. 19: Quadrotor movement in square trajectory pattern (a) using LQR control (b) using LQR Integrator control.

Based on Table 14, the lack of the LQR control system applied to the quadrotor to trace the waypoint coordinates is corrected by adding an Integrator control to the LQR control. Using LQR and Integrator control, the quadrotor can reduce the steady-state error and multiple overshoots that occur, followed by an increase in the accuracy of tracking aircraft movements on the trajectory from 64.84% to 94.96%. The steady-state error is minimized from 2 meters to 0.54. meters and the average undershoot is -1.04, so there are no multiple overshoots when the quadrotor takes advantage of this control. Based on the

description in the previous paragraph, the Integrator can compensate for the control signal generated by the LQR. The control signal has calculated from an error value multiplied by the last gain integrator. So, the system response does not only depend on giving the current read state value. Besides, this control can accommodate the quadrotor's attitude towards the regulator with the energy required by the system specifications for the 12 steady states.

Table 14: Comparison of Characteristics Movement Quadrotor using LQR and LQR Integrator Control Method in Square Trajectory Pattern

Waypoint	Length of Track (m)	LQR				LQR Integrator			
		Over shoot (m)	Unders hoot (m)	Steady state error (m)	Accu racy (%)	Over shoot (m)	Unders hoot (m)	Steady state error (m)	Accu racy (%)
wp1 to wp2	13	0	0	1.51	86.40	0	0	0.39	93.58
wp2	0	0	-0.15	0	92.22	0	0	0	100
wp2 to wp3	13	0	0	2.10	66.67	0	0	0.45	94.59
wp3	0	0	-2.25	0	20.62	0	0	0	100
wp3 to wp4	13	0	0	2.54	40.29	0	0	0.29	72.73
wp4	0	0	-1.74	0	48.42	0	0	0	100
wp4 to wp1	13	0	0	1.80	65.78	0	0	1.02	98.78
wp1	0	0	-0.01	0	98.34	0	0	0	100
Average		**0**	**-1.04**	**2.00**	**64.84**	**0**	**0**	**0.54**	**94.96**

6.3.4 Comparison between LQR and LQR Integrator Control Method Performance in Zig – Zag Trajectory Pattern

Comparison of translational motion control is also carried out in zig-zag trajectory tracing, where the quadrotor provides flight characteristics interpreted in Fig. 20 (a, b).
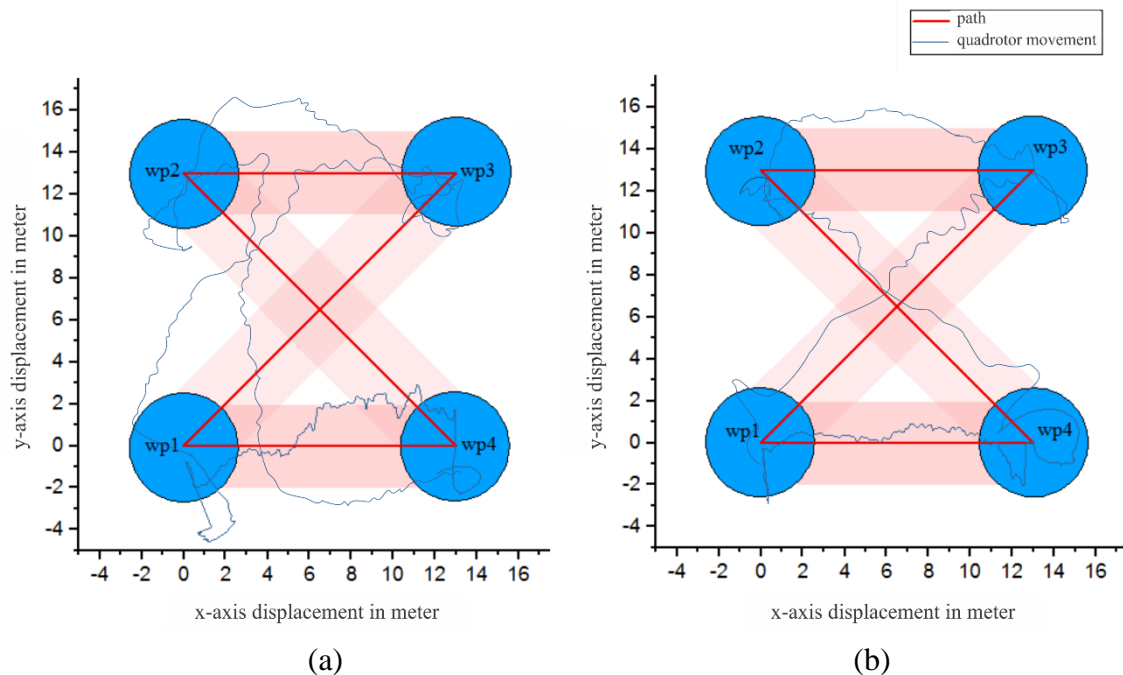
Fig. 20: Quadrotor movement in zig-zag trajectory pattern (a) using LQR method (b) using LQR Integrator method.

Based on Fig. 20 (a, b), the quadrotor has been able to enter within the tolerance of the zig-zag waypoint path when carrying out a search strengthened by the acquisition of data analysis results in Table 15.

Table 15: Comparison of characteristics movement quadrotor using LQR and LQR Integrator control method in Zig – Zag trajectory pattern

Waypoint	Length of Track (m)	LQR				LQR Integrator			
		Over shoot (m)	Unders hoot (m)	Steady state error (m)	Accu racy (%)	Over shoot (m)	Unders hoot (m)	Steady state error (m)	Accu racy (%)
wp1 to wp2	13	0	0	0.76	73.72	0	0	0.18	98.47
wp2	0	0	0	0	100	0	0	0	100
wp2 to wp3	18.38	0	0	4.70	16.15	0	0	0.90	92.36
wp3	0	0	-0.86	0	41.67	0	-0.02	0	93.33
wp3 to wp4	13	0	0	2.24	40.48	0	0	1.84	92.36
wp4	0	0	-0.42	0	84.61	0	-0.1	0	92.85
wp4 to wp1	18.38	0	0	5.08	0	0	0	1.29	95.45
wp1	0	0	-2.45	0	17.24	0	-0.41	0	76
Average		0	-1.12	3.19	46.73	0	-0.18	1.06	86.49

Referring Table 15, it indicates that controlling a quadrotor on a zig-zag line is more complicated than tracing a straight path pattern. This result is evidenced by the more minor accuracy results for the two control method applications. Quadrotor control with LQR control has decreased tracking accuracy to 46.73% with steady-state error, and the average undershoot is getting greater to be 3.19 and -1.12 meters. Likewise, quadrotor control using LQR and Integrator experienced a decrease in tracking accuracy to 86.49% with a steady-state error and an undershoot that occurred at 1.06 and -0.18 meters.

This condition occurs because the zig-zag trajectory pattern requires the quadrotor to rotate by maintaining a direction that exceeds 90°. The results in the yaw torque were significantly affecting the pitch and roll torque being unstable with a greater force. This instability cannot be handled by quadrotor translation control, which has a more extended control update rate than other state controls and makes the quadrotor have a more significant deviation than before. The condition does not necessarily increase the value of gain K, that resulting torsional the greater torque. The torque can make the quadrotor more responsive rotate in the direction of the x-axis or y-axis even slammed [30]. Therefore, the best system response is presented using the results of the Q element tuning with a gain K as in controlling the translation motion at a specific location.

7. CONCLUSION

Implementing the LQR control method with the Integrator on the waypoint mission has successfully minimized steady-state error and multiple-overshoot. LQR Integrator can increase the accuracy to 94.96% with a steady-state error of 1.06 meters in square track pattern and 86.49% with a steady-state error of 0.54 meters in zig-zag trajectory. The compensation of Integrator has higher accuracy that can sign to provide minimum error, but it no more effective to increase precision state in translation movement.

In the future, this research needs to develop other methods that can enhance the precision state in quadrotor systems. We will implement an artificial intelligence approach

to combine in anatomy structure LQR control method. So, the system has a self-learning ability that can adapt to the environment dynamically.

REFERENCES

[1]   Kenzo N, Farid K, Satoshi S, Wei W, Daisuke N. (2010) Autonomous flying robot - unmanned aerial vehicle and micro aerial vehicle. Springer Tokyo Dordrecht Heidelberg London New York. doi: 10.1007/978-4-431-53856-1

[2]   Tri KP, Agfi EP, Andi D. (2015) Optimizing control based on ant colony for quadrotor stabilization. IEEE International Conference on Aerospace Electronics and Remote Sensing Technology, pp 1-4. doi: 10.1109/ICARES.2015.7429820

[3]   Luis RGC, Alejandro EDL, Rojrlio L, Claude P. (2013) Quad rotorcraft control (vision - based hovering and navigation), Springer Verlag London. doi: 10.1007/978-1-4471-4399-4

[4]   Jhon O, Rolf R. (2005) Waypoint guidance for small UAVs in wind, AIAA Virginia University of Washington, 6951: 1-12. https://doi.org/10.3182/20131120-3-FR-4045.00005

[5]   Richard S, Mark K, Qi G. (2016) Unscented guidance for waypoint navigation of a fixed-wing UAV, American Control Conference (ACC) Boston, pp 473-478. doi: 10.1109/ACC.2016.7524959

[6]   Anibal O, Bruno S. (2020) Aerial robotic manipulation (research, development and applications), Springer Tracts in Advanced Robotics, 129. doi: 10.1007/978-3-030-12945-3

[7]   When-Ci L, Wun-Shin W. (2016) Design of an automatic docking system for quadcopters, Asia-Pacific Conference on Intelligent Robot, pp 199-203. doi: 10.1109/ACIRS.2016.7556212

[8]   Nurul AI, Nor LO, Dwi P, Z MZ, Luhur B. (2015) Attitude Control of Quadrotor, ARPN Journal of Engineering and Applied Sciences, 10(22): 17206-17211.

[9]   Oktaf AD, Andi D, Tri KP. (2017) Model of linear quadratic regulator (LQR) control method in hovering state of quadrotor. Journal of Telecommunication, Electronic and Computer Engineering, 9(3): 135-143. https://jtec.utem.edu.my/jtec/article/view/1589/1891

[10]   Lucas A, Willian CR, Paulo ES, Renato AA. (2013) PID, LQR and LQR-PID on a quadcopter platform. IEEE International Conference on Informatics, Electronics and Vision, pp 1-6. doi: 10.1109/ICIEV.2013.6572698

[11]   Emre CS, Ali TK. (2014) Optimal path tracking control of a quadrotor UAV, IEEE International Conference on Unmanned Aircraft Systems, pp. 115-125. doi: 10.1109/ICUAS.2014.6842246

[12]   Josias GB, Darielson AS, Laurinda LN, Lucas VOF, Kaio MR, Antonio BSJ, Wilkley BC. (2019) Performance comparison between the PID and LQR controllers applied to robotic manipulator joint. IEEE 45th Annual Conference of the IEEE Industrial Electronics Society, pp 479-484. doi: 10.1109/IECON.2019.8927059

[13]   Michael FE. (2015) LQR with integral feedback on a parrot mini-drone, MIT Cambridge, 02139.

[14]   Gusna HT, Andi D. (2017) Sistem kendali autopilot pada quadrotor untuk menuju titik koordinat dengan memanfaatkan GPS, Universitas Gadjah Mada, Indonesia.

[15]   Anup V, Pabba S, Jansi KR. (2017) Fully autonomous UAV. IEEE International Conference on Technical Advancements in Computers and Communications, pp 41-44. doi: 10.1109/ICTACC.2017.20

[16]   Lucas VS, Alexandre SB, Mario S-F. (2015) Outdoor waypoint navigation with the AR. Drone quadrotor. IEEE International Conference on Unmanned Aircraft Systems, pp 303-311. doi: 10.1109/ICUAS.2015.7152304

[17]   Tri KP, Andi D, Oktaf AD, Nur ASP. (2016) Optimizing control based on fine-tune PID using ant colony logic for moving control UAV systems. American Institute of Physics Conference Proceedings, 1755, 170011. https://doi.org/10.1063/1.4958613

[18]   Mohamad RR, Saeide H, Davoud S. (2013) Designing and simulation for vertical moving control of UAV system using PID, LQR and Fuzzy logic, International Journal of Electrical and Computer Engineering, 3(5):651-659. http://dx.doi.org/10.11591/ijece.v3i5.3440

Dhewa et al.

[19] James WF. (2007) Modelling and linear control of a quadcopter, Cranfield University.

[20] Katsuhiko O. (2010) Modern control system, 5th Edition, Prentice-Hall.

[21] Russell CH. (2016) Dynamics, 14th Edition, Hoboken, New Jersey: Pearson Prentice Hall.

[22] Zoran B, Petar P, Denis K. (2016) Mathematical modelling of unmanned aerial vehicle with four rotors. Journal of Interdisciplinary Description of Complex Systems, 14(1): 88-100. Retrieved from https://ideas.repec.org/a/zna/indecs/v14y2016i1p88-100.html

[23] Gesang N, Andi D. (2017) Undesirable rolling minimization on the EDF missiles flight based on LQR methods, International Conference on Advanced Mechatronics, Intelligent Manufacture, and Industrial Automation, pp 85-90. doi:10.1109/ICAMIMIA.2017.8387563

[24] Andi D, Agfi EP, I MT, Agung W. (2019) The obstacle avoidance system in a fixed-wing UAV when flying low using LQR method. International Conference on Computer Engineering, Network and Intelligent Multimedia, pp 1-7. doi: 10.1109/CENIM48368.2019.8973292

[25] Robert S. (2018) Design and development of the LQR optimal controller for the unmanned aerial vehicle. Obuda University, Budapest, Hungaria, 1(36): 45-54. doi:10.19062/1842-9238.2018.16.1.7

[26] Thomas S, Stefan R. (2017) Eliminating the effect of magnetic disturbances on the inclination estimates of inertial sensors. IFAC-PapersOnLine, 50(1): 8798-8803. https://doi.org/10.1016/j.ifacol.2017.08.1534

[27] Karl JA, Tore H. (2006) Advanced PID control, ISA Publishing.

[28] Ariesa BZ, Andi D. (2017) Sistem kendali penghindar rintangan pada quadrotor menggunakan konsep linear quadratic. Indonesian Journal of Electronics and Instrumentations Systems, 7(2): 219-230. https://jurnal.ugm.ac.id/ijeis/article/view/25503/17912

[29] Daniele G, Marc SA, Irene A, Maria A, Paolo A, Marco B, Pierluigi DB, Donatella D, Danilo G, Peter Hobbs, Veronika L, Tomasz N, Marco P, Marianna R, Riccardo S, Valerio S, Bernadette S, Fabrizio T. (2020) The use of unmanned aerial vehicles (UAVs) for engineering geology applications, Springer Bulletin of Engineering Geology and the Environment, 79: 3437-3481. https://doi.org/10.1007/s10064-020-01766-2

[30] Andi D, Ahmad A, Agfi EP. (2018) Translation movement stability control of quad tiltrotor using LQR and LQG, International Journal of Intelligent Systems and Applications, 10(3): 10-21. doi:10.5815/ijisa.2018.03.02

MAINTAIN AGENT CONSISTENCY IN SURAKARTA CHESS USING DUELING DEEP NETWORK WITH INCREASING BATCH

RIAN ADAM RAJAGEDE

Department of Informatics, Universitas Islam Indonesia, Sleman, Indonesia

*Corresponding author: rian.adam@uii.ac.id

ABSTRACT: Deep reinforcement learning usage in creating intelligent agents for various tasks has shown outstanding performance, particularly the Q-Learning algorithm. Deep Q-Network (DQN) is a reinforcement learning algorithm that combines the Q-Learning algorithm and deep neural networks as an approximator function. In the single-agent environment, the DQN model successfully surpasses human ability several times over. Still, when there are other agents in the environment, DQN may experience decreased performance. This research evaluated a DQN agent to play in the two-player traditional board game of Surakarta Chess. One of the drawbacks that we found when using DQN in two-player games is its consistency. The agent will experience performance degradation when facing different opponents. This research shows Dueling Deep Q-Network usage with increasing batch size can improve the agent's performance consistency. Our agent trained against a rule-based agent that acts based on the Surakarta Chess positional properties and was then evaluated using different rule-based agents. The best agent used Dueling DQN architecture with increasing batch size that produced a 57% average win rate against ten different agents after training for a short period.

ABSTRAK: Pembelajaran Peneguhan Mendalam adalah terbaik apabila digunakan bagi mewujudkan ejen pintar dalam menyelesaikan pelbagai tugasan, terutama jika ia melibatkan algoritma Pembelajaran-Q. Algoritma Rangkaian-Q Mendalam (DQN) adalah Pembelajaran Peneguhan berasaskan gabungan algoritma Pembelajaran-Q dan rangkaian neural sebagai fungsi penghampiran. Melalui persekitaran ejen tunggal, model DQN telah beberapa kali berjaya mengatasi kemampuan manusia. Namun, ketika ejen lain berada dalam persekitaran ini, DQN mungkin kurang berjaya. Kajian ini melibatkan ejen DQN bermain papan tradisional iaitu Catur Surakarta dengan dua pemain. Salah satu kekurangan yang dijumpai adalah konsistensi. Ejen ini akan kurang bagus ketika berhadapan lawan berbeza. Kajian menunjukkan dengan penggunaan Rangkaian-Q Dwipertarungan Mendalam bersama peningkatan saiz kumpulan dapat meningkatkan konsistensi prestasi ejen. Ejen ini telah dilatih untuk melawan ejen lain berasaskan peraturan dan sifat kedudukan Catur Surakarta. Kemudian, ejen ini diuji berpandukan peraturan berbeza. Ejen terbaik adalah yang menggunakan rekaan DQN Dwipertarungan bersama peningkatan saiz kumpulan. Ianya berhasil memenangi permainan dengan purata 57% berbanding sepuluh agen lain melalui latihan jangka masa pendek.

1. INTRODUCTION

Deep reinforcement learning has been able to produce agents that can solve a variety of complex problems, such as simulated car driving [1], video games [2], or natural language processing [3]. A game is an environment that is often used to evaluate reinforcement learning agents' ability to interact with other agents and make decisions to achieve specific goals. Researchers can focus on algorithms with a relatively more straightforward environment before implementing them in more complex environments such as self-driving cars.

The deep learning approach successfully captures richer features and improves agent performance when combined in reinforcement learning algorithms. For example, in [2] the produced agent uses Deep Q-Learning, the combination of Convolutional Neural Network [4] and Q-Learning [5] to play and win Atari games. Another quite phenomenal one is Alpha Go [6], an agent that manages to beat the best human players in the world in a reasonably complex game, Go, using deep reinforcement learning. In various types of board games, human-level abilities have also been surpassed by intelligent agents, such as in Othello [7,8], Mancala [9], Chess [10,11], Go [6,12], or even in a game with incomplete information, such as Poker [13]. Those agents are trained using reinforcement learning, deep learning, or a combination of both. In [8], the Othello game is seen as a classification problem. The agent trained on the game database using a deep convolutional neural network to decide the best action in the given state. In contrast to [7], agents in the Othello game trained using neural fitted temporal difference learning, which is a method in reinforcement learning. In chess, the previous studies also use deep learning [11] or deep reinforcement learning [10] to produce a good performance agent.

Board games have different characteristics compared to Atari single-player video games previously researched [2]. In the majority of board games, the agent must interact with one or more players. This environmental behaviour is called a Markov Game [14]. The presence of other players in the game dramatically affects the agent in making decisions and can make it difficult for us to produce intelligent agents. In [12], agents are trained using Convolutional Neural Network and Monte Carlo Tree Search (MCTS) by self-playing in the Go game without being given explicit information by humans. Self-playing means the agent plays games against itself. The method is effective as the agent produced using this method successfully defeats humans in the Go game and the agent from the previous research [6] with a shorter training time. Another form of the agent training process that can be used is to train the agent against the rule-based player who moves based on the positional values of the board game [15] or uses a database that stores records of previous matches [8].

This research will implement and evaluate the reinforcement learning algorithm, Deep Q-Learning, in the two-player board game of Surakarta Chess. Surakarta Chess has unique game characteristics. One of them is that some positions on the board can be very profitable to defeat the opponent. From those properties, we can make rule-based agents train the reinforcement learning agent. The making of intelligent agents in Surakarta Chess has been studied previously. In those studies, agents were made based on two search methods, αβ-search [16–18] and based on MCTS [19,20]. We proposed to use Deep Q-Learning as a different approach to creating an agent in Surakarta Chess. Deep Q-Learning differs from the other methods mentioned earlier as Q-learning is not based on the search method. The use of Q-Learning on two-player board games has been studied before in several different types of games [9,15,21-24]. In [22], Deep Q-Learning still found it difficult to beat the searching method in the Hex game even though it has been trained for two weeks (about

60,000 episodes). The long training process is also shown in [24]. The model was trained to over 500,000 episodes to achieve about a 50% winning rate against heuristic agents.

This research explored Deep Q-Learning architecture variants, including Dueling Q-Network [24], and proposed increasing batch size method [25] as a regularization technique in Deep Q-Learning to speed up the training process and improve the agent performance. We trained the agent against a rule-based agent instead of a random agent, as done in [9]. In previous studies, agents were trained and evaluated against the same opponent [9,24]. In this study, to see the agent's consistency in dealing with different opponents, our agent was evaluated against different rule-based agents. Agent consistency in facing other agents in achieving a goal is crucial in various tasks, not only in games.

2. RESEARCH METHOD

The process of interaction and training in the reinforcement learning agent (RL agent) is shown in Fig.1. Agents will be trained to use Deep Q-Learning against a rule-based agent in the Surakarta Chess environment. At a timestep *t*, the RL agent will receive a board condition (a state *S*) and then perform one of the valid actions *A* based on its policy. In the next turn, the opponent will do the same thing: see the game's condition and then take action. The results of RL agent action on time steps *t* and opponent actions on time step *t*+1 make a new game state, *S′*. The agent will get two types of rewards, *R*, reward when winning a game, and reward when capturing the opponent's pieces that the system environment already defines. The RL agent learns from a collection of experiences represented by the tuple of (*S*, *A*, *R*, *S′*). All agents are implemented using PyTorch [26] and trained on Google Colab's GPU.
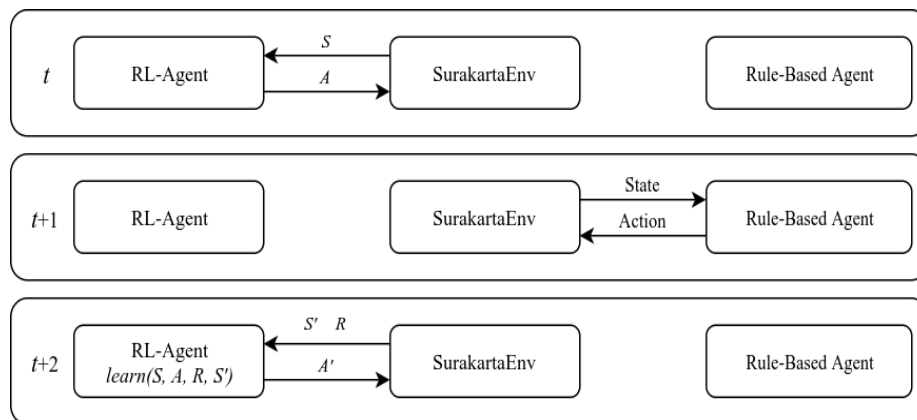
Fig. 1: Interaction between RL agent, the opponent and the environment.

2.1 Surakarta Chess

Surakarta Chess is a chess-like game from Surakarta, Indonesia, contested annually by the International Computer Game Association (ICGA). Surakarta Chess is played by two players on a 6x6 board with 8 curves and 12 pieces. The starting position of each player on the board is shown in Fig. 2 (a). In each turn, players can move their piece or capture the opponent's piece. The player can move his piece to eight adjacent positions if another piece has not occupied the destination. A player can capture the opponent's piece by moving a piece along a horizontal or vertical line then through at least one curve to reach the opponent's piece without being blocked by another piece. Illustrations of piece movement and capture are shown in Fig. 2 (b) and Fig. 2 (c).
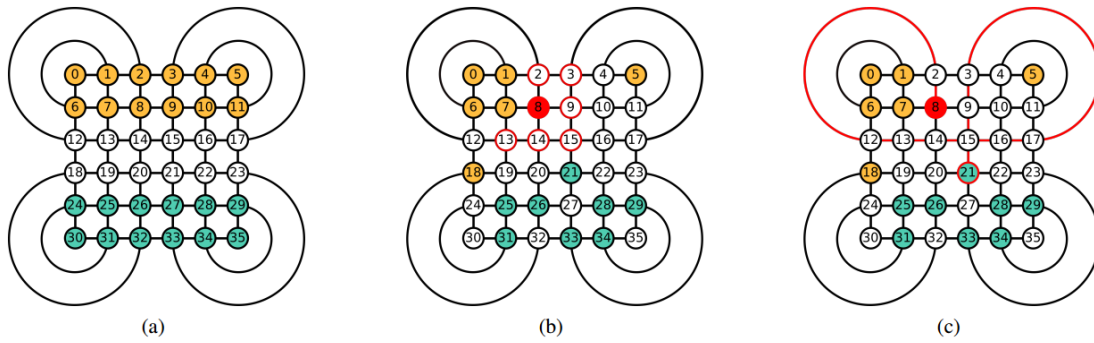
Fig. 2: (a) Surakarta Chess initial state; (b) available move for a piece in 8 shown as circles with red border; (c) capturing path from 8 to 21 shown as red path.

Because a piece must be in a particular position to capture, in previous studies, they use position values to measure how good a piece's position is [17,19]. There are three types of positions in Surakarta Chess based on their relationship to the curve. The three types of positions are shown in Fig. 3, distinguished by red, white, black, and yellow.
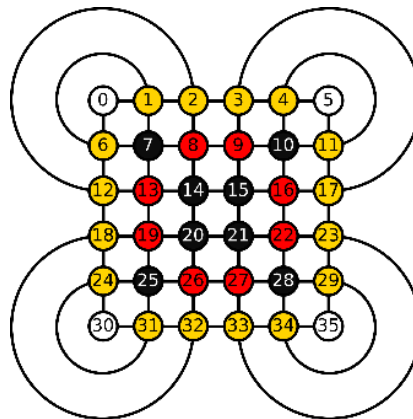
Fig. 3: Positional value in Surakarta Chess.

Surakarta Chess consists of three phases [16], namely the opening phase, the middle phase, and the final phase. In the opening phase, the player will focus on placing their pieces in an advantageous position. This is crucial because the player needs to make an unblocked path to capture the opponent's piece. The middle phase occurs after pathways are created. In this phase, players will begin to attack and defend their pieces from their opponent. The final phase is indicated by the small number of pieces on the board. In this phase, the pieces are free to move and capture the opponent's piece because the path to capture is already open.

2.2 Surakarta Chess Environment

In this study, we use *SurakartaEnv* part of Gapoera API [27], a publicly available game environment toolkit. Players can access current board information using available functions. One aspect of the information provided to players through *SurakartaEnv* is the position of the piece. *SurakartaEnv* maps the game board to a matrix with a value of -1, 0, or 1. A value of 0 is given to a position if no pieces are occupying it. A value of 1 or a value of -1 indicates the player's pieces' position depending on the player's perspective. The value 1 indicates the first player's position, while the value of -1 indicates the second player's position. Each

position on the board is numbered from 0 to 35, as shown in Fig. 2. From each of these positions, 12 actions can be done, 8 of which are actions to move without capturing in 8 directions and 4 of which are actions to move across the line horizontally or vertically until reaching the curve to capture. Therefore, there are a total of 432 available actions. *SurakartaEnv* accepts an action A in the form of an integer between 0 to 431.

In addition to the position of the pieces, both players can also access other information through *SurakartaEnv*. Players can get information on which pieces that player can capture, which player pieces that the opponent can capture, and which actions are valid in each turn for both players. The rule-based agent will later use that information to make decisions in every turn. *SurakartaEnv,* by default, sets rewards to both players for each action. We use a +10 reward if the player wins the match, and -10 if the player loses, and +0.5 when the player captures the opponent's piece.

2.3 Rule-Based Agent

A rule-based agent decides its action based on game information available at the time. In this research, three rule-based agents are made that take action based on a particular priority. When an agent cannot perform any valid moves based on its priority, the agent will make a valid random move. The explanation of each priority for each agent is shown in Table 1. The red and black positions refer to Fig. 3. A safe place is a place where the player's piece is safe from opponent's attacks.

Table 1: The priority of each rule-based agent

Agent Name	RB1		RB2		RB3	
Movement Priority	1.	Capture	1.	Capture	1.	Capture
	2.	Move to black	2.	Move to red	2.	Move to red
	3.	Move to a safe place	3.	Move to black	3.	Move to a safe place
			4.	Move to a safe place		

Each agent has an exploration probability parameter ε that gives agents the possibility to make a random move that is not based on their priorities. This random action is intended to create variations both in the training process and in the testing process. In this study, RL-agents will be trained against RB1 with $\varepsilon = 0.1$.

2.4 Reinforcement Learning Agent

Reinforcement learning agents were trained using the Deep Q-Learning method [2]. Deep Q-learning is the improvement of the Q-Learning algorithm [5] that uses a deep neural network as an approximator of the action-value function. The neural network architecture used in [2] is Convolutional Neural Network (CNN) [4]. This study will compare CNN architecture with a simple neural network without convolutional layers or commonly called multi-layer perceptron (MLP). Both architectures are shown in Fig. 4. Both architectures are simpler than those proposed in [2], given that the Surakarta Chessboard size is smaller than the Atari game image matrix. In [2], 84x84x4 inputs represent pixels on the screen from the last four frames, while in Surakarta, the input is only a 6x6 matrix. It also makes consideration for comparing MLP with CNN in Surakarta Chess.
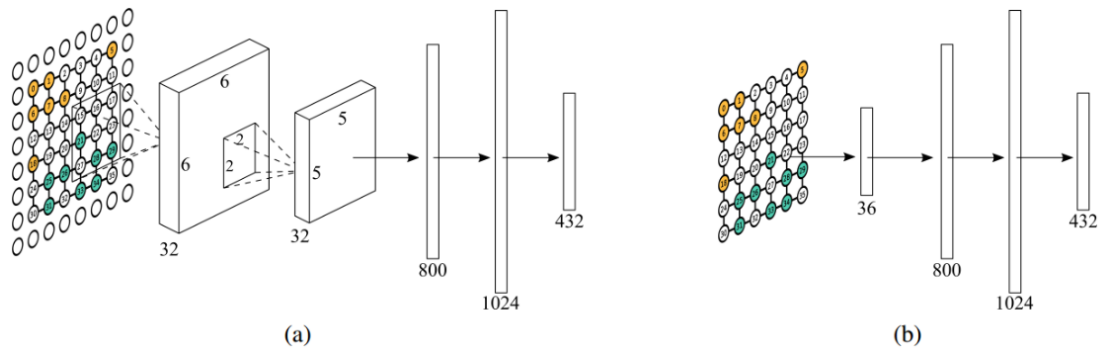
Fig. 4: (a) Q-Network Architecture with Convolutional Layer, (b) Q-Network Architecture
using Multi-Layer Perceptron.

Figure 4 (a) shows the architecture consisting of one convolution layer, one pooling layer, and a fully connected layer. Inputs are padded to keep the output size the same after the convolutional process. The convolutional layer uses a 3x3 kernel size and 32 feature maps, while the pooling layer uses a 2x2 size pooling window. The neural network output is a vector with 432 elements, representing all possible actions in Surakarta Chess. In the MLP architecture, two hidden layers are used with the number of neurons similar to the neurons from the convolutional process on the CNN architecture.

We use two techniques proposed in [2], experience replay and the use of two neural networks as policy and target networks in one agent. Experience replay uses a replay memory with a capacity C to store the agent's experiences in the form of (S, A, R, S'). In this study, all agents are set to have the same memory replay capacity of 50,000 experiences. During the training process, the agent will take a batch of data from the replay memory as training data. We also explore the effect of increasing batch data size [25] on the model performance. Increasing batch size means that samples of experience drawn from replay memory will increase through episodes. In [25], this method can help speed up the model training process. The second technique we use is the use of policy and target networks in one agent that can increase the stability of the model. Initially, the target network is a clone of the policy network, but its weight is only updated after the policy network is updated N times. The algorithm used to optimize network policy is Adam Optimizer [28], with an initial learning rate of 0.0001. The weights and biases of the networks are initialized using the methods proposed in [29, 30].

We also compared another architecture called Duelling Deep Q-Network [24]. The duelling network has two separate streams. One will produce a scalar state value $V(s)$, and the other will produce action advantages $A(s, a)$. State values will provide information on whether a state is valuable or not, while action advantages provide information about the advantages of each action. The two values are then combined to get $Q(s, a)$ using Eq. (1). In previous research [24], a duelling network was proposed using CNN. This research will also compare the model performance when using MLP on the duelling network. The Duelling Network architecture is shown in Fig. 5.

$$Q(s,a) = V(s) + \left(A(s,a) - \frac{1}{|A|} \sum_{a'} A(s,a') \right) \tag{1}$$

During the training process, both agents that use DQN and Duelling Q-Network will use ε-greedy as a policy to decide the action in a state. The value of ε is the agent's

probability of taking random actions to explore states. In this study, the value of ε initially used was 13%. This value will be reduced after some episodes, so the agent acts based more on the state action value. Each agent was trained for 1250 episodes. In episodes 75, 150, and 250, the value of ε will be reduced by 3.7%. As a result, after 250 episodes, the value of ε is only 1.9%.
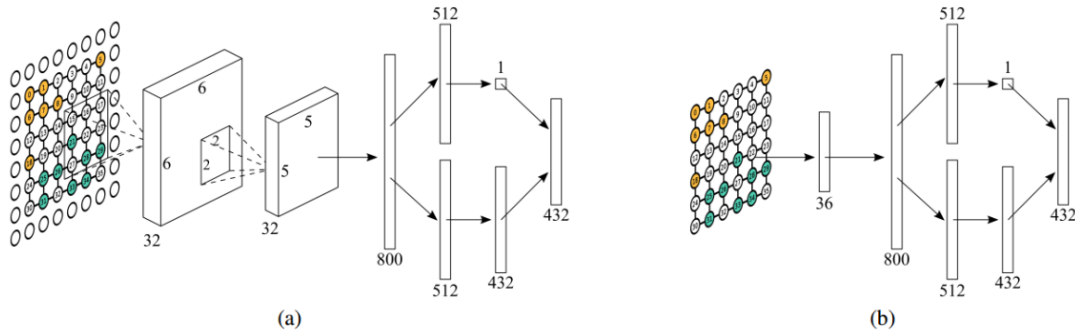
Fig. 5: (a) Dueling Q-Network Architecture with Convolutional Layer,
(b) MLP on Dueling Q-Network Architecture.

3. RESULTS AND DISCUSSION

3.1 Model Performance

RL agents will be trained and their parameters tuned against RB1 and their performance evaluated against other agents. In the first experiment, we compared the effect of increasing batch size [25]. This experiment used DQN with a convolutional network as a model architecture. Three agents were compared. The first was an agent without increasing batch size, the second was an agent with a less frequently increasing batch size, and the third was a model with a more frequent increasing batch size. The result of the agents against RB1 is shown in Table 2.

Table 2: Performance comparison of increasing batch size usage

	Increase frequency	Average score from last episodes			
		Last 50	Last 100	Last 150	Last 200
Model 1	-	5.80	5.39	5.39	5.60
Model 2	250	5.40	4.82	5.53	5.96
Model 3	150	**6.80**	**6.45**	**6.59**	**6.38**

The agent's score is the number of opponent pieces captured by the agent until the game is finished. Model 1 did not use increasing batch size, while models 2 and 3 used it. Model 2 used a less frequently increasing batch size that increases the batch size 50% from the current size every 250 episodes, while Model 3 used a more frequently increasing batch size that increased the batch size 50% every 150 episodes. This process was conducted until it reached 1000 episodes. All models had an initial batch size of 48. The graph of increasing batch size is shown in Fig. 6. Table 2 shows that increasing the batch size during training can help the model improve its performance.

Another parameter that affects the agent's performance is the value of *N*, which is the number of updates made on the policy network before updating the target network. We tested three *N* values: 10, 210, and 700. The *N* values used were much smaller than those used in [2] because we used fewer iterations in the training phase. In a single game, we assumed the agent had 70 turns so that when $N = 210$, the target network was updated around every three games. The score for each model against RB1 for each episode appears in Fig. 7. It showed that if we used a too small or too large *N*, the agent performance became unstable and tended to decrease over episodes. Whereas when $N = 210$, the score obtained by the model was ascending with relatively more stability. The three agents shown in Fig. 7 used DQN with a convolutional layer and increasing batch size.
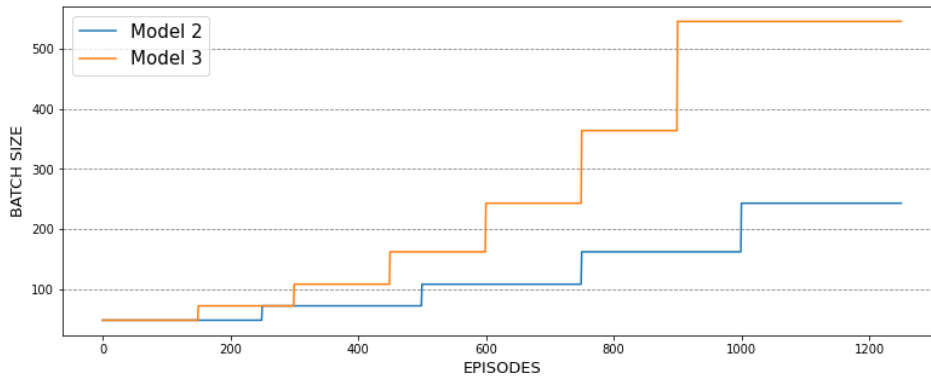
Fig. 6: Batch size throughout episodes.

Fig. 7: Performance comparison of N, using moving average scores for every 150 episodes.

This research also compared four agents with different neural network architectures. Table 3 shows that the use of the duelling network significantly increased the agent's performance. The scores shown are averages of the last few scores. For example, in the "last 50" column, the value in that column is the average of the RL agent scores for the last 50 episodes, from episodes 1201 to 1250.

The use of a duelling network with a convolutional layer outperformed other agents. Even the duelling network without a convolutional layer still outperformed the regular DQN with a convolutional layer. Scores of each model for every episode are shown in Fig. 8.

Table 3: Performance comparison of network architecture

Model type	Average score from last episodes			
	Last 50	Last 100	Last 150	Last 200
DQN-CNN	6.80	6.45	6.59	6.38
DQN-MLP	5.78	5.55	5.49	5.49
Dueling-CNN	**9.36**	**8.69**	**8.25**	**8.21**
Dueling-MLP	8.08	7.45	**8.25**	6.63
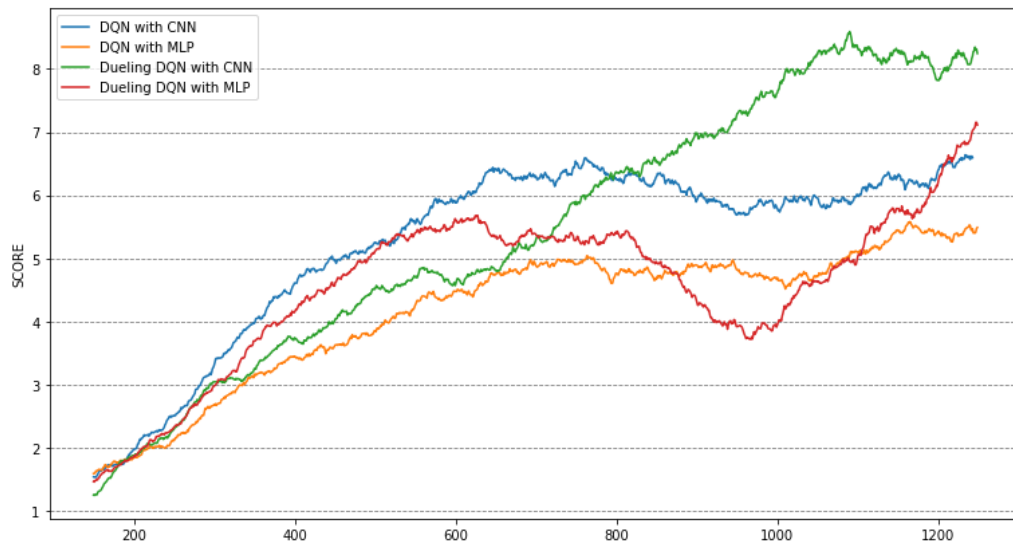
Fig. 8: Performance comparison of Q-Learning models, using moving average scores for every 150 episodes.

3.2 Score Against Other Agents

After completing the training process, we evaluated four RL agents with different network architectures using the parameter settings mentioned earlier. These agents competed against five different rule-based agents and one random agent. The random agent was an agent that always took a valid random movement in each turn. Each RL agent played 30 games for each rule-based agent. The RL agent played as the first player who makes the first move. In Table 4, it shows the number of RL agent wins in 30 games against other agents. We evaluated five agents:

- two agents without duelling networks (DQN-CNN and DQN-MLP)
- two agents with duelling networks (Duelling-CNN and Duelling-MLP)
- an agent for Duelling-CNN that was trained without an increasing batch

The last agent we mentioned was used to compare the effect of an increasing batch on agent performance.

From the table, we can see that all five agents can defeat the random agent (RA) in all games for a 100% win rate. It also shows that agents trained using the duelling network had the most wins against nine other agents. When an opponent had a greater ε value, meaning that the opponent had a greater chance of moving randomly, agents were expected to exploit this vulnerability to win more. However, as shown in the table, only agents who used the duelling network tended to be able to use it as an opportunity to win the match, whereas, in the DQN-MLP or DQN-CNN model, an increase in the value of ε did not benefit the model

significantly. The agent that did not use increasing batches had poor performance because of difficulties in the training process, as shown in Table 4.

Duelling network agents can also adapt to agents that have different rules, RB2 and RB3. Both rule-based agents had a slight difference in priority for determining their action compared to RB1. This adaptation did not occur in other models that experienced a high number of losses against rule-based agents aside from the training process. The average win rate is calculated by averaging the win rate of an RL agent against the other agents.

Table 4: Performance comparison of models against other rule-based agents. The shaded column is the agent that is countered during the training process

| Model type | Number of RL agent wins | | | | | | | | | Avg. Win. Rate (%) |
| | RA | RB1 | | | RB2 | | | RB3 | | |
		ε=0.1	ε=0.2	ε=0.3	ε=0.1	ε=0.2	ε=0.3	ε=0.1	ε=0.2	ε=0.3	
DQN-CNN	30	2	7	5	1	3	2	3	2	1	18.6
DQN-MLP	30	7	4	0	0	0	1	0	0	0	13.9
Dueling-CNN	**30**	**13**	**16**	**23**	**12**	**12**	**19**	**9**	**18**	**19**	**57.0**
Dueling-MLP	30	11	13	13	5	10	11	4	7	13	39.0
Dueling-CNN (no inc. batch)	30	0	1	1	0	4	1	0	0	0	12.3

3.3 Model Consistency

To see an agent's consistency in facing other agents, we used the Coefficient of Variations (CV), as shown in Eq. (2), where σ is the standard deviation, and μ is the mean of the data. The smaller the CV value, the more consistent the model. We calculated the CV between the three rule-based agents by separating them based on their epsilon value. The results are shown in Table 5.

$$CV = \frac{\sigma}{\mu} \times 100 \qquad (2)$$

For example, in Table 5, Duelling-CNN had a CV of 14.99 in column with ε = 0.1. This was calculated from {13, 12, 9}, the number of Duelling-CNN agent wins against RB1 ε = 0.1, RB2 ε = 0.1, and RB3 ε = 0.1, respectively. From Table 5, we can see that the Duelling-CNN model had a relatively small CV value compared to other agents. Except when the value ε = 0.3, the Duelling-MLP agent had the smallest CV value. The CV value of agent Duelling-CNN without increasing batch in column ε=0.1 could not be calculated because the agent had no victory.

Table 5: Coefficient of variations between rule-based agents

| Model type | Coefficient of variation | | |
	ε=0.1	ε=0.2	ε=0.3
DQN-CNN	40.82	54.00	63.73
DQN-MLP	141.42	141.42	141.42
Duelling-CNN	**14.99**	**16.26**	9.27
Duelling-MLP	46.36	24.49	**7.64**
Duelling-CNN w/o increasing batch	-	101.98	70.71

Rajagede

4. CONCLUSION

In this research, a deep reinforcement learning approach was implemented to create agents in Surakarta Chess. We explored several Deep Q-Learning architectures to find the best agent. The results show that the use of duelling networks and increasing batch size can improve agent performance and consistency in the Surakarta Chess game. In a short period, agents with duelling network architecture and increasing batch size mechanisms succeeded in obtaining a high average win rate, 57%, against ten different agents. We also found that the best model had better consistency even though it played against agents with different strategies. In the future, duelling networks and increasing batch size can be evaluated in more complex environments.

REFERENCES

[1]   Lillicrap TP, Hunt JJ, Pritzel A, Heess N, Erez T, Tassa Y, Silver D, Wierstra D Continuous control with deep reinforcement learning. In 4th International Conference on Learning Representations: 2-4 May 2016; San Juan, Puerto Rico. Retrieved from http://arxiv.org/abs/1509.02971.

[2]   Mnih V, Kavukcuoglu K, Silver D, Rusu AA, Veness J, Bellemare MG, Graves A, Riedmiller M, Fidjeland AK, Ostrovski G, Petersen S, Beattie C, Sadik A, Antonoglou I, King H, Kumaran D, Wierstra D, Legg S, Hassabis D. (2015) Human-level control through deep reinforcement learning. Nature, 518 (7540): 529–533. doi: 10.1038/nature14236.

[3]   Yogatama D, Blunsom P, Dyer C, Grefenstette E, Ling W Learning to compose words into sentences with reinforcement learning. In 5th International Conference on Learning Representations: 24-26 April 2017; Toulon, France. Retrieved from https://openreview.net/forum?id=Skvgqgqxe.

[4]   LeCun Y, Bottou L, Bengio Y, Haffner P. (1998) Gradient-based learning applied to document recognition. Proceedings of the IEEE, 86 (11): 2278–2324.

[5]   Watkins CJ, Dayan P. (1992) Q-learning. Machine learning, 8 (3–4): 279–292.

[6]   Silver D, Huang A, Maddison CJ, Guez A, Sifre L, van den Driessche G, Schrittwieser J, Antonoglou I, Panneershelvam V, Lanctot M, Dieleman S, Grewe D, Nham J, Kalchbrenner N, Sutskever I, Lillicrap T, Leach M, Kavukcuoglu K, Graepel T, Hassabis D. (2016) Mastering the game of Go with deep neural networks and tree search. Nature, 529 (7587): 484–489. doi: 10.1038/nature16961.

[7]   van den Dries S, Wiering MA. (2012) Neural-fitted TD-leaf learning for playing othello with structured neural networks. IEEE Transactions on Neural Networks and Learning Systems, 23 (11): 1701–1713. doi: 10.1109/TNNLS.2012.2210559.

[8]   Liskowski P, Jaskowski W, Krawiec K. (2018) Learning to play othello with deep neural networks. IEEE Transactions on Games, 10 (4): 354–364. doi: 10.1109/TG.2018.2799997.

[9]   Kasim MF. (2016) Playing the game of congklak with reinforcement learning. In Proceedings of 8th International Conference on Information Technology and Electrical Engineering (ICITEE). IEEE. pp 1–5. doi: 10.1109/ICITEED.2016.7863309.

[10]   Lai M. (2015) Giraffe: Using deep reinforcement learning to play chess. Master's thesis, Imperial College London, Retrieved from https://arxiv.org/pdf/1509.01549.pdf.

[11]   David OE, Netanyahu NS, Wolf L. (2016) DeepChess: End-to-End Deep Neural Network for Automatic Learning in Chess. In Villa AEP, Masulli P, Pons Rivero AJ eds Artificial Neural Networks and Machine Learning – ICANN 2016. Cham, Springer International Publishing. pp 88–96. doi: 10.1007/978-3-319-44781-0_11.Retrieved from http://link.springer.com/10.1007/978-3-319-44781-0_11.

[12]   Silver D, Schrittwieser J, Simonyan K, Antonoglou I, Huang A, Guez A, Hubert T, Baker L, Lai M, Bolton A, Chen Y, Lillicrap T, Hui F, Sifre L, van den Driessche G, Graepel T, Hassabis D. (2017) Mastering the game of Go without human knowledge. Nature, 550 (7676): 354–359. doi: 10.1038/nature24270.

Rajagede

[13] Moravčík M, Schmid M, Burch N, Lisỳ V, Morrill D, Bard N, Davis T, Waugh K, Johanson M, Bowling M. (2017) DeepStack: Expert-level artificial intelligence in heads-up no-limit poker. Science, 356 (6337): 508. doi: 10.1126/science.aam6960.

[14] Littman ML. (1994) Markov games as a framework for multi-agent reinforcement learning. In Machine learning proceedings 1994. Elsevier. pp 157–163.Retrieved from https://doi.org/10.1016/b978-1-55860-335-6.50027-1.

[15] Somasundaram TS, Panneerselvam K, Bhuthapuri T, Mahadevan H, Jose A. (2018) Double Q–learning Agent for Othello Board Game. In Proceedings of 10th International Conference on Advanced Computing (ICoAC). IEEE. pp 216–223. doi: 10.1109/ICoAC44903.2018.8939117.

[16] QIU H, WANG Y, GAO F, Quan QIU. (2013) Research on search engine techniques of Surakarta game. The Journal of China Universities of Posts and Telecommunications, 20 117–120. doi: 10.1016/S1005-8885(13)60235-6.

[17] Liu C, Wang J, Zhang Y. (2014) Search strategy research and analysis for surakarta chess game. In Proceedings of The 26th Chinese Control and Decision Conference (2014 CCDC). IEEE. pp 3362–3366.

[18] Winands MH. (2015) The Surakarta bot revealed. In Computer Games. Springer. pp 71–82.

[19] Zuo G, Wu C. (2016) A heuristic Monte Carlo tree search method for surakarta chess. In Proceedings of Chinese Control and Decision Conference (CCDC). IEEE. pp 5515–5518. doi: 10.1109/CCDC.2016.7531982.

[20] Li S, Qi Y, Bo J, Fu Y. (2019) Design and Implementation of Surakarta Game System Based on Reinforcement Learning. In Proceedings of Chinese Control and Decision Conference (CCDC). IEEE. pp 6326–6329. doi: 10.1109/CCDC.2019.8832340.

[21] Draskovic D, Brzakovic M, Nikolic B. (2019) A comparison of machine leaming methods using a two player board game. In Proceedings of IEEE EUROCON 2019-18th International Conference on Smart Technologies. IEEE. pp 1–5. doi: 10.1109/EUROCON.2019.8861927.

[22] Young K, Vasan G, Hayward R. (2016) Neurohex: A deep q-learning hex agent. In Computer Games. Springer. pp 3–18.Retrieved from https://doi.org/10.1007/978-3-319-57969-6_1.

[23] Arvidsson O, Wallgren L. (2010) Q-Learning for a Simple Board Game. PhD Thesis, Bachelor's Thesis, School of Computer Science and Engineering, KTH Royal Institute of Technology, Retrieved from http://www.csc.kth.se/utbildning/kandidatexjobb/datateknik/2010/rapport/arvidsson_oskar_OCH_wallgren_linus_K10047.pdf.

[24] Wang Z, Schaul T, Hessel M, Hasselt H, Lanctot M, Freitas N. (2016) Dueling network architectures for deep reinforcement learning. In Proceedings of International conference on machine learning. PMLR. pp 1995–2003.Retrieved from http://proceedings.mlr.press/v48/wangf16.html.

[25] Smith SL, Kindermans P-J, Ying C, Le QV. (2018) Don't Decay the Learning Rate, Increase the Batch Size. In 6th International Conference on Learning Representations: 30 April - 3 May 2018; Vancouver, BC, Canada. Retrieved from https://openreview.net/forum?id=B1Yy1BxCZ.

[26] Paszke A, Gross S, Massa F, Lerer A, Bradbury J, Chanan G, Killeen T, Lin Z, Gimelshein N, Antiga L, Desmaison A, Kopf A, Yang E, DeVito Z, Raison M, Tejani A, Chilamkurthy S, Steiner B, Fang L, Bai J, Chintala S. (2019) PyTorch: An Imperative Style, High-Performance Deep Learning Library. In Wallach H, Larochelle H, Beygelzimer A, Alché-Buc F d\textquotesingle, Fox E, Garnett R eds Proceedings of Advances in Neural Information Processing Systems 32. Curran Associates, Inc. pp 8026–8037.Retrieved from http://papers.nips.cc/paper/9015-pytorch-an-imperative-style-high-performance-deep-learning-library.pdf.

[27] Rajagede RA, Mahardhika GP. (2021) Gapoera: Application Programming Interface for AI Environment of Indonesian Board Game. In arXiv. Retrieved from https://arxiv.org/abs/2110.11924.

[28] Kingma DP. (2015) Adam: A Method for Stochastic Optimization. In 3rd International Conference on Learning Representations; San Diego, CA, USA. Retrieved from http://arxiv.org/abs/1412.6980.

[29]   Glorot X, Bengio Y. (2010) Understanding the difficulty of training deep feedforward neural
        networks. In Proceedings of the 13th international conference on artificial intelligence and
        statistics. JMLR Workshop and Conference Proceedings. pp 249–256.
[30]   He K, Zhang X, Ren S, Sun J. (2015) Delving deep into rectifiers: Surpassing human-level
        performance on imagenet classification. In Proceedings of the IEEE international conference
        on computer vision. pp 1026–1034.

DEVELOPMENT OF RAINFALL FORECASTING MODEL USING MACHINE LEARNING WITH SINGULAR SPECTRUM ANALYSIS

**PUNDRU CHANDRA SHAKER REDDY[1*], YADALA SUCHARITHA[2]
AND GODDUMARRI SURYA NARAYANA[3]**

[1]*Department of Computer Science and Engineering,
CMR College of Engineering & Technology, Hyderabad, India*
[2]*Department of Computer Science and Engineering,
CMR Institute of Technology, Hyderabad, India*
[3]*Department of Computer Science and Engineering,
Vardhaman College of Engineering, Hyderabad, India*

*Corresponding author: chandu.pundru@gmail.com

ABSTRACT:Agriculture is the key point for survival for developing nations like India. For farming, rainfall is generally significant. Rainfall updates are help for evaluate water assets, farming, ecosystems and hydrology. Nowadays rainfall anticipation has become a foremost issue. Forecast of rainfall offers attention to individuals and knows in advance about rainfall to avoid potential risk to shield their crop yields from severe rainfall. This study intends to investigate the dependability of integrating a data pre-processing technique called singular-spectrum-analysis (SSA) with supervised learning models called least-squares support vector regression (LS-SVR), and Random-Forest (RF), for rainfall prediction. Integrating SSA with LS-SVR and RF, the combined framework is designed and contrasted with the customary approaches (LS-SVR and RF). The presented frameworks were trained and tested utilizing a monthly climate dataset which is separated into 80:20 ratios for training and testing respectively. Performance of the model was assessed using Root Mean Square Error (RMSE) and Nash–Sutcliffe Efficiency (NSE) and the proposed model produces the values as 71.6 %, 90.2 % respectively. Experimental outcomes illustrate that the proposed model can productively predict the rainfall.

ABSTRAK:Pertanian adalah titik utama kelangsungan hidup negara-negara membangun seperti India. Untuk pertanian, curah hujan pada amnya ketara. Kemas kini hujan adalah bantuan untuk menilai aset air, pertanian, ekosistem dan hidrologi. Kini, jangkaan hujan telah menjadi isu utama. Ramalan hujan memberikan perhatian kepada individu dan mengetahui terlebih dahulu mengenai hujan untuk menghindari potensi risiko untuk melindungi hasil tanaman mereka dari hujan lebat. Kajian ini bertujuan untuk menyelidiki kebolehpercayaan mengintegrasikan teknik pra-pemprosesan data yang disebut analisis-spektrum tunggal (SSA) dengan model pembelajaran yang diawasi yang disebut regresi vektor sokongan paling rendah (LS-SVR), dan Random-Forest (RF), ramalan hujan. Menggabungkan SSA dengan LS-SVR dan RF, kerangka gabungan dirancang dan dibeza-bezakan dengan pendekatan biasa (LS-SVR dan RF). Kerangka kerja yang disajikan dilatih dan diuji dengan menggunakan set data iklim bulanan yang masing-masing dipisahkan menjadi nisbah 80:20 untuk latihan dan ujian. Prestasi model dinilai menggunakan Root Mean Square Error (RMSE) dan Nash – Sutcliffe Efficiency (NSE) dan model yang dicadangkan menghasilkan nilai masing-masing sebanyak 71.6%,

90.2%. Hasil eksperimen menggambarkan bahawa model yang dicadangkan dapat meramalkan hujan secara produktif.

1. INTRODUCTION

India's welfare is farming, where most the agribusiness is subject to rainfall as its standard wellspring of water, the time and proportion of rainfall hold high significance and can affect the whole economy of the country. Weather plays a major part in our regular day to day life. Climate estimating is one of the most testing issues seen by the world, in the latest couple of centuries in the field of science and innovation. As India's economy notably relies upon cultivation, rainfall has a significant impact [1]. Variation in the timing of rainfall and its quantity makes estimating rainfall is a challenge for meteorological researchers. Predicting is one the greatest difficulties for researchers from an assortment of fields, for example, climate data mining, ecological machine learning, functional-hydrology, and numerical prediction, to make a forecast model for precise rainfall. Climate anticipation stands apart for all nations around the world in all the advantages and administrations gave by the meteorological department [2].

Rainfall anticipation is significant because severe and sporadic rainfall can have numerous effects like obliteration of yields and farms, harm of property so a superior anticipating model is crucial for an early notice that can limit dangers to life and property and also dealing with the farming a better way. This forecasting predominantly helps ranchers and furthermore, water assets can be used proficiently [3]. Rainfall forecast is a difficult task and the outcomes ought to be precise. There are numerous equipment tools for anticipating rainfall by utilizing the climate conditions like temperature, humidity, pressure and so on. These customary strategies can't work in a proficiently so by utilizing ML-based strategies we can design for exact outcomes. We can only do it by having the past data examination of rainfall and can foresee the rainfall for future seasons [4]. Taking into account that farming activities and crop yield depend on the rainfall distribution, monthly rainfall estimating is significant for farming planning and flood control. Monthly rainfall anticipation with a suitable technique is a fundamental prerequisite to help water management. Accordingly, monthly rainfall estimating is broadly appropriate in the field of hydrology. A few procedures for predicting time series have been designed on a worldwide scale [5].

Machine Learning (ML) or Artificial Intelligence (AI) and stochastic techniques dependent on information extraction procedures are the mainly utilized time-series modeling for hydrological estimating. Nonetheless, ML has been given more consideration in weather anticipating, predominantly because stochastic approaches consider that the time-series are fixed and have a restricted capacity to catch profoundly nonlinear qualities of rainfall series. Climatology time-series in tangible utilize are normally non-fixed and non-linear, so foreseeing the greatest values is very complex [6]. The hypothesis of the modular approach and the incorporation of various models have presently increased more enthusiasm for rainfall estimating to address this issue. Regression, Artificial Neural Network (ANN), Decision Tree, Random Forest, Fuzzy logic and group cycle of data handling methods are the majority utilized computational strategies utilized for climate forecasting. Even though ANN or SVM in such non-linear issues is generally applied, direct elucidation of the guidelines is complex. Then again, classification utilizing decision tree methods is helps display complex associations among attributes with the additional focal points of recognizing the significance of every attribute

[7]. RF and SVR are computationally quick, effectively reasonable and don't need earlier knowledge of the data. Because of these reasons, the utilization of RF in the case of prediction is picking up popularity. Further, because of its ability to recognize the persuasive part of various features, it's rather beneficial to utilize RF in prediction applications. Techniques dependent on data-driven, ML frameworks are broadly and effectively practical in numerous fields. ML has to turn into general inductive practice in rainfall estimation outstanding to its incredibly non-linear, adaptable, and data-driven method training without first receiving catchment and flow methods. Notwithstanding the fame of ML techniques for time-series anticipation, they are not an effective device to foresee long-standing rainfall [8]. The most commonly utilized ML-based approaches for rainfall prediction include SVM, Genetic-Programming, ANN, and Fuzzy-Logic. Cross-breed methodologies for tending to various climatology issues have been supported by meteorologists. Least-square SVR has newly got extensive consideration in different forecasting issues. In this research, LS-SVR was picked because it is computationally more engaging than the conventional SVR. In light of the utilization of quadratic programming by non-linear conditions, the conventional SVR has computational challenges to choose the best possible solution. The hybrid reproduction approach dependent on LS-SVR as an estimating model conveys incredible results.

The Singular Spectrum Analysis (SSA) is a proficient device that can divide the original time-series into a number of discrete segments, together with pattern designs, oscillating segments, and noise. SSA is applied to yearly, monthly, and hourly water temperature time-series to assess its ability and prediction capability to recognize major data from those series. SSA is used to extract the trend and it is a striking trend-extraction procedure, since it needs no approach portrayal of time-series and pattern, mines noisy time-series patterns through unsure motions in time-series, and susceptible to outliers. The noteworthiness of utilizing an appropriate SSA to translate unrefined input data to gracefully superior quality data earlier than being actualized as a design input [9]. Existing methods have been led to investigate the benefit of united data pre-processing and ML; evidently, this is the unique that SSA combined among LSSVR and RF has been utilized for rainfall estimation.

We have seen that the majority of the works claiming higher accuracy have labeled rainfall into three or under three parts or have predicted rainfall utilizing ML methods but have not done rainfall anticipating utilizing ML strategies, very few of them have utilized barely any meteorological parameters for the anticipation of the rainfall [10]. Most of the existing works are utilized the regression methods for forecasting rainfall and outcomes are not up to the mark due to selection of correct parameters for modeling. We have proposed a model to foresee the rainfall utilizing a combination ML-based techniques. The expectation of rainfall relies upon different climate attributes. Categorizing the rainfall gives us great classification precision but our definitive objective is to anticipate the rainfall utilizing the other climate attributes [11]. In this investigation, objective isn't just to accurately classify rainfall but additionally effectively foresee the rainfall utilizing different climate attributes.

There is persuading proof that the hybrid design dependent on LS-SVR and RF is solid and that the SSA generates excellent results. Subsequently, for enhancing the prediction efficiency of the state-of-art models, the data pre-processing procedure is implemented in the present investigation. The main objectives of the study are:

1. Connecting SSA with ML-based methods (i.e., LS-SVR and RF) to build hybrid models (SSA-LSSVR and SSA-RF) for rainfall prediction.

2. Comparison among the crossbreed models and the conventional models to assess the effectiveness of the data pre-processing strategy.

The Proposed work is concentrated around understanding the impacts of various meteorological attributes in rainfall estimation alongside an investigation of approaches that were utilized for anticipating rainfall, ML, and their restriction. The proposed model predicts the rainfall for the following season utilizing ML and forecasting approaches. Our contribution to this problem is to predict the monthly rainfall using ML-based techniques and compare the performance of the model with state-of-the-art approaches.

2. LITERATURE REVIEW

In this section, the existing works on rainfall forecasting proposed by various researchers are presented. Abbot et al. [12] designed a rainfall forecasting model by artificial neural networks which produce more precise results compared to conventional statistical and numerical techniques. Fahimi et al. [13] developed a hybrid framework called an Adaptive-Neuro-Fuzzy-Inference-System (ANFIS) for accurate long-term rainfall prediction. The outcome shows that the ANFIS is fit for catching the rainfall data-dynamic behavior and produces agreeable results. Kisi et al. [14] presented a framework, which combines ANNs with wavelet examination (WA) to estimate rainfalls and the model performance was compared with standard ANFIS. The outcomes exhibit that the proposed model is more productive than the ANFIS and is reasonable for rainfall anticipating. Pandhiani et al. [15] described a rainfall anticipation model by SSA and SVR for seasonal rainfall anticipation. The outcomes illustrate a noteworthy growth in model effectiveness contrasted to the standard SVR approach. Chan et al. [16] presented a monthly rainfall forecasting model by LS-SVR. The investigation demonstrates that the SVR design is better than the ARIMA approach. The investigation infers that the clarification for SVR acceptable execution lies in the non-direct quality of the caught and utilized SVR space. Karthikeyanet al. [17] described a comparative study of ML-based techniques on rainfall forecasting. They concluded has ANN, SVR, and RF exhibitions all in all good and RF conveyed the finest output. Finally, there is no investigation of RF-dependent models with a data pre-processing strategy for rainfall prediction, which timely this recent research to present a crossbreed model pairing RF with a data pre-processing approach. Ji et al. [18] designed a rainfall prediction model by a decision tree with CART and C4.5 techniques. The proposed strategy predicts rainfall and it is characterized into three classes in hourly rainfall 0.0 to 0.5 mm as level 1, 0.5 to 2.0 mm as level 2, > 2.0mm as level 3.

Min Minet al. [19] explored and designed an algorithm called quantitative rainfall estimates (QPEs) based on random forest (RF), machine learning (ML) techniques for summer-time rainfall forecasting utilizing the Himawari study dataset, cloud substantial properties products, and GFS-NWP data. In this study, they used a hybrid forecasting model that incorporates regression techniques with RFs classification for rainfall forecasting. The proposed method works tremendously and is different from the traditional and existing models because it utilizes the RFs ML approach for nowcasting. Navidet al.[20]proposed amultiple linear regressions (MLR) technique for forecasting the rainfall in Bangladesh. In MLR, first, apply correlation investigation and then regression analysis. MLR is very useful in future rain prediction and the results are very helpful to the agriculture sector for crop management. Finally, they concluded has rainfall is influenced by many climate factors and utilized those factors in the forecasting of rainfall to increase accuracy. Rodrigueset al. [21] designed the Multiple Linear Regression (MLR) technique

and time-series ARIMA techniques for monthly rainfall anticipation. The experimental results demonstrate that MLR and ARIMA produce accurate forecast results over the traditional forecasting methods. In the end, the proposed performance of the two models is evaluated in terms of MAPE and the outcomes and the exactness of predictions made for rainfall by MLR (1.14) is found to be greater over ARIMA (19.61). Swainet al. [22] developed a multiple linear regression model (MLRM) to anticipate the yearly rainfall over the Cuttack region, Odisha, India, utilizing the annual average rainfall data of the previous three years. The proposed model results describe that it is capable to generate precise accuracy matching with the actual data values and the proposed model acquired high R^2 (0.974) and adjusted R^2 (0.963) when compared to the existing models.Razeef Mohdet al.[23]presented a rainfall forecast model utilizing Nonlinear Auto- Regressive with External Input (NARX), which was trained by the proposed Self Adaptive Levenberg-Marquardt (Self Adaptive LM) framework and to make it more adaptive, the LM approach was customized with the learning rate to make it more precise for predicting rainfall. The rainfall data were gathered from Kashmir and Jammu, India. The experiments were conducted and model performance was evaluated with RMSE (1.721%) and MSE (1.721%) values.

Faulinaet al. [24] designed a hybrid monthly rainfall prediction framework by using ARIMA and ANFIS at particular locations in Indonesia, namely Pujon and Wagir. The proposed model was executed and the performance of the model was compared in terms of accuracy against the existing works. The experimental outcomes display that the ANFIS model is more precise in forecasting the monthly rain-data of Pujon, whereas the ARIMA technique outcomes were superior in forecasting the monthly rain-data of Wagir. Crameret al. [25] describe an intelligent machine learning system for rainfall forecasting where the forecasts of a few target parameters are decisive to a particular purpose. The proposed model was applied and compared with the forecast performance of the base-lines and six other well-liked ML prediction models called M5 Model trees, K-Nearest Neighbours (KNN), Radial Basis Neural Networks (RBNN), SVR, Genetic Programming, and M5 Rules. The investigation results state that the ML prediction models are capable to do better than the conventional models. Riveroet al. [26] implemented a short –term rain forecast model using Bayesian Enhanced Modified Approach (BEMA) with relative entropy. The experimental outcomes state the accuracy of the proposed methodology through diverse forecasting models utilizing the SMAPE index for short term rainfall sequence and chosen sequence from standards.

Mehr et al. [27] presented a new model called hybrid regression for advance month precipitation forecasting in northwest Iran. It is designed using SVR-FFA and it is trained and tested using monthly rainfall data. Johny et al. [28] designed a framework named AEEMD-ANN for rainfall forecasting and the experimental outcomes show that it is flourishing in predicting SWM precipitation of year 2002. Samantaray et al. [29] used RNN, ANFIS and SVM combinations for precipitation investigation. They conclude that SVM is gives good performance compared to others. Zhao et al. [30] developed an enhanced precipitation prediction model using five predictors. The experimental outcomes display that the IRFM gives good accuracy with five predictors inside of one predictor.

3. STUDY AREA AND DATA COLLECTION

Weather data is in extremely enormous amount and it includes forty-seven (47) general parameters such as rainfall, temperature, humidity, sunshine and cloudy hours, wind speed, etc. The major problem of this section is to investigate and process theclimate

data of the study region, Nellore district, Andhra Pradesh, India. The attributes have to be selected in such a way that it includes the effect of seasonal rainfall. We have to select different input and output variables and find a correlation between those variables using various strategies such as probability distribution method, Karl Pearson's coefficient, etc. and preprocess the data using appropriate methods.

3.1 Case Study Region

Nellore zone of Andhra Pradesh State in India is the investigation region for the evaluation of rainfall anticipation. Nellore station (latitude 14°26' N/longitude 79°92' E) is located in the coastal Andhra Pradesh region and it is surrounded on the South and North by Chittoor and Prakasam districts, on the west by Veligonda hills neighboring Kadapa district and on the east by the Bay of Bengal as shown in Fig. 1. The total area of the Nellore region covers 1307600 hectares and 39 % of the region is bound to farming. The major crops around there are rice, sugarcane, cotton, sunflower, groundnut, and tobacco. Rainfall got during the southwest monsoon (June-September) is one of the main factors for the groundwater and the average annual rainfall of the Nellore is around 835 mm [31].

The study area is one of the most significant agricultural regions in the nation. Rapid and independent industrialized development projects have caused environmental changes in the earlier period, consequently raised the need to evaluate elements impacting the present climate anticipation. The daily rainfall information, estimated in millimeters (mm), was acquired from the IMD, Hyderabad, TS, and India. Severe rainfall is seen in many regions during June to September period because of the Southwest Monsoon (SWM). During the SWN monthly rainfall at certain regions goes up to 700 mm however during the lean time it stays under 50 mm. The Nellore district encounters substantial rainfall and floods each year which causes river-bank erosions and landslides in several parts of the district. Farming plays a significant job in the economy of the State. Farming which is the principal livelihood of the individuals who establish almost 90% of the all-out populace is additionally influenced by the rainfalls and floods [32].
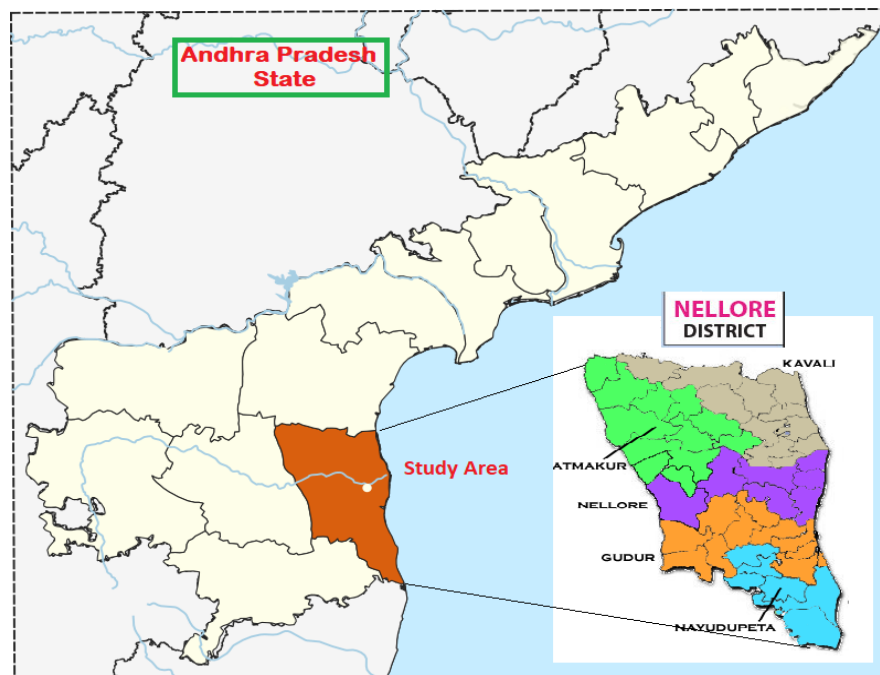

Fig. 1: Geographical area of Nellore district (Source: en.wikipedia.org).

3.2 Dataset Description

To predict seasonal monthly rainfall, we have to portray various elements which indirectly or directly influence the rainfall. The input variables of rainfall estimation are maximum, minimum and average temperature (ºC), vapor pressure (hPa), wind speed (km/h), humidity (%) and cloud cover (%). The dataset details are shown in Table 1.

Table 1:List of input and output parameters

SNO	Variable	Name of the attribute	Short name	Type
1	X_1	Minimum Temperature (°C)	MinTemp	Input
2	X_2	Maximum Temperature (°C)	MaxTemp	Input
3	X_3	Average Temperature (°C)	AvgTemp	Input
4	X_4	Vapor Pressure (hpa)	VP	Input
5	X_5	Wind Speed (Km/h)	WS	Input
6	X_6	Relative Humidity (%)	RH	Input
7	X_7	Cloud Cover (%)	CC	Input
8	Y	Rainfall (mm)	RF	Output

3.3 Primary Source of Data

In this research, the 110 years of climate data (1901-2012) of Nellore region, AP, India is taken from the Indian Meteorological Department (IMD), Hyderabad, TS, India at http://www.imdhyderabad.gov.in, and National Climatic Data Center, Asheville, the USA at ncdc.noaa.gov in the form of monthly means. Parameters like MinTemp, MaxTemp, AvgTemp, VP, WS, RH and CC are considered as input values and rainfall as output parameter which relies on input attributes. We considered just the relevant, required elements for design the forecasting model. Table 3.1 portrays the climate data depiction utilized in the rainfall prediction model. In our proposed model, we considered extended Southwest monsoon season sets in by June and lasts till October while the Northeast monsoon begins in October and ends in December. To figure out the attributes of the monthly rainfall series in Nellore Dist., the evocative statistics were utilized for investigating their rainfall properties.

4. PROPOSED METHODOLOGY

The problem examined in this section is that of anticipation of precise monthly rainfall for the accompanying season dependent on the past climate dataset, by using relating prior data. The combined SSA with LSSVM and RF framework is applied over this data so as to build up a model to anticipate the monthly rainfall value to the Nellore region which is situated on the southeast coast of India, with the water of the Bay of Bengal.

4.1 Least-Squares Support Vector Machine

In this segment, we quickly discuss the basic hypothesis on LS-SVR in time-series anticipation. Given a training set as input x_i and output y_i, the regression equation that interfaces the input vector to the output can be defined as:

The LS-SVR, a novel kind of SVR, involves a series of same supervised strategies that investigate data and recognize trends. It works well in solving convex quadratic issues with more intensity and produces good results for linear equations. Further, it has the advantages of shortening the issue and solution finding without losing exactness. In this investigation, the LS-SVR is utilized to anticipate monthly rainfall. In the accompanying

sector, we discuss the essential hypothesis on LS-SVR in time-series anticipating. Because of a trainingset as input x_i and output y_i, the regression equation is defined as follows in Eq. (1).

$$F(y) = w^T \mathbb{0}(x) + b \tag{1}$$

Where, $\mathbb{0}(x)$ is a nonlinear mapping function. Converting the regression issue in Eq. (1) into a constrained-quadratic optimization issue, by diminishing the cost element, w and b can be determined. In the structural minimization rule, the regression issue can be originated in Eqs. (2) and (3):

$$\text{Min } J\,(w, e) = \frac{1}{2}w^T w + \frac{\acute{r}}{2}\sum_{i=1}^{m} e_i^2 \tag{2}$$

Subject to the following limitations:

$$y_i = w^T \mathbb{0}\,(x_i) + b + e_i \, (i = 1, 2, :::, m) \tag{3}$$

Where $\acute{r}$ represents the consequence term and e_i is the training-error for x_i. To crack the optimization problem, the answer for optimizing the LS-SVM is to generate a Lagrangian equation expressed in Eq. (4):

$$L\,(w, b, e, \alpha) = J(w, e) - \sum_{i=1}^{m} \alpha_i \{ w^T \mathbb{0}\,(x_i) + b + e_i - y_i \} \tag{4}$$

Where α_i represents the Lagrange values.

By constructing the kernel function $K(x, x_i)$; Mercer's theorem can be fulfilled. Next, the LS-SVR method is executed in Equation (5):

$$f(x) = \sum_{i=1}^{m} \alpha_i K(x, xi) + b \tag{5}$$

4.2 Random Forest

Random-Forest is the most remarkable ML technique for analytics, including a collection of basic trees. RF is an improved version of the decision-tree dependent on the strategy for bagging. In bagging, numerous stochastic-error situations are performed by picking training-sets independently and arbitrarily from the training set; totaling the anticipation of every individual trained model is cultivated by taking its average value. RF can likewise evaluate the noteworthiness of disclosing factors to the estimate as per the straightforward guideline, "the more pertinent the illustrative variable, the more significant the impact on the prediction" to utilize the RF model for the selection of factors. In bootstrap-sampling, the annotations are isolated into two parts for every approach: in-bag-subset and out-of-bag subset [33]. The out-of-bag subsets might be utilized to decide the noteworthiness for every testing attribute: (1) randomizing the qualities for one picked logical attribute in the out-of-sack subset; (2) utilizing the randomized out-of-sack-subset and the first example to make new expectations; (3) testing the importance of the picked illustrative attribute by expanding the MSE of the new conjecture.

4.2 Singular Spectrum Analysis

SSA illustrates a powerful way to deal with time-series investigation in numerous fields of research. It is especially significant when time-series are disintegrated into significant parts like trends, motions, and noise. A significant advantage of the SSA method is that it is non-parametric, which means it tends to be custom fitted to the basic informational index and refuses the requirement for an earlier method [34]. Consequently, the SSA is viewed as a model-free technique. As indicated by, two valuable stages are engaged with the SSA strategy: decomposition and reconstruction. The method of decomposition consists of two stages: combining and singular-value-decomposition

(SVD). This disintegration is the fundamental outcome of the SSA technique and it is significant when every restored sub-section can be sorted as either a sample design or as a part of the noise. Embedding is the first stage in the SSA technique. This strategy changes the fitted time-series to a   multi-dimensional vector series. Singular Value Decomposition (SVD) is the trajectory-matrix is the principal module of the decomposition procedure.

4.3 Linking SSA with LS-SVR and RF

The monthly rainfall values were normalized by their particular means and standard-deviations earlier to training the standard approaches (LS-SVR and RF). To train these approaches, the normalized rainfall values are utilized. Two elements, the penalty-term and the kernel-width should be chosen in the calibration procedure of the LS-SVR. The matrix-search strategy is used for improving elements for the period of the calibrating time of the LS-SVR. It is fit for delivering optimum element set and can conquer the issues of over-fitting of the approach through the cross-validation system. RF has two elements, the number of factors $\sqrt{M}$ and the number of trees (ntree), which should be estimated. $\sqrt{M}$ would for the most part produce close ideal outcomes, so the estimation of $\sqrt{M}$ was chosen by experimentation utilizing the incentive around $\sqrt{M}$ (estimation of M is 4). The scope of ntree from 0 to 3000 was utilized to look through the best worth. Be that as it may, no significant change was accomplished contrasted with the default incentive for ntree of 750. Subsequently, the estimation of 750 for ntree was embraced in this research.

The monthly rainfall of Nellore station was taken from 1925–2000 and the initial 60-years of rainfall data were applied for training and the leftover 15 years of rainfall data were utilized for validation. The areal rainfall prediction for the Nellore station was executed utilizing the LS-SVR and RF.

The set of suitable inputs is a significant worry for LS-SVR and RF modelling. Diverse mix of forerunner values of the rainfall data were considered as inputs (i.e., (1) $P_{(t)}$; (2) $P_{(t)}$, $P_{(t-1)}$; (3) $P_{(t)}$, $P_{(t-1)}$, $P_{(t-2)}$). The output is rainfall time-series data to be predicted with 1-, 2-, and 3-month lead-time (i.e., $P_{(t+1)}$, $P_{(t+2)}$, and $P_{(t+3)}$).

The crossbreed models were acquired by consolidating two distinct strategies. Taking into account the SSA's strength, these approaches are intended to progress determining execution and dependability. The outcomes of the normal and crossbreed models are contrasted to evaluate the accuracy of the model in rainfall anticipation.
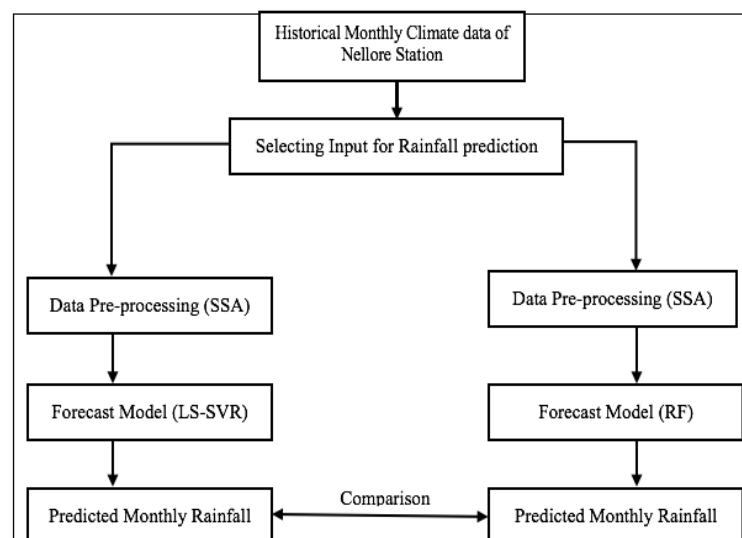

Fig. 2: The famework of the proposed rainfall prediction model.

The proposed framework has the following steps and is depicted in Fig. 2.

1. At first, the time-series of rainfall data was rotten into various principle components (PCs) utilizing SSA.

2. The appropriate PCs are determined based on the pattern or time of every series and new series of each parameter is established by including the essential parts to be characterized.

3. LS-SVR and RF approaches are designed for each part of the reconstruction so the design of LS-SVR and RF is distinctive for every segment of the restoration.

4. At last, LS-SVR and RF approaches are fed with the new series to anticipate the future rainfalls for 1-, 2-, and 3, 4-month lead-time. This is the main thought of pairing SSA with ML strategies.

4.4 Forecast Verification

The proposed model performance is assessed in terms of RMSE and NSE, for the calibration and testing duration. The formulas are represented in Eqs. (6) and (7) respectively.

$$\text{RMSE} = \sqrt{\frac{1}{n}\sum_{i=1}^{n}(X-Y)^2} \tag{6}$$

Where, X and Y are the fitted and predicted values correspondingly. Lesser values of RMSE recommend higher precision.

$$\text{NSE} = 1 - \frac{\sum_{i=1}^{n}(X-Y)^2}{\sum_{i=1}^{n}(X-M)^2} \tag{7}$$

Where M is the mean of the fitted values. An NSE of 0.75–1.0 relates to "excellent" accuracy, 0.65–0.75 to "good" precision, and 0.5–0.65 to a "sensible precision", while values below 0.5 imitate unacceptable precision. In spirit, the nearer NSE is to 1, the more precise is predicted.

5. RESULTS AND DISCUSSION

In this article, we designed the monthly rainfall prediction approaches for 1, 2, 3, 4-month lead time for the Nellore station. The performance of the standard and hybrid models is compared. The variation is that the customary approaches utilized the direct noisy data as model input, while the crossbreed models utilized the deteriorated input data produced by SSA rather than unrefined data. Table 2 displays the prediction performances for 1, 2, and 3, 4- month intervals for the customary and hybrid models in terms of RMSE and NSE.

Table 2:Prediction performances of the proposed models

Model	RMSE				NSE			
	1-month	2-month	3-month	4-month	1-month	2-month	3-month	4-month
LSSVR	194.58	193.31	199.56	199.85	0.04	0.06	0.05	0.07
SSA-LSSVR	**72.29**	**69.48**	**71.09**	**73.54**	**0.96**	**0.95**	**0.86**	**0.84**
RF	197.87	199.24	194.18	200.54	0.04	0.05	0.04	0.03
SSA-RF	**111.76**	**126.77**	**132.83**	**142.56**	**0.73**	**0.59**	**0.49**	**0.65**

In Table 3, it is seen that RMSE and NSE display extremely deprived values for the customary methods utilizing raw data when contrasted with the crossbreed models utilizing data created by SSA. There is additional proof that the customary approaches have been inadequately approved for each interval. The LS-SVR outcome is noise-sensitive and might not be successful when the degree of clamor is lofty. Thusly, the LS-SVR pairing with the SSA separating the crude rainfall data will diminish the noise impacts and its helpful in enhancing the model performance. Figures 3(a,b) and 4(a,b) outline the time-series charts of the fitted and one-month lead-time anticipated rainfall by the customary and hybrid approaches of Nellore station. From the figures, we uncover that the predicted values from the crossbreed models are nearer to fitted values than the values estimated by the standard models. The rainfalls anticipated by the crossbreed models were discovered to be firmly restricted to the line of uniformity, though the rainfall determined by the customary models is not near the line of balance.

5.1 Comparative Analysis

The proposed hybrid models are predicted the monthly rainfall reasonably and produced significant results. The proposed model accuracy is assessed by RMSE and NSE and the results display that the SSA-LSSVR and SSA-LSRF are good compare to LSSVR and LSRF respectively. In this section, the proposed model performance is compared with existing models in terms of RMSE, NSE. The results show that the proposed hybrid framework looking good compared to existing techniques in monthly rainfall prediction of Nellore station. Here we had taken the average values of 1-, 2-, 3-, 4- month percentages RMSE, and NSE values for comparison of the proposed method. These comparison values are displayed in Table 3.

Table 3:The proposed model performance comparison with existing techniques

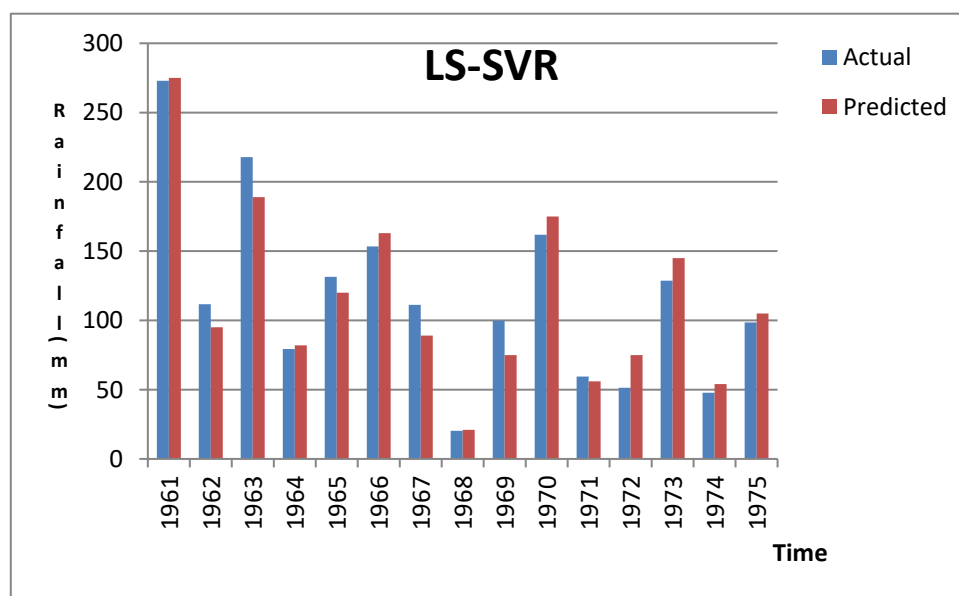| SNo	Model Name	RMSE (%)	NSE
1	Deep ESN Model (Echo state Network) [9] (2019)	1.51	0.02
2	Multiple Linear Regression [8] (2020)	26.5	0.837
3	Artificial Neural Network [11] (2018)	68.49	0.69
4	**The proposed model (SSA-LSSVAR, SSA-LSRF)**	**0.716**	**0.902**

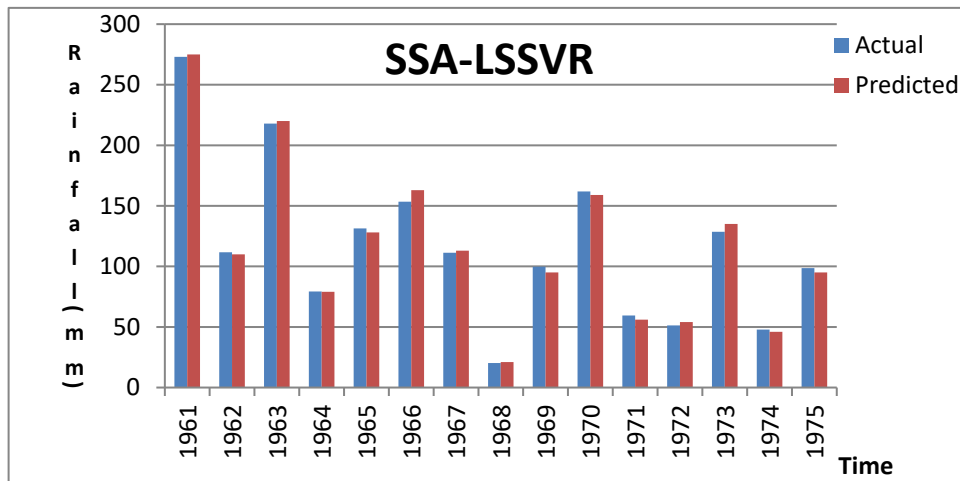Fig. 3a: Fitted and predicted values for LSSVR model.

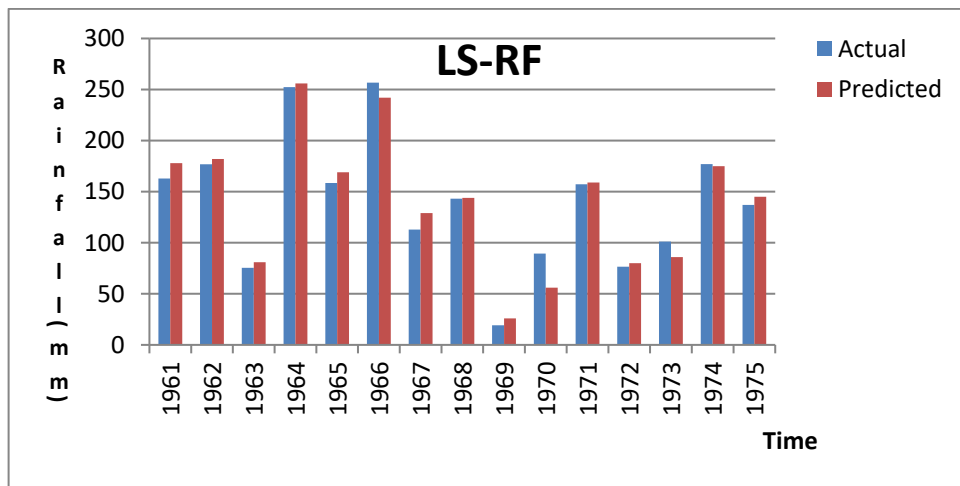Fig. 3b: Fitted and Predicted values for SSA-LSSVR model.

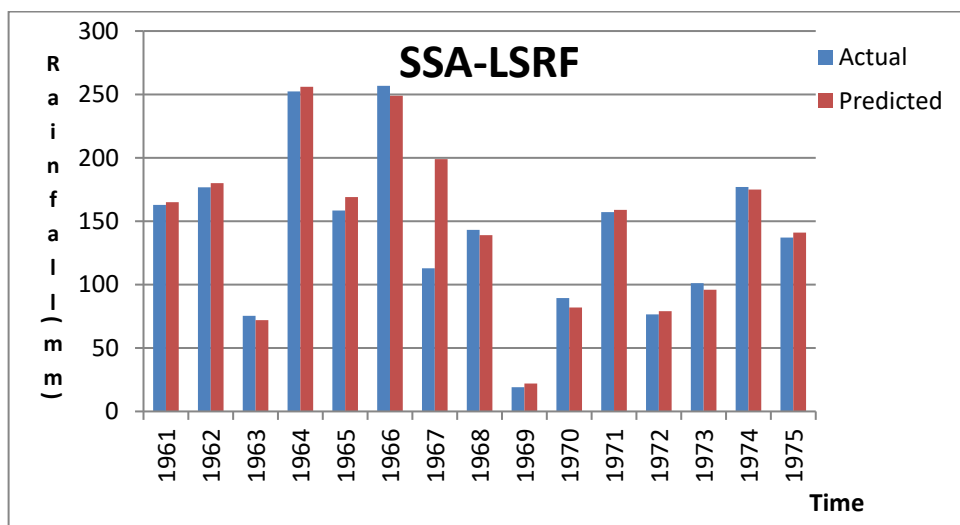Fig. 4a: Fitted and predicted values for LSRF model.

Fig. 4b: Fitted and predicted values for SSA-LSRF model.

6. CONCLUSION AND FUTURE WORK

The current research investigated the dependability of integrating a data preprocessing approach (SSA) with ML-based strategies, LSSVR and RF, for monthly rainfall estimating in Nellore station, India. The study infers that the SSA can acquire and give magnificent forecasts to noteworthy hydrological time series segments with unique uneven practices, for example, rainfall and runoff series. One of the significant discoveries is that the crossbreed approaches (SSA-LSSVR and SSA-RF) have superior accuracy over the customary approaches (LS-SVR and RF). It tends to be inferred that the crossbreed models are a potential modelling procedure that can be applied to anticipate the monthly rainfall in the current examination area. Connecting the rainfall properties of the study area to the estimating design exhibitions is recommended to be additionally examined in future research. Further, only one data pre-processing strategy has been accepted; consequently, future work may consider different pre-processing methods and contrast their accuracies with accomplishing added exact prescient results. Additionally, just the areal monthly rainfall data from one station was utilized in the present research. More study regions ought to be incorporated for testing the findings.

REFERENCES

[1]   Bojang PO, Yang TC, Pham QB, Yu PS. (2020)Linking singular spectrum analysis and machine learning for monthly rainfall forecasting. Applied Sciences, 10(9):1-20.

[2]   Kashiwao T, Nakayama K, Ando S, Ikeda K, Lee M, Bahadori A. (2017) A neural network-based local rainfall prediction system using meteorological data on the Internet: A case study using data from the Japan Meteorological Agency. Applied Soft Computing, 56(1):317-330.

[3]   Reddy PC, Babu AS. (2017) Survey on weather prediction using big data analytics. InSecond International Conference on Electrical, Computer and Communication Technologies (ICECCT), IEEE: pp 1-6.

[4]   Basha CZ, Bhavana N, Bhavya P, Sowmya V. (2020) Rainfall prediction using machine learning & deep learning techniques. InInternational Conference on Electronics and Sustainable Communication Systems (ICESC), IEEE: pp 92-97.

[5]   Choi C, Kim J, Kim J, Kim D, Bae Y, Kim HS. (2018) Development of heavy rain damage prediction model using machine learning based on big data. Advances in Meteorology, 2018 (2):1-11.

[6]   Reddy PC, Babu AS. (2020) An enhanced multiple linear regression model for seasonal rainfall prediction, International Journal of Sensors, Wireless Communications and Control, 10(1):473-483.

[7]   Das S, Chakraborty R, Maitra A. (2017) A random forest algorithm for nowcasting of intense rainfall events. Advances in Space Research, 60(6):1271-82.

[8]   Moulana M, Roshitha K, Niharika G, Sai MS. (2020) Prediction of rainfall using machine learning techniques. International Journal of Scientific & Technology Research, 9(3):236-240.

[9]   Yen MH, Liu DW, Hsin YC, Lin CE, Chen CC. (2019) Application of the deep learning for the prediction of rainfall in Southern Taiwan. Scientific Reports, 9(1):1-9.

[10]   Reddy PC, Sureshbabu A. (2019) An applied time series forecasting model for yield prediction of agricultural crop. InInternational Conference on Soft Computing and Signal Processing, Springer: pp 177-187.

[11]   Shah U, Garg S, Sisodiya N, Dube N, Sharma S. (2018) Rainfall prediction: Accuracy enhancement using machine learning and forecasting techniques. InFifth International Conference on Parallel, Distributed and Grid Computing (PDGC), IEEE: pp 776-782.

[12]   Abbot J, Marohasy J. (2013) The potential benefits of using artificial intelligence for monthly rainfall forecasting for the Bowen Basin, Queensland, Australia. Water Resources Management VII, 171:287.

[13] Fahimi F, Yaseen ZM, El-shafie A. (2017) Application of soft computing based hybrid models in hydrological variables modeling: a comprehensive review. Theoretical and Applied Climatology, 128(3-4):875-903.

[14] Kisi O, Shiri J. (2011) Rainfall forecasting using wavelet-genetic programming and wavelet-neuro-fuzzy conjunction models. Water Resources Management, 25(13):3135-3152.

[15] Pandhiani SM, Shabri AB. (2013) Time series forecasting using wavelet-least squares support vector machines and wavelet regression models for monthly stream flow data. Open Journal of Statistics, 3: 183-194.

[16] Chan JC, Paelinckx D. (2008) Evaluation of random forest and adaboost tree-based ensemble classification and spectral band selection for ecotope mapping using airborne hyperspectral imagery. Remote Sensing of Environment, 112(6):2999-3011.

[17] Karthikeyan L, Kumar DN. (2013) Predictability of nonstationary time series using wavelet and EMD based ARMA models. Journal of Hydrology, 502:103-119.

[18] Ji SY, Sharma S, Yu B, Jeong DH. (2012) Designing a rule-based hourly rainfall prediction model. InIEEE 13th International Conference on Information Reuse & Integration (IRI), IEEE, pp 303-308.

[19] Min M, Bai C, Guo J, Sun F, Liu C, Wang F, Xu H, et al. (2018) Estimating summertime rainfall from Himawari-8 and global forecast system based on machine learning. IEEE Transactions on Geoscience and Remote Sensing, 57(5): 2557-2570.

[20] Navid MAI, Niloy NH. (2018) Multiple linear regressions for predicting rainfall for Bangladesh. Communications, 6(1): 1-4.

[21] Rodrigues J, Deshpande A. (2017) Prediction of rainfall for all the states of India using auto-regressive integrated moving average model and multiple linear regression. In International Conference on Computing, Communication, Control and Automation (ICCUBEA), IEEE: pp 1-4.

[22] Swain S, Patel P, Nandi S. (2017) A multiple linear regression model for rainfall forecasting over Cuttack district, Odisha, India. In 2nd International Conference for Convergence in Technology (I2CT), IEEE: pp 355-357.

[23] MohdRazeef, Butt MA, and Baba MZ. (2018) SALM-NARX: Self Adaptive LM-based NARX model for the prediction of rainfall. In 2nd International Conference on I-SMAC (IoT in Social, Mobile, Analytics and Cloud)(I-SMAC) I-SMAC (IoT in Social, Mobile, Analytics and Cloud)(I-SMAC), IEEE:pp 580-585.

[24] Ria F, Lusia DA, Otok BW, Kuswanto H. (2012) Ensemble method based on anfis-arima for rainfall prediction. In International Conference on Statistics in Science, Business and Engineering (ICSSBE), IEEE: pp 1-4.

[25] Cramer S, Kampouridis M, Freitas AA, Alexandridis AK. (2017) An extensive evaluation of seven machine learning methods for rainfall prediction in weather derivatives. Expert Systems with Applications, 85(2): 169-181.

[26] Rivero CR, Pucheta JA, Baumgartner JS, Laboret SO, Sauchelli VH, Patiño HD. (2016) Short-series Prediction with BEMA Approach: application to short rainfall series. IEEE Latin America Transactions,14(8): 3892-3899.

[27] Mehr AD, Nourani V, Khosrowshahi VK, Ghorbani MA. (2019) A hybrid support vector regression–firefly model for monthly rainfall forecasting. International Journal of Environmental Science and Technology, 16(1):335-346.

[28] Johny K, Pai ML, Adarsh S. (2020) Adaptive EEMD-ANN hybrid model for Indian summer monsoon rainfall forecasting. Theoretical and Applied Climatology, 18(1):1-7.

[29] Samantaray S, Tripathy O, Sahoo A, Ghose DK. (2020) Rainfall forecasting through ANN and SVM in Bolangir Watershed, India. InSmart Intelligent Computing and Applications, Springer: pp 767-774.

[30] Zhao Q, Liu Y, Ma X, Yao W, Yao Y, Li X. (2020) An improved rainfall forecasting model based on GNSS observations. IEEE Transactions on Geoscience and Remote Sensing, 58(7):4891-900.

[31] https://en.wikipedia.org/wiki/Nellore_district. 15.01.2021

[32] https://en.climate-data.org/asia/india/andhra-pradesh/nellore-6270/. 15.01.2021

[33] Abdel-Kader H, Abd-El Salam M, Mohamed M. (2021) Hybrid Machine Learning Model for Rainfall Forecasting. Journal of Intelligent Systems and Internet of Things, 1(1):5-12.

[34] Pham QB, Yang TC, Kuo CM, Tseng HW, Yu PS. (2021) Coupling singular spectrum analysis with least square support vector machine to improve accuracy of SPI drought forecasting. Water Resources Management, 35(3):847-868.

Mohammad Samuri et al.

CLASSIFICATION MODEL FOR BREAST CANCER MAMMOGRAMS

Suzani Mohamad Samuri[1,3]*, Try Viananda Nova[2], Bahbibi Rahmatullah[1,3], Wang Shir Li[1,3], Ziadoon Tareq Al-Qaysi[4]

[1]*Department of Computing, Faculty of Art, Computing and Creative Industry, Sultan Idris Education University, Malaysia*
[2]*Department of Informatic, Universitas Ibn Kaldun Bogor, Jawa Barat, Indonesia*
[3]*Data Intelligence and Knowledge Management Special Interest Group, Faculty of Art, Computing and Creative Industry, Sultan Idris Education University, Malaysia*
[4]*Computer Science Department, College of Computer Sciences and Mathematics, Tikrit University, Iraq*

*Corresponding author: suzani@fskik.upsi.edu.my

ABSTRACT: Machine learning has been the topic of interest in research related to early detection of breast cancer based on mammogram images. In this study, we compare the performance results from three (3) types of machine learning techniques: 1) Naïve Bayes (NB), 2) Neural Network (NN) and 3) Support Vector Machine (SVM) with 2000 digital mammogram images to choose the best technique that could model the relationship between the features extracted and the state of the breast ('Normal' or 'Cancer'). Grey Level Co-occurrence Matrix (GLCM) which represents the two dimensions of the level variation gray in the image is used in the feature extraction process. Six (6) attributes consist of contrast, variance, standard deviation, kurtosis, mean and smoothness were computed as feature extracted and used as the inputs for the classification process. The data has been randomized and the experiment has been repeated for ten (10) times to check for the consistencies of the performance of all techniques. 70% of the data were used as the training data and another 30% used as testing data. The result after ten (10) experiments show that, Support Vector Machine (SVM) gives the most consistent results in correctly classifying the state of the breast as 'Normal' or 'Cancer', with the accuracy of 99.4%, in training and 98.76% in testing. The SVM classification model has outperformed NN and NB model in the study, and it shows that SVM is a good choice for determining the state of the breast at the early stage.

ABSTRAK: Pembelajaran mesin telah menjadi topik yang diminati dalam penyelidikan yang berkaitan dengan pengesanan awal kanser payudara berdasarkan imej mamogram. Dalam kajian ini, kami membandingkan hasil prestasi dari tiga (3) jenis teknik pembelajaran mesin: 1) Naïve Bayes (NB), 2) Neural Network (NN) dan 3) Support Vector Machine (SVM) dengan 2000 imej digital mammogram hingga teknik terbaik yang dapat memodelkan hubungan antara ciri yang diekstraksi dan keadaan payudara ('Normal' atau 'Cancer') dapat diperoleh. Grey Level Co-occurrence Matrix (GLCM) yang mewakili dua dimensi variasi tahap kelabu pada gambar digunakan dalam proses pengekstrakan ciri. Enam (6) atribut terdiri dari kontras, varians, sisihan piawai, kurtosis, min dan kehalusan dihitung sebagai fitur yang diekstrak dan digunakan sebagai input untuk proses klasifikasi. Eksperimen telah diulang selama sepuluh (10) kali untuk memeriksa kesesuaian prestasi semua teknik. 70% data digunakan sebagai data latihan dan 30% lagi digunakan sebagai data ujian. Hasil setelah sepuluh (10) eksperimen menunjukkan bahawa, Support Vector Machine (SVM) memberikan hasil yang paling konsisten dalam mengklasifikasikan keadaan payudara dengan betul sebagai 'Normal' atau 'Kanser', dengan akurasi 99.4%,

dalam latihan dan 98.76% dalam ujian. Model klasifikasi SVM telah mengungguli model NN dan NB dalam kajian ini, dan ia menunjukkan bahawa SVM adalah pilihan yang baik untuk menentukan keadaan payudara pada peringkat awal.

KEYWORDS: *machine learning; breast cancer detection; mammogram images; data mining; data-driven modelling*

1. INTRODUCTION

Breast cancer screening which is commonly made by mammography is a limited series of x-rays taken of the breast. Radiologist sees for any anomalous signs or patterns on the mammogram that might be breast cancer. These signs normally show up on the mammogram before any lump may be thought at the breast. If there is anything odd on this mammogram, more tests get to be made. These tests may add another mammogram, imaging, or a biopsy. Whether testing mammograms will change the probability of women dying from breast cancer has been argued for decades [1]. It is definitely not an ideal test. Some cancers are failed to be detected by the mammogram. This false-positive mammogram effects lead to more experimentation, which is time-consuming and may have unnecessary apprehension. Since mammographic X-ray images are 2D projections of a 3D object, localization of features identified within the breast volume is not trivial. Furthermore, mammograms represent highly deformed configurations of the breast due to compression, thus the tumor localization process relies on the expertise of the clinicians. Breast cancer-related studies have long been conducted by researchers around the world.

In the last few decades, various information production and machine learning techniques have been produced for breast cancer discovery and categorization, which may be separated into three important phases: Preprocessing, feature extraction, and classification. To facilitate explanation and analysis, the preprocessing of mammography images helps improve the clarity of peripheral regions and level system, and various methods have been reported to help in the process. Several transform-based quality analysis techniques are used to change the image into a new structure using the spatial frequency properties of the component level variations. In fact, there are many studies related to early detection is possible to show whether the state of the breast to be 'Normal' or 'Abnormal'. Among the most common classifier used for classification and early detection of breast cancer is Neural Network (NN). It is a model made to imitate the function of learning that owned the human brain. As stated by [2], the Neural classifier developed able to perform well by successfully classifying cancer and non-cancer (normal) images with an accuracy of 97%. However, this study did not show any comparison between the developed NN classifier and other types of the classifier. With regard to a single technique, [3] mentioned that in his mapping study, found that Decision Trees (DT), Support Vector Machines (SVM) and Artificial Neural Networks (ANN) were those most frequently adopted to build ensemble classifiers.

Therefore, in this paper on cancer detection, the focus will be on the classification part, whereby the use of three classifiers namely Naive Bayes (NB), Neural Network (NN) and Support Vector Machines (SVM), to accurately classify the mammographic images of the breast as Normal or Cancer will be presented. The results of this research will be useful for tracking visible tumors between images, as well as to help radiologists in their tasks to detect subtle abnormalities in a mammogram.

2. METHODOLOGY

This research methodology uses a data mining approach to classify data. In this case, there is an important phase that must be done to get the best research results. There are four phases involved namely sample selection, image enhancement and feature extraction, model development, and evaluation.

2.1 Sample Selection

A total of two thousand (2000) 2d-digital mammogram images were collected from the Central Pertamina Hospital, Indonesia (1000 normal breast images and 1000 cancer images) as shown in Fig. 1. These 2d-digital mammogram images were then converted to 3d-digital mammogram images for better analysis.
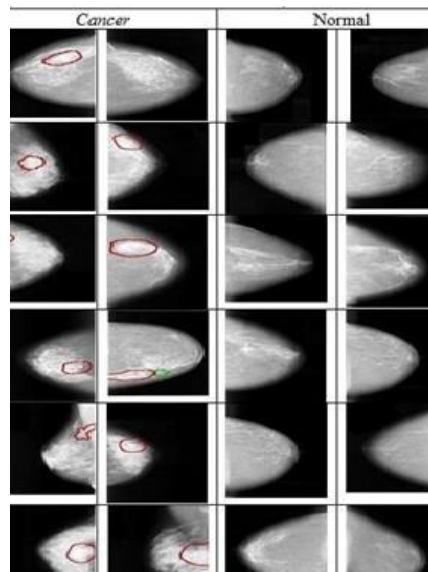

Fig. 1: Some of the mammogram of normal and cancer images.

2.2 Image Enhancement and Feature Extraction

In preprocessing phase, the possibility distribution algorithm [4] is used for image enhancement using logical approach fuzzy with 5 parameters, namely α, $\beta1$, γ, $\beta2$ and max as shown in Fig. 2.

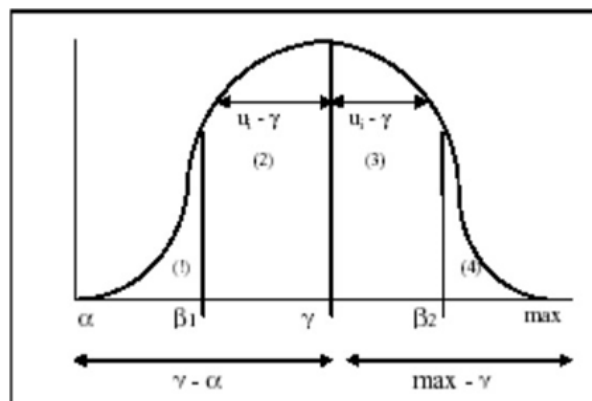Fig. 2: Possibility distribution function [4].

From the required parameters, α represents the minimum value of the distribution, γ represents the average value of the distribution and max represents the maximum value of the distribution. The fuzzy transformation function used to get the entire value is defined as follows:

$$\alpha \quad = \min \tag{1}$$

$$\beta 1 \quad = (\alpha + \gamma)/2 \tag{2}$$

$$\gamma \quad = \text{mean} \tag{3}$$

$$\beta 2 \quad = (\max + \gamma)/2 \tag{4}$$

$$\max = \max \tag{5}$$

The purpose of using the possibility distribution algorithm in improving image quality is to lower the level of pixel grayness that has a grayish value between β1 and β2. The way to do this is to provide a new intensity value in pixels between β1 and γ, γ and β2 with the opposite board value to the mean γ. The fuzzy rule below is used to perform image contrast enhancement based on Fig. 2:

$$\text{Rule 1: If } \alpha \le u_i \le \beta 1 \text{ then } P = 2((u_i - \alpha)/(\gamma - \alpha))2 \tag{6}$$

$$\text{Rule 2: If } \beta 1 \le u_i \le \gamma \text{ then } P = 1 - 2((u_i - \gamma)/(\gamma - \alpha))2 \tag{7}$$

$$\text{Rule 3: If } \gamma \le u_i \le \beta 2 \text{ then } P \tag{8}$$
$$= 1 - 2((u_i - \gamma)/(\max - \gamma))2$$

$$\text{Rule 4: If } \beta 2 \le u_i \le \max \text{ then } P = 2((u_i - \gamma)/(\max - \gamma))2 \tag{9}$$

where $u_i = f(x,y)$ is the intensity of the i-i pixel. Regulations that lower the level of pixel grayness that has a grayish value between β1 and β2 are represented by Eqs. (7) and (8). The steps of possibility distribution algorithm can be explained as the following:

Step 1: Initialize parameter data matrix set by image to be improved. From the image, the minimum, maximum and average (mean) grayish values were obtained. The value β1 is set with the result of (min + mean)/2. Whereas the value of β2 is set with the result of (mean + max)/2.

Step 2: Fuzzification for all pixels. In this step, fuzzy rules were applied (Eq. 6, Eq. 7, Eq. 8 and Eq. 9) to get a new grayish value.

Step-3: Modification for all pixels were executed, the fuzzy value of the data obtained from the new grayish value is powered by two.

Step-4: Defuzzification for all pixels. The new contrast data derived from fuzzy data values is calculated and multiplied by the matrix of the initial image data.

In this phase, feature extraction also being done to extract the important variables to be used in the next step which is development of classification model. For feature extraction, GLCM (Grey Level Co-occurrence Matrix) is being used. GLCM is the two dimensions represent the level variation gray at the image. GLCM is one of the popular statistical methods of extracting textural feature from images. According to [5], by extracting the features of an image by GLCM approach, the image compression time can be greatly

reduced in the process of converting RGB to Gray level image when compared to other discrete wavelet transform (DWT) techniques. In this study, measurement of the contrast, variance, standard deviation, kurtosis, mean, and smoothness are computed as features extracted and shall be used in the classification stage.

2.3 Development of Data-driven Classification Model

In this work, Matlab software is used for developing the classification model and analysis. The three (3) machine learning techniques investigated to produce a data-driven classification models, were Neural Network (NN), Support Vector Machine (SVM) and Naïve Bayes (NB). Figure 3 shows an example of the 'Breast Image Extracted Features – Breast State' modelling structure. The inputs identified for the classification model were contrast, variance, standard deviation, kurtosis, mean, and smoothness. These features were extracted using GLCM methods explained in the previous section [5]. Whereas the output for this classification model is the state of the breast itself, whether it is 'Normal' or 'Cancer'.
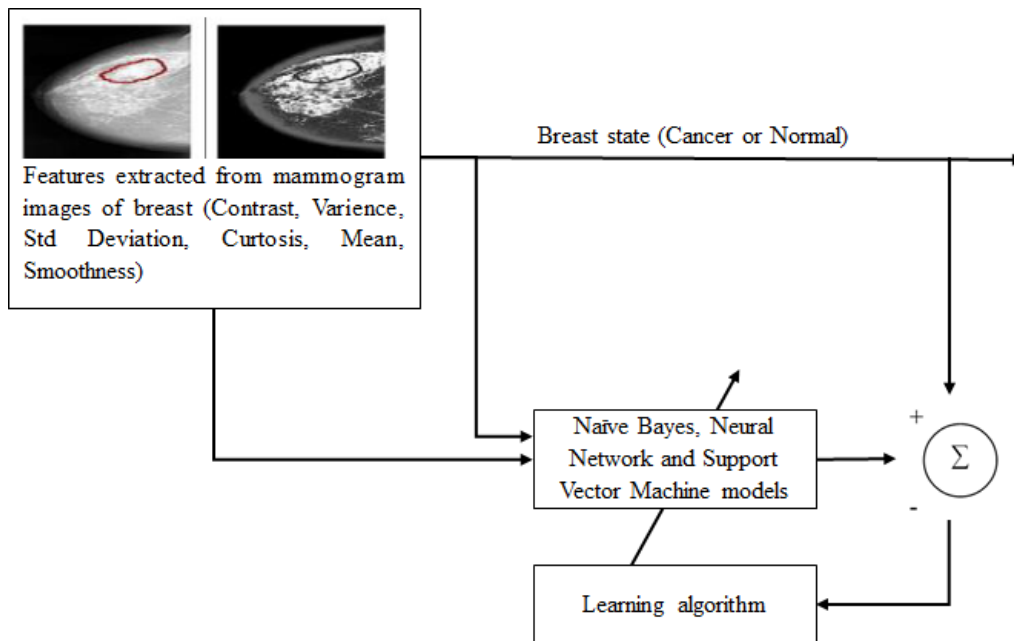
Fig. 3: Model structure for 'Breast Image Extracted Features – Breast State'. $\varepsilon(t)$ = error between actual and predicted breast category.

2.3.1 Naïve Bayes (NB)

The Naive Bayesian classifier is based on Bayes Theorem assuming independence among predictors. The Naive Bayesian model is easy to build, without the estimation of complex iterative parameters that make it very useful for very large datasets. Despite its simplicity, the Naive Bayesian classification often works very well and is widely used because it often outperforms more sophisticated classification methods.

Bayes Theorem provides a way of calculating the probability of posterior, P (c | x), of P (c), P (x), and P (x | c). The basis of the Naïve Bayes theorem used is the Bayes formula as follows [6]:

$$P(C|X) = \frac{P(x|c)P(c)}{P(x)} \qquad (10)$$

The Bayes Naïve classification assumes that the influence of predictor value (x) on a particular class (c) does not depend on the values of other predictors. This assumption is called class conditional independence.

2.3.2 Neural Network (NN)

Neural network is a model created to mimic the learning functions of the human brain. In the Neural Network, neurons are grouped into layers, called neuron layers. Usually, each neuron of a layer is connected to all neurons in the back and front layers (except inputs and outputs). Information sent in a NN, propagated layers – per – layers ranging from inputs to outputs without or through one or more hidden layers. Depending on the algorithm used, information can also be propagated backwards (backpropagation). Figure 4 shows the Neural Network with three neuron layers.
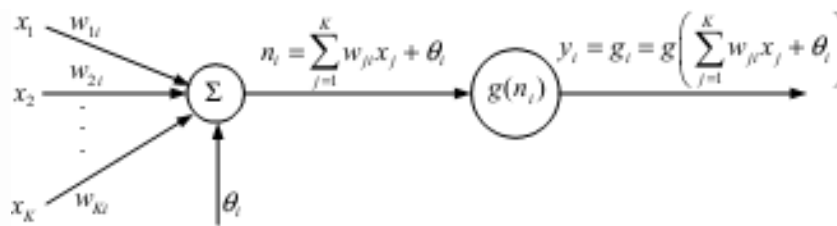
Fig. 4: Algorithm for Neural Network.

2.3.3 Support Vector Machine (SVM)

Support Vector Machine (SVM) is one of the prediction techniques, both in the case of classification and regression [7]. SVM has a basic principle of linear classifier that is a classification case that can be linearly separated, but nowadays SVM is also able to solve non-linear problems by adding kernel concepts to high-resolution workspaces. In this space, a hyperplane (hyperplane) will be searched to maximize the distance between data classes.

SVM can actually work on linearly separated data only. When the data is nonlinear then, the way that can be used is to use the kernel on the data. Kernel can be interpreted as a function that remaps data in the original dimension space into more dimensional space as shown in Fig. 5.
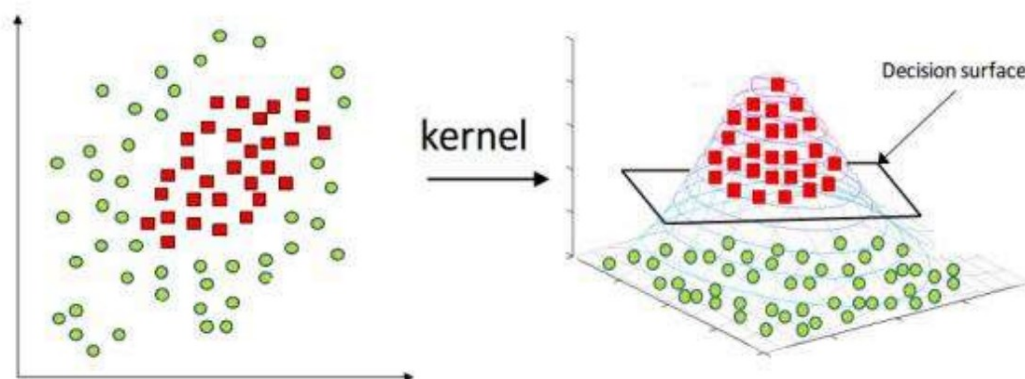
Fig. 5: Representation for Support Vector Machine (SVM).

2.4 Experimental Procedure

As shown in Fig. 3, the features extracted from 2000 mammogram breast images were experimented with different classifiers that are Neural Network (NN), Support Vector

Machine (SVM) and Naïve Bayes (NB). The data has been randomized and the experiment has been repeated for ten (10) times to check for the consistencies of the performance of all techniques. 70% of the data were used as the training data and another 30% used as testing data. Accuracy based on confusion matrix is used as the performance indicator, to show which technique can best model the classification of normal and abnormal state of the breast.

3. FINDINGS

In this section, findings from three (3) different classification models NB, NN and SVM) will be presented. The inputs identified for all models were the contrast, variance, standard deviation, kurtosis, mean, and smoothness based on the GLCM approach applied to 2000 3d-digital breast mammogram images reported in the previous section. The outputs for all models were the breast state: 'Normal' or 'Cancer', which represented by '1' and '2' in the modelling process respectively. The extracted features with the breast states were then randomized. 70% of the data were used for training and another 30% were used as testing. The objective of this modelling is to mimic the behavior of the expert in identifying the state of the breast whether it is 'Normal' or 'Cancer' by training the model with the extracted features (contrast, variance, standard deviation, kurtosis, mean, and smoothness) from the 3d-digital mammogram images and the identified breast state. The following subsections report the findings on all the training and testing work conducted.

3.1 Naïve Bayes Model Training and Testing Results

The first classification model built in this study is using the NB. The scatterplots for training and testing of NB model are shown in Fig. 6(a) and (b). While the detail results for the accuracy of the model for each experiment in the training and testing are shown in Table 1 and Table 2. In Table 1, it can be seen, that out of 1400 sample data used for training (70% of the total sample data), there are average of 964 correct predictions and average of 436 incorrect predictions for training. Thus, the average accuracy for the training is about 68.83%. Whereas for the testing, out of 600 sample data used for testing (30% of the total sample data), there are average of 420 correct predictions and average of 180 incorrect predictions for the whole 10 experiments. Therefore, the average accuracy for the NB model testing is about 70.07%.
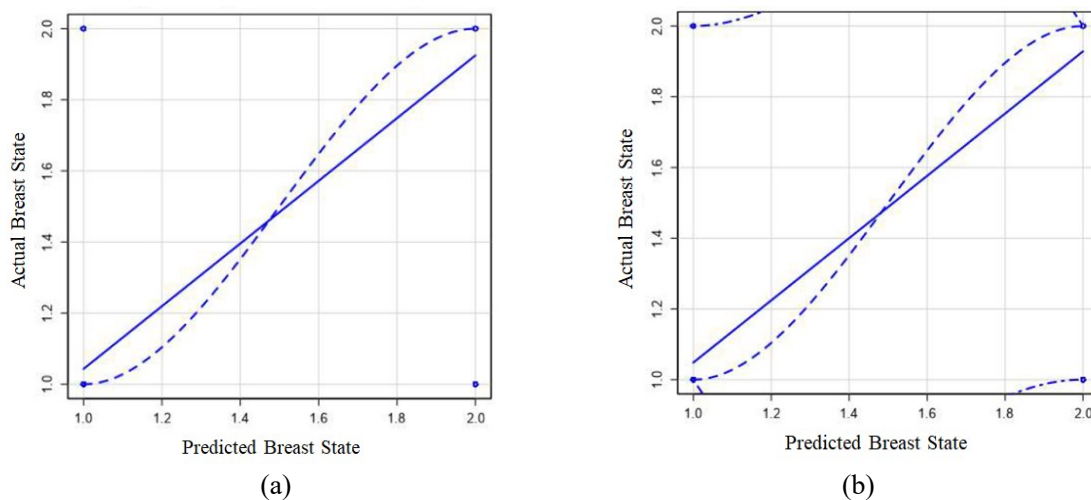

(a)   (b)

Fig. 6: Scatterplots for (a) Training of the NB Model, (b) Testing of the NB Model.

Table 1: NB model training results for 10 experiments.

	Naïve Bayes Model Training Results																		
	Predicted																		
Actual	Exp 1		Exp 2		Exp 3		Exp 4		Exp 5		Exp 6		Exp 7		Exp 8		Exp 9		Exp 10	
	1	2	1	2	1	2	1	2	1	2	1	2	1	2	1	2	1	2	1	2
1	540	194	540	194	580	165	579	166	520	209	576	168	545	191	536	197	580	166	574	170
2	272	394	271	395	231	424	233	422	291	380	235	421	267	397	276	391	231	423	237	419
Acc	66.69%		66.77%		71.70%		71.51%		64.28%		71.23%		67.31%		66.22%		71.62%		70.95%	

Table 2: NB model testing results for 10 experiments.

	Naïve Bayes Model Testing Results																		
	Predicted																		
Actual	Exp 1		Exp 2		Exp 3		Exp 4		Exp 5		Exp 6		Exp 7		Exp 8		Exp 9		Exp 10	
	1	2	1	2	1	2	1	2	1	2	1	2	1	2	1	2	1	2	1	2
1	228	86	228	86	252	68	253	67	248	71	256	66	223	90	232	83	253	68	258	64
2	120	166	120	166	96	184	95	185	100	181	91	187	125	162	116	169	95	184	90	188
Acc	65.68%		65.75%		72.74%		73.06%		71.44%		73.77%		64.21%		66.82%		72.87%		74.41%	

3.2 Neural Network (NN) Model Training and Testing Results

The next classification model built in this study is using the NN. Figure 7(a) and (b) show the scatterplots for training and testing of NN model, while Table 3 and 4 show the detail results of the NN model accuracy for each experiment in training and testing. As seen in Table 3 and 4, there are average of 1237 correct predictions and average of 163 incorrect predictions for training. Thus, the average accuracy for the training is about 88.38%. Whereas for the testing, out of 600 sample data used for testing (30% of the total sample data), there are average of 530 correct predictions and average of 70 incorrect predictions for the whole 10 experiments. Therefore, the average accuracy for the NN model testing is about 88.27%.
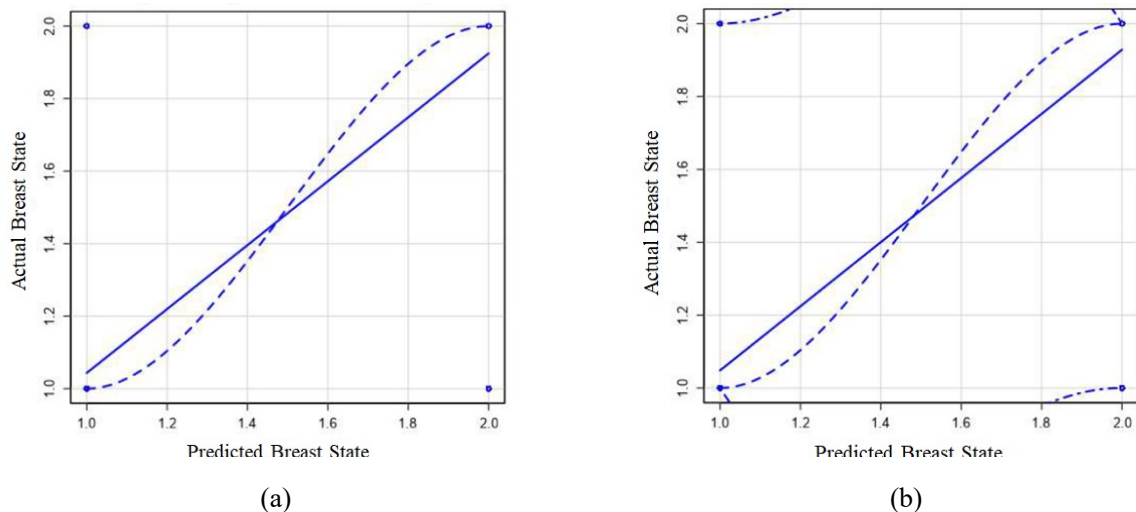

(a)   (b)

Fig. 7: Scatterplots for (a) Training of the NN Model. (b) Testing of the NN Model.

Table 3: NN model training results for 10 experiments.

	Neural Network Model Training Results																		
	Predicted																		
Actual	**Exp 1**		**Exp 2**		**Exp 3**		**Exp 4**		**Exp 5**		**Exp 6**		**Exp 7**		**Exp 8**		**Exp 9**		**Exp 10**	
	1	2	1	2	1	2	1	2	1	2	1	2	1	2	1	2	1	2	1	2
1	708	73	717	66	716	67	729	58	711	71	697	81	721	64	718	66	714	68	719	65
2	101	518	93	524	94	523	81	532	99	519	113	509	88	527	93	523	96	522	90	526
Acc	87.55%		88.66%		88.51%		90.04%		87.89%		86.17%		89.11%		88.68%		88.29%		88.90%	

Table 4: NN model testing results for 10 experiments.

	Neural Network Model Testing Results																		
	Predicted																		
Actual	**Exp 1**		**Exp 2**		**Exp 3**		**Exp 4**		**Exp 5**		**Exp 6**		**Exp 7**		**Exp 8**		**Exp 9**		**Exp 10**	
	1	2	1	2	1	2	1	2	1	2	1	2	1	2	1	2	1	2	1	2
1	314	24	304	31	302	32	299	34	319	20	308	28	308	28	301	33	306	29	300	33
2	33	229	43	222	46	220	48	219	29	232	39	225	38	226	47	219	41	224	47	220
Acc	90.48%		87.60%		87.01%		86.29%		91.91%		88.88%		88.95%		86.73%		88.27%		86.62%	

3.3 Support Vector Machine (SVM) Model Training and Testing Results

The final classification model developed in this study is using the SVM. The scatterplots result of SVM model for training and testing are shown in Fig. 8 (a) and (b), while Table 5 and 6 show the detail results for the accuracy of the model for each experiment during training and testing.

From Table 5, it was found that, the majority of the outputs were correctly predicted by the SVM model, with average of 1392 correct predictions and average of only 8 incorrect predictions for training. Thus, the average accuracy for the training is about 99.40%. Interestingly, Table 6 also shown that the SVM model is able to correctly predict the output of the testing sample data with average of 593 correct predictions as against the incorrect predictions of only 7. This has made the average percentage of the testing accuracy to be 98.76%, slightly lower than its training accuracy.

Table 5: SVM model training results for 10 experiments.

	Support Vector Machine Model Training Results																		
	Predicted																		
Actual	**Exp 1**		**Exp 2**		**Exp 3**		**Exp 4**		**Exp 5**		**Exp 6**		**Exp 7**		**Exp 8**		**Exp 9**		**Exp 10**	
	1	2	1	2	1	2	1	2	1	2	1	2	1	2	1	2	1	2	1	2
1	799	7	799	7	809	0	809	0	799	7	809	0	799	7	799	7	809	0	809	0
2	10	584	10	584	0	591	0	591	10	584	0	591	10	584	10	584	0	591	0	591
Acc	98.80%		98.80%		100.00%		100.00%		98.80%		100.00%		98.80%		98.80%		100.00%		100.00%	

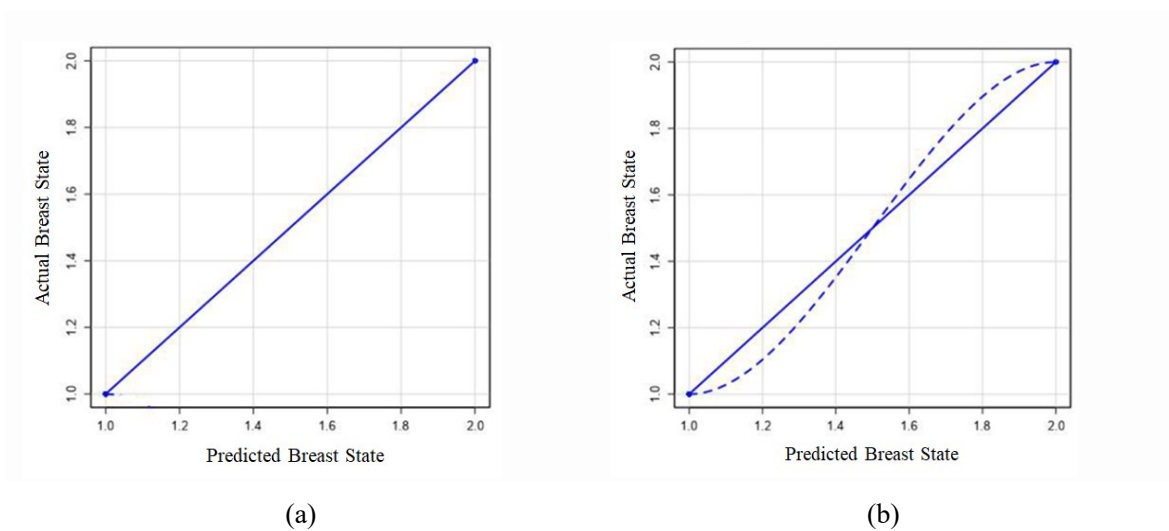(a)   (b)

Fig. 8: Scatterplots for (a) Training of the SVM Model, (b) Testing of the SVM Model.

Table 6: SVM model testing results for 10 experiments.

	Support Vector Machine Model Testing Results																		
Actual	**Predicted**																		
	Exp 1		**Exp 2**		**Exp 3**		**Exp 4**		**Exp 5**		**Exp 6**		**Exp 7**		**Exp 8**		**Exp 9**		**Exp 10**	
	1	2	1	2	1	2	1	2	1	2	1	2	1	2	1	2	1	2	1	2
1	336	8	340	5	347	0	347	0	342	3	342	3	339	6	342	3	342	3	347	0
2	10	246	7	248	0	253	0	253	5	250	5	250	7	248	5	250	5	250	0	253
Acc	97.00%		98.00%		100.00%		100.00%		98.70%		98.70%		98.70%		98.70%		98.70%		100.00%	

4. DISCUSSION

In this study, the 2d-digital mammography images were first transformed into 3d-digital mammography and GLCM approach is applied to these 3d-digital breast images to extract the contrast, variance, standard deviation, kurtosis, mean, and smoothness as features to be input to the models. The supervised learning technique is used to train the models that infer a function from input data with labeled breast state, 'Normal' or 'Cancer'. 2000 digital mammogram images of the breast have been analyzed.

Naive Bayes, Neural Network, and Deep Learning are among the most common machine learning techniques used in cancer detection [2,8-11]. However, in this study, ten (10) experiments have been conducted using the three (3) machine learning techniques namely Naïve Bayes, Neural Network and Support Vector Machine and the accuracy of each model in providing correct prediction for each experiment was recorded as shown in Section 3.

The result after ten (10) experiments show that the Support Vector Machine (SVM) gives the most consistent results in predicting or classifying correctly the state of the breast as 'Normal' or 'Cancer', with an average accuracy of 99.40% in training and 98.76% in testing. The SVM classification model has outperformed NN and NB models in the study, and it shows that SVM is a good choice for determining the state of the breast at the early stage.

As compared to the previously developed NN model reported by [2], the currently developed SVM model outperformed their NN model. Their study also not considering any other machine learning techniques but just focusing on NN model only.

However, these single classifier models can be further experiment and improved. For example, as reported by [3], the majority of research have reported positive results concerning the accuracy of ensemble classifiers as compared to the single classifiers. The following research have supported the given statement [12-21].

Apart from that, the performance index used can also be varied, not just focusing on the accuracy of the model but to consider other aspect like computational time for the training and testing to be done, as well as Precision-Recall curve to capture the exact capability of the classifiers investigated [22-25].

Transfer learning has also seen as the alternative to the conventional supervised learning for breast cancer detection and classification as reported by [3]. Therefore, comparison of model performance developed based on the supervised learning with transfer learning would be interesting to be explored in the near future.

Besides testing procedure that has been implemented in this study, validation with expert (radiologist) is seen crucial. The expert validation is time consuming, but it is important to be done in order to further validate the reliability of the developed models.

5. CONCLUSION

Today, the need for machine learning is rising in the field of breast cancer research. It has been used to screen and differentiate normal breast with cancer. The process of diagnosis can be very complicated. That is why for decades, researchers have developed various machine learning algorithms and architectures that can screen and differentiate cancerous images from normal ones by training the algorithms with various features extracted from the image of the breast. In particular, breast cancer diagnosis is more important than ever because the classification results will affect the treatment and safety of the patients. It requires not only a high prediction of accuracy, but also a high reliability and robustness.

In this study, ten (10) experiments have been conducted using the three (3) machine learning techniques namely Naïve Bayes, Neural Network and Support Vector Machine, using 2000 2d-digital mammogram images that have been converted into 3d-images. The accuracy of each model in providing correct prediction based on the confusion matrix has been reported for each experiment. The SVM classification model has outperformed NN and NB models in the study, and it shows that SVM is a good choice for determining the state of the breast at the early stage. However, further improvements can be done to the classifier models in producing more accurate and reliable results, for example, by exploring the ensemble classifier by combining different algorithm from the same type of classifier or different type of classifier to leverage the strength of individual classifiers.

As part of the future work, these models can also be extended to further classify the stage of the breast cancer (Stage 0, 1, 2, 3 and 4) by using the laboratory results of the patients as well as the auto measured diameter of the detected abnormality extracted from the digital mammogram images.

ACKNOWLEDGEMENT

REFERENCES

[1] Rubin R. (2017) Do Screening Mammograms Cut Breast Cancer Deaths or Lead to Overtreatment? Probably Both. *Forbes*. Retrieved from https://www.forbes.com/sites/ritarubin/2017/01/10/do-screening-mammograms-cut-breast-cancer-deaths-or-lead-to-overtreatment-probably-both/

[2] Mohamad Samuri, Suzani, Megariani TV. (2019) Intelligent 3D Analysis for Detection and Classification of Breast Cancer. JITCE (Journal of Information Technology and Computer Engineering), 3(2): 96-103. https://doi.org/https://doi.org/10.25077/jitce.3.02.96-103.2019

[3] Hosni M, Abnane I, Idri A, de Gea JMC, Alemán JLF. (2019) Reviewing ensemble classification methods in breast cancer. Computer methods and programs in biomedicine, 177: 89-112.

[4] Dubois D, Prade, H. (2016) Practical Methods for Constructing Possibility Distributions. Int. J. Intell. Syst., 31: 215-239. https://doi.org/10.1002/int.21782

[5] Mohanaiah P, Sathyanarayana P, GuruKumar L. (2013) Image texture feature extraction using GLCM approach. International journal of scientific and research publications, 3(5): 1.

[6] Han J, Kamber M, Pei J. (2012) Data Mining Concepts and Techniques (3rd ed). USA: Elsevier Inc.

[7] Brereton R, Gavin L. (2010) Support Vector Machines for classification and regression. The Analyst. 135: 230-267. 10.1039/b918972f.

[8] Hamidinekoo A, Denton E, Rampun A, Honnor K, Zwiggelaar R. (2018) Deep Learning in Mammography and Breast Histology, an Overview and FutureTrends, Medical Image Analysis. doi:10.1016/j.media.2018.03.006.

[9] Sahiner B, Pezeshk A, Hadjiiski LM, Wang X, Drukker K, Cha KH, Summers RM, Giger ML. (2019).Deep learning in medical imaging and radiation therapy. Med Phys. 46(1):e1-e36. doi: 10.1002/mp.13264. Epub 2018 Nov 20. PMID: 30367497.

[10] Sechopoulos I, Teuwen J, Mann R. (2020) Artificial intelligence for breast cancer detection in mammography and digital breast tomosynthesis: State of the art. Seminars in Cancer Biology. https://doi.org/10.1016/j.semcancer.2020.06.002.

[11] Arcadu F, Benmansour F, Maunz A. Willis J, Haskova Z, Prunotto,M. (2019) Deep learning algorithm predicts diabetic retinopathy progression in individual patients. NPJ digital medicine, 2(1): 1-9.

[12] Wang H, Zheng B, Yoon SW, Ko HS. (2018) A support vector machine-based en- semble algorithm for breast cancer diagnosis, Eur. J. Oper. Res., 267: 687–699.
doi: 10.1016/j.ejor.2017.12.001.

[13] Huang, M-W, Chen C-W, Lin W-C, Ke S-W, Tsai C-F. (2017) SVM and SVM ensembles in breast cancer prediction, PLoS One 12: e0161501. doi: 10. 1371/journal.pone.0161501

[14] Tsirogiannis GL, Frossyniotis D, Nikita KS, Stafylopatis A. (2004) A meta-classifier approach for medical diagnosis, in: Methods Appl. Artif. Intell. pp 154–163.
doi: 10.1007/978- 3- 540- 24674-9_17.

[15] Tan AC, Gilbert D. (2003) Ensemble machine learning on gene expression data for cancer classification. Appl. Bioinform. 2 :1–10. doi: 10.1186/ 1471-2105-9-275.

[16] Janghel RR, Shukla A, Sharma S, Gnaneswar AV. (2014) Evolutionary ensemble model for breast cancer classification. doi: 10.1007/978-3-319-11897-0_2.

[17] Joanna J, Piotr J. (2008) GEP-induced expression trees as weak classifiers using gene expression programming to induce, in: Lect. Notes Comput. Sci., pp. 129–141.

[18] Schaefer G, Nakashima T. (2015) Strategies for addressing class imbalance in en- semble classification of thermography breast cancer features, in: 2015 IEEE Congr. Evol. Comput. CEC 2015 –Proc, pp. 2362–2367. doi: 10.1109/CEC. 2015.7257177.

[19] Lederman D, Wang XW, Zheng B, Sumkin JH, Tublin M, Gur D. (2011) Fusion of classifiers for REIS-based detection of suspicious breast lesions, in: Med. Imaging 2011 Image Perception, Obs. Performance, Technol. Assess., pp. 1–9. doi:79661c \ n10.1117/12.877368.

[20] Nguyen TT, Liew AWC, Tran MT, Pham XC, Nguyen MP. (2014) A novel genetic algorithm approach for simultaneous feature and classifier selection in multi classifier system, in: Proc. IEEE Congr. Evol. Comput. CEC 2014, pp. 1698–1705.
doi: 10.1109/CEC.2014.6900377.

[21] Ghorai S, Mukherjee A, Sengupta S, Dutta PK. (2011) Cancer classification from gene expression data by NPPC ensemble, IEEE/ACM Trans. Comput. Biol. Bioinform. 659–671, doi: 10.1109/TCBB.2010.36.

[22] Ferri C, Hernández-Orallo J, Modroiu R. (2009) An experimental comparison of per- formance measures for classification, Pattern Recognit. Lett., 30: 27–38.
doi: 10.1016/j.patrec.2008.08.010.

[23] Davis J, Goadrich M. (2006) The relationship between precision-recall and ROC curves, in: Proc. 23rd Int. Conf. Mach. Learn.

[24] Zaidan AA, Ahmad NN, Abdul Karim H, Larbani M, Zaidan BB, Sali A. (2014) On the multi-agent learning neural and Bayesian methods in skin detector and pornography classifier: An automated anti-pornography system. Neurocomputing, 131: 397-418.
https://doi.org/10.1016/j.neucom.2013.10.003.

[25] Alamoodi, A. H.; Garfan, Salem; Zaidan, B. B.; Zaidan, A. A.; Shuwandy, Moceheb Lazam; Alaa, Mussab; Alsalem, M. A.; Mohammed, Ali; Aleesa, A. M.; Albahri, O. S.; Al-Hussein, Ward Ahmed; Alobaidi, O. R. (2020). A systematic review into the assessment of medical apps: motivations, challenges, recommendations, and methodological aspect. Health and Technology, (), doi:10.1007/s12553-020-00451-4

AN IMMERSIVE AUGMENTED REALITY SYSTEM TO STUDY THE EFFICIENCY OF DYNAMIC EXIT SIGNAGE

AZHAR MOHD IBRAHIM[*], MUHAMMAD ARIF KAMARUDDIN
AND AZNI NABELA WAHID

*Department of Mechatronics Engineering, International Islamic University Malaysia,
Jalan Gombak, 53100 Kuala Lumpur, Malaysia*

[*]Corresponding author: azhar_ibrahim@iium.edu.my

ABSTRACT: Every year, many disasters occur to buildings causing their destruction and leading to huge casualties. One way of preventing casualties is by evacuation drill activity. Although accurate evacuation drills could enhance the efficiency of the process during the real event, these drills are not fully effective because participants miss the sense of being stressed or under pressure while in action. Several gaming concepts have been introduced to train the participants on how to cope with and evacuate effectively during an emergency. For instance, Augmented Reality (AR) and Virtual Reality (VR) interfaces could provide virtual content to enhance the effectiveness of evacuation drills. However, accurate representation of different evacuation scenarios and its impact analysis during emergency using the above technologies are still debatable, mainly due to immersion quality. Thus, this study proposes an Immersive Augmented Reality (IAR) application that is mainly the amalgamation of AR and VR in realizing fast and safe evacuation during on-site building emergencies. A virtual dynamic exit signage system is also developed in the proposed "Smart Evacuation application". This work evaluated the efficiency of a virtual dynamic exit signage and also a proposed "Smart Evacuation" system by analysing on-site emergency evacuation processes. By setting up various scenarios imitating real life disasters, this research analysed the time taken and level of stress of the occupants during the evacuation of a chosen site. The proposed "Smart Evacution" achieved 33.82% better perfomance compared to normal evacuation thus indicating a faster and safer evacuation.

ABSTRAK: Secara statistik, kebanyakan bencana kemusnahan bangunan yang berlaku setiap tahun telah menyebabkan kerugian besar. Salah satu cara bagi mengelak kejadian ini adalah melalui aktiviti latih tubi evakuasi. Walaupun latih tubi evakuasi ini dapat menambah proses kecekapan semasa kejadian sebenar, latih tubi ini tidak benar-benar berkesan kerana peserta kurang mendalami perasaan tertekan atau di bawah tekanan semasa kejadian. Pelbagai konsep permainan telah diperkenalkan bagi melatih peserta bagaimana perlu bertindak dan evakuasi secara efektif semasa kecemasan. Sebagai contoh, antarmuka Realiti Terimbuh (AR) dan Realiti Maya (VR) mungkin dapat menghasilkan simulasi secara maya bagi menambah keberkesanan latih tubi evakuasi. Walau bagaimanapun, ketepatan representasi pelbagai senario evakuasi dan analisis tekanan semasa kecemasan menggunakan teknik-teknik di atas adalah masih boleh dipertikaikan terutama kerana kualiti kedalamannya. Oleh itu, kajian ini mencadangkan aplikasi Realiti Terimbuh Mendalam (IAR) di mana tumpuan adalah pada kombinasi AR dan VR dibuat dengan secara evakuasi pantas dan selamat semasa kecemasan pada bangunan kejadian. Sistem maya penunjuk arah keluar dinamik turut dicipta dalam "Aplikasi Evakuasi Pintar" yang dicadangkan ini. Kajian ini menilai keberkesanan sistem maya penunjuk arah keluar secara dinamik dan juga sistem "Evakuasi Pintar" dengan menganalisa proses evakuasi

kecemasan pada tempat kejadian. Dengan mengadakan pelbagai jenis senario dan meniru bencana sebenar, kajian ini menganalisa masa yang diambil dan tahap tekanan penghuni bangunan semasa proses evakuasi berlaku pada tapak pilihan. "Evakuasi Pintar" ini mencapai 33.82% keberkesanan pada prestasi berbanding evakuasi biasa. Ia membuktikan proses evakuasi ini lebih pantas dan selamat.

1. INTRODUCTION

Signages or legends have been used in various locations to aid people in recognizing their location, for navigation, for immediate notices, and other purposes. The most crucial signage that every building should install is the exit signage that is made compulsory by the Occupational Safety and Health Administration (OSHA) and the National Fire Protection Association (NFPA). In its guideline, OSHA states that "Exit signs must be clear of decorations, equipment which may impair visibility to means of an exit. Access to exits must be marked by visible signs in all cases where the exit or way to reach it is not immediately visible to the occupants" [1]. However, most of the time during emergency situations, such as natural disaster or fire, these exit signages lose their functionality due to the damage incurred by the event that caused visual impairment to the occupants. In addition, these static signages have fixed images that are unable to react to the immediate situation, possibly causing the evacuees to choose a dangerous route. A research conducted by the Fire Safety Engineering Group of The University of Greenwich found that only 38% of evacuees saw the emergency signage during the emergency situations, which shows the low effectiveness of the sign. From those numbers, 100% of them will obey the sign immediately although they did not confirm whether the designated path is safe or not [2].

Due to the incompetence of the signage during emergency, a lot of accidents and casualties have been recorded throughout the years when the occupants were trapped, suffocated, stampeded by a panicked crowd, etc. The US Fire Administration recorded that from 2013 to 2015, the number of fire fatalities from 1800 fatal fires in residential buildings was around 2695 civilians [3]. In China, the average number of fire fatalities for each year hit around 2500 people while the fire incidents occurred around 140 000 to 260 000 times every year [4]. In Malaysia, it has been recorded that fire incidents occurred to 1024.67 per 1 000 000 population for each year between 2006-2015. Fire fatalities have been recorded at around 7.53 for each 1 000 000 population per year. The record also shows that there is an increasing trend of about 30% of fire victims from 2012 to 2014 [5].

One of the main problems during evacuation management is dynamic human behavior, which is unpredictable and difficult to calculate. Various researchers have done numerous experiments and data collecting from surveillance video and surveys to grasp the understanding of human behavior in crowd [6]. For safety purposes during real data collection, theoretical analysis via simulations are normally conducted to analyze unforeseen problems during the evacuation. However, the problem with simulation is that it lacks immersion and understanding of real scenarios causing varying reactions and behaviors and thus affecting the result of the studies [7-9]. Another fundamental problem during evacuation is unfamiliarity with the structure of the building, which slows down movement to the exit. The presence of legends around the building plays a big role to lead those people, however, during the real event, the visibility of the signs will be hindered and therefore misleading [10].

Augmented Reality has indeed served humans in improving their abilities to do tasks. The wide range of AR capabilities in various sectors shows its competency and importance to the developed community. Among those, AR plays a major role for certain industries to achieve their objectives i.e. safety inspection, hazard identification and safety training [11]. Augmented Reality (AR) interfaces could provide virtual content to enhance the effectiveness of evacuation drills. However, accurate representation of different evacuation scenarios and its impact analysis during emergencies using AR is still debatable, mainly due to immersion quality. Thus, this research aims to develop an Immersive AR application with dynamic signage function that can guide building occupants to evacuate the building faster and safely. Besides that, this research also aims to study the effect of dynamic exit signage during an emergency toward the safety of evacuees and their evacuation time by using an augmented reality approach.

Here, we reviewed four recent AR based applications related to evacuation and navigation. First, "RescueMe" gave a good approach by connecting the application into a cloud server in which any real-time situation could be updated in an instant and thus notify the user on current condition of the building. The program created a 2D map of the building, which was designed by the developer beforehand, hence the existing map offered huge benefits to the user [12]. "MARA" on the other hand, used surrounding objects to guide the user during the evacuation. For every object, there was sign or legend image overlaid onto the object which led the user toward the right direction [13]. "MARA" also used user's feedback to analyze the effectiveness of the program. This method is a good approach to collect insights of the program for later improvement. "Mixed Reality Emergency Management" used a different practice as it mainly focused on simulated agents as a guide for users to follow [14]. By directing the smartphone onto the building structure, agents emerge into the real world via the smartphone screen and the user can follow these agents straight away a safe area is reached. Lastly, "IVR SGs" emphasized on disaster simulation to evaluate the human behavior during a crisis situation [15]. "IVR SGs" developed numerous realistic hazard situations such as falling desks or rooftops, simulated fire, falling debris to obstruct a pathway, and others. These models gave users experience on how to handle different hurdles during a catastrophe. In contrast, our proposed "Smart Evacuation" will focus on the efficiency of dynamic exit signages towards different evacuation scenarios to realize a higher probability of safe and fast evacuation.

2. METHODS

A mobile application called "Smart Evacuation" is introduced here (as shown in Fig. 1) and will be center of the research that all the research methodologies (as shown in Fig. 2 and Fig. 3) are based on. This application was developed using "Unity3D" and mainly uses an AR during most of its operation. The program consists of several main components that function to lead the user during the evacuation process. The components of such dynamic signage will overlay onto the existing signage to show the correct route from user's position toward the destination of either a safer area or an assembly point. Figure 1 shows examples of the "Smart Evacuation" application's icon and its interface.

The "Unity 3D 2018.4.23f1" engine is used as the main medium as it has built-in navigation mesh to create a surface for simulation of the agents. The realistic looking features provided by "Unity" is also a strong advantage as the modelled object in simulation should resemble its real-life counterpart as much as possible to help the user feel familiar in the augmented world.
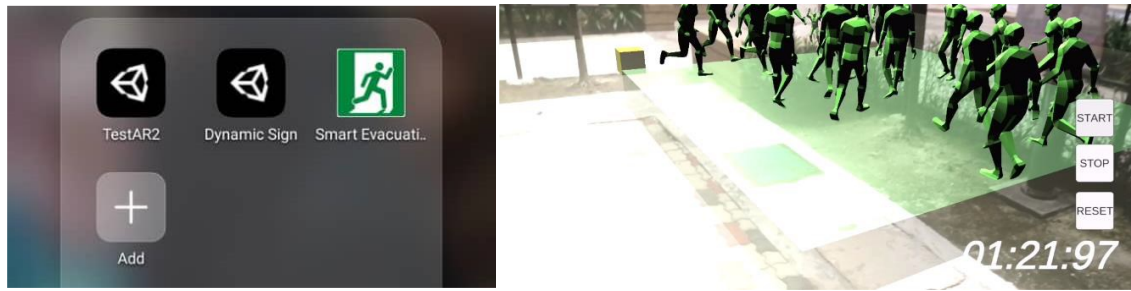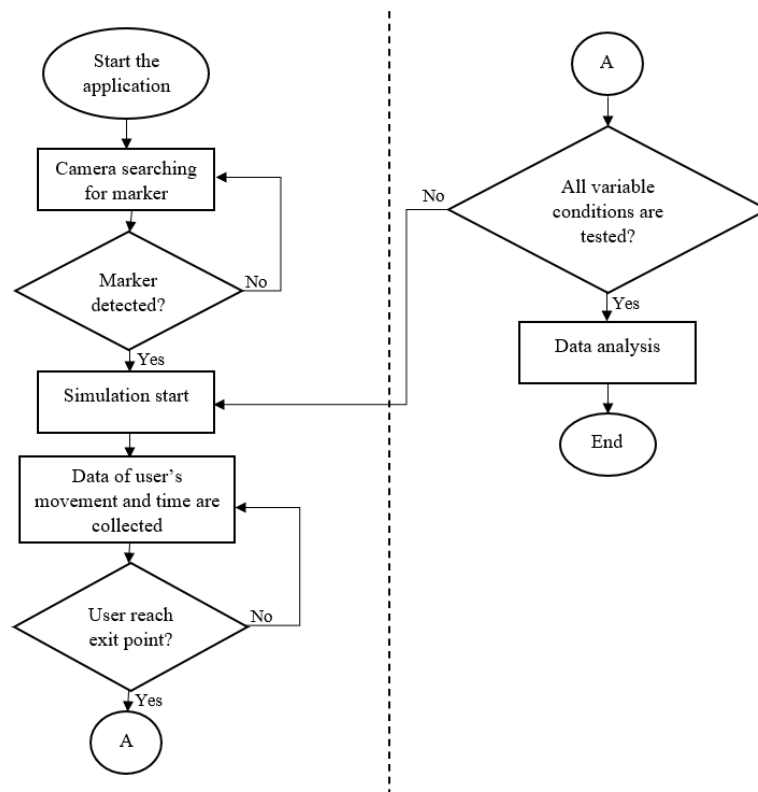
Fig. 1: Smart evacuation application.

Fig. 2: Process flow of the proposed method.

For the proposed "Smart Evacuation", there are several scripts of code that determine the evacuation movement flow. All scripts are designed for different "GameObjects" (fundamental objects in "Unity") such as timer function, marker detection function for signage and defining location function, but they are correlated with each other and served as one main process flows, as depicted in Fig. 3. The "GameObjects" agents have their own flow process that is not affected by other processes. The purpose of these agents is to create a visual evacuation scenario for the user in which the user could feel as if there are other people running to the safer place during the process. When the virtual environment is synchronized, agents will be generated onto the scene. Then, agents start running to the safe area. Upon reaching the safe area, agents will be in stand still motion indicating completion of their process flow in the proposed method. Meanwhile, the whole evacuation flow will end only when the user itself reaches the safe area.
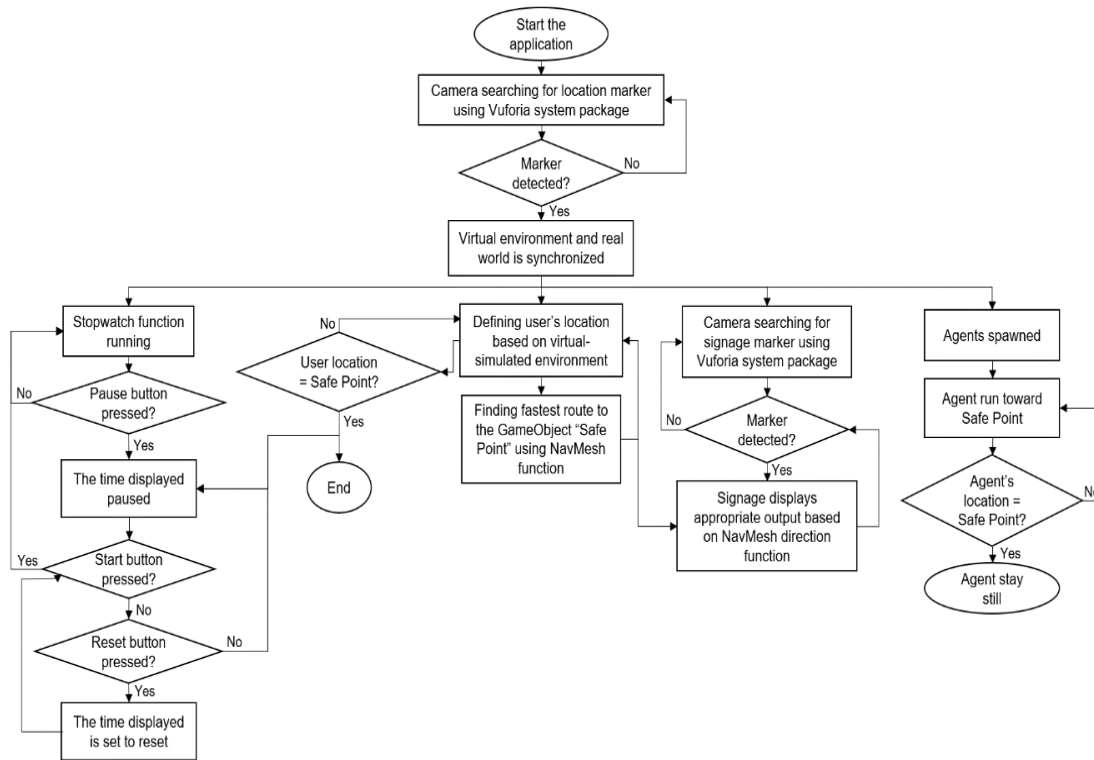
Fig. 3: Flow chart of the proposed Smart Evacuation.

2.1 Evacuation Simulation

To develop a realistic simulation of humans moving around the designated environment in "Unity", the pathfinding system is needed so that they only will move along to the desired path [16]. "Unity" provides two main features: Agents and Navigation Mesh. Agents are the objects that will move within the desired area while Navigation Mesh is the system that will indicate the walkable area for the agent. But before that, the environment of the simulation must be created first.

2.1.1 Floor Plan

Here, the simulation site used is the second floor of the E1 Engineering building in the International Islamic University Malaysia. This site has a suitable design with good movement flow and a decent amount of exit paths. The parameters of the hallways are also suited to the test where the width of the hallway is 3.44 m, which can fit about 2 agents with 0.5m of spacing between them. The size of the door is 1.81 m, which allows one agent to pass through it at a time. For the stairs, the width of the stairs is about 1.8 m. For the simulation, the design of the actual floor plan is modified to a simpler one due to the abundance of parts of the structure that are unrelated to the evacuation drill. The final design of the floor plan is shown in Fig. 4.

2.1.2 Agents

The developed Virtual Agents are designed to have similar body vectors to human bodies i.e. their movement is approximately similar to how human bodies move. They will then run according to their navigated path to imitate how normal residents would run towards the outside of the building when a disaster occurred.
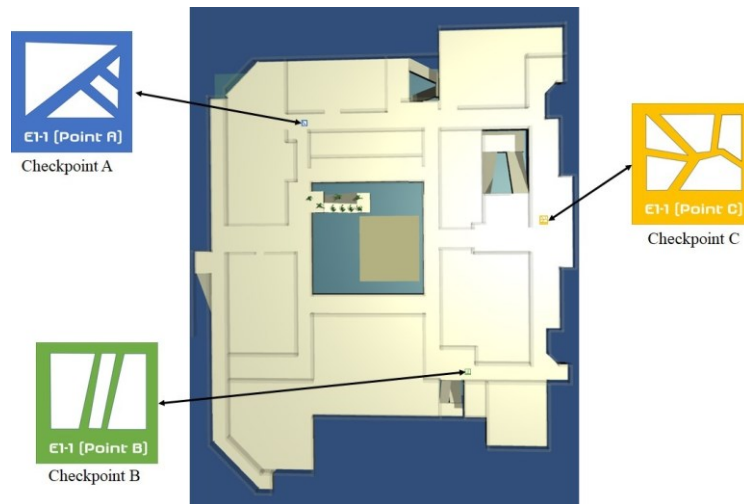
Fig. 4: Floor plan of the simulated environment according to the actual floor plan.

For the agent design, some standards had to be followed. These standards were necessary for the perfection of movement during the evacuation simulation to avoid any faults or errors, such as collisions. The standard suggested by Berg et al. [17] requires two circles around each agent; a reserved radius and a safety radius for collision avoidance purposes. All agents also should move at the same speed [17]. Thus, the agent speed is set at 1.43 ms^{-1} following the mean speed of human gait [18]. Figure 5 shows the "GameObject" of the agent where it is surrounded by a collider capsule, used for detecting another object that interacts with it which will trigger the programmed event. In this case, the capsule acts as collision avoidance, where the agent will stop moving if it enter another agent's parameter. The radius for the collider is 0.5 m while the height is set to 2 m.

Fig. 5: Capsule collision of agent.

2.1.3 Navigation Mesh

Navigation Mesh is provided by "Unity" 3D to help ease the developer in creating a pathfinder in a complex space for the simulation program. The Navigation Mesh or "Navmesh" also helps automatically program the agent so that it will avoid collisions with its environment. "Navmesh" is a 2D polygon mesh that defines a walkable area for the chosen agent. Agents can only walk or pass-through "Navmesh" areas in the simulation, no other areas.

The 'baked' function will automatically create the walkable surface for the agent, but the layer must first be set to differentiate what objects in the environment will be the surface

and what will be obstacle. After the execution of the 'baked' function, there will be a blue polygon filling up the surface, as seen in Fig. 6. In the figure, Object A is a wall (object) that agents cannot move through, that thus creates a room and hallway in the simulated environment. Area B is the limit boundaries created by "Navmesh" so that it has collision avoidance tolerance between the agent and wall. Surface C is the walkable area for the agent.
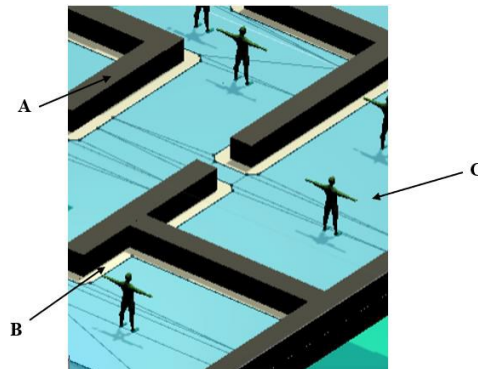

Fig. 6: 'Baked' Navmesh surface.

2.1.4 Marker Detection

This section will describe how the image tracking works. The processes are categorized into four phases, as shown in Fig. 7. The four phases include data collection, marker design, marker detection, and overlay process. The first phase is data collection, which is used to point out the problem on AR tracking. Pilet [19], in his research, mentioned that some features of the marker's surface that should accounted for are the geometry and texture. To make even tiny holes acceptable for the system, the continuity of the object surface must be emphasized. He also highlights that the camera angle towards the objects should be approximately 35 to 45 degrees for the determination of marker placement [19]. Thus, a marker-based type is chosen due to its ease of programming and its variety of source code that can lead to an infinity of outputs.

Fig. 7: Flow of image tracking phases.

Fig. 8: Exit sign marker with dimension.

In this work, Qualcomm Vuforia Software Development Kit (SDK) is chosen as the medium to program the augmented image due to its recognition compared to other tool software. For the second phase, internal structure of the program is designed. The image marker that will be tested is an Exit Sign. This signage is a normal exit sign with the word "EXIT" and a vector of a person running in green and white color (Fig. 8). This image will be printed on a paper with dimensions of 25 cm width and 12.9 cm height and will be used for image tracking tests later.

Fiala [20] stated that markers should be in hybrid semi-rigid arrays during the execution of ARTag marker-based detection on the objects with non-rigid surfaces. Thus, to create a specified array, the placement of marker must be paired with correct the alignment onto the surface. Hence, an image splitting method is used to extract the features of the exit sign.

Figure 9 shows how the image is extracted and the image is identified by its distinct features [20].

Fig. 9: The marker's features after extraction.

In phase three, the marker detection will be applied onto the surface. First, the marker will be registered into the system and the image will be saved into the system's database. The application then will give the most appropriate tracking method to detect the marker on the surface. The marker registration system is a method to define an image to be recognized by the system as an AR marker so that the application can recognize it. So, "Vuforia SDK" is an appropriate software to be used as it provides tracking features for natural feature marker-based detection. This software allows the programmer to use their own image to be the marker by storing the image as image target data in the target database of the system. Thus, this method provides unlimited input and variables for the programmers while it helps during image feature extraction by reducing the restrictions on the variety in marker representation.

Vuforia SDK is a built-in tool inside "Unity" 3D Engine software (refer Fig. 10). "Unity" will handle both the Vuforia image tracking system and AR camera functionality. The image from the extraction of the exit sign in the target database will be imported into "Unity". Then, the camera functionality will capture the image and send it to the tracker, frame by frame. The image will be converted from camera format to rendering and tracking format. Vuforia SDK tracker also has a computer vision algorithm that is able to recognize real-world objects in captured frames. Thus, from there, Vuforia is able to detect the markers from the target database and save it into the video renderer for later use.
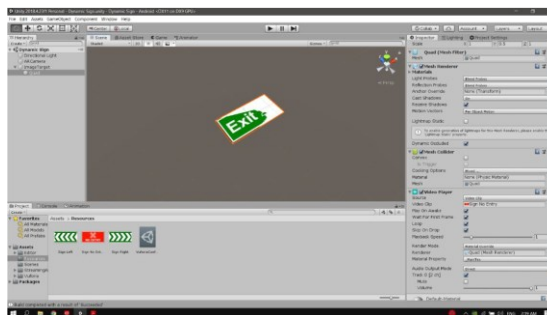

Fig. 10: "Unity" user interface with Vuforia SDK built-in.

In the last phase, the marker taken by the tracker will call the image stored in database and used it in the application code. The image is then layered by intended output layer according to the program code. Figure 11 shows some of the output layers that will aid the user in their evacuation. (a) No Entry; indicates that user should not advance onward or enter the space behind the door. This may be due to blockage from the disaster (such as fire or fallen debris) or due to the pathway onward being an unsuitable path to the safe area. (b) Go Right; indicates that user should proceed moving onto the right-side path to get to the safe area. (c) Go Left; as with Go Right, but the user should turn left. (d) Enter Here; user should enter the pathway of the sign or enter the room indicated by the sign. Finally, the application was installed into the smartphone from "Unity" software and tested and

evaluated. There are several aspects that were evaluated to specify the condition and limitation of the AR tracking from the coded program.
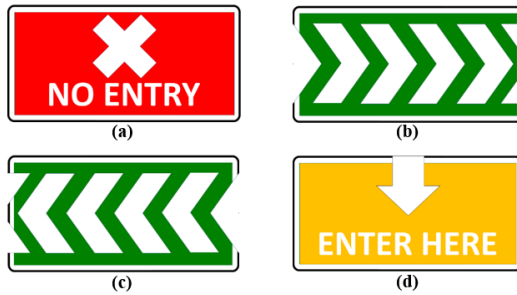
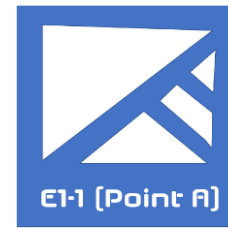

Fig. 11: Output sign of exit marker.

Fig. 12: Example of location detection-marker.

2.1.5 Location Detection Marker

Detection marker is used for initial start-up of the simulation. Figure 12 shows one of the location detector markers. By using the image tracking method as mentioned above, the image target is registered into the database and will be called out if the AR marker detection is able to track it. Thus, the image is applied as location detection that is used to identify the user's exact location in the building. Although current smartphones have built-in GPS, use of GPS is an unreasonable approach in detecting user exact location inside the building [21].

The image tracking-based location detection method is much simpler and gives a precise position. Firstly, the image target will be set in the "Unity" software and the image will be placed in the simulation at the desired positions. The chosen positions are based on a commonly used intersection, as shown in Fig. 13, so that no matter the user's location in the building, they can go to a marker's position in the shortest time. There will be different markers on each position so the AR can identify the location. Thus, for the chosen site floor map, there will be three detection-marker locations positioned around the site with logical and strategic reasoning.
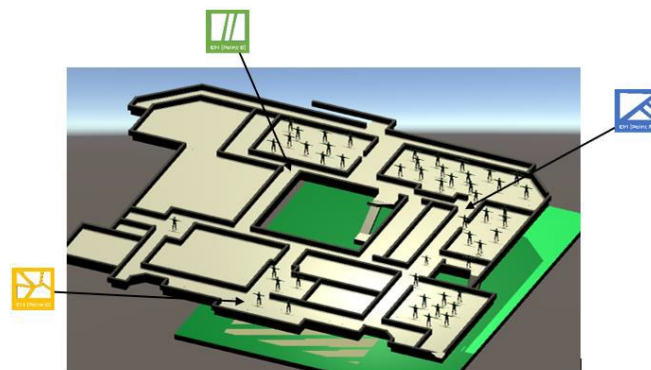
Fig. 13: The markers are placed around the building for user's convenience.

This method involves the synchronization of the marker's position between the simulation site and the real world. In "Unity", the marker is placed on the desired location. Then the real-world marker is placed on the same coordinate (refer to Fig. 14). By adjusting the scale, rotation and positioning of the marker, both markers are approximately synchronized. Thus, the wall and ground of the simulation are also synchronized with the real-world.

Fig. 14: The marker is placed in the simulated environment.

2.1.6 Implementation of Dynamic Signage

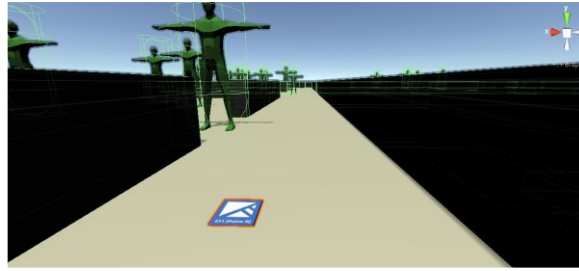The main purpose of the dynamic signage is to lead the occupants to the exit in the fastest way possible using an optimum safe path. In a real-life situation, fire break-out can happen anywhere within the building. For fire detection, a lot of fire detectors and alarms (such as heat detectors, smoke detectors, carbon monoxide detectors) are normally installed in rooms and hallways for the maximum detection. When any of the detectors detects the fire, a signal is sent to the fire alarm control panel, and then the alarm is triggered to notify the building occupants of the fire detection.

With the implementation of dynamic signage, the building will have a different fire alarm system, shown in Fig. 15. Each of the fire detectors in the building will be assigned one identification that will determine its own precise location to the control panel. Our proposed "Smart Evacuation" aims to provide the optimum navigation to lead the user to exit the building in the safest and fastest way possible. Thus, the dynamic signage will be pre-set manually by the designer on where to lead the user throughout the building. The presence of this dynamic signage will then be compared to the evacuation without dynamic signage during the simulation. The data for both methods of evacuation will be taken for analysis.
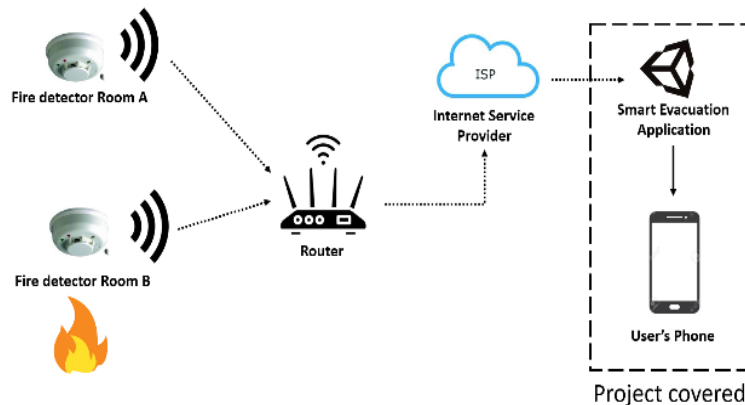
Fig. 15: Fire alarm system with dynamic signage system.

2.2 Available Safe Egress Time (ASET) and Required Safe Egress Time (RSET)

The Available Safe Egress Time, or ASET, and Required Safe Egress Time, or RSET, have been widely applied for fire safety assessment inside a building based on fire safety engineering design [22]. The basic idea of life safety in a building through designed safe egress is that the occupants will be safe if they are able to evacuate from the building before the fire is out of control or the space within the building is too hazardous for humans, t_{HAZ}. The human is expected to start the evacuation process following the detection of fire, t_{DET}

(fire alarm) which is subsequent to the fire breaking out. Thus, $\text{ASET} = t_{\text{DET}} - t_{\text{HAZ}}$ can be defined as the time between the detection of the fire and the hazard condition starting to prevail [23].

RSET, on the other hand, is interpreted as the time between the detection of the fire and the time the occupant successfully evacuates from the hazardous space. Thus, the life of occupant can be ensured safe if a building has a safe design with an RSET lower than its ASET [23]. The understanding of ASET and RSET is essential for fire safety assessment of a building. This research focused solely on the movement time of the occupant following their response to the alarm until they reach the safe exit.

3. RESULTS

3.1 Simulation in "Unity" Engine

To simulate the evacuation drill in the AR based simulation, the simulation will first be tested in "Unity" to monitor the evacuation flow of the agents. Upon starting, the agents will start running to the safe area. The collider cylinder will detect nearby agents and each agent will not invade another agent's parameters; thus, they will not collide or overlap. The agents' avoidance system will slow down their movement, thus leading to agent crowds and jammed pathways, as shown in Fig. 16. This situation is similar to real-life evacuations where lots of people moving in a single space creates a congested path. The safe area or assembly point is situated on the ground floor with a big rectangular area as depicted in Fig. 17.
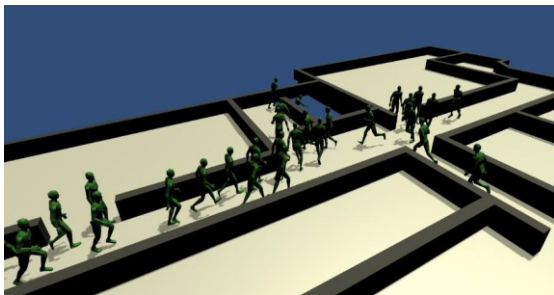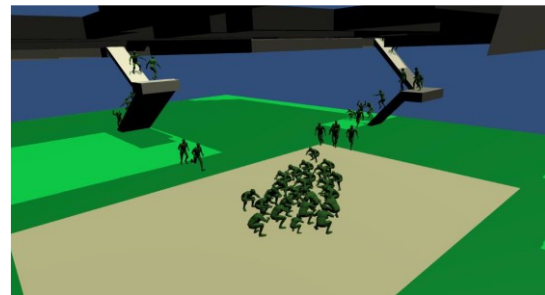

Fig. 16: Crowded area slowing the movement flow.

Fig. 17: Agents rushing to the safe area.

3.2 AR Based Simulation

To obtain the analysis of human behavior during the evacuation drill, the user should experience a situation as similar as possible to a real disaster. Thus, in this section, we will go further down to the actual AR application by using the smartphone to overlay the animated simulation into the real-world. Upon detecting the marker, the system will track the image by extracting the image features and fetching the description from the system database. Then the simulation environment, such as walls and floors, will be superimposed onto the real-world image. The real-world image is in real time as the camera is functioning and capturing the moment frame by frame.

The simulation will start automatically when the marker is detected, the user will experience the evacuation drill by seeing the virtual agents running through the real-world hallway, the fire spreading and the smoke obscuring the user's vision through the mobile app. When the animated environment is prepared and successfully overlaid, as in Figure 18, the simulation for the evacuation is ready.
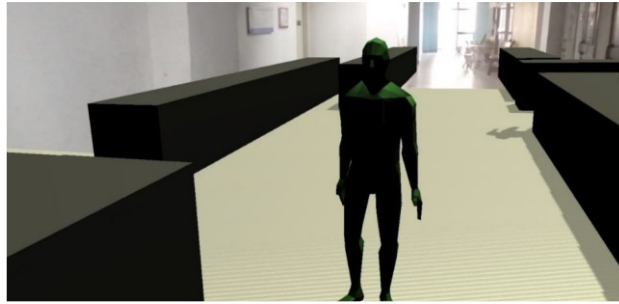
Fig. 18: Environment and agent are overlaid on the real-world image.

There are several aspects that will be evaluated in this research. The first aspect is the time taken for the evacuation. Upon starting at the location detection-marker, the user needs to go to the safe area immediately. The time will be recorded from the start of simulation until the user steps into safe area. A second aspect is the stress level of the user. The emotional strain of the users will be examined according to each area of the site. There are three checkpoints that will be analyzed, all three of which are located throughout the chosen site. For this simulation, the method of evacuation will be compared between a normal evacuation (the user will start from checkpoint and finish at the safe area without any assistance) and with AR Evacuation help (upon start, user will use the proposed application and check for the signage and follow the direction of the dynamic signage).

During the disaster, there will be numerous situations and unexpected accidents that may emerge and hinder the evacuees. Thus, in this simulation, there will be several scenarios that will be tested to evaluate on how human's reaction and behavior towards different kind of situations during the disaster. The chosen scenarios to be tested constitute the main factor contributing to fatalities during building evacuation such as low visibility, congested paths, and blocked paths.

3.2.1 Normal Scenario

For the first scenario, as seen in Fig. 19, there is not much additional hindrance to be put into the simulation except some of the agents running with the user. This scenario is to test the familiarity of the user toward the building's pathway and their knowledge of the evacuation path.

Fig. 19: Normal scenario with no additional obstacle.
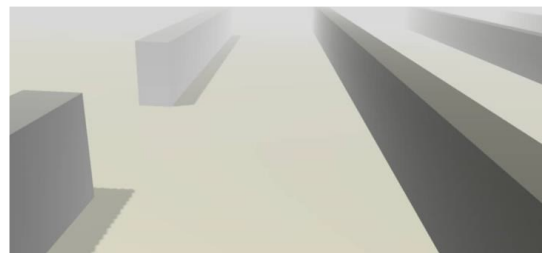
Fig. 20: Hazy environment causing low visibility to the user.

3.2.2 Low Visibility

For this scenario, the user will experience the low visibility problem (refer to Fig. 20). This is to resemble the smoke that emerges during the fire in the building. Besides the exposure of toxicity in the smoke, the high density level of the smoke can also lower people's visibility, thus making them harder to find the correct exit route [24]. The time taken, movement flow, and the level of stress of user will all be recorded.

3.2.3 Congested Path

This scenario is similar to the first scenario except that there are an additional 40 agents in the simulation. This high number of agents is to create a heavily congested pathway such as in Fig. 21, which is one of the main factors that slow people down when evacuating the building [3]. This scenario is to test on how the user will adapt and think critically on how to figure out the optimum path when each pathway is congested with agents.

Fig. 21: Congested path scenario.

3.2.4 Blocked Path

The path blockage scenario is one of the common incidents that can occur during fire breakout in a building. There will be some paths that are filled with fire and wreckage of the building, which could fully block and limit the evacuation route (refer Fig. 22). This test will evaluate how the user finds the available route when most of the paths are sealed off.
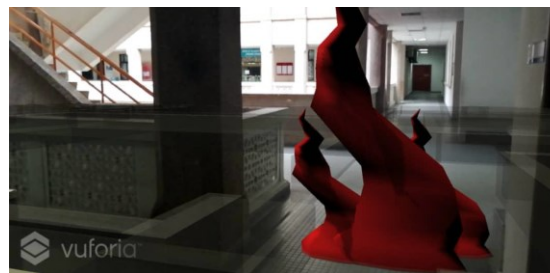

Fig. 22: Fire blocking the user from using a route.
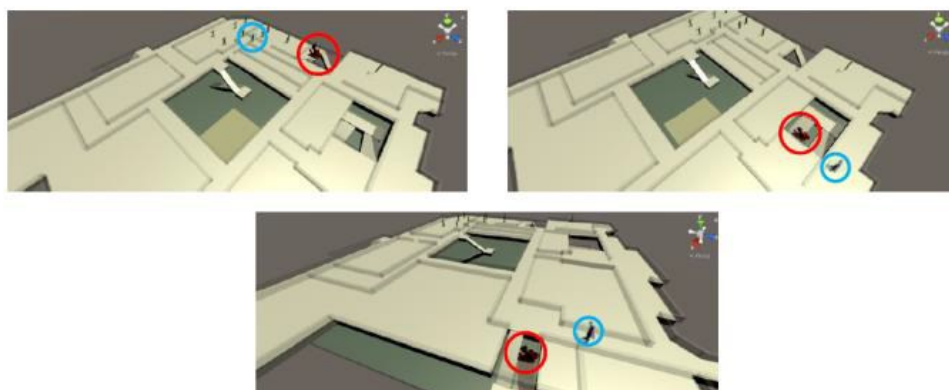

Fig. 23: Location of fire in Blocked Path scenario.

There are 3 different fire locations that will block the user's path relative to the starting point of the user. The location of fire (red circle) and the user's respective starting point (blue circle) are as seen in Fig. 23.

3.3 Participants

The experimental test will be done by three participants all of whom are 23 years old. All three participants are male with similar height and normal healthy bodies. So, the speed of each participant walking is approximately same. The value taken from the participants then will be averaged for the further analysis.

3.4 Time Taken

Time taken will start when the location detection-marker is detected and will stop when the user reaches the safe area. The results are shown in Table 1 below.

Table 1: Result for time taken for user to reach safe point (Please refer Fig. 3 for the location of Checkpoint A, B and C). The time unit is minute (m): second (s): millisecond (ms).

Normal Scenario

	Checkpoint A		Checkpoint B		Checkpoint C	
	Normal Evacuation (m:s:ms)	With AR (m:s:ms)	Normal Evacuation (m:s:ms)	With AR (m:s:ms)	Normal Evacuation (m:s:ms)	With AR (m:s:ms)
Participant 1	00:35:84	00:39:93	00:31:75	00:32:36	00:50:97	00:46:18
Participant 2	00:37:49	00:38:13	00:40:60	00:40:25	00:48:37	00:45:20
Participant 3	00:34:08	00:30:45	00:38:95	00:34:52	00:52:01	00:45:45
Average	**00:35:80**	**00:36:17**	**00:37:10**	**00:35:71**	**00:50:45**	**00:45:61**

Low Visibility

	Checkpoint A		Checkpoint B		Checkpoint C	
	Normal Evacuation (m:s:ms)	With AR (m:s:ms)	Normal Evacuation (m:s:ms)	With AR (m:s:ms)	Normal Evacuation (m:s:ms)	With AR (m:s:ms)
Participant 1	00:31:71	00:38:89	00:29:58	00:34:79	00:46:82	00:41:32
Participant 2	00:32:25	00:30:58	00:29:92	00:29:92	00:39:84	00:44:65
Participant 3	00:38:34	00:34:01	00:30:84	00:36:15	00:42:04	00:40:97
Average	**00:34:10**	**00:34:49**	**00:30:11**	**00:33:62**	**00:42:90**	**00:42:31**

Blocked Path

	Checkpoint A		Checkpoint B		Checkpoint C	
	Normal Evacuation (m:s:ms)	With AR (m:s:ms)	Normal Evacuation (m:s:ms)	With AR (m:s:ms)	Normal Evacuation (m:s:ms)	With AR (m:s:ms)
Participant 1	01:29:72	1:10:25	02:20:75	01:34:57	02:08:35	01:28:12
Participant 2	01:33:65	1:04:76	01:39:87	01:35:35	01:42:15	01:39:98
Participant 3	01:33:22	1:02:84	02:46:52	01:44:58	02:06:65	01:38:02
Average	**01:32:53**	**01:05:95**	**02:15:71**	**01:38:17**	**01:59:05**	**01:35:37**

Congested Path

	Checkpoint A		Checkpoint B		Checkpoint C	
	Normal Evacuation (m:s:ms)	With AR (m:s:ms)	Normal Evacuation (m:s:ms)	With AR (m:s:ms)	Normal Evacuation (m:s:ms)	With AR (m:s:ms)
Participant 1	00:39:74	00:36:53	00:34:99	00:29:12	00:42:82	00:37:39
Participant 2	00:25:31	00:37:15	00:36:49	00:33:41	00:37:17	00:41:58
Participant 3	00:28:56	00:25:24	00:27:30	00:29:27	00:46:88	00:42:28
Average	**00:31:20**	**00:32:97**	**00:32:93**	**00:30:60**	**00:42:29**	**00:40:42**

3.5 Level of Stress

To calculate the level of stress for each scenario, the user will be immediately asked some questionnaire (refer to Appendices A and B) after completing the experimental test.

The survey will be used to evaluate the level of stress upon going through the evacuation drill. The survey is based on the System Usability Scale (SUS) format where the answer ranges from (1) calm to (5) stress. The value of the response from all the question will be averaged to obtain the level of stress of the users (refer Table 2).

Table 2: Result data for level of stress analysis

Scenario		Participant 1	Participant 2	Participant 3	**Average**
Normal Scenario	Normal Evacuation	1.40	1.00	2.80	1.73
	With AR	**1.33**	**1.00**	**2.33**	**1.55**
Low Visibility	Normal Evacuation	2.20	1.60	3.60	2.47
	With AR	**1.83**	**1.16**	**2.00**	**1.66**
Blockage Path	Normal Evacuation	3.80	2.60	4.00	3.47
	With AR	**2.17**	**1.67**	**3.00**	**2.28**
Jammed Path	Normal Evacuation	1.60	2.60	3.00	2.40
	With AR	**1.50**	**1.83**	**2.33**	**1.89**

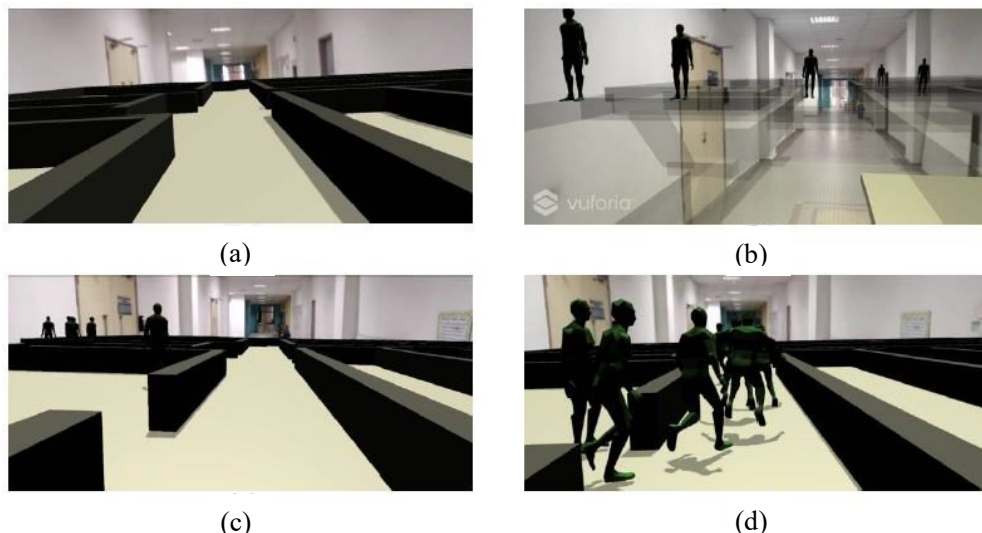## 5. DISCUSSION

(a)

(b)

(c)

(d)

Fig. 24: Various output of agents upon detecting marker.

Upon detecting the image, the application will superimpose the virtual simulation onto the real world in less than 1 second. The walls, ground, and agents are placed onto the scene and approximately synchronized with the real world's environment. The agents are randomly generated onto the scene although during the simulation in "Unity", the agents are perfectly spawned in their programmed locations and start running to safe area. During the AR simulation, there are four situations imposed during the initial start-up of the simulation, which can be seen in Fig. 24: (a) No agent is generated on the scene. (b) The agents are spawned but in wrong place (on the wall, in the sky, etc.). (c) Agents spawned on the right position, but their movement is wrong or there is no movement at all. (d) Perfect simulation where agents are spawned correctly and move according to the program. The

inconsistency of the agents spawned is related to how the camera is positioned during marker detection. Thus, the user needs to rescan the marker until that fourth case is obtained.

From simulation results for each scenario, the different values indicate how it affects the users differently. For the time taken to finishing the simulation, the average times taken for the participants are shown Figs. 25 and 26.

	Checkpoint A	Checkpoint B	Checkpoint C		Checkpoint A	Checkpoint B	Checkpoint C		Checkpoint A	Checkpoint B	Checkpoint C		Checkpoint A	Checkpoint B	Checkpoint C
		Normal Scenario				Low Visbility				Blocked Path				Jammed Path	
Normal Evacuation	35.8	37.1	50.45		34.1	30.11	42.9		92.53	135.71	119.05		31.2	32.93	42.29
AR	36.17	35.71	45.61		34.49	33.62	42.31		65.95	98.17	95.37		32.97	30.6	40.42

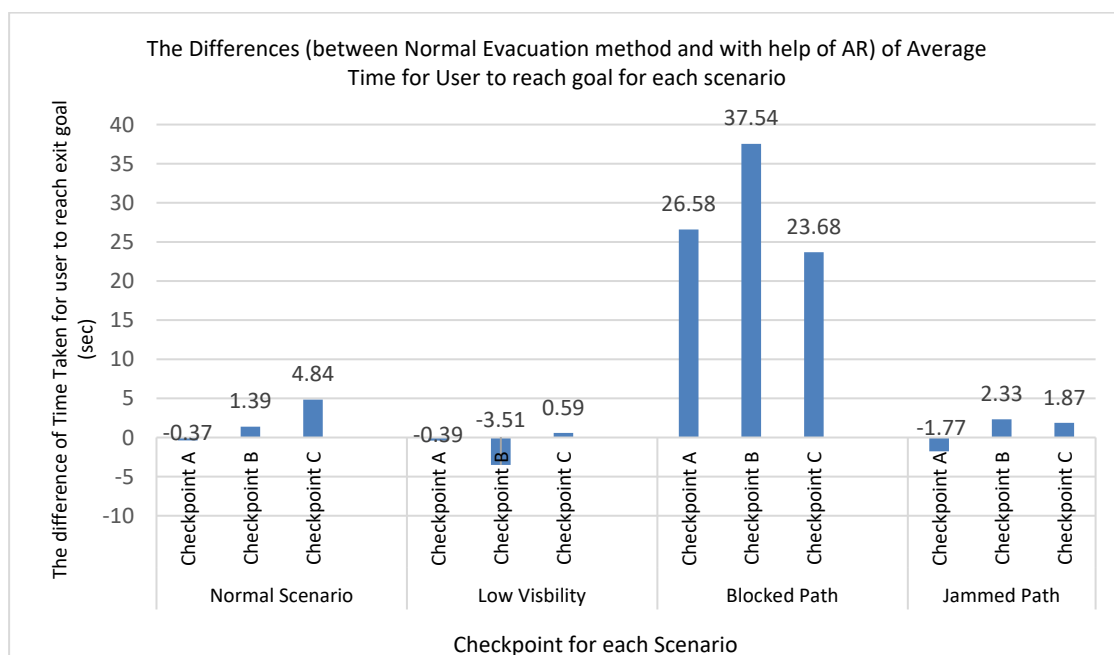Fig. 25: Average time taken for user to reach the safe area.

Fig. 26: Differences between normal evacuation method and with AR Evacuation method.

For a normal scenario, the time difference between the normal evacuation method versus the "Smart Evacuation" application is small. This is due to the high familiarity level of the three participants toward the simulation site i.e. they are aware of the fastest route to the safe area, which led them to use the same route that proposed by the AR without any difficulty. For the low visibility scenario, as the simulation of smoke was only displayed in

the phone screen, participants could still see the real-world route that was still clear without any smoke. This scenario also leads to the same result as our first scenario where the differences of time for each checkpoint are relatively small. The jammed path scenario also faced a similar situation as the packed agents in the simulation did not affect the participants as the small screen of phone could not affect the human's wide field of view. The participants still see the clear real-world's hallway without any agents, as illustrated in the Fig. 27.
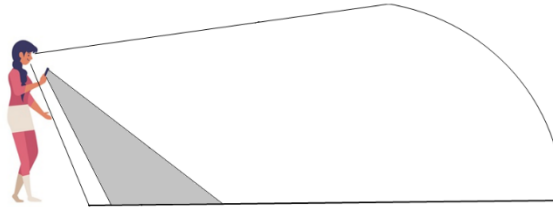

Fig. 27: Human field of vision (white) versus area covered by smartphone (grey).

For these types of scenarios, it is best for the participant to use AR head gear, so the user's field of vision is fully enclosed with the AR display. Lastly, for the blocked path scenario, we can see the huge differences in the time taken which using the 'Smart Evacuation" application led the participant faster to the exit compared to the normal evacuation method. Although the high level of familiarity of the participants toward the site simulation, they did not anticipate the location of simulated fire that blocked their path thus leading them onto the wrong path and making several turns to reach the safe area. With the big gap of differences in time between the two methods, this proved that the 'Smart Evacuation" application was a huge help to lead the user to safe area faster. In general, the efficiency of the Smart Evacuation application can be calculated as

$$Performance = \frac{1}{Execution\ time}. \tag{1}$$

The performance value is then ratioed between the two methods; Normal evacuation and evacuation with Smart Evacuation application.

$$\%\ Performance = \frac{Actual\ performance}{Possible\ performace} \times 100 \tag{2}$$

Taken from blocked path scenario data in Table 1, the average time taken for three checkpoints for normal evacuation and evacuation with Smart Evacuation apps are 115.76s and 86.50s, respectively. The performance of both can be calculated with Equation (1), thus we obtain 0.008639 and 0.011561 respectively. Equation (2) is used to calculate the efficiency of the Smart Evacuation compared to normal evacuation,

$$Efficiency\ of\ Smart\ evacuation\ performance = \frac{0.011561}{0.008639} \times 100$$
$$= 133.82\ \%$$

Thus, for the blocked path scenario, Smart Evacuation has a 33.82% better performance compared to normal evacuation.

On the other hand, for level-of-stress analysis (refer to Fig. 28), the 'Smart Evacuation" application proved to give less stress to the user compared to the normal evacuation method. With the range of 5 from 1 (calm), 2 (somewhat calm), 3 (normal), 4 (somewhat stress) and 5 (stress), the average level of stress for the normal scenario, low visibility, blocked path, and jammed path with help of AR is 1.55, 1.6, 2.28, and 1.89 respectively, which are lower than the normal evacuation method (1.73, 2.47, 3.47, and 2.4, respectively). This

demonstrates that the 'Smart Evacuation" application aids in lowering the stress of the user during the emergency evacuation.
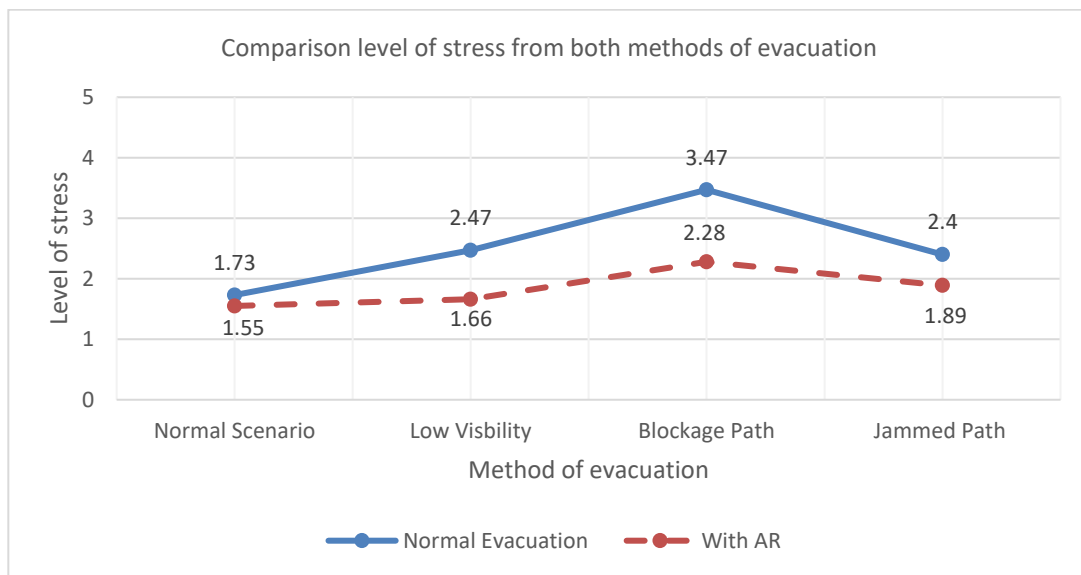

Fig. 28: Differences in stress level between the two methods of evacuation.

6. CONCLUSION

This research proposed an Immersive Augmented Reality (IAR) application for assisting in the evacuation process during building emergencies. With the inclusion of virtual dynamic exit signage, the performed simulation was able to give the desired result for data analysis on human behavior during evacuation drills. During the progression of the research, there are some limitations and flaws that can be pointed out in this study. The limitation of the materials in studying human behavior gives a big impact in obtaining an accurate result. For example, the unavailability of devices and programs for level-of-stress readings for the simulation's user causes the developer to use alternate methods that depend on survey and questionnaire data. Based on the result data obtained after the simulation, there are still many flaws in the result due to the incompetence of various factors during the research. Overall, the implementation of augmented reality of dynamic signage still gives a distinct outcome for some cases, which proves the efficiency of the proposed method. The main application of this proposed "Smart Evacuation" is that it can be used for real-life on-site emergency situations in assisting evacuees to reach a safer area faster. Besides that, the proposed application can also be used for on-site evacuation training purposes. Furthermore, the authority of a building can use the proposed application in analyzing movement time for the calculation of RSET, which can be used for the Fire Safety Assessment of the building.

The causes of error in the simulation results are as follows:

I. Asynchronization of the simulation world with the real world due to a small margin of error in the placement of the marker.
II. Poor built-in motion tracker of the device that could not detect the floor and the wall of the real world perfectly.
III. Agent placement error on the Navmesh surface that causes the agent to start moving weirdly.
IV. Lighting issues during the signage scanning.

V. The familiarity of the user with the chosen site did not much affect some testing scenarios such as the smoke scenario, the normal scenario, and the jammed path scenario.

For future work, the errors above could be restored and some possible improvements that could be made include:

I. Readjusting the location detection-marker and considering the perspective view where the far object will be seen as smaller.
II. Recheck every agent on the simulation site so that its collision detection does not overlap.
III. Use a more complex building for the simulation test so the difference between each scenario will be much noticeable.
IV. Use of AR device headgear so that the user will have 100% field of vision based on the AR display.
V. Use of a variety of participants with different heights, backgrounds, or ages.

ACKNOWLEDGEMENT

REFERENCES

[1] ESW exit sign warehouse. Available: https://www.exitsignwarehouse.com/pages/exit-sign-regulations-requirements.
[2] Hui X, Galea ER, Lawrence PJ (2014). Experimental and survey studies on the effectiveness of dynamic signage systems. Fire Safety Science, 11: 1129-1143. doi: 10.3801/IAFSS.FSS.11-1129.
[3] Civilian fire fatalities in residential buildings (2008-2010). Available: https://nfa.usfa.fema.gov/downloads/pdf/statistics/v13i1.pdf.
[4] Wang F, Lu S, Li C (2005). Analysis of fire statistics of China: Fire frequency and fatalities in fires. In Proceedings of the eighth international symposium on fire safety science, IAFSS: 353-362. doi: 10.3801/IAFSS.FSS.8-353.
[5] Tan YR, Akashah FW, Mahyuddin N (2012). The analysis of fire losses and characteristics of residential fires based on investigation data in Selangor. In MATEC Web of Conferences, 66: 00109.
[6] Kinateder M, Wirth TD, Warren WH (2018). Crowd dynamics in Virtual Reality. Crowd Dynamics, 1: 15-36.
[7] Warren WH (2018). Collective motion in human crowds. Current directions in psychological science, 27(4): 232-240.
[8] Nizam M, Ibrahim AM (2020). Augmented Reality-Based Evacuation Simulation To Study Crowd Behaviors. International Journal of Advanced Research in Engineering and Technology (IJARET), 11(10): 374-383.
[9] Ibrahim AM, Saifullah M, Romlay MRM, Venkat I (2019). Hybrid Social Force-Fuzzy Logic Evacuation Simulation Model for Multiple Exits. In 2019 7th International Conference on Mechatronics Engineering (ICOM): 1-5.
[10] Chen X (2006). Microsimulation of evacuation strategies. Ph.D. thesis, Texas State University San Marcos.
[11] Li X, Yi W, Chi HL, Wang X, Chan APC (2018). A critical review of virtual and augmented reality (vr/ar) applications in construction safety. Automation in Construction, 86: 150-152.
[12] Ahn J, Han R (2012). An indoor augmented-reality evacuation system for the Smartphone using personalized Pedometry. Human-Centric Computing and Information Sciences, 2(1): 1-23.

doi: 10.1186/2192-1962-2-18.

[13] Stigall J, Sharma S (2019). Evaluation of mobile augmented reality application for building evacuation. In Proceedings of 28th International Conference, 64: 109-118.

[14] Lochhead I, Hedley N (2019). Mixed reality emergency management: bringing virtual evacuation simulations into real-world built environments. International journal of digital earth, 12(2): 190-208. doi: 10.1080/17538947.2018.1425489.

[15] Feng Z, González VA, Amor R, Spearpoint M, Thomas J, Sacks R, Lovreglio R, Cabrera-Guerrero G (2020). An immersive virtual reality serious game to enhance earthquake behavioral responses and post-earthquake evacuation preparedness in buildings. Advanced Engineering Informatics, 45: 101118.

[16] Kristinsson KV (2015). Social Navigation in Unity 3D. M.Sc. Project Report, Reykjavík University.

[17] van den Berg J, Guy SJ, Lin M, Manocha D (2012). Reciprocal collision avoidance for multiple mobile robots. In IEEE International Conference on Robotics and Automation: pp. 1–16.

[18] Bohannon RW, Andrews AW (2011). Normal walking speed: a descriptive meta-analysis. Physiotherapy, 97(3): 182-189.

[19] Pilet J (2008). Augmented reality for non-rigid surfaces. Doctoral Dissertation. Available: http://www.hvrl.ics.keio.ac.jp/~julien/publi/PiletPhd.pdf.

[20] Fiala M (2007). Magic mirror system with hand-held and wearable augmentations. In 2007 IEEE Virtual Reality Conference: 251-254.

[21] Wu C, Yang Z, Xu Y, Zhao Y, Liu Y (2014). Human mobility enhances global positioning accuracy for mobile phone localization. IEEE Transactions on Parallel and Distributed Systems, 26(1): 131-141.

[22] Poon SL (2014). A dynamic approach to ASET/RSET assessment in performance based design. Procedia Engineering, 71: 173-181.

[23] Cooper LY (1983). A concept for estimating available safe egress time in fires. Fire Safety Journal, 5(2): 135-144.

[24] Alarifi AAS, Phylaktou HN, Andrews GE (2016). What kills people in a fire? heat or smoke? In the 9th Saudi Students Conference, University of Leeds. Available: https://eprints.whiterose.ac.uk/96795/1/Alarifi%20SSC9%20What%20Kills%20people%20in%20a%20Fire%20Heat%20or%20Smoke%20(final%20version)%20-corrected.pdf.

APPENDIX A:
STRESS DATA SURVEY USING GOOGLE FORM

APPENDIX B:
RESULT FOR LEVEL OF STRESS SURVEY USING GOOGLE FORM

Please choose your participant number	Scenario	Method of evacuation	Early confusion when experiencing simulated drill during initial simulation	Finding the safest route	The agents running through hallway	The chaotic surrounding (smoke and fire)	After the simulation	Problem with detecting signage (For AR only)
Participant 1	Normal Scenario	Normal evacuation	2	1	1	1	2	
Participant 1	Normal Scenario	With help of AR	1	1	2	1	2	1
Participant 1	Low Visibility	Normal evacuation	3	2	1	3	2	
Participant 1	Low Visibility	With help of AR	3	2	1	2	2	1
Participant 1	Blocked Path	Normal evacuation	4	5	2	5	3	
Participant 1	Blocked Path	With help of AR	3	2	2	2	2	2
Participant 1	Jammed Path	Normal evacuation	2	1	2	1	2	
Participant 1	Jammed Path	With help of AR	2	1	2	1	2	1
Participant 2	Normal Scenario	Normal evacuation	1	1	1	1	1	
Participant 2	Normal Scenario	With help of AR	1	1	1	1	1	1
Participant 2	Low Visibility	Normal evacuation	3	1	1	1	2	
Participant 2	Low Visibility	With help of AR	2	1	1	1	1	1
Participant 2	Blocked Path	Normal evacuation	3	5	1	2	2	
Participant 2	Blocked Path	With help of AR	3	1	1	1	2	2
Participant 2	Jammed Path	Normal evacuation	3	1	4	3	2	
Participant 2	Jammed Path	With help of AR	2	2	2	2	2	1
Participant 3	Normal Scenario	Normal evacuation	3	3	4	1	3	

COMPUTATIONLESS PALM-PRINT VERIFICATION USING WAVELET ORIENTED ZERO-CROSSING

JITENDRA PRABHAKAR CHAUDHARI[1*], HIREN KANTILAL MEWADA[2]
AMIT VINUBHAI PATEL[1], KEYUR KAMALDASJI MAHANT[1],
ALPESH DUDABHAI VALA[1]

[1]*CHARUSAT Space Research and Technology Centre,
Department of Electronics and Communication Engineering, CSPIT,
Charotar University of Science and Technology , Changa, Gujarat, India*
[2]*Department of Electrical Engineering, Prince Mohammad Bin Fahd University,
Kingdom of Saudi Arabia*

*Corresponding author: jitendrachaudhari.ec@charusat.ac.in

ABSTRACT: Palmprints can be characterized by their texture and the patterns of that texture dominate in a vertical direction. Therefore, the energy of the coefficients in the transform domain is more concentrated in the vertical sideband. Using this idea, this paper proposes the characterization of the texture features of the palmprint using zero-crossing signatures based on the dyadic discrete wavelet transform (DWT) to effectively identify an individual. A zero-crossing signature of 4 x 256 was generated from the lower four resolution levels of dyadic DWT in the enrolment process and stored in the database to identify the person in recognition mode. Euclidean distance was determined to find the best fit for query palmprints zero-crossing signature from the dataset. The proposed algorithm was tested on the PolyU dataset containing 6000 multi-spectral images. The proposed algorithm achieved 96.27% accuracy with a lower recognition time of 0.76 seconds.

ABSTRAK: Pengesan Tapak Tangan boleh dikategorikan berdasarkan ciri-ciri tekstur dan corak pada tekstur yang didominasi pada garis tegak. Oleh itu, pekali tenaga di kawasan transformasi adalah lebih penuh pada jalur-sisi menegak. Berdasarkan idea ini, cadangan kajian ini adalah berdasarkan ciri-ciri tekstur pada tapak tangan dan tanda pengenalan sifar-silang melalui transformasi gelombang kecil diadik yang diskret (DWT) bagi mengecam individu. Pada mod pengecaman, tanda pengenalan sifar-silang 4 x 256 yang terhasil daripada tahap diadik resolusi empat terendah DWT digunakan dalam proses kemasukan dan simpanan di pangkalan data bagi mengenal pasti individu. Jarak Euklidan yang terhasil turut digunakan bagi memperoleh padanan tapak tangan paling sesuai melalui tanda pengenalan sifar-silang dari set data. Algoritma yang dicadangkan ini diuji pada set data PolyU yang mengandungi 6000 imej pelbagai-spektrum. Algoritma yang dicadangkan ini berjaya mencapai ketepatan sebanyak 96.27% dengan durasi pengecaman berkurang sebanyak 0.76 saat.

KEYWORDS: *multi-scale edge detection; palmprint recognition; feature extraction*

1. INTRODUCTION

People authentication is now a necessity in the digital world. Biometric-based identification is considered to be a most reliable system for protection and reliable authentication. In the current mechanization era, artificial intelligence systems prepare

data about everything and use it to solve several complex problems. Although many organizations have built state of the art security systems, recent terrorist attacks have uncovered significant vulnerabilities in complex security schemes. Consequently, various organizations look to the uniqueness of each human body to establish information frameworks, often called biometrics, because they are more "real" or more difficult to counterfeit. Automatic personal identity recognition can be accomplished through the use of different biometric identifiers. In many biometric baseline systems, anatomical individuality such as thumbprints, fingerprints, and morphology of the iris, retina, head, nose, or hand or behavioral characteristics such as signature, keystroke mechanics, and gait are used for identification. Each biometric innovation has its own particular merits and constraints, and therefore no system exists with better performance for all applications [1].Biometric System, which uses the iris, is one of the mainstream biometric frameworks with exceptionally high precision [2]. Since the iris acquisition method is costly, it requires very high cooperation from the user and has a high failure rate of enrolment. Because of their simplicity, good accuracy, and low cost, face and finger print recognition have gained a large popularity. However, the present COVID situation makes these systems fail from occlusion due to masks hiding the facial features and frequent sanitization reducing the fingerprint features [3]. Recently, a hand geometry-based identification has been proposed in [4]. However, this system is tedious, sensitive to the acquisition process, and computationally complex. New emerging ear trait recognition is explained in [5]. Mewada et al. [5] used CNN for learning and discriminating between ear features. A moving human leg angle-based gait recognition system, explained in [6], uses average statistical features of eight frames.

A palmprint-based identification system has many advantages compared to other biometric systems: 1) Hand features of the human have high stability and uniqueness. 2) For data, acquisition needs extremely minimal support from clients. 3) Non-intrusive data collection. 4) Inexpensive devices are sufficient to acquire good data quality. 5) The mechanism provides high accuracy and uses low-resolution images. 6) More features can be extracted from palmprints as it allows for a larger surface area compared to fingerprints. 7) Since low-resolution imaging sensors are used for acquiring palmprint images, the computation required for pre-processing and extracting features is minimal. 8) palmprints can be considered a trustworthy human identifier as these patterns are unique in monozygotic twins [7].

Therefore, this paper presents a unique approach requiring less computation and complexity in the palmprint recognition process. The proposed system is sustainable with low memory devices and makes it suitable for embedded platform implementation.

2. LITERATURE STUDY

A recent advancement in machine learning has obtained the greatest attention in classification models. Various deep learning based neural networks outperformed the traditional methods of classification, achieving enormous classification accuracy. Jia et al. [8] presented a detailed study on various deep learning-based palmprint recognition algorithms. All these algorithms succeeded in achieving classification accuracy ranging from 80% to 100%. From the computation study, it has been observed that GPU based computation efficient architecture requires at least 390M FLOP operations (i.e. ScarletNAS architecture) and minimum identification time of 183 ms for NASNet architecture (excluding training time). Thus, deep learning provides the highest accuracy at the cost of computation time and hardware complexity.

Another comparative analysis of palmprint recognition was presented in [9]. This study involved all traditional methods used in multispectral recognition including principle component analysis, Fisher linear discrimination, fuzzy method, edge map generation, radon transform, etc. Bounneche et al. [10] used oriented log-Gabor filters to enhance the recognition rate. Features obtained from the log-Gabor filters were matched using hamming distance for palm identification. The feature extraction required an average time of 894 ms and a matching time of around 5.6 ms.

To tackle the problem of misalignment, a Local Micro-structure Tetra Pattern (LMTrP) based local feature extraction was proposed in [11]. Initially, Gabor based features were obtained and later a histogram using LMTrP in local regions was generated for matching purposes. Raghavendra et al. [12] proposed discrete wavelet transform based multi-spectral fusion of palm features. They extracted the average coefficients from DWT from each spectrum of the palm and fused these coefficients based on a weighted function. Then inverse DWT was calculated to get a fusion of ROI from the wavelet domain. For identification purposes, Gabor filters were used with distance calculation. They achieved a 5.97 error rate in classification. The overall method was complex, as it requires multiple spectrum's DWT feature fusion.

The moving human leg angle-based gait recognition system is explained in [13] and uses average statistical features of eight frames. A least square regression model named salient and discriminative descriptor learning method described in [14] solved the sparse nonnegative noise interference error problem. Kokila et al. used PCA to extract the features and an ANN model for matching purposes [15]. A simple basic operation (additions and subtractions) based method that forms code for a palmprint is described in [16]. Chaudhari et al. [17] used a Histogram of Radon transform for feature extraction from low resolution images.

Jaafar et al. [18] touched on a less recognized algorithm, where a mobile camera was used for palm acquisition. They used histogram equalization and thresholding for feature extraction. A Fuzzy based nearest centroid neighbor was proposed for palm recognition achieving accuracy of 98.78%. Hong et al. [19] de-blurred palm images using a Gaussian Focused degradation model and a Vese–Osher decomposition model was used to extract the texture features from ROI. The normalized correlation coefficient was calculated to find the similarity between two palms and obtained 0.9210 EER.

A sparse based image enhancement, PCA based dimensionality reduction and voting based recognition, was proposed in [20]. This algorithm was tested on a PolyU dataset and obtained a 99.87% accuracy. Tamrakar and Khanna [28] used approximation coefficients obtained from the Haar wavelet for feature extraction. Further, the image was processed with a Gaussian derivative to obtain local phase information. Later,a block-based histogram was used as a feature vector for recognition. They claimed 100% recognition rate on PolyU dataset. Their extraction time and recognition time were lower (i.e. 16.942 ms and 188.4471 ms) but the training time requirement was 3502 ms.

This paper presents a unique approach where feature extraction and matching require less time and make the system approachable to real-time. The proposed system uses dyadic wavelet transform, which is fast and compatible with hardware as it works in discrete and power of 2. The discriminative features obtained using signature formation makes it robust for intra-variation. Further, reduction in matching time is obtained with exclusion of the coarsest level features.

3. DISCRETE DYADIC WAVELET TRANSFORM

Edges of the palm print are important features in the recognition process. An edge can be thought of as a series of fast transitions in image amplitude. For a given image f(x,y), the image gradient $|\nabla f(x,y)|$ takes a local maximum value indicating the edge. However, image texture also obtains a similar transition. Therefore, to discriminate the edge from the texture, scale factor needs to be considered in the calculation. The dyadic wavelets that account for the scaling and smoothing function can easily discriminate the edges from the texture regions. The DDWT of image f(x,y) calculated multi-scale edge at point (s,t) can be expressed as

$$W_j^k(s,t) = < f(x,y)\varphi_j^k(x-s, y-t) > \tag{1}$$

where j and k =1, 2 are integers and φ is the wavelet function which can be expressed as

$$\varphi_j^k(x,y) = 2^{\frac{j}{2}}\varphi(2^j(x,y) - k) \tag{2}$$

The modulus of DDWT $|W_j^k(s,t)|$ reaches a maximum value locally in the neighbourhood of point (s,t). Similar to the 1D example, the scale dependency of the magnitude of the modulus maxima is applied to the Hölder exponent of f(x,y) and hence provides knowledge to differentiate between edges and textures.

For a certain decision of wavelets, the DDWT change can be executed inside a fast hierarchical digital filtering scheme using multi-resolution analysis. A Mallat pyramid based hierarchical filtering to obtain DDWT is shown in Fig.1.
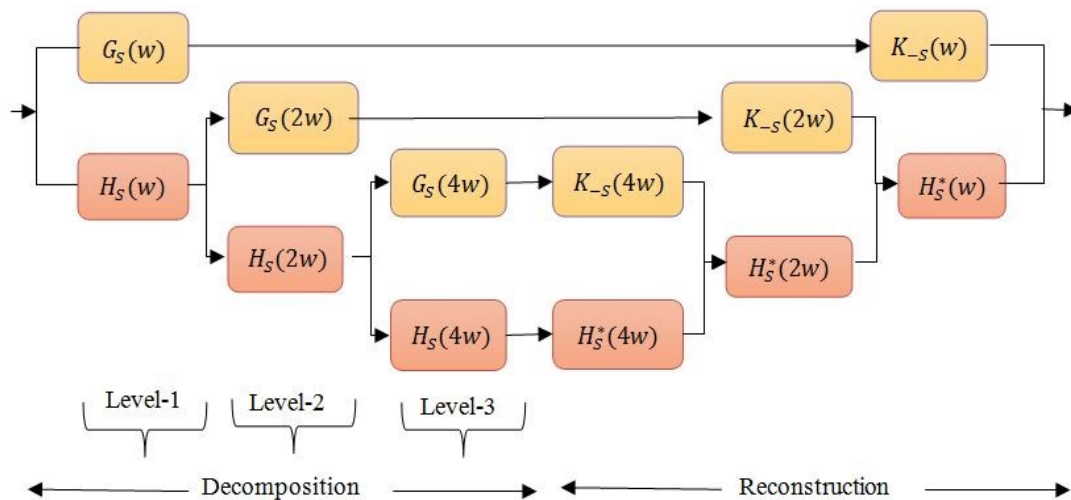
Fig.1: Filter bank realization of a 1-D dyadic DWT at three levels (left) of DWT decomposition and (right) DWT reconstruction, where G(w) is a complex conjugate of H(w).

In Fig.2, $H(\omega)$ is a low pass filter, $G(\omega)$ is a high pass filter, and $K(\omega)$ is a high pass filter for $r = 1$ and a low pass filter when $r = 2$ and $p > 0$. Figure 2 represents the successive partition of the frequency spectrum. The initial frequency spectrum of $[0, \pi]$ is divided into equivalent subintervals i.e. $[0, \pi/2]$ and $[\pi/2, \pi]$. The upper spectrum has T/2 DDWT coefficients. These coefficients are the basis for the next level. In the next level of the decomposition from the previous level-1, the lower spectrum is further subdivided into two equal subintervals i.e. $[0, \pi/4]$ and $[\pi/4, \pi/2]$. The subdivision process proceeds, successively separating the lower subintervals until it can no longer go any further.

Let the sampling shifted digital filter be expressed as $F_s(\omega) = e^{-j\omega s}F(\omega)$. This digital filter can be formulated to divide the spectrum into two intervals. The required condition in the design of these filters is that filters should be asymmetrical and they should have small compact support. The family $G(\omega), H(\omega)$ *and* $K(\omega)$ that satisfy these conditions is expressed as

$$H(\omega) = e^{j\omega/2}\left(\cos\left(\frac{\omega}{2}\right)\right)^{2p+1} \quad G(\omega) = 4Je^{j\omega/2}\left(\sin\left(\frac{\omega}{2}\right)\right)^{r} \quad K(w) = \frac{1 - |H(w)|^2}{G(w)}$$

In the opposite operation of the decomposition referred as reconstruction, the signals are up-sampled to obtain the signal back. A unique approach of signature formation from these wavelet decompositions and reconstructions has been proposed in next section.

(a)   (b)

(a)   (b)

(a)   (b)
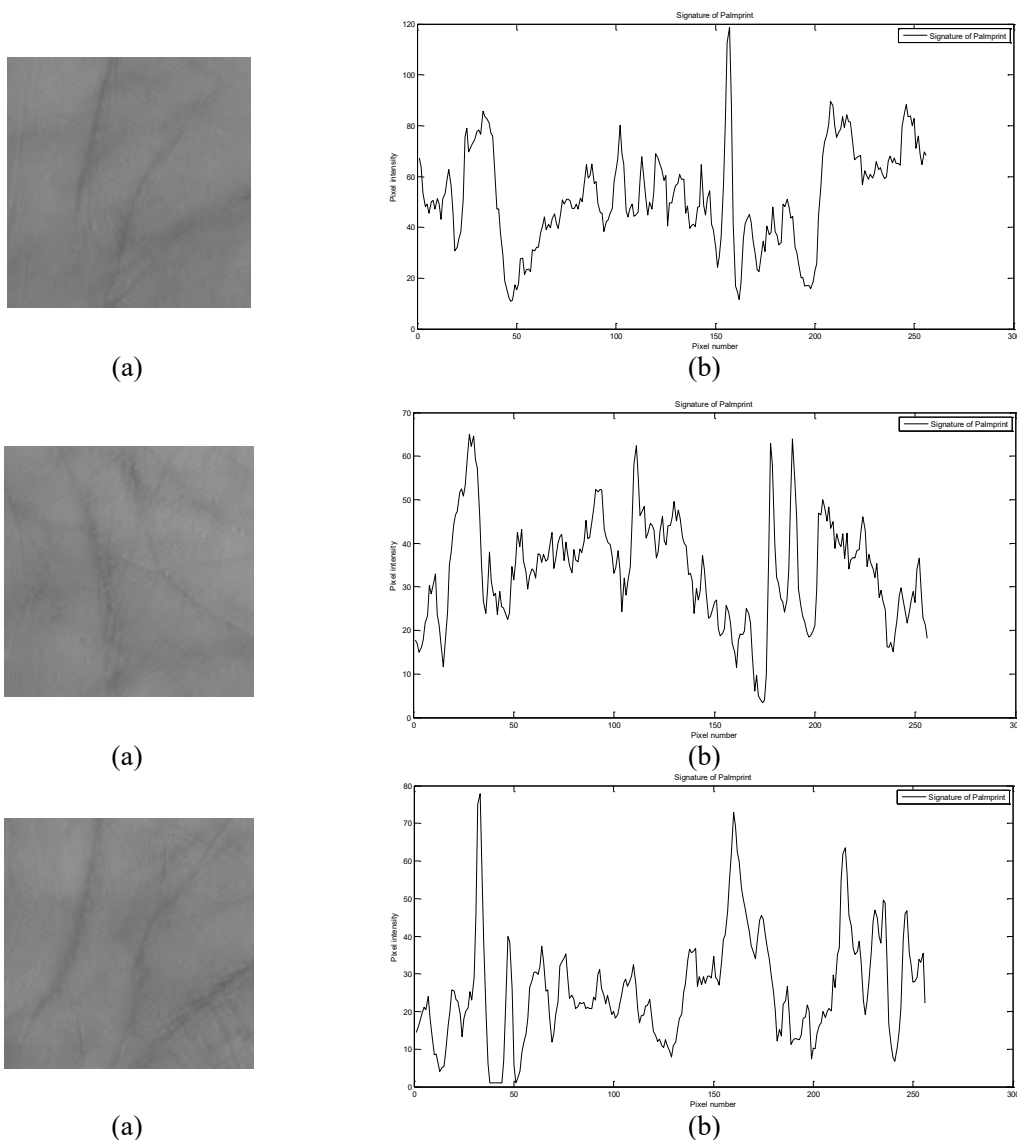
Fig.2: Sample palm print signatures (a) palmprint ROI (b) corresponding PS obtained with reference to the horizontal line passed from the center of the extracted ROI.

4. PALMPRINT FEATURE EXTRACTION USING DDWT

The basic requirement in palmprint recognition is that obtained features shall be translation and rotation invariant. Therefore, the region providing distinguished features

must be obtained first to extract these features. This region extraction process, consisting of five steps, is well explained in [21]. The main contribution of this paper lies here. The traditional wavelet approach uses multi-resolution edge-oriented features i.e. principle lines of palms, ridges i.e. loop, arch and whorl or cores and delta in the recognition process. This paper proposes the formation of zero-crossing signatures using DDWT. The DDWT is applied to this region providing unique features for recognition. These steps to obtain the zero-crossing signature of each palm are as follow:

The palmprint's extracted ROI has been used to plot the signature in the pre-processing operation step. To get the signature, a horizontal line is passed through the center of the ROI. The pixel intensities are recorded on that line and a corresponding unique signature has been generated for each palmprint. Figure 2 demonstrates the unique signatures obtained from three different palmprints.
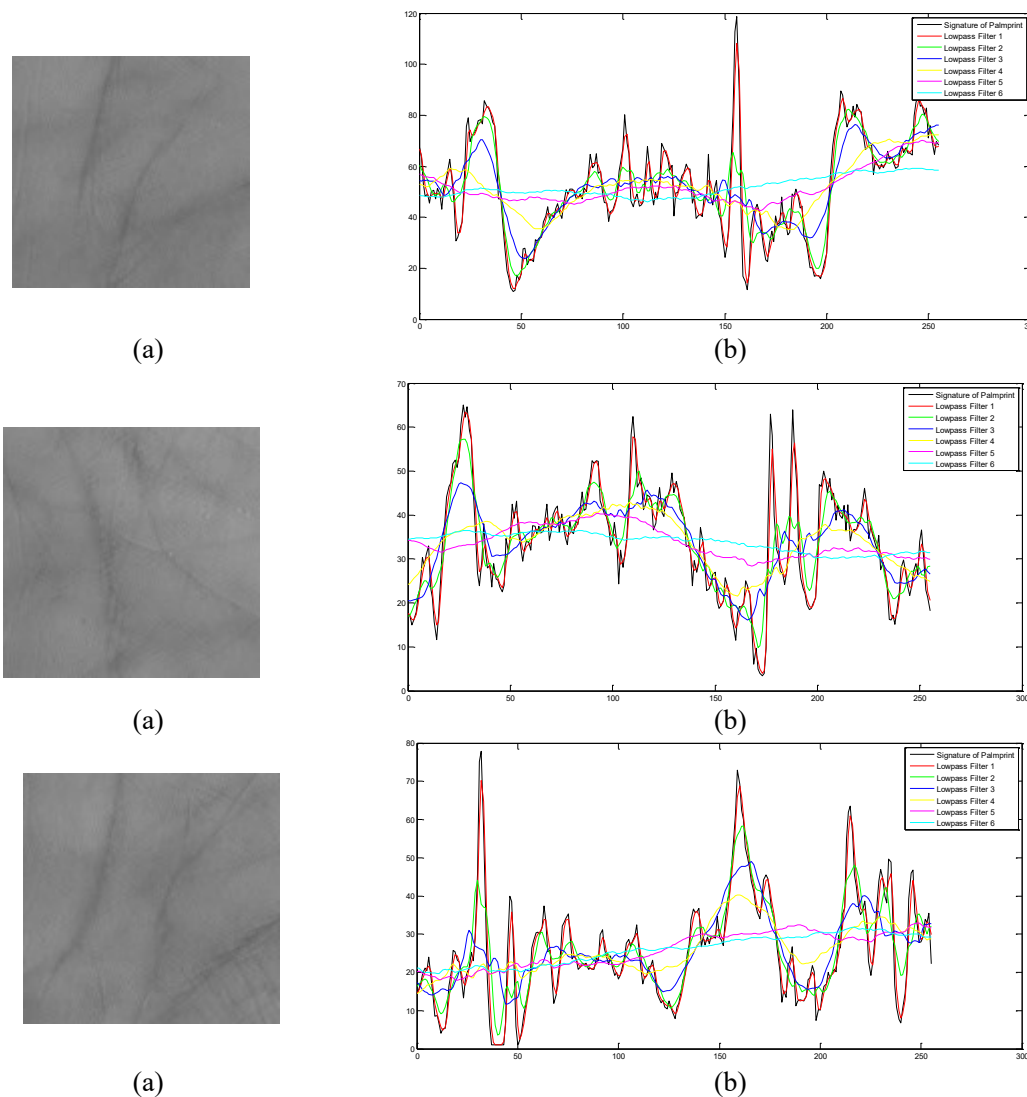
Fig.3: The palmprint signatures at various scales (a) extracted ROI of palmprint, (b) corresponding PS along with six resolution levels of the DDWT.

The signals obtained using a piecewise constant function between sequences of two consecutive zeros are used as unique features to represent the palmprint instead of the zero-crossing of the wavelet transform at various scales. This signal is referred to as a Piecewise Constant function of Palmprint Signature (PCPS). For DDWT, all scales are restricted

with power of 2 only. The PS has been calculated with a finite resolution that forces a finer scale while calculating the dyadic wavelet transform instead of computing the wavelet transform on all scales of 2^j for j varying from -∞ to +∞. The resolution is restricted by the finite larger scale and a nonzero finer scale. For implementation purposes, the finer scale is equal to 1 and the largest scale is 2^j. Further experimentation has been carried out at different resolution/scales of DDWT. Figures 3 and 4 present the PS and corresponding PCPS obtained using DDWT at various scales.

(a)   (b)

(a)   (b)

(a)   (b)
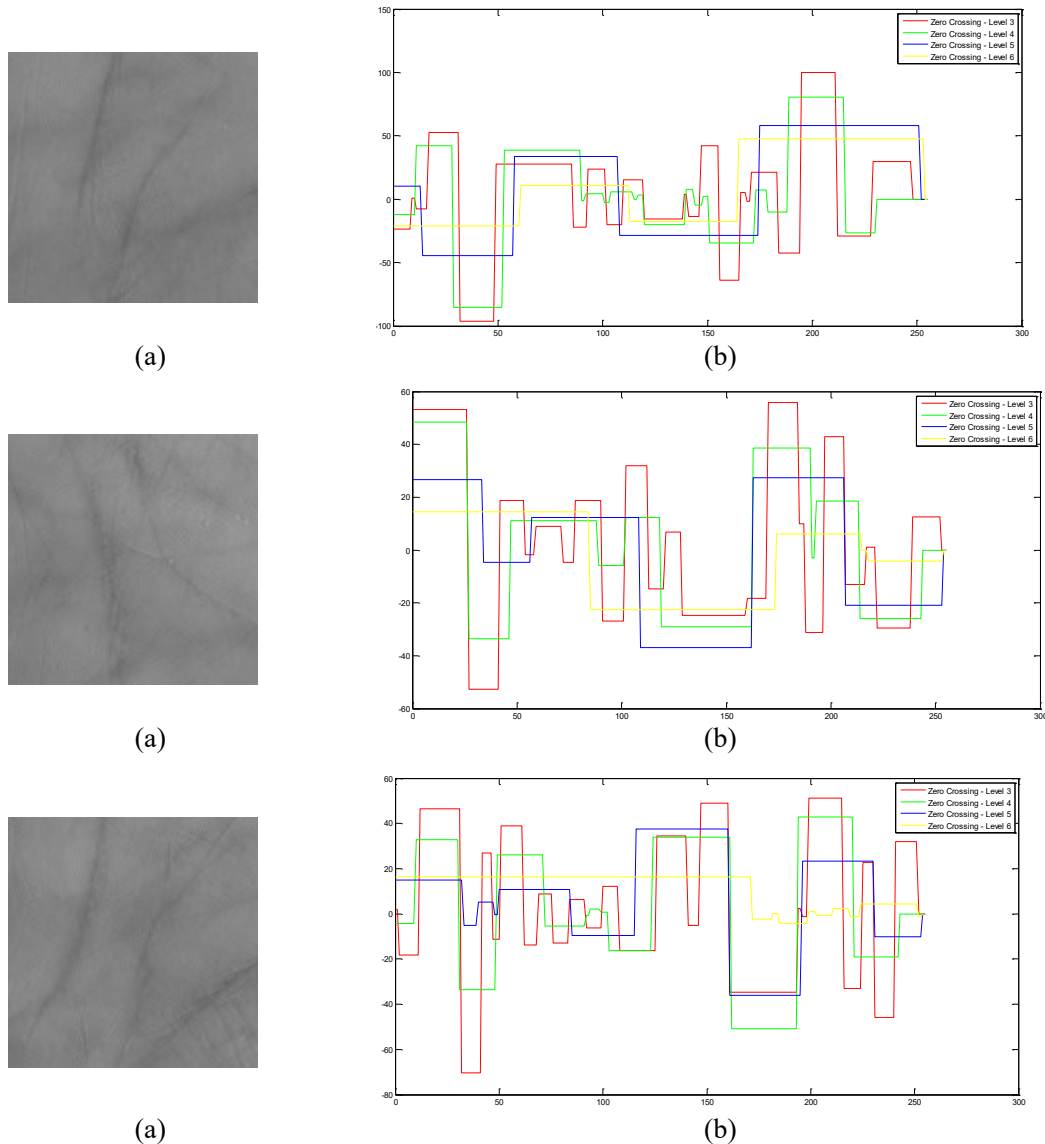
Fig.4: Piecewise constant function representation of PS (a) extracted ROI of palmprint, (b) PCPS corresponding to the lowest four resolution levels of the dyadic wavelet transform.

5.   RESULTS AND DISCUSSION

PolyU database [23], available on the internet, has been used for dyadic DWT testing for palmprint images as unimodal biometrics. In the experiment, 4 level dyadic decomposition was used. Features based on discrete dyadic wavelets were measured to evaluate the performance accuracy of the proposed algorithm. When testing the algorithm, each image from the database was matched with the same dataset's remaining images.

If the test image matched another image in the dataset, it was counted as correct matching. Otherwise, it will be counted as incorrect matching. In the matching method, the Euclidean distance between the feature sets was used. The minimum Euclidean distance amongst two palmprints' features was considered the best fit for the test image for stored prototypes. The system's performance was calculated using false acceptance ration (FAR) and genuine acceptance ration (GAR).

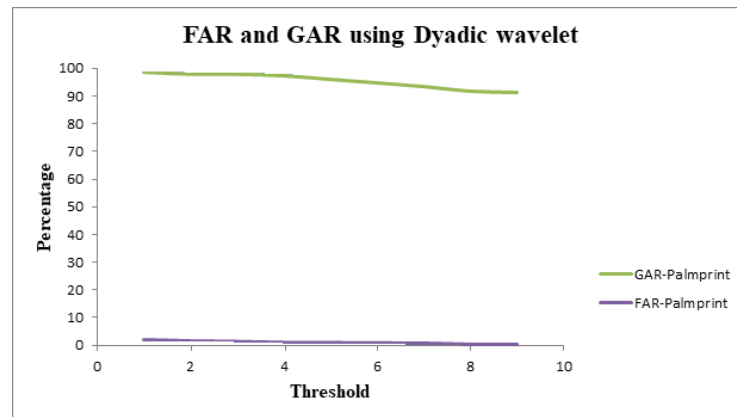Fig.5: Performance of the proposed algorithm of person identification using discrete dyadic wavelet transform in terms of percentage FAR and GAR plotted at various thresholds.

FAR represents that the system has accepted and recognized the imposter, and its values must be as low as possible. GAR means true acceptance of the user. The FAR and GAR percentages for palmprints were plotted, taking into account various threshold values. Fig.6 shows this performance plot. The maximum recognition accuracy of 96.27% is achieved for palmprint images from the PolyU database using dyadic DWT. The testing time of 0.76 seconds indicates the computational efficiency of the algorithm. The Table 1 discusses the comparative analysis of the proposed DWT based signature model with other DWT based palmprint recognition models.

Table 1: Palmprint recognition accuracy comparison using DWT approaches

Authors	Key Points	Max. Accuracy
Kozik and Choraś [24]	Haar wavelet transform based geometrical feature extraction	94%
Giełczyk et al. [25]	Computationless geometric feature extraction	91%
L. Zhang and D. Zhang [26]	Fusion of signatures of gravity, density, spatial disperse and energy in DWT domain	98%
Agrawal et al. [27]	Curvelet transform based energy computation	85%
Chaudhari et al. (Proposed method)	Zero crossing signature using Dyadic DWT	96.27%

Kozik and Choraś [24] developed geometric characteristics from the Haar wavelet transform and Giełczyk et al. [25] proposed a further reduction in computation. Zhang and Zhang [26] calculated the statistical signatures across all the DWT scale using the density, energy, gravity, and dispersivity and achieved an accuracy of 98% at the cost of high future sets. In contrast, the proposed method uses the zero-crossing points to establish a

signature size of 4X 256 and can achieve near-by precision at the lower future level. Thus, the strategy proposed is more effective than other methods focused on the DWT.

Table 2 presents the computational time requirement from the literatures section. As discussed, machine learning approaches can achieve better performance but at the cost of long computation i.e. training time. Table 2 suggests that the accuracy of the traditional methods is also better and require less execution time. Here, the extraction of the palm region has not been considered and computation has been partitioned into two parts: the feature extraction process and the matching process. Gabor-based approaches require a long time for feature extraction since the large number of orientations and scales in Gabor forms the large number of features. Therefore, their feature extraction time is large. Wavelet has only four bands per unit decomposition and therefore, it requires less execution time in comparison with Gabor. Therefore, the proposed approach requires shorter execution time of 21.04 ms including only feature extraction and matching.

Table 2: Computation time comparison with related techniques

Reference	Method	Feature extraction time (ms)	Recognition time (ms)	Accuracy (%)
Bounneche et al. [10]	Gabor filter and Hamming Distance	894	5.6	99.33
Li et al. [11]	Gabor filter + LMTrP histogram + Euclidean distance	82.68	-	95.60
Raghavendra et al. [12]	Fusion of Haar DWT features from multiple spectrum	-	42000 (Total)	96.52
Tamrakar et al. [28]		16.94	304	99.98
Hong et al. [18]	Debluring + Vese–Osher decomposition model	30.9	0.059	99.07
Jaafar et al. [19]	Histogram equalization + Thresholding + Fuzzy K nearest centroid neighbor	-	255 (Total)	98.78
Imad et al. [20]	Sparse Representation+ PCA+ 2D-LDA + Voting	-	600 (total)	99.87
Proposed	DWT + Palmprint Signature	20.25	0.76	96.27

6. CONCLUSION AND FUTURE SCOPE

The fusion of features, i.e. multi-modal biometric, improves the accuracy at the cost of complexity and execution time. This paper presented an alternative to these two problems. Dyadic DWT has been used in palmprint retrieval and identification. The energy of dyadic DWT is more concentrated in the vertical sideband. Therefore, a DWT based multi-resolution analysis is performed to obtained coefficients characterizing the palm. A zero-crossing signature is created to represent the texture features of the palm ROI using this sideband. The goal is to cut out recognition time and ensure recognition accuracy. The recognition accuracy has been improved to 96.27% without the fusion of

multiple features. Therefore, we can say that it provides a light-weight palmprint verification framework. This may be aimed for mobile applications in the future.

REFERENCES

[1] Zhang DD. (2004) Palmprint authentication. Springer Science & Business Media.
[2] Kim D, Jung Y, Toh KA, Son B, Kim J. (2016) An empirical study on iris recognition in a mobile phone. Expert systems with Applications, 54: 328-339.
[3] Lunter J. (2021) Everyday biometrics: can face replace fingerprint recognition?. Biometric Technology Today, 2021(4): 7-10.
[4] Shawkat SA, Al-Badri KSL, Turki AI. (2019) The new hand geometry system and automatic identification. Periodicals of Engineering and Natural Sciences, 7(3): 996-1008.
[5] Mewada HK, Patel AV, Chaudhari J, MahantK, Vala A. (2020) Wavelet features embedded convolutional neural network for multiscale ear recognition. Journal of Electronic Imaging, 29(4): 043029.
[6] Shaban Al-Ani M, Mohammadi M, AlyanNezhadi MM. (2020) Gait Recognition based on Measurements of Moving Human Legs Angles. International Journal of Engineering, 33(5): 975-983.
[7] Kong A, Zhang D, Lu G. (2006) A Study of identical twins' palmprints for personal authentication. In International Conference on Biometrics (pp. 668-674). Springer, Berlin, Heidelberg.
[8] Jia W, Xia W, Zhao Y, Min H, Chen YX. (2021) 2D and 3D Palmprint and Palm Vein Recognition Based on Neural Architecture Search. International Journal of Automation and Computing, 18(3): 377-409.
[9] Aberni Y, Boubchir L, Daachi B. (2019) Multispectral palmprint recognition: a survey and comparative study. Journal of Circuits, Systems and Computers, 28(07): 1950107.
[10] Bounneche MD, Boubchir L, Bouridane A, Nekhoul B,Ali-Chérif A. (2016) Multi-spectral palmprint recognition based on oriented multiscale log-Gabor filters. Neurocomputing, 205: 274-286.
[11] Li G, Kim J. (2017) Palmprint recognition with local micro-structure tetra pattern. Pattern Recognition, 61: 29-46.
[12] Raghavendra R, Busch C. (2014) Novel image fusion scheme based on dependency measure for robust multispectral palmprint recognition. Pattern recognition, 47(6):2205-2221.
[13] Shaban Al-Ani M, Mohammadi M, AlyanNezhadi MM. (2020) Gait Recognition based on Measurements of Moving Human Legs Angles. International Journal of Engineering, 33(5): 975-983.
[14] Zhao S, Zhang B. (2020) Learning salient and discriminative descriptor for palmprint feature extraction and identification. IEEE transactions on neural networks and learning systems, 31(12): 5219-5230.
[15] Kokila MK. (2020) Accurate Palm Print Verification with Adaptive Histogram Equalization and Deep Learning Algorithm. Journal of Critical Reviews, 7(19): 3701-3710.
[16] Almaghtuf J, Khelifi F, Bouridane A. (2020) Fast and efficient difference of block means code for palmprint recognition. Machine Vision and Applications, 31(6): 1-10.
[17] Chaudhari J, Patil PM, Kosta YP. (2012) Feature extraction using Histogram of Radon Transform for Palmprint matching. International Journal of Advances in Engineering & Technology, 5(1): 416.
[18] Jaafar H, Ibrahim S, Ramli DA. (2015) A robust and fast computation touchless palm print recognition system using LHEAT and the IFkNCN classifier. Computational intelligence and neuroscience, 2015.
[19] Hong D, Liu W, Wu X, Pan Z, Su J. (2016) Robust palmprint recognition based on the fast variation Vese–Osher model. Neurocomputing, 174: 999-1012.
[20] Rida I, Al-Maadeed S, Mahmood A, BouridaneA, Bakshi S. (2018) Palmprint identification using an ensemble of sparse representations. IEEE Access, 6: 3241-3248.

[21] Zhang D, Kong WK, You J, Wong M. (2003) Online palmprint identification. IEEE Transactions on pattern analysis and machine intelligence, 25(9): 1041-1050.

[22] Černá D, Finěk V. (2017) Quadratic spline wavelets with short support satisfying homogeneous boundary conditions. arXiv preprint arXiv:1712.03643.

[23] The Hong Kong Polytechnic University (PolyU) Multispectral Palmprint Database [Online](2013). http://www.comp.polyu.edu.hk/~biometrics/MultispectralPalmprint/MSP.htm, 2013.

[24] Kozik R, Choras M. (2010) Combined shape and texture information for palmprint biometrics. ratio, 1(d2), d2.

[25] Giełczyk A, Choraś M, Kozik R. (2019) Lightweight verification schema for image-based palmprint biometric systems. Mobile Information Systems, 2019.

[26] Zhang L, Zhang D. (2004) Characterization of palmprints by wavelet signatures via directional context modeling. IEEE Transactions on Systems, Man, and Cybernetics, Part B (Cybernetics), 34(3): 1335-1347.

[27] Agarwal S, Sharma V, Verma PK. (2019) Palm Print Recognition Using CEDA. In 2019 3rd International Conference on Computing Methodologies and Communication (ICCMC) (pp. 929-932). IEEE.

[28] Tamrakar D, Khanna P. (2016) Kernel discriminant analysis of block-wise Gaussian derivative phase pattern histogram for palmprint recognition. Journal of Visual Communication and Image Representation, 40: 432-448.

Latif et al.

A STUDY OF CHANNEL AND DELAY-BASED SCHEDULING ALGORITHMS FOR LIVE VIDEO STREAMING IN THE FIFTH GENERATION LONG TERM EVOLUTION-ADVANCED NETWORK

LIZA ABDUL LATIFF[1], HUDA ADIBAH MOHD RAMLI[2*], ANI LIZA ASNAWI[2] AND NUR HALIZA ABDULWAHAB[3]

*[1]Razak Faculty of Technology and Informatics,
Universiti Teknologi Malaysia, Kuala Lumpur, Malaysia
[2]Department of Electrical and Computer Engineering, International Islamic University Malaysia,
Jalan Gombak, 53100 Kuala Lumpur, Malaysia
[3]Faculty of Engineering, Universiti Teknologi Malaysia, Johor Bahru, Malaysia Malaysia*

*Corresponding author: hadibahmr@iium.edu.my

ABSTRACT: This paper investigates the performance of a number of channel and delay-based scheduling algorithms for an efficient QoS (Quality of Service) provision with more live video streaming users over the Fifth Generation Long-Term Evolution-Advanced (5G LTE-A) network. These algorithms were developed for use in legacy wireless networks and minor changes were made to enable these algorithms to perform packet scheduling in the downlink 5G LTE-A. The efficacies of the EXP and M-LWDF algorithms in maximizing the number of live video streaming users at the desired transmission reliability, minimizing the average network delay and maximizing network throughput, are shown via simulations. As the M-LWDF has a simpler mathematical equation as compared to the EXP, it is more favoured for implementation in the complex downlink 5G LTE-A.

ABSTRAK: Kertas ini menyiasat prestasi sebilangan saluran dan algoritma penjadualan berdasarkan kelewatan untuk penyediaan QoS (Kualiti Perkhidmatan) yang cekap dengan banyak pengguna video secara langsung melalui rangkaian Generasi Kelima Long-Term Evolution Advanced (5G LTE-A). Algoritma-algoritma yang disiasat di dalam kertas ini dicadangkan untuk digunakan dalam generasi rangkaian tanpa wayar yang lama dan sedikit perubahan dibuat untuk membolehkan algoritma ini menyokong penjadualan paket dalam downlink 5G LTE-A. Keberkesanan EXP dan M-LWDF algoritma dalam memaksimumkan jumlah pengguna pada kebolehpercayaan transmisi yang diinginkan dari streaming video secara langsung, meminimumkan kelewatan rangkaian, dan memaksimumkan truput rangkaian ditunjukkan melalui simulasi. Namun, dengan M-LWDF mempunyai formula matematik yang mudah dibandingkan dengan EXP, ia lebih sesuai untuk digunakan dalam downlink 5G LTE-A yang lebih kompleks.

KEYWORDS: *scheduling algorithms; 5G; orthogonal frequency division multiple access; quality of service; long term evolution-advanced (LTE-A)*

1. INTRODUCTION

Fifth Generation (5G) is the most current standard of wireless networks [1] deployed in Malaysia. 5G was expected to provide satisfactory Quality of Service (QoS) for a large

number of users [2] and be more resilient in terms of network flexibility and (re)configurations. To date, there is no formal definition for 5G radio access networks, but the majority of the studies extended the Long-Term Evolution-Advanced (LTE-A) by embracing innovative features relevant to 5G (referred to as 5G LTE-A). The 5G LTE-A aggregates the available bandwidth (also known as Component Carriers (CCs)) to significantly increase data rates. Moreover, another important 5G feature for meeting the desired QoS for more mobile internet users is by packet scheduling. In each scheduling period, the packet scheduler in the downlink LTE-A uses a scheduling algorithm to choose the packets of a user for transmission on each radio resource on each CC.

The scheduling algorithms currently available in the extant literature are channel-based, delay-based, channel-and-delay-based or none of those. The decision whether to consider channel quality or packet delay or neither depends on the network performance to be maximized or the desired QoS to be satisfied. For example, Round Robin (RR) [3] is neither a delay-based nor a channel-based scheduling algorithm that aims to fulfill the fairness requirement while Maximum Rate (Max-Rate) [3] is a well-known channel-based scheduling algorithm developed for maximizing throughput performance. On the other hand, the Delay Prioritized Scheduling (DPS) [4] is a delay-based scheduling algorithm. The DPS does not account for the channel quality when selecting a user to receive its packets. The current trend in mobile internet usage shows an explosive request for live video streaming especially during this Covid-19 era where most daily activities have migrated to the online domain. This video streaming traffic is delay-sensitive and demands for the provision of high transmission reliability (as described in the 3GPP specifications [5]) for a huge number of live mobile video users whilst ensuring the network performance is maximized. It was shown in [6,7] that channel and delay aware scheduling algorithms are the best candidates for meeting the desired QoS of this delay-sensitive live video streaming traffic and are hence considered in this paper.

An extensive number of channel and delay-based scheduling algorithms have been proposed for the legacy of wireless networks. Quite a number of these channel- and delay-based scheduling algorithms showed excellent performance in the wireless networks for which they were developed and there is a likelihood that these scheduling algorithms may perform well in the 5G LTE-A. Implementing these scheduling algorithms in the 5G LTE-A may require minor amendments because the 5G LTE-A is a new wireless network and has different frameworks and features as compared to legacy wireless networks. Therefore, the contribution of this paper is the study on the adaptations of the legacy channel- and delay-based scheduling algorithms for use in the 5G LTE-A network when streaming live video.

2. DOWNLINK 5G LTE-A NETWORK MODEL

This paper considers the downlink 5G LTE-A given that an enormous volume of mobile internet traffic is communicated in the downlink. Orthogonal Frequency Division Multiple Access (OFDMA) is the multiple access technique employed in the downlink 5G LTE-A. This technique divides the wide bandwidth into multiple narrowband sub-carriers. The 5G LTE-A modeled in this paper modifies the legacy 4G LTE-A that performs packet scheduling at every 1 ms Transmission Time Interval (TTI). A total of 12 sub-carriers of 15 kHz width each are used to carry the user packets. This group of sub-carriers (12 sub-carriers) in the frequency domain and 1 ms TTI (that contains 14 Orthogonal Division Multiple Access (OFDM) symbols) in the time domain is referred to as Physical Resource Block (PRB).

On the other hand, the downlink 5G LTE-A, has a variable TTI size (as illustrated in Table 1). The packet scheduler may choose to perform scheduling every 0.14 ms TTI for the case of delay-sensitive mobile internet traffic or every 4.0 ms TTI for a more delay-relaxed mobile internet traffic. This paper considers modeling the 0.14 ms TTI size as it aims to evaluate the scheduling algorithms for delay-sensitive live video streaming. The 0.14 ms TTI size constitutes 2 Orthogonal Division Multiple Access (OFDMA) symbols in the time domain and 12 sub-carriers in the frequency domain (see Fig. 1) for each PRB. At this TTI size also, there will be a total of 8 PRBs (as illustrated in Table 1) that map to 192 Resource Elements (REs) that will be used to carry user packets. Additionally, to further increase the 5G LTE-A performance as compared to the legacy wireless networks, the Round Trip Time (RTT) of Hybrid Automatic Repeat Request (HARQ) is shortened from 8 ms to 4 ms [8].

Table 1: TTI and Sub-band size [9].

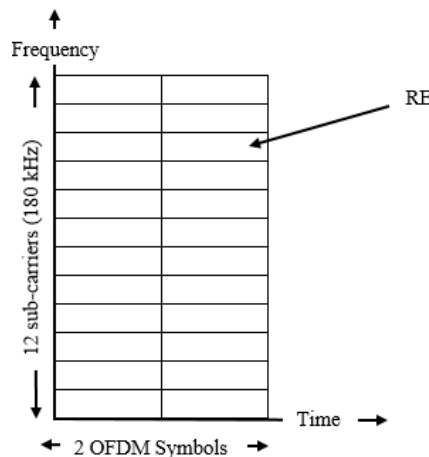| TTI size (ms)	Frequency domain scheduling block size (subband size)	Resource Elements (REs) per block size
0.14	8 PRBs (1440 Hz)	192
0.5	4 PRBs (720 Hz)	336
1.0	3 PRBs (540 Hz)	432
2.0	2 PRBs (360 Hz)	576
4.0	1 PRB (180 Hz)	576

Fig. 1: PRB time and frequency domain representation.

3. CHANNEL AND DELAY-BASED SCHEDULING ALGORITHMS

This paper studies eight channel- and delay-based scheduling algorithms for possible implementation in the downlink 5G LTE-A when providing the desired QoS of the delay-sensitive live video streaming traffic. These algorithms are described in the following section.

3.1 Modified-Largest Weighted Delay First (M-LWDF) Algorithm

The M-LWDF [10] is a prominent scheduling algorithm proposed for a single-user wireless network. It should be noted that at each scheduling period, only one user is selected to receive its packets in this single-user wireless network. This is contrary to the downlink 5G LTE-A that performs packet scheduling in both time and frequency domains (i.e., more than one user can receive its packets at each scheduling period). The M-LWDF

algorithm chooses the packets of a user that maximize Eq. (1) at each scheduling period and transmits the chosen user packets on the entire bandwidth.

$$priority_i(t) = a_i * W_i(t) * \left(\frac{cqi_i(t)}{R_i(t)}\right) \tag{1}$$

$$a_i = -\left(\frac{\log \delta_i}{PDT_i}\right) \tag{2}$$

$$R_i(t) = \left(1 - \frac{1}{t_c}\right) R_i(t-1) + I_i(t) * \frac{1}{t_c} * cqi_i(t) \tag{3}$$

where $priority_i(t)$ is the priority of the ith user at scheduling period t, a_i is the desired QoS of the ith user, δ_i is the Packet Loss Ratio (PLR) threshold of the ith user and PDT_i is the packet delay threshold of the ith user, $W_i(t)$ is the Head-of-Line (HOL) packet delay of the ith user at scheduling period t, $cqi_i(t)$ is the channel quality of the ith user at scheduling period t, $R_i(t)$ is the average throughput of the ith user at scheduling period t, t_c is a constant and $I_i(t)$ is a function indicating whether the ith user is scheduled or not at scheduling period t.

3.2 Exponential (EXP) Algorithm

Like the M-LWDF, the EXP [11] was proposed for the single-user wireless network. The decision on which user packets to be transmitted at each scheduling period is made according to:

$$priority_i(t) = a_i * \frac{cqi_i(t)}{R_i(t)} exp\left(\frac{a_i * W_i(t) - aW}{1 + \sqrt{aW}}\right) \tag{4}$$

$$aW = \frac{1}{N} \sum_{i=1}^{i=N} a_i * W_i(t) \tag{5}$$

where $priority_i(t)$ is the priority of the ith user at scheduling period t, a_i is the desired QoS of the ith user (as defined in Eq. (2)), $cqi_i(t)$ is the channel quality of the ith user at scheduling period t, $R_i(t)$ is the average throughput of the ith user at scheduling period t (see Eq. (3)), $W_i(t)$ is the HOL packet delay of the ith user at scheduling period t and N is the maximum number of available users.

3.3 Channel-Aware Earliest Deadline (C-AED)

The provision of the desired QoS for more users whilst maximizing network performance is the most challenging issue in the design of a packet scheduling algorithm. This is further complicated by the diverse QoS requirement of mobile internet traffic as well as the nature of the time and frequency variation of mobile wireless channels. The C-AED [12] is another algorithm developed to address this complicated challenge in a single-user wireless network. Decisions on which user to receive its packets at each scheduling period are made according to:

$$priority_i(t) = a_i * \frac{cqi_i(t)}{R_i(t)} \left(\frac{W_i(t)}{PDT_i - W_i(t)}\right) \tag{6}$$

where $priority_i(t)$ is the priority of the ith user at scheduling period t, a_i is the desired QoS of the ith user (as defined in Eq. (2)), $cqi_i(t)$ is the channel quality of the ith user at scheduling period t, $R_i(t)$ is the average throughput of the ith user at scheduling period t (see Eq. (3)), $W_i(t)$ is the HOL packet delay of the ith user at scheduling period t and PDT_i is the packet delay threshold of the ith user.

When compared with M-LWDF and EXP that used the desired QoS, channel quality, HOL packet delay, and average throughput criteria in their priority equations, the C-AED includes additional criterion of the packet delay threshold in its priority calculation, with the goal of improvement in performance.

3.4 Exponential Based Packet Scheduling (EBPS) Algorithm

The EBPS [13] algorithm was developed for use in multi-user satellite downlink Long Term Evolution (LTE) networks. The satellite LTE network aims to complement the limitations of terrestrial wireless networks by providing global coverage to users including in remote areas. This LTE network contains only one CC, and similar to the 4G LTE-A, packet scheduling in this wireless network is performed in every 1 ms TTI. However, contrary to single-user wireless networks, the LTE is a multi-user wireless network where more than one user can be scheduled in each TTI due to the usage of OFDMA as its multiple access technique. Packet scheduling in this LTE network is performed per PRB and time basis and the EBPS schedules packets of a user on each PRB and at each TTI according to Eq. (7).

$$priority_{i,j}(t) = \frac{cqi_{i,j}(t)}{R_i(t)} exp\left(\left(\frac{e}{0.99 * PDT_i}\right) * \left(\frac{PDT_i - W_i(t)}{W_i(t)}\right)\right) \quad (7)$$

where $priority_{i,j}(t)$ is the priority of the ith user on j^{th} RB at TTI t, $cqi_{i,j}(t)$ is the channel quality of the ith user on j^{th} RB at TTI t, $R_i(t)$ is the average throughput of the ith user at TTI t (see Eq. (3)), $W_i(t)$ is the HOL packet delay of the ith user at TTI t and PDT_i is the packet delay threshold of the ith user. It can be observed that when compared with M-LWDF, EXP and C-AED, the algorithms developed for LTE networks makes scheduling decision on each PRB and at each TTI.

3.5 Joint User Scheduling (JUS) Algorithm

The JUS [14] is another variation of EBPS in which the algorithm was developed by the same authors for supporting the desired QoS of delay-sensitive mobile internet traffic in the satellite LTE network. At each TTI and on each PRB the scheduling decisions are carried out based on:

$$priority_{i,j}(t) = \frac{cqi_{i,j}(t)}{R_i(t)} exp\left(\frac{W_i(t) * (cqi_{i,j}(t) * PDT_i - 1) + PDT_i}{2W_i(t) * (1 + cqi_{i,j}(t) * PDT_i)}\right) \quad (8)$$

where $priority_{i,j}(t)$ is the priority of the ith user on j^{th} RB at TTI t, $cqi_{i,j}(t)$ is the channel quality of the ith user on j^{th} RB at TTI t, $R_i(t)$ is the average throughput of the ith user at TTI t (see Eq. (3)), $W_i(t)$ is the HOL packet delay of the ith user at TTI t and PDT_i is the packet delay threshold of the ith user.

3.6 Exponential Maximum-Largest Weighted Delay First (EXP-MLWDF)

The EXP-MLWDF [15] was developed for use in the LTE for high mobility and dense area scenarios. The aim was to reduce congestion in LTE wireless networks due to the high use of delay-sensitive mobile internet traffic such as video streaming and voice. It was shown via a series of computer simulations that the EXP-MLWDF outperformed the M-LWDF algorithm in meeting the desired QoS for more mobile users. This algorithm decides priority of each user according to:

$$priority_{i,j}(t) = a_i * \frac{cqi_{i,j}(t)}{R_i(t)} exp\left(\frac{PDT_i}{PDT_i - W_i(t)}\right) \quad (9)$$

where $priority_{i,j}(t)$ is the priority of the ith user on j^{th} RB at TTI t, a_i is the desired QoS of the ith user (as defined in Eq. (2)), $cqi_{i,j}(t)$ is the channel quality of the ith user on j^{th} RB at TTI t, $R_i(t)$ is the average throughput of the ith user at TTI t (see Eq. (3)), PDT_i is the packet delay threshold of the ith user and $W_i(t)$ is the HOL packet delay of the ith user at TTI t.

3.7 Downlink Scheduler Based on Deadlines (DSBD)

Similar to the previously discussed algorithms, the DSBD [16] was developed to efficiently utilize the limited LTE radio resources and meeting the desired QoS of delay-sensitive mobile internet traffic for more users. This algorithm has the following equation:

$$priority_{i,j}(t) = \frac{cqi_{i,j}(t)}{R_i(t) * (PDT_i - W_i(t))} \tag{10}$$

where $priority_{i,j}(t)$ is the priority of the ith user on j^{th} RB at TTI t, $cqi_{i,j}(t)$ is the channel quality of the ith user on j^{th} RB at TTI t, $R_i(t)$ is the average throughput of the ith user at TTI t (see Eq. (3)), PDT_i is the packet delay threshold of the ith user and $W_i(t)$ is the HOL packet delay of the ith user at TTI t.

3.8 Efficient Downlink Packet Scheduling (EDPS)

The last algorithm considered in this paper is EDPS [17] where this algorithm combines the well-known Earliest Deadline First (EDF) and Proportional Fair (PF) algorithms so as to support the transmission of delay-sensitive mobile internet packets via the downlink LTE wireless network. It should be noted that the EDF does not take channel quality into account whereas the PF does not consider packet delay in its algorithm. On each PRB and at each scheduling period, the user with the highest priority of Equation (11) will be selected to receive its packets.

$$priority_{i,j}(t) = \frac{d_i * W_i(t)}{log\left(1 + \frac{b_i}{W_i(t)}\right) + c_i} * \left(\frac{1}{PDT_i - W_i(t)}\right) * \frac{cqi_{i,j}(t)}{R_i(t)} \tag{11}$$

where $priority_{i,j}(t)$ is the priority of the ith user on j^{th} RB at TTI t, $cqi_{i,j}(t)$ is the channel quality of the ith user on j^{th} RB at TTI t, $R_i(t)$ is the average throughput of the ith user at TTI t (see Eq. (3)), $W_i(t)$ is the HOL packet delay of the ith user at TTI t and PDT_i is the packet delay threshold of the ith user. It was shown in [17] that when b_i, c_i and d_i are set to 1, the EDPS achieved good scheduling performance.

It can be observed in sub-section 3.3 through sub-section 3.8 that the conventional scheduling algorithms manipulated similar scheduling criteria but devised different priority metrics calculations in an attempt to maximize the number of users that received the desired QoS of delay-sensitive mobile internet traffic. These algorithms showed good performance in the mobile network environments they were evaluated in. However, their performance in the downlink 5G LTE-A may vary because the downlink 5G LTE-A supports slightly distinguished frameworks and features as compared to the legacy wireless networks.

As such, the contribution of this paper is to study the performance of these channel and delay-based scheduling algorithms in the downlink 5G LTE-A where minor revisions were made to these algorithms to enable them to carry out packet scheduling in this wireless network. This includes the usage of variable TTI size in which 0.14 ms TTI size is assumed in this paper. This, therefore, requires packet scheduling to be performed in each 8 PRBs. Moreover, the average channel quality computed from all PRBs for each CC will be considered for these algorithms instead of computing the channel quality across the

whole bandwidth for the M-LWDF, EXP and C-AED and the channel quality on each PRB for the rest. The example of average channel quality computation is represented in Equation (12).

$$cqi\_avg_i(t) = \frac{\sum_{j=1}^{j=max\_RB} cqi_{i,j}(t)}{max\_RB} \tag{12}$$

where $cqi\_avg_i(t)$ is the average channel quality of the *ith* user at TTI *t*, $cqi_{i,j}(t)$ is the channel quality of the *ith* user on *jth* RB at TTI *t* and *max_RB* is the total number of available RBs.

4. SIMULATION ENVIRONMENTS

This paper adopted a simulation method [18-20] to evaluate the performance of the studied channel and delay-based scheduling algorithms as discussed in Section 3. The downlink 5G LTE-A network was modeled to comprise of only one base station. This base station used 43.01 dB transmit power and operated at 2 GHz and 2.6 GHz CCs. Each CC had 5 MHz bandwidth that mapped to a total of 50 PRBs available to be used by the downlink users. CQI was reported by the downlink users in every 5 ms interval. These CQI reports reached the base station after 2 ms duration. Erroneously received packets at the user end could be retransmitted 4 times and the RTT of HARQ process was constrained to 4 ms. This simulation software prioritized pending HARQ retransmission over new packets and new packets of users would only be transmitted if remaining PRBs were available after retransmission of pending HARQ packets was completed. The simulation assumed live video streaming of 512 kbps average data rate as the delay-sensitive mobile internet traffic. The delay threshold for the video users was capped at 80 ms and the QoS provision of the video users was met when the transmission reliability was maintained above 99.99%. Table 2 summarizes the assumptions used for simulation.

Table 2: A summary of simulation assumptions

Description	Assumption
Frequency spectrum	2 GHz and 2.6 GHz
Bandwidth	5 MHz
Number of available RBs	50 RBs (25 RBs each from each CC)
Base station transmit power	43.01 dB
CQI	Periodic CQI every 5 ms with 2 ms delay
HARQ RTT	4 ms
Maximum number of HARQ retransmissions	4 times
Video delay packet threshold and the desired transmission reliability	80 ms and 99.99%

Transmission reliability, average network delay, and network throughput metrics, which are considered as common metrics for the video streaming QoS provision, were used to evaluate the performance of each channel and delay-based scheduling algorithm. For example, the transmission reliability must be maintained above the 99.99% threshold to ensure that received video packets were not distorted during live streaming and hence guaranteed the desired QoS received by the live video users. The transmission reliability, as well as other metrics, are defined next:

$$Transmission\ reliability = 100 - \frac{\sum_{i=1}^{i=N} \sum_{t=1}^{t=T} p\_discard_i(t)}{\sum_{i=1}^{i=N} \sum_{t=1}^{t=T} p\_total_i(t)} \qquad (13)$$

$$Average\ network\ delay = \frac{1}{T} \sum_{t=1}^{t=T} \frac{1}{N} \sum_{i=1}^{i=N} W_i(t) \qquad (14)$$

$$Network\ throughput = \frac{1}{T} \sum_{i=1}^{i=N} \sum_{t=1}^{t=T} p\_received_i(t) \qquad (15)$$

where *p_discard$_i$(t)* is the size of discarded packets of the *ith* user at time *t*, *p_total$_i$(t)* is the total size of packets of the *ith* user that arrive at the base station at time *t*, *Wi(t)* is the HOL packet delay of the *ith* user at time *t*, *p_received$_i$(t)* is the size of correctly received packets at the *ith* user at time *t*, *T* is the maximum simulation time and *N* is the maximum number of users.

5.   RESULTS AND DISCUSSION

The transmission reliability, average network delay, and network throughput performances of the channel- and delay-based scheduling algorithms in the downlink 5G LTE-A when streaming video are shown in Fig. 2, Fig. 3, and Fig. 4, respectively. Though all these scheduling algorithms consider the same scheduling criteria (i.e., channel quality, packet delay, etc.), the manipulation of these criteria into their respective mathematical equations map to a slight variation in performance. For example, if the QoS provision of the live video users is to be satisfied, then the transmission reliability should be kept above 99.99%. It can be observed in Fig. 2 and Table 3 that the EXP is superior to other channel and delay-based scheduling algorithms where it supports 16% more users compared to C-AED, DSBD and EDPS (i.e., EXP supports 29 video users whereas the C-AED, DSBD, and EDPS support up to 25 users). Furthermore, it can be observed in Fig. 3 and Fig. 4 that both EXP and M-LWDF are capable of minimizing the average network delay as well as maximizing the network throughput. Both EXP and the M-LWDF prioritize the most urgent packets to avoid these packets from being discarded for delay violations and hence minimize the average network delay. The network throughput on the other hand is the most important metric for the network operator for profit maximization. Therefore, the EXP and M-LWDF are preferred as these algorithms provide higher network throughput as compared to the other evaluated scheduling algorithms.

The achievement accomplished by EXP and M-LWDF, as illustrated in Table 3, is significant given that mobile users are streaming live video at an average rate of 512 kbps. The EXP outperforms other scheduling algorithms because EXP computes the average of the desired QoS and the HOL packet delay. This, however, incurs additional computational complexity because the extra step is needed in determining the priority of each user at each TTI (the downlink 5G LTE-A network is already complex and additional complexity in a scheduling algorithm is not preferred). The M-LWDF algorithm, on the other hand, has a simple mathematical equation and achieves slightly lower performance compared to the EXP. It supports 12% more video users as compared to C-AED, DSBD and EDPS and is capable of minimizing average network delay whilst maximizing the network throughput (as demonstrated in Fig. 3 and Fig. 4). It also does not come with additional computational complexity as does EXP. Other variations of mathematical equations lead to worse performance as in C-AED, DSBD, and EDPS whereas more complex mathematical equations do not necessarily map to good video performance (see the EBPS, JUS, EXP-MLWDF algorithms).
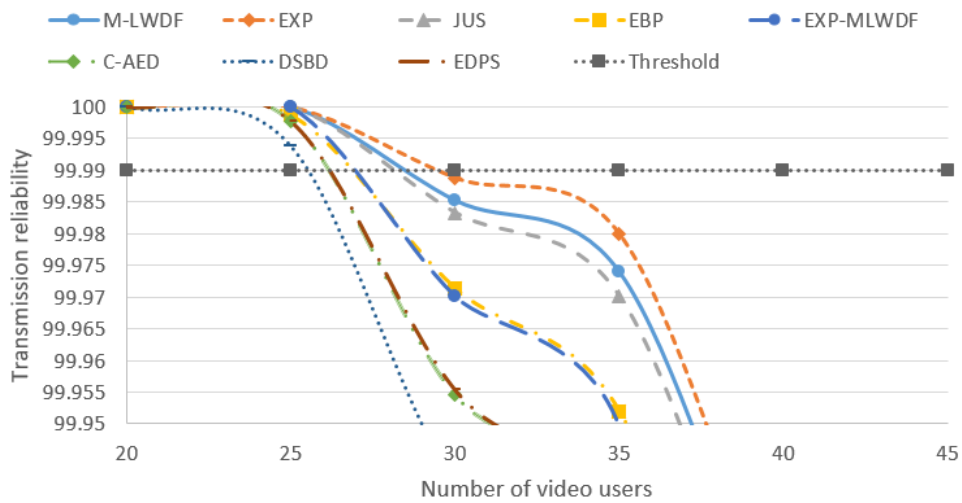
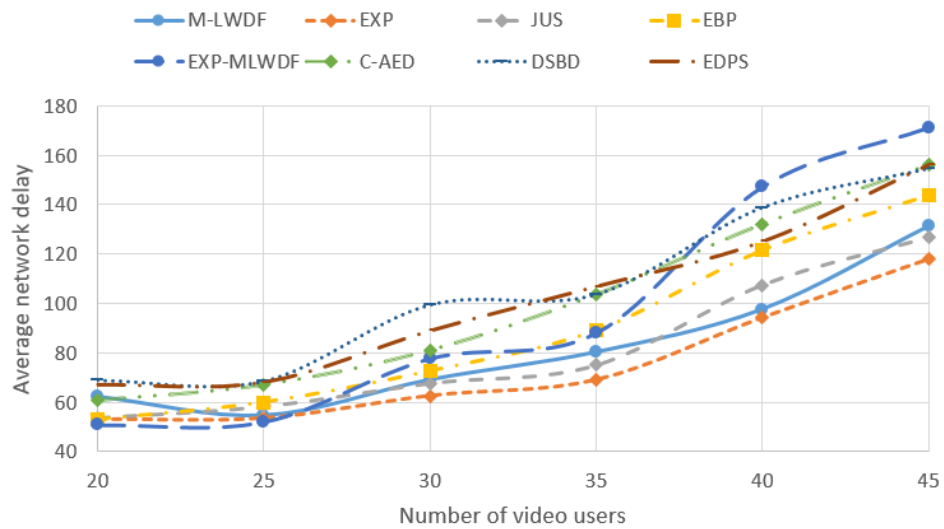Fig. 2: Transmission reliability vs number of video users.

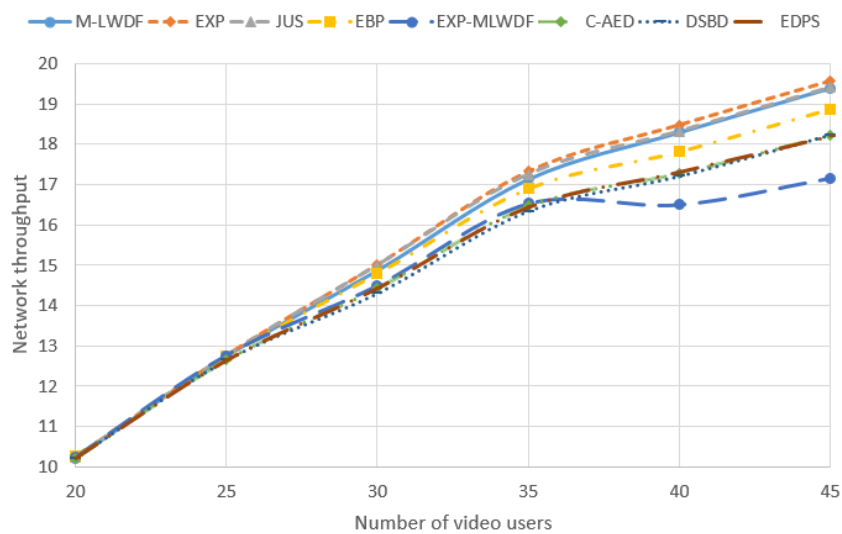Fig. 3: Average network delay vs number of video users.

Fig. 4: Network throughput vs number of video users.

Table 3: Maximum number of users at desired video QoS provision

Scheduling algorithms	Maximum number of users at desired live video QoS provision
M-LWDF	28
EXP	29
C-AED	25
EBPS	26
JUS	27
EXP-MLWDF	26
DSBD	25
EDPS	25

6. CONCLUSION

The enormous demand for video streaming traffic has accelerated the standardization of 5G wireless networks. Packet scheduling is of paramount importance in the 5G wireless to efficiently utilize the scarce radio resources and provide satisfactory QoS provisions of the diverse mobile internet traffic. This paper studies the performance of channel- and delay-based scheduling algorithms in the downlink 5G LTE-A wireless network when streaming live video. Minor amendments were made to these algorithms because the frameworks and features of the downlink 5G LTE-A are slightly different from legacy wireless networks. A series of computer simulations demonstrated that the EXP outperforms other scheduling algorithms however, this algorithm incurs additional complexity for calculating the average of the desired QoS and the HOL packet delay at every TTI. The M-LWDF seems the most eligible candidate because its performance is comparable to EXP, and it does not come with an additional complexity cost. It supports 12% more users streaming video at 512 kbps average data rate, minimizing the average network delay and maximizing the network throughput. It can also be concluded, based on this study, that complex mathematical equations sometimes do not necessarily map to a good scheduling performance. What is most important is the exploitation of these scheduling criteria to effectively meet the desired QoS for a huge number of users and maximizing the network performance. Future works will investigate the performance of these algorithms in a multiple cell scenario, considering diverse mobile internet traffic.

ACKNOWLEDGEMENT

REFERENCES

[1] Nordin MAM, Ramli HAM. (2020) Performance analysis of 5G path loss models for rural macrocell environment. IIUM Eng. J., 21(1): 85-99.

[2] Antonioli RP, Fodor G, Soldati P, Maciel TF. (2021) Decentralized Joint Beamforming, User Scheduling, and QoS Management in 5G and Beyond Systems. IEEE Commun. Stand. Mag., 5(1):62-69.

[3] Dahlman E, Parkvall S, Skold J, Beming P. (2007) 3G Evolution: HSPA and LTE for Mobile Broadband. Elsevier Ltd.

[4] Sandrasegaran K, Ramli HAM, Basukala R. (2010) Delay-Prioritized Scheduling (DPS) for Real Time Traffic in 3GPP LTE System, in IEEE Wireless Communication and Networking Conference, pp. 1-5.

[5] 3GPP (2019) Technical Specification Group Services and System Aspects; System

architecture for the 5G System (5GS); Stage 2 (Release 16).

[6] Ramli HAM, Basukala R, Sandrasegaran K, Patachaianand R. (2009) Performance of well known packet scheduling algorithms in the downlink 3GPP LTE system, in 2009 IEEE 9th Malaysia international conference on communications (MICC), pp. 815-820.

[7] Ramli HAM, Isa FNM. (2016) Improving real-time multimedia scheduling in practical mobile cellular channels, in IEEE 6th International Conference on Intelligent and Advanced Systems (ICIAS), pp. 1–6.

[8] Pocovi G, Soret B, Pedersen KI, aMogensen P. (2017) MAC layer enhancements for ultra-reliable low-latency communications in cellular networks, in IEEE International Conference on Communications Workshops, pp. 1005–1010.

[9] Pedersen KI, Niparko M, Steiner J, Oszmianski J, Mudolo L, Khosravirad SR. (2016) System level analysis of dynamic user-centric scheduling for a flexible 5G design, in IEEE Global Communications Conference, pp. 1–6.

[10] MathewA, Kumaran K, Ramanan K, Stolyar A, Whiting P. (2001) Providing Quality of Service over a Shared Wireless Link. IEEE Commun., 39(2):150–154.

[11] Shakkotai S, Stolyar A. (2000) A Study of Scheduling Algorithms for a Mixture of Real- and Non-Real-Time Data in HDR, Bell Labs Tech Memo.

[12] Elsayed KMF, Khattab AKF. (2006) Channel-Aware Earliest Deadline Due Fair Scheduling for Wireless Multimedia Networks. Wirel. Pers. Commun., 38:233–252.

[13] Aiyetoro G, Takawira F. (2017) An exponential based packet scheduling scheme for real time traffic in satellite LTE networks, in IEEE AFRICON, pp. 215–220.

[14] Aiyetoro G, Takawira F. (2018) Joint User Scheduling and PRB Mapping Scheme in Satellite LTE Networks, in 4th International Wireless Communications & Mobile Computing Conference (IWCMC), pp. 24–29.

[15] Angri I, Mahfoudi M, Najid A, El Bekkali M. (2018) Exponential M-LWDF (EXP-MLWDF) Downlink Scheduling Algorithm Evaluated in LTE for High Mobility and Dense Area Scenario. Int. J. Electr. Comput. Eng., 8(3):1618–1627.

[16] Ashidani PJ, Guardieiro PR. (2013) Downlink Scheduler Based on Deadlines for LTE Networks, in International workshop on telecommunications (IWT), pp. 1–5.

[17] Liu B, Tian H, Xu L. (2013) An Efficient Downlink Packet Scheduling Algorithm for Real Time Traffics in LTE Systems, in IEEE 10th Consumer Communications and Networking Conference (CCNC), pp. 364–369.

[18] Ramli HAM, Isa FNM, Asnawi AL, Jusoh AZ, Azman AW. (2019) Urgency-Aware Scheduling Algorithm for Downlink Cognitive Long Term Evolution-Advanced, in IEEE 89th Vehicular Technology Conference (VTC Spring), pp. 1–5.

[19] Ramli HAM, Mansor MIH. (2020) An enhanced packet scheduling algorithm for the downlink cognitive long term evolution-advanced. IIUM Eng. J., 21(1):51-60.

[20] Ramli HAM. (2020) A study on packet scheduling algorithms for healthcare contents over fifth generation (5G) mobile cellular network. Int. J. Electron. Telecommun., 66(4):1–7.

DETECTION OF TRAFFIC DENSITY WITH IMAGE PROCESSING USING PIN HOLE ALGORITHM

MOCHAMAD ADITYA IRAWANTO, CASI SETIANINGSIH* AND BUDHI IRAWAN

*Computer Engineering, School of Electrical & Engineering,
Telkom University, Indonesia*

*Corresponding author: setiacasie@telkomuniversity.ac.id

ABSTRACT: Intelligent traffic monitors have developed and have become more attractive in recent years. A detection system in the monitoring traffic system is proposed using different algorithms. Pin Hole Algorithm used to detect the car that passes the road (the studied area). A fixed camera mounted at a predetermined point is used with known height (of the camera), the intensity of the light, and the visibility of the camera. The classification process is important to know the traffic congestion status. The traffic congestion status will be sent to the server address already provided. In the congestion detection test, results were obtained with an accuracy value of 85% using the 64x64 grid division and obtaining good detection results for susceptible light intensity values between 5430 and 41379 LUX with an accuracy value of between 60% and 90%.

ABSTRAK: Sejak beberapa tahun ini, sistem pengawasan trafik pintar telah dibina dan terus berkembang luas. Sistem pengesanan dalam sistem trafik pengawasan telah dicadangkan menggunakan pelbagai algoritma. Algoritma lubang pin digunakan bagi mengesan kereta yang melalui jalan (kawasan kajian). Kamera dipasang tetap pada titik tertentu iaitu dengan menyelaras ketinggian kamera, keamatan cahaya, dan kebolehlihatan kamera. Proses klasifikasi sangat penting bagi menentukan status kesesakan trafik. Status kesesakan trafik akan dihantar ke alamat pelayan yang telah disediakan. Nilai ketepatan ujian pengesanan kesesakan yang diperoleh adalah 85% iaitu menggunakan pembahagi grid 64x64 dan dapatan kajian menunjukkan pengesanan yang baik bagi nilai keamatan cahaya antara 5430 dan 41379 LUX dengan nilai ketepatan antara 60% dan 90%.

KEYWORDS: *intelligent traffic density; pin hole algorithm; congestion monitor; car detection; traffic details; image processing*

1. INTRODUCTION

Traffic lights with less efficient distribution can cause overcrowding at crossroads and can cause congestion that causes traffic jams to the detriment of road users [1]. Congestion is a condition where there is a stagnant or interrupted flow of vehicles passing through the road due to the accumulation of vehicles exceeding the existing traffic capacity [2].

Congestion problems are caused by a lack of available facilities and infrastructure such as road monitoring systems, road widths, traffic signs. Generally, traffic monitoring systems that are running today still use traditional systems. The system used now is to use cameras installed at various points, which are monitored manually by the Transportation Agency. Overall, this system can work well, detecting congestion in accordance with the

rules of the city of Bandung in Indonesia. It's just that congestion validation is still a bit challenging because there is no definite data comparison yet.

Pin Hole algorithm was used to obtain the congestion status for traffic control on the toll road section. Before that, the camera is fixed to take images (video) for the studied area, pre-processing of the image, contrast limited adaptive histogram equalization, edge detection, enhancement, then image segmentation and classification. The presented algorithm can work with different city roads.

2. RELATED WORK

To maximize the detection of traffic jams using Image Processing, according to previous research that has been done [3], several factors must be considered. The first is the camera settings. This setting is required to be able to determine the shooting results. The accuracy depends on many factors such as the width of the road, the height of the camera installation and the angle of the camera. The second is image segmentation. In object detection, before filtering using a certain algorithm, the initial process is to convert the data format. The data in MPEG form is converted to JPEG. In the form of JPEG format will be searching the edge value or background image, edge value is used to distinguish between road and object to be processed [4]. The edge value taking is done continuously in order to get perfect results [5].

Detection of vehicle objects on a road segment to determine the status of traffic jams can use the Pin Hole Algorithm [6]. Pin Hole algorithm works by using an IP camera. The result of detection from the camera will be MPEG4 which will be converted back into MJPEG to be processed to the next stage [7]. Then the obtained image is filtered using a Greyscale filter to determine the background value of the image. The background value is used to separate where the object is to be detected and which image is just the background of the image [7]. The picture shooting takes place within three minutes, and it is because if the image is taken less than three minutes sometimes still has data that is not yet valid and not perfect. Then determined the parameters of the results in an emphasis on three parameters, namely the first parameter is the size of the image based on terms of connection, the speed of data as a data source. The second parameter is the large image download and the third parameter is the pixel pin hole size.

Another method that can be used in vehicle counting in traffic control is Blob analysis [8]. The Blob Filter algorithm is able to detect congestion well. The steps required in this algorithm are as follows:

1. Vehicle Segmentation, settings in a location of picture shooting on camera.

2. Background Updating, define the background of the image by segmenting.

3. Feature Extraction and Vehicle Classification used to be able to define different objects when detecting images.

4. Vehicle Tracking is used to determine the amount of vehicle current based on the distance of each vehicle.

5. Vehicle Flow Analysis and Counting is used for the final count of the number of vehicles and the speed of the coming vehicle on the line.

The output of this method is the number of vehicles outside the track with the average speed of the vehicle so that it can be concluded whether the situation can be said to be

stuck or not. This method also has an average accuracy value in three conditions of 90% with an estimated error of less than 5 km/hour.

Detecting traffic jams in the city in real-time with the help of a UAV can be chosen as another alternative in analyzing traffic conditions. Traffic data in the form of videos taken from drones is then detected using a Deep Learning Algorithm, namely Mask RCNN. Several steps must be taken, namely, firstly counting the number of vehicles, and estimating the speed of the vehicle. Second, estimate the geometric space for pixels in the image to perform vehicle recognition and tracking [9].

3. RESEARCH METHOD

3.1 Illustrations

Acquisition Video is the process of taking the recording of toll road conditions taken with the *.mp4 video format then saved in a personal computer. The video acquisition is taken based on the entrance to the Bandung city with the criteria of having one common goal and having multiple branches as an alternative way. The video acquisition was taken using GoPro Hero5 Black with 720 pixels video quality and 1280 x 720 pixels resolution at 30 fps. The video acquisition is taken at the top of a person crossing the bridge (JPO) which is on a 5.1 m highway toll road. An illustration of video acquisition can be seen in Fig. 1.
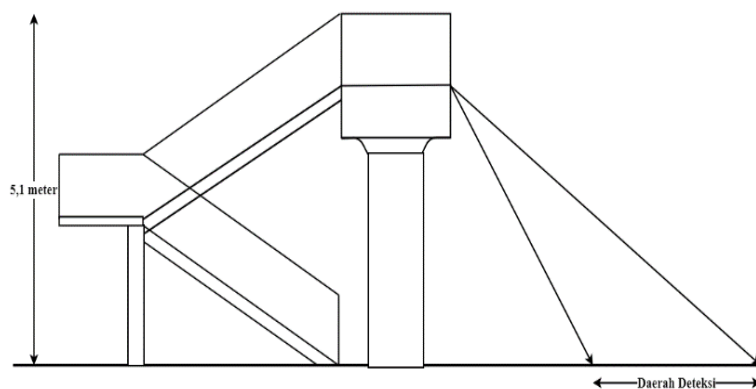

Fig. 1: Illustration of video acquisition.

3.2 Algorithm Steps

Traffic congestion detection is achieved by many steps such as image acquisition from video acquisition, pre-processing on image, Pin Hole processing to perform vehicle calculation on image and result from classification. The process of the suggested algorithm can be described as follows:

3.2.1 Image Acquisition

The image acquisition process is a step to get a sample image based on video recording. Image captured with *.mp4 format and stored in *.png format. Figure 2 shows the acquisition of the saved image with the format of *.png given region Region of Interest (ROI) to detect congestion. ROI is an area marked as the boundary area of toll roads that will be calculated using digital image processing. The original image that has been given the ROI region can be seen in Fig. 2.

Fig. 2: Image acquisition with ROI.

3.2.2 Pre-Processing

The pre-processing step is used to perform calculations by processing the image by combining filters in the image processing. The process that runs in this stage is like capturing the image of the video, changing the grayscale filter, inserting the image into the CLAHE filter, determining the border of the image, inserting the image into the low pass filter, and performing the image segmentation.

a. Greyscale

Greyscale is a color in pixels that are still between the range of black and white values 0-255 which means 0 is a value in black and 255 is white. Gray degree in greyscale can be done by using digital image processing by adjusting the gray degree of the image using a threshold value. Thresholding is the method used to be able to adjust the number of gray-degree values in digital images [10]. The colored image has a matrix value for each pixel in which each pixel has a value of red, green, and blue (r, g, b). To be able to change the color image into greyscale and set the gray degree using thresholding will be explained as follows

- Calculate the value of greyscale using the equation

$$s = \frac{r \times g \times b}{3} \qquad (1)$$

where S is greyscale value

- Calculate the value of thresholding using the equation

$$x = \frac{W}{b} \qquad (2)$$

Where x is gray degree values after thresholding, W is gray degree values before thresholding, and b is the desired quantization values.

The result of color image processing being the greyscale image can be seen in Fig. 3.

Fig. 3: Greyscale image result.

b. Contras Limited Adaptive Histogram Equalization (CLAHE)

CLAHE is a digital image processing process that improves image contrast by increasing contrast in local images by providing a maximum threshold value [11]. The CLAHE process functions to divide the local image contrast in a symmetrical grid called the area size. The image's division region size can be divided into sections such as CR for the corner region, BR for border region, IR for the inner region [12]. The existence of the division of region sizes due to the division of the grid there are different characteristic values for each value of the neighborhood. The structure of region size can be seen in Fig. 4.

CR	BR	BR	CR
BR	IR	IR	BR
BR	IR	IR	BR
CR	BR	BR	CR

Fig. 4: Region size CLAHE.

After dividing the local image into a symmetric grid, the calculation is performed by obtaining a new gray level on each local grid using the cumulative function distribution of histograms used in each local region (i, j).

- Calculates the distribution using an equation

$$(k) = \frac{(N-1)}{M} \cdot \sum_{k=0}^{n} h(k); n = 1,2,3,\dots,N-1 \tag{3}$$

where M is the number of pixels, N is the greyscale value, and h(k) is the histogram on grey value.

After calculating the distribution of cumulative function, then regional on local image give maximal threshold limit on the image using CLAHE.

- Calculates threshold limits using equations

$$\beta = \frac{M}{N}(1 + \frac{a}{100}(S_{max} - 1)) \tag{4}$$

Where M is wide of region size, N is greyscale value, and a is minimum and maximum limit values of histograms ranging from 0-100.

The result of image processing into CLAHE filter can be seen in Fig. 5.

Fig. 5: CLAHE image result.

c. Edge Detection Using Canny Method

Edge Detection or abbreviated as ED is an object detection process in digital image processing that produces an edge output of the image object used to mark the detail part of the image [13]. ED is processed using Canny method. The Canny method is used because it produces a visible edge shape compared to Robert, Sobel, Prewitt, and LoG methods after being processed using the Global Thresholding method [13]. ED in the process is done by giving gaussian filter greyscale image which then convoluted by using method of Canny to get result of fine edge image. Gaussian filter is done by using gaussian filter equation as follows [14]:

- Calculate Gaussian filters using equations

$$G(x) = \frac{1}{\sqrt{2\pi\sigma^2}} e^{-\frac{x^2 + y^2}{2\sigma^2}} \qquad (5)$$

σ = standard deviation distribution (σ = 1,4)

e = exponential value (e = 2,71828183)

(x,y) = the midpoint of the Gaussian function

- Convolution with the Canny method is done by equation

$$\frac{1}{159}\begin{pmatrix} 2 & 4 & 5 & 4 & 2 \\ 4 & 9 & 12 & 9 & 4 \\ 5 & 12 & 15 & 12 & 5 \\ 4 & 9 & 12 & 9 & 4 \\ 2 & 4 & 4 & 4 & 2 \end{pmatrix} \qquad (6)$$

- Calculate magnitude gradient using equation

$$G = |G_X| + |G_y| \qquad (7)$$

- Determining the edges by using the equation

$$q = tan^{-1}\left(\frac{G_x}{G_y}\right) \qquad (8)$$

- Gives the threshold value of the threshold to the ED by using equations

$$g(x,y) = f(x) = \begin{cases} 1, if\ T_{min}, & \leq f(x,y) \leq T_{max} \\ 0, & otherwise \end{cases} \qquad (9)$$

The results from image processing in canny method can be seen in Fig. 6.

Fig. 6: Edge detection image result.

d. Low Pass Filter Using Bilateral Filter

Low Pass Filter is a method by using a filter type that passes low-frequency frequencies and dampens high-value frequencies in imagery [15]. In the process, LPF uses the Bilateral filter method. The BF method is a noise reduction filter on the ash image and also maintains edge detection for smoother image results [16]. Benefits of using the Bilateral filter method include:

- Maintain edge detection while eliminating image disturbance and refining the resulting image
- Eliminate the opacity of the color image
- An easy method to apply [16].

The Bilateral filter method is calculated using the kernel filter equation

$$K = \frac{1}{Ksize.w \; x \; Ksize.h} \begin{pmatrix} 1 & 1 & ... & 1 \\ 1 & 1 & ... & 1 \\ ... & ... & ... & ... \\ 1 & 1 & ... & 1 \end{pmatrix} \tag{10}$$

K = kernel bilateral filter

Ksize = wide of blur in the kernel

w = width image

h = high image

The result of image processing in the Bilateral filter can be seen in Fig. 7.

Fig. 7: Bilateral filter image result.

e. Image Segmentation

Image segmentation is the process for recognition of objects in images and also feature extraction [13]. By doing image segmentation in the final stage, it will show the results of objects and backgrounds on the image. Segmentation is done by assigning a threshold value (threshold) that applies to all parts of the input image. Segmentation is done using the following equation

$$g(x,y) = f(x) = \begin{cases} 1, & f(x,y) \geq T_{max} \\ 0, & f(x,y) < T_{max} \end{cases} \tag{11}$$

g(x,y) = image after thresholding

f(x,y) = edge detection image result

T = limit threshold value

Fig. 8: Segmentation image result.

3.2.3 Pin Hole Algorithm Processing

Determination of the area in the image is the process of determining the area by following the length and width of the toll road to be detected. After the image acquisition process, area masking is carried out by providing a detection area limit on the toll road section. The masking area is done by connecting the four coordinates in the image so that it becomes a 2D shape. Then the detection area is calculated using the equation for the area of an irregular trapezoid.

The preprocessed black and white image is divided into a small symmetrical grid (Pin Hole). The number of grids used is 8x8, 16x16, 32x32, 64x64 pixels. The process of dividing into a grid is done when inserting the CLAHE filter into the grayscale image.

The next step is to find the centroid point (middle value) in the image in each grid area (Pin Hole). To calculate the vehicle capacity in the area to be detected, it can be done using Background Elimination (BE) [17]. BE is processed by eliminating everything that is considered, not including the object in the image so that the value of the object and the background of the image will be separated [17]. BE can be done by first calculating the mean of the RGB value of the image with the *p*-value in the selected background image using equation

$$B(p) = \sum_k \frac{I_B(k,p)}{n} \tag{12}$$

$I_B(k,p)$ = pixel color value for point p in frame k

Then BE from the process   was calculated with equation

$$D(k,p) = \{I_B(k,p) - B(P)\} \tag{13}$$

{.} = value Euclidean Distance between I_B and I_B

After the BE value is obtained, the image of the result of the process is only the centroid value of the object of the detected vehicle object. To obtain the value of congestion capacity in the area specified, then used equation

$$G(x) = 1 - \frac{D(k,p)}{I_B(k,p)} \tag{14}$$

G(x) = congestion value

After doing the calculation on the input image, we will get the result of the number of centroid values contained in the box Pin Hole of the filled capacity of the box.

3.2.4 Classification

Results classification is an advanced process of calculating the number of centroids from the Pin Hole area by grouping the calculation results into several categories determined based on the amount of capacity of the detected object. According to Rudi Herianto (2018), as the Head of the Satlatas Bojongsoang Unit, the congestion category can be grouped into 3, namely:

a. **Traffic Jam**

The jam status is used when the resulting value of the congestion capacity calculation reaches a value of more than 70%.

b. **Crowded Smoothly**

The current status is smoothly used when the value of the result of the congestion capacity calculation reaches a value of more than 10% and less than 70%.

c. **Fluent**

The current status is used when the value of the calculation of congestion capacity reaches less than 10%.

4. RESULTS

4.1 Testing the Conversion of Pixel Values into Meter Units

Testing the conversion of pixel values into units of meters aims to see the effect of the results of the detection performed using imagery with the existing conditions significantly. To do this test needs to be done in several stages by taking several image samples that have a smooth and crowded classification smoothly. The stages that need to be done can be described as follows:

a. **Determine the true value of the actual detection**

The actual detection area value is obtained by calculating the area of the road that is on the Moh. Toha Toll Road based on Toll Road Geometry Standard [18].

b. **Calculate the actual detection area**

The image ROI is calculated using the formula of building a free trapezoidal space. Where both sides of the trapezoid are the length of the toll road and the height of the trapezoid is the width of the toll road.

c. **Calculate pixel area and conversion to meters**

Calculating the area of pixels then converting them into meter units is done by calculating the area obtained from the image of the detection result into the equation

$$area = LP \ \times dpi \ \times pixel\ to\ cm \tag{15}$$

dpi = dot per inch

pixel to cm = 0.0264583333 cm

d. **Determine the Image Scale Value**

Determine the value of the image scale by dividing the original area by the area of the pixel area converted into meters. It is helpful as a comparator value between the image of the detection result and the condition on the actual toll road.

Based on the process of testing the conversion of pixel values to meters, the results are obtained for the actual detection area as shown in Table 1. The result of the pixel value conversion to the unit meter can be seen in Table 2. After getting each of the required values as in Tables 1 and 2, conclusions can be drawn based on the sampling of the detected images. Conclusions can be seen in Table 3.

Table 1: Wide actual toll roads

No.	Explanation	Value
1.	DPI	72 pixels per inch camera
2.	Actual Toll Road Length	91 m
3.	Actual Toll Road Width	10.5 m
4.	Actual Toll Road Area	955.5 m^2

Table 2: Scale and area of conversion

No.	Area (pixels)	Area of Conversion Area (m^2)	Actual Toll Road Area (m^2)	Conversion Area Scale with Real Area
1.	237900 pixels	4531.93	955.5	4:1

Table 3: The final conversion result to the pixel value

No	Pixel Value			Value After Conversion (m^2)			
	Area	Object Area	Percentage of Congestion	Classi-fication	Area	Object Area	Percentage of Congestion
1.	237900	17900	7.52%	Fluent	4531.93	340.9907	7.52%
2.	237900	34800	14.62%	Smoothly	4531.93	662.939	14.62%

4.2 Pin Hole Grid Testing

The value of detection accuracy for 20 frames can be seen in Fig. 9. Pin Hole grid test aims to see the effect of the number of Pin Hole boxes during the image segmentation process. This step is used to detect congestion when segmentation in the image entered in the CLAHE filter on the accuracy obtained in the process. CLAHE filter was used because the filter input image is divided into the symmetrical grid where the number of grids affects the Pin Hole's accuracy.

a. Image Conformity Results

This test is done by running 5 different Pin Hole grid values, i.e., grid images 8x8, 16x16, 32x32, and 64x64 with the image without grid division. The grid value used for the original image and the segmentation image of the CLAHE filter results. The following results from the process can be seen in Table 4.

Based on the segmentation image conformity using CLAHE filters with the original image in Table 4, the results of segmentation images have a lot of noise due to the inadequate CLAHE filters caused by the small number of grids that cause excess calculation results when the process is done The Histogram Equalizer that causes the calculated vehicle object does not match the input

image. Many noises in the results image are obtained in the image with a grid of 8x8, 16x16 and 32x32.
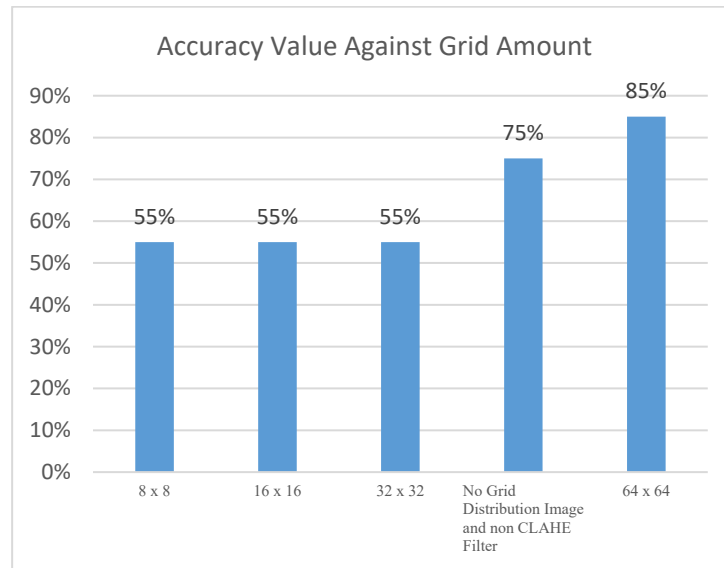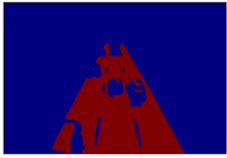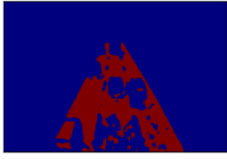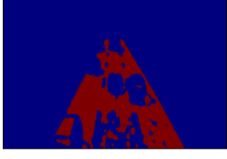

Fig. 9: Value of accuracy to the number of grids.

Table 4: Image conformity results

No.	Grid Amount	Results		Similar	Not Similar
		Original Image	**CLAHE Segmentation Image**		
1.	0x0			✓	
2.	8x8				✓
3.	16x16				✓
4.	32x32				✓
5.	64x64			✓	

a. **Image Detection Results**

This was done by comparing the detection value of the image with the correct value to get the accuracy value. The correct value is obtained from interviews conducted with Mr. Rudi Herianto is the Chief of the Indonesian National Police Traffic Department in Bandung.

4.3 Light Intensity Testing

Testing will be carried out by taking sample data on the results of recording traffic conditions on the toll road with different light intensity values. Different light intensity values will be obtained by detecting at different times, i.e., morning, afternoon, evening, and night. After that, the comparison of results will be made based on the accuracy values obtained. From this stage, the conclusion will be drawn based on high accuracy values on the value of the light intensity obtained by concluding the vulnerable value of the appropriate light intensity to detect congestion. The results of this test can be seen in Fig. 10.
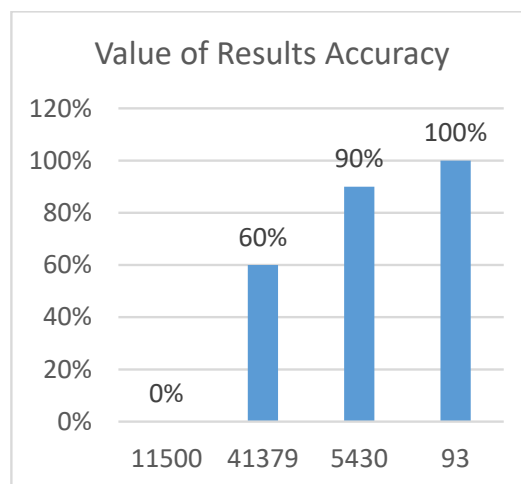
Fig. 10: Value accuracy of results based on light intensity.

Based on the graph in Fig. 10, the value of light intensity affects the result of the accuracy value obtained from the detection of congestion. The difference in the value of accuracy obtained is based on several factors as follows:

a. **Toll Road Conditions**

As seen in Fig. 10 that the detection error that occurred on the Toll road segment at light intensity is 11500 with an accuracy value of 0%. This is due to the detection of the image background as an object; after an analysis of the original image and the segmentation results obtained results that the error lies in the color of the uneven markers.

b. **Car Light**

Although in Fig. 10 the detection at night, the accuracy value reaches 100%, because the results of true values obtained from subjective opinions do not guarantee that the results are always correct. Reflection of light from car lights is considered to have an excessive amount of light intensity from the specified threshold. Therefore, the value of the excess light intensity is detected as an

object when image segmentation and is calculated in the search for congestion capacity values.

5. CONCLUSION

Based on the results of the analysis of the testing scenario on the congestion detection system using image processing with Pin Hole algorithm, which is carried out on 5 toll roads that will enter the city of Bandung, the following conclusions are obtained:

1. Based on the conversion of pixel values into units of meter obtained results from the image of the sample taken that the area of detection value using the image of 237900 pixels equal to the area of 4531.93 m^2 on the actual condition with a scale of 1:4

2. The congestion capacity for the classification results smoothly in the sample image will be the same value when the total object value of 340.9907 m is in the area of the detection area of 4531.93 m^2 in the real condition.

3. The implementation of the system can produce an accuracy value of 85% by using symmetrical 64x64 grid images with an average computing time of 5 seconds.

4. The detection results are assessed in the light intensity range from 5.430 to 41.379 LUX, assuming good road conditions.

5. The algorithm used still require modification with other algorithms in order to do detection at night.

6. Based on the weather obtained when sampling is not so influential as long as the light intensity values obtained are still in the susceptible 5.430 to 41.379.

7. This system is helpful as an alternative to find the value of congestion capacity based on the number of vehicles that will enter the city of Bandung through the highway.

REFERENCES

[1] Royani, Tahere, Haddadnia J, Pooshideh MR. (2010) A simple method for calculating vehicle density in traffic images. In 6th IEEE Iranian Conference on Machine Vision and Image Processing: October 2010; pp 1-4.
[2] Fibriliyanti, Yanita, Faradila LR, Taqwa A. (2017) Implementasi Pengolahan Citra dengan Metode Histogram Of Oriented Gradient (Hog) untuk Pengaturan Waktu pada Traffic Light Berdasarkan Deteksi Kepadatan Kendaraan. In Prosiding SNATIF: 2017; pp 403-412.
[3] Directorate General of Land Transportation Ministry of Transportation Republic of Indonesia. (2008) Technical Instructions for the Implementation of Road Equipment. Jakarta.
[4] Nurhadiyatna A, Hardjono B, Wibisono A, Sina I, Jatmiko W, Ma'Sum MA, Mursanto P. (2013) Improved vehicle speed estimation using gaussian mixture model and hole filling algorithm. In 2013 IEEE International Conference on Advanced Computer Science and Information Systems (ICACSIS): September 2013; pp 451-456.
[5] Kim KI, Jung K, Kim JH. (2002) Color texture-based object detection: an application to license plate localization. In Springer International Workshop on Support Vector Machines: August 2022; Berlin, Heidelberg. pp 293-309.
[6] Bas E, Tekalp AM, Salman FS. (2007) Automatic vehicle counting from video for traffic flow analysis. In 2007 IEEE intelligent vehicles symposium: June 2007; pp 392-397.
[7] Mahatmaputra S, Permata E, William. (2011) Deteksi kemacetan lalu lintas melalui kamera menggunakan pin hole algorithm. ComTech., 2:821-834.

[8] Cucchiara R, Massimo P, Paola M. (2000) Image analysis and rule-based reasoning for a traffic monitoring system. IEEE transactions on intelligent transportation systems, 1(2):119-130.

[9] Chen TH, Lin YF, Chen TY. (2007) Intelligent vehicle counting method based on blob analysis in traffic surveillance. In Second IEEE International Conference on Innovative Computing, Informatio and Control (ICICIC): September 2007; pp 238-238.

[10] Zhang H, Liptrott M, Bessis N, Cheng J. (2019) Real-time traffic analysis using deep learning techniques and uav based video. In 16th IEEE International Conference on Advanced Video and Signal Based Surveillance (AVSS): September 2019; pp. 1-5.

[11] Saepudin D, Rizal A. (2014) Analisis Contrast Limited Adaptive Histogram Equalization (Clahe) Dan Region Growing Dalam Deteksi Gejala Kanker Payudara Pada Citra Mammogram. Jurnal Elektro Unika Atma Jaya., 7(1):15-28.

[12] Reza AM. (2004) Realization of the contrast limited adaptive histogram equalization (CLAHE) for real-time image enhancement. Journal of VLSI signal processing systems for signal, image and video technology., 38(1):35-44.

[13] Junior RA, Nurhasanah N, Sanubary I. (2014) Perbandingan Penggunaan Beberapa Metode Deteksi Tepi Pada Pengolahan Citra Radiologi Fraktur Tulang. Prisma Fisika., 5(3):122-130.

[14] Triono P, Murinto M. (2015) Aplikasi Pengolahan Citra Untuk Mendeteksi Fraktur Tulang Dengan Metode Deteksi Tepi Canny. Jurnal Informatika Ahmad Dahlan., 9(2):103-842.

[15] Panda DK, Sukadev M. (2013) A gaussian mixture model with gaussian weight learning rate and foreground detection using neighbourhood correlation. In 2013 IEEE Asia Pacific Conference on Postgraduate Research in Microelectronics and Electronics (PrimeAsia): December 2013; pp. 158-163.

[16] Tomasi C, Manduchi R. (1998) Bilateral filtering for gray and color images. In Sixth IEEE international conference on computer vision (IEEE Cat. No. 98CH36271): January 1998; pp. 839-846.

[17] Deswal S, Gupta S, Bhushan B. (2015) A survey of various bilateral filtering techniques. International Journal of Signal Processing, Image Processing and Pattern Recognition., 8(3):105-120.

[18] Atkočiūnas E, Blake R, Juozapavičius A, Kazimianec M. (2005) Image processing in road traffic analysis. Nonlinear Analysis: Modelling and Control., 10(4):315-332.

[19] The Directorate General of Directorate General of Marga The Ministry of Public Works and Housing Republic of Indonesia. (2008) Standar geometri jalan bebas hambatan untuk jalan tol. Jakarta.

BIODEGRADATION OF MANGO SEED STARCH FILMS IN SOIL

Nur'Aishah Ahmad Shahrim*, Norshahida Sarifuddin, Ahmad Zahirani Ahmad Azhar and Hafizah Hanim Mohd Zaki

Department of Manufacturing and Materials Engineering, Kulliyyah of Engineering, International Islamic University Malaysia, Jalan Gombak, 53100 Kuala Lumpur, Malaysia

**Corresponding author: nuraishahahmadshahrim@gmail.com*

ABSTRACT: The typical petroleum-based plastics have triggered environmental problems. For this purpose, biodegradable polymers such as starch are often used to manufacture biodegradable plastics. At present, the efforts are underway to extract starch as a promising biopolymer from mango seeds and subsequently to produce a biodegradable starch film to be used as plastic packaging. As such, in this work, glycerol-plasticized mango starch films were prepared using a solution casting process, using different amounts of citric acid as a cross-linking agent. The blend ratio of starch to glycerol was set at 3:5 wt. each, while the amount of citric acid ranged from 0 to 10 wt.%. Then, the casted films underwent 21 days of soil burial testing in the natural environment to determine their biodegradability behavior. The soil burial test is one of the common methods chosen to assess the biodegradability of polymers. The idea is that, by burying samples in the soil for a fixed time, samples are exposed to microorganisms (i.e. bacteria and fungi) present in the soil that serve as their food source. This is somehow likely to facilitate the process of deterioration. For this reason, the soil burial test can be regarded as an authentic approach to the process of deterioration in the natural environment. The films' susceptibility to biodegradation reactions was assessed within intervals of seven days through their physical appearance and weight loss. Interestingly, it was found that the cross-linked starch films have been observed to degrade slower than the non-cross-linked starch films as burial time progressed. The declining percentages of weight loss, as well as the presence of microorganisms and eroded surface on the films observed by SEM, explained the degradation behavior of the cross-linked starch films compared to the non-cross-linked starch films. Hence it is believed that cross-linked starch-glycerol films are biodegradable in soil, henceforth, the potential to be commercialized as a biodegradable packaging material soon. At the same time, this plastic packaging is expected to be recognized as a value-added product since the raw materials ergo mango seeds utilized to develop this product are from waste, therefore, environmentally friendly.

ABSTRAK: Plastik yang berasaskan petroleum telah mencetuskan masalah persekitaran. Untuk tujuan ini, polimer biodegradasi seperti kanji sering digunakan untuk membuat plastik yang boleh terurai. Pada masa ini, usaha sedang dilakukan untuk mengekstrak pati sebagai biopolimer yang menjanjikan dari biji mangga dan kemudiannya menghasilkan filem pati yang terbiodegradasi untuk digunakan sebagai kemasan plastik. Oleh yang demikian, dalam karya ini, filem pati mangga plastik-gliserol disusun menggunakan proses pemutus larutan, menggunakan jumlah asid sitrik yang berlainan sebagai agen penghubung silang. Nisbah campuran pati dan gliserol ditetapkan pada 3:5 wt.% masing-masing, sementara jumlah asid sitrik berkisar antara 0 hingga 10 wt.% berat. Kemudian, sampel plastik tersebut ditanam di dalam tanah selama 21 hari di persekitaran semula jadi untuk menentukan tingkah laku biodegradasinya. Ujian penguburan tanah adalah salah

satu kaedah biasa yang dipilih untuk menilai biodegradasi polimer. Ideanya adalah bahawa, dengan menguburkan sampel di tanah untuk waktu yang tetap, sampel terdedah kepada mikroorganisma (iaitu bakteria dan jamur) yang terdapat di dalam tanah yang berfungsi sebagai sumber makanan mereka. Ini mungkin memudahkan proses kemerosotan. Atas sebab ini, ujian penguburan tanah dapat dianggap sebagai pendekatan yang sahih terhadap proses kemerosotan di persekitaran semula jadi. Kerentanan filem terhadap reaksi biodegradasi dinilai dalam selang waktu tujuh hari melalui penampilan fizikal dan penurunan berat badan. Menariknya, didapati bahawa filem-filem pati berangkai silang telah dilihat menurun lebih perlahan daripada filem-filem pati yang tidak bersilang ketika masa pengebumian berlangsung. Peratusan penurunan berat badan yang menurun, serta kehadiran mikroorganisma dan permukaan yang terhakis pada filem yang diperhatikan oleh SEM, menjelaskan tingkah laku degradasi filem pati berangkai silang berbanding dengan filem pati yang tidak bersilang. Oleh itu, dipercayai bahawa filem kanji-gliserol berangkai silang dapat terbiodegradasi di dalam tanah, dan seterusnya, potensi untuk dikomersialkan sebagai bahan pembungkusan yang boleh terurai tidak lama lagi. Pada masa yang sama, pembungkusan plastik ini diharapkan dapat diakui sebagai produk bernilai tambah kerana bahan mentah ergo mangga yang digunakan untuk mengembangkan produk ini adalah dari sisa, oleh itu, mesra alam.

1. INTRODUCTION

Over the past several years, due to the rise in environmental concerns, research has been focused on biodegradable materials in reducing the reliance on petroleum-based materials. For this purpose, a biopolymer has been widely developed as an alternative to conventional materials due to their attractive benefits such as biodegradability and sustainability towards the environment [1]. At present, the development of biodegradable materials based on polymers has been attempted in several approaches [2]. One of the approaches is to produce polymeric materials based on inherently biodegradable materials. This has been attracting rising interest in the utilization of starch as a biopolymer. Consequently, the biodegradable constituent is predicted to be degraded rapidly by environmental factors such as biological activity, chemical conditions, moisture, heat, and light, initiating an overall deterioration of the polymeric matrix, which in turn boosts the disintegration of the whole material [2,3].

In this analysis, mango seeds were used to get native starch. Mango (*Mangifera indica*) belongs to the genus *Mangifera* in the *Anacardiaceae* family of flowering plants, is a common tropical fruit, and is widely grown practically. Throughout the world's tropical and subtropical regions like Malaysia, Thailand, and India [4]. These types of fruits are usually consumed as fresh or processed into juices, and their seeds are discarded as waste. Interestingly, these seeds are rich in starch and protein [5]. Therefore, the seeds fit as a viable source of starch. Because starch does not possess thermoplastic properties, polyols, such as glycerol, are often used as plasticizers to improve the workability and flexibility, as well as to overcome the brittleness of the native starch [6]. However, the usage of starch in developing biodegradable plastics may have several drawbacks. Its hydrophilic characteristic may cause the synthesized materials to have a high-water sensitivity, poor moisture barrier properties, and high retrogradation over some time. Hence, poly-carboxylic acids, such as citric acid, are introduced as cross-linking agents during the blending of thermoplastic starch to overcome the retrogradation phenomenon and improve its performance in numerous applications. Citric acid is known as a natural organic acid, is nutritionally harmless compared with other substances, and consists of multi-carboxylic structures [7].

Soil burial biodegradability behavior of starch incorporated with biopolymers such as starch grafted low-density polyethylene (LDPE) [8], corn starch with chitosan [9], and corn starch with polyvinyl alcohol (PVOH) [10] have been demonstrated. A similar approach by crosslinking cassava starch with citric acid has been reported its biodegradability properties through soil burial [7]. From these literatures, it can be concluded that starch-based films prepared from different sources of starch exhibited biodegradable behavior. However, study related to the biodegradability behavior of mango seed starch-based films is rarely reported. Hence, in this research, the utilization of starch from mango seeds specifically obtained at the local market in Malaysia have been processed to prepare the films. The extraction processes of the mango seeds included the separation between the kernel (outer) and cotyledon (inner), in which only the inner seeds were further processed and blended with glycerol and citric acid to fabricate films. This is to differentiate the findings obtained in this work with the mango kernel starch plasticized with glycerol and sorbitol that has been reported previously [11], which does not consider the biodegradation testing. The primary objective of this research was to develop a biodegradable starch-based film for packaging materials applications via solution casting method. Prior to the main objective, a biodegradability analysis was conducted using a soil burial test to investigate the effect of cross-linking on the degradation rate of the glycerol-plasticized thermoplastic mango seed starch (GTPS) films. It is expected that the non-cross-linked and cross-linked GTPS films will experience weight loss during the soil burial test, proving that these films are biodegradable and sustain the environment after usage as packaging.

2. MATERIALS AND METHODS

2.1 Raw Materials

Mango seeds had been collected from the local market as a source of starch. 85% pure glycerol was procured from Merck Sdn. Bhd. (Selangor, Malaysia) and reagent-grade citric acid (≥99% purity) was procured from Sigma-Aldrich Sdn. Bhd. (Selangor, Malaysia).

2.2 Extraction of Mango Seed Starch via Distillation Method

The starch from mango seed was extracted with minor modifications according to the procedure defined by Noor et al. [5]. Initially, 5 g of mango seed flour was introduced to 100 ml of distilled water at room temperature, with continuous stirring for 6 h. Then, the slurry was filtered with a cloth bag (about 200 μm mesh), and the excess residues were rinsed three times with distilled water. The filtrate was immersed and precipitated at 4 °C overnight. Finally, the starch obtained was filtered and dried in the oven for 24 h at 40 °C. The starch was crushed with a mortar and pestle, wrapped in a sealed plastic bag, and held at room temperature for further use.

2.3 Preparation of Starch-Glycerol Film Cross-linked with Citric Acid

Starch-glycerol films that were cross-linked with citric acid were processed with some modifications using the solution casting method recommended by Seligra et al. [7] and Reddy & Yang [8]. The starch-to-glycerol ratio was set at 3:5 (wt.%), while the citric acid content ranged from 0 wt.% to 10 wt.%. The total input mass was kept at 100 g. Abbreviations of the material and corresponding sample compositions are presented in Table 1. The blends were heated to 90 °C on a hot plate and kept with continuous stirring at 250 rpm during this temperature for 20 min. The formulations then were cooled to 65 °C and poured on an acrylic sheet. The cast films were allowed to dry in an oven at 40 °C and then peeled off plates after around 24 hours. The peeled films were preserved at 23 °C and 30% relative humidity in a desiccator before characterization.

Table 1: Abbreviations and corresponding compositions of each sample

Material	Abbreviation	Weight Proportion (g)			
		Starch	Glycerol	Citric Acid	Distilled Water
GTPS-CA0	G5	3.0	0.5	0	96.5
GTPS-CA1	CA2	3.0	0.5	0.2	96.3
GTPS-CA2	CA4	3.0	0.5	0.4	96.1
GTPS-CA3	CA6	3.0	0.5	0.6	95.9
GTPS-CA4	CA8	3.0	0.5	0.8	95.7
GTPS-CA5	CA10	3.0	0.5	1.0	95.5

2.4 Fourier-Transformed Infrared (FT-IR) Spectroscopy

FT-IR spectroscopy was used to examine the functional properties of non-cross-linked and cross-linked GTPS films (Spectrum 100, Perkin Elmer; USA). FT-IR spectra were recorded using an attenuated total reflection (ATR) method to study the functional groups in starch. The analysis was performed in the $4000 \text{ cm}^{-1} – 600 \text{ cm}^{-1}$ range, with a resolution of 8 cm^{-1} and a scanning frequency of 32 per sample.

2.5 Soil Burial Degradation

Degradation behavior of starch-based film incorporated with 5 wt.% glycerol crosslinked with 0, 2, 4, 6, 8, and 10 wt.% citric acids was carried out by soil burial test using procedures mentioned by Azahari et al. [9] with slight modification. The soil will cover a grid from all the sides of the grid by cutting three samples of each film measuring between 20 mm and 20 mm. Samples of every composition were then buried in separate pots of composted soil at a depth of 50 mm. The soil was then exposed to the natural weather and positioned in the open area.

The weight loss of all samples was calculated at regular intervals of time (7 days) for the degradation rate of samples. The samples were carefully separated from the soil and washed away soil from the film with distilled water. The sample was left to dry, and the electronic mass balance was used to measure the weight of the dried sample. During the soil burial test, the weight loss of the sample was assessed according to Eq. (1):

$$Weight\ loss\ (\%) = \frac{W_i - W_d}{W_i} \times 100 \tag{1}$$

where W_i is the sample's initial weight (g) and W_d is the sample's weight (g) after seven days.

2.6 Scanning Electron Microscopy (SEM) Test

The morphology of the film surfaces before and after the soil burial test were examined using a scanning electron microscope (JEOL, JSM-IT 100; Japan), operated at an acceleration voltage of 7 kV. The samples were sputter-coated with palladium (SC7620 Sputter Coater, Quorum Technologies Ltd, Lewes, United Kingdom).

3. RESULTS AND DISCUSSION

3.1 Functional Properties

Figure 1 shows the FT-IR spectra of cross-linked mango seed starch-glycerol films. The observed peaks are the functional groups of starch, glycerol, and citric acid, with minor variations in intensity and band position. The following characteristic bands were visible in all spectra: $3270 – 3315 \text{ cm}^{-1}$ corresponds to the stretching of the O-H group of starch,

glycerol, and water, 2924 – 2928 cm^{-1} corresponds to the stretching of the C-H group due to the formation of intermolecular and intramolecular bonds between starch and glycerol hydroxyl groups, and 1611 – 1633 cm^{-1} corresponds to water related absorbance.
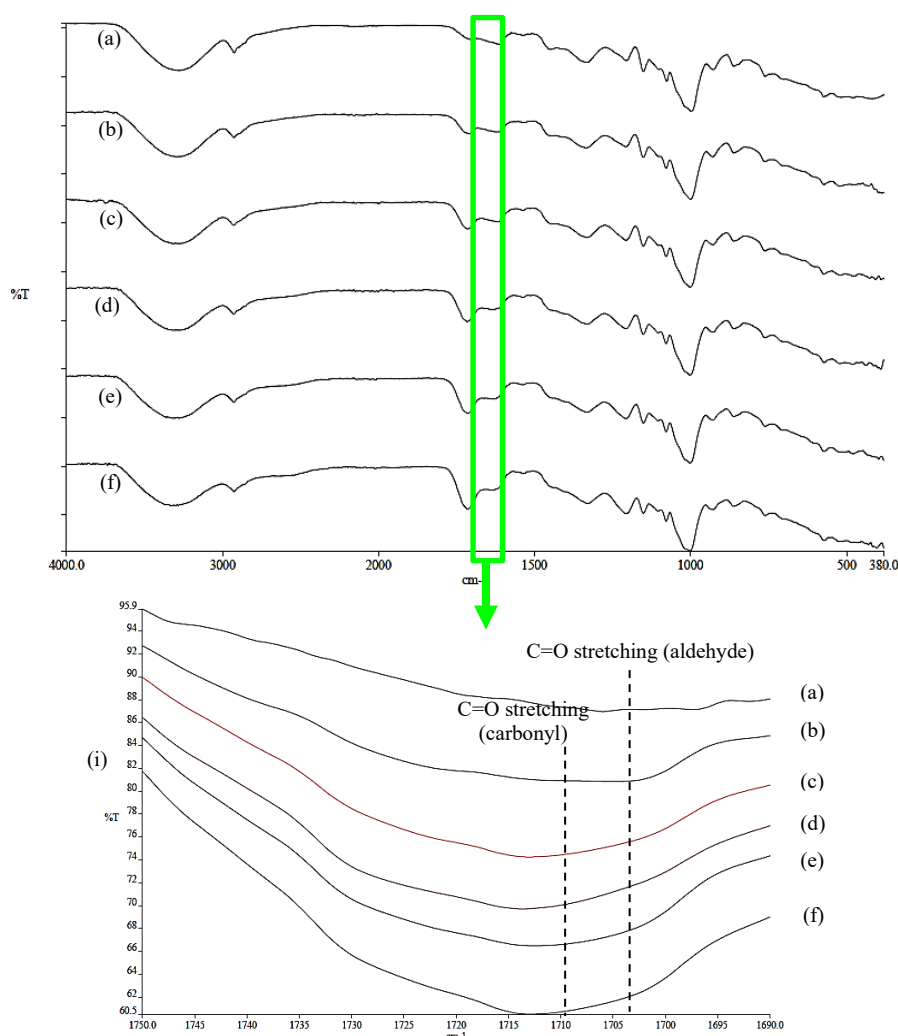

Fig. 1: FT-IR spectra of mango seed starch-glycerol cross-linked with citric acid concentrations of (a) 0, (b) 2, (c) 4, (d) 6, (e) 8, and (f) 10 wt.%.

The addition of citric acid to the blend causes changes in the peaks. The hydroxyl group-related peak at 3270 – 3315 cm^{-1} was wider and less intense. This meant that there were more O-H in the blend that could easily vibrate, resulting in more O-H forming hydrogen bonds [7]. Furthermore, the addition of citric acid to the GTPS resulted in peaks shifting from 998.30 cm^{-1} to 1000.23 cm^{-1}. This demonstrates that the interactions of citric acid's hydroxyl and carboxyl groups with C-O groups of C-O-C in starch are weaker than those of glycerol [6]. It is also observed that both non-cross-linked (Fig. 1(a)) and cross-linked films (Fig. 1(b) – 1(f)) have similar peaks, except for the additional peak in the cross-linked film at 1712 – 1713 cm^{-1}. The C=O peak was attributed to the carboxyl and ester carbonyl bands, where there was chemical linkage from acid groups esters between citric acid and glycerol, as well as esters between starch and citric acid [7,12]. This suggests that crosslinking occurred in the starch-glycerol films. The addition of citric acid resulted in more intense peaks, implying that citric acid is more capable of disrupting starch chains' intermolecular and intramolecular hydrogen bonds [13,14].

3.2 Visual Observation

The pictorial view of the samples retrieved after being subjected to natural soil burial test for 21 days is presented in Fig. 2. This denoted that the visual changes of samples can be used as the first indication of any surface degradation.

From the figure, it was observed that the non-cross-linked films and cross-linked films at 2 wt.% to 10 wt.% citric acid contents started to experience deterioration in the first seven days. The deterioration of starch-based films in soil was governed by hydrolytic degradation, in which the excess water permeated through the soil and diffused into the samples, causing films to become soft and swelled. This could be described by the appearance of samples that seemed fragile and brittle and diminished in size. Specifically, after being buried 21 days in soil, GTPS-CA0 showed major deterioration compared to GTPS-CA2. Increasing citric acid content from 2 wt.% to 10 wt.%, making the cross-linked films more resistant to deterioration. At the same time, it was also noticed that there are white particles spotted on films, which are believed as micro-organisms on the surface of all samples. By some means, the deterioration of samples was boosted by the microbial attack, evidenced by SEM images (Fig. 3). Moreover, the macro-organisms like fungus gnat larvae, the worm-like creatures that squirm their way around in soil and fungi to feed the decaying samples, hence boost up the degradation rate. These results imply that the films were degraded and decomposed in the soil environment, although the degradation rates were significantly varied among the starch-based films.
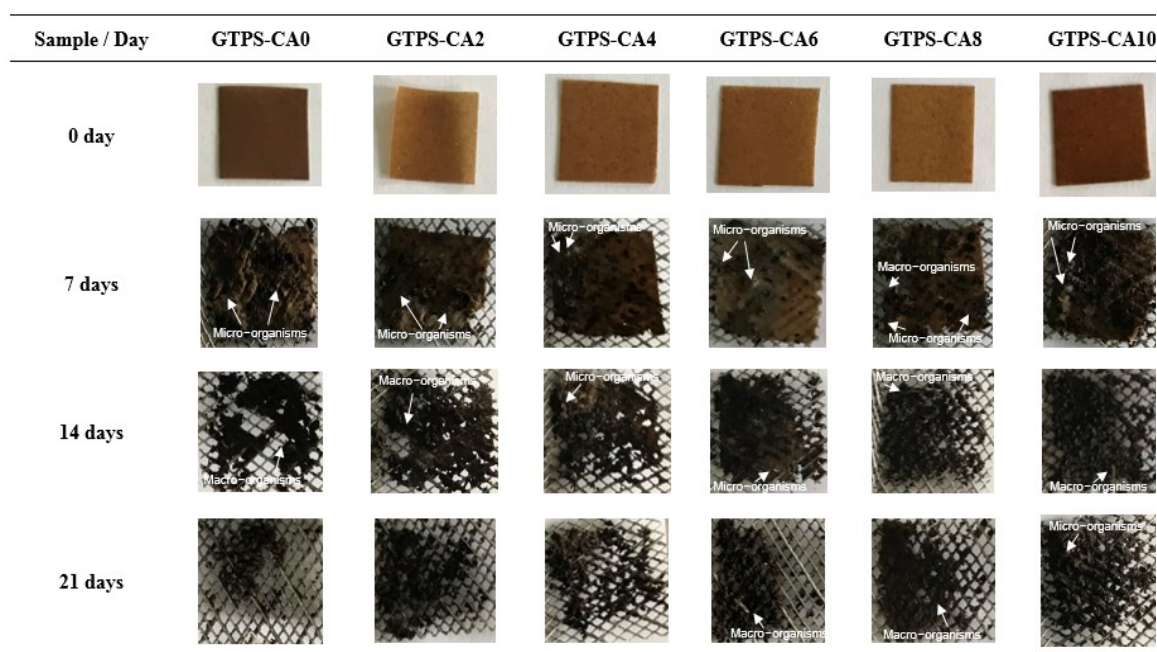

Fig. 2: Macroscopic appearance of non-cross-linked and cross-linked mango seed starch-glycerol films after being buried for 21 days.

3.3 Morphological Properties

SEM micrographs are shown in Fig. 3(a) – 3(f) visualized the morphological changes of mango seed starch-glycerol-citric acid films after being subjected to a soil burial test for 7 days. The observation was done in short-term degradation due to the unfeasibility in observing the morphology of films after 21 days since there were only tiny pieces of films left when retrieved from the soil, shown previously.

The morphology of starch-glycerol films with 0 wt.% citric acids displayed a significantly eroded surface with plentiful filamentous fungus, fungus colonization, and pores (Fig. 3(a)). The addition of citric acid from 2 wt.% to 10 wt.% in starch and glycerol blend (Fig. 3(b) – 3(f)) revealed the surface of the samples were colonized by micro-organisms, however, with the existence of less filamentous fungus, fungus colonization, puffball spores, and pores. Thus, it seems that starch-glycerol films with higher citric acid content degrade slowly, consequently had a lower percentage of weight loss (Section 3.4).

During the exposure of samples in soil within 7 days, the formation of numerous pores and microbial biofilm with many cells growing on the starch-based films appeared. The presence of pores on the deteriorated samples upon the biodegradation process is associated with the starch consumption by the microorganisms, lead to enhancement of microorganisms, water, and oxygen accessibility into the polymer matrix, and caused weight loss of samples. At the same time, the exposed films' surface facilitates moisture permeation that fosters microbial attack on the starch and hydrolysis of the matrix component [15]. Furthermore, the deterioration of starch-based films was also contributed by the fungal strains [16]. It is noted that the fungal species that existed in the film was identified as *Aspergillus* sp. It is noticed in the form of the filamentous and unicellular arrangement was reproduced by spores. These micro-organisms are believed to exploit the starch film as a sole carbon source, causing degradation of films in the soil condition. A similar type of micro-organisms associated with polymer degradation in the soil was reported earlier [16] on cassava starch-based films. Besides, the existence of filamentous fungus, spores, and fungus colonization on the film surface concurs with the fact that fungi are pervasive and very effective in influencing the film's biodegradability behavior, especially in the soil condition. The observation is per the findings reported previously [17].
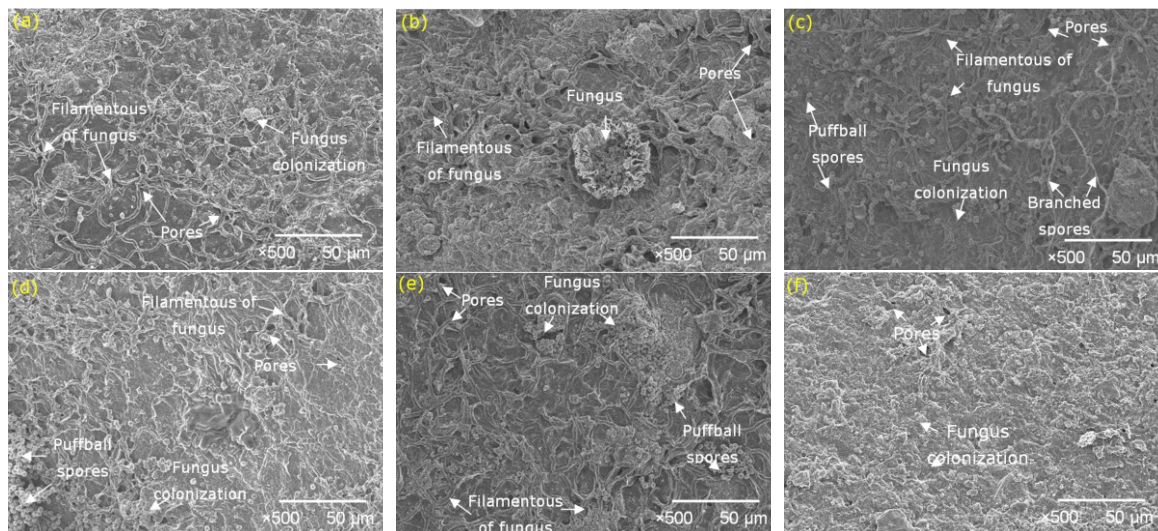

Fig. 3: SEM micrographs at 500× magnification of cross-linked mango seed starch films with various citric acid concentrations (a) 0, (b) 2, (c) 4, (d) 6, (e) 8, and (f) 10 wt.%.

3.4 Weight Loss

The percent weight loss of mango seed starch-glycerol films cross-linked with different amounts of citric acid after being buried in soil for 21 days is illustrated in Fig. 4. It was noticed that the percent weight loss of all samples progressed continuously over time.

The result revealed that the non-cross-linked films (GTPS-CA0) achieving the highest weight loss, thus denote the fastest rate of degradation compared to cross-linked films. The addition of citric acid to starch and glycerol blend resulted in a low percentage of weight

Ahmad Shahrim et al.

loss. It was also remarked that the maximum weight losses were 91.76%, 91.41%, 90.32%, 87.93%, 86.44%, and 85.94% for GTPS-CA0, GTPS-CA2, GTPS-CA4, GTPS-CA6, GTPS-CA8, and GTPS-CA10, respectively after 21 days of soil burial.
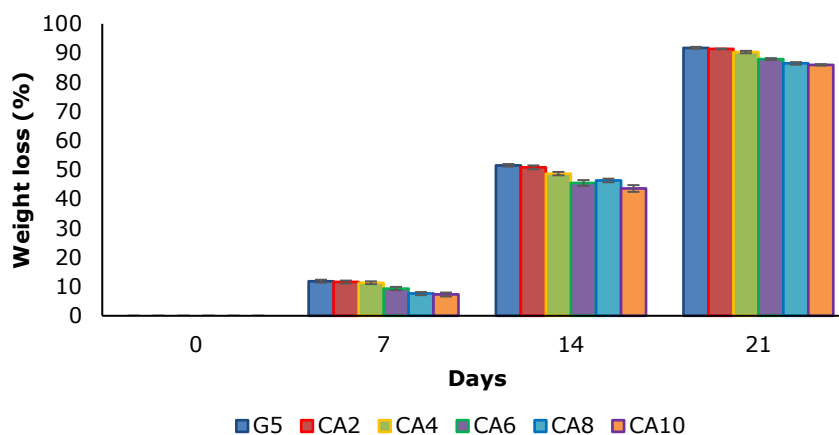

Fig. 4: Weight loss of non-cross-linked and cross-linked mango seed starch-glycerol films after buried in soil for 21 days.

Based on Fig. 4, it was found that the weight loss observed after 21 days of soil burial was decreased with increasing citric acid content. Within the burial time, the starch-glycerol films might absorb adequate water because of their hydrophilic characteristics, which facilitates microbial attack and hydrolysis of the matrix component. As a result, the hydrolytic depolymerization of starch chains to monomeric units occurs, and the probable deterioration of films is caused by microorganisms [18]. Eventually, the formation of pores on the film surfaces as being viewed in SEM micrographs (Fig. 3) indicates the starch consumption by microorganisms. It is also important to note that the starch also might be attacked by micro-organisms as being visually observed (Fig. 2), which might feed on the starch as a source of food, henceforth deteriorate the films. Increasing citric acid content in starch and glycerol blend leads to a slower degradation rate because lesser microorganisms invade the films and weaker interaction of hydrogen bonds within the starch chains.

However, the weight losses may underestimate because the soil and debris have adhered to the film surface. The weight loss of the cross-linked starch-glycerol films at 21 days of soil burial proved that they are biodegradable. This is in agreement with the findings reported [7] in cassava starch-glycerol cross-linked with citric acid, who observed that cross-linked films degrade slower in soil than non-cross-linked films.

4. CONCLUSION

From the present study, it is confirmed that the cross-linked mango seed starch-glycerol films are proved by the FT-IR spectra and its biodegradability by soil burial tests. The results obtained from the visual observation after exposure to soil burial test revealed that cross-linked starch films degrade slower which has been justified by the decreasing weight loss percentages as well as the presence of microorganisms and eroded surface on the films detected by SEM. It is therefore hoped that the fabrication of mango seed starch-based films as biodegradable plastic packaging would soon minimize the environmental pollution mainly caused by typical petroleum-based plastics, specifically single-use plastics. Having said that, the use of mango seeds as raw materials to produce biodegradable plastics will also offer a value-added material and reduce the production cost. Overall, the extent of

starch-based film degradation following exposure to soil burial has been extensively inferred in this work.

ACKNOWLEDGEMENT

REFERENCES

[1] Lu DR, Xiao CM, Xu SJ. (2009). Starch-based completely biodegradable polymer materials, 3(6):366–375. https://doi.org/10.3144/expresspolymlett.2009.46

[2] Sutivisedsak N, Cheng HN, Dowd MK, Selling GW, Biswas A. (2012) Evaluation of cotton byproducts as fillers for poly (lactic acid) and low-density polyethylene. Industrial Crops and Products, 36(1):127–134. https://doi.org/10.1016/j.indcrop.2011.08.016

[3] Orhan Y, Hrenović J, Büyükgüngör H. (2004) Biodegradation of plastic compost bags under controlled soil conditions. Acta Chimica Slovenica, 51(3): 579–588.

[4] Hassan LG, Muhammad AB, Aliyu RU, Idris ZM, Izuagie T, Umar KJ, Sani NA. (2013) Extraction and Characterisation of Starches from Four Varieties of Mangifera indica Seeds. IOSR Journal of Applied Chemistry, 3(6):16–23.

[5] Noor F, Rahman J, Mahomud S, Akter MS, Talukder AI, Ahmed M. (2014) Physicochemical properties of flour and extraction of starch from jackfruit seed. International Journal of Nutrition and Food Sciences, 3(4): 347–354. https://doi.org/10.11648/j.ijnfs.20140304.27

[6] Jiugao Y, Ning W, Xiaofei M. (2005) The effects of citric acid on the properties of thermoplastic starch plasticized by glycerol. Starch/ Staerke, 57(10):494–504.
https://doi.org/10.1002/star.200500423

[7] Seligra PG, Jaramillo CM, Fama L, Goyanes S. (2016) Biodegradable and non-retrogradable eco-films based on starch-glycerol with citric acid as cross-linking agent. Carbohydrate Polymers, 138:66–74. https://doi.org/10.1016/j.carbpol.2015.11.041

[8] Gautam N, Kaur I. (2013) Soil burial biodegradation studies of starch grafted polyethylene and identification of *Rhizobium meliloti* therefrom. Journal of Environmental Chemistry and Ecotoxicology, 5(6):147–158. https://doi.org/10.5897/JECE09.022

[9] Coniwanti P, Laila L, Alfira MR (2014). Pembuatan Film Plastik Biodegredabel Dari Pati Jagung Dengan Penambahan Kitosan Dan Pemplastis Gliserol. Jurnal Teknik Kimia, 20(4):22–30.

[10] Azahari NA, Othman N, Ismail H. (2011) Biodegradation Studies of Polyvinyl Alcohol / Corn Starch Blend Films in Solid and Solution Media, 22(2):15–31.

[11] Nawab A, Alam F, Haq MA, Hasnain A. (2016) Biodegradable film from mango kernel starch: Effect of plasticizers on physical, barrier, and mechanical properties. Starch - Stärke, 68 (9 - 10):919–928. https://doi.org/10.1002/star.201500349

[12] Reddy N, Yang Y. (2010) Citric acid cross-linking of starch films. Food Chemistry, 118(3):702–711. https://doi.org/10.1016/j.foodchem.2009.05.050

[13] Shi R, Zhang Z, Liu Q, Han Y, Zhang L, Chen D, Tian W. (2007) Characterization of citric acid/glycerol co-plasticized thermoplastic starch prepared by melt blending. Carbohydrate Polymers, 69(4):748–755. https://doi.org/10.1016/j.carbpol.2007.02.010

[14] Zuraida A, Anuar H, Yusof Y. (2011) The Study of Biodegradable Thermoplastics Sago Starch. Key Engineering Materials, 471-472:397–402.
https://doi.org/10.4028/www.scientific.net/kem.471-472.397

[15] Sarifuddin N, Ismail H, Ahmad Z. (2014) Incorporation of Kenaf Core Fibers into Low-Density Polyethylene/Thermoplastic Sago Starch Blends Exposed to Natural Weathering. Molecular Crystals and Liquid Crystals, 603(1):180–193. https://doi.org/10.1080/15421406.2014.976516

[16] Maran JP, Sivakumar V, Thirugnanasambandham K, Sridhar R. (2014) Degradation behavior of biocomposites based on cassava starch buried under indoor soil conditions. Carbohydrate Polymers, 101(1):20–28. https://doi.org/10.1016/j.carbpol.2013.08.080

[17] Nuradibah MA, Sam ST, Noriman NZ, Ragunathan S, Ismail H. (2015) Degradation assessment of natural weathering on low-density polyethylene/thermoplastic soya spent powder blends. AIP Conference Proceedings, 1669:020040. https://doi.org/10.1063/1.4919178

[18] Obasi HC, Igwe IO, Madufor IC. (2013) Effect of Soil Burial on Tensile Properties of Polypropylene / Plasticized Cassava Starch Blends. Advances in Materials Science and Engineering, 2013:2–5.

EXPERIMENTAL INVESTIGATION OF THE INFLUENCE OF MULTI-RECYCLING ON THE FRACTURE BEHAVIOR OF POST CONSUMER HIGH IMPACT POLYSTYRENE FROM DISPOSABLE CUPS EVALUATED BY THE J-INTEGRAL APPROACH

HANAN EL BHILAT[1]*, HASSAN MABCHOUR[2], HOUDA SALMI[1], ABDELILAH HACHIM[2] AND KHALID EL HAD[2]

[1]*National higher school of electricity and mechanics, ENSEM, Laboratory of Control and Mechanical Characterization of Materials and Structures, Casablanca, 20232, Morocco.*
[2]*Institute of Maritime Studies, Laboratory of Materials and Structures, Casablanca, 20232, Morocco.*

*Corresponding author: h.elbhilat@ensem.ac.ma.

ABSTRACT: The aim of the present paper is to study the effect of multi-recycling on the fracture behavior of high impact polystyrene from disposable cups. After collecting and washing the material, it was subjected to six cycles of recycling. After each cycle, it was subjected to tensile tests to determine the R-curves. The theory of the J-integral contour has been used for the development of a characterization method of the fracture strength appropriate to the case of this non-linear elastoplastic polymer material. To this end, the method of multiple specimens (Single edge notch tension SENT) of thin thickness was used, by introducing cracks of the same lengths to several identical test pieces. The results suggested a slight decrease in crack resistance of recycled high impact polystyrene, especially during the first cycle, demonstrated by a comparison of J_{IC} values related to initiation of crack propagation. The fracture energy absorbed as a function of the cycles suggested a weakening within the material.

ABSTRAK: Tujuan kajian ini adalah bagi mengkaji kesan tindak balas pada pelbagai peringkat-kitar semula ke atas kerapuhan polisterin berimpak tinggi pada cawan pakai buang. Selepas mengumpul dan membasuh cawan ini, terdapat enam peringkat kitar semula. Pada setiap peringkat, ianya akan melalui ujian tegangan bagi mendapatkan lengkung-R. Teori kamiran-J kontur telah digunakan bagi mencipta kaedah khas bagi mengkaji kekuatan retakan bersesuaian bagi kes bahan polimer elastoplastik yang tidak-linear. Sehingga kini, kaedah Regangan Tepi Takuk Tunggal (SENT) telah digunakan pada spesimen berketebalan rendah, dengan menghasilkan keretakan sama panjang di permulaan kajian di buat pada pelbagai bahan uji yang serupa. Dapatan kajian menunjukkan rintangan pada retakan telah berkurang sedikit pada polisterin kitar semula berimpak tinggi, terutama pada kitaran pertama, yang ditunjukkan pada nilai J_{IC} pada permukaan rambatan retakan awal. Tenaga kerapuhan yang meresap pada setiap kitaran menunjukkan bahan telah melemah dari dalam.

1. INTRODUCTION

The 19th and 20th centuries marked the appearance of plastics. These new materials are the result of advances in petrochemicals and awakened a particularly strong interest in the aftermath of the Second World War, a period during which the industry had to cope with the growing demand for raw materials. Consequently, the various properties, ease of processing, and advantageous costs presented by these materials encourage their application in all fields of industrial production in order to meet the growing needs of consumers.

The oil shock occurring in the 1970s marked the beginning of consumer polymers. However, this massive exploitation is not without consequences. Indeed, the main drawback of polymeric materials lies in the fact that they are not biodegradable and thus create the problem of managing their industrial or consumer waste, which accumulates in a worrying manner. It is only in the last thirty years that the treatment of plastic waste has become a primary concern in preserving the environment. The recovery of plastic materials is then the subject of all attention, especially in the scientific world where many studies have looked at this global phenomenon.

The general characteristics of plastic waste and recycled polymers, from a mechanical point of view, are established by the fact that they have undergone, during their previous uses, two major phenomena. On the one hand, used or recycled polymeric resins have experienced degradation due to aging (fatigue, temperature...), oxidation, or water absorption. This degradation is manifested by chain breaks and crosslinks occurring at the level of macromolecules. The consequence of these phenomena is the gradual deterioration of the thermomechanical properties of plastic materials [1-5]. On the other hand, pollution depending on the clean or dirty origin of the previous use of this waste can lead to a retention of impurities which influences, among other things, negatively, their thermal and mechanical properties.

Although these two factors are closely linked, their more or less extensive existence depends, of course, on the origin of the waste. For example, it makes perfect sense that industrial plastic waste undergoes very little degradation and has extremely low impurities. Their existence and influence may even turn out to be negligible with regard to production waste (directly from polymerization reactors). Too high temperatures or even too long a residence time could have a degradation effect [6-10]. That's why this paper is only focused on the influence of multi-recycling on the fracture behavior of high impact polystyrene.

High impact polystyrene (HIPS), is a specific polystyrene because of its opacity and above all, its impact resistance. It is also called impact polystyrene (SB). Styrene is the basic element in the manufacture of polystyrene and its compatibility with other monomers and polymers makes it possible to imagine many styrenic compounds with various properties. HIPS is one of them. It incorporates 15 to 25% polybutadiene and is also obtained by grafting polybutadiene during the production of polystyrene. HIPS is an inexpensive plastic material that is easy to produce and shape. Thus, it has a wide forming temperature range and is particularly suitable for thermoforming. In addition, it can have a glossy, satin or matte finish. It is also easily pigmentable; characteristics that make impact polystyrene widely used in various fields. It is used to manufacture displays, containers, toys, roof boxes, food packaging, etc.

Most of the scientific articles treating the influence of recycling on thermoplastics are interested in mechanical properties in particular: elongation at break, elastic limit, maximum stress and impact resistance. All of this data was determined by stress testing and pendulum impact testing in Charpy and Izod mode. Also, various analyses with a scanning electron

microscope or even with an electronic transmission microscope have also been identified in certain works. The information found as a result of these tests was aimed at determining whether or not there was an improvement in mechanical properties [11-22]. However very limited studies have treated the elasto-plastic fracture behavior of post-costumer high impact polystyrene, especially in the case of multi-recycling. In this study, we investigated the effect of multi-recycling on the fracture behavior of high impact polystyrene from disposable cups, using the multi-specimen method that finds its application in Elastoplastic Fracture Mechanics.

A strained metal or polymer can undergo certain damage and alternations. This damage can lead, in some cases, to the appearance of macroscopic cracks. These cracks are often of sufficiently large size to satisfy the assumptions of continuity of the mechanics of a continuous medium. We can then place ourselves within the framework of fracture mechanics to characterize the harmfulness of this defect [23].

The goals of linear fracture mechanics are:

- The characterization of the stress fields and singular deformations at a crack point
- Establishing the relationships between the crack point fields, the geometry of the test specimen and the overall field (measurable quantity)
- The energy conditions necessary for the (re)-initiating of the crack
- Description of the crack propagation (stable or unstable)
- The determination of a critical size of the defects beyond which the failure (especially unstable) will be triggered

Initially, one will endeavor to present the cases where the factor K_I: the factor of intensity of the stresses, and G the rate of restitution of energy, provide solutions in the understanding of the initiation mechanisms of polymers. In this paper, we will then be interested in the parameter J and its uses in fracture mechanics in the case where the material has a non-linear elastic behavior, which is the case of high impact polystyrene.

Unlike resilience, an integral characteristic depending on the experimental conditions, toughness is an intrinsic characteristic of materials and a quantity that can be used in design (like a Young's modulus). The determination of the toughness is carried out on specimens notched by different theoretical approaches depending on the mechanical behavior of the material. Indeed, for a brittle material, toughness is evaluated from the concepts of Linear Elastic Fracture Mechanics (LEFM) while it is studied according to the concepts of Elastoplastic Fracture Mechanics (Post-Yield Fracture Mechanics: PYFM) when the material is ductile.

PYFM requires the introduction of the concept of Cracking Resistance curve or R curve. It was established by Irwin [24] in order to characterize the resistance to slow cracking of materials with some ductility at the crack head. An R curve is a curve of variation of the toughness with the crack advance (Δa). In general, a crack can start and then progress when a parameter (K, G, or J), representing the action of the external environment at the crack head, becomes equal to the resistance to cracking (KR, GR, or JR) of the material. In the case of a brittle material (LEFM), the structure of the material and its resistance to cracking do not change during propagation due to the absence of plastic deformation at the crack head. On the other hand, in the case of a ductile material (PYFM), the progressive increase in the plastic deformation at the crack head during initiation and propagation causes an increase and then a stabilization of its resistance to cracking. The toughness of the material

can no longer be represented by a single critical parameter (K_c or G_c) but rather by an R curve (KR, GR or JR = f (Δa)) (Fig. 1).
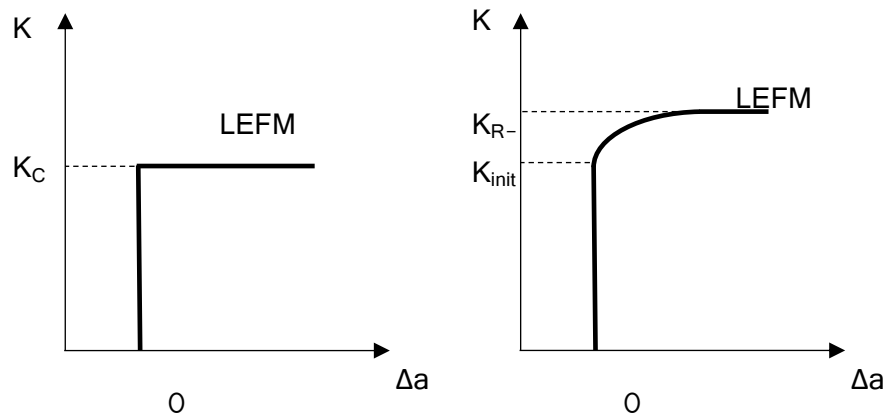

Fig. 1: R curves in LEFM and PYFM.

Rice [25] demonstrated that, in the case of a crack located in the xz plane and whose front is parallel to the axis z (Fig. 2), the integral J (Eq. (1)) is independent of contour Γ and null when this contour is closed (there is no crack). We can consider that J represents the component of the energy flow crossing Γ, due to the singularity related to the presence of the crack.

$$J = \int_{\Gamma} \left(W dy - T_i \, \frac{\partial u_i}{\partial x} \, ds \right) \tag{1}$$

with: W, the strain energy density,

T_i the outwardly oriented traction vector,

u_i, the displacement vector of the arc ds,

s, the curvilinear abscissa on the contour Γ,
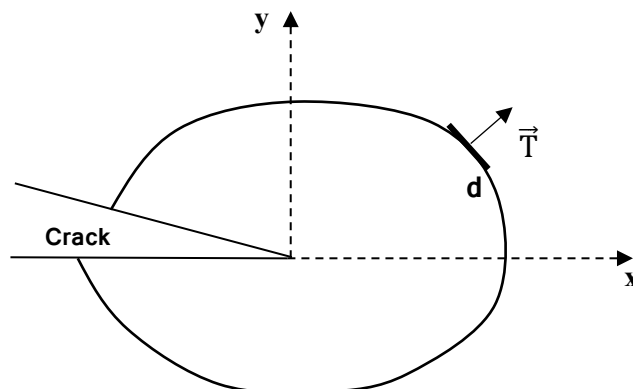
x, y and z the Cartesian coordinates.

Fig. 2: Illustration of the concept of integral J.

Note that W = $\int \sigma_{ij} \, d\varepsilon_{ij}$, with σ_{ij} and ε_{ij} the stress and strain components, respectively.

J is calculated from the energy U necessary to propagate the crack (energy supplied by the external environment) (Eq. (2)).

$$J = -\frac{1}{b}\frac{dU}{da} \tag{2}$$

with "b", the thickness of the specimen and "a" the crack length. From this equation (Eq. (2)), Begley and Landes [26-28] have shown that J is identical to G in the case of a linearly elastic and brittle material and that J can be a criterion of rupture for elastoplastic materials. The crack is initiated when J reaches a critical value J_{IC} which is an intrinsic characteristic of the material. Although J_{IC}'s calculation methods are very controversial, the ASTM E813-81 standard that considers the case of metals seems to be applicable to polymers. This standard assumes that the curve $J = f(\Delta a)$ is a line and that J_{IC} corresponds to the intersection of this line with the blunt line (Fig. 3) having for equation:

$$J = 2\sigma_y \Delta a \tag{3}$$

with σ_y being the stress at the tensile yield point of the material. On the other hand, the ASTM E 813-87 standard states that the curve $J = f(\Delta a)$ follows a power law of the form $J = A.\Delta a^n$ and that J_{IC} corresponds to the value of J taken at the intersection of this curve with the straight line of Eq. (4) (Fig. 3):
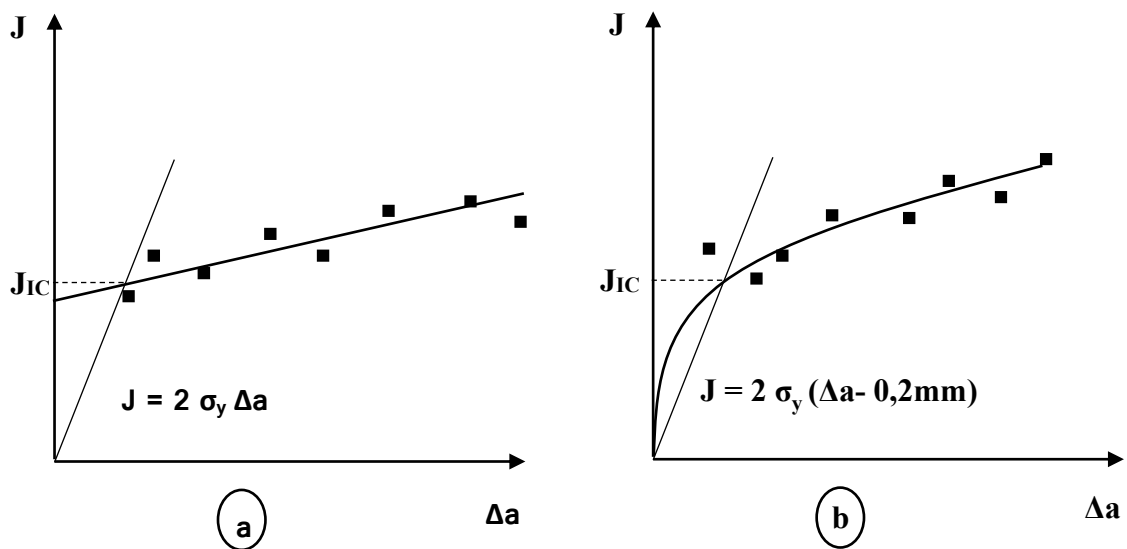
$$J = 2\sigma_y(\Delta a - 0,2mm) \tag{4}$$

Fig. 3: Method for determining J_{IC} according to ASTM E 813-81 (a) and ASTM E 813-87 (b).

In practice, the procedure for obtaining J-R curves is identical to that used in LEFM. To construct the J-R curves, it is necessary to perform the tests on multiple samples (7 minimum) up to different levels of deflection or crack opening. These tests will be followed by an optical measurement of the fracture surface in order to determine the actual crack advances. Each test piece tested leads to the determination of a pair of values (J, Δa), i.e. at a point on the J-R curve. Next, we calculate the integral J.

2. MATERIALS AND METHODS

In this section, we present our experimental study, divided into two parts:

- The first is to study the effect of several extrusion/recycling cycles on the toughness properties of high impact polystyrene from disposable cups, mainly the J-Δa curves.
- The second is devoted to the study of the effect of the six recycling cycles on the J_{IC} parameter then compare the results to virgin material.

The work plan thus followed is presented below. The various experimental techniques used and their operating conditions, as well as the ways of using the results are also presented in this paper.

2.1 Disposable Cups Recycling

The high impact polystyrene disposable cups collected for this study by the recycling company have undergone mechanical recycling carried out at the level of the same recovery company.

The process involves washing and then shredding the cups into small pellets. These pellets are then crushed using a grinder. The granulation (Fig. 4) of the ground material obtained is carried out in a twin-screw granulating extruder by the material provider.

Fig. 4: HIPS Granules and pellets from disposable cups.

The extruder (Leistritz) is equipped with a cylinder filter changer. The filtering system helps prevent unmelted granules or other impurities from entering the extrudate. The extrusion parameters are as follows:

- Extrusion temperature: from 220 to 230 °C;

- Screw speed: 35 rpm.

- A maximum injection pressure of 2,500 bars.

The extrudates are cooled in a water tank before being transformed into granules using a cutter. These granules, considered to be the first cycle of extrusion, are then made into specimens destined for various thermo-mechanical tests by molding process as shown in Fig. 5.

The specimens obtained are treated in the same way and with the same conditions described above. These operations were repeated six times without any change under all conditions. Therefore, the total number of extrusion cycles, to which the virgin resin is subjected, is equal to 6.
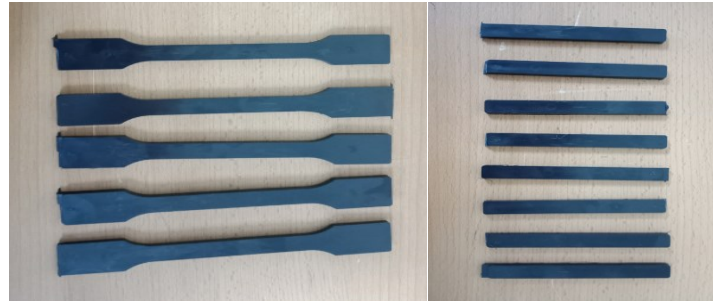
Fig. 5: Tests specimens according to ISO 294-1 and ISO 294-2.

2.2 Choice of Specimens for Fracture Behavior Analysis

The ISO 13586 and ASTM D 5045 standards suggest that to evaluate the J_{IC} of a thermoplastic and thermosetting material, the tests must be carried out on CT (Compact Tension) specimens, or on SENT (Single Edge Notched Tension) specimens. The dimensions of the test pieces are given by the standards. Although the specifications and recommendations of the two standards ISO 13586 and ASTM D 5045 are only applicable for linear fracture mechanics, the choice and sizing of specimens has been maintained by standard ASTM D 6068 for the determination of JR curves of elastoplastic polymer materials. In our experimental study, the JR curve of both virgin and recycled high impact polystyrene is drawn by adopting the operating mode described by the standard ASTM D 6068, but the general configuration of the test (type of test piece, experimental device, etc.) is identical to that performed in LEFM (ASTM D 5045, ISO 13586). The SENT (Fig. 6) specimens were molded by a SINTESI molding machine.
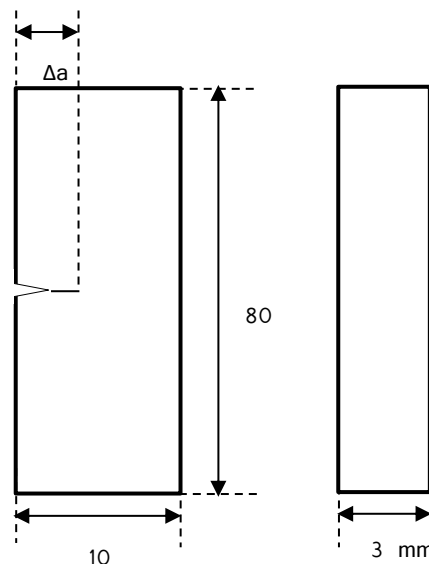

Fig. 6: Cracked tensile test piece on the side (SENT).

The last stage of preparation of the specimens is carried out using a razor blade. A pre-crack is introduced into the notched area of the specimen, the cutter blade of which, 0,4 mm thick, is changed after 5 specimens. The condition of the blade is essential to avoid residual stresses following this operation.

Un-notched SENT specimens were machined for tests that correct the results obtained on notched and pre-cracked specimens.

2.3 Test Methodology and J-R Curve

The principle of the construction method of the experimental JR curve is to load a pre-cracked specimen until an imposed displacement (displacement of the cross member), of the order of a few tenths of a millimeter, is reached with a fixed loading speed. The tensile tests were carried out using a ZwickRoell tensile machine with a 2,5 kN load cell.

The fracture face is then optically examined to calculate the advance of the crack. Consequently, two types of data are to be recovered on a test:

- The load displacement curve, which leads to calculate J.

- The fracture surfaces, which makes it possible to measure the crack advance Δa.

The crack advance measurements, being of very low values, were performed with KSM off-line measuring device that measures thinly cut cross sections (slices) of specimens, as shown in Fig. 7.
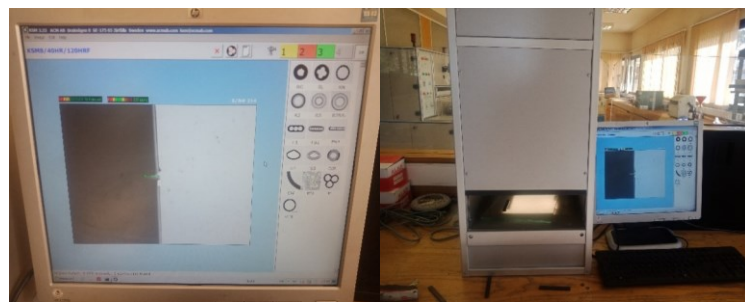

Fig. 7: KSM off-line measuring device.

Thus, each specimen makes it possible to obtain a pair of values (J, Δa) that represent a point on the J-R curve.

This method, shown in Fig. 8, (proposed by the ASTM D 6068) standard, provided that the loading speed adopted causes a clear and stable propagation of the crack. To ensure this condition, the ISO 13586 standard recommends using, at a temperature of 23 ° C, a speed of 10 mm/min.

The J integral is calculated from the area under the load displacement curve - using Grapher 14 software, which represents the total energy U_T. A single tensile test is carried out on a non-notched SENT specimen of the same size as the notched specimen. The unique load displacement curve from this test is used to calculate the indentation energy "U_i" for each specimen. Indeed, U_i is the area under the curve between zero until the displacement corresponding to the maximum force applied to the notched and pre-cracked specimen. This amount of energy is dissipated by phenomena other than cracking.

Using U_T and U_i, J can be calculated for each test by Eq. (5):

$$J = \frac{\eta(U_T - U_i)}{b(w - a_0)} \tag{5}$$

η is a geometrical dimensionless parameter. Garcia et al [29] state that to calculate J of polymers, the factor η depends only on the ratio between the length of the crack and the width of the specimen (a_0 / w).

For the geometry of the test piece, Clarke and Landes [30] succeeded in obtaining an approximation of η through the formula:

For CT specimens

$$\eta = 2 + 0{,}522 \left(1 - \frac{a_0}{w}\right) \tag{6}$$

For SENT specimens

$$\eta = 2 \tag{7}$$

2.4 Tests on SENT Specimens

The SENT specimens are loaded by applying a tensile force through the two symmetrical bores and a suitable mounting on the ZwickRoell tensile machine equipped with a 2,5 kN load cell. The test is stopped once the imposed displacement (u) is reached (Fig. 8). The load-displacement curve is recovered and the cracking area is examined in the KSM instrument to facilitate the measurement of the different crack advance lengths Δa. Finally, the test piece is completely torn into two parts.
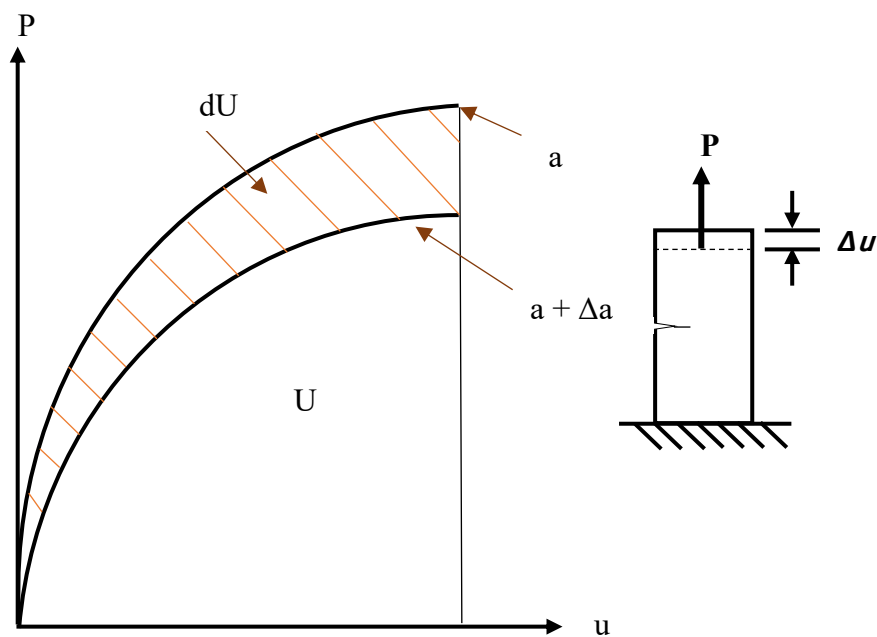

Fig. 8: Variation of dissipated energy with constant displacement.

Eight restraints (u) are studied ranging from 2,5 mm to 10 mm. For displacements smaller than 2,5 mm, we did not observe an advance of the crack. The eight tries give us 8 points, with one or two extra specimens if needed. The standard requires a minimum of 7 points to draw the J-R curve. The maximum force and total energy are deduced and calculated from these curves. The values obtained are corrected by the indentation energy. So, J is calculated for each test specimen by applying Eq. (5).

The fracture areas of the two parts of the specimen are then observed. The depth of the pre-cracks (or initial crack) is not controlled during the preparation of the specimen, but measured precisely after each test under the KSM device. It is the average of three measurements of the distance between the notch tip and the crack tip. The distance between the final crack front and the initial crack front is measured at five equidistant points. The extension of the crack Δa is the average of this value.

The J-R curve given by the tensile tests on SENT specimens is plotted. This curve characterizes the resistance to cracking of HIPS. The most useful information that can be

derived from this curve is the starting toughness J_{IC}, a characteristic of the material. It defines the initiation point of a crack.

The ASTM E 813 standard recommends, for the calculation of J_{IC}, a graphic method that consists of shifting the blunt line to a $\Delta a = 0,2$. J_{IC} is the intersection of this straight line with curve J. In addition to the blunt line method, some authors define J_{IC}, for polymer materials, as the value of the curve J - Δa which corresponds to an advanced 0,2 mm or 0,4 mm crack [31,32]. HUAND [32] asserted that $J_{0,2}$ can also be taken as the characteristic value representative of crack initiation.

3. RESULTS AND DISCUSSION

A significant shift is noted between the J-R curve given by the tests on test pieces of virgin HIPS, and that obtained with recycled material. On the other hand, a slight decrease of J_{IC} is noticed amongst different cycles as shown in Fig. 9 and Fig. 10, thus demonstrating that the mechanical properties in terms of fracture energy, represented by the energy sufficient to initiate the fracture, decreases with the increase in the number of cycles performed. The material changes from a ductile state to a brittle state. Embrittlement occurs abruptly by the combined effect of the drop in molar mass and the increase in crystallinity (entanglement), thus reducing the amorphous phase, which prevents crack growth within the material.

Through the number of recycling cycles, high impact polystyrene undergoes thermo-mechanical-chemical degradation inducing chain scissions, the molar weight decreases creating more chain ends. These extremities represent concentrates of fracture energy that absorb the energy and cannot propagate it any longer, initiating the fracture. In addition, a large difference in molecular mass produces a heterogeneous whole favoring fracture. The low number of entanglements that were the usual consolidation of high impact polystyrene propagates the tear easily creating the fracture while the fracture of virgin HIPS was relatively difficult.
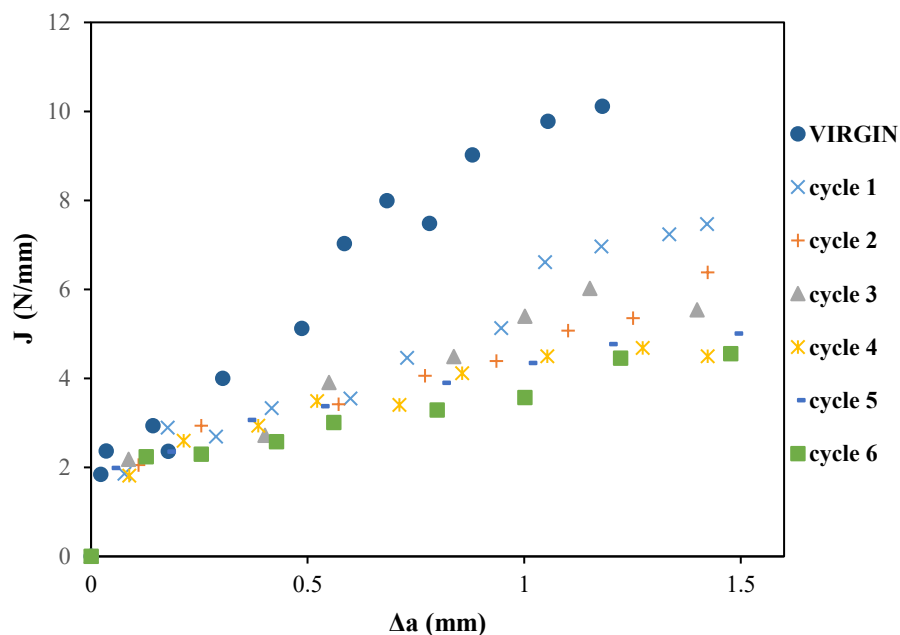

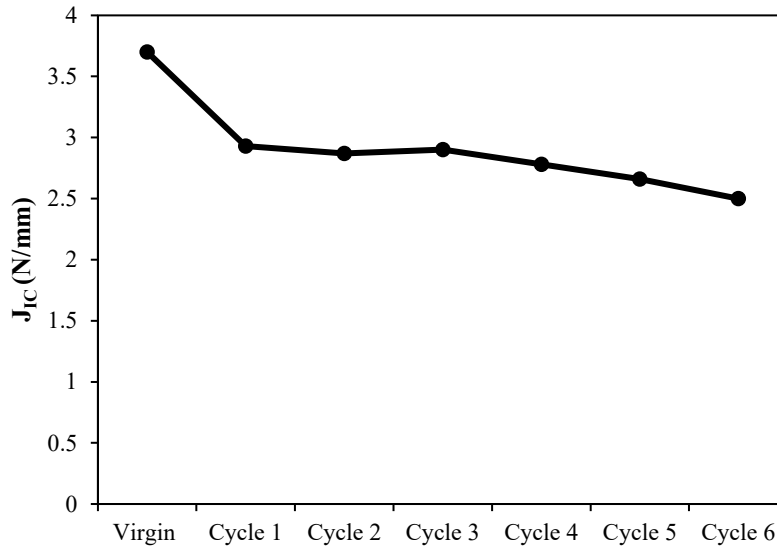Fig. 9: The J-Δa curve of recycled HIPS during different cycles.

Fig. 10: The evolution of J_{IC} as a function of number of cycles.

Degradation During Recycling/Extrusion

It is well known that extrusion is one of the most severe processes that a polymer can withstand [33], shear forces and high temperatures cause mechanical and thermal splitting of the polymer chain, resulting in the formation of end of chain radicals (initiation of propagation phenomenon) as shown in Fig. 11.
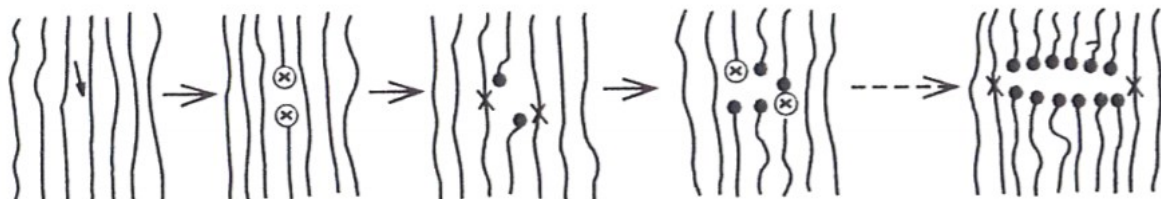

Fig. 11: Splitting of the polymer chains due to mechanical and thermal degradation.

Polymers are generally recycled in the molten state, at a temperature above the melting temperature but obviously well below the decomposition temperature. This does not prevent thermal and mechanical degradation from prevailing during the short implementation period (processing):

- thermal: the high friction shear can locally increase the temperature above the nominal processing temperature and chemical bonds can be thermally strained until they break.
- mechanical: when the rate of deformation of chemical bonds is much greater than the rate of relaxation of macromolecules, the activation energy of the fracture of the bonds and consequently the induced degradation time (t_i), are reduced to the intensity of the applied stresses.

The consequence of such degradation is the reduction in molar mass by 1/2, 1/4, or 1/8 of the initial molar mass [34], in fact, the molar mass of polymers plays a significant role in terms of durability. It has been generally recognized that high impact polystyrene becomes more stable when its molar mass increases or when the fraction of low masses decreases. Shorter chains result in a greater number of chain ends. These ends provide elements very

sensitive to aging and to degradation in general. They are even capable of locally catalyzing degradation reactions.

A high molar mass induces the following properties:

- an increase in the entanglement rate (knots) which serves to counter the propagation of cracks in the material
- a drop in gas permeability and therefore a drop in the progression of reactive elements through the material [35].

Our previous work [36] on characterizing of multi-recycled high impact polystyrene indicated an increase of the Melt Flow Index as well as a decrease in molecular weight which supports the results of the present paper.

4. CONCLUSION

The study of the mechanical properties, in particular the fracture behavior of multi-recycled high impact polystyrene from disposable cups, allowed us to specify the influence of the degradation phenomenon on the drop in J_{IC} values. Mechanical degradations in the recycling/processing of polymers have been the least studied, no doubt because of their complexity; however, they play a very important role and their control is essential in the recycling operation. The growing demand from users for the quality and reliability of plastics, gives the study of degradation an increasingly important place, particularly from the perspective of recycling, which is becoming more and more inevitable.

The multi-specimen method based on Elastoplastic Fracture Mechanics, revealed a slight degradation in terms of fracture resistance, of the various recyclates, especially during the first cycle, this is explained by chain breaking, oxidation, and decreasing of the molar mass of high impact polystyrene. On the other hand, the present analysis strongly supports our previous work on the effect of multi-recycling on the material-flowing index as it showed an increase in melting flow index and therefore the decrease in viscosity with the number of recycling cycles.

REFERENCES

[1] Azwa ZN,Yousif BF,Manalo AC, Karunasena W. (2013), A review on the degradability of polymeric composites based on natural fibres, Materials & Design, 47(1): 424-442. https://doi.org/10.1016/j.matdes.2012.11.025

[2] Celina M, Linde E, Brunson D, Quintana A, Giron N. (2019) Overview of accelerated aging and polymer degradation kinetics for combined radiation-thermal environments, Polymer Degradation and Stability,166 (1): 353-378. https://doi.org/10.1016/j.polymdegradstab.2019.06.007

[3] Saikrishnan S, Jubinville D, Tzoganakis C, Mekonnen TM. (2020) Thermo-mechanical degradation of polypropylene (PP) and low-density polyethylene (LDPE) blends exposed to simulated recycling. Polymer Degradation and Stability, 182(1). https://doi.org/10.1016/j.polymdegradstab.2020.109390

[4] Ito M, Nagai K. (2008) Degradation issues of polymer materials used in railway field, Polymer Degradation and Stability, 93(10): 1723-1735. https://doi.org/10.1016/j.polymdegradstab.2008.07.011

[5] Verdu J. (2011) Vieillissement chimique des plastiques : aspects généraux, Techniques de l'Ingénieur. https://www.techniques-ingenieur.fr/base-documentaire/archives-th12/archives-plastiques-et-composites-tiaam/archive-1/vieillissement-chimique-des-plastiques-aspects-generaux-am3151/

[6] Vranjes N, Rek V. (2007) Effect of EPDM on morphology, mechanical properties, crystallization behavior and viscoelastic properties. Macromolecular Symposia, 258(1): 90-100. https://doi.org/10.1002/masy.200751210

[7] Kallel T, Massardier-Nageotte V, Jaziri M, Gérard J F, Elleuch B. (2003) Compatibilization of PE/PS and PE/PP blends. I. Effect of processing conditions and formulation. Journal of Applied Polymer Science, 90(9): 2475-2484. https://doi.org/10.1002/app.12873

[8] Lin Y, Marchand G R, Hiltner A, Baer E. (2011) Adhesion of olefin block copolymers to polypropylene and high density polyethylene and their effectiveness as compatibilisers in blends. Polymer, 52(7) :1635-1644. https://doi.org/10.1016/j.polymer.2011.02.012

[9] Siddiqui M, Antonakou E, Redhwi H, Achilias D. (2019) Kinetic analysis of thermal and catalytic degradation of polymers found in waste electric and electronic equipment. Thermochimica Acta, 675 (1): 69-76. https://doi.org/10.1016/j.tca.2019.03.001.

[10] Sawaguchi T, Sasaki D, Takamura A. (2019) On the entanglement-based mechanism in thermal degradation of vinyl polymers, Polymer Degradation and Stability, 169(1): 108990. DOI: https://doi.org/10.1016/j.polymdegradstab.2019.108990.

[11] Hirayama D, Clodoaldo S. (2018) Morphologic and mechanical properties of blends from recycled acrylonitrile-butadiene-styrene and high-impact polystyrene, Polymer, 135 (1): 271-278. https://doi.org/10.1016/j.polymer.2017.12.038.

[12] Lin Y, Yakovleva V, Chen H, Hiltner A, Baer E. (2009) Comparison of olefin copolymers as compatibilizers for polypropylene and high-density polyethylene. Journal of Applied Polymer Science, 113(3): 1945-1952. https://doi.org/10.1002/app.30190

[13] Zweifel H. (2000) Plastics Additives Handbook Munich. Hanser. (5th Edition) :900.

[14] Mehrabzadeh M, Farahmand F. (2001) Recycling of commingled plastics waste containing polypropylene, polyethylene, and paper. Journal of Applied Polymer Science. 80(13): 2573-2577. https://doi.org/10.1002/app.1367

[15] Ku H, Wang N, Pattarachaiyakoop N, Trada M. (2011) A review on the tensile properties of natural fiber reinforced polymers composites. Composites, Part B,42(4): 856-873. https://doi.org/10.1016/j.compositesb.2011.01.010

[16] Grein C, Gahleitner M, Bernreitner K. (2012) Mechanical and optical effects of elastomer interaction in polypropylene modification: ethylene-propylene rubber, poly-(ethyleneco-octene) and styrene-butadiene elastomers. eXPRESS Polymer Letters, 6(9): 688-696. DOI: 10.3144/expresspolymlett.2012.74

[17] Ubonnut L, Thongyai S, Praserthdam P. (2007) Interfacial adhesion enhancement of polyethylene-polypropylene mixtures by adding synthesized diisocyanate compatibilizers. Journal of Applied Polymer Science,104(6): 3766-3773. https://doi.org/10.1002/app.25945

[18] Radonjic G, Gubeljak N. (2002) The use of ethylene/propylene copolymers as compatibilizers for recycled polyolefin blends. Macromolecular Material and Engineering, 2(287): 122-132. https://doi.org/10.1002/1439-2054(20020201)287:2<122::AID-MAME122>3.0.CO;2-A

[19] Colbeaux A, Kotek J, Fenouillot F, Taha M, Wautier H, Gérard J F. (2001) Compatibilisation de mélanges polypropylène/polyéthylène par extrusion réactive. Thèse doctorat INSA Lyon, 338 p. http://theses.insa-lyon.fr/publication/2001ISAL0058/these.pdf

[20] Almishal S, Mohamed T, Shazly M. (2020) Experimental and statistical study of the effect of temperature and waste ratio on the mechanical properties and cost of polystyrene polypropylene plastic blends, Heliyon, 6(6): e04166. https://doi.org/10.1016/j.heliyon.2020.e04166.

[21] Mehat NM, Kamaruddin S. (2011) Optimization of mechanical properties of recycled plastic products via optimal parameters using the Taguchi methods. Journal of Materials Processing Technology, 211(12): 1989-1994. https://doi.org/10.1016/j.jmatprotec.2011.06.014

[22] Krulis Z, Kokta V B, Horak Z, Michalkova D, Fortelny I. (2001) Compatibilization as a procedure for recycling of commingled polyolefin waste. Macromolecular Materials and Engineering, 286(3): 156-160. https://doi.org/10.1002/1439-2054(20010301)286:3<156::AID-MAME156>3.0.CO;2-J

[23] Ritchie R, Liu D. (2021) Chapter 2 - Foundations of fracture mechanics, Introduction to Fracture Mechanics, Elsevier: 3-9. https://doi.org/10.1016/B978-0-323-89822-5.00008-6.

[24] Irwin GR. (1957) Analysis of stresses and strains near the end of a crack traversing a plate, Journal of Applied Mechanics, 24:361-364.

[25] Rice JR. (1968) A path independent integral and approximate analysis of strain concentration by notches and cracks. Journal of Applied Mechanics, 35(2):379-386.
DOI: 10.1115/1.3601206

[26] Begley JA, Landes JD. (1971) The effect of specimen geometry in JIc. Fracture toughness, American Society of Testing and Materials, Special Technical Publication, 514: 24-39. https://doi.org/10.1520/STP38817S

[27] Begley JA, Landes JD. (1971) The J-integral as a fracture criterion. Fracture toughness, American Society of Testing and Materials, Special Technical Publication, 514: 1-23. https://doi.org/10.1520/STP38816S

[28] Begley JA, Landes JD. (1974) Test Results from J-lntegral Studies: An Attempt to Establish a JIC Testing Procedure. Fracture Analysis, American Society for Testing and Materials, Special Technical Publication, 560:170-186.   https://doi.org/10.1520/STP33140S

[29] Brosa V, Bernal C, Frontini P. (1999) Calibration of fracture mechanics parameters and J–R curve determination in polyethylene side-grooved arc-shaped specimens. Eng. Fract. Mech,62(2-3): 231-248. https://doi.org/10.1016/S0013-7944(98)00094-0

[30] Clarke G, Landes J. (1979) Evaluation of the J Integral for the Compact Specimen. J. Test. Eval,7(5): 264-269. https://doi.org/10.1520/JTE10222J

[31] Tancrez J, Pabiot J, Rietsch F. (1996) Damage and fracture mechanisms in thermoplastic-matrix composites in relation to processing and structural parameters. Compos. Sci. Technol, 56(7): 725-731. https://doi.org/10.1016/0266-3538(96)00013-9

[32] Huang D. (1996) The application of fracture mechanics to materials selection. Polym. Eng. Sci, 36(18): 2270-2274. https://doi.org/10.1002/pen.10625

[33] Kumar S, Singh R. (2003) Primary and Secondary Recycling of Thermosetting Polymers: A Review. Reference Module in Materials Science and Materials Engineering, 73(9): 1775. https://doi.org/10.1002/mame.200390005

[34] Wrozynski RJ, Rubinsztajn M, Potyrailo RA. (2004) Evaluation of Process Degradation of Polymer Formulations Utilizing High-Throughput Preparation and Analysis Methods. Macromolecular rapid communication, 2(1): 264-269.
https://doi.org/10.1002/marc.200300167

[35] Bartolomeo P. (2003) Deriving a prediction of the life cycle of géosynthrtic polymers. Bulletins des laboratoires des Pont et Chaussées, N°243-Réf 4456, p.51.

EFFECT OF STERILIZATION ON MECHANICAL AND BLOOD PROPERTIES OF MEDICAL GRADE POLYVINYL CHLORIDE

MARYAM POOSTCHI AND HAMED BAGHERI*

*Faculty of Interdisciplinary Sciences and Technologies,
Tarbiat Modares university,Tehran,Iran*

*Corresponding author: hbagheri@modares.ac.ir

ABSTRACT: The use of phthalates as a plasticizer in plasticized polyvinyl chloride (PVC) always poses the threat of migration of phthalates into the environment through medical equipment. Phthalates can be used with natural-based plasticizers, such as Epoxidized soybean oil (ESBO) known as phthalate's scavenger and PVC stabilizers. PVC formulations were characterized by different combinations of di (2-ethylhexyl) phthalate (DEHP) 30-40% with 5% ESBO. PVC flexibility increased significantly in the presence of ESBO, without a change in strength (tensile test). The decrease of the Tg temperature by adding ESBO in Differential Scanning Calorimetry indicated that ESBO preserved DEHP in the polymer. Also, it was shown that the sterilization process with Ethylene Oxide, similar to ESBO, decreased the Tg of polymer. DEHP migration was evaluated at a maximum level to the environment using the Gas Chromatography test. Samples containing ESBO showed less hemolysis.

ABSTRAK: Penggunaan phthalates sebagai plasticizer dalam plastik polyvinyl chloride (PVC) selalu menimbulkan ancaman penghijrahan phthalates ke alam sekitar melalui peralatan perubatan. Phthalates boleh digunakan dengan plasticizer berasaskan semula jadi, seperti minyak kacang soya Epoxidized (ESBO) yang dikenali sebagai pemulung phthalate dan penstabil PVC. Formulasi PVC dicirikan oleh kombinasi yang berbeza di (2-ethylhexyl) phthalate (DEHP) 30-40% dengan 5% ESBO. Fleksibiliti PVC meningkat dengan ketara di hadapan ESBO, tanpa perubahan kekuatan (ujian tegangan). Penurunan suhu Tg dengan menambahkan ESBO dalam Calorimetri Pengimbasan Berbeza menunjukkan bahawa ESBO mengekalkan DEHP dalam polimer. Juga, ditunjukkan bahawa proses pensterilan dengan Etilena Oksida, serupa dengan ESBO, menurunkan Tg polimer. Penghijrahan DEHP dinilai pada tahap maksimum ke lingkungan menggunakan uji Kromatografi Gas. Sampel yang mengandungi ESBO menunjukkan kurang hemolisis.

1. INTRODUCTION

In the years before 1970, glass bottles were used as containers for human blood preservation and were reused after cleaning and sterilization [1]. Now containers are special plastic bags with appropriate properties that meet today's needs regarding the maximum stability of the product and cell survival [2]. Today, all blood containers are sterilized and disposable. Blood bags used for blood preservation are made of polyvinyl chloride (PVC) [1–3].

PVC has a wider range of use in the construction and auto industries, as well as in the medical industry due to its characteristics, i.e. inert properties, transparency, easy sterilization,

compatibility with chemical compositions, and low cost [3–6]. Semi-hard and soft PVC comprises numerous parts of plastic materials used in the medical industry. Many sterilized disposable containers and tools, such as catheters, preservation bags for injecting fluids, medical tubes, preservation bags for blood and plasma, and dialysis equipment, are made of PVC. Materials used in these tools, especially blood preservation bags and medical tubes, cannot be replaced with other polymers [7–10].

PVC is considered a hard polymer with high Tg that is required to be plasticized for medical equipment, such as medical tubes and bags [11]. Various plasticizers, such as phthalates, are utilized in PVC. Phthalates are compounds formed as a result of phthalic acid esterification, which adds about 30-40% weight to PVC and plays a major role in its flexibility [9, 12]. Di-(2-ethylhexyl)-phthalate (DEHP) is the most widely used plasticizer. Most concerns are about the migration of DEHP to the environment due to the non-covalent bond between DEHP (phthalates) molecules and vinyl chlorides [5, 6, 10, 13–16].

Epoxidized soybean oil (ESBO) is an organic compound produced by soybean oil epoxidation [17]. The compound is used as a lubricant and stabilizer in PVC [5, 18–20]. Food products preserved in glass containers are sealed with PVC films or linings. ESBO is an additive used during PVC manufacture. ESBO can resist the release of HCl molecules due to its bonding with chlorine atoms in PVC [6, 15, 20, 21].

The United States Food and Drug Administration announced that the DEHP study on lab animals did not prove the safe use of DEHP for human beings. Thus, DEHP is used only for medical instruments with no continual contact with fluids in a patient's body. Furthermore, it is strongly advised not to utilize PVC–DEHP containing medical instruments for vulnerable patients, such as infants and pregnant women. Medical instrument manufacturing companies are also advised to remove DEHP from their products [22].

Sterilization is a major process in manufacturing medical tools. Most soft PVC products should be sterilized before use. Regarding the significance of the sterilization process in producing medical PVC tools, this study investigated the sterilization process effect on the migration of the plasticizer in the PVC bulk. The migration of the plasticizer probably increases due to special conditions in the sterilization process related to pressure and temperature.

The present study mainly discussed how to modify PVC blood preservation bags and find suitable polymer compositions with higher safety, flexibility, and blood compatibility, as well as lower migration rate. The study also evaluated the effect of various factors, including sterilization with ethylene oxide gas and addition of secondary plasticizers, such as ESBO, on the migration rate of plasticizers into the blood. We investigated certain properties of blood preservation bags and their stability and flexibility, including the release rate of plasticizers into the blood and blood compatibility (as clot formation for each PVC film with different percentages of plasticizers).

2. MATERIALS AND METHODS

2.1 Materials:

The materials were used PVC S6058 with the K-value 60 manufactured by Iranian Petrochemical Industries Co., di-2 (ethylhexyl) phthalate manufactured by Azar Shimi Co. (Iran), 2,6-di-tert-butyl-4-methylphenol with Vulkanox BHT manufactured by LanXess (Germany), ESBO manufactured by MBT (South Africa), Ca-Zn stearate manufactured by Poorya Exir Co. (Iran), chloroform with CAS No. 3-66-67 and the molecular mass of 119.38g/mol manufactured by Merck (Germany), Ethanol of 98% purity manufactured by

Jahan Khorram Co. (Iran), distilled water and physiologic serum manufactured by Sepidaj Pharmaceutical Co. (Iran), and sheep blood obtained from Darvash Co. (Iran).

2.2 Sample preparation:

The plasticizer percentage of each sample (30-40%) was determined based on previous studies [16, 23, 24]. The three samples contained 30%, 35%, and 40% DEHP. The test was also repeated with ESBO, which was added as much as 5% to the samples four, five, and six as a secondary plasticizer (at the same DEHP content). The number of samples along with their plasticizer contents is listed in Table 2.1. The samples zero and seven were used as evidence samples; none of the two samples contained DEHP, although the sample seven contained 5% ESBO.

Table 2.1: Percentage of each plasticizer was used in samples.

Sample No.	Primary plasticizer (DEHP) %	Secondary plasticizer (ESBO) %
0	0	0
1	30	0
2	35	0
3	40	0
4	30	5
5	35	5
6	40	5
7	0	5

After determining the plasticizer percentage in each sample, its component was measured in 100 units (phr), as shown in Table 2.2. The weight of each sample was kept at 60g to fit the capacity of an internal mixer device. The fraction of each component, including PVC, a stabilizer, an antioxidant, a plasticizer, and ESBO, was calculated based on 100 units(phr), as shown in Table 2.2.

Table2.2: Components of a sample weighing 60g

Sample No.	Composition	Sample No.	Composition
1	PVC+30%DEHP (Non-sterilized)	7	PVC+30%DEHP (sterilized)
2	PVC+35%DEHP (Non-sterilized)	8	PVC+35%DEHP (sterilized)
3	PVC+40%DEHP (Non-sterilized)	9	PVC+40%DEHP (sterilized)
4	PVC+30%DEHP+5%ESBO (Non-sterilized)	10	PVC+30%DEHP+5%ESBO (sterilized)
5	PVC+35%DEHP+5%ESBO (Non-sterilized)	11	PVC+35%DEHP+5%ESBO (sterilized)
6	PVC+40%DEHP+5%ESBO (Non-sterilized)	12	PVC+40%DEHP+5%ESBO (sterilized)

Each sample was mixed with a W50 Brabender mixer (Germany) to obtain a homogeneous mixture. The mixing device was set at 160°C and 80 rpm, and the samples were mixed for two min. The sample without the plasticizer was selected as a control sample of zero migration. However, the sample was removed from the study because of its poor properties.

Sample films with 5mm thickness were prepared. Hot pressing was conducted with a device manufactured by Sanjesh Baspar Novin Co. (Iran), while cold pressing was performed with a device manufactured by Toyo Seiki (Japan).

Each sample was fixed in two dumbbell-shaped casts where their dimensions were worked out according to ISO 6621 standards—length 15cm, width 2cm, and thickness 3mm. The samples then underwent hot pressing at 165°C for four min under 60Nm torque, followed by cold pressing (room temperature) for three min under 60Nm torque.

Half of the dumbbell samples were sterilized to compare the characteristics before and after sterilization. Each sample was put into a sterilized tank (Jiangyin Huaqing Machinery, China) of 90% ethylene oxide gas at 50°C and 50KP for eight h.

Table 2.3 shows the composition of each prepared sample, including figures attributed to it, which were utilized later.

Table 2.3: Sample nomenclature and abbreviations

Sample No.	PVC		DEHP		ESBO		Ca-Zn St		BHT	
	gr	phr	gr	phr	Gr	phr	Gr	Phr	gr	phr
0	58.53	100	0	0	0	0	01.17	2	0.29	0.5
1	40.96	100	18.02	44	0	0	0.82	2	0.25	0.5
2	38.10	100	20.95	55	0	0	0.76	2	0.19	0.5
3	34.99	100	24.14	69	0	0	0.70	2	0.17	0.5
4	37.85	100	18.17	48	03.03	8	0.76	2	0.19	0.5
5	34.78	100	21.22	61	03.13	9	0.70	2	0.17	0.5
6	31.83	100	24.19	76	03.18	10	0.64	2	0.16	0.5
7	55.81	100	0	0	05.00	5	02.00	2	0.50	0.5

2.3 Mechanical testing:

Both sterilized and non-sterilized samples underwent examination separately, based on ISO-527 standards, using TCS2000 Universal Testing (Gotech Testing Machines, Taiwan). The study samples had an average thickness of 2.4mm and width of 10mm.

2.4 Differential scanning calorimetry (DSC):

Differential Scanning Calorimetry (DSC) measurements were carried out on a DSC-1 unit manufactured by Mettler Toledo, Switzerland. About 4-5mg of the polymer sample was sealed in an aluminum pan. The polymer sample was first heated to 130 °C at a rate of 10°C/min under nitrogen atmosphere for three min to erase the thermal history. Then, it was cooled to -70°C at

a rate of 10°C/min for five min, and subsequently, heated to 130°C at a rate of 10°C/min. Both the cooling and heating traces were recorded.

2.5 Gas chromatography analysis (GC):

2.5.1   Sample extraction

All glassware was washed in 70% alcohol solutions and then put into the laboratory oven at 70°C for 15 min. The samples were cut in certain pieces using sterilized scissors and then put into a watch glass. The samples were weighed individually, and sterilized forceps were used to place the samples in an Erlenmeyer flask immediately after it was filled with as much as 50cc chloroform solution. The samples were tapped, and the flask was placed in the oven at 25°C for 24 h. Then, the flask was removed from the oven, and the pieces were taken out of the chloroform solution and put back in a watch glass. The pieces were again put into the oven at 70°C for 30 min to be dried. The solutions were preserved in other tapped dishes to be analyzed by gas chromatography.

2.5.2 Preparation of standard solution

Dodecane, with the chemical formula $C_{12}H_{26}$, was utilized to prepare standard solutions. The solutions were prepared at 100, 200, and 500ppm concentrations. The 500ppm solution was more like the samples than the other two solutions.

Chromatography was performed on the CP3800 gas chromatograph manufactured by Varian, USA. The injector temperature was set at 280°C with split-less mode, and the detector temperature was 300°C. The column was CP-Sil 5 CB made from silica with an inner diameter of 0.25mm and a length of 25m. Nitrogen-bearing gas at 40psi pressure and 1µl injection volume was applied to a flame Ionization detector. The test was conducted with the following temperature condition passing through the liquid column:

The initial temperature of 90°C was held for three min and increased at a heating rate of 15°C/min up to 280°C, which was held for five min. The total heating time was 20.67 min.

2.6 Hemolysis test:

The samples were cut into 1cm × 1cm films with sterilized scissors and a knife under sterilized conditions. The cut films were added to 100 million red globules lacking serum. Then, they were delivered to a container with 1 mL biological buffer using physiologic buffer and put in a SHIN SAENG Finetech rotary oven, (South Korea) at 37°C for one h at 100rpm. After an hour, the samples were centrifuged at 10,000rpm for five min in a Sigma3-30K centrifuge (ATR, USA). The supernatant was tested using the WPA Biowave II spectrophotometer (Biochrom, UK) at a 540nm wavelength to determine the released hemoglobin.

3. RESULTS AND DISCUSSION

3.1 Tensile test

Increasing the plasticizer to PVC led to increased flexibility (Figs. 1a, b) by decreasing the tensile stress and increasing the maximum stain at break. Considerable flexibility was observed in the samples 5 and 6 to which ESBO was added, confirming the ESBO plasticizer effect on PVC.
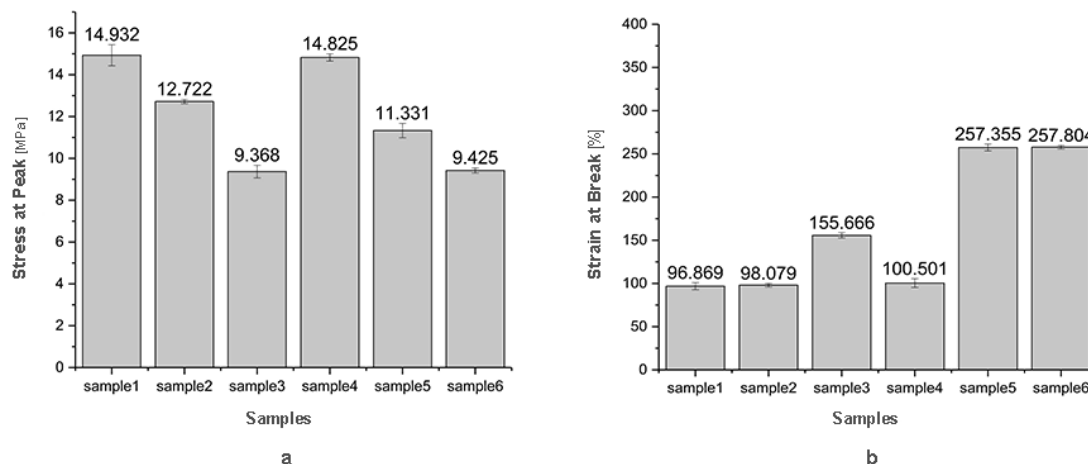
Poostchi et al.

Figure 3.1 mechanical properties of stretch PVC films evaluated: Yield stress (a) and strain at breakpoint (b) before sterilization process.

The stress-strain diagram demonstrated that ultimate stress decreased with increasing the plasticizer in the samples 1 to 6. Furthermore, by adding ESBO to the samples, ultimate stress decreased continually with increasing the plasticizer.

Both samples 2 and 4 with the same plasticizer content had different strains at break so that the maximum strain was 2% more in the sample 4 compared to the sample 2. The strain rate difference was insignificant in these samples due to the low plasticizer content. However, increasing the plasticizer content up to 40% led to a meaningful difference in the samples 3 and 5. In other words, replacing 5% DEHP with 5% ESBO increased the polymer strain from 156% to 257%. Accordingly, ESBO had higher plasticizing effect than DEHP and its plasticizing characteristics in PVC. When a plasticizer (such as DEHP) is added, its molecules will be placed in various sites between polymer chains. This helps PVC become more flexible and leads to a decrease in Tg.

The effect of plasticizers on Tg is attributed to the increase in the free volume that enhances molecular mobility. Although plasticizers reduce chain entanglement density, the length scale of the chain contributing to Tg (~50 C-C bond) is smaller than the entanglement Mw (~200 C-C). It means that the chain entanglement density effect should not be considerable in typical plasticizer contents (~10-20%); unless one uses much higher plasticizer contents or co-plasticizers such as ESBO.

All the samples represented similar behavior both before and after sterilization. The mechanical behavior of the samples after sterilization is shown in Figure 3.2.

The sterilization process did not have considerable effects on maximum strain at the break of the samples. The sample strains considerably increased after sterilization, indicating that sterilization tended to increase its flexibility. Moreover, samples with 5% ESBO better preserved their mechanical properties.
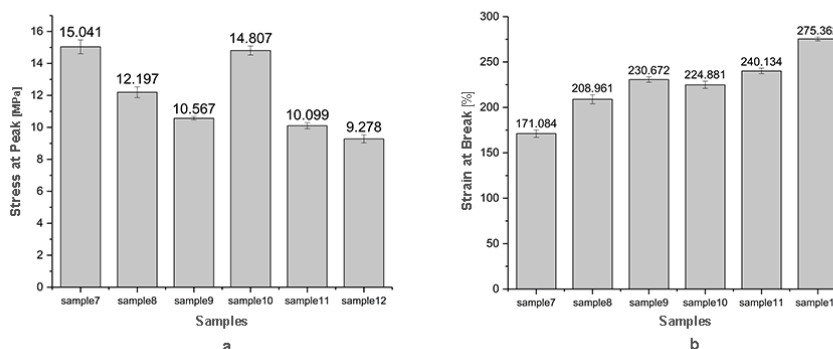
Figure 3.2 mechanical properties of stretch PVC films evaluated; Yield stress (a) and strain at breakpoint (b) after sterilization process.

The results of mechanical testing after sterilization confirmed that the strain increased at the break of the polymer with the ESBO plasticizer. The other plasticizers did not show such a maximum strain level at break. However, DEHP showed maximum strain at break after sterilization.

These results can be attributed to the fact that DEHP molecules diffuse to polymer chains because of more heating during the sterilization process and lead to increasing the distance of polymer chains and thus increasing maximum strain at break. Increasing DEHP provides more void spaces between chains, leading to improving chain sliding against each other and increasing polymer flexibility.

When ESBO was added to the polymer, it caused higher increased molecular distances between PVC chains by the combined effect of ESBO and DEHP molecules. DEHP was emplaced between PVC chains and, finally, increased polymer flexibility. Actually ESBO has a synergistic effect when used with DEHP and increases the polymer flexibility.

Sarath Josh et al. (2012) studied the temperature effect on the DEHP migration and release in blood preservation bags and confirmed the increased DEHP penetration index with increasing the temperature [25, 26]. In other words, DEHP molecules were stabilized between PVC chains with increasing the temperature. During the sterilization process, the temperature increased to 60°C when ethylene oxide gas was penetrated to the polymer bulk. Therefore, during the sterilization process, DEHP molecules were better mixed with PVC molecules with increasing the temperature up to 60°C. The polymer was annealed, and its mechanical properties were improved.

3.2 DEHP release from PVC

3.2.1 DSC analysis

Table 3.3 and Figure 3.1 show the second heating DSC curves of the four samples. As shown in Table 3.3, the Tg temperature decreased with increasing ESBO (Table 3.1). Accordingly, the Tg temperature decreased 4°C in the sample 5 compared to the sample 2 and more than 13°C in the sample 11 compared to the sample 8.

Decreasing the Tg temperature with increasing ESBO indicates that ESBO, used as a stabilizer for DEHP, can be simultaneously used as a secondary plasticizer. Furthermore, the

existence of ESBO in the PVC polymer bulk not only stabilizes DEHP into the PVC structure but also reduces the Tg temperature in the samples.

Table 3.1 Tg comparison in the samples 2, 5, 8 and 11

Sample No.	T_{start} (^{o}C)	T_{final} (^{o}C)	T_g (^{o}C)
2	-23.10	-4.73	-13.38
5	-37.50	-27.43	-17.09
8	-24.45	-5.13	-14.22
11	-31.27	-23.63	-27.29

The results showed that the Tg temperature of the polymer decreased after sterilization because of more molecular diffusion of the plasticizer into the polymer bulk.

The above findings are confirmed by the tensile test results, where the samples exhibited a higher maximum strain after sterilization. As shown in the mechanical test results, maximum strain at break increased with an increase in the plasticizer content. The DSC test results indicated that maximum strain at break increased by decreasing Tg and increasing the free volume in the polymer chains.

In other words, the DSC test results confirmed the tensile test results. A decrease in Tg indicated an increase in the plasticizer effect on PVC because of the synergistic effect of ESBO and the sterilization process (Fig. 3.3).
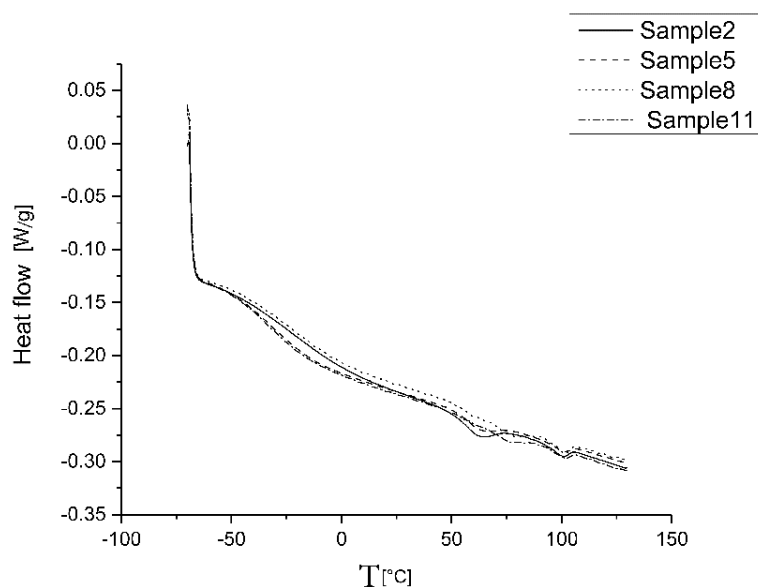

Figure 3.3: DSC curve of the samples 2, 5, 8 and 11

3.2.2 *Gas chromatography test analysis*

The DEHP concentration in the samples 8 and 11 was calculated to be 1333.4948 ppm and 1362.5368 ppm, respectively, with a difference of 30 ppm that can be neglected (Fig. 3.4)
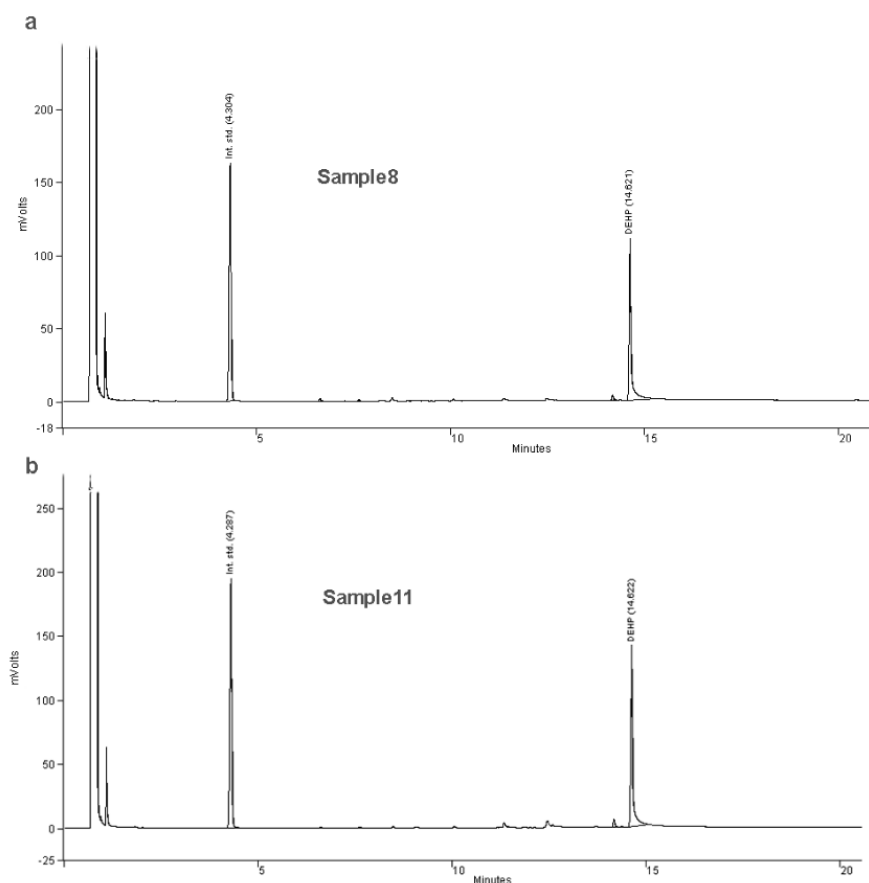
Figure 3.4 Chromatograms of samples 8 (a) and 11 (b).

Given the results in Figure 3.4 showing the release rate of DEHP into the extraction solution, it can be concluded that ESBO has no role in the migration of DEHP from the polymer bulk.

3.3 Hemolysis analysis

Samples with hemolysis more than 2% are considered slightly hemolytic, according to analysis standards of medical tools. According to the results, the samples had no considerable hemolysis effect; maximum hemolysis was in the sample 7 at 3.3%, containing 30% DEHP (Fig. 3.5). However, it appears that adding ESBO to PVC decreased the PVC hemolysis effect. Thus, the sample 10 with 0.22% hemolysis percentage and the samples 11 and 12 with 0.88% hemolysis percentage were known as non-hemolytic samples, while the samples 7 and 8 were slightly hemolytic with 3.3% and 2% hemolysis percentages, respectively. Therefore, the results indicated that the samples were non-hemolytic.

Haishima et al. demonstrated that PVC plasticizers, including a 6-carbon ring such as DEHP, had an effective role in suppressing blood cell hemolysis [27]. Moreover, Miller et al. reported that adding small amounts of DEHP to red blood cells reduced their hemolysis to 20%, which were preserved at 4°C for 35 days [28, 29]. The present study confirms these results.
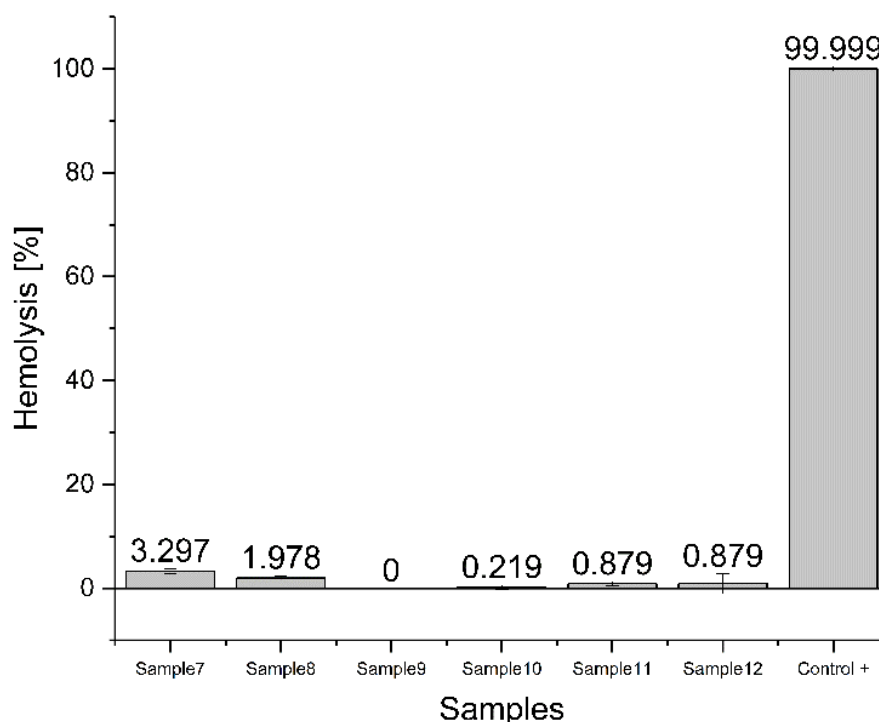
Figure 3.5 Hemolysis of the samples 7 – 12

4. CONCLUSION

For more than 50 years, DEHP has been used as a plasticizer in PVC in blood preservation bags and also in most medical tools. Ethylene oxide sterilization is an essential process in manufacturing medical tools.

The results of tensile tests and heat analysis on the samples demonstrated that 5% ESBO led to DEHP stabilization within the polymer structure and improved its mechanical properties with decreasing temperature (Tg) and increasing polymer flexibility. Moreover, sterilization using ethylene oxide gas improved mechanical properties of the samples.

The results of the gas chromatography test on solutions extracted from the sterilized samples, both with and without ESBO, indicated that ESBO had no effect on the migration of DEHP molecules into the non-polar environment.

According to the hemolysis test results, DEHP release into the blood was extremely low, as DEHP is a non-polar molecule whereas blood is a polar one. Moreover, all samples containing 5% ESBO were non-hemolytic.

Finally, it can be summarized that sterilization has no significant effect on the migration of the plasticizer from the polymer bulk; however, its annealing effects help improve the mechanical properties of PVC medical tools.

REFERENCES

[1]   Van der Meer PF, Reesink HW, Panzer S, Wong J, Ismay S, Keller A, (2014) Should DEHP be eliminated in blood bags?. Vox Sang 106(2):176-95,doi: 10.1111/vox.12099.

[2]   Dumont LJ, Baker S, Dumont DF, (2012)., Exploratory in vitro study of red blood cell storage containers formulated with an alternative plasticizer. Transfusion 20(7):1439-45, doi:10.1111/j.1537-2995.2011.03506.x.

[3]   Chiellini F, Ferri M, Morelli A, Dipaola L, Latini G. (2013) Perspectives on alternatives to phthalate plasticized poly(vinyl chloride) in medical devices applications. Prog in Polym Science 38(7): 1067-1088, doi:10.1016/j.progpolymsci.2013.03.001.

[4]   Hakkarainen M, (2003) New PVC materials for medical applications—the release profile of PVC/polycaprolactone–polycarbonate aged in aqueous environments. Polym Degrad Stab 80(3):451-458, doi:10.1016/S0141-3910(03)00029-6.

[5]   Coltro L, Pitta JB, Madaleno E, (2013) Performance evaluation of new plasticizers for stretch PVC films. Polym Test 32(2):272-278, doi:10.1016/j.polymertesting.2012.11.009.

[6]   Radaniel T, Genay S, Simon N, et al., (2014) Quantification of five plasticizers used in PVC tubing through high performance liquid chromatographic-UV detection. J Chromatogr B Analyt Technol Biomed Life Sci 965:158-63, doi: 10.1016/j.jchromb.2014.06.027.

[7]   Lamba NM, Courtney JM, Gaylor JD, Lowe GD. (2000)In vitro investigation of the blood response to medical grade PVC and the effect of heparin on the blood response. Biomater 21(1):89-96, doi:10.1016/S0142-9612(99)00145-3.

[8]   Labed V, Obeid H, Ressayre K. (2013) Effect of relative humidity and temperature on PVC degradation under gamma irradiation: Evolution of HCl production Yields. Radiat Phys Chem 84:26-29, doi:10.1016/j.radphyschem.2012.06.052.

[9]   Haishima Y, Matsuda R, Hayashi Y, Hasegawa C, Yagami T, Tsuchiya T. (2004) Risk assessment of di(2-ethylhexyl)phthalate released from PVC blood circuits during hemodialysis and pump-oxygenation therapy. Int J Pharm 274(1-2):119-29, doi:10.1016/j.ijpharm.2004.01.009.

[10]   Al Salloum H, Saunier J. Tfayli A. Yagoubi N. (2016) Studying DEHP migration in plasticized PVC used for blood bags by coupling Raman confocal microscopy to UV spectroscopy. Mater Sci Eng C Mater Biol Appl 61:56-62, doi: 10.1016/j.msec.2015.12.008.

[11]   Khorasani MT, Mirzadeh H. (2007) Effect of oxygen plasma treatment on surface charge and wettability of PVC blood bag—In vitro assay. Radiat Phys Chem 76(6):1011-1016, doi:10.1016/j.radphyschem.2006.10.002.

[12]   Mankidy R., Wiseman S. Ma H, Giesy JP. (2013) Biological impact of phthalates. Toxicol Lett 217(1): 50-8, doi:10.1016/j.toxlet.2012.11.025.

[13]   Wang Q, Storm BK. (2005) Separation and analysis of low molecular weight plasticizers in poly(vinyl chloride) tubes. Polym Test 24(3):290-300, doi:10.1016/j.polymertesting.2004.12.002.

[14]   Haishima Y, Seshimo F, Higuch T, (2005) Development of a simple method for predicting the levels of di(2-ethylhexyl) phthalate migrated from PVC medical devices into pharmaceutical solutions. Int J Pharm 298(1): 126-42, doi: 10.1016/j.ijpharm.2005.04.009.

[15]   Zygoura PD, Paleologos EK, Kontominas MG. (2011) Migration levels of PVC plasticisers: Effect of ionising radiation treatment. Food Chem 128(1):106-13, doi: 10.1016/j.foodchem.2011.03.002.

[16]   Burgos N, Jiménez A. (2009) Degradation of poly(vinyl chloride) plasticized with non-phthalate plasticizers under sterilization conditions. Polym Degrad Stab 94(9):1473-1478, doi:10.1016/j.polymdegradstab.2009.05.004.

[17]   Fankhauser-Noti A, Fiselier K, Biedermann-Brem S, Grob, K. (2006) Assessment of epoxidized soy bean oil (ESBO) migrating into foods: comparison with ESBO-like epoxy fatty acids in our normal diet. Food Chem Toxicol 44(8):1279-86, doi: 10.1016/j.fct.2006.02.005.

[18]   Karmalm P, Hjertberg T, Jansson A, Dahl R. (2009) Thermal stability of poly(vinyl chloride) with epoxidised soybean oil as primary plasticizer. Polym Degrad Stab 94(12):2275-2281, doi:10.1016/j.polymdegradstab.2009.07.019.

[19] Yu BY, Lee AR, Kwak SY. (2012) Gelation/fusion behavior of PVC plastisol with a cyclodextrin derivative and an anti-migration plasticizer in flexible PVC. Eur Polym J 48(5):885-895, doi:10.1016/j.eurpolymj.2012.02.008.

[20] Bueno-Ferrer C, Garrigós MC, Jiménez A. (2010) Characterization and thermal stability of poly(vinyl chloride) plasticized with epoxidized soybean oil for food packaging. Polym Degrad Stab 95(11):2207-2212, doi:10.1016/j.polymdegradstab.2010.01.027.

[21] Hammarling L, Gustavsson H. Svensson K, Karlsson S, Oskarsson A. (1998) Migration of epoxidized soya bean oil from plasticized PVC gaskets into baby food. Food Addit Contam 15(2):203-8, doi: 10.1080/02652039809374631.

[22] SANCO D. European Commission, Health & Consumer Protection Directorate-General. Opinion on Medical Devices Containing DEHP Plasticised PVC 2002, doi: 10.2772/45179.

[23] Sunny MC, Ramesh P, Mohanan PV, George KE. (2010) Metallocene based polyolefin: a potential candidate for the replacement of flexible poly (vinyl chloride) in the medical field. Polym for Advanced Technologies 21(9):621-631, doi:10.1002/pat.1475.

[24] Al Salloum H, Saunier J, Aymes-Chodur C, Barakat H, Yagoubi N. (2015) Impact of the nature and concentration of plasticizers on the ability of PVC to sorb drug. Int J Pharm 496(2):664-75, doi:10.1016/j.ijpharm.2015.11.004.

[25] Sarath Josh MK, Pradeep S. Balachandran S, Sudha Devi R, Vijayalakshmi Amma KS, Benjamin S. (2012). Temperature- and solvent-dependent migrations of di(2-ethylhexyl) phthalate, the hazardous plasticizer from commercial PVC blood storage bag. J Polym Res 19(7), doi:10.1007/s10965-012-9915-4.

[26] Jérémy P et al (2019). New SPE-LC-MS/MS method for the simultaneous determination in urine of 22 metabolites of DEHP and alternative plasticizers from PVC medical devices, talanta, 198:377-389

[27] Haishima Y, Kawakami T, Hasegawa C, Tanoue A, Yuba T, Isama K, Matsuoka A, Niimi S. (2014). Screening study on hemolysis suppression effect of an alternative plasticizer for the development of a novel blood container made of polyvinyl chloride. J Biomed Mater Res B Appl Biomater 102(4):721-8, doi: 10.1002/jbm.b.33052.

[28] Estep TN, Pedersen RA, Miller TJ, Stupar KR. (1984) Characterization of erythrocyte quality during the refrigerated storage of whole blood containing di-(2-ethylhexyl) phthalate. Blood 64(6): 1270-6, doi:10.1182/blood.V64.6.1270.1270

[29] Amandine D et al. (2019). Simultaneous determination of di(2-ethylhexyl) phthalate and diisononylcyclohexane-1,2-dicarboxylate and their monoester metabolites in four labile blood products by liquid chromatography tandem mass spectrometry, Journal of Pharmaceutical and Biomedical Analysis, 181:1-11, doi:10.1016/j.jpba.2019.113063.

MAGNETICALLY MODIFIED SUGARCANE BAGASSE DISORDERED CARBON AS A CADMIUM REMOVAL AGENT IN WATER

**Izzaty Syahirah Baharudin[1], Noraini Mohamed Noor[2*],
Ezzat Chan Abdullah[1], Raihan Othman[2] and
Mubarak Nasibab Mujawar[3]**

*[1]Malaysia - Japan International Institute of Technology,
Universiti Teknologi Malaysia, Jalan Semarak, 54100 Kuala Lumpur, Malaysia
[2]Science in Engineering Department, Kulliyyah of Engineering,
International Islamic University Malaysia,
Jalan Gombak, 53100 Kuala Lumpur, Malaysia
[3]Department of Chemical Engineering, Curtin University,
Sarawak Campus CDT 250, 98009 Miri, Sarawak, Malaysia*

[*]Corresponding author: norainimnoor@iium.edu.my

ABSTRACT: Heavy metals are hazardous to health at certain levels. Currently, heavy metals are removed by physicochemical treatments, such as adsorption, flotation, and electrochemical deposition, and also biological treatments, such as algal biofilm reactor and anaerobic ammonium oxidation. In this study, magnetic biochar was produced to enhance the effectiveness and performance of the adsorbent for heavy metal removal. This study aimed to synthesise high-performance magnetic biochar, to determine the optimum parameters and conditions for high yield of magnetic biochar and high removal of cadmium (Cd^{2+}) from aqueous solution, and to determine the adsorption kinetics and isotherms for Cd^{2+} removal. Nickel oxide (NiO)-impregnated sugarcane bagasse was subjected to slow pyrolysis to produce magnetic biochar. The impregnated metal, pyrolysis temperature, and pyrolysis time were varied to determine the optimum parameters and conditions to produce high-performance magnetic biochar. The removal of Cd^{2+} from aqueous solution and batch adsorption study were conducted. The synthesised magnetic biochar was characterised using field-emission scanning electron microscopy (FESEM), energy dispersive X-ray (EDX), X-ray diffraction (XRD), Brunauer-Emmett-Teller (BET) surface area, Fourier transform infrared (FTIR), and vibrating sample magnetometer (VSM). The adsorption data agreed well with the pseudo-second-order model and followed the Langmuir isotherm model. This study achieved 88.47% removal efficiency of Cd^{2+} from aqueous solution. Thus, the removal of this heavy metal as a human carcinogen reduces the hazardous effects on human health and reduces the toxicity in the environment.

ABSTRAK: Logam berat adalah berbahaya bagi kesihatan di peringkat tertentu. Pada masa ini, logam berat disingkirkan melalui rawatan fizikokimia, seperti penyerapan, pengapungan, dan deposit elektrokimia, dan rawatan biologikal, seperti reaktor biofilem alga dan oksidasi ammonium anerobik. Kajian ini menghasilkan biochar magnetik bagi meningkatkan keberkesanan dan prestasi penyerapan penyingkiran logam berat. Kajian ini bertujuan bagi mengsintesis biochar magnetik pada prestasi tinggi, bagi menghasilkan parameter optimum dan keadaan pengeluaran tinggi biochar magnetik dan penyingkiran tinggi kadmium (Cd^{2+}) daripada larutan akues, dan bagi mendapatkan penyerapan kinetik dan isoterma penyingkiran Cd^{2+}. Nikel oksida (NiO)-impregnat hampas tebu adalah

berdasarkan pirolisis perlahan bagi menghasilkan biochar magnetik. Logam yang terimpregnat, suhu pirolisis dan tempoh pirolisis dipelbagaikan bagi mendapatkan parameter optimum dan keadaan bagi menghasilkan biochar magnetik berprestasi-tinggi. Penyingkiran Cd^{2+} daripada larutan akues dan kajian penyerapan berkumpulan telah dibuat. Biochar magnetik yang disentisis diklasifikasikan menggunakan mikroskopi elektron imbasan medan-pancaran (FESEM), tenaga sebaran X-ray (EDX), pembelauan X-ray (XRD), kawasan permukaan Brunauer-Emmett-Teller (BET), Penjelmaan Fourier inframerah (FTIR), dan sampel getaran magnetometer (VSM). Data penyerapan menunjukkan persetujuan dengan model aturan-kedua-pseudo dan mengikuti model isoterma Langmuir. Kajian ini mencapai 88.47% keberkesanan penyingkiran Cd^{2+} daripada larutan akues. Oleh itu, penyingkiran logam berat ini sebagai karsinogen manusia mengurangkan kesan teruk pada kesihatan manusia dan pengurangan toksik pada alam sekitar.

1. INTRODUCTION

Heavy metals are hazardous to health at certain concentrations in water. In order to meet the discharge requirements, lead, mercury, silver, chromium, cadmium, zinc, nickel, and tin are heavy metals that need to be removed from wastewater until specific allowable concentrations are achieved. These heavy metals cause serious health risks and affect the environment negatively [1,2]. The treatment of water containing heavy metals is important to reduce health risks [2]. Wastewater with high concentrations of heavy metals is hazardous to humans and the environment. Wastewater treatment is vital in providing a sustainable and safe environment. Various treatment methods have been studied in the past decade. Adsorbents from different biomass types, such as magnetic biochar, can be used for heavy metal removal from wastewater.

Studies on magnetic biochar have attracted attention as the adsorbent possesses high adsorption capability to remove heavy metals from wastewater. Moreover, the removal performance of magnetic biochar is relatively higher than biochar. Magnetic biochar can be produced from biomass sources, such as pine sawdust, palm kernel shell, cottonwood, and pineapples [1,3-5,6]. Several methods are available to synthesise magnetic biochar, but the most used method is pyrolysis, which is the burning of a sample in the absence of oxygen.

Cadmium is a human carcinogen, which can cause cancer and lead to death [7]. The main cause of death in 2012 was cancer, which is mainly due to genomic instability [8,9]. Other than that, the inhalation of high levels of cadmium can severely affect lungs [7]. Furthermore, consuming high levels of cadmium can cause stomach pain, resulting in diarrhoea and vomiting [7]. Prolonged exposure to cadmium, even at lower concentrations, can also lead to lung damage, fragile bones, and kidney disease [7].

Many studies have focused on wastewater treatment, including physicochemical treatment, and there is a growing interest in biological treatment. Several physicochemical treatment methods have been studied and are currently used, such as electrooxidation, chemical precipitation, adsorption, flotation, electrochemical deposition, and shales from coal mines [10-12]. Meanwhile, biological treatment methods include anaerobic ammonium oxidation, sequencing batch biofilter reactor, algal biofilm reactor, natural biofiltration, and photo-anaerobic membrane bioreactor have been studied [13-17].

Activated carbon is preferred for heavy metal removal, which becomes one of the most popular adsorbents in the wastewater industry [18]. However, high-quality activated

carbon is more expensive and cost-inefficient [18]. Low-cost adsorbents have been introduced as alternatives to the expensive activated carbon [18]. These include adsorbents from natural materials and waste products, such as industrial by-products and modified agricultural and biological wastes [12]. Among examples of low-cost adsorbents are natural materials (e.g., chitosan, zeolites, and clay), waste products (e.g., coal, fly ash, and oxides), and biosorption products (e.g., hazelnut shells, rice husk, and pecan shells) [12,18]. These adsorbents are inexpensive and cost-efficient due to their availability in large quantities.

Therefore, in this study, magnetic biochar produced from modified agriculture and biological waste was used to remove cadmium in wastewater. The study of magnetic biochar for heavy metal removal from wastewater is new in Malaysia. Sugarcane bagasse was selected as the biomass source in this study because this waste material is usually discarded in Malaysia. Hence, sugarcane bagasse is easy to obtain and cost-effective. The waste also has favourable physicochemical characteristics that can assist in wastewater treatment. Chemical modification and impregnation with metals on sugarcane bagasse through slow pyrolysis can enhance the effectiveness and performance of the adsorbent.

Besides food, sugarcane is also a major source of bioethanol production that is widely used to replace gasoline in several countries, including Brazil. However, there is an issue of using food as a biomass source due to the competition between energy and food [19]. Sugar is produced from either sugar beet or sugarcane [19]. Various by-products are produced during the process, such as molasses, bagasse, pressmud, lime sludge, and beet pulp, and these by-products are renewable raw materials [19]. Therefore, these by-products are preferred as biomass sources to avoid fuel and food competition. In Mexico, a study was conducted to simulate the potential of sugarcane and blue agave bagasse in bioethanol production by replacing food with biomass sources [20].

Several studies involving magnetic biochar as an effective heavy metal adsorbent have been conducted. Until now, several modifications have been made in various studies to improve the properties of biochar, primarily to enhance its adsorption properties for better performance. Moreover, the number of studies on sugarcane bagasse adsorbent and magnetic adsorbent has been growing since 2007. However, the studies were more favourable towards magnetic absorbent, except in 2015, where the studies on sugarcane bagasse as absorbent were higher than magnetic absorbent.

2. MATERIALS AND METHODS

2.1 Materials

Sugarcane bagasse was obtained directly from the juice stall, where the bagasse is the solid waste from the mechanical extraction of sugarcane. First, the raw sugarcane bagasse was air-dried and crushed to obtain smaller-sized biomass. The crushed bagasse was washed thrice using tap water. Then, this sample was oven-dried for 24 h at 70 °C and left in room temperature drying rack for 1 week. This study used a synthetic wastewater sample prepared with a similar concentration of pure Cd^{2+} instead of industrial wastewater to evaluate the removal efficiency of Cd^{2+} using magnetic biochar. This synthetic wastewater sample can help simulate the real industrial wastewater behaviour.

In this work, sugarcane bagasse was impregnated with three types of nickel metals {nickel oxide (NiO), nickel chloride ($NiCl_2$), and nickel sulfate ($NiSO_4$)}. The impregnation produced sugarcane bagasse magnetic biochar, which was later used for Cd^{2+} adsorption in aqueous solution.

2.2 Synthesis of Magnetic Biochar

The dried sugarcane bagasse was magnetised by the impregnation of metal salts on the biomass surface. The metal salt solutions of NiO, NiCl$_2$, and NiSO$_4$ were prepared and biomass was immersed in the solutions with the metal salt-to-biomass ratio of 0.45:1, where the ratio was kept constant throughout the experiment. Next, the immersed biomass was placed in a shaker for 1 h at 170 rpm. After completion, the sample was filtered and oven-dried at 70 °C for 24 h prior to slow pyrolysis. The ratio of metal salt per biomass was maintained and the holding time was 10 and 20 min. Approximately 5 and 10 g of the impregnated sugarcane bagasse were weighed for the experiments with pyrolysis time of 10 and 20 min, respectively.

Magnetic biochar was synthesised in oxygen-free conditions through slow pyrolysis in a WiseTherm muffle furnace. A vacuum pump was used for degassing prior to pyrolysis to achieve oxygen-free conditions. Various temperatures ranging from 400 to 700 °C (400, 450, 500, 550, 600, 650, and 700 °C) were used for the determination of optimum temperature to produce magnetic biochar with high adsorption capacity at 25 °C/min heating rate. This temperature range was selected because the pyrolysis working temperature is between 400 and 700 °C. Sugarcane bagasse cannot be magnetised when the temperature is lower than 400 °C, where carbonisation occurs at this temperature range. Similarly, gasification occurs when the temperature exceeds 700 °C.

After pyrolysis, the magnetic biochar was cooled to room temperature before it was crushed to smaller size. Next, the crushed magnetic biochar was rinsed with distilled water several times until it reached the neutral state. Finally, the magnetic biochar was oven-dried and stored in an airtight plastic container prior to characterisation.

2.3 Characterisation of Magnetic Biochar

Prior to adsorption, magnetic biochar was characterised using Brunauer-Emmett-Teller (BET) surface area, field-emission scanning electron microscopy (FESEM), X-ray diffraction (XRD), Fourier transform infrared (FTIR), and vibrating sample magnetometer (VSM). After Cd^{2+} removal from wastewater, only FESEM, XRD, and FTIR were conducted to characterise the samples. BET analysis was performed to calculate the surface area of magnetic biochar. The optimum condition to produce magnetic biochar was analysed using FTIR to determine the surface functional groups before and after the adsorption of Cd^{2+}. FESEM was used to observe the porosity and structure of the sample's surface after synthesising magnetic biochar. This characterisation is also required to observe the condition of magnetic biochar after Cd^{2+} adsorption from synthetic wastewater. The phase identification and structure of magnetic biochar before and after adsorption were studied using XRD. Meanwhile, VSM was applied to measure and determine the magnetic properties of the synthesised magnetic biochar.

2.4 Cadmium Adsorption

About 0.3 g of each sample was weighed and synthetic wastewater solution with 20 ppm of cadmium concentration was prepared. The samples were added into capillary tubes filled with 10 ml of cadmium solution. The samples in the capillary tubes were agitated at 200 rpm for 1 h using an incubator shaker (IKA KS 3000 i control). After completion, the samples were filtered and 10 ml of the solution was collected in smaller capillary tubes. Atomic absorption spectroscopy (AAS) was utilised to analyse the samples. The optimum time and temperature were selected for the sample with the highest cadmium removal.

2.5 Batch Adsorption Study

After obtaining the AAS results, the sample with the optimum time and temperature was selected to conduct a batch adsorption study. Cadmium solutions of 20, 40, 60, 80, and 100 ppm were prepared and each solution was filled in a conical flask. Then, 0.6 g of the selected sample was added into each conical flask containing 200 ml solution.

3. RESULTS AND DISCUSSION

3.1 Magnetic Biochar Yield and Cd^{2+} Removal Percentage of Magnetic Biochar

The yield of magnetic biochar was determined by weighing the magnetic biochar before and after pyrolysis (Eq. 1). Meanwhile, the Cd^{2+} removal percentage was determined by measuring the concentration of Cd^{2+} after adsorption using AAS (Eq. 2).

$$\% \, magnetic \, biochar \, yield = \frac{(Weight_{after} - Weight_{before})}{Weight_{before}} \times 100 \, \% \tag{1}$$

$$\% \, removal = \frac{(Concentration_{Cd^{2+},after} - Concentration_{Cd^{2+},before})}{Concentration_{Cd^{2+},before}} \times 100 \, \% \tag{2}$$

Figure 1a illustrates the yields of magnetic biochar over pyrolysis temperature using different types of sugarcane bagasse impregnated for 10 min. NiO-impregnated sugarcane bagasse showed the highest yield (46.5%) compared to other metals at 400 °C, followed by NiO-impregnated sugarcane bagasse at 500 °C with 42.53% yield. The finding clearly shows that a higher pyrolysis temperature will result in a lower yield of magnetic biochar. The percentage of yield decreased with pyrolysis temperature. At elevated temperatures from 400 to 600 °C, biomass decomposed and produced lower magnetic biochar yields, nearly 50% reduction from the initial yield. This result suggests that most of the volatile matter in sugarcane bagasse decomposed at higher temperatures, leaving a small amount of magnetic biochar with high carbon content. On the other hand, slow heating exposed sugarcane bagasse to heat for a longer time, allowing more volatile matter to decompose and form more surface pores [21].

According to Fig. 1b, $NiSO_4$-impregnated sugarcane bagasse achieved the highest yield of 36.03% at 400 °C. From the figure, different anions of metal salts affected the percentage of yield produced, indicating the changes in the primary degradation of the biomass.

Figure 2a presents the graph of Cd^{2+} removal percentage versus temperature at 10 min of pyrolysis time. NiO-impregnated magnetic biochar demonstrated the highest Cd^{2+} removal efficiency of 88.57% at 500 °C, followed by $NiSO_4$-impregnated magnetic biochar (88.55%) at 400 °C and $NiCl_2$-impregnated magnetic biochar (87.69%) at 500 °C. The removal efficiency decreased as the impregnated magnetic biochars were heated from 400 to 500 °C, except NiO-impregnated magnetic biochar. In contrast to the impregnated magnetic biochars produced at 20 min of pyrolysis time (Fig. 2b), the removal percentage started to increase after 450 °C and decrease beyond 600 °C. The reason for such behaviour is that the development of the pore structure and active sites are insufficient at high pyrolysis temperatures [22].

The best metal to be impregnated with magnetic biochar and the optimum parameters and conditions were determined from the metal-impregnated magnetic biochar producing the best yield and Cd^{2+} removal percentage. Therefore, NiO-impregnated magnetic biochar

was chosen due to its high yield of 40.24% and high Cd^{2+} removal efficiency of 88.57% at 500 °C.
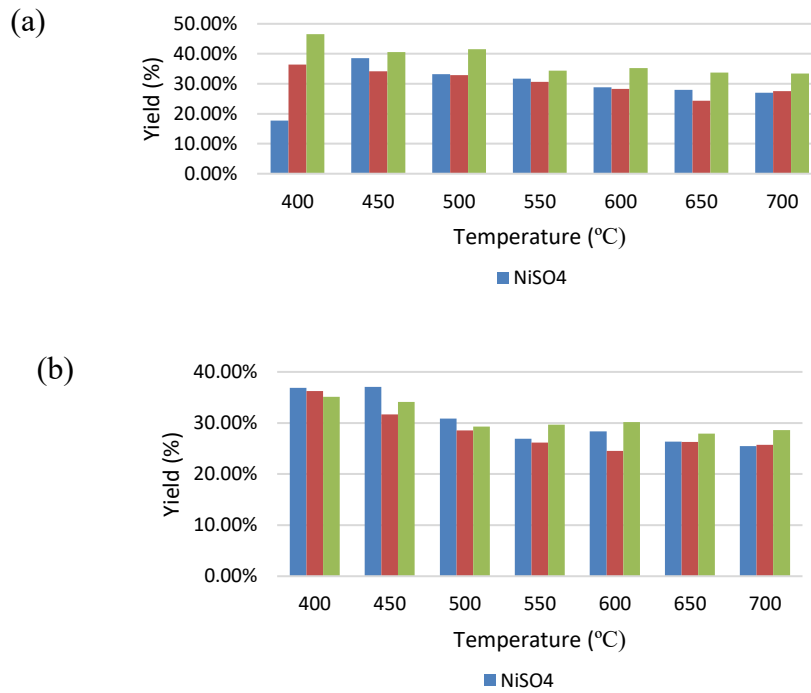

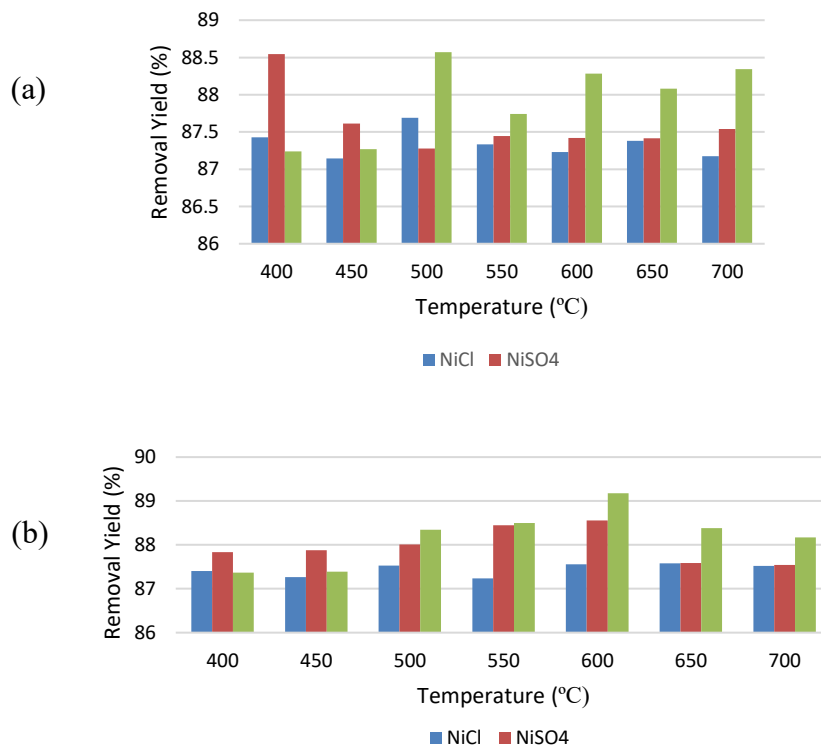Fig. 1: Yield of magnetic biochar at (a) 10 min and (b) 20 min of pyrolysis time.

Fig. 2: Cd^{2+} removal percentage of magnetic biochar at (a) 10 min and (b) 20 min of pyrolysis time.

3.2 Characterisation of Magnetic Biochar

3.2.1 Field-Emission Scanning Electron Microscopy and Energy Dispersive X-ray Spectroscopy Analysis

The surface structure of raw sugarcane bagasse and magnetic biochar was studied using FESEM. Figure 3(a-d) depict the morphology of raw sugarcane bagasse, sugarcane bagasse biochar, magnetic biochar before adsorption, and magnetic biochar after adsorption, respectively. Raw sugarcane bagasse has a more blocked and smooth surface [23], but the structure is more porous and agglomeration could be observed (Fig. 3d) after impregnation and pyrolysis of sugarcane bagasse. This finding suggests that the metals are impregnated on raw sugarcane bagasse after the synthesis process. The widening of pores could be seen from the figures, indicating the extraction of some materials, such as the dissolution of lignin and other components from the bagasse during impregnation. The loss of volatile compounds from within the particles increased gradually when the final temperature increased during heating.
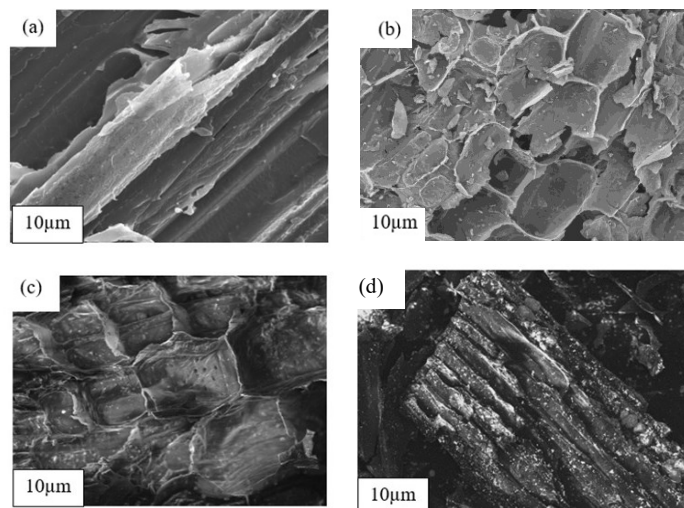

Fig. 3: Morphology of (a) raw sugarcane bagasse, (b) sugarcane bagasse biochar, (c) magnetic biochar before adsorption, and (d) magnetic biochar after adsorption.

Figure 4 presents the EDX analysis of magnetic biochar after Cd^{2+} adsorption, which shows the presence of cadmium element in the magnetic biochar. This analysis agrees that magnetic biochar can remove heavy metals from aqueous solution.
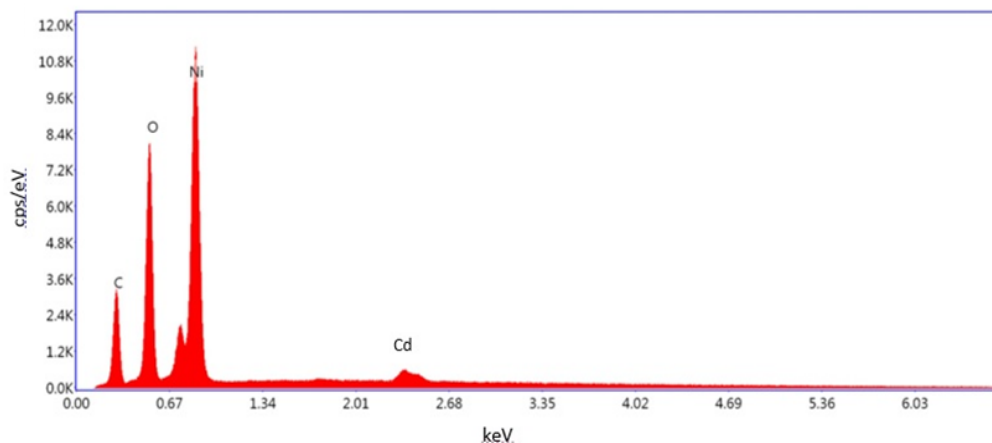

Fig. 4: EDX analysis of magnetic biochar after Cd^{2+} adsorption.

3.2.2 Vibrating Sample Magnetometer Analysis

In this study, VSM analysis was conducted to measure the magnetisation of magnetic biochar. Figure 5 depicts the magnetic hysteresis cycles of magnetic biochar. The magnetic biochar recorded the coercive field of 163.96 G, saturation magnetisation (Ms) of 0.24093 emu/g, and retentivity (Mr) of 0.07377 emu/g. Meanwhile, raw sugarcane bagasse did not give any magnetisation value.
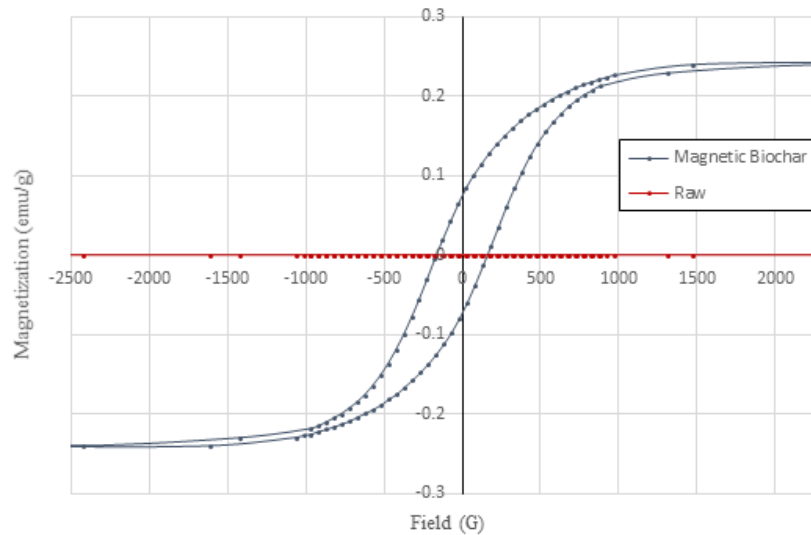

Fig. 5: Magnetic hysteresis cycles of magnetic biochar.

The magnetic hysteresis cycles prove that raw sugarcane bagasse does not have ferromagnetic properties, whereas magnetic biochar shows ferromagnetic properties. Therefore, magnetic biochar can be recovered using magnets. A magnet bar was placed outside of glass bottles containing magnetic biochar to test its magnetic separation ability (Fig. 6). This phenomenon can be considered a combination of superparamagnetic, ferromagnetic, and paramagnetic behaviours [24].
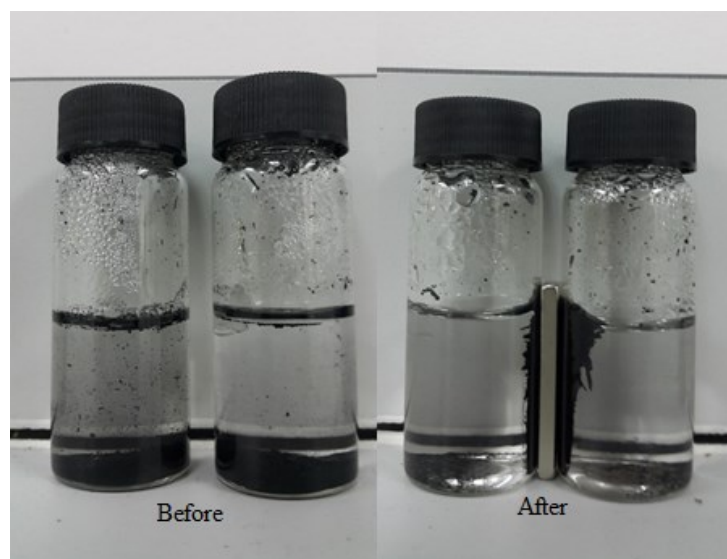

Fig. 6: Magnetic separation ability of magnetic biochar before
and after putting the magnetic bar.

3.2.3 Fourier Transform Infrared Spectroscopy Analysis

FTIR analysis was carried out to determine the functional groups available in raw sugarcane bagasse and magnetic biochar before and after Cd^{2+} adsorption. Figure 7(a) presents the FTIR spectra of raw sugarcane bagasse and Fig. 7(b) illustrates the FTIR spectra of magnetic biochar before and after Cd^{2+} adsorption. The spectra are different in the raw sugarcane bagasse compared to the synthesised magnetic biochar. Therefore, the internal structure of magnetic biochar and their functional groups changed during synthesis.
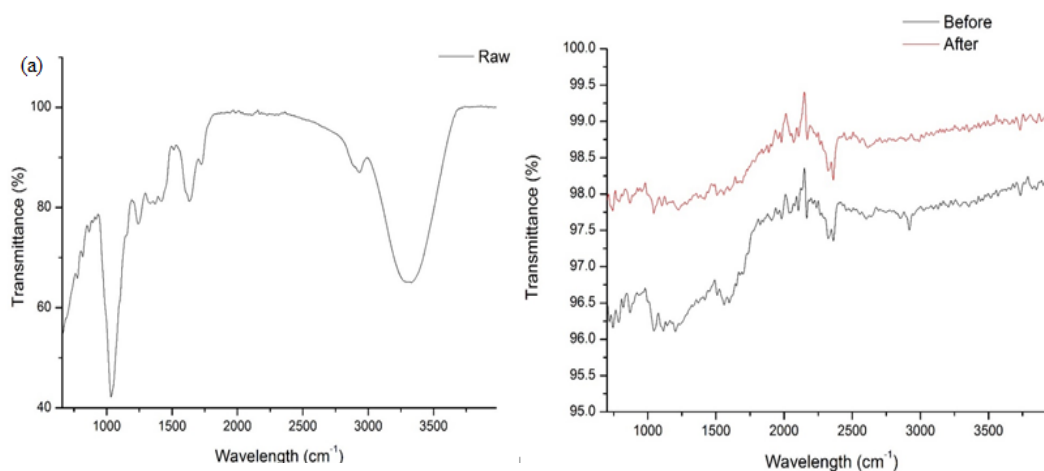

Fig. 7: FTIR spectra for (a) raw sugarcane bagasse and (b) magnetic biochar before and after Cd^{2+} adsorption.

Table 1 shows the possible functional groups present before Cd^{2+} adsorption. For the FTIR spectra before Cd^{2+} adsorption, there is a peak present around $2{,}921$ cm^{-1}, suggesting the presence of CH stretch. Meanwhile, the peak at $1{,}653$ cm^{-1} indicates C=C stretch, which is present due to pyrolysis. Other than that, the C–N stretch is present at $1{,}041$ cm^{-1}, showing that organic compounds are present in the magnetic biochar. It is observed that these functional groups are absent after Cd^{2+} adsorption in aqueous solution. This finding indicates that the adsorption of heavy metals breaks the bonds of the functional groups.

Table 1: Possible functional groups of the identified peaks

Peak Position (cm^{-1})	Possible Functional Group
2,921	CH stretch
1,653	C=C stretch
1041	C–N stretch

3.2.4 Brunauer-Emmett-Teller Surface Area Analysis

BET surface area analysis was conducted to calculate the surface area of raw sugarcane bagasse and magnetic biochar. Table 2 lists the surface area and porosity of raw sugarcane bagasse and magnetic biochar. The results showed higher surface area, total pore volume, and average pore diameter of magnetic biochar than raw sugarcane bagasse. This finding indicates that the pyrolysis of sugarcane bagasse to magnetic biochar increased the surface area and porosity, resulting in higher adsorption capacities. The significant improvement in the surface area and pore volume in magnetic biochar may be due to the significant increase in volatile released [25]. In addition, the NiO impregnated

on the surface of magnetic biochar increased the surface area due to the combustion of the organic molecules trapped in the particles and recrystallization of NiO [26]. Therefore, magnetic biochar has higher adsorption capacity than conventional biochar or raw sugarcane bagasse.

Table 2: Main textural characteristics of raw sugarcane bagasse and magnetic biochar

Properties	Raw Sugarcane Bagasse	Magnetic Biochar
Specific surface area (m^2/g)	1.8058	10.6364
Total pore volume (cm^3/g)	0.0011	0.03437
Average pore diameter (nm)	2.3330	11.5499

3.2.5 X-Ray Diffraction Analysis

XRD analysis was carried out to identify phase characteristics. Figure 8 illustrates the XRD patterns of magnetic biochar. The figure suggests that crystalline NiO formed in magnetic biochar with the highest intensity of $2\theta = 43.3302°$ at (200) plane. Other than that, the NiO peaks are observed at $2\theta = 37.2722°, 62.8562°, 75.4142°,$ and $79.3662°$ at (111), (220), (311), and (222) planes, respectively. The formation of Ni is also shown at the peaks around $2\theta = 44.5262°$ and $51.9102°$ at (111) and (200) planes, respectively.
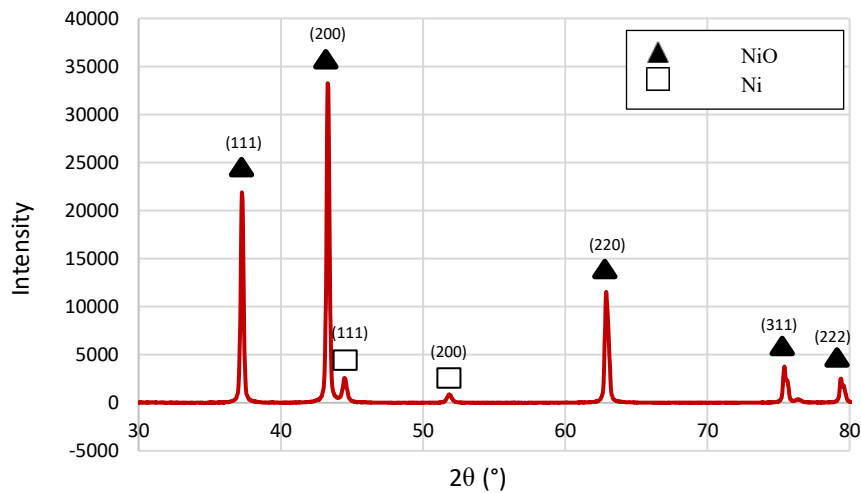

Fig. 8: XRD patterns of magnetic biochar.

At 400–500 °C, NiO is reduced to metallic Ni as magnetic biochar most probably acts as a reducing agent [27]. The analysis shows the formation of magnetic biochar, as confirmed by the existence of NiO and metallic Ni in magnetic biochar.

3.2 Batch Adsorption Study

Adsorption kinetics and isotherms were examined in the batch adsorption study. According to Fig. 9, Cd^{2+} adsorption reached equilibrium at 120 min. The figure also shows that the higher the concentration, the higher the amount of Cd^{2+} absorbed by magnetic biochar due to the increases in adsorption capacity. The increase in the mass transfer driving force where the movement of Cd^{2+} ion into the magnetic biochar surfaces, leading to high adsorption rates [28].
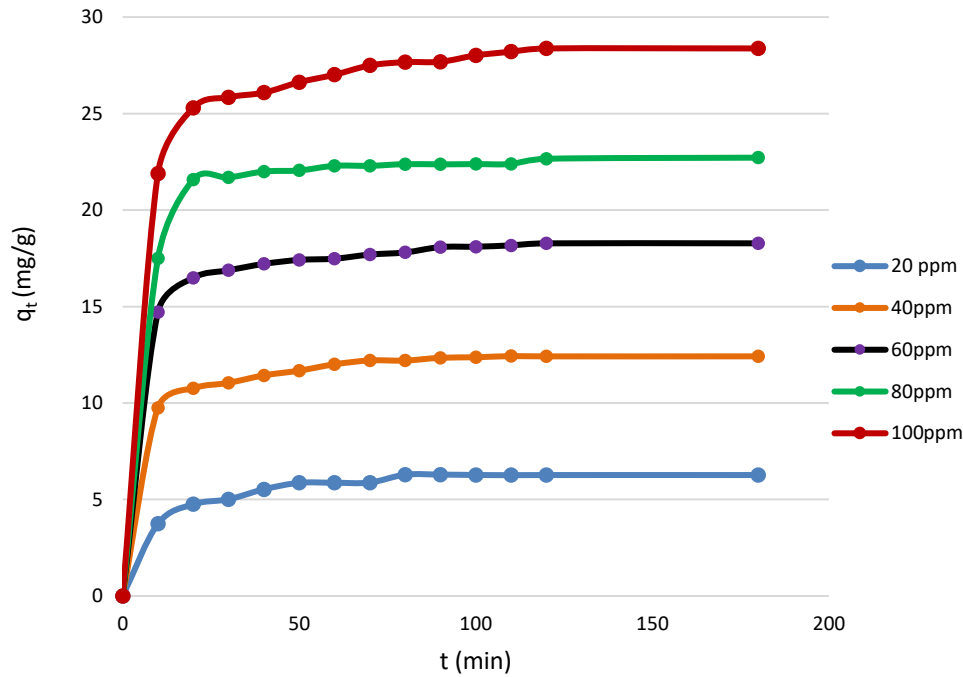
Fig. 9: Effect of time on cadmium adsorption capabilities.

3.3 Adsorption Kinetics

The effect of cadmium adsorption kinetics on the magnetic biochar was simulated using two mathematical models: pseudo-first-order (Eq. 3) and pseudo-second-order (Eq. 4) models. Figure 10 (a,b) presents the adsorption kinetics for the pseudo-first-order and pseudo-second-order models, respectively, for Cd^{2+} adsorption on magnetic biochar.

$$\ln\left(\frac{q_e}{q_e - q_t}\right) = k_1 t \tag{3}$$

$$\frac{1}{(q_e q_t)} = \frac{1}{q_e} + k_2 t \tag{4}$$

where:

q_e = amount of Cd^{2+} adsorbed at time t;
q_t = amount of Cd^{2+} adsorbed at equilibrium;
k_1 = pseudo-first-order rate constant; and
k_2 = pseudo-second-order rate constant.

Tables 3 and 4 tabulate the kinetic parameters of Cd^{2+} adsorption for pseudo-first-order and pseudo-second-order models, respectively. The correlation coefficient (R^2) values for both kinetic models clearly show that the experimental data follow the pseudo-second-order model with $R^2 \approx 1$. Therefore, the pseudo-first-order model could not describe the adsorption kinetics of this study. It is assumed that the amount of Cd^{2+} on the surface of magnetic biochar affects the adsorption, and the pseudo-second-order model suggests that the adsorption process is chemisorption as visualised in FTIR analysis previously, where Cd^{2+} adsorption in this study is due to the chemical bonds formed [1].
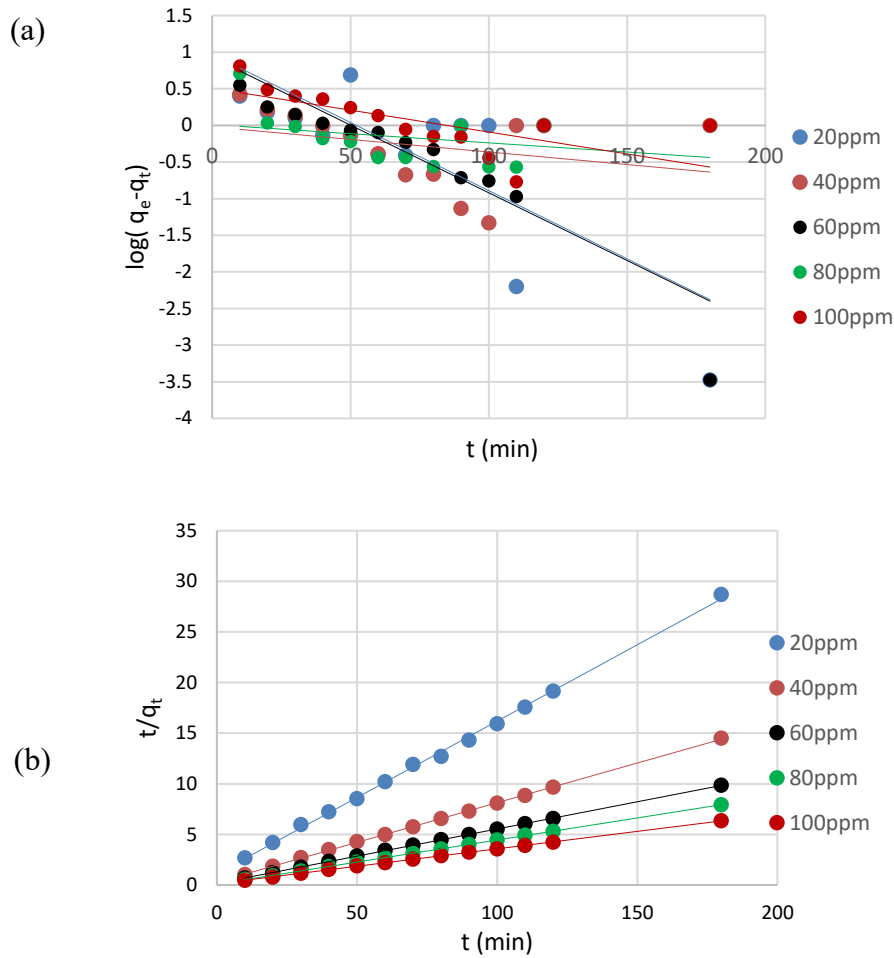
Fig. 10: (a) Pseudo-first-order and (b) pseudo-second-order models of Cd^{2+} adsorption.

Table 3: Kinetic parameters of Cd^{2+} adsorption for the pseudo-first-order model

C_o (mg/L)	q_e (mg/g)	k_1	q_e	R^2
20	60.2683	-2.2364	0.9581	0.5798
40	12.4177	0.0451	0.9922	0.0917
60	18.2750	-2.1395	0.9583	0.7415
80	22.6550	0.1145	0.9915	0.0828
100	28.3737	-1.1692	0.9863	0.4615

Table 4: Kinetic parameters of Cd^{2+} adsorption for the pseudo-second-order model

C_o (mg/L)	q_e (mg/g)	k_2	q_e	R^2
20	60.2683	0.0206	6.6313	0.9986
40	12.4177	0.0210	12.7551	0.9998
60	18.2750	0.0173	18.6220	0.9999
80	22.6550	0.0212	22.9358	0.9999
100	28.3737	0.0091	28.9855	0.9998

The kinetic parameters for the adsorption of heavy metals are insignificant because the experimental data did not fit well with the pseudo-first-order model.

3.4 Adsorption Isotherms

The isotherm models studied were the Freundlich (Eq. 5) and Langmuir isotherm models (Eq. 6).

$$q_e = \frac{Q_m K_L C_e}{1 + K_L C_e} \tag{5}$$

$$q_e = \ln K_F + \frac{1}{n} \ln C_e \tag{6}$$

where:

C_e = concentration of solution at equilibrium;
q_e = adsorption of Cd^{2+} at equilibrium;
K_L = Langmuir model's constant; and
K_F = Freundlich affinity coefficient.

Both isotherm models assume different adsorption mechanics. The Freundlich isotherm model assumes the chemisorption of Cd^{2+} on the heterogeneous surface of magnetic biochar, while the Langmuir isotherm model describes the homogeneous surface of magnetic biochar by monolayer adsorption for Cd^{2+} removal. Figure 11(a,b) illustrate the Freundlich and Langmuir isotherm models for Cd^{2+} adsorption of this study, respectively.

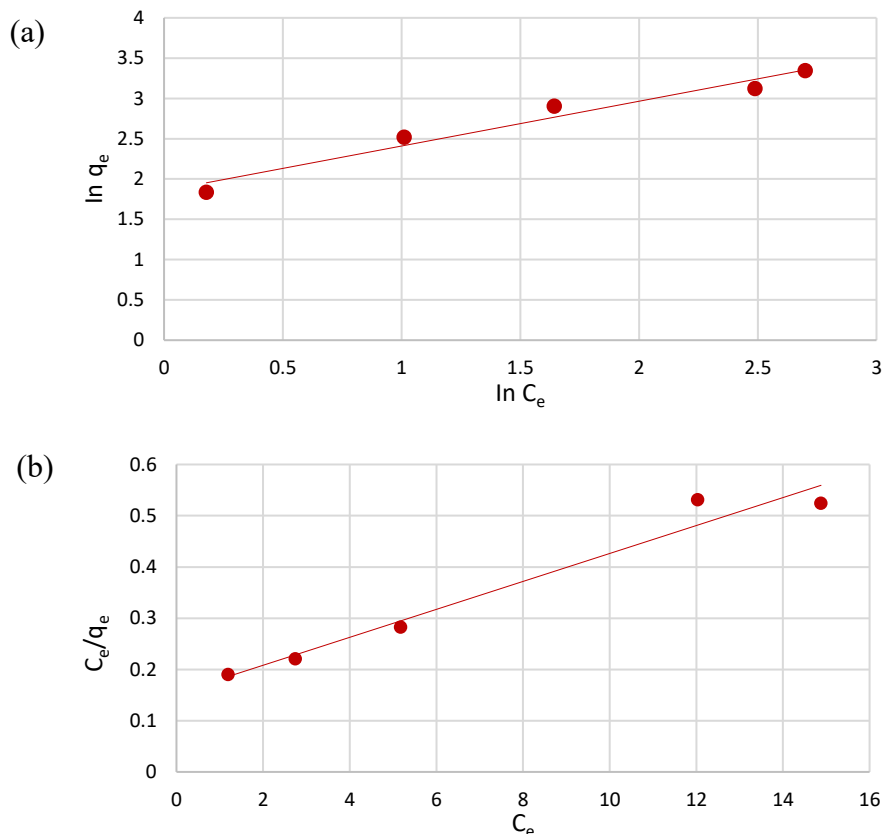Fig. 11: (a) Freundlich and (b) Langmuir isotherm models for Cd^{2+} adsorption.

Table 5 presents the isotherm constants and correlation coefficients of Cd^{2+} adsorption for the Freundlich and Langmuir isotherm models. The R^2 values of the Langmuir and Freundlich isotherm models for Cd^{2+} adsorption are excellent, explaining that the experimental data are best described by both isotherm models. Therefore, the adsorption

mechanism of this study agrees with both chemisorption and monolayer adsorption on the surface of magnetic biochar.

Table 5: Freundlich and Langmuir isotherm constants and correlation coefficients for Cd^{2+} adsorption

Freundlich	1/n	K_F	R^2
	0.5555	6.3859	0.9593
Langmuir	Q_{max}	K_L	R^2
	36.6300	0.1777	0.9647

4. CONCLUSION

High yield of magnetic biochar was synthesised from NiO-impregnated sugarcane bagasse via slow pyrolysis for heavy metal removal in aqueous solution. The optimum temperature and time to synthesise high-performance magnetic biochar were 500 °C at 10 min. High cadmium removal up to 88.47% was obtained using magnetic biochar. The batch adsorption study was conducted for Cd^{2+} removal in aqueous solution using magnetic biochar. The experimental data followed the pseudo-second-order model ($R^2 \approx 1$) and both Freundlich and Langmuir isotherm models achieved the best fitting of $R^2 \approx 1$.

For future work, a study on the synthesised NiO-impregnated magnetic biochar can be done on industrial wastewater instead of simulated aqueous solution to determine the removal efficiency of the process. Furthermore, a study considering various biomass sources can be conducted to determine the biomass with high yield of magnetic biochar and high heavy metal removal efficiency because Malaysia has abundant biomass resources, especially agricultural waste.

ACKNOWLEDGEMENT

REFERENCES

[1] Li T, Su X, Yu X, Song H, Zhu Y, Zhang Y. (2018) La (OH) 3-modified magnetic pineapple biochar as novel adsorbents for efficient phosphate removal. Bioresource Technology, 263: 207-213.

[2] Rai PK, Lee SS, Zhang M, Tsang YF, Kim KH. (2019) Heavy metals in food crops: Health risks, fate, mechanisms, and management. Environment International, 125: 365-385.

[3] Reguyal F, Sarmah AK, Gao W. (2017) Synthesis of magnetic biochar from pine sawdust via oxidative hydrolysis of $FeCl_2$ for the removal sulfamethoxazole from aqueous solution. Journal of Hazardous Materials, 321: 868-878.

[4] Hao Z, Wang C, Yan Z, Jiang H, Xu H. (2018) Magnetic particles modification of coconut shell-derived activated carbon and biochar for effective removal of phenol from water. Chemosphere, 211: 962-969.

[5] Wang S, Gao B, Li Y, Creamer AE, He F. (2017) Adsorptive removal of arsenate from aqueous solutions by biochar supported zero-valent iron nanocomposite: batch and continuous flow tests. Journal of Hazardous Materials, 322: 172-181.

[6] Wang B, Jiang YS, Li FY, Yang DY. (2017) Preparation of biochar by simultaneous carbonization, magnetization and activation for norfloxacin removal in water. Bioresource Technology, 233: 159-165.

[7]   Engwa GA, Ferdinand PU, Nwalo FN, Unachukwu MN. (2019) Mechanism and health effects of heavy metal toxicity in humans. Poisoning in the modern world-new tricks for an old dog, 10.

[8]   Ferlay J, Colombet M, Soerjomataram I, Mathers C, Parkin DM, Piñeros M., ... & Bray, F. (2019) Estimating the global cancer incidence and mortality in 2018: GLOBOCAN sources and methods. International Journal of Cancer, 144(8): 1941-1953.

[9]   Franken C, Koppen G, Lambrechts N, Govarts E, Bruckers L, Hond ED, Loots I, Nelen V, Sioen I, Nawrot TS, Baeyans W, Larebeke NV, Boonen F, Ooms D, Wevers M, Jacobs G, Covaci A, Schettgen T, Schoeters G. (2017) Environmental exposure to human carcinogens in teenagers and the association with DNA damage. Environmental Research, 152: 165-174.

[10] Kazeminezhad I, Mosivand S. (2017) Elimination of copper and nickel from wastewater by electrooxidation method. Journal of Magnetism and Magnetic Materials, 422: 84-92.

[11] Suto R, Ishimoto C, Chikyu M, Aihara Y, Matsumoto T, Uenishi H, Yasuda T, Fukumoto Y, Waki M. (2017) Anammox biofilm in activated sludge swine wastewater treatment plants. Chemosphere, 167: 300-307.

[12] Naeem M, Mujahid M, Umer A, Ahmad S, Ahmad G, Ali J, ... & Khalid I. (2019) New trends in removing toxic metals from drinking and wastewater by biomass materials and advanced membrane technologies. J. Bio. Env. Sci, 15(3): 10-17.

[13] Suto R, Ishimoto C, Chikyu M, Aihara Y, Matsumoto T, Uenishi H, Yasuda T, Fukumoto Y, Waki M. (2017) Anammox biofilm in activated sludge swine wastewater treatment plants. Chemosphere, 167: 300-307.

[14] Bani-Melhem K, Al-Shannag M, Alrousan D, Al-Kofahi S, Al-Qodah Z, Al-Kilani MR. (2017) Impact of soluble COD on grey water treatment by electrocoagulation technique. Desalination and Water Treatment, 89: 101-110.

[15] Hom-Diaz A, Jaén-Gil A, Bello-Laserna I, Rodríguez-Mozaz S, Vicent T, Barceló D, Blánquez P. (2017) Performance of a microalgal photobioreactor treating toilet wastewater: pharmaceutically active compound removal and biomass harvesting. Science of the Total Environment, 592: 1-11.

[16] Hülsen T, Barry EM, Lu Y, Puyol D, Keller J, Batstone DJ. (2016) Domestic wastewater treatment with purple phototrophic bacteria using a novel continuous photo anaerobic membrane bioreactor. Water Research, 100: 486-495.

[17] Domingues A, Rosa IC, da Costa JP, Rocha-Santos TA, Gonçalves FJ, Pereira R, Pereira JL. (2020) Potential of the bivalve *Corbicula fluminea* for the remediation of olive oil wastewaters. Journal of Cleaner Production, 252: 119773.

[18] Joseph L, Jun BM, Flora JR, Park CM, Yoon Y. (2019) Removal of heavy metals from water sources in the developing world using low-cost materials: A review. Chemosphere, 229: 142-159.

[19] Kamzon MA, Abderafi S, Bounahmidi T. (2016) Promising bioethanol processes for developing a biorefinery in the Moroccan sugar industry. International Journal of Hydrogen Energy, 41: 20880-20896.

[20] Barrera I, Amezcua-Allieri MA, Estupiñan L, Martínez T, Aburto J. (2016) Technical and economical evaluation of bioethanol production from lignocellulosic residues in Mexico: Case of sugarcan and blue agave bagasses. Chemical Engineering Research and Design. 107: 91-101.

[21] Zhang Y, Song X, Xu Y, Shen H, Kong X, Xu H. (2019) Utilization of wheat bran for producing activated carbon with high specific surface area via NaOH activation using industrial furnace. Journal of Cleaner Production, 210: 366-375.

[22] Deng CH, Gong JL, Zeng GM, Niu CG, Niu QY, Zhang W, Liu HY. (2014) Inactivation performance and mechanism of *Escherichia coli* in aqueous system exposed to iron oxide loaded graphene nanocomposites. Journal of Hazardous Materials, 276**:** 66-76

[23] Jiang W, Xing Y, Zhang L, Guo X, Lu Y, Yang M, ... & Wei G. (2021) Polyethylenimine-modified sugarcane bagasse cellulose as an effective adsorbent for removing Cu (II) from aqueous solution. Journal of Applied Polymer Science, 138(7): 49830.

[24] Reitz JR, Milford FJ, Christy RW. (2008) Foundations of Electromagnetic Theory, 4th edn. Addison-Wesley Publishing Company.

[25] Foo KY, Hameed BH. (2012) Mesoporous activated carbon from wood sawdust by K_2CO_3 activation using microwave heating. Bioresource Technology, 111: 425-432. doi:10.1016/j.biortech.2012.01.141

[26] Zhu T, Chen JS, Lou XW. (2012) Highly efficient removal of organic dyes from waste water using hierarchical NiO spheres with high surface area. The Journal of Physical Chemistry C, 116(12): 6873-6878. doi:10.1021/jp300224s

[27] Collard FX, Bensakhria A, Drobek M, Volle G, Blin J. (2015) Influence of impregnated iron and nickel on the pyrolysis of cellulose. Biomass and Bioenergy, 52-62.

[28] Chen B, Zhou D, Zhu L. (2008) Transitional adsorption and partition of nonpolar and polar aromatic contaminants by biochars of pine needles with different pyrolytic temperatures. Environ. Sci. Technol., 42: 5137-5143

APPLICATION OF HOUSE OF QUALITY IN THE CONCEPTUAL DESIGN OF BATIK WAX EXTRUDER AND PRINTER

NURUL ANISSA MOHD ASRI [1], ABDUL MALEK ABDUL HAMID[1], NORHASHIMAH SHAFFIAR[1], NOR AIMAN SUKINDAR[1], SHARIFAH IMIHEZRI SYED SHAHARUDDIN[1*] AND FARID SYAZWAN HASSAN[2]

[1]*Department of Manufacturing and Materials Engineering, Kulliyyah of Engineering, International Islamic University Malaysia, Jalan Gombak, 53100 Kuala Lumpur, Malaysia*
[2]*3D Gens Sdn Bhd, Bukit Jelutong, 40150 Shah Alam, Malaysia*

Corresponding author: shaimihezri@iium.edu.my

ABSTRACT: Malaysian batik production is dominated by two techniques known as hand-drawn batik, or batik tjanting, and stamp batik, or batik block. In comparison to batik block, the more popular batik tjanting takes a longer time to produce. A Standardized Nordic Questionnaire (SNQ) for musculoskeletal symptom examination involving batik artisans in Kelantan and Terengganu identified high rates of musculoskeletal disorders in respondents due to their working posture during the batik tjanting process. It was also observed that the number of workers and artisans willing to participate in the traditional batik industry is on the decline. These problems have led to a systematic Quality Functional Deployment approach to facilitate the decision-making process for the conceptual design of an automatic batik printer. In this study, house of quality (HOQ) was applied to identify the critical features for a batik printer based on the voice of the customer (VOC). A survey done to rate the importance of VOC using an 8-point Likert scale revealed that the batik practitioners topmost priority for the batik printer feature is the 'ability to adjust and maintain the temperature of wax' (17.54%) while the non-batik practitioners chose 'ability to deliver a variety of complex designs' (15.94%). The least required feature for the batik printer was related to the size of the batik printer. The mapping between customer requirements (VOC) and technical requirements identified that the extruder design (21.3%), the heating element (18%), and nozzle diameter (17.8%) were the most critical components for the batik printer. Several conceptual designs of the extrusion unit, cartesian-based batik printer, and 2D image conversion using open-sourced software were proposed at the end of this work.

ABSTRAK: Pengeluaran batik Malaysia telah didominasi oleh dua teknik yang dikenali sebagai batik lukisan-tangan (batik canting) dan batik cap (batik blok). Sebagai perbandingan, batik canting yang popular mengambil masa lebih lama bagi dihasilkan. Soal Selidik Nordic Standad (SNQ) bagi meneliti gejala muskuloskeletal melibatkan tukang batik di Kelantan dan Terengganu telah menunjukkan persamaan kadar muskuloskeletal yang tinggi pada postur badan semasa bekerja canting batik. Bilangan pekerja yang terlibat dalam industri tradisional batik ini turut terjejas. Masalah-masalah ini telah mengarah kepada kaedah Pengerahan Fungsi Kualiti bagi membantu proses membuat keputusan dalam rekaan konsep pencetak batik automatik. Kajian ini telah mengadaptasi Kualiti Rumah (HOQ) bagi mengesan ciri-ciri kritikal pada pencetak batik berdasarkan suara pelanggan (VOC). Kaji selidik telah dilakukan bagi menilai kepentingan VOC menggunakan skala Likert 8-poin. Didapati keutamaan yang diperlukan

oleh 17.54% ahli batik adalah; ciri pencetak batik ini perlu mempunyai 'keupayaan dalam menyelaras dan menetapkan suhu lilin', manakala sebanyak 15.94% bukan ahli batik memilih 'keupayaan pencetak ini harus berjaya menghasilkan pelbagai rekaan yang kompleks'. Ciri yang kurang diberi tumpuan adalah berkaitan saiz pencetak batik. Persamaan antara kehendak pelanggan (VOC) dan kehendak teknikal dalam mengenal pasti komponen-komponen penting bagi pencetak batik adalah rekaan penyemperit (21.3%), elemen pemanas (18%), dan diameter nozel (17.8%). Pelbagai rekaan konsep bagi unit penyemperit, pencetak batik canting, dan imej konversi 2D menggunakan perisian sumber terbuka telah dicadangkan di bahagian akhir kajian ini.

1. INTRODUCTION

The establishment of the Rural and Industrial Development Authority (RIDA) in 1951 marked the Malaysian government's formal initiative to develop the handicraft industry as part of rebuilding the rural community's economy and society. In the Fourth Malaysia Plan (1981-1984), handicraft activity was given due recognition as an 'industry sector' that required revitalization to aid in the eradication of rural poverty. The initiated rural urbanization strategy was extended in the 'Halacara Baru' (New Direction) program in 1984, which led to significant progress in the handicraft industry [1]. This scenario granted an opportunity for the batik industry to reap the benefits from the larger economic movement and became a major contributor to the overall sales of the handicraft industry [2]. The production of batik in Malaysia is dominated by two techniques: hand-drawn batik, also known as batik tjanting, and stamp batik, or batik block. In comparison to batik block, batik tjanting allows for greater freedom in design, has a longer production time, and is sold at a higher price.

Tjanting is a tool designed with a small container head made from copper with a spouted end that is attached to a wooden handle, as shown in Fig. 1. The copper head acts as a reservoir that supplies molten wax to a copper spout. The main problem in using tjanting in the waxing process arises from the lack of thermal control of the molten wax which then affects the quality of the wax lines drawn on the fabric [3]. The initial wax lines drawn on the fabric tend to be thick and as the wax in the copper container gradually cools down, the wax's increase in melt viscosity causes the rendered wax line to become thinner, unsmooth, and penetrates less into the fabric.

Fig. 1: The batik artisan holds the tjanting tool at an angle whilst rendering
the batik wax on the fabric [4].

A body map adapted from a Standardized Nordic Questionnaire (SNQ) for musculoskeletal symptom examination was used to evaluate work-related musculoskeletal symptoms amongst batik tjanting workers in Kelantan and Terengganu [5,6]. Musa et. al [5] observed that postural movement of the batik workers includes standing for more than four hours, continuous hand/wrist movements as well as bending/stooping. While Yusof et al. [6] noted that the majority of the batik workers did not get enough rest during the tjanting phase. These working postures and long-standing hours have led to work-related musculoskeletal disorder (MSD) symptoms amongst batik workers. A study on batik workers in Kelantan revealed the feeling of discomfort occurred mostly at the shoulders (41.0%), lower back (34.4%), and ankles or feet (34.4%) whilst Terengganu batik workers revealed that discomfort was frequently felt at the shoulders (64.5%), sole (61.3%), upper back (51.6%), hand (51.6%), legs (51.6%), knee (48.4%) and wrist (45.2%).

Several automatic batik printing systems such as the Integrated Computer-Aided Tjanting system (ICATS)[7] and the batik Kelowong Machine [8] have been developed. An automated Batik Colouring System [9] had also been built to achieve a similar coloring effect and aesthetic as hand-coloring. However, the application of these automated batik systems has been lacking in the local batik communities. According to Affanti and Hidayat [10], the acceptance of any new form of batik tool is influenced by the batik craftsmen's requirements such as comfort and efficiency. Hence, it is necessary to systematically identify end-user requirements and market segments to increase new batik tools' performance and values. A literature search revealed that the end-user requirements for batik printers have never been systematically investigated qualitatively and quantitatively for the Malaysian market. Table 1 summarizes the possible attributes for a batik printer model based on numerous studies which include printing speed, printing quality, operation, temperature, and cost.

Table 1: Attributes of a batik printer

	Batik printer features	References
Printing speed	Ability to produce batik at a high production rate.	[11]
Printing quality	Consistency in wax line thickness and quality	[3]
	Consistency in drawing repeated and complex design	[3,11,12]
Operation	Minimum fabrication skill	[11,13]
	Ease of use	[8, 12]
Temperature	Ability to adjust the temperature of the wax	[12]
Cost	Low cost	[12,14]

Commonly used tools to obtain inputs from end-users or stakeholders in the design process include Pugh method (PM), decision matrix (DM), quality function deployment (QFD), and analytical hierarchy process (AHP)[15]. QFD was developed more than 25 years ago in Japan and is used in product planning, design deployment, process planning, and production planning of newly designed products. QFD can be used to transform customer requirements into technical design parameters, to compare the product's strengths and weaknesses with available competitors' products, to improve product performance, and to offer shorter product development time at an effective cost [17,18]. One of the vital components in QFD is the house of quality (HOQ), a cross-functional tool that embeds consumer preferences in the new product design specification [18]. Both PM and DM

approaches identify the relative ranking among design alternatives based on weighted attributes [21,22]. In comparison to PM and DM, the HOQ approach enables proper identification and relative ranking of the product's technical requirements that need to be urgently improved, hence, the product can be developed in a targeted or focused manner to achieve customer satisfaction [21]. The method also does not require a very large number of comparisons to make a decision, as seen in AHP [22]. QFD and HOQ have been deployed to design and improve various batik-related products such as batik coloring machines [23], batik designs [24], batik merchandise [27,28], and natural batik dies [27].

This study intends to identify the critical features of a batik printer according to the customer or end-user requirements, employs HOQ to aid in the decision-making process, and proposes a conceptual design for a customer-based batik printer. The outcome of this study can be used to increase the market value of the batik printer and promotes the growth of the batik industry.

2. METHODOLOGY

The overall process flow used to derive the conceptual design is shown in Fig. 2. The process flow starts with determining the market survey and ends with the conceptual design of the most critical component based on engineering specifications.
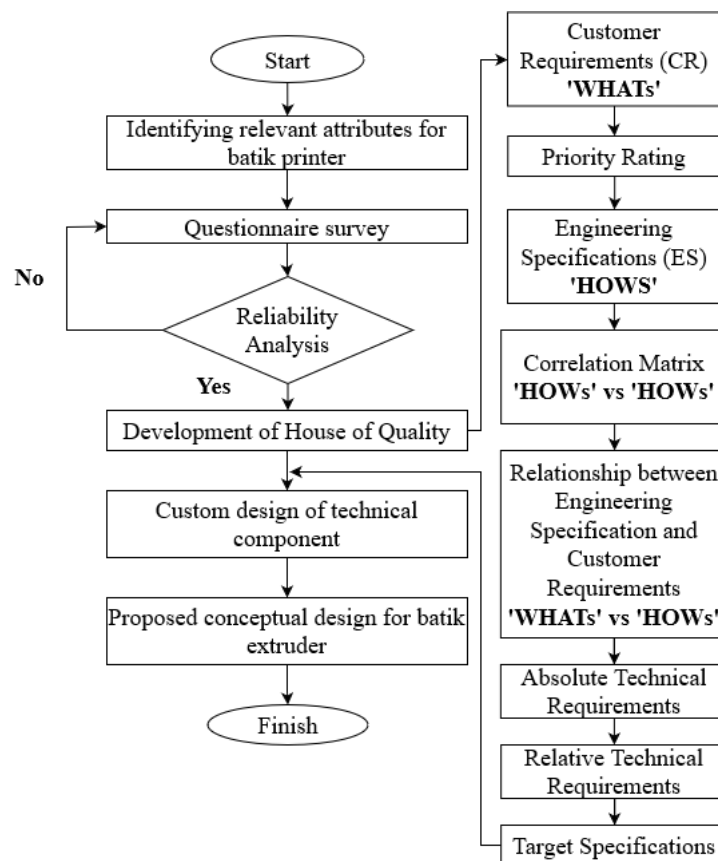

Fig. 2: Overall process flow used to develop the conceptual design of batik printer.

2.1 Questionnaire Survey

A quantitative method via questionnaire was designed based on batik printer features including printing speed, ability to adjust and maintain the temperature of the wax, ease of operation, ability to maintain consistency of wax line thickness and quality, ability to deliver

a variety of complex design, cost of equipment, size of equipment and maintenance (refer to Table 2). The survey aims to identify the rating of importance of these printer features on a Likert scale of 1-8. Questionnaires were administered via Google form as well as manual handout. The sample population for the survey was determined based on Eq. (1) due to the unknown number of customers.

$$n = \frac{P(1-P)Z^2}{d^2} \qquad (1)$$

where n = size of sample

P = standard deviation/ expected proportion at 30% = 0.3

Z = normal random variables = (1.645)

d = margin of error in estimating P [28] = (0.05)

Equation 1 proposes that at 90% of the confidence interval [29] the total number of participants in the survey should be at least 227. In this study, the survey received was compiled based on a total of 241 respondents and the demographic of the respondents is shown in Table 3.

Table 2: Questionnaire developed based on the required attributes of a batik printer

Note: Kindly rank in terms of importance for each printer feature according to 1 (least preferred) to 8 (highly preferred).										
Table 1 attributes	Questionnaire attributes	Scale								
		1	2	3	4	5	6	7	8	
Printing speed	Printing speed									
Temperature	Ability to adjust and maintain the temperature of the wax									
Operation	Ease of operation									
Printing quality	Ability to maintain consistency of wax line thickness and quality									
	Ability to deliver a variety of complex design									
Cost	Cost of equipment									
Operation	Size of equipment									
	Maintenance									

Table 3: Demographics of the survey population

Profession	Frequency
Batik Practitioner	64
Non-batik Practitioner	177

Batik practitioner		Non-batik practitioner	
Gender	Frequency	Gender	Frequency
Female	52	Female	130
Male	12	Male	47

Age (years)	Frequency	Age (years)	Frequency
20 – 30	44	20 – 30	118
31 – 40	13	31 – 40	24
41 – 50	5	41 – 50	32
51 – 60	2	51 – 60	3

2.2 Reliability Analysis

Cronbach alpha is an important concept for the evaluation of assessment and questionnaires [30]. The reliability of the measurements was assessed by computing Cronbach's alpha by using IBM SPSS Statistics 26.0 to analyze the statistics.

2.3 House of Quality

The design structure for HOQ is very flexible and contains the same basic building components shown in Fig. 3 below. In this study, the features for the HOQ are depicted in Fig. 4 and involve input from a focus group with relevant experience in the development of a 3D printer from the university and industry. The description of each process for each room to design the batik printer features is explained below.
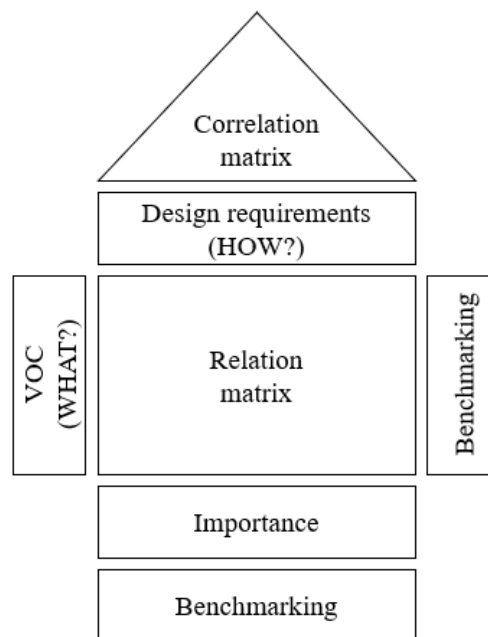

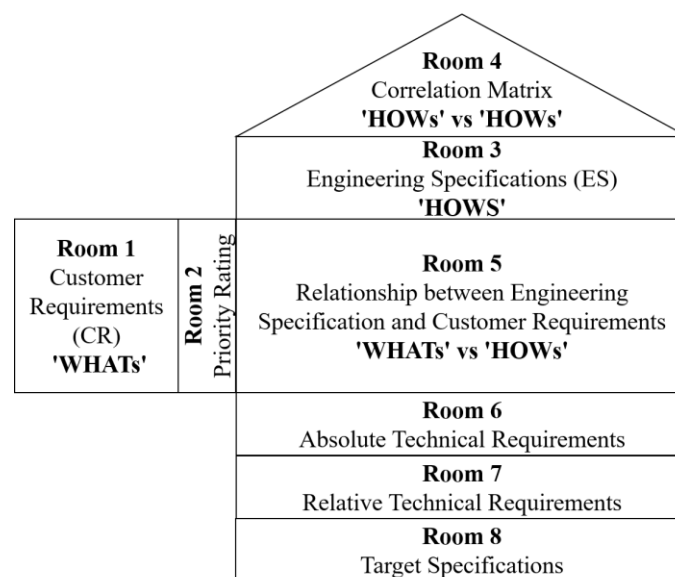Fig. 3: Basic building structure for HOQ [31].

Fig. 4: Adapted HOQ matrix for the conceptual design of the batik printer.

a. **Room 1:** Customer requirements (CR).

The characteristics of product features and functions are not necessarily the same for the designers as for the customers. The customer requirements ('WHATs') represent the voice of customers (VOC) for the batik printer features and were determined based on bibliographic and literature searches [32]. These features are summarized in Table 2 and are used to develop the questionnaire for the market survey.

b. **Room 2:** Customer requirement priority rating.

The priority rating for customer requirements can be deliberated via the team's direct experience with the customer or determined based on a survey [33]. In this study, each CR is prioritized by assigning a numeric value called the degree of importance on a scale of 1-8 based on a market survey.

c. **Room 3:** Engineering specifications (ES).

Engineering specification (How's) represents the product requirements in measurable technical terms. In this study, ES is the result of brainstorming sessions with a focus group consisting of industry experts in 3D printing, 3D Gens SDN BHD, and the additive manufacturing unit at the International Islamic University Malaysia (IIUM).

d. **Room 4:** Correlation matrix.

The matrix of correlation illustrates the relationship between the features of engineering ('How vs. How'). The intensity of the correlation is provided by symbols that imply positive or negative interaction while other features remain unchanged. The double-positive symbol (++) implies a strong positive correlation, (+) a positive correlation, (--) a strong negative correlation, and (-) a negative correlation. This allows a better understanding of the relationship of various ES and negates any contradictions and unnecessary increases in cost. The correlation was evaluated by the researcher and experts [34] from the addictive manufacturing focus group at IIUM.

e. **Room 5:** Relationship between customer requirements (CR) and engineering specifications (ES).

The main relationship between customer requirements and engineering specifications ('What vs How') was determined as shown in the product architecture in Fig. 5. The relationship matrix was then developed to include a list of how the engineering specifications serve the needs of each customer using a commonly employed 1-3-9 scale [35]. Rating scale 1 is a minor or potential relationship, 3 is a moderate relationship, and 9 is a solid relationship. The evaluation was assisted by the researcher and experts [38, 36] from the additive manufacturing focus group at IIUM and 2D printer from the industry as it requires technical insight and understanding of the relationship between CR and ES.

f. **Room 6:** Absolute technical requirements

The importance of the significance level of the absolute technical requirement (SL_ABS) reflects the engineering specifications required to satisfy the customer's requirements and can be determined using Eq. 2 [29].

$$SL\_ABS = \sum (\text{value of relationship between customer requirements and engineering specifications x important ranking value}) \quad (2)$$

g. **Room 7:** Relative technical requirements

The value of the significance level of the relative technical requirements (SL_REL) can be evaluated as follows in Eq. 3 [29].

$$SL\_REL = \frac{(\text{significance level of absolute technical requirements}) \times 100}{\sum (\text{total of the significance level of absolute technical requirement}} \quad (3)$$

The absolute and relative technical requirements are used to rank the engineering specification (ES). The priority list of ES enables the designer/manufacturer to optimize the product design.

h. **Room 8:** Target specification

Target specification represents objectives for product design or improvement. They summarize the basic data that reflect the customer requirements and can be used to identify strategic design opportunities.

2.4 Conceptual Design for the Batik Extruder and Printer

The main component for the conceptual design of the batik printer was prioritized based on the ranking obtained in ES and CR. A systematic exploration was adopted using a combination table that integrates the relative technical attributes and the printing features based on the result of the HOQ. Autodesk Fusion 360 is used to generate the conceptual designs of the extruder and the overall framework of the batik printer.

3. RESULTS AND DISCUSSION

3.1 Questionnaire Survey

Cronbach's analysis provides a measure of the internal consistency of a test or scale, expressed as a number between 0 to 1. The acceptable values of alpha range from 0.70 to 0.90. The result for alpha in this study is 0.948, therefore the reliability analysis on a questionnaire survey of 241 respondents is confirmed.

The batik printer features used in the survey correlate to the customer requirements (CR) or the voice of customers (VOC) in the HOQ matrix. The respondent demographics can be divided into two types. In this study, batik practitioners are clarified as respondents who have theoretical and practical knowledge of batik production and are directly involved in the batik making lifecycle either in the design, production, and distribution of batik fabrics. In contrast, non-batik practitioners refer to respondents that do not have theoretical knowledge of batik production, lack experiential and practical knowledge, and are not directly involved in the batik production life cycle. The survey data presented in Fig. 6(a) and Fig. 6(b) demonstrates that the distribution of preferences for printer features differs in ranking between the batik practitioners and non-batik practitioners. It was found that 17.54% of the batik practitioners agreed that the most important feature for the batik printer is the ability to 'adjust and maintain the temperature of the wax' whilst 15.94% of the non-batik practitioners prioritized the 'ability to deliver a variety of complex designs' attribute.

Both groups deliberated that the 'size of the equipment' attribute is of the least importance. The distribution of percentage for each feature for the batik printer was translated into the priority rating in Table 4. It is proposed that the high priority rating of the batik practitioners for a batik printer that can adjust and maintain its wax temperature is attributed to the experiential or practical exposure to wax rendering activity using tjanting. The traditional tjanting is not equipped with isothermal control of the wax melt which leads to inconsistent quality and variation in wax line thickness rendered on the fabric. Previously, the traditional tjanting tool was innovated by incorporating an electrical heating system [10,39]. However, the improved version did not take off amongst batik artisans due to ergonomic issues and insufficient exposure to the tool's operation and performance [10].
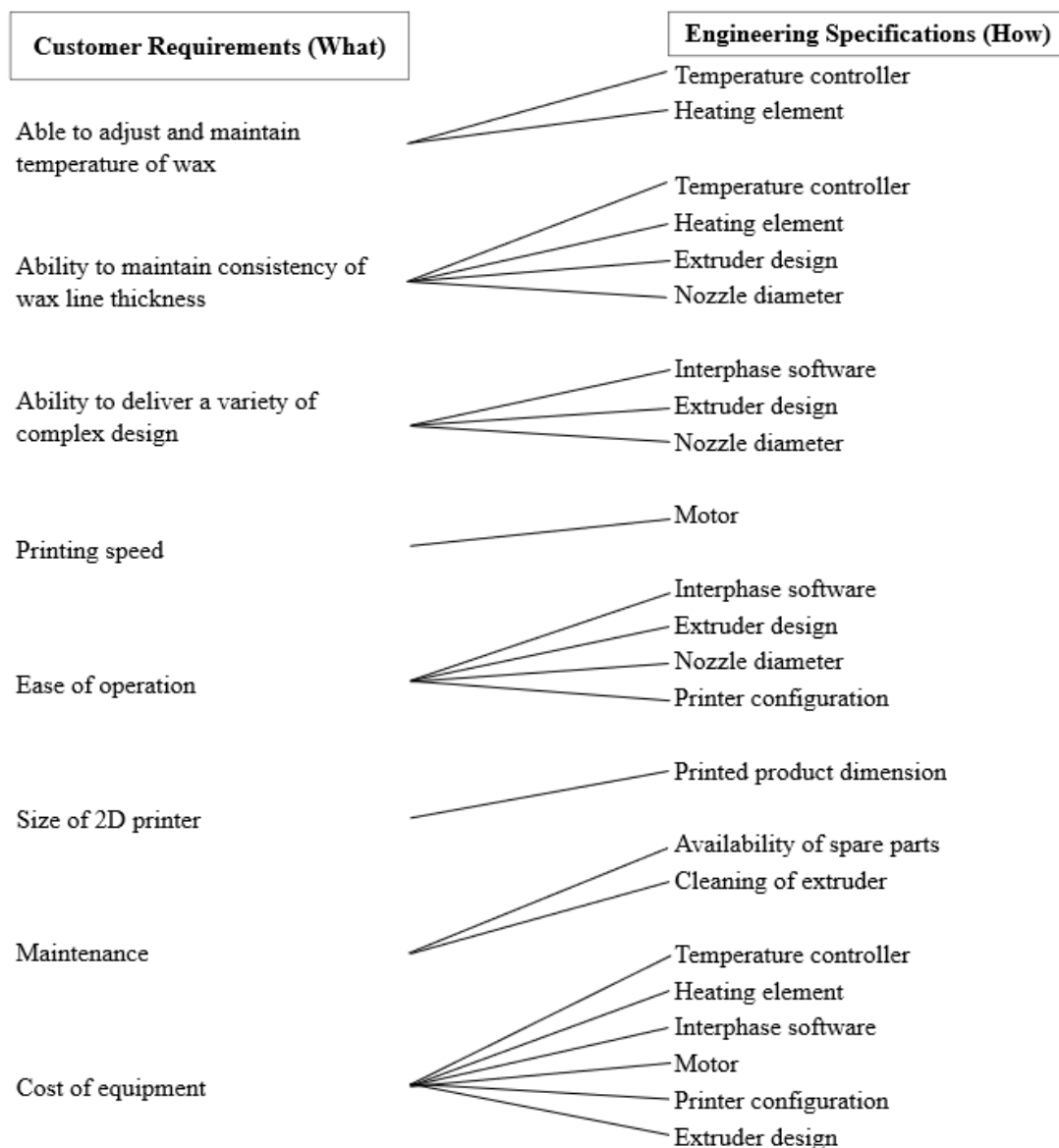

Fig. 5: Main correlation between engineering specification (How) and customer requirements (What) for the batik printer.
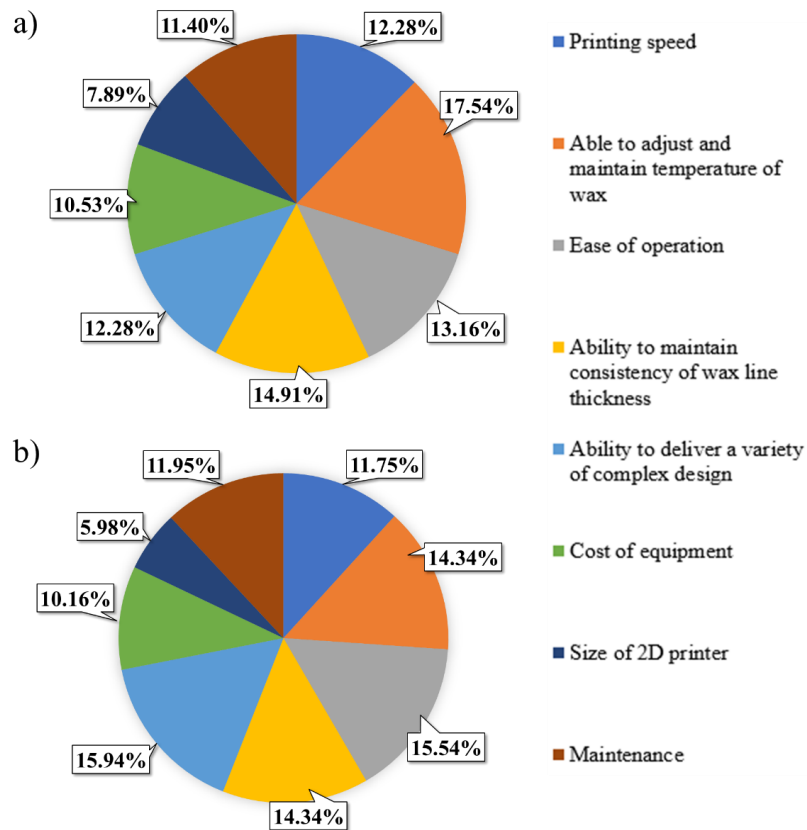
Fig. 6: The distribution of preferences for the batik printer attributes for
(a) batik practitioners and (b) non-batik practitioners.

The non-batik practitioner's high preference for a batik printer that is capable to deliver a variety of complex designs is consistent with the local's aesthetic appreciation towards batik products. Poon's [38] study on determinant factors for the demand in batik products identified that design is the most crucial element followed by quality and price. The apparent differences in the ranking of priorities prove that human perception in prioritizing product attributes can be vague [39] due to personal taste and usage [40].

Table 4: The batik practitioners and non-batik practitioner's priority ratings of
batik printer features based on survey.

	Scale	Batik practitioner	Non-batik practitioner
High	8	Able to adjust and maintain the temperature of the wax	Ability to deliver a variety of complex design
	7	Ability to maintain consistency of wax line thickness	Ease of operation
	6	Ease of operation	Able to adjust and maintain the temperature of the wax
	5	Ability to deliver a variety of complex design	Ability to maintain consistency of wax line thickness
	4	Printing speed	Maintenance
	3	Maintenance	Printing speed
	2	Cost of equipment	Cost of equipment
Low	1	Size of 2D printer	Size of 2D printer

Priority rating (left axis label)

Table 5: Overall priority ratings for the batik printer feature with percentage based on survey

	Scale	Features	
High	8	Ease of operation	(15.3%)
	7	Ability to deliver a variety of complex design	(15.1%)
	6	Able to adjust and maintain the temperature of wax	(14.9%)
	5	Ability to maintain consistency of wax line thickness	(14.5%)
	4	Printing speed	(11.9%)
	3	Maintenance	(11.9%)
	2	Cost of equipment	(10.2%)
Low	1	Size of the 2D printer	(6.3%)

Scale 8, 7, 6 grouped as — Extruder unit. Priority rating: High ↑ Low.

The main target market for the batik printer is for both batik and non-batik practitioners such as entrepreneurs, hobbyists, and art faculties in higher academic institutions. Considering the inputs from the non-batik practitioner is essential to avoid myopic product design since the batik practitioners are only represented by a small group of experts [40]. Therefore, despite the differences in preferences, it is necessary to consider a consensus or overall performance rating, as shown in Table 5 to ensure that the new product is attractive and satisfactorily captures the voice of customers in the market segment [40]. The overall results show that both `ease of operation 'and `ability to deliver a variety of complex design' share similar percentages at 15.3% and 15.1%, respectively. The least favorable attribute is the size of the 2D printer at 6.3%. The priority ratings obtained for the batik printer feature are then integrated into the HOQ matrix.

3.2 House of Quality

The number of sections or rooms applied in the HOQ varies from as simple as 4 sections to a more complex matrix with more than 8 sections [41]. Fig. 7 represents the HOQ used in the decision-making process for the development of conceptual designs for the batik printer. In this study, benchmarking and competitive assessment was not conducted for the batik printer. Benchmarking and competitive assessments are commonly deduced from a formal market survey and present the customer's comparative assessment of the new product with those available in the market [42]. Vairaktarakis [43] highlighted that it is crucial that customers can and should only assess products that they use and are accustomed to. However, as batik printers are highly customized products and are not commonly used, competitive assessment based on customer feedback was not performed to avoid faulty judgment. Several HOQ studies have also been performed without benchmarking and competitive assessments [45,46].

The customer's requirements (CR) for a batik printer include printing speed, the ability to adjust and maintain wax temperature, ease of operation, ability to maintain consistency of wax line thickness and quality, ability to deliver a variety of complex designs, equipment costs, 2D printer size, and maintenance (Room 1). The priority ratings in Room 2 were determined by the overall survey results. Based on the survey result, the top three (3) priorities for the batik printer features are ease of operation, ability to deliver complex design, and ability to maintain and control the wax temperature. The engineering specifications (ES) in Room 3 include a temperature controller, heating element, extruder design, interface software, nozzle diameter, motor, printer configuration, printed product dimension, spare parts availability, and cleaning tools. The correlation matrix, i.e., the roof of the house of quality (Room 4), is formed to define the interrelationship between each of the engineering specifications. All the highly rated customer requirements show a strong relationship with the design of extruders on engineering specifications. The relationship

between engineering specifications and customer requirements in Room 5 reveals that there are two primary engineering specifications: the heating element and the extruder, which are highly linked to various customer requirements.
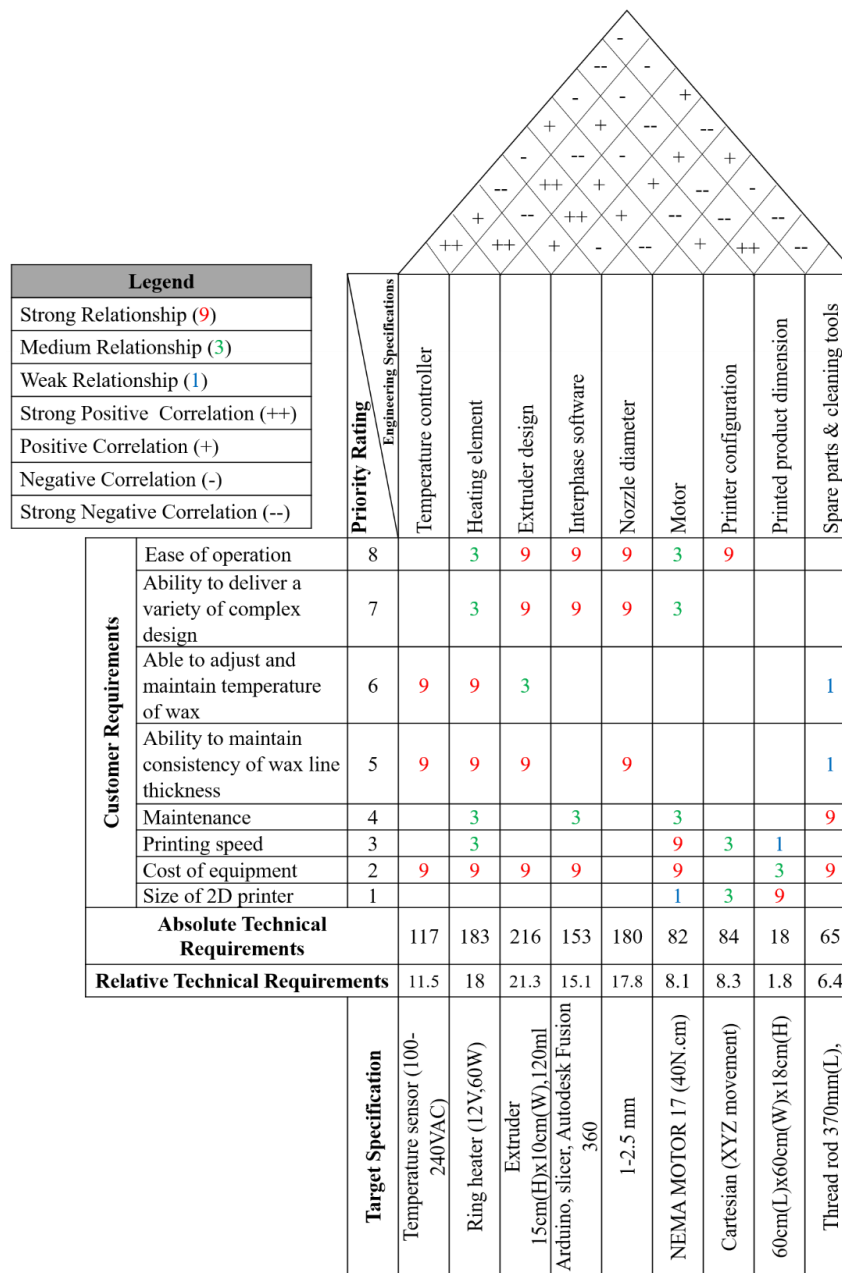
Legend

Strong Relationship (9)	
Medium Relationship (3)	
Weak Relationship (1)	
Strong Positive Correlation (++)	
Positive Correlation (+)	
Negative Correlation (-)	
Strong Negative Correlation (--)	

Customer Requirements	Priority Rating	Temperature controller	Heating element	Extruder design	Interphase software	Nozzle diameter	Motor	Printer configuration	Printed product dimension	Spare parts & cleaning tools
Ease of operation	8		3	9	9	9	3	9		
Ability to deliver a variety of complex design	7		3	9	9	9	3			
Able to adjust and maintain temperature of wax	6	9	9	3						1
Ability to maintain consistency of wax line thickness	5	9	9	9		9				1
Maintenance	4		3		3		3			9
Printing speed	3		3				9	3	1	
Cost of equipment	2	9	9	9	9		9		3	9
Size of 2D printer	1						1	3	9	
Absolute Technical Requirements		117	183	216	153	180	82	84	18	65
Relative Technical Requirements		11.5	18	21.3	15.1	17.8	8.1	8.3	1.8	6.4
Target Specification		Temperature sensor (100-240VAC)	Ring heater (12V,60W)	Extruder 15cm(H)x10cm(W),120ml	Arduino, slicer, Autodesk Fusion 360	1-2.5 mm	NEMA MOTOR 17 (40N.cm)	Cartesian (XYZ movement)	60cm(L)x60cm(W)x18cm(H)	Thread rod 370mm(L),

Fig. 7: The HOQ matrix for the batik printer.

Determining the ratings for the HOQ structure is crucial as it aids in developing a product that is marketable and attracts customers [46]. Evaluation on absolute technical requirements in Room 6 indicates that the extruder design (216), the heating element (183), nozzle diameter (180) are the top three (3) engineering elements. The corresponding relative technical requirements in Room 7 are presented in Fig. 8. Based on these absolute and relative assessments in Fig. 8, it is evidenced that the extruder body, heating element, and nozzle diameter which form the extrusion unit are the most critical engineering components for the batik printer.
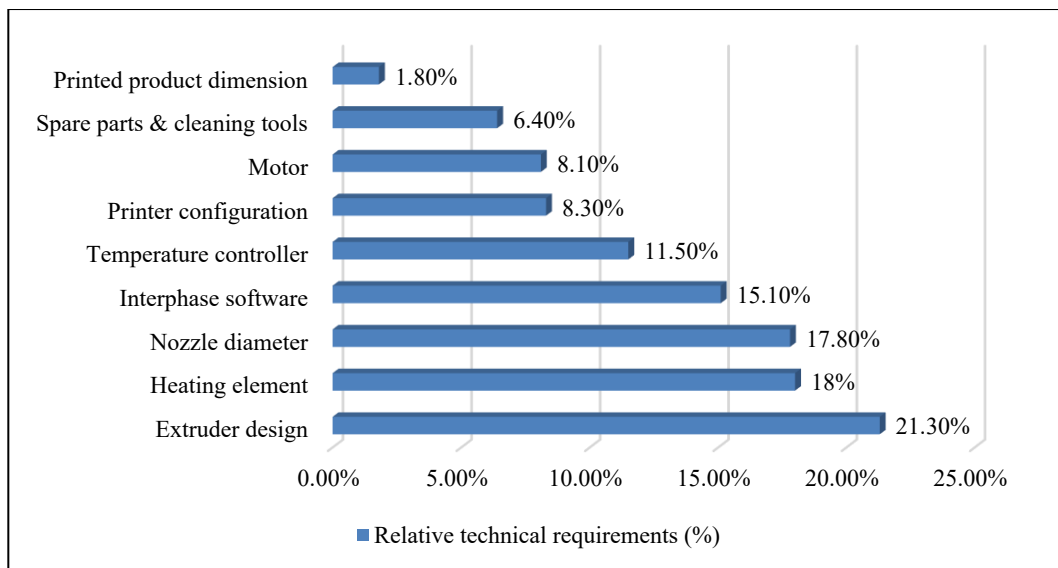
Fig. 8: Relative technical requirements (%) based on engineering specifications for the batik printer.

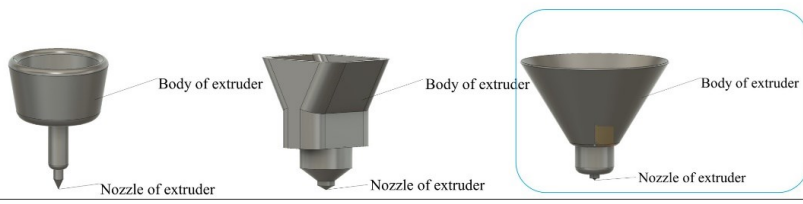## 3.3 Conceptual Design of the Batik Extruder and Printer Based on HOQ

Conceptual design is a key activity in the product development process and significantly affects the accuracy, cost, manufacturability, and life cycle features of the product [47]. In this work, the conceptual design of the extrusion unit (extruder body, heating element, and nozzle diameter) is prioritized and mapped against relevant customer requirements such as ease of operation, adjustment and maintaining of wax temperature, consistency of wax line thickness, and delivery of complex designs (specified in Table 5). A combination table with possible solutions that meet both engineering specifications (i.e., extrusion system) and customer requirements are presented in Table 6. Possible designs of the extruder body were identified, and concept C was selected to ease cleaning operation and was further developed into the final concept as shown in Fig. 9. A ceramic ring heater with a feedback thermocouple (12 V, 60 Watt) was selected, as the size is compatible with the extruder body and can control the required range of melting temperature for the batik wax (70 °C – 100 °C). This will ensure the consistency and quality of the wax line rendered on the fabric. The extruder's nozzle diameter was determined by taking into consideration of available tjanting design. The traditional tjanting tool can be categorized into three types based on its function, diameter, and the number of nozzles. Complex designs can be delivered using a modular approach in which the extruder body is interchangeable with the extruder head. Hence the extruder head was designed with (i) a medium-size nozzle diameter of 1 mm and 2.5 mm adapted from tjanting *rengrengan* design and (ii) single and multiple nozzles.

The priority ratings in HOQ highlighted that 'ease of operation' is one of the topmost desirable features for the batik printer. Besides extruder design and nozzle diameter, 'ease of operation' also has a strong relationship with printer configuration and software interface. The structural framework for the batik printer in this study is based on 3D printer configurations. The three common types of configurations for the 3D printer are cartesian, delta, and polar. In this study, a cartesian-based system is adopted as it allows for the left to right movement (X-axis motion), front to back movement (Y-axis motion), and up and down movement (Z-axis motion). A batik printer having a cartesian configuration provides 'ease of operation' as it is easier to maintain and calibrate. The design is also supported by various hardware resources and can be integrated with various open-sourced software for printing

path configuration. The three possible conceptual designs for the batik printer are presented in Fig. 10.

Table 6: Combination table based on engineering specifications and customer requirements for the extrusion unit

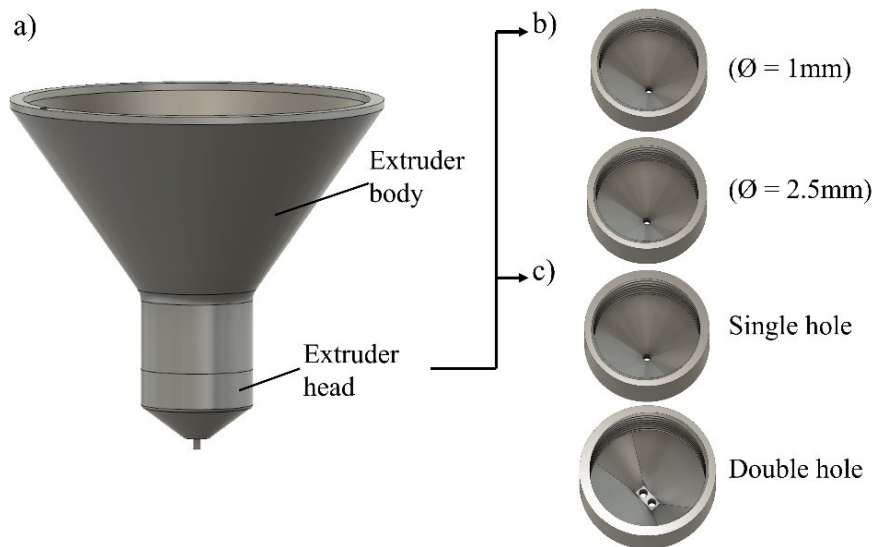| Customer Requirements (CR)	Engineering Specifications (ES)		
Ease of operation	Body of extruder / Nozzle of extruder	Body of extruder / Nozzle of extruder	Body of extruder / Nozzle of extruder
Ability to deliver a variety of complex design	**Fixed** (Ø = 1mm)	**Modular** Interchangeable nozzle. Diameter = 1 mm, 2.5mm	**Modular** Interchangeable nozzle. Single hole / Double hole
Able to adjust and maintain temperature of wax	Ring heater with TEC feedback controller (12V, 60W)	Peltier with TEC feedback controller (12V, 60W)	
Ability to maintain consistency of wax line thickness and quality	Ring heater with TEC feedback controller (12V, 60W)	Peltier with TEC feedback controller (12V, 60W)	

Fig. 9: Modular extruder unit design consisting of (a) extruder body and extruder head assembly, (b) extruder head with different nozzle diameter, (c) extruder head with different nozzle opening.
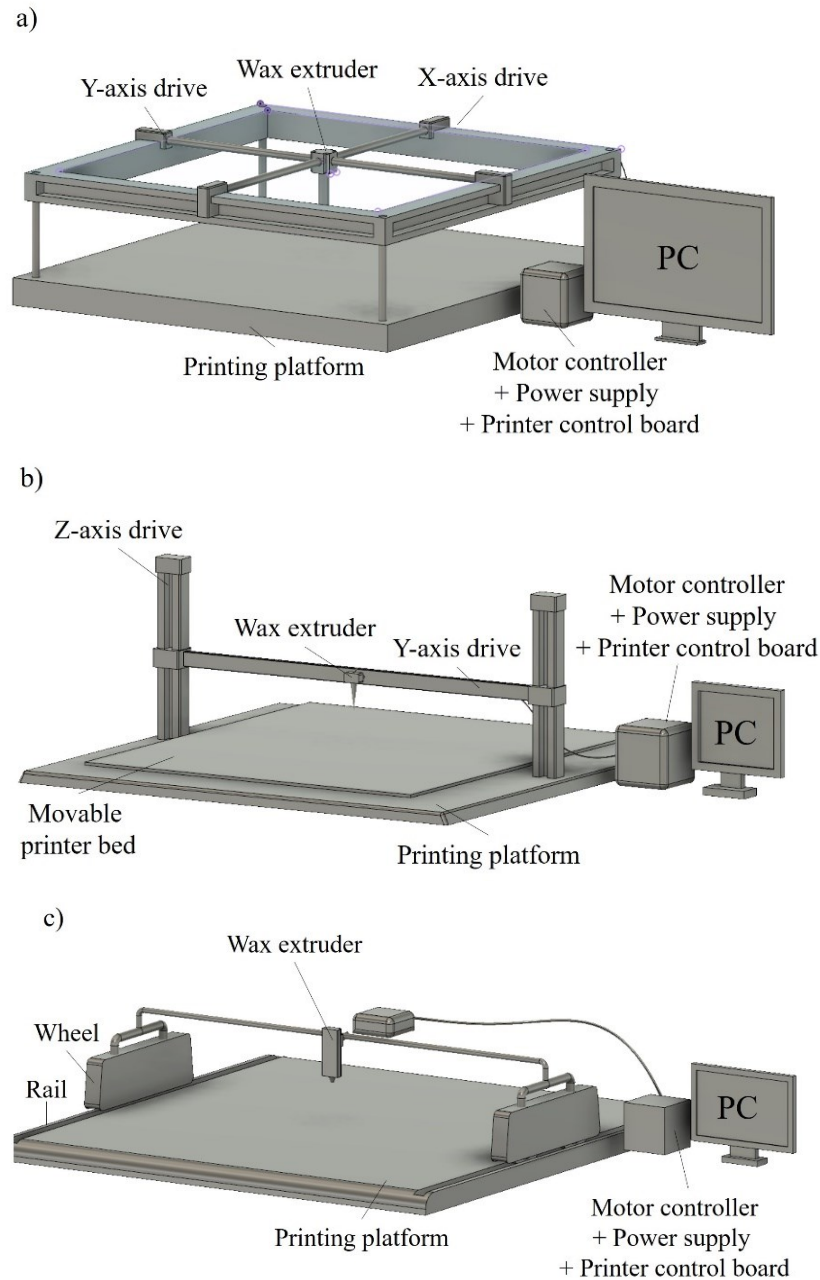
a)

b)

c)

Fig. 10: Cartesian-based conceptual designs (a-c) for the batik printer.

The expiration of various 3D printer patents has partly contributed to the development of an increasing number of open-sourced interface software. The process flow and examples of image generation based on open-sourced software for the batik printer are proposed in Fig. 11. There are 3 main components for any 2D images to be converted into printed images, i.e., image converter, slicer software, and printer interface. Firstly, the format of any 2D images (.jpg, .gif, etc.) based on drawings or illustrations need to be converted into STL format using image converter software (3D Builder, selva3d.com, Ultimaker Cura, imagetostl.com, etc). The STL software is then assessed by the slicer software (Ultimaker Cura, Ideamaker, etc) to create the sequence of G-codes in a program that integrates movement, wax extrusion rate, wax melt temperature, and sensor data. The G-code program is then uploaded into the batik printer and executed using printer interface such as Pronterface.
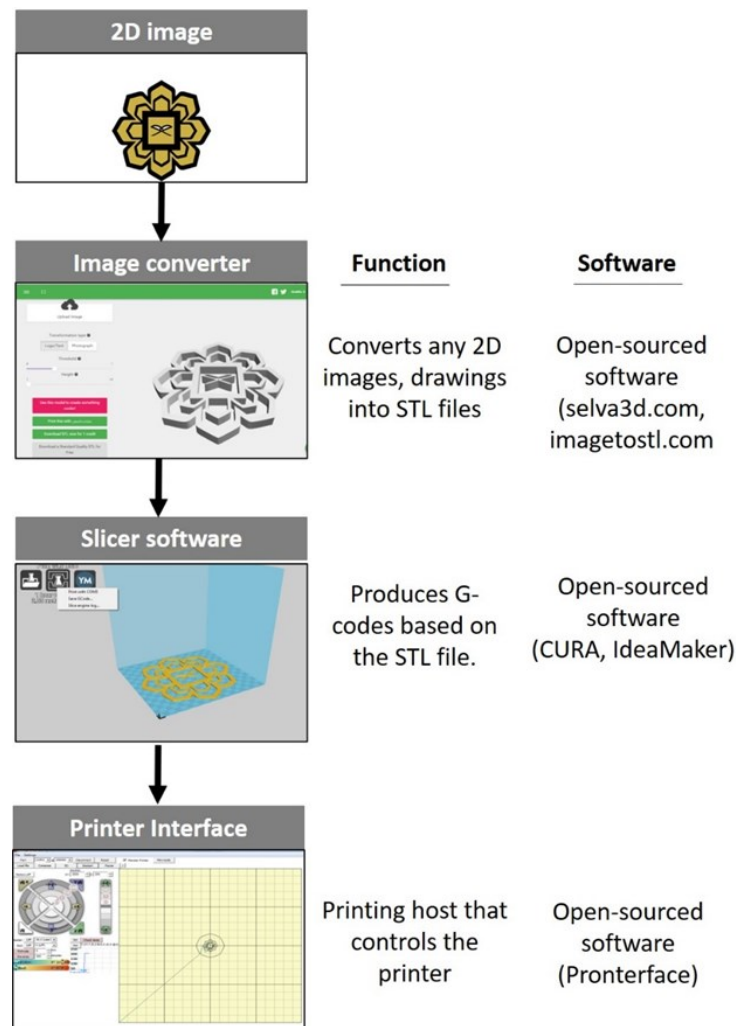
Fig. 11: Process flow for 2D image conversion using open-sourced software for the batik printer.

4. CONCLUSION

The house of quality is a vital component that forms the quality functional deployment. The voice of customer (VOC) or customer requirements were translated from survey questionnaires. Results showed that the topmost priority feature for the batik practitioners is 'ability to adjust and maintain the temperature of the wax' whilst the non-batik practitioners responded with 'ability to deliver a variety of complex designs'. The overall voice of customers was considered to ensure that the new product is satisfactory and able to attract a larger market. These voices of customers were integrated into the decision-making process via the house of quality. The absolute and relative assessments performed revealed that the extruder body, heating element, and nozzle diameter which form the extrusion unit were the most critical engineering specified components for the batik printer. The technical requirements of the extrusion unit (extruder body, heating element, and nozzle diameter) were then mapped against relevant customer requirements to aid the design of the extruder system. As a result, a modular-based extruder system operated using a ceramic ring heater (12 V, 60 Watt) with multiple detachable heads was proposed. Since `ease of operation` is a highly desirable printer feature for the customers, several cartesian-based batik printer configurations were proposed at the end of this study. Further performance assessment-based study will be conducted with actual integrated software and hardware for the batik printer.

ACKNOWLEDGEMENT

REFERENCES

[1] Redzuan M, Aref F. (2011) Constraints and potentials of handicraft industry in underdeveloped region of Malaysia," Afr. J. Bus. Manag., 5(2): 256-260.

[2] Anon. (2017) The Malaysian Handicraft Annual Report 2017, Kuala Lumpur, Malaysia.

[3] Teng YY. (2018) Making batik her life's purpose. The Star Online. [Online]. Available: https://www.thestar.com.my/metro/focus/2018/12/15/making-batik-her-lifes-purpose

[4] Benzin K. (2016) Batik – an ancient indonesian tradition. Reddduckpost. [Online]. Available: https://www.redduckpost.com/batik-an-ancient-indonesian-tradition/

[5] Musa R, Kyi W, Rampal KG. (2000) Work-related musculoskeletal symptoms among batik workers in Kelantan. Malays. J. Med. Sci., 7(2):13-17.

[6] Yusof N, Yusof R, Ahmat Basri FMF, Soin N. (2013) Ergonomic evaluation of postural assessment among 'canting' batik workers," Adv. Eng. Forum., 10: 226-230.

[7] Rahman AAA, Pillai S. (1996) Mahathir: Leadership and Vision in Science & Technology. Academy of Sciences Malaysia, Universiti Putra Malaysia Press.

[8] Muthi'ah W. (2018) Study of computerized-batik technique using 'Batik Kelowong' machine in Batik Adelia, Bekasi, IOP Conference Series: Materials Science and Engineering, 453(1): 012022.

[9] Morris AS, Elamvazuthi I. (1998) Automating the batik colouring process, Part I: An investigation of colouring kinetics on woven fabrics. In UKACC International Conference on Control'98: 1-4 September 1998; Swansea., 1:224–228.

[10] Affanti TB, Hidayat SR. (2018) Batik innovations in Surakarta Indonesia. In 3rd International Conference on Creative Media, Design and Technology: 25 September 2018; Surakarta., pp. 138–141.

[11] Mohd NH, Shuib NH, Baharin HB. (2019) Industri batik tempatan 'dibunuh. BH Online. [Online].Available:https://www.bharian.com.my/berita/nasional/2019/03/539919/industri-batik-tempatan-dibunuh

[12] Ya'kub EM, Wibisono K. (2019) Canting batik elektrik 'made in' Arek Surabaya. Antara News. [Online]. Available: https://www.antaranews.com/berita/156642/canting-batik-elektrik-made-in-arek-surabaya

[13] Nair N. (2014) A boost for batik. The Star Online. [Online]. Available: https://www.thestar.com.my/news/community/2014/09/26/a-boost-for-batik-designers-work-lifts-profile-of-traditional-fabric

[14] Zakaria R. (2019) Make wearing batik a culture. NST Online. [Online]. Available: https://www.nst.com.my/news/nation/2019/01/451180/make-wearing-batik-culture

[15] National Research Council (2001) Theoretical foundations for decision making in engineering design. National Academy Press.

[16] Wolniak R. (2018) The use of QFD method advantages and limitation. Prod. Eng. Arch., 18:14-17.

[17] Wolniak ER, Sędek A. (2009) Using QFD method for the ecological designing of products and services. Qual. Quant., 43(4):695-701.

[18] Park T, Kim KJ. (1998) Determination of an optimal set of design requirements using house of quality. J. Oper. Manag., 16(5): 569-581.

[19] Chang KH. (2014) Design theory and methods using CAD/CAE: The computer aided engineering design series. London, Academic Press.

[20] Dieter GE, Schmidt LC. (2009) Engineering design. Boston, McGraw-Hill Higher Education.

[21] Li X, Zhao W, Zheng Y, Wang R, Wang C. (2014) Innovative product design based on comprehensive customer requirements of different cognitive levels. Sci. World. J. 2014: 627093.

[22] Leal JE. (2020) AHP-express: A simplified version of the analytical hierarchy process method. MethodsX, 7:100748.

[23] Siswiyanti S, Rusnoto R. (2018) Penerapan ergonomi pada perancangan mesin pewarna batik untuk memperbaiki postur kerja. J. Optimasi Sist. Ind., 17(1):75-85.

[24] Fauziyah F. (2021) The development of Yogyakarta special batik design to meet customer desire and satisfaction using quality function deployment. In Proceedings of the 4th International Conference on Sustainable Innovation 2020-Accounting and Management: 13-14 October 2020; Yogyakarta., pp. 399–405.

[25] Kamal M, Wang Y, Kennon R. (2016) Redesigning cultural product by applying quality function deployment, WIT Trans. Eng. Sci., 113: 413-419.

[26] Adieba MH, Dwiyanto BM. (2016) Analisis peningkatan kualitas produk batik menggunakan pendekatan quality function deployment (QFD) (Studi Kasus Batik BL di Pekalongan). Diponegoro J. Manag., 5(3):198-209.

[27] Rinawati DI, Sari DP, Pujotomo D, Kasih PH. (2018) Natural dyes product design using green quality function deployment II method to support batik sustainable production. In E3S Web of Conferences: January 2018. 73:04014.

[28] Cochran WG. (2007) Sampling techniques. John Wiley & Sons.

[29] Homkhiew C, Ratanawilai T, Pochana K. (2012) Application of a quality function deployment technique to design and develop furniture products. Songklanakarin J. Sci. Tech., 34(6):663-668.

[30] Tavakol M, Dennick R. (2011) Making sense of Cronbach's alpha. Int. J. Med. Educ., 2:53-55.

[31] Bernal L, Dornberger U, Suvelza A, Byrnes T. (2009) Quality function deployment (QFD) for services. International SEPT Program, Leipzig, Germany.

[32] Ramírez Y, Cisternas LA, Kraslawski A. (2017) Application of house of quality in assessment of seawater pretreatment technologies. J. Clean. Prod., 148:223-232.

[33] Hauser JR, Clausing D. (1988) The house of quality. Harv. Bus. Rev., 66:63–73.

[34] Aomar R, Dhanhani J, Ali S. (2013) An enhanced QFD approach for improving water tanks sustainability at a local water distributor. Ind. Eng. Manag., 2(4):54-64.

[35] Park T, Kim KJ. (1998) Determination of an optimal set of design requirements using house of quality. J. Oper. Manag., 16(5): 569-581.

[36] Lee AW, Lin GT, Kuo WH, Lee SJ. (2017) The application of quality function deployment to smartwatches: the house of quality for improved product design. In Portland International Conference on Management of Engineering and Technology: Oregon; 9-13 July 2017., pp. 1–6.

[37] Aditya F, Agatha YV, Shamsuddin SA, Dhelika R, Aulia DC. (2018) Temperature control of canting with electric heating for batik making. In International Electronics Symposium on Engineering Technology and Applications: 29-30 October 2018; Bali., pp. 48–54.

[38] Poon ST. (2017) The journey to revival: thriving revolutionary batik design and its potential in contemporary lifestyle and fashion. Int. J. Hist. Cult. Stud., 3(1): 48–59.

[39] Büyüközkan G, Ertay T, Kahraman C, Ruan D. (2004) Determining the importance weights for the design requirements in the house of quality using the fuzzy analytic network approach. Int. J. Intell. Syst., 19(5): 443-461.

[40] Vairaktarakis GL. (1999) Optimization tools for design and marketing of new/improved products using the house of quality. J. Oper. Manag., 17(6): 645-663.

[41] Prasad B. (1998) Review of QFD and related deployment techniques. J. Manuf. Syst., 17(3): 221-234.

[42] Griffin A, Hauser JR. (1993) The voice of the customer. Mark. Sci., 12(1): 1-27

[43] Chan LK, Wu ML. (2002) Quality function deployment: a comprehensive review of its concepts and methods. Qual. Eng., 15(1):23–35.

[44] Peters MH, Kethley BR, Bullington K. (2005) Course design using the house of quality, J. Educ. Bus. 80(6): 309–315.

[45] Isaac OT, Olumide OT, Rasaki OO. (2015) Application of house of quality matrix to material selection for engineering designs, Br. J. Appl. Sci. Technol., 10(4): 1-11.

[46] Prasad KD, Subbaiah KV. (2011) Prioritization of customer needs in house of quality using conjoint analysis. In 5th International Quality Conference: 20 May 2011; Kragujevac., pp. 693–699.

[47] Betteridge M, Maropoulos PG. (1995) A review of conceptual design research and industrial practice in concurrent. In Proceedings of the Eleventh National Conference on Manufacturing Research: 12-14 September; Leicester., pp. 693–697.

MECHANICAL CHARACTERIZATION OF POLYESTER/ E-GLASS FIBER REINFORCED/MWCNTS NANOCOMPOSITES

NAGUIB G. YAKOUB

Faculty of Engineering, Beni-Suef University, Beni-Suef, Egypt

*Corresponding author: Nagibgergeous@eng.bsu.edu.eg

ABSTRACT: Mechanical properties of polyester/glass fiber reinforced by multiwalled carbon nanotubes (MWCNTs) were studied. MWCNTs nano particles are mixed within resin in various weight fractions of 0.1, 0.2, 0.4 and 0.6 % using sonication. E-Glass fiber (chopped strand mat) is used in various weight fractions within the composite like 80/20 wt%, 70/30 wt%, 50/50 wt% to fabricate polyester/CSM/MWCNTs composites. The effect of the addition of MWCNTs nanoparticles on the mechanical characteristics such as hardness and tensile strength were investigated. The effect of various E-glass fiber chopped strand mat (CSM) wt.% reinforcement is also investigated. A scanning electron microscope (SEM) was used to show the nanocomposites morphological properties such as reinforcement orientation and the bonding between matrix and fiber. It was found that the addition of 0.4 wt% MWCNTs improves the mechanical properties of composites, especially the 50 wt% polyester / 50 wt% CSM composite. The tensile strength improved by 39.8%, and the hardness improved by 38%.

ABSTRAK: Ciri-ciri mekanikal bagi poliester / gelas fiber diperkukuh dengan dinding berbilang karbon nanotiub (MWCNTs) dikaji. Partikel nano MWCNT telah dicampur ke dalam resin pelbagai berat pada pecahan 0.1, 0.2, 0.4 dan 0.6 % menggunakan sonikasi. Gentian Kaca-E (potongan lembaran) telah digunakan dalam pelbagai pecahan berat dalam komposit 80/20 wt%, 70/30 wt%, 50/50 wt% bagi menghasilkan komposit poliester/CSM/MWCNT. Kesan penambahan nanopartikel MWCNT pada ciri-ciri mekanikal seperti kekerasan dan kekuatan tensil diuji. Kesan pelbagai gentian Kaca-E (potongan lembaran) (CSM) wt.% bersama agen pengukuh turut dikaji. Pengimbas Mikroskop Elektron (SEM) digunakan bagi menilai ciri-ciri morfologi komposit nano seperti orientasi pengukuh dan ikatan antara matrik dan gentian. Dapatan kajian menunjukkan dengan penambahan sebanyak 0.4 wt% MWCNT dapat memperbaiki ciri-ciri mekanikal komposit terutama komposit campuran (50 wt% polyester / 50 wt% CSM). Ketahanan tensil meningkat sebanyak 39.8%, dan kekerasan telah bertambah sebanyak 38%.

1. INTRODUCTION

Glass fiber-reinforced composite materials (GFRPs) are increasingly used due to their high rigidity, high durability limit, high corrosive resistance, low thermal expansion coefficient and close-net shape, and greater production viability compared to conventional engineering materials [1]. Nanocomposites became significant, in the last few decades in particular, to boost mechanical properties for different applications [2]. Such

nanomaterials are capable of improving mechanical, thermal, and electrical characteristics. Recent research has been carried out to investigate the utility of polyester/glass fiber/MWCNTs composites in many fields like aerospace and automotive industries because of their light weight and high performance [3-6]. Composites based on CNTs have been widely studied using a variety of matrix materials like ceramics [4-6], metals [7], and polymers [8-12]. Breton [13] improved epoxy resin by adding different kinds of MWCNTs and subsequently mechanical characteristics of MWCNTs were tested. The results showed that a higher tensile modulus was acquired by the enhancement of MWCNTs within epoxy resin of 1, 3, and 6 weight percentage. Liu et al. [14] dispersed 2 wt.% of MWCNTs in a nylon-6 matrix, they found that the tensile modulus increased about 214% and the yield strength about 162%.

Allaoui et. al. [15] investigated the mechanical and electrical characteristics of the MWCNTs/epoxy composite and concluded that 1 wt.% and 4 wt.% of carbon nano-tubes greatly enhanced the composite's young's modulus and yield strength. Zhou [16] filled epoxy resin of 0.1 wt%, 0.2 wt%, 0.3 wt%, and 0.4 wt% CNTs and studied the loading effects on the mechanical properties of composites. The results show the increased modulus with a higher CNT material content, while the maximum strength was reached by the 0.3 wt% CNT. Schadler et. al. [17] investigated the load transition in epoxy composite reinforced by MWCNTs and observed that the compression modulus was significantly scattered; its maximum value was 6 MPa which was large compared to the tension modulus of 4.2 MPa. Shekar et al. [18] used a sonication technique to distribute MWCNTs within polymer matrices efficiently and homogenously. The author also pointed out that the flexural force and flexural modulus of nanocomposites were increased by amino functionalized MWCNT in the epoxy composites. The calendar technique for standardized distribution of MWCNTs in epoxy resin was introduced by Gojnyet et al. [19] the mechanical properties were improved by the addition of a small wt% of nanotubes compared to the same wt% of carbon black dispersed in the epoxy resin. Results indicated that nanotube-filled epoxy resin had improved fracture toughness, tensile strength, and elasticity modulus under ductility retention.

Shokrieha et al. [20] studied the effect of adding MWNTs on properties of mat/polyester composites. They concluded that the flexural strength of the composites was improved by 45% at only 0.05 wt.% of MWNT. Furthermore, increasing the amount of MWNTs in composites enhanced their tensile, flexural, and compressive moduli.

Multi-wall carbon nanotubes (MWCNTs) were used as a secondary improvement in the current study to strengthen the mechanical properties of the polyester/CSM composite. polyester/CSM laminate was developed using a hand-layup technique. It was discovered that adding 0.4 wt% MWCNTs to composites improved their mechanical properties, especially in 50/50 wt% composites.

2. MATERIALS

2.1 Fabrication of MWCNTs Based Nanocomposites

Chopped strand mat (CSM) has a fiber length between 20 and 30 mm. Fiber mass of 450 g/m^2 was used as a first reinforcement and polyester as a matrix. Multiwalled carbon nano tubes MWCNTs (93%, diameter 10–40 nm and length 5–20 μm) were provided by Sigma-Aldrich and were used as secondary reinforcement. Figure 1 shows the fiber and the MWCNTs nanofiller used to fabricate polyester/CSM nanocomposites. Methyl ethyl ketone peroxide (MEKP) was added as a catalyst to the orthophthalic unsaturated

polyester as a cure for ambient temperature. Both fibers and polyester materials were purchased from Al-Joumhouria Co. Cairo, Egypt. The polyester/CSM/MWCNTs nano composites were manufactured using a hand-layup technique [21] these composites were manufactured using a flat wooden mold, as shown in Fig. 2, which was horizontally mounted and covered with a thin layer of a release agent of liquid polyvinyl acetate (PVA). Firstly, MWCNTs were added to polyester resin using sonication, then a first layer of MWCNTs/polymer resin was rolled across a single roller. Next, a layer of CSM was laid on top of the first layer of nano-MWCNTs/polyester resin. The layer was subsequently mounted on the mold surface. A smooth steel roller was employed to squeeze air out of the layers, which also ensured that the polyester resin layers were evenly distributed across the surfaces. An additional layer of MWCNTs / polyester resin was added to the glass fiber sheet. Polyester/CSM/MWCNTs nanocomposites were made up of three layers of CSM. Glass fibers, were constructed at 4 mm of thickness during the same process. The substance was then treated for 24 hours at room temperature.

The composites are produced in various fractions of weight such as:

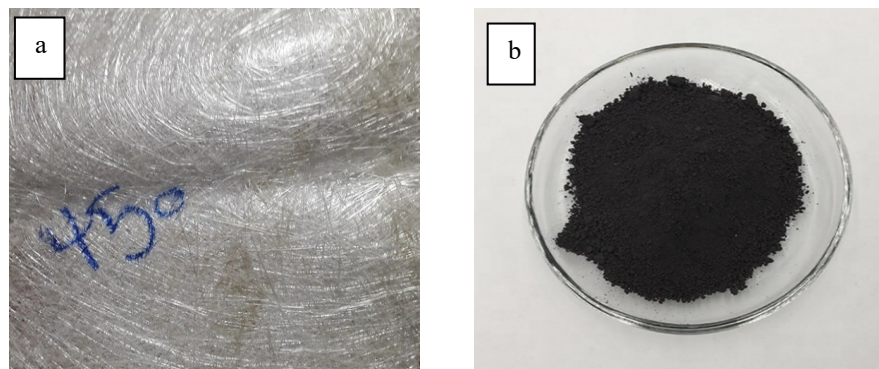| Sample code	Polyester (wt%)	CSM (wt%)	MWCNTs (wt%)
S1	80	20	0
S2	80	20	0.1
S3	80	20	0.2
S4	80	20	0.4
S5	80	20	0.6
S6	70	30	0
S7	70	30	0.1
S8	70	30	0.2
S9	70	30	0.4
S10	70	30	0.6
S11	50	50	0
S12	50	50	0.1
S13	50	50	0.2
S14	50	50	0.4
S15	50	50	0.6

Fig. 1: (a) E-glass fiber chopped strand mat glass fiber, (b) MWCNTs nano-powder.

Fig. 2: Hand-layup technique.

3. TESTING

3.1 Tensile Strength

MWCNTs nanoparticles in various percentages as 0.1%, 0.2%, 0.4% and 0.6% were introduced to various weight percentages of polyester/glass fiber like 80/20 wt%, 70/30 wt%, and 50/50 wt% then tensile test was conducted using WAW-300B (300 kN, Zhejiang Jingyuan Mechanical Equipment Co., Ltd., Jinhua, China) tensile testing machine with a constant strain rate of 1 mm/min, according to ASTM D3039. Six samples were tested and an average value was chosen for each nanocomposite. The model tensile specimens are presented in Fig. 3 before conducting the tensile test.

3.2 Hardness

Hardness tester (Barcol hardness test type 934-1) was used to test specimens according to the ASTM D638 type IV (Fig. 4). About six samples were checked and the average value was chosen for each nanocomposite. The specimen was put under the Barcol hardness tester indentor and the specimen was subjected to a uniform pressure up to meeting the optimum dial indicator. The deep penetration was converted to absolute numbers of Barcol to obtain hardness in Brinell. Different weight percent of MWCNTs nanoparticles were introduced to investigate different (polyester/CSM/MWCNTs) composites hardness.
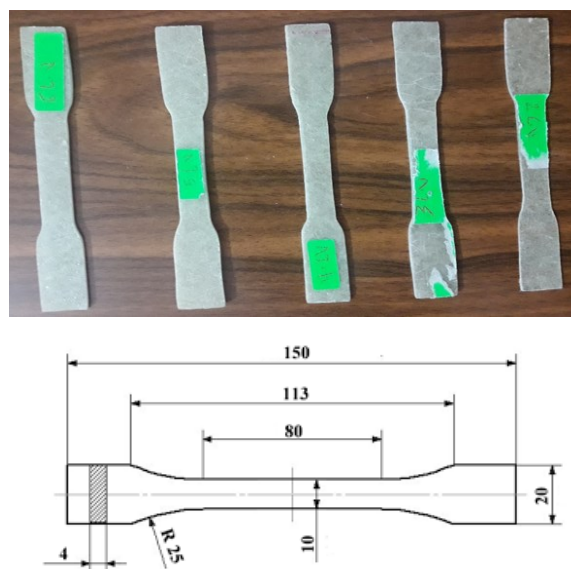

Fig. 3: The standard tensile specimens.

Fig. 4: ASTM D638 Type IV standard specimen using Barcol tester.

4. RESULTS AND DISCUSSION

4.1 Tensile Strength of Polyester/CSM/MWCNTs Nanocomposites

The tensile strength variations versus the weight percent of MWCNTs nanoparticles are shown in Figs. 5(a-c), various wt.% of polyester/CSM/MWCNTs specimens were fabricated. Fig.5(a) indicates that the tensile strength of (80 wt.% polyester / 20 wt.% CSM) without MWCNTs has a value of 75.4 MPa. While in case of (80 wt.% polyester / 20 wt.% CSM + 0.1 wt.% of MWCNTs) the tensile strength value increased from 75.4 MPa to 101 MPa. The maximum tensile strength is then observed to be 104.5 MPa at 0.4 wt.% of MWCNTs specimen, that means the tensile strength is improved by 38.5%. by more reinforcement with MWCNTs. Over 0.4 wt.% the tensile strength was then reduced and it reached a low value of 77.03MPa when MWCNTs were added by 0.6 wt.%.

It is observed from Fig. 5(b) that tensile strength of polyester/fiber (70/30 wt.%) composite has a value of 97.01 MPa. By being reinforced up to 0.1 wt.% with MWCNTs nanoparticles, the tensile strength value was increased from 97.01 MPa to 123.11 MPa and reached a maximum value of 140.07 with the addition of MWCNTs up to 0.4 wt.% (tensile strength of composite improved by 44%). It was observed that tensile strength decreased by further addition of MWCNTs nanoparticles over 0.4 wt.%, and dropped to 94.74 MPa at the 0.6 wt.% of MWCNTs. This is close to the pattern of 80/20 wt.% of Polyester/CSM shown in Fig. 5(a).

Figure 5(c) shows a similar pattern of tensile strength variation of polyester/CSM 50/50 weight percentage and the tendency for variation in strength of nanoparticles with various wt.% of the MWCNT. As discussed previously, results were found to be similar. This shows that the percentage value of the material composition changed its tensile strength. Also, the addition of MWCNTs nanoparticles affects the polyester/CSM composite tensile strength values. It is observed that the further increase of MWCNTs nanoparticles leads to decrease in tensile strength for all polyester/CSM composites.

Figure 6 indicates a comparison between tensile strength variation vs different wt. percentages of MWCNTs nanoparticles reinforces polyester/CSM (80/20 wt.%, 70/30 wt.% and 50/50 wt.%). It is concluded that the nanocomposite of 50/50 wt.% of polyester/CSM/MWCNTs at the same content of 0.4 wt.% of MWCNTs has a tensile strength value of 170 MPa compared to 80/20 wt% (about 105 MPa) and 70/30 wt.% composite (about 140 MPa).
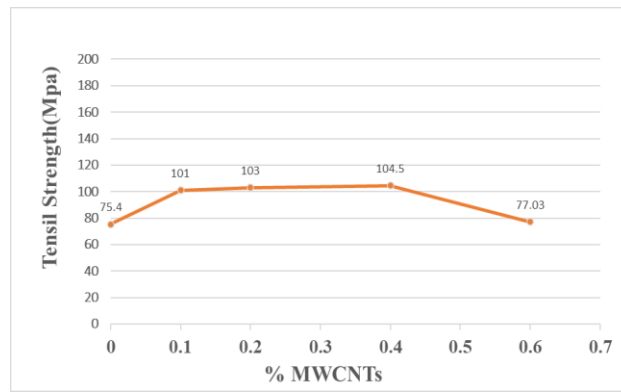
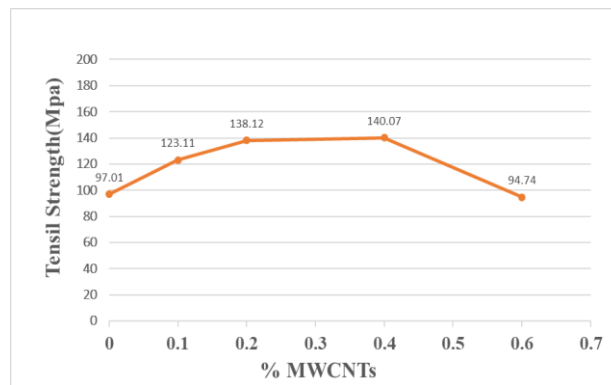Fig. 5: (a) Tensile strength vs % MWCNTs of polyester/CSM (80/20 wt.%).

Fig. 5: (b) Tensile strength vs % MWCNTs of polyester/CSM (70/30 wt.%).
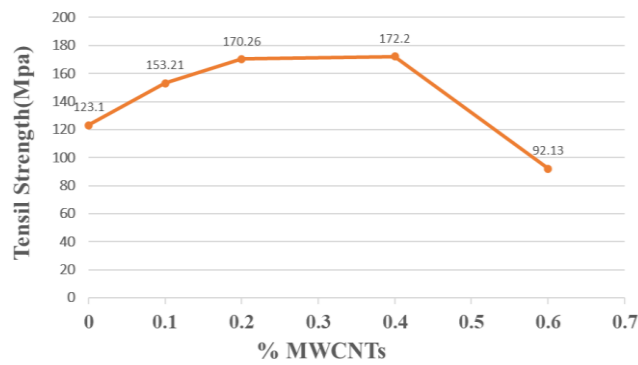

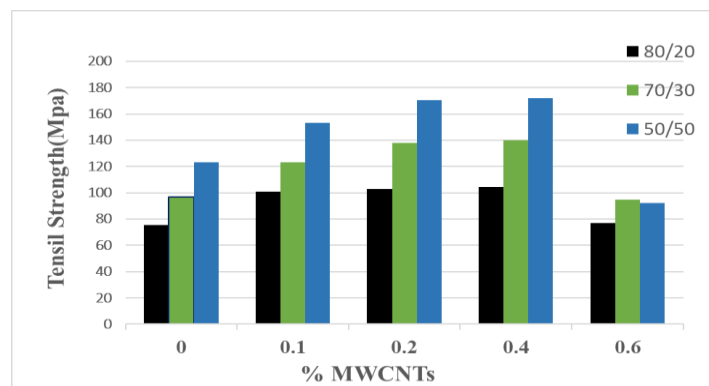Fig. 5: (c) Tensile strength vs % MWCNTs of polyester/CSM (50/50 wt.%).

Fig. 6: Comparison between tensile strength variation and different wt. percentages of MWCNTs reinforces polyester/CSM (80/20 wt.%, 70/30 wt.% and 50/50 wt.%).

4.2 SEM Microscopy

Figure 7(a) shows an SEM image of 0.4 wt.% MWCNT-reinforced 50/50 wt.% of polyester/CSM. From this figure, a matrix-fiber adhesion is observed. This explains the higher value of tensile strength of this composite. Figure 7(b) shows SEM image of 0.6 wt.% MWCNT-reinforced 50/50 wt.% of polyester/CSM. From Fig. 7(b) it is clear that introduction of more MWCNTs causes agglomeration of particles and leads to decrease in mechanical properties, explaining the reduced value of tensile strength by further addition of MWCNTs.
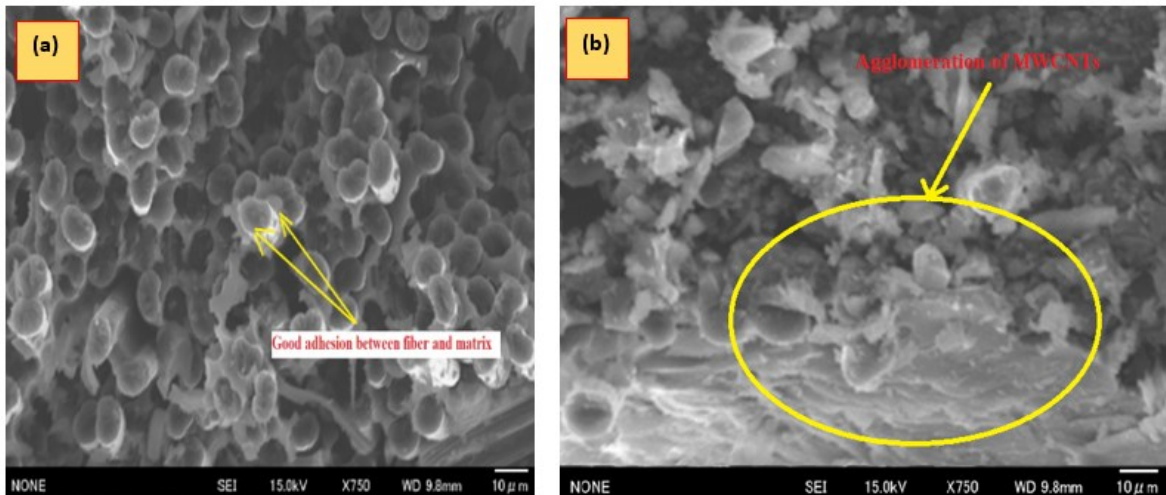

Fig. 7: SEM image of 50/50 wt.% of polyester/CSM reinforced by (a) 0.4 wt.% MWCNTs., (b) 0.6 wt.% MWCNTs.

4.3 Hardness Test

4.3.1 Hardness of Polyester/CSM/MWCNTs Nanocomposites

Figure 8(a) shows hardness variation of wt.% nano MWCNT-reinforced polyester/CSM (80/20 wt.%). It is observed that by the addition of 0.1 wt.% of MWCNTs, the hardness value is increased from 32.3 to 40.01 and by adding 0.4 wt.% of MWCNTs, the hardness is increased to 41.5%. Therefore, the hardness improved by 23.8% and 28.4% by reinforcing with 0.1 wt.% and 0.4 wt.% of MWCNTs, respectively. It is obvious that the hardness of 0.1 wt.% and 0.4 wt.% of MWCNTs composites is improved. It is also observed that the hardness values are decreased after 0.4 wt.%. Figure 8(b) and Fig. 8(c) show the hardness variation of MWCNTs reinforced (60 wt.% polyester / 40 wt.% CSM) and (50 wt.% polyester / 50 wt.% CSM), respectively. From the graphs, it is clear that hardness values increase by increasing the weight percent of MWCNTs. However, further increase up to 0.6 wt.% of MWCNTs leads to a decrease in hardness values for both (60 wt.% polyester / 40 wt.% CSM) and (50 wt.% polyester / 50 wt.% CSM) composites. Comparative plots show that the (50 wt.% polyester / 50 wt.% CSM) composite has higher values of hardness about 47 BHN as demonstrated in Fig. 9. It is noted from the previous data that, with the increase in MWCNTs nanoparticles, tensile strength and hardness first increase and then decrease with more addition of MWCNTs nanoparticles. The maximum tensile strength value is seen at 0.4 wt.% of MWCNTs nanoparticles and the characteristics are reduced with a higher introduction of MWCNTs nanoparticles. The increase in the adhesion of fiber matrix is due to tensile characteristic enhancement by introducing MWCNTs. Nano particles have an increasing, unique surface and low surface

strength. Thus, they can react with the macro-molecular chain chemically and physically to improve the connection between the matrix and the fiber. The reduction of the tensile strength for composites reinforced by 0.6 wt% MWCNTs could be attributed to nano filler accumulation in the glass fiber polyester matrix. However, with an increase of MWCNTs nanoparticle material, the accumulation activity increased, suggesting that nanocomposites of polyester/CSM/MWCNTs were more incompatible with an excess of MWCNTs nanoparticles addition.
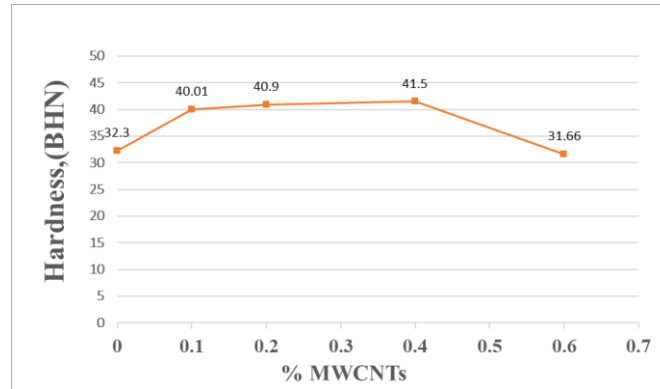

Fig. 8: (a) Hardness variation of wt.% nano MWCNTs reinforces polyester/CSM (80/20 wt.%).
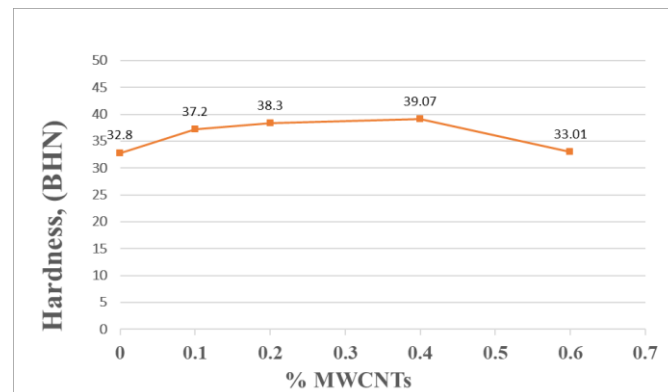

Fig. 8: (b) Hardness variation of wt.% nano MWCNTs reinforces polyester/CSM (70/30 wt.%).
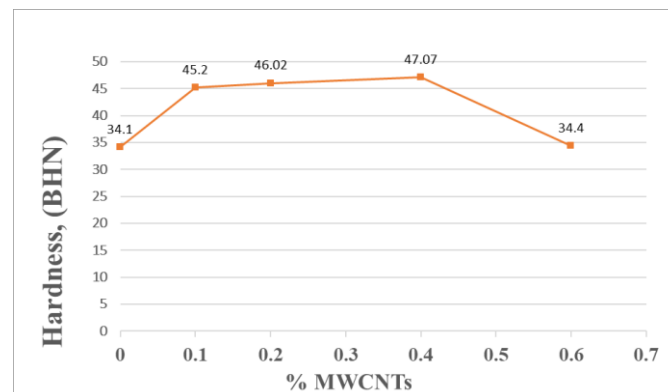

Fig. 8: (c) Hardness variation of wt.% nano MWCNTs reinforces polyester/CSM (50/50 wt.%).
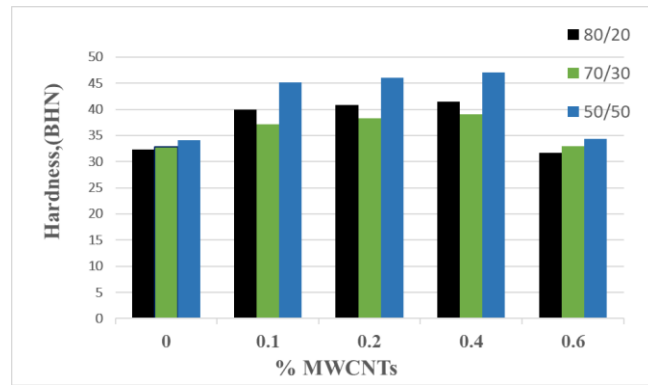
Fig. 9: Comparison between hardness variation and different weight percentages of MWCNTs reinforces polyester/CSM (80/20 wt.%, 70/30 wt.% and 50/50 wt.%).

5. CONCLUSION

Polyester reinforced by E-glass fiber CSM composites were manufactured by means of the hand layup method. Different wt.% of MWCNTs nanoparticles were used to reinforce composites. Tensile and hardness tests were conducted to investigate the effect of MWCNTs addition. The experimental data support the following conclusions:

1. The mechanical properties of (polyester/CSM/MWCNTs) are enhanced due to the presence of MWCNTs nanoparticles. Adding up to 0.4 wt.% of MWCNTs nanoparticles greatly improves the strength and hardness of various composites, especially in the 50 wt.% polyester / 50 wt.% CSM composite, where it enhanced both the tensile strength and the hardness by 39.8% and 38%, respectively. However, further addition of MWCNTs nanoparticles reduced tensile strength and hardness values. The addition of MWCNTs nanoparticles gives strong adhesion between matrix and fiber. It also leads to the improvements of the mechanical properties for different composites. Nanoparticle agglomerates cause the decrease in values of both tensile strength and hardness. The presence of further wt.% of MWCNTs nanoparticles leads to decrease in mechanical properties as nanoparticles agglomerate and leads the polymer matrix to weaken. In the 50 wt.% polyester / 50 wt.% CSM composite, tensile strength decreased by 25.1% by adding 0.6 wt.% of MWCNTs over polyester / CSM without MWCNTs addition. Also, hardness value of 50 wt.% polyester / 50 wt.% CSM without MWCNTs addition was slightly enhanced by 0.8% when 0.6 wt.% of MWCNTs was added.

2. For 80/20, 70/30 and 50/50 wt.% of polyester/CSM adding MWCNTs nanocomposites up to 0.4 wt.%, enhanced hardness and tensile strengths for all composites compared to polyester/CSM composites without MWCNTs nano particles.

3. 50/50 wt.% of polyester/CSM + 0.4 wt.% MWCNTs nanocomposite has a hardness of 47 BHN and a tensile strength of 172 MPa and these are the highest values, above all other composites.

REFERENCES

[1] Palanikumar K. (2010) Modeling and analysis of delamination factor and surface roughness in drilling GFRP composites. Mater Manuf Process., 25:1059–1067.

[2] Murugan S, Rajendran R, Fei W. (2016) Graphene-zinc oxide (G-MWCNTs) nanocomposite for electrochemical supercapacitor applications. J. Sci. Adv. Mater. Dev., 1:454-460.

[3] Sandhya CP, John B, Gouri C. (2017) Sn/Al$_2$O$_3$/C/CNT composite prepared by wet milling as anode material for lithium-ion cells, J. Sci. Adv. Mater. Dev., 2:210-214.

[4] Peigney A, Laurent C, Flahaut E, Rousset A. (2000) Carbon nanotubes in novel ceramic matrix nanocomposites. Ceramics International., 26(6):677-683.

[5] Flahaut E, Peigney A, Laurent C, Marliere C, Chastel F, Rousset A. (2000) Carbon nanotubemetal- oxide nanocomposites: microstructure, electrical conductivity and mechanical properties. Acta Materialia., 48(14):3803-3812.

[6] Peigney A, Flahaut E, Laurent C, Chastel F, Rousset A. (2002) Aligned carbon nanotubes in ceramic-matrix nanocomposites prepared by high-temperature extrusion. Chemical Physics Letters., 352(1-2):20-25.

[7] Xu CL, Wei BQ, Ma RZ, Liang J, Ma XK, Wu DH. (1999) Fabrication of aluminum-carbon nanotube composites and their electrical properties. Carbon., 37(5):855-858.

[8] Cochet M, Maser WK, Benito AM, Callejas MA, Martínez ME, Benoit JM, Schreiberb J, Chauvet O. (2001) Synthesis of a new polyaniline/nanotube composite: ''in-situ'' polymerization and charge transfer through site selective interaction. Chem Comm., 16:1450-1451.

[9] Jin Z, Sun X, Xu G, Goh SH, Ji W. (2000) Nonlinear optical properties of some polymer/multiwalled carbon nanotube-based composites. Chem Phys Lett., 318:505-510.

[10] Jin Z, Pramoda KP, Xu G, Goh SH. (2001) Dynamic mechanical behavior of melt-processed multi-walled carbon nanotube/poly (methyl methacry-late) composites. Chem Phys Lett., 337(1-3):43-47.

[11] Kumar S, Doshi H, Srinivasarao M, Park JO, Schiraldi DA. (2002) Fibers from polypropylene/ nano carbon fiber composites. Polymer, 43(5):1701-1733.

[12] Lourie O, Wagner HD. (1999) Evidence of stress transfer and formation of fracture clusters in carbon nanotube-based composites. Composite Science and Technology., 59(6):975-977.

[13] Breton Y, Esarmot GD, Salvetat JP, Delpeux S, Sinturel C, Béguin F, Bonnamy S. (2004) Mechanical properties of multiwall carbon nanotubes/epoxy composites: influence of network morphology. Carbon., 42(5-6):1027-1030.

[14] Liu T, Phang I, Shen L, Chow S, Zhang W. (2004) Morphology and mechanical properties of multiwalled carbon nanotubes reinforced nylon-6 composites. Macromolecules, 37(19):7214-7222.

[15] Allaoui A, Bai S, Cheng HM, Bai JB. (2002) Mechanical and electrical properties of a MWNT/epoxy composite. Composites Science and Technology, 62:1993-1998.

[16] Zhou Y, Pervin F, Lewis L, Jeelani S. (2006) Experimental study on the thermal and mechanical properties of multi-walled carbon nanotube- reinforced epoxy. Materials Science and Engineering., 452-453:657-664.

[17] Schadler LS, Giannaris SC, Ajayan PM. (1998) Load transfer in carbon nanotube epoxy composites. Appl Phys Lett., 73(26):3842-3844.

[18] Shekar KC, Prasad BA, Prasad NE. (2014) Effect of amino multiwalled carbon nanotubes reinforcement on the flexural properties of neat epoxy. Appl Mech Mater., 592:912-916.

[19] Gojny FH, Wichmann MHG., Fiedler B, Schulte K. (2005) Influence of different carbon nanotubes on the mechanical properties of epoxy matrix composites – a comparative study. Compos Sci Technol., 65:2300-2313.

[20] Shokrieh MM, Saeedi A, Chitsazzadeh M. (2014) Evaluating the effects of multi-walled carbon nanotubes on the mechanical properties of chopped strand mat/polyester composites, Materials & Design, 56:274-279.

[21] El-Tayeb NSM, Yousif BF, Yap TC. (2006) Tribological studies of polyester reinforced with CSM 450-R-glass fiber sliding against smooth stainless steel counterface. Wear., 261:443-452.

INFLUENCE OF IPNS (VINYLESTER / EPOXY / POLYURETHANE) ON THE MECHANICAL PROPERTIES OF GLASS / CARBON HYBRID COMPOSITES

KARJALA SANTHOSH PRIYA[1], KUTTYNADAR RAJAMMAL VIJAYA KUMAR[1], *GOPI SURESH[2], RAJESH RAVI[3], CHOCKALINGAM DEVANATHAN[4], CHINATHAMBI MUTHUKARUPPAN MEENAKSHI[5]

[1]*Department of Mechanical Engineering, Dr. M.G.R. Educational and Research Institute, Chennai, India.*
[2]*Department of Mechanical Engineering, Rajalakshmi Institute of Technology, Chennai, India.*
[3]*School of Aerospace and Automotive Engineering, Universite International de-Rabat (UIR), Rabat – 11100, Morocco.*
[4]*Department of Mechanical Engineering, Rajalakshmi Engineering College, Thandalam, India.*
[5]*Department of Mechanical Engineering, Bharath Institute of Higher Education and Research, Chennai, India.*

*Corresponding author: saisuresh1979@gmail.com

ABSTRACT: The main objective of this study is to compare the interpenetrating polymer networks' (IPNs) physical strengths with different variants of fibers. In this study, E-glass, carbon, and a combination of E-glass and carbon fiber (hybrid) have been taken as the reinforcement. Similarly, three combinations of the IPNs were chosen as the matrix material, namely epoxy / polyurethane (EP), vinyl ester / polyurethane (VP) and epoxy/vinyl ester (EV) as IPN blends. In order to thoroughly understand the physical characteristics of the combination of blends and fibers, nine variants (laminates) were fabricated: combinations of epoxy / polyurethane / E-glass (EPG), epoxy / polyurethane / carbon (EPC), epoxy / vinyl ester / glass / carbon (EPGC-hybrid), vinyl ester / polyurethane / glass (VPG), vinyl ester / polyurethane / carbon (VPC), vinyl ester / polyurethane / glass / carbon (VPGC), epoxy / vinyl ester / glass (EVG), epoxy / vinyl ester / carbon (EVC), and epoxy / vinyl ester / glass / carbon (EVGC-hybrid), all with help of a hand-layup technique. Furthermore, mechanical tests such as tensile, flexural, impact, and HDT (heat distortion temperature) were performed on all the variants as per the ASTM standards. Results shows that carbon fiber reinforcement with all IPN combinations has shown extraordinary performance (double fold) over the E-glass fiber reinforcement, whereas the hybrid (combination of E-glass/carbon) laminates have shown excellent characteristics over E-glass fiber reinforcement, irrespective of IPN matrix material. All the results were compared with each other and their corresponding variations were plotted as bar charts.

ABSTRAK: Objektif utama kajian ini adalah bagi membandingkan kekuatan fizikal rangkaian polimer saling menusuk (IPN) dengan pelbagai jenis gentian berbeza. Kajian ini mengguna pakai gentian kaca-E, karbon dan gabungan kaca-E dan gentian karbon (hibrid) sebagai penguat. Begitu juga, tiga kombinasi IPN dipilih sebagai bahan matrik, iaitu epoksi / poliuretan (EP), ester vinil / poliuretan (VP) dan epoksi / ester vinil (EV) sebagai campuran IPN. Bagi tujuan memahami secara mendalam ciri-ciri fizikal gabungan campuran dan gentian, sembilan varian (lamina) dihasilkan, malaui kombinasi seperti epoksi / poliuretan / kaca-E (EPG), epoksi / poliuretan / karbon (EPC), epoksi / ester vinil

/ kaca / karbon (EPGC-hibrid), ester vinil / poliuretan / kaca (VPG), ester vinil / poliuretan / karbon (VPC), ester vinil / poliuretan / kaca / karbon (VPGC), epoksi / ester vinil / kaca (EVG), epoksi / ester vinil / karbon (EVC), epoksi / ester vinil / kaca / karbon (EVGC-hibrid) dengan teknik susun atur lapisan menggunakan tangan. Selain itu, ujian mekanikal seperti tegangan, lenturan, hentaman dan HDT (suhu kelenturan panas) dilakukan pada semua varian mengikut piawaian ASTM. Dapatan kajian menunjukkan bahawa, penguat gentian karbon dengan semua kombinasi IPN telah menunjukkan prestasi luar biasa (dua kali ganda) daripada penguat gentian kaca-E, manakala lamina hibrid (campuran kaca-E / karbon) telah menunjukkan ciri-ciri sangat baik berbanding penguat gentian kaca-E tanpa mengira bahan matrik IPN. Semua hasil dapatan dibandingkan antara satu sama lain dan padanan variasi diplot sebagai carta bar.

1. INTRODUCTION

Considerable research activity has been initiated in the area of materials, with the goal of finding new materials that can deliver high performance in the way that high performance engineering materials have, for example, composites. Meanwhile, the application of these composite materials is among the most important developments in the engineering field in recent years. These materials have become essential to different engineering applications, for example automobile part manufacturing and marine & aerospace applications. Since the composite materials explicitly have very high strength to weight ratio, are lightweight, and resistant to high temperatures, they are indeed considered to be pioneer materials in all applications. When compared with traditional metallic materials, composite materials present a wide spectrum of advantages over metallic materials, because metallic materials are prone corrosion when employed in corrosive environments [1-3]. In recent decades, thermoset polymer composites have become recognized and perhaps the most notably desirable materials in all sectors. The inherent properties like modulus to weight ratio, corrosion resistance, and fatigue resistance have further bolstered its wide acceptance in all sectors of engineering applications. On the other hand, thermoset FRPs (fiberglass reinforced plastics) have lower toughness when compared with traditional metallic materials and alloys. This adverse effect of strength gain is mainly due to interfacial bonding and linkages between the fiber and matrix materials. This is purely based on the property of the modifications on the matrix. Meanwhile, researchers have kept trying various synthesis methodologies in the area of matrix modifications as well as adopting the newer techniques such as blending and concept of Interpenetrating polymer networks [4-6].

Generally, composites are explained as being a mixture of two or more materials that are combined to yield better characteristics than the individual materials in the mix. In contrast to traditional metallic alloys, each mixed material separately keeps its physical, chemical, and mechanical properties. Aside from the phase mixing of both materials, reinforcement agents are added that are usually much stronger, stiffer, and harder than the matrix material. Normally the reinforcement will be a fiber or a particulate. In the fabrication of particulate composites, the particulates uniformly occupy all areas of the composite material, whereas the strength of fiber-reinforced composites is completely based on the reinforcement direction, size, and shape. Different types of fiber and matrix materials are available on the market, where the traditional fibers like glass and carbon fibers are most common in the area of FRP fabrication. Similarly, in the area of matrix selection, common synthetic resins like epoxy, polyurethane and vinyl ester are often the only resin components considered for a fabricator. Each resin has its own unique nature of application in the

fabrication of versatile components. Epoxy resin is considered to be the highest performance resin due to its inherent properties and resistance to environmental degradation. Generally, epoxy consists of a cross-linking reaction group, originally derived from the epoxy group [7-9].

Mostly, epoxy is used in the coating and fabrication industries because it shows good adhesion with fiber reinforcement. Epoxy also boasts very good chemical resistance, mechanical strength and electrical insulation property. Likewise, vinyl ester resin is considerably used in most polymeric industries. Basically, vinyl ester is produced by esterification process, where epoxy resin has been chosen as the prime ester substituent. Engineers widely consider vinyl ester to be an acceptable substitute material for epoxy resin since it has a comparatively lower cost than the epoxy resin. It is also commonly used in marine industries due to its corrosion resistance and reduced water uptake characteristics, and is extensively used in FRP tank vessel manufacturing and their allied components. Other classic resins in this series are polyurethane resins (PUR), from the family of thermoset and thermoplastic resins. PUR is predominately accepted as a versatile material throughout the world due to its inherent properties like toughness, durability, and tear resistance. It is important to remember that all resins have their own positive and negative impact on component fabrication. In order to tap the benefits of two resins, the concept of interpenetrating polymer networks has been suggested and research activity has been successfully initiated in that field. While undergoing the polymerization, each resin would undergo separate curing and have mutual entanglement with the mutual resin [10-12].

In this present work, instead of choosing an individual polymer as the matrix material, the combination or blending of two resins has been implemented in order to fabricate the laminate. Three sets of combinations have been taken for physical examination in this study. Initially, epoxy with polyurethane was kept as the constant blend for glass, carbon, and glass / carbon fiber reinforcement. Then, a vinyl ester and polyurethane blend was taken as the blend for glass, carbon, and glass/carbon fiber reinforcement. Finally, epoxy and vinyl ester with a specific proportion was kept as the blend for the reinforcement of glass, carbon, and glass / carbon fiber. All the combinations underwent physical examination in order to have a detailed comparison of all the reinforcements with all blends. Tests like tensile, flexural, impact, and moisture exhibit the relative coherence of all the reinforcements [13].

2. MATERIALS AND METHODS

2.1 Materials

The epoxy resin used in the experimental process as well as diglycidyl ether bisphenol A, vinyl ester resin with corresponding hardener, promotor, and catalyst, and polyurethane and E-glass / carbon fiber with aerial density of 350 GSM were purchased from Sakthi fibers, Chennai. All fibers and resins used for fabrication were received from the supplier as shown in Fig. 1.

2.2 Sample Preparation

Initially, the epoxy with hardener was mixed with a ratio of 10:6 wt%. Similarly, the vinyl ester and its corresponding hardener (methyl ethyl ketone peroxide), promotor, and accelerator were mixed with a ratio of 100:2:2. Finally, the polyurethane prepolymer was mixed with its respective hardener MOCCA. All the mixtures with their corresponding hardeners were kept for blending as mentioned in the Table 1.
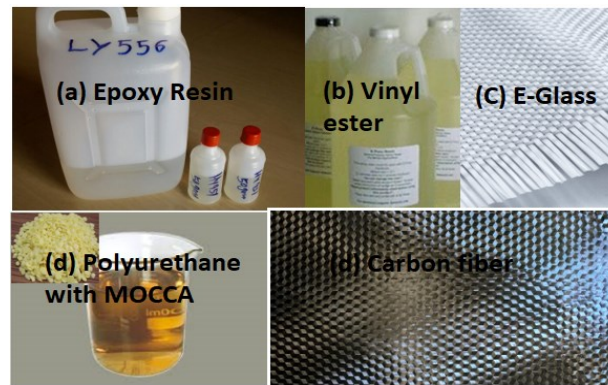
Fig. 1: Raw materials used to fabricate the IPN laminate.

Table 1: IPN – Blend with reinforcement combinations

Notations	IPN – Blending Combination	Fiber Reinforcement
EPG	Epoxy + Polyurethane	Glass
EPC	Epoxy + Polyurethane	Carbon
EPGC	Epoxy + Polyurethane	Glass/Carbon
VPG	Vinyl ester + Polyurethane	Glass
VPC	Vinyl ester + Polyurethane	Carbon
VPGC	Vinyl ester + Polyurethane	Glass/Carbon
EVG	Epoxy + Vinyl ester	Glass
EVC	Epoxy + Vinyl ester	Carbon
EVGC	Epoxy + Vinyl ester	Glass/Carbon

2.3 Fabrication Technique

Nine different types of composites, as mentioned in Table 1, were made by the hand-layup technique. Six plies of biaxial woven mat of the fibers were cut. To fabricate the laminate, the woven mat was initially placed on the flattened aluminum plate then completely covered with a polypropylene sheet. Following this, the blend was applied over the polypropylene sheet and the respective fiber mat was placed over the wet surface of the combination of IPN laminate. The mats were placed one over another until a 3 mm thickness was obtained. After every combination set was made, the specimens were kept at atmospheric temperature to ensure the complete polymerization. Also, laminates were kept in the hot air oven for a period of 2 hours to further enhance the complete polymeric condensation. All the specimens were cut to the sizes mentioned in Table 2 in order to subject the specimens to physical examinations. The specimens were cut with help of a diamond saw cutter with utmost care and accuracy [14].

Table 2: ASTM Standards with size of the specimens

ASTM Standards	Size of the specimen (length x breadth x thickness) in "mm"
ASTM D 3039 - Tensile	250 x 25 x 3.2
ASTM D 790- Flexural	127 x 12.7 x 3.2
ASTM D 256 – Impact	63 x 12.8 x 3.2
ASTM D 648 – HDT	125 x 12.7 x 3.2

2.4 Experimental Analysis

The tensile and flexural tests were done according to ASTM D3039 for all set of specimens by a universal testing machine, as mentioned in Table 2. In each test, five samples were tested and averages were noted down as the final value. The sample specimens of all the hybrid composites are shown in Fig. 2.
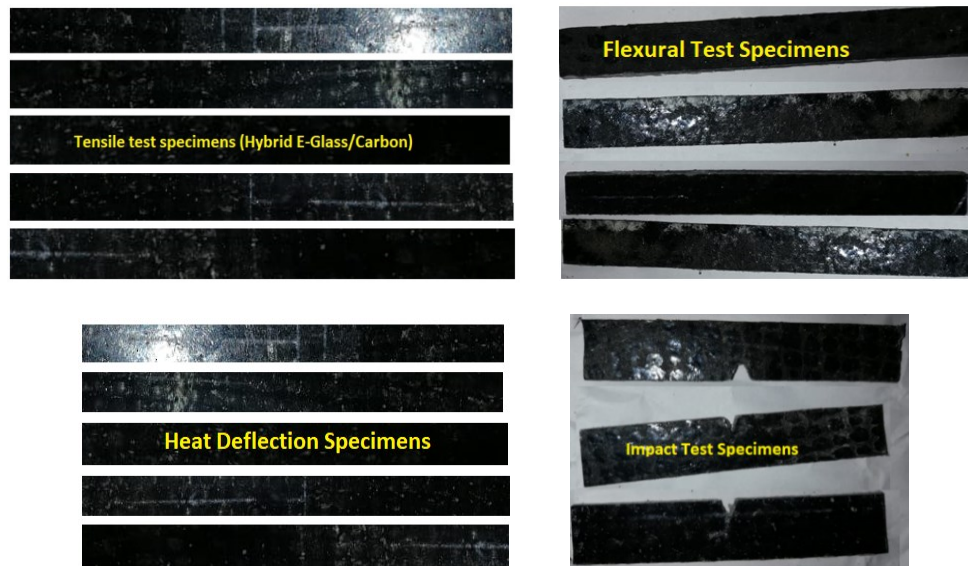

Fig. 2: Hybrid test specimens of IPN composite.

3. RESULTS AND ANALYSIS

Table 3 illustrates test results of the various IPN blends with E-glass and carbon fiber reinforcements. All physical property tests were conducted at ambient temperature.

Table 3: IPN – Blend (E-Glass/Carbon – reinforced) physical properties

IPN – Blending Combination	Mechanical Properties			
	Tensile (MPa)	Flexural (MPa)	Impact (kJ/m^2)	HDT (°C)
Epoxy + Polyurethane + Glass (EPG)	625	415	16	74
Epoxy + Polyurethane + Carbon (EPC)	1025	752	19	89
Epoxy + Polyurethane + Glass/Carbon (EPGC)	834	554	17	81
Vinyl ester + Polyurethane + Glass (VPG)	452	376	12	68
Vinyl ester + Polyurethane + Carbon (VPC)	854	725	19	79
Vinyl ester + Polyurethane + Glass/Carbon (VPGC)	667	501	16	72
Epoxy + Vinyl ester + Glass (EVG)	554	386	15	76
Epoxy + Vinyl ester + Carbon (EVC)	954	786	20	88
Epoxy + Vinyl ester + Glass/Carbon (EVGC)	776	512	17	81

3.1 Tensile Strength Analysis of IPN Laminate

The results of the tensile strength of the E, E/SF, E/BF, E/CF, and E/SBCF fiber-reinforced composites are shown in Fig. 3. It was observed that the tensile strength of the pure EPG composite had a value of 625 MPa. However, during this test, it was observed that the fracture on the specimen occurred at the gauge length of the specimen. Though epoxy is known for its good strength and stiffness, due to the loading of the polyurethane on the epoxy, the strength of the specimen showed a little dip when its tensile strength is considered. Past studies have shown that the pure epoxy with glass reinforcement show a predominant tensile strength value against all other sets of thermoset resins. Similarly, the fracture purely relied on the phenomenon of crack initiation on the matrix, with subsequent loss of the interfacial strength between the fiber and matrix. Also, it was common to notice that the fibers were broken as pull out fractures on the gauge length. The EPC specimen showed a tensile strength value of 1025 MPa; this value was nearly 64% higher than the EPG specimens. This high tensile strength shows that carbon fiber reinforcement has caused the rise in the tensile strength value.

Normally, carbon fibers are known for their higher strength, lower weight, and stiffness ratio. The characteristics of the carbon fiber showed the overwhelming response, when present, in its hike in tensile strength. The same failure mechanism seen in the EPG was observed in EPC. The EPGC specimen showed a mixed response, where half of its strength seems due to the glass fiber and half due to the carbon fiber.

The specimen showed a 45% increase over previous EPC specimens. However, the values obtained on the vinyl ester matrix material showed a different trend, unlike the epoxy-based composites. Proof of this is seen in the VPG tensile strength value of 452 MPa. This value was nearly 88% lower than the value obtained from the EPGC. Although the vinyl ester resin was proven to have a good toughness and impact resistant matrix, it showed a dip in tensile strength value even when loaded with polyurethane matrix. For a second time, it was interesting to note that the VPC had a tensile strength value of 854 MPa, which was nearly 22% higher than the value obtained from VPG.
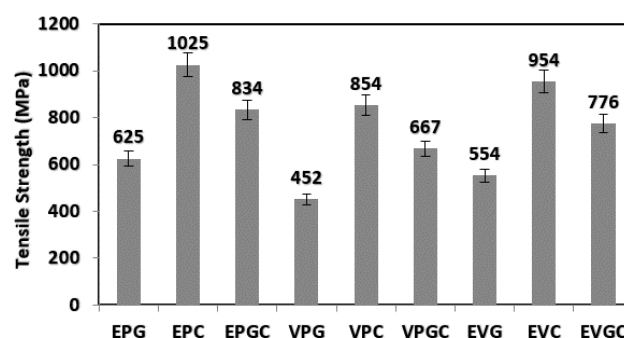

Fig. 3: Tensile strength analysis of E-glass / carbon fiber reinforced IPN (EP/VP/EV) laminate.

From the results, it is proven that the carbon fiber reinforcement maintained a high value when reinforced, irrespective of the matrix material. On the contrary, the VPGC showed an increase in the tensile strength value against the VPC. The obtained value was 667 MPa; this was nearly 17% lower than the carbon fiber reinforcement. From all the results, it was observed that, irrespective of matrix, carbon fiber often offers a very high and good strength bearing capability. In line of the above, the EVG shows a tensile strength value as 554 MPa. The obtained value was not higher than EPG, but not lower than VPG, from the obtained value, it was proven that the epoxy holds a greater load bearing capability

than the other two matrices, namely, the polyurethane and the vinyl ester. The EVC exhibits the tensile strength value of 954 MPa, and this was higher than the corresponding EPC and VPC. At last, the EVGC shows a tensile strength value of 776 MPa, this value is nearly 19% lower than the value of EVC. All the results clearly show that the carbon fiber holds the higher load bearing capacity irrespective of IPN matrix materials, similarly the hybridization on the composites increases the laminate strength to many folds greater than the glass fiber and many folds lower than the carbon reinforced IPN laminate [15].

3.2 Flexural Strength Analysis of IPN Laminate

The obtained results of the flexural strength of the E, E/SF, E/BF, E/CF and E/SBCF fiber-reinforced composites are shown in Fig. 4. The specimen was held between the two rollers in a horizontal direction and the load was applied in the vertical direction. Similar trends were seen in the flexural analysis as were seen in the previous tensile strength analysis. The EPG showed the flexural strength value of 415 MPa, this was mainly due to the epoxy matrix. Epoxy would usually have good interfacial strength; thus, the inter-laminar strength was further increased in all combinations. The carbon fiber reinforced IPN laminate exhibited a higher value than the glass fiber reinforcement. This increased percentage (81%) in the EPC was due to the carbon fiber reinforcement's stiffness characteristics. The carbon fiber played a major role in increasing the strength of the laminates to higher levels.
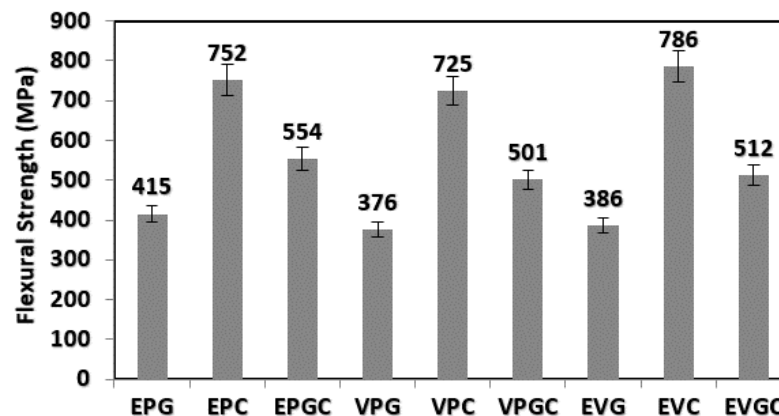

Fig. 4: Flexural strength analysis of E-glass / carbon fiber reinforced IPN (EP/VP/EV) laminate.

The hybrid IPN laminate, with a combination of glass and carbon fiber reinforcement showed a lower value than the neat carbon fiber reinforcement. The obtained value shows that the load bearing capacity of the hybridization was based on the tailoring property of the glass and carbon fiber. Nevertheless, the VPG, VPC, VPGC showed the flexural strength values of 376 MPa, 725 MPa, and 501 MPa, respectively. The obtained value for VP (vinyl ester and polyurethane) showed again that the matrix influences the load bearing strength of the laminate as discussed in the tensile strength analysis. However, the EV (Epoxy and vinyl ester) showed that, for every epoxy-based IPN, the strength of the IPN laminate largely increased the load bearing capacity to a massive level [16].

3.3 Impact Strength Analysis of IPN Laminate

Figure 5 shows the result of impact strength analysis of different variations of IPN blends with E-glass / carbon fiber reinforced laminates.
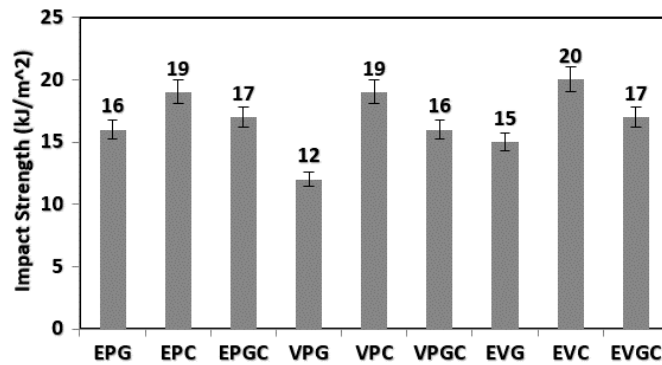
Fig. 5: Impact strength analysis of E-glass/carbon fiber reinforced IPN (EP/VP/EV) laminate.

The EPG specimen showed an impact strength value of 16 kJ/m^2. This obtained value was comparatively high with respect to all sets of IPN specimens. Similarly, the EPC showed a value of 19 kJ/m^2. This value was much higher than the glass fiber reinforcement. Again, this study proves that the carbon fiber reinforcement has better entanglement and adhesion property with all sets of IPN matrixes. EPGC showed a comparatively lower value than that of EPG and EPC. Similarly, the VPG, VPC, VPGC showed an impact strength value of 12 kJ/m^2, 19 kJ/m^2, 16 kJ/m^2, respectively. Though vinyl ester is universally accepted as being a good impact resistant material, when it is mixed with the epoxy, the showed values of 15 kJ/m^2, 20 kJ/m^2, and 17 kJ/m^2, respectively. From all the tests, it was clearly observed that the IPNs with hybridization significantly provided higher impact strength than the individual fiber reinforcement [17].

3.4 Heat Deflection Test of the IPN Laminate

The heat deflection temperature (HDT) was measured in order to find out the distortion temperature of the respective composites under elevated temperature (0.25 mm deflection), while the specimen was subjected to a standard load. Results are shown in the Fig. 6. While doing the test on the EPG specimen, it exhibited an HDT value of 74 °C. Though the neat epoxy reinforced composite exhibited higher HDT value in previous literature, in this study, it showed a lower value than the original neat epoxy-based composites. The main reason behind the lesser distortion was the loading of the polyurethane into the hybrid composite. Variation in HDT value was far less than variation in the strength tests. Since polyurethane is an elastic material, it loosens its entanglement with the epoxy very quickly as the temperature increases into the system.
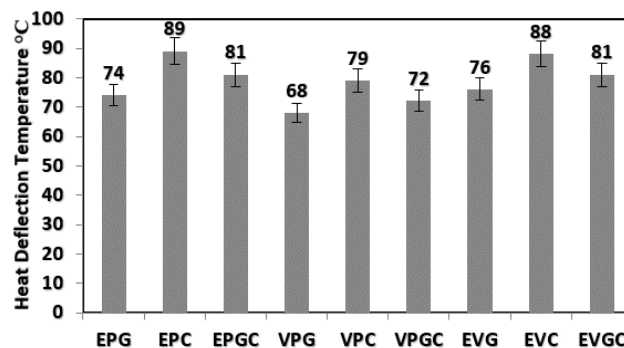

Fig. 6: Flexural strength analysis of E-glass / carbon fiber reinforced IPN (EP/VP/EV) laminate.

The EPC hybrid composite showed an HDT value of 89 °C, this value was nearly 9% higher than the EPG. Although the EPC laminate contains polyurethane, its HDT value was

higher than the EPG. This was due to the carbon reinforcement into the laminate. However, the carbon reinforcement sustained maximum transverse load when the laminate was subjected to the transverse load. The EPGC showed a mixed response much like the value obtained from tensile and flexural tests. The combination shows the mixed strengthened value of E-Glass and Carbon fiber. This value was 16% lower than the EPC. Correspondingly, the VPG exhibited an HDT value of 68 °C and the VPC showed an HDT value of 79 °C. Though it exhibited a 16% higher value than the earlier reinforcements, the increase in the HDT value clearly showed that the carbon fiber reinforcement takes the maximum load. It also showed the better adhesion characteristics over the matrix material. In the same way, the EPGC also showed a reduction in their HDT value as comparted with the VPC. As with the EPGC, the glass fiber took less load and the carbon fiber took the maximum load. This is the reason why the specimen showed a mixed response of glass fiber and carbon fiber. The EVG showed an HDT value of 76 °C whereas its corresponding carbon fiber reinforcement exhibited a value of 88 °C. From all the tests, it was clearly shown that the polyurethane resin-loaded hybrid composite showed a predominantly lower HDT value as compared with the neat laminates. By the same token, the carbon fiber reinforced IPNs showed a higher value, irrespective of the type of IPN used. Equally, the hybrid laminates showed mixed responses from glass and carbon fiber reinforcement.

4. CONCLUSION

The three sets of IPNs (epoxy / polyurethane, vinyl ester / polyurethane, epoxy / vinyl ester) were prepared with a ratio of 70:30 with the variant reinforcements of E-glass, carbon, E-glass / carbon fiber reinforcement. All the variants were subjected to physical tests and their corresponding results are drafted below:

1. During tensile test, EP (epoxy/polyurethane) and EV (epoxy/vinyl ester) specimens showed better tensile strength values as compared to VP (vinyl ester/polyurethane) specimens. This is because of the matrix contributions to the IPN blends.

2. Similarly, in flexural stress analysis, the EP (epoxy/polyurethane) specimens exhibited excellent flexural strength values over the remaining set of IPN blends.

3. On the contrary, during the impact strength analysis, the EV (epoxy/vinyl ester) showed better impact resistance value as compared with the remaining set of two variants. This was mainly because of the toughness characteristics of the vinyl ester.

4. While doing the HDT test, it was observed that polyurethane significantly played a role in terms of negative dip in the HDT value. However, carbon fiber reinforcement into the epoxy-based composite cumulatively increased the HDT value.

5. Overall, important findings were that carbon fiber reinforcement into the IPN blend significantly increased the physical strengths of the laminates to double fold that of the E-glass fiber reinforcement. This shows that the carbon fiber had considerably better adhesion property with all sets of IPNs.

REFERENCES

[1] Mat Serudin A, Othuman Mydin MA, Abdul Ghani AN. (2021) Influence of fiberglass mesh on physical properties of lightweight foamcret. IIUM Engineering Journal, 22(1): 23-34.
[2] Zarinkolah Z, Bagheri H, Hosseinkhani S. (2021) Investigation on the mechanical, thermal, bio-degradation, and bio-compatibility properties of poly (lactic acid)/poly (ethylene glycol) blend. IIUM Engineering Journal, 22(1): 223-233.

[3]   Tiwari A, Wiener J, Arbeiter F, Pinter G, Kolednik O. (2020) Application of the material inhomogeneity effect for the improvement of fracture toughness of a brittle polymer. Eng. Fract. Mech., 224: 106776. https://doi.org/10.1016/j.engfracmech.2019.106776

[4]   BNVS Ganesh Gupta, Hiremath MM, Prusty RK, Ray BC. (2020) Development of advanced fiber-reinforced polymer composites by polymer hybridization technique: emphasis on cure kinetics, mechanical, and thermomechanical performance. J. Appl. Polym. Sci., 137(43): 1–11. https://doi.org/10.1002/app.49318.

[5]   Ke H, Zhao L, Zhang X, Qiao Y, Wang G, Wang X. (2020) Performance of high-temperature thermosetting polyimide composites modified with thermoplastic polyimide, Polym. Test., 90: 106746. https://doi.org/10.1016/j.polymertesting.2020.106746.

[6]   Liu Y, Wu Q, Wang C, Zhou D, Liang R, Kang Y. (2018) Curing behaviors' characterization of strong and weak crosslinking systems by thermal and dynamic mechanical methods, Polym. Test., 70: 1-7. https://doi.org/10.1016/j.polymertesting.2018.06.022.

[7]   Shukla MJ, Kumar DS, Rathore DK, Prusty RK, Ray BC. (2016) An assessment of flexural performance of liquid nitrogen conditioned glass/epoxy composites with multiwalled carbon nanotube, J. Compos. Mater., 50: 3077-3088. https:// doi.org/10.1177/0021998315615648

[8]   Suresh G, Jayakumari LS. (2015) Evaluating the mechanical properties of E-Glass fiber/ carbon fiber reinforced interpenetrating polymer networks. Polimeros, 25: 49-57. https://doi.org/10.1590/0104-1428.1650.

[9]   Suresh G. (2016) Analyzing the mechanical behavior of E-glass fibre-reinforced interpenetrating polymer network composite pipe. J. of Composite Materials, 50: 3053-3061.

[10] Ramesh M. (2017) Mechanical and water intake properties of banana-carbon hybrid fiber reinforced polymer composites. Materials Research, 20: 365-376.

[11] Sumesh KR, Kanthavel K, Vivek S. (2019) Mechanical/thermal/vibrational properties of sisal, banana and coir hybrid natural composites by the addition of bio synthesized aluminium oxide nano powder. Mater Res Exp., 6(4): 045318. https://doi.org/10.1088/2053-1591/aaff1a.

[12] Vivek S, Kanthavel K. (2018) Effect of bagasse ash filled epoxy composites reinforced with hybrid plant fibres for mechanical and thermal properties. Compos B, 160: 170-176.

[13] Suresh G, Vivek S, Ganesh Babu L. (2019) Evaluation of mechanical behaviour of carbon fiber reinforced nanoclay filled IPN matrix composite. Materials Res Exp, 6(12): 125311. https://doi.org/10.1088/2053-1591/ab54ec

[14] Shayan Asenjan M, Sabet SAR, Nekoomanesh M. (2020) Mechanical and high velocity impact performance of a hybrid long carbon/glass fiber/polypropylene thermoplastic composite. Iran Polym J., 29: 301-307.

[15] Alikhani A, Hakim S, Nekoomanesh M. (2017) Modified preparation of HDPE/clay nanocomposite by in situ polymerization using a metallocene catalyst. Iran Polym J., 26: 721-731.

[16] Ramakrishna HV, Padma Priya S, Rai SK. (2006) Effect of fly ash content on impact, compression, and water absorption properties of epoxy toughened with epoxy phenol cashew nut shell liquid–fly ash composites. J Reinf Plast Compos., 25(5): 455-462.

[17] Srinivasan T, Suresh G. (2020) Experimental analysis of mechanical properties of banana fibre/epoxy (particulate) reinforced composite. Materials Today Proceedings, https://doi.org/10.1016/j.matpr.2020.05.103.

EVALUATION OF SURFACE ROUGHNESS AND MATERIAL REMOVAL RATE IN ELECTRICAL DISCHARGE MACHINING OF AL-ALLOY WITH 10% *SiC*

ABBAS FADHIL IBRAHIM

*Production Engineering and Metallurgy Department,
University of Technology, Baghdad, Iraq*

*Corresponding author: 70011@uotechnology.edu.iq

ABSTRACT: Aluminum-based metallic matrix compounds are widely used in industrial and aircraft manufacturing due to their advanced characteristics, such as toughness and high strength resistance to weight ratio, etc. Silicon carbide is an important industrial ceramic and it is the fourth hardest ceramic after diamond, boron nitride, and boron carbide. Owing to its low fracture toughness, it is difficult to machine silicon carbide using traditional machining processes. Electrical discharge machine can machine such materials irrespective of their hardness. Aluminum alloy 6061 and 10% SiC based-metal matrix composite were used as a workpiece that was produced by stir casting. In the experimental investigation, pulse current Pc (10, 20, and 30 A), pulse on (Pon) duration (100, 150, and 200 µsec), and pulse off (Poff) duration (6, 12, and 24 µsec) were treated as the input variables. The output responses were surface roughness (SR) and material removal rate (MRR). The best value for surface roughness (Ra) reached (1.032 µm) at Pc (10 A), Pon duration (100 µsec) and Poff (15 µsec). Also, the best result for the productivity of the process (MRR) reached (69.49 × 10⁻³ g/min) at Pc (30 A) Pon, (200 µsec) and (6 µsec) Poff. Therefore, the experimental outcomes were optimized for surface roughnes and material removal rate by adding 10% SiC to aluminum alloy 6061.

ABSTRAK: Sebatian matrik logam berasaskan aluminium telah digunakan secara meluas dalam industri pembuatan dan pesawat kerana ciri-cirinya yang canggih, seperti ketahanan dan daya rintangan yang tinggi kepada nisbah berat, dan lain-lain. Silikon karbida adalah seramik industri yang penting dan ia merupakan seramik keempat terkuat setelah berlian, boron nitrida dan boron karbida. Disebabkan ketahanan frakturnya yang rendah, adalah sukar bagi menghasilkan mesin silikon karbida menggunakan proses pemesinan tradisional. Mesin pelepasan elektrik mampu menghasilkan mesin menggunakan bahan tersebut tanpa mengira kekerasan. Aloi aluminium 6061 dan komposit matrik logam berasaskan SiC 10% telah digunakan sebagai bahan kerja yang terhasil melalui tuangan kacauan. Melalui penyelidikan eksperimen, detik arus Pc (10, 20, dan 30 A), detik hadir (Pon) berdurasi (100, 150, dan 200 µsec), dan detik henti (Poff) berdurasi (6, 12, dan 24 µsec) dirawat sebagai pemboleh ubah input. Respon pengeluaran adalah kekasaran permukaan (SR) dan kadar penyingkiran bahan (MRR). Nilai terbaik bagi kekasaran permukaan (Ra) telah mencapai (1.032 µm) pada Pc (10 A), berdurasi Pon (100 µsec) dan Poff (15 µsec). Tambahan, hasil terbaik bagi proses produktiviti (MRR) mencapai (69.49 × 10⁻³ g/min) pada Pc (30 A) Pon, (200 µsec) dan (6 µsec) Poff. Oleh itu, hasil eksperimen dioptimumkan bagi permukaan kasar dan kadar penyingkiran bahan dengan tambahan 10% SiC ke aloi aluminium 6061.

1. INTRODUCTION

Electrostatic discharge treatment is one of the most used unconventional manufacturing processes. Thermoelectric power is used to remove the unwanted materials from the workpiece by a sequence of electrical sparks between on the workpiece and the electrode. Electrical discharge happens between the workpiece and the electrode in a small gap that separates the undesirable metal from the original workpiece during melting and evaporation. The work piece and electrode must have electrical conductivity to create the spark [1]. The electrostatic discharge generates an impulse pressure by blasting an insulator to expel the molten particles. Thus, the amount of material removed can be effectively controlled to produce a complex and precise machine element [2]. The removed material is incompletely discarded, and the remaining material collects to form drainage pits. As a result, the machined surface has small pores and cracks caused by a high temperature gradient which reduces the quality of the surface finish. There have been several published studies dealing with the surface finishing of EDM materials. It was observed that several machining parameters affect the surface roughness, and it was difficult to determine the best surface quality that would result from any possible combination of parameters, such as the wear of the workpiece and the wear occurring at the corners of Gr and Cu materials observed after the average values of pulse current (Pc) and Pulse on time (Pon). Therefore, the generated sparks were concentrated in the middle of the machined area causing arcing and short circuit. Investigations indicated that the EDM output parameters increased with increasing pulse current, and the best curing rates were achieved using copper and aluminum electrodes [1, 3]. The advantage of EDM compared to other traditional methods is the ability to penetrate very hard metals, the ability to machine complex shapes, and the reduction of distortion on fine features [2, 4, 5].

This technology is widely used to manufacture elements for critical parts, like the copier parts, gearboxes, etc. These components operate under the parameters of temperature and dynamic forces, thus high-strength materials are used, such as thermally hardened steel alloys, titanium-aluminum-tungsten-based alloys and others. Metal Matrix Compounds (MMCs) are compound materials, such as alloys based on Al, Mg, or Ti and stiffeners, like Al_2O_3 molecules, SiC, TiB_2, and TiC [6,7]. MMCs provide support to the structure and distribute the load, while the particles or fiber stiffeners provide beneficial thermal performance, physical, or mechanical properties. They have high specific properties, such as light weight, high strength, high toughness, high durability, and excellent heat resistance. The evolution of MMCs leads to their use in the nuclear, aerospace, and automotive industries as an alternative to conventional materials. MMCs are created by different manufacturing processes, such as friction stir welding process, metal injection molding, pressure casting technology, mechanical alloying, and continuous binder powder coating [7,8]. Conventional machines for MMCs offer relatively high engineering precision; therefore, due to the mechanical nature of the process, they generate excessive heat and that causes plastic deformation which in turn reduces the quality of the workpiece surface layer [9-11]. EDM is a contactless process, and the processing powers are humble, therefore it is used for thin, fragile, and aspect ratio machines [12]. Studies showed a selection of process variables, and fixing the appropriate range of parameters to machine every product decides the quality of the product. Haris et al. [13] analyzed the effect of nozzle size and inlet pressure supplied on the flushing efficiency to avoid improper flushing and enhance the material removal rate in the EDM process. Rino et al. [14] investigated the effect of different types of electrode, including Cu (ordinary electrode) and Cu-Ni (newly proposed graphitization catalyst electrode), on

the electrical discharge machining performance, material removal rate and surface roughness. The copper-nickel electrode recorded a 35% better material removal rate than the copper electrode, though with a higher short-circuiting rate. Copper-nickel also provided the lowest surface roughness value with 10% better than the best surface roughness produced by the copper electrode [14]. Abdul-Azeez et al. [15] studied the optimization of parameters for siliconized silicon carbide (SiSiC) on the output quality responses: MRR, tool wear rate (TWR) and SR. Face centered central composite (FCCC) design was used in the experiment planning. Pc and Pon were found to be significant on all the responses. In addition to Pc and Pon, Sv was also significant on MRR. Pc-Pon interaction is significant on MRR and TWR, while Pon-Sv interaction is significant on Ra. [15]. Sulaiman et al. [16] investigated the surface characteristics of a functionally graded Titanium (Ti-6Al-4V) alloy during (EDM). The results showed an average micro-layer thickness of 24.47 μm with a current of 7.5 A when machined at -1600°C. Also, an increase in the crack formation with the highest current of 7.5 A for the surfaces machined at subzero temperature was recorded for both the workpieces and electrode materials [16]. Ahsan et al. [17] studied the effect of nickel powder mixed dielectric fluid on the electrical discharge machining performance of mild steel. Peak current, tool/electrode diameter and concentration of powder were the process parameters. The process performance was measured in terms of material removal rate (MRR), tool wear rate (TWR), and surface roughness (SR). According to them, increasing the current had a negative effect on both the TWR and surface roughness in contrast, and the current increase had a positive effect on the MRR [17]. This study sought to evaluate the effect of the electrostatic discharge mechanism of an aluminum alloy with silicon carbide stiffeners. Peak current, pulse on time, and pulse off time were chosen as process parameters, while the material removal rate and the surface roughness were chosen as process performance indicators.

2. EXPERIMENTAL WORK

The work material was made of aluminum alloy matrix (AA6061) and 10% silicon carbide, which was produced by stirring casting method. Silicon carbide reinforced MMCs have high hardness, low density, high strength (also at high temperature), and high corrosion resistance. Thus, aluminum alloy with silicon carbide parts are used in highly demanding applications (such as pistons and pressure arms). The composite porosity was about 5%, and the average grain size was 50 μm. The experiment was designed and analyzed using the screening method in Minitab 19 software. Also, three variables of factors, including the pulse current (Pc), pulse on duration (Pon), and the pulse off duration (Poff) were selected for the investigation.

The experimental works were conducted on a CM 323C EDM machine, seen in Fig. 1, with kerosene as the dielectric solution. A copper electrode was used as the tool material in the experimental work with (ϕ40 × 100 mm), seen in Fig. 2, with its chemical composition shown in Table 1. According to the design of experiments (DOE) with screening method, the research consisted of thirteen tests. The machining conditions for experimental work are listed in Table 2.

The value of MRR was calculated from the weighting method. The workpiece sample was weighed before machining (wp_1) and after machining (wp_2), and the MRR was calculated from the following formula [18]:

$$MRR = \frac{Wp1 - Wp2}{T} \tag{1}$$

where, T represents the time of machining. The value of SR of the samples was measured by using a portable device (pocket surf), and the test was carried out in the laboratories of the University of Technology, Baghdad.
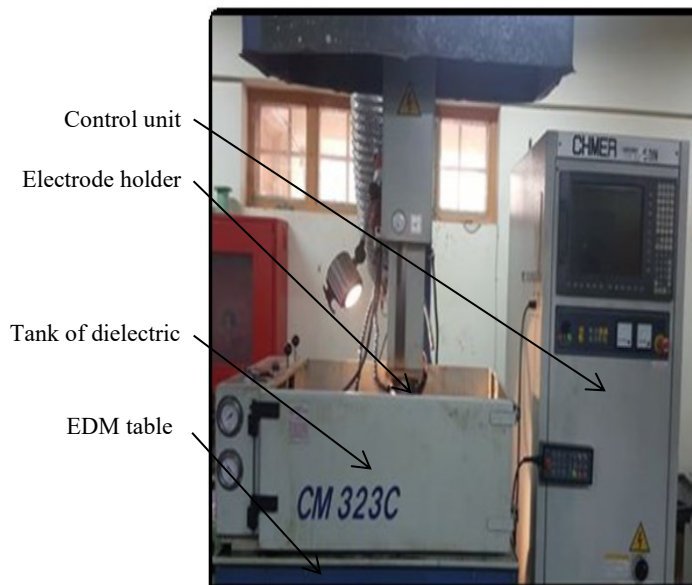

Fig. 1: EDM (CM323C type).

Fig. 2: Copper electrode tool.

Table 1: Chemical composition of copper electrode

Material	Zn%	Pb%	Sn%	Au%	Si%	Bi%	Sb%	Te%	Cu%
Weight%	0.0029	<0.005	0.003	0.0004	0.010	0.003	0.033	0.015	Rem

Table 2: Machining conditions for experimental work

Factors of code consideration	Symbol	Grade		
		1	**2**	**3**
Current (A)	Pc	10	20	30
Pulse on duration (μs)	Pon	100	150	200
Pulse off duration (μs)	Poff	6	12	24

3. RESULTS AND DISSCUSION

Depending upon the experimental results given in Table 3, the effect of the process parameters on the two responses that are (Ra) and (MRR) using copper electrodes was analyzed by analysis of variance (ANOVA) from screening approach with the help of

MINITAB 19 software. According to the theory of experiment, the research was performed and a response surface full quadratic polynomial was selected.

Table 3: Design of experiments and response result

Run order	Pc (A)	Pon (μsec)	Poff (μsec)	Ra (μm)	MRR× 10^{-3} (g/min)
1	30	100	6	1.543	67.45
2	10	100	15	1.032	58.21
3	10	150	6	1.153	60.93
4	20	150	15	1.384	63.71
5	10	200	6	1.611	59.52
6	30	200	6	1.744	69.49
7	20	100	6	1.226	65.36
8	10	200	24	1.372	63.12
9	30	150	24	1.421	64.56
10	20	200	24	1.463	64.62
11	30	200	15	1.711	68.28
12	30	100	24	1.274	62.78
13	10	100	24	1.086	58.41

3.1 Analysis of Variance (ANOVA)

ANOVA has been used to check the null hypothesis of the predicted data at a point of (95) per cent confidence and to test the defined dominant conditions and the efficacy of the second-order model for increasing the machining process reaction. Fishers statistical test (F-test) tested the importance of the function, its strength. If p-value ≤ 0.05, the factor was concluded to have a statistically significant impact. Tables 4 and 5 indicate the information of analysis of variance for the Ra and MRR of EDM process. The mathematical relation between the variables and the surface roughness and material removal rate was obtained from the non-linear regression models that are given in Eqs. 2 and 3, respectively.

Table 4: Analysis of variance (ANOVA) for Ra

Exporter	Degree of Freedom	Adj. Sum. Square	Adj Mean Square	F-Value	P-Value
Model	4	0.57094	0.14273	21.45	0.000
Linear	3	0.55352	0.184508	27.73	0.000
A	1	0.20707	0.207072	31.12	0.001
B	1	0.30276	0.302760	45.50	0.000
C	1	0.04369	0.043692	6.57	0.034
Square	1	0.01741	0.017413	2.62	0.144
B*B	1	0.01741	0.017413	2.62	0.144
Error	8	0.05323	0.006654	/	/
Total	12	0.62417	/	/	/

3.2 Predicted Model of Surface Roughness

The results for (Ra) response were assessed, which were given in the analysis of variance in Table 4 using the three levels of factors for the backward convert model for the minimum p-value. The F-value Model (21.45) indicated that the model was significant.

Values of "Prob> F" less than 0.05 imply the model terms are significant. In this case, A, B, C were significant model terms. The predicted final empirical equation is:

$$Ra = 1.401 + 0.01439\,(Pc) - 0.00694\,(Pon) - 0.00734\,(Poff) + 0.000035(Pon)^2 \qquad (2)$$

The 3D graphs presented in Fig. 3, 4, and 5 illustrate the effect of EDM factors on the Ra. Figure 3 manifested that when using pulse current (10 A) and pulse over duration (100 μs), the lower SR was reduced when using copper electrodes and kerosene insulator to 1.032 μm, and the lower surface roughness occurred due to the interaction effects of low peak Pc and low Pon. The intensity of spark energy increased with Pon, which resulted in recast layers and the formation of large craters on the machined surface tending to increase the surface roughness. Kerosene dielectric produced a better surface finish than that of the distilled water dielectric, possibly due to the slow oxidation rate and the fine surface morphology. Figure 4 depicts the 3D graphs of the Ra using pulse current (10 A) and pulse duration (6 μs), and the lower Ra obtained when using the values of 1.032 μm. Figure 5 reveals the 3D graphs of Ra using pulse over duration (100) and pulse duration (24 μs), and the lower Ra obtained reached the value (1.086 μm). This is due to the long pulse duration that furnished good cooling effect and enough time for flushing away the molten material and debris from the gap between the workpiece and electrode.
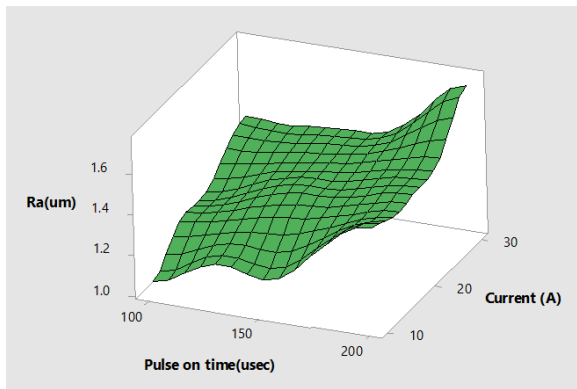

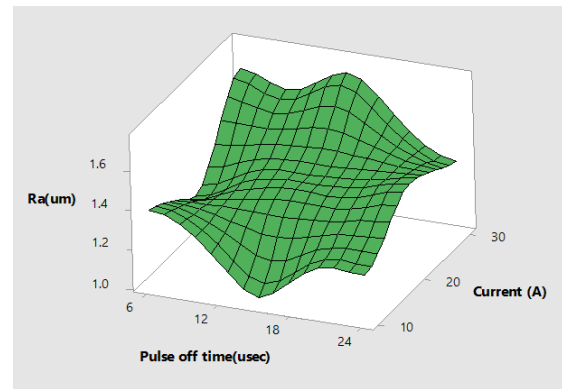Fig. 3: 3D plot for relationship between SR, Pc, and Pon.

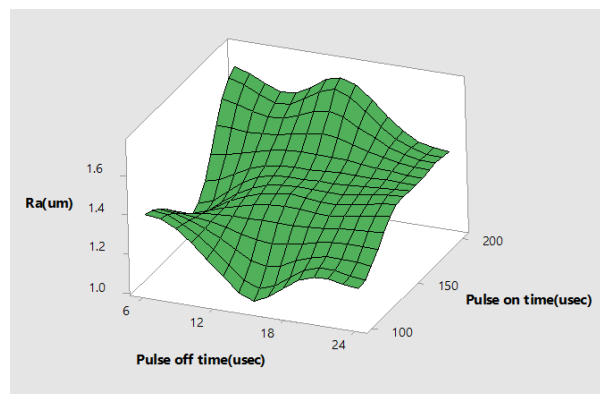Fig. 4: 3D plot for relationship between SR, Poff, and Pc.

Fig. 5: 3D plot for relationship between SR, Poff, and Pon.

3.3 Predicted Model of MRR

In order to assess the outcomes of the material removal rate response in Table 5 using the three levels of parameters, the F-value of 40.66 indicated that the pattern is significant.

In this case, A, B, C, AC, BC were important model terms. The expected final empirical equation is:

$$MRR = 56.32 + 0.5035 \, (Pc) - 0.0085 \, (Pon) - 0.204 \, (Poff) - 0.01199 \, (Pc*Poff) + 0.002276 \, (Pon*Poff) \tag{3}$$

In Eqs. 2 and 3, it was also apparent that the coefficient of current amplitude was the most significant machining parameter and influence on the predicted (Ra) and (MRR), respectively. Higher pulse current values created melted craters on the surface of the workpiece, visible to the naked eye.

Table 5: Analysis of variance (ANOVA) for MRR

Exporter	DF	Adj SS	Adj MS	F-Value.	P -Value
Model	5	151.914	30.383	40.66	0.000
Linear	3	129.792	43.264	57.89	0.000
A	1	104.782	104.782	140.21	0.000
B	1	16.435	16.435	21.99	0.002
C	1	8.575	8.575	11.47	0.012
2-way interactions	1	22.122	11.061	14.80	0.003
A*C	1	8.732	8.732	11.68	0.011
B*C	1	7.864	7.864	10.52	0.014
Error	7	5.231	0.006654	/	/
Total	12	157.145	0.747	/	/

The three-dimensional diagrams presented in Fig. 6, 7, and 8 were used to evaluate and interpret the experimental group model. These numbers demonstrated the influence of EDM factors on the MRR. Figure 6 displays that the value of material removal rate increases with increasing Pc (up to 30 A) and Pon (up to 200 μsec) reaching the value of 69.49×10^{-3} g/min, due to higher Pc, which produces maximum spark discharge power combined with higher thrust in the spark gap, which tends to heat the workpiece and cause melting and vaporization resulting in higher material removal rate. An increase in Pon proportionally increases the spark or the amount of heat energy to transfer heat to the workpiece, which causes the melting of material resulting in higher MRR. Figure 7 shows the 3D graphs of MRR using current (30 A) and pulse duration (6 μsec), and the maximum material removal rate obtained when using the value of 69.49×10^{-3} g/min, due the interaction between maximum current and lower pulse duration. Figure 8 clarifies the 3D graphs for MRR using the Pon (200) and Poff (6 μsec), and the maximum material removal rate obtained when using the kerosene dielectric reached the value of 69.49×10^{-3} g/min. MRR increased after the increasing of pulse on time value due the increased energy density at the points of the electrical discharge instantaneously after the time of the discharge, and as a result, the plasma channel expanded continuously with the Pon.

The amount of heat energy generated was large and increased the dissolving and abrasive treatment to remove the successive layers from the surface of the workpiece, and this means that the productivity increased with the current and the pulse on time.
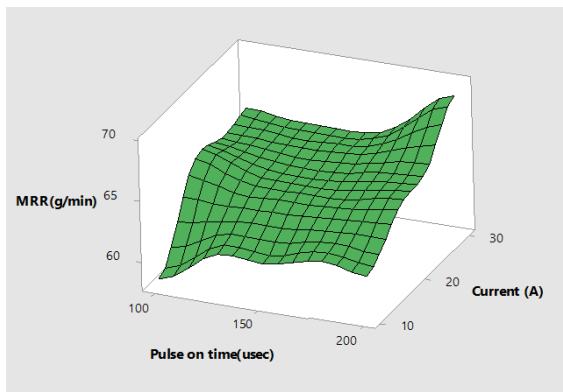
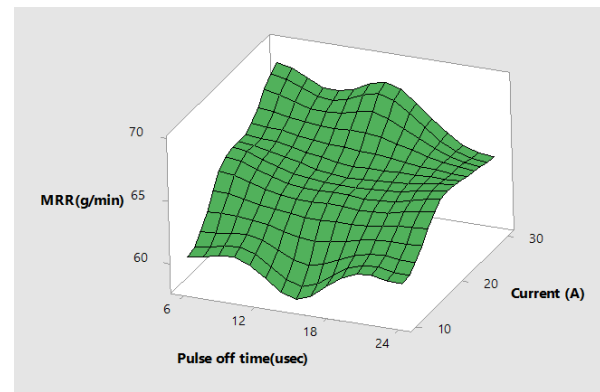Fig. 6: 3D plot for Relationship between MRR, Pc, and Pon.

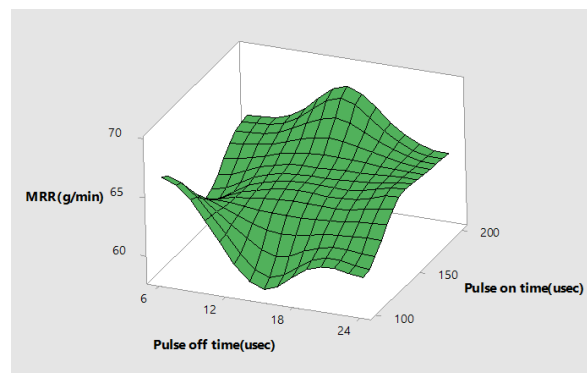Fig. 7: 3D plot for Relationship between MRR, Pc, and Poff.

Fig. 8: 3D plot for relationship between MRR, Pon, and Poff.

4. CONCLUSIONS

The machining characteristics of Al-alloy with 10% SiC MMCs in electrical discharge machining (EDM) were investigated with the help of the screening design method. It was found that the pulse current has a more significant influence on the SR and MRR than the other inputs, namely Pon duration and Poff duration. The values of the coefficients of correlation and the analysis of variance indicated a good statistical analysis for the non-linear regression models of the responses. The best value for the surface roughness (Ra) reached (1.032 μm) at pulse current (10 A), pulse on duration (100 μsec) and pulse off (15 μsec). The best result for the productivity of the process (MRR) reached $(69.49 \times 10^{-3}$ g/min) at Pc (30 A), Pon (200 μsec) and Poff (6 μsec). The desirability process elucidates that the best predicting response values were roughly the same as those obtained through the experiments as mentioned in the two items above, and this confirmed the results of the present work.

REFERENCES

[1] Bains P, Sidhu S, Payal H. (2016) Fabrication and machining of metal matrix composites, IKG Punjab Technical University, 31: 553-573.
[2] Pramanik A, Basak K, Littlefair G, Debnath S, Prakash C, Meinam S, Deepak M, Ramesh S. (2020),Methods and variables in electrical discharge machining of titanium alloy – A review, Heliyon, 6: 1-15.
[3] Manjunath P, Sandeep K, Jagadish Danil Y, Khaled G. (2021) Experimental analysis and optimization of EDM parameters on HcHcr steel in context with different electrodes and

dielectric fluids using hybrid Taguchi-based PCA-utility and CRITIC-utility approaches, Metals, 11(419): 1-23.

[4] Smolentsev V. (1983) EDM and electrochemical methods of processing materials, Moscow: Higher School.

[5] Yeliseyev Y, Savushkin B. (2010) EDM of aerospace products ,Moscow: Moscow State Technical University.

[6] Liao Z., Abdelhafeez A., Li H., Yang Y., Diaza O. G., and Axinte D. (2019) State-of-theart of surface integrity in machining of metal matrix composites, International Journal of Machine Tool Manufacturing, 143:63-91.

[7] Kandpal B, Kumar J, and Singh H. (2014) Production technologies of metal matrix composite: A review, International Journal of Research in Mechanical Engineering & Technology, 4(2): 27-32.

[8] Manikandana K, Ranjithkumarb P, Kumarb D, Palanikumarc K. (2020) Machinability evaluation and comparison of Incoloy 825, Inconel 603 XL, Monel K400 and Inconel 600 super alloys in wire electrical discharge machining, Journal of Material Research and Technology, 9(6): 12260-12272.

[9] Uthayakumar M, Kumaran T, Khan A, Skoczypiec S, Bizon W. (2018) Microdrilling of AA (6351)-SiC-B4C composite using hybrid micro-ECDM process, Journal of Testing and Evaluation, 48(4): 3073-3086. https://doi.org/10.1520/JTE20180216.

[10] Gore S, Patil G. (2018) Wire electro discharge machining of metal matrix composites: A review. Procedia Manufacturing, 20:41-52.

[11] Skoczypiec S, Machno M, Bizon W. (2015) The capabilities of electrodischarge microdrilling of high aspect ratio holes in ceramic materials, Management and Production Engineering Review, 6(30):61-69.

[12] Sivasankar S, Jeyapau R. (2012) Application of grey entropy and regression analysis for modelling and prediction on tool materials performance during EDM of hot pressed ZrB2 at different duty cycles, Procedia Engineering, 38:3977-3991.

[13] Haris R, Rasidi I, Kee M, Al Emran I, Zulafif R, Worapong S. (2020) Design and investigate of flushing system for electrical discharge machining (EDM) application, International Journal of Integrated Engineering, 12(2):218-225.

[14] Rino A, Ahmad M, Rahim M, Rha H, Sabri A, Aziz N, Ahmad T, Al Emran I, Rasidi I. (2020) The influence of graphitization catalyst electrode in electrical discharge machining of polycrystalline diamond-finishing condition. International Journal of Integrated Engineering, 12(2):211-217.

[15] Abdulazeez A, Jafri R, Ahmad A, Hamidon M. (2017) Optimization of electrical discharge machining parameters of SISIC through response surface methodology. Jurnal Teknologi, 799(1):119-129.

[16] Sulaiman A, Ahsan K, Mohamed K. (2018) Analysis of microlayer defects of a functionally graded titanium alloy by electrical discharge machining, Engineering and Applied Science Research, 45(1):17-22.

[17] Ahsan K, Muataz F, Mohiuddn A, Nurfathhah A, Mohd D. (2018) Performance of electrical discharge machining (EDM) with nickel added dielectric fluid. IIUM Engineering Journal, 19(1):215-222.

[18] Prasanna J, Rajamanickam S, Amit K, Karthick G, Sathya V. (2017) MRR and TWR evaluation on electrical discharge machining of Ti-6Al-4V using tungsten: copper composite electrode, Frontiers in Automobile and Mechanical Engineering, IOP Conference Series: Materials Science and Engineering, pp. 197–208.

FLOW INDUCED VIBRATION IN SQUARE CYLINDER OF VARIOUS ANGLES OF ATTACK

NUR AIN SHAFIZA RAMZI[1], LEE KEE QUEN[1*], NUR AMIRA BALQIS MOHD ZAINURI[1], HOOI-SIANG KANG[2,3], NOR'AZIZI OTHMAN[1] AND KENG YINN WONG[2]

[1]*Mechanical Precision Engineering, Malaysia-Japan International Institute of Technology, Universiti Teknologi Malaysia, Kuala Lumpur, Malaysia*
[2]*School of Mechanical Engineering, Faculty of Engineering, Universiti Teknologi Malaysia, Malaysia*
[3]*Marine Technology Center, Institute for Vehicle System and Engineering, Universiti Teknologi Malaysia, Malaysia*

*Corresponding author: lkquen@utm.my

ABSTRACT: An experimental study was carried out to identify the effect of angle of attack on flow-induced vibration (FIV) of square cylinders. The experiment was conducted at the Aeronautical and Wind Engineering Laboratory (AEROLAB), UTM Kuala Lumpur using a wind tunnel that was free from external wind conditions. A supporting structure was designed and fabricated to conduct this experiment. The importance of this support structure was to enable the rigid cylinder to suspend and vibrate freely upon excitation of wind speed. The results were analysed through the response of amplitude and frequency of the rigid cylinder over a velocity range of 0.5m/s to 4.0m/s. The results showed that for a square cylinder of $\alpha=0°$, vortex-induced vibration (VIV) occurred at low reduced velocity (U_R) in range of $5 \leq U_R \leq 10$ and galloping occurred at higher reduced velocity which started at $U_R=15$. A tranquil zone was found between VIV and galloping in the reduced velocity range of $10 \leq U_R \leq 15$. As for $\alpha=22.5°$ and $45°$, only VIV response was found at low reduced velocity in range of $4 \leq U_R \leq 9$.

ABSTRAK: Satu kajian eksperimentasi telah dilakukan bagi mengenal pasti pengaruh sudut serangan oleh getaran cetusan-aliran (FIV) dalam silinder persegi. Eksperimen ini dijalankan di Makmal Kejuruteraan Aeronautika dan Angin (AEROLAB), UTM Kuala Lumpur dengan menggunakan terowong angin yang bebas dari pengaruh angin luar. Struktur sokongan telah direka dan difabrikasi bagi tujuan eksperimen ini. Ini penting bagi membolehkan silinder pegun tergantung dan bergetar dengan bebas semasa ujian kelajuan angin. Dapatan kajian dianalisis melalui tindak balas amplitud dan frekuensi silinder pegun pada kadar halaju 0.5m/s sehingga 4.0m/s. Hasil kajian menunjukkan bahawa bagi silinder persegi $\alpha = 0°$, getaran pengaruh-vorteks (VIV) berlaku pada halaju rendah (U_R) dalam julat $5 \leq U_R \leq 10$ dan getaran lebih teruk telah ketara berlaku pada kadar halaju berkurang iaitu bermula pada $U_R = 15$. Zon tenang dijumpai antara VIV dan getaran teruk pada kadar halaju berkurang $10 \leq U_R \leq 15$. Adapun pada $\alpha = 22.5°$ dan $45°$, hanya tindak balas VIV dijumpai pada halaju rendah dalam kadar $4 \leq U_R \leq 9$.

1. INTRODUCTION

Flow-induced vibration (FIV) of a bluff body has received huge attention in various fields such as the aerospace industry, bridges, tall buildings, smokestacks, power generation, and engineering infrastructure. Therefore, FIV has been a hot topic for researchers for the past 20 years and various methods have been undertaken such as experiments and simulations to investigate FIV on cylindrical structures [1-2]. VIV and galloping can be categorized under FIV phenomenon, where VIV occurs at steady conditions while galloping can be considered as unsteady FIV phenomenon that usually arises in asymmetrical bodies. Previous study has reported that galloping usually occurs at high flow speeds [3-10]. Failures or problems that may occur from FIV are usually due to improper design. Therefore, understanding on the characteristic of flow induced vibration is of utmost importance because of its physical applications and the possibility of causing severe damage if improper design is applied. The collapse of the Tacoma Narrows Bridge in 1940 was a well-known accident that was caused by FIV. Due to its catastrophic effects, continuous research on FIV is highly demanded to provide a better understanding of its characteristics in order to avoid such accidents from happening again.

In civil engineering, consideration of wind path over buildings and other rectangular structures is particularly vital as it leads to variation in the structure's angle of attack. Angle of attack can be described as the angle between the reference line of the body and the relative oncoming motion flow such as air and water. The angle of attack may result in uneven pressure distributions that can lead to unpredictable loading patterns. Based on the previous research, study on the effect of angle of attack is very limited.

Nemes et al. [11] is one of the few teams that have investigated the interaction between flow-induced vibration mechanisms of a square cylinder with different angles of attack. The experiment was conducted in a free surface recirculating water channel and reported that VIV and galloping occurred over a narrow range of angles of incidence. Hu et al. [12] conducted an experiment with various angles from $0°$ to $\pm 30°$ and found that as the forward inclination increased, the crosswind responses of the cylinder decreased, while for the backward inclination, the crosswind response did not reduce evenly. On the other hand, Kawai, [13] conducted an experiment in a boundary wind tunnel with three types of flow (smooth flow, turbulent boundary layer flow over open terrain, and turbulent boundary layer flow over urban area). From the results, strong VIV was noticed at angles of attack of $0°$ and $15°$. When the angle of attack exceeded $15°$, VIV became weak and could not be detected in the smooth flow. As for turbulent boundary layer flow over urban area, the weak VIV was still seen for angles of attack greater than $15°$. Galloping was also found in this experiment when the angle of attack was $0°$ with reduced velocity equal to 10. Zhao et al. [14] studied FIV on a square cylinder with two angles of incidence of $0°$ and $45°$. The results showed that galloping occurred at $0°$ while VIV occurred at $45°$. In the literature review, some conflicts of the outputs are found. For example, Obasaju et al. [15] found a tranquil zone between VIV and galloping for $\alpha = 0°$, but Nemes et al. [11] reported no tranquil zone in their study. Other studies did not show relative outputs on this issue [16-20]. Hence, this gains our interest for further investigation of the issue. The main purpose of the present study is to identify the characteristic of the FIV around a square cylinder based on various angles of attack, at the same time clarifying whether the galloping occurs right after VIV or there is a resting gap without the occurrence of galloping and VIV.

2. METHODOLOGY

2.1 Experimental Details

The experiments were conducted in the AF100 subsonic wind tunnel of the Aeronautical and Wind Engineering Lab (AEROLAB) in the University Technology Malaysia, Kuala Lumpur, as shown in Fig. 1. The test section size was 33 cm in width, 35 cm in height, and 70 cm in length. The main objective of this experiment was to identify the effect of different angles of attack towards the FIV of a rigid cylinder with one degree of freedom (1dof). By using three different angles of attack, the behavior of FIV could be observed.

A clear acrylic was used as the material for the square cylinder. Acrylic was chosen because the material is lightweight. The cylinder was attached on the supporting structure using circular acrylic plate with a diameter of 6 cm. Fig. 2 shows the schematic diagram of the angle of attack for the rigid square cylinder.

To analyse the effect of angle of attack, three angles, namely 0 °, 22.5°, and 45°, were tested in the present study. The reason for using these angles is that they correspond to the conditions where the reactions are dominated by VIV and galloping [21]. Table 1 shows the specification of the cylinders.

In order to attach the coiled spring, holes were made at the end of each circular plate. The function of the coiled spring was to suspend the cylinder on the supporting structure. The coiled springs were attached in parallel for both sides. Using laser cutting, 6 holes were made at the circular plate to allow the rigid cylinders to hang in the pre-set angles. The steel supporting structure was made with the dimensions of 29 cm x 29 cm x 29 cm in length, width, and depth, respectively. For the coiled spring, low stiffness was used in the experiment to generate the lock-in condition. The dimensions, the set-up of the rig, and schematic diagram of the experiment are shown in Fig. 3(a), 3(b), and 3(c), respectively.
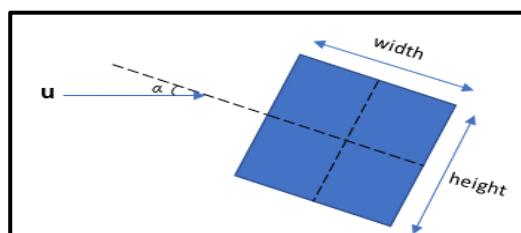

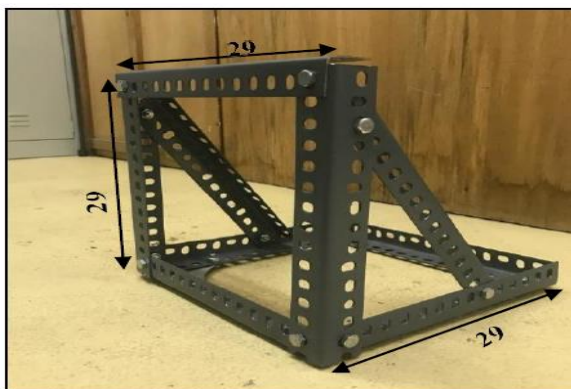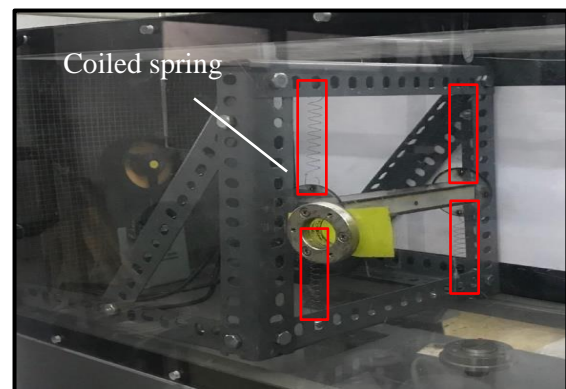Fig. 1: The overview of AF100 Subsonic Wind Tunnel.

Fig. 2: The angle of attack of a square rigid cylinder.

Table 1: Specification of the cylinder

Overview	Dimension (cm)	Weight (g)
	Aspect ratio=1 Width = 3.0 Height = 3.0 Length = 17.5	77.237

(a)

(b)
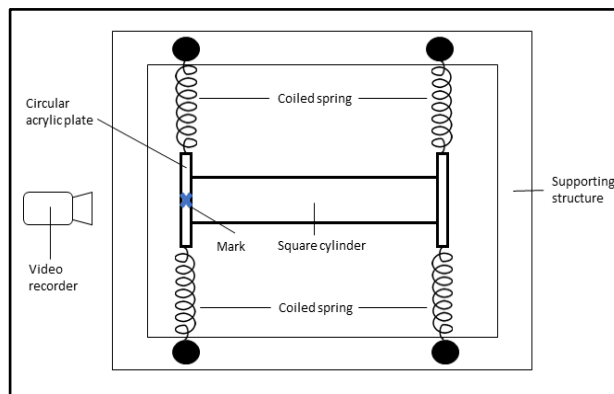
(c)

Fig. 3: (a) The dimensions of the rig. (b) the set-up of the rig and
(c) schematic diagram of the experiment.

2.2 Measuring Equipment

To record all the data obtained from the experiment, it was important to use proper measuring equipment. The equipment used must be sensitive to the vibration test in order to find the dynamic responses of the rigid cylinders. The equipment that was used to gain the results was the GES-28004 anemometer, pitot-static probe, video recorder, and laptop equipped with tracker video analysis and modelling tool software. The uniformity of the wind tunnel was checked using an anemometer and pitot tube as shown in Fig. 4 and Fig. 5, respectively. Anemometer was used to measure the air speed (m/s) in the wind tunnel while

the pitot-static probe was used to measure the pressure (Pa) of air in the wind tunnel. To record the vibration response of the cylinder, a video recorder was used. The video was converted into the amplitude of the vibration using the tracker video analysis modelling tool software, as shown in Fig. 6. In addition, in order to obtain the frequency response of the cylinder, the amplitude data needed to be converted from the time domain into the frequency domain using Fast Fourier Transform (FFT). An FFT Spectrum Analyzer implemented Fourier's basic theorem that denotes any waveform in the time domain by weighting the sum of pure sine waves of all frequencies. From the Discrete Fourier Transform, FFT is developed with the Eq. (1):

$$A(r) = \sum_{k=0}^{N-1} X(s) e^{\frac{-j2\pi}{N^{rs}}} , r = 0,2, \dots , N \qquad (1)$$

In which, $X(s)$ is the periodic wake that is sampled at Nyquist frequency or higher and s is the number of samples collected from original signals.
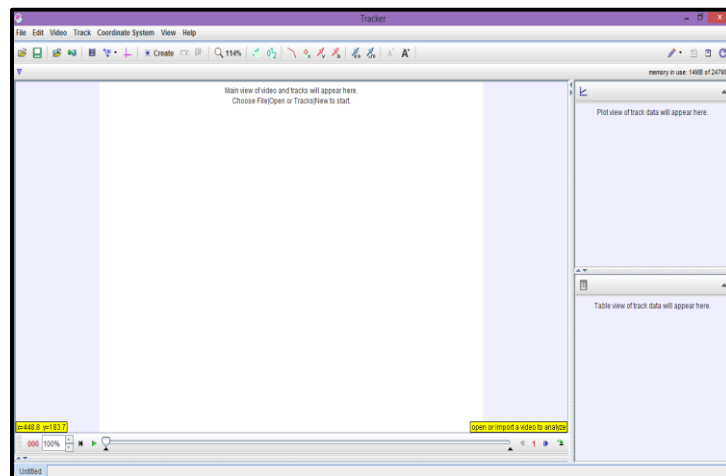

Fig. 4: Anemometer.

Fig. 5: Pitot-static probe.

Fig. 6: Tracker video analysis and modelling tool software.

The supporting structure was placed inside the wind tunnel, while the video recorder was used to record the video of the vibration of the cylinder. The recorder was held by the tripod outside the wind tunnel. The experiments were over a range of velocities from 0.5 m/s to 4.0 m/s, corresponding to the Reynolds number ranging from 16853~134831. The experiment was conducted with three different angles of attack on the square cylinder. The sampling frequency of the video recorder was 30 Hz, which is adequate to collect the motion of the cylinder. The angle was changed in order to observe the dynamic responses at each

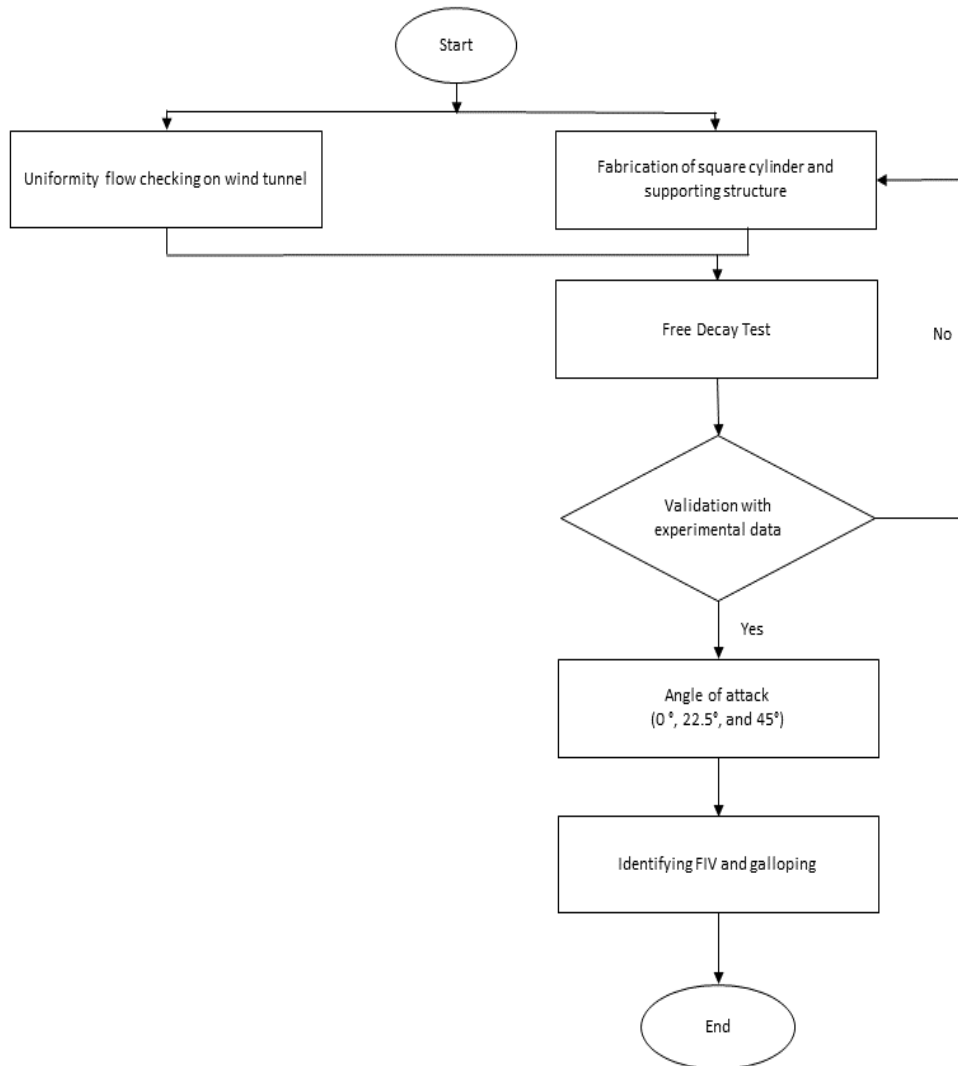angle of attack. The process of the experimental work can be summarized in the flow chart shown in Fig. 7.

Fig. 7: The process of experimental work.

3. RESULTS AND DISCUSSION

3.1 Uniformity of the Flow in Wind Tunnel

Before conducting the experiments, the uniformity of the wind tunnel needed to be checked to ensure the flow was in a uniform condition. Three different velocities were observed, which is 9 m/s, 6 m/s, and 3 m/s.

After obtaining the data, the uniformity of each velocity of the experiment was calculated using this Eq. (2) [22]:

$$\Phi = \sqrt{\sum_{i=1}^{n} \frac{(\beta_i - \overline{\beta})^2}{n}} \qquad (2)$$

where; β_i = Measured value (velocity) $\overline{\beta}$ = Average value (average velocity) n = Number of samples. From the calculations, the results for non-uniformity (Φ) are shown in Table 2. Based on the calculated results, all of the data shows small values, indicating low non-

uniformity of the air flow. Hence, the flow uniformity in the wind tunnel was in good condition, and suitable for use to investigate the effect of FIV on the square cylinders.

Table 2: Non-uniformity at different speeds

Velocity (m/s)	Φ
3	0.149
6	0.103
9	0.063

3.2 Free Decay Test

In this present study, the natural frequency value is important because as the value of the shedding frequency slowly reaches the natural frequency, the vibration of the rigid cylinder will increase to high values. To obtain the natural frequency, a free decay test was conducted by pulling the cylinder downward and allowing it to vibrate freely until it stopped. The natural frequency of the square cylinder was obtained from the power spectrum graph. To verify the experimental value of the natural frequency, the theoretical value of the natural frequency was calculated using Eq. (3):

$$f_n = \frac{\sqrt{\frac{K_{Total}}{m_{Total}}}}{2\pi} \tag{3}$$

where k_{Total} is the stiffness of the system while m_{Total} is the mass of the system. This equation was adopted from previous study of VIV with similar experimental settings [23]. The value obtained for spring stiffness of the system was 119.6 N/m as the springs were attached in parallel. Table 3 shows the value obtained from experiment and calculation. The percentage error is found to be 9.81%. Similar error percentages were also reported in [23] where up to 11.55% of error percentage was achieved using the same equation. Since the error percentage was less than 20%, the experimental value should be acceptable [24]. Hence, the design of the experimental rig was verified. Based on the free decay test, the damping ratio was found to be 0.008185. Because the damping ratio was very low, the damping effect was unaccounted in the present study.

Table 3: The comparison between experimental and theoretical value of the natural frequency

Natural frequency (Hz)		Percentage of error (%)
Experimental value	Theoretical value	
6.783	6.177	9.81

3.3 Verification of the Experiment Data

Strouhal number is a non-dimensional parameter that describes the oscillation of a cylinder. In the present study, the Strouhal number considering the VIV condition was found at 0.1257, as shown in Fig. 8(a) for α=0°. This was in agreement with Okajima [25], who suggested that the Strouhal number of alternating vortices shed from a square cylinder can be estimated to be about 0.13 in the Reynolds-number range between 10^2 and 3.4×10^5.
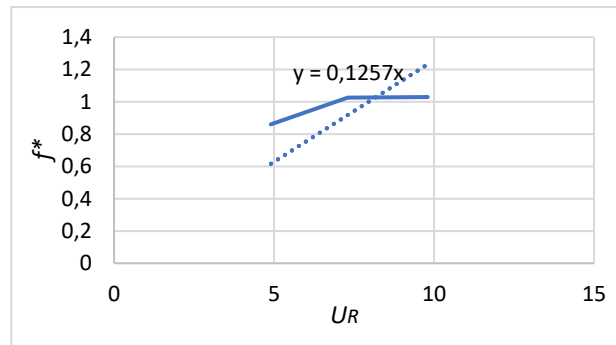
Fig. 8: Frequency ratio versus reduced velocity with angle
of attack $\alpha= 0°$.

Maruai et al. [26] conducted a series of experimental measurements of flow-induced vibration using a square cylinder with a downstream flat plate. In their study, they stated that for an isolated square cylinder, only two significant flow-induced vibration behaviours can be observed, namely, VIV that occurs at lower branch velocity and galloping that occurs at higher branch velocity. To verify the data of the present study, the existing amplitude ratio of an isolated square cylinder [26] was compared with the square cylinder response of the present study, as shown in Fig. 9. The amplitude ratio was defined as $A^*=y/d$ where y is the standard deviation of amplitude and d is the cylinder height. A very similar trend was found with small deviation. The patterns of both studies were in good agreement. The occurrence of VIV in both studies was at a reduced velocity range of $5 \leq U_R \leq 11$ and galloping at $U_R > 15$. The reduced velocity is defined as $U_R=U/f_nd$, where U is free stream velocity, f_n is the natural frequency and d is the cylinder height. However, the amplitude of the present study was slightly lower than the previous study because of the different damping ratio value. Based on Fig. 9, the current experimental work was verified.
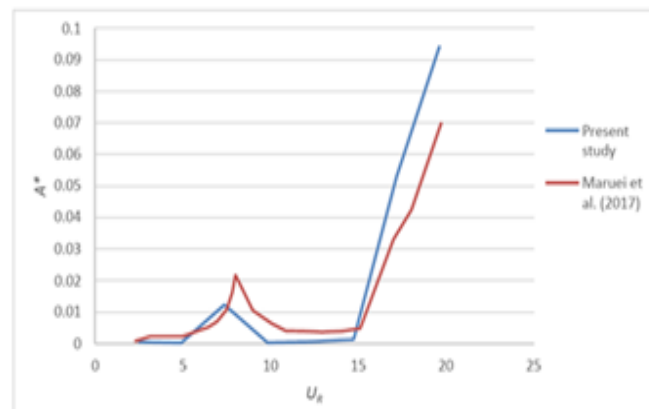

Fig. 9: Amplitude ratio versus reduced velocity of the previous study
[26] and the present study.

3.4 Effect of the Angle of Attack

To investigate the effect of angle of attack on the FIV of the square cylinder, experiments were carried out over a wide range of reduced velocities at angles of attack of $\alpha=0°$, 22.5°, and 45°. Fig. 10 shows the comparison of the amplitude response of various angle of attacks. From the graph, it can be observed that galloping response was only found at $\alpha=0°$ as the vibration amplitude of the cylinder increased with increasing reduced velocity

at U_R =15. Other than that, VIV response was also observed at lower branch of reduced velocity in the range of $5 \leq U_R \leq 10$. On other hand, only VIV behavior was found for square cylinder of α=22.5° and 45° where galloping is absent. Nevertheless, the occurrence of VIV for both angle of attacks is at low reduced velocity range $4 \leq U_R \leq 9$, which was slightly earlier than the cylinder of α=0°. It was also observed that the amplitude of the cylinder at α=22.5° was lower compared to the amplitude of cylinder at α=45°. Based on this finding, it can be concluded that the cylinder of α=22.5° had less tendency towards the VIV response. In fact, Cui et al. [27] also has shown the similar results, where in their study, cylinder of α=22.5° had lower VIV amplitude compared to the others. Next, a region free from VIV and galloping was found at reduced velocity in the range of $10 \leq U_R \leq 15$ for α=0°, which is in agreement with Maruai et al. [26]. Therefore, it can be said that for a square cylinder, a tranquil zone was found between the phenomena of VIV and galloping.
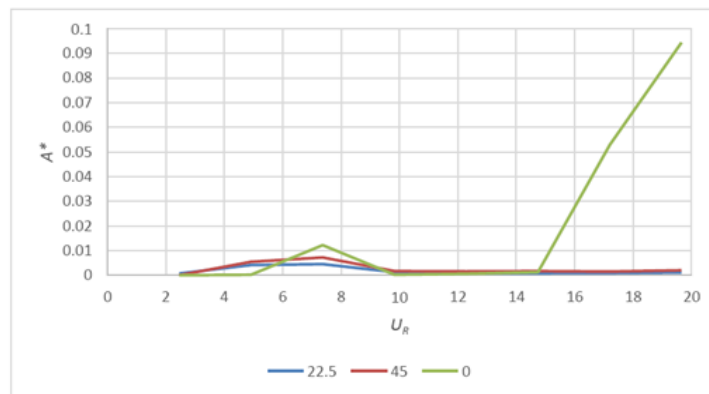

Fig. 10: Amplitude ratio of the rigid cylinder of various angles of attack.
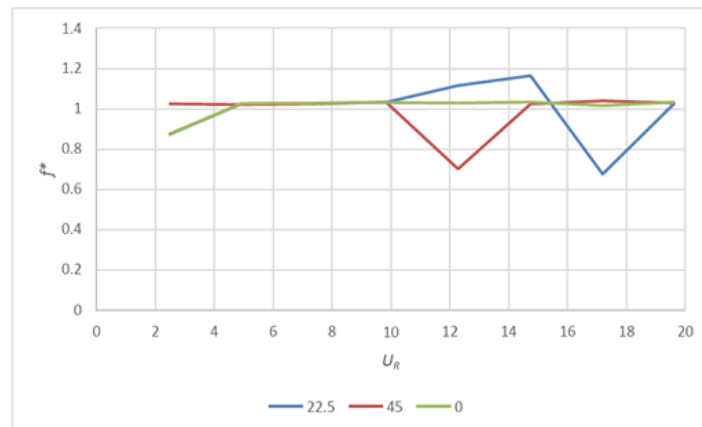

Fig. 11: Frequency ratio of the rigid cylinder of various angles of attack.

Fig. 11 shows the comparison of the frequency ratio of the different angles of attack where frequency ratio is defined as $f^*=f/f_n$, f is the vibrating frequency, and f_n is the natural frequency of the cylinder. As shown in Fig. 11, the frequency ratio was close to 1 as the U_R >5 for α=0°. This indicates that the cylinder underwent lock-in phenomena. Supposedly, the frequency ratio would be slightly higher or lower than 1 when galloping occurred at U_R >15. The same goes for the frequency ratio for α=22.5° and 45°. The frequency ratio of the cylinder was supposedly higher than 1 when U_R>10 and increased monotonically with increasing reduced velocity to indicate that it was outside the lock-in regime and galloping did not occur [27]. However, in the present study, the described condition did not happen. Therefore, the power spectrum graph obtained from the FFT method were investigated in

detail to identify the energies that were possessed by the cylinder at different angles of attack.
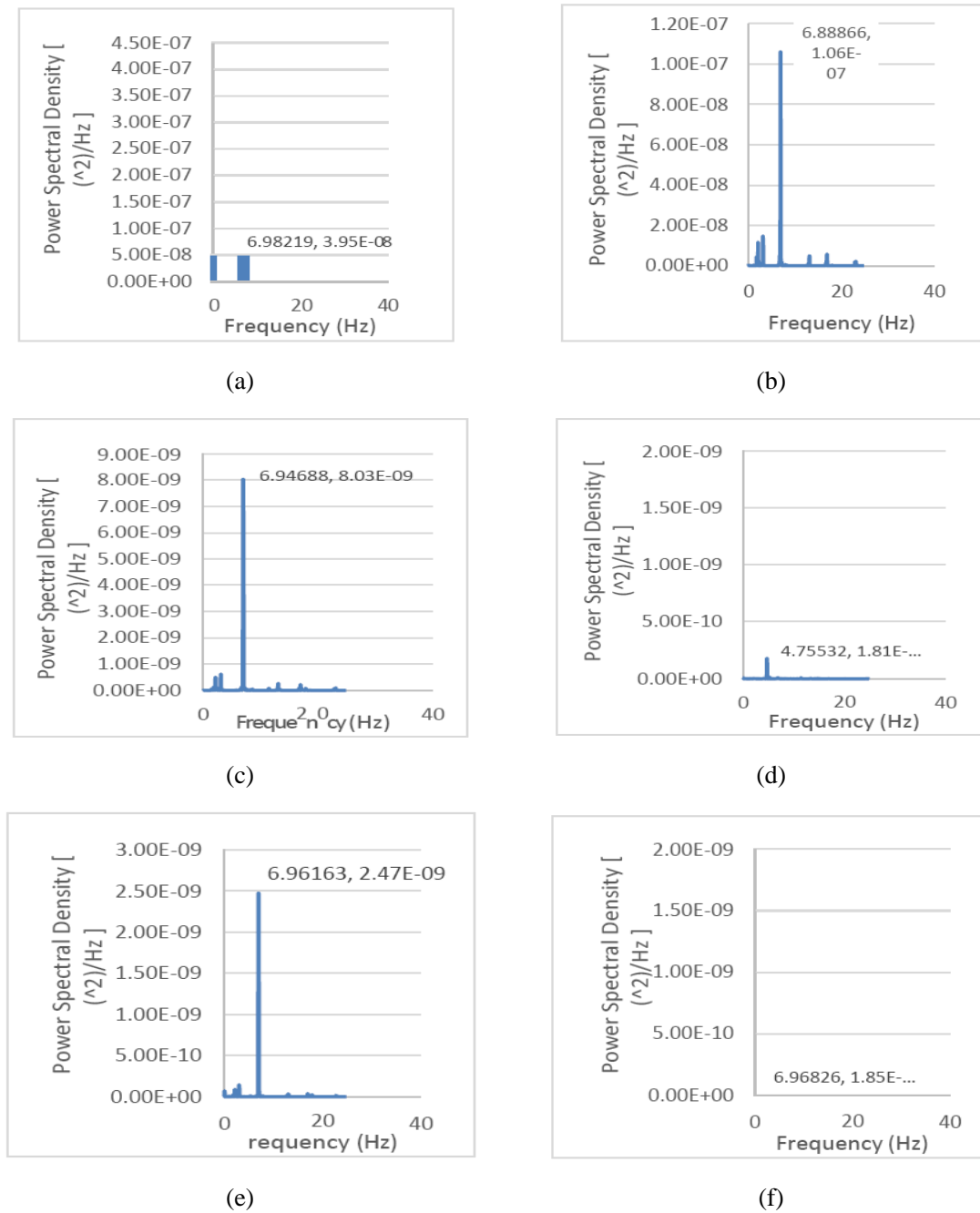

Fig. 12: (a) and (b): U_R =7 and 17 for α=0°; (c) and (d): U_R =7 and 17 for α=22.5°; (e) and (f): U_R =7 and 17 for α=45°.

Fig. 12(a) and (b) show the power spectrum graph of α=0° when U_R =7 and U_R =17 respectively. For the case of α=0°, both VIV and galloping occurred. It was observed that the value of power spectrum density (PSD) at U_R =7 (where the lock-in condition occurred) was lower than the value of the power spectrum density at U_R =17 (where the galloping occurred). This condition can be justified as galloping possesses higher vibration energy than VIV. Fig. 12(c) and (d) show the power spectrum graph of α=22.5° at U_R =7 and 17 respectively, while Fig. 12(e) and (f) show the power spectrum density of α=45° at U_R =7 and 17 respectively. Based on Fig. 12(c-f), it can be seen that the value of power spectrum

density at U_R =17 was lower than U_R =7. This is because there is no occurrence of galloping at U_R =17. In addition, Fig. 12(c) and Fig. 12(e) show a significant PSD peak during lock-in condition (U_R =7). On the contrary, multiple peaks with relatively small PSD values were found at U_R =17 (Fig. 12(d) and (f)). Hence, this justifies that although the frequency ratio remained close to 1 for α=22.5° and 45°, no occurrence of galloping was found and the PSD values were small with multiple frequency peaks.

ACKNOWLEDGEMENT

REFERENCES

[1] Bearman PW, Gartshore IS, Maull DJ, Parkinson GV. (1987) Experiments on flow-induced vibration of a square-section cylinder. Journal of Fluids and Structures, 1(1):19-34. doi:https://doi.org/10.1016/S0889-9746(87)90158-7

[2] A Rahman MA, Wan Hussin WN, Mohd MH, Noor Harun F, Quen LK, Paik JK. (2019) Modified wake oscillator model for vortex-induced motion prediction of low aspect ratio structures. Ships and Offshore Structures, 14(Sup1):1-9. doi:10.1080/17445302.2019.1593308

[3] Khalak A, Williamson CH. (1999) Motions, forces and mode transitions in vortex-induced vibrations at low mass-damping. Journal of fluids and Structures, 13(7-8):813-851. doi:https://doi.org/10.1006/jfls.1999.0236

[4] Bearman PW. (1984) Vortex shedding from oscillating bluff bodies. AnRFM, 16:195-222. doi:https://doi.org/10.1146/annurev.fl.16.010184.001211

[5] Sarpkaya T. (2004) A critical review of the intrinsic nature of vortex-induced vibrations. Journalof fluids and structures, 19(4): 389-447. doi:https://doi.org/10.1016/j.jfluidstructs.2004.02.005

[6] Carberry J, Sheridan J, Rockwell D. (2005) Controlled oscillations of a cylinder: forces and wake modes. Journal of Fluid Mechanics, 538: 31-69. doi:https://doi.org/10.1017/S0022112005005197

[7] Govardhan RN, Williamson CHK. (2006) Defining the 'modified Griffin plot' in vortex-induced vibration: revealing the effect of Reynolds number using controlled damping. Journal of fluid mechanics, 561: 147-180. doi:https://doi.org/10.1017/S0022112006000310

[8] Ng YT, Luo SC, Chew YT. (2005) On using high-order polynomial curve fits in the quasi-steady theory for square-cylinder galloping. Journal of fluids and structures, 20(1): 141-146. doi:https://doi.org/10.1016/j.jfluidstructs.2004.02.008

[9] Klamo JT, Leonard A, Roshko A. (2006) The effects of damping on the amplitude and frequency response of a freely vibrating cylinder in cross-flow. Journal of Fluids and Structures, 22(6-7): 845-856. doi:https://doi.org/10.1016/j.jfluidstructs.2006.04.009

[10] Shirakashi M, Chua CP, Salim SAZS. (2016) Design and fabrication of fiv apparatus for classroom lecture demonstration. Jurnal Teknologi, 78(9): 1-7. doi:https://doi.org/10.11113/jt.v78.4933

[11] Nemes A, Zhao J, Jacono DL, Sheridan J. (2012) The interaction between flow-induced vibration mechanisms of a square cylinder with varying angles of attack. doi:https://doi.org/10.1017/jfm.2012.353

[12] Hu G, Li C, Tse KT, Kwok KCS. (2018) Vortex induced vibration of an inclined finite-length square cylinder. European Journal of Mechanics-B/Fluids, 68:144-152. doi:https://doi.org/10.1016/j.euromechflu.2017.12.004

[13] Kawai H. (1995) Effects of angle of attack on vortex induced vibration and galloping of tall buildings in smooth and turbulent boundary layer flows. Journal of Wind Engineering and Industrial Aerodynamics, 54: 125-132. doi:https://doi.org/10.1016/0167-6105(94)00035-C

[14] Zhou J, Nemes A, Jacono DL, Sheridan J. (2010) The effect of incidence angle variation of a square cylinder on its dynamic response and wake states. In Proceedings of the 17th Australasian Fluid Mechanics Conference, pp. 724-727). Auckland, New Zealand: AFMC

[15] Obasaju ED, Ermshaus R, Naudascher E. (1990) Vortex-induced streamwise oscillations of a square-section cylinder in a uniform stream. Journal of Fluid Mechanics, 213:171-189. doi:http://dx.doi.org/10.11113/jt.v79.9987

[16] Du X, Chen R, Dong H, Ma W, Xu H, Zhao Y. (2021) Aerodynamic characteristics of two closely spaced square cylinders in different arrangements. Journal of Wind Engineering and Industrial Aerodynamics, 208: 104462. doi: https://doi.org/10.1016/j.jweia.2020.104462

[17] Yanovych V, Duda D, Uruba V. (2021) Structure turbulent flow behind a square cylinder with an angle of incidence. European Journal of Mechanics-B/Fluids, 85: 110-123. doi: https://doi.org/10.1016/j.euromechflu.2020.09.003

[18] Cao Y, Tamura T. (2020) Low-frequency unsteadiness in the flow around a square cylinder with critical angle of 14° at the Reynolds number of 2.2× 104. Journal of Fluids and Structures, 97:103087. doi : https://doi.org/10.1016/j.jfluidstructs.2020.103087

[19] Peng S, Wang H, Zeng L, He X. (2019) Low-frequency dynamics of the flow around a finite-length square cylinder. Experimental Thermal and Fluid Science, 109: 109877. doi: https://doi.org/10.1016/j.expthermflusci.2019.109877

[20] Zhao J, Leontini J, Jacono DL, Sheridan J. (2019) The effect of mass ratio on the structural response of a freely vibrating square cylinder oriented at different angles of attack. Journal of Fluids and Structures, 86:200-212. doi: https://doi.org/10.1016/j.jfluidstructs.2019.02.008

[21] Zhao J, Leontini JS, Jacono DL, Sheridan J. (2014) Fluid–structure interaction of a square cylinder at different angles of attack. Journal of Fluid Mechanics, 747: 688-721. doi: https://doi.org/10.1017/jfm.2014.167

[22] Hassan JM, Mohamed TA, Mohammed WS, Alawee WH. (2014) Modeling the uniformity of manifold with various configurations. Journal of Fluids, 2014. https://doi.org/10.1155/2014/325259

[23] Shaharuddin NMR, Darus IM. (2015) Experimental study of vortex-induced vibrations of flexibly mounted cylinder in circulating water tunnel. Acta Mechanica, 226(11): 3795-3806. doi: https://doi.org/10.1007/s00707-015-1438-8

[24] Cecconi M, Rhodes A, Poloniecki J, Della Rocca G, Grounds RM. (2009) Bench-to-bedside review: the importance of the precision of the reference technique in method comparison studies–with specific reference to the measurement of cardiac output. Critical Care, 13(1):1-6. doi:https://doi.org/10.1186/cc7129

[25] Okajima A. (1982) Strouhal numbers of rectangular cylinders. Journal of Fluid Mechanics, 123: 379-398. doi: https://doi.org/10.1017/S0022112082003115

[26] Maruai NM, Mat Ali MS, Ismail MH, Shaikh Salim SAZ. (2017) Downstream flat plate as the flow-induced vibration enhancer for energy harvesting. Journal of Vibration and Control, 24(16): 3555-3568. doi:https://doi.org/10.1177/1077546317707877

[27] Cui Z, Zhao M, Teng B, Cheng L. (2015) Two-dimensional numerical study of vortex-induced vibration and galloping of square and rectangular cylinders in steady flow. Ocean Engineering, 106:189-206. doi:https://doi.org/10.1016/j.oceaneng.2015.07.004

VEHICLE AIR CONDITIONER (VAC) CONTROL SYSTEM BASED ON PASSENGER COMFORT: A PROOF OF CONCEPT

SUROTO MUNAHAR[1], BAGIYO CONDRO PURNOMO[1], MUHAMMAD IZZUDIN[1],
MUJI SETIYO[1*] AND MADIHAH MOHD SAUDI[2]

[1]*Department of Automotive Engineering, Universitas Muhammadiyah Magelang, Magelang 56172, Indonesia*
[2]*Faculty of Science and Technology, Universiti Sains Islam Malaysia, Bandar Baru Nilai 71800, Nilai, Negeri Sembilan, Malaysia*

*Corresponding author: muji@unimma.ac.id

ABSTRACT: The air conditioning system (AC) in passenger cars requires precise control to provide a comfortable and healthy driving. In an AC system with limited manual control, the driver has to repeatedly change the setting to improve comfort. This problem may be overcome by implementing an automatic control system to maintain cabin temperature and humidity to meet passenger's thermal comfort. Therefore, this paper presents the development of a laboratory-scale prototype air conditioning control system to regulate temperature, humidity and air circulation in the cabin. The experimental results show that the control system is able to control air temperature in the range of 21 °C to 23 °C and cabin air humidity between 40% to 60% in various simulated environmental conditions which indicate acceptance for comfort and health standards in the vehicle. In conclusion, this method can be applied to older vehicles with reasonable modifications.

ABSTRAK: Sistem penyejuk udara (AC) pada kenderaan penumpang memerlukan ketepatan kawalan bagi menyediakan keselesaan dan kesejahteraan pemanduan. Melalui sistem AC dengan kawalan manual terhad, pemandu perlu berulang kali mengubah penyesuaian latar bagi meningkatkan keselesaan. Masalah ini dapat diatasi dengan menerapkan sistem kawalan automatik bagi menjaga suhu dan kelembapan kabin agar memenuhi keselesaan suhu penumpang. Oleh itu, kajian ini merupakan pembangunan prototaip sistem kawalan AC skala laboratari bagi mengawal suhu, kelembapan dan peredaran udara dalam kabin. Hasil eksperimen menunjukkan sistem kawalan ini mampu mengendali suhu udara pada kitaran 21 °C hingga 23 °C dan kelembaban udara kabin antara 40% hingga 60% pada pelbagai keadaan persekitaran simulasi yang menunjukkan penerimaan standard keselesaan dan kesejahteraan kenderaan. Sebagai kesimpulan, cara ini dapat diaplikasi pada kenderaan lama dengan modifikasi bersesuaian.

KEYWORDS: *air conditioner; control system; humidity; temperature*

1. INTRODUCTION

The vehicle air conditioner (AC) system was developed to provide passenger comfort. Initially, the AC system was only used to regulate temperature but that is not enough anymore. Although the thermal comfort of building occupants has been studied extensively, in-vehicle thermal comfort is continuously being developed due to its dynamics. Since vehicles operate in a dynamic environment, therefore passenger comfort in the vehicle is very important to ensure people travel safely [1–3]. Moreover, as climate change causes

temperature extremes, a study proposes to formulate new guidelines for car design based on passengers' thermal comfort to avoid health impacts [4].

Apart from temperature, to provide passenger comfort in the targeted cabin, humidity and air circulation speed are also important parts that must be considered [5,6]. Humidity greatly affects health [7,8] and changes in extreme humidity lead to new disease symptoms [9]. Maintaining humidity in the cabin can be done by opening the windows while driving [10]. However, in extreme weather such as summer, connecting cabin space with environment will add excessive load to air conditioning system. On the other hand, if the humidity is too low it can cause dehydration and endanger driving safety due to driving errors [11]. Another method is to put phase change material (PCM) to control humidity and temperature in the car, but it works passively [12]. Temperature-humidity- air circulation speed is interrelated air property [13,14]. The speed of air circulation in vehicle air conditioners is generally controlled manually via a knob on the dashboard, except in modern cars equipped with sophisticated sensors. Manual controls cannot provide good thermal comfort, as airspeed reset is based solely on feedback from the passenger or driver. Therefore, air speed control in an AC system also needs to be developed.

Increasing passenger comfort in the cabin by maintaining temperature has been discussed extensively, both while the vehicle is running and when the vehicle is from a parking location [2,4,12,13,15]. However, the discussion on the integration of temperature-humidity-air speed control systems based on effective human comfort is still very limited, except at the simulation stage [16-18]. Therefore, this study aims to develop a specific air conditioning control system used in vehicles to adjust temperature-humidity-air speed based on effective human comfort (22 °C; 40% to 60% of relative humidity, RH). The lab-scale prototype is tested in a simulation room, conditioned to resemble real environmental conditions. Furthermore, the room temperature was measured using a thermometer, humidity was evaluated by humidity meter, and the airflow meter was applied to estimate airflow.

2. METHOD

2.1 System Description
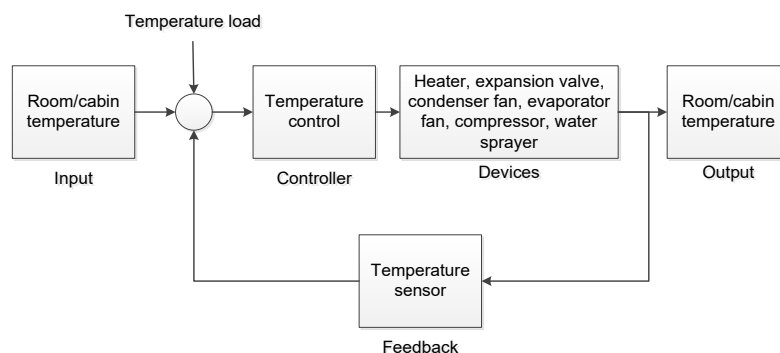
Fig. 1: The block diagram of temperature control.

The system developed is presented in Fig. 1 and Fig. 2. This system has five main blocks including the input, controller, devices, feedback, and output. Temperature control uses a closed loops system, and the feedback mechanism uses a sensor. The prototype has five components, encompassing the heater, condenser fan, evaporator fan, expansion valve, and compressor. The confounding factor of temperature control is the heat load from the

outside. The humidity control system consists of a heater, water sprayer and humidity sensor to provide feedback.

Fig. 2: The block diagram of humidity control.

2.2 Experiment Set-up

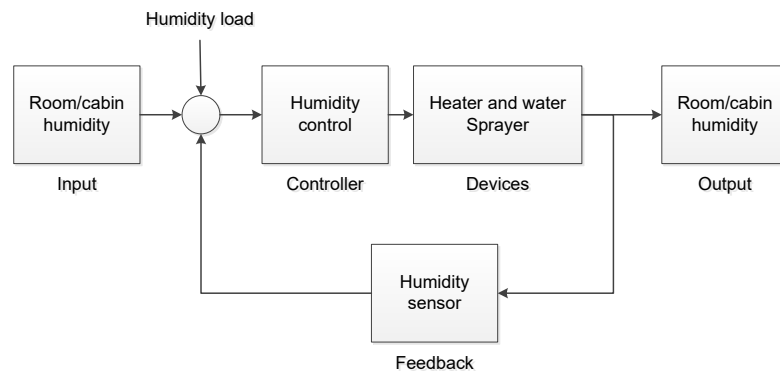Figure 3 shows the experimental set-up which includes the electronic control module (1), evaporator (2), compressor (3), condenser (4), and expansion valve (5). The specifications of each equipment are shown in Table 1. The electronic control module (ECM) consists of a microcontroller, relay, and electronic circuits that are programmed based on the desired needs. The ECM works based on input from temperature and humidity sensors, and produces output to the water sprayer, condenser fan, evaporator fan, heater, and compressor. The performance mechanism of this air conditioning system follows the process shown in Fig. 4. This figure shows a psychometric diagram used to explain the conditions of the cabin space. When the cabin room has a high temperature and humidity (at point 1), the AC system will regulate temperature and humidity in a condition of thermal comfort (point 3). Process from point 1 to point 3 is a process of dehumidifying (1 to 2) and cooling (2 to 3). When a vehicle suddenly passes a highly cold temperatures area, the AC system will turn on the heater (R) to increase the temperature. Likewise, when a vehicle suddenly passes through an immensely low humidity area, the AC system turns on the water sprayer which will spray water (in the form of fog) to increase the humidity in order to achieve thermal comfort conditions.

Table 1: Specifications of the tools used in the study

No	Parts	Specification
1.	Evaporator	Evaporator Unit A3 Toyota; DENSO
2.	Compressor	Type SD505 - SD 505 - Universal Model Sanden, piston type, driven by a 220-volt AC motor with a power of 2 HP.
3.	Expansion valve	TEV type (thermo expansion valve)
4.	Temperature sensor	Sensor type DS18B20; Wrapped in stainless steel pipe; Dimensions 6 x 50 mm; Cable length 100 cm; Power supply 3-5.5V; Temperature range -55 to + 125C; Analog type
5.	Humidity sensor	Dimension: 28.2 x 13.1 x 10 mm; Weight: 6 g; Working voltage: 3V ~ 5.5V; Output signal: digital signal; Temperature measurement range: -40°C to 80 C; Accuracy: 0.5 °C; Humidity range: 0 ~ 100%; RH Accuracy: 2%
6.	Heater	12 volts 300 W with coil type heating element
7.	Simulation environment	Dimension: 1.5 x 1.5 x 3 m

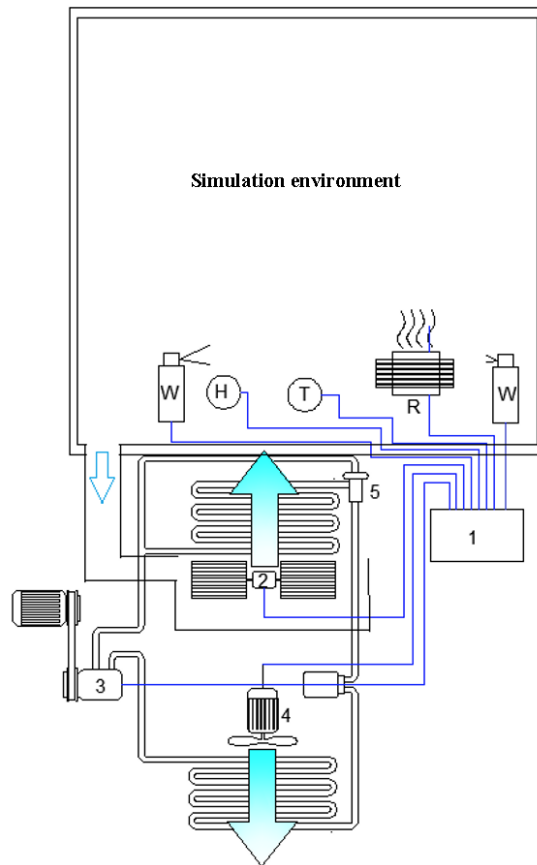Fig. 3: Set up experiment: 1-electronic control module (ECM); 2-evaporator;
3-compressor; 4-condenser; 5-expansion valve; T-temperature sensor;
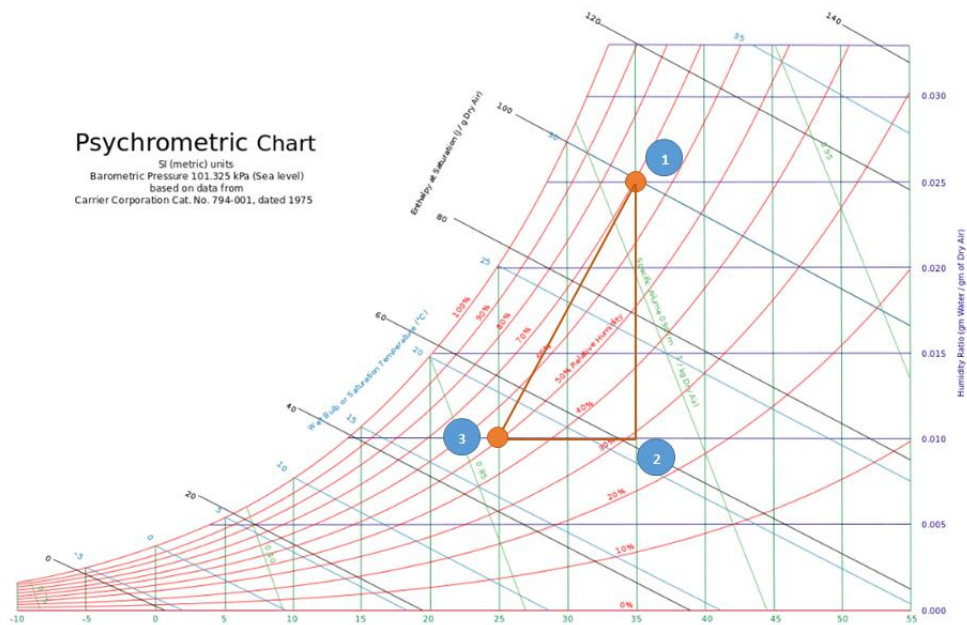H-humidity sensor; W-water sprayer; and R-heater.

Fig. 4: Psychometric chart of AC system.

Installation of heating sensors, water spray, temperature and humidity sensors are paired adjacent to the evaporator. The ECM input includes temperature and humidity

sensors, while the evaporator is mounted in series against the condenser and compressor. This prototype was tested during hot climates with a location in Indonesia which has a longitude position of -7.520639969601074 and latitude 110.22739445901612.

2.3 Logic Rule of Control System

The control system has two subsystems to control temperature and humidity of cabin air as shown in Fig. 5 and Fig. 6. The logic rule of temperature control has a working structure as follows. If the temperature is below 16 °C, the programming statement is set to turn on the heater (R) and turn off the air conditioner but the evaporator fan is on (P1). The length of time the heater runs depends on the high and low temperature of the cabin space, so if the temperature of the cabin space is very low, it takes a longer heater lifetime to achieve thermal comfort. If the temperature of the cabin space is in the range of 17 to 20 °C, then the statement program is set to activate the AC compressor and heater with the evaporator fan at very low speed (P2). The statement program is set to turn on the evaporator fan in a very low position speed to reach a range of 21 to 24 °C (P3) and so on according to Fig. 5.
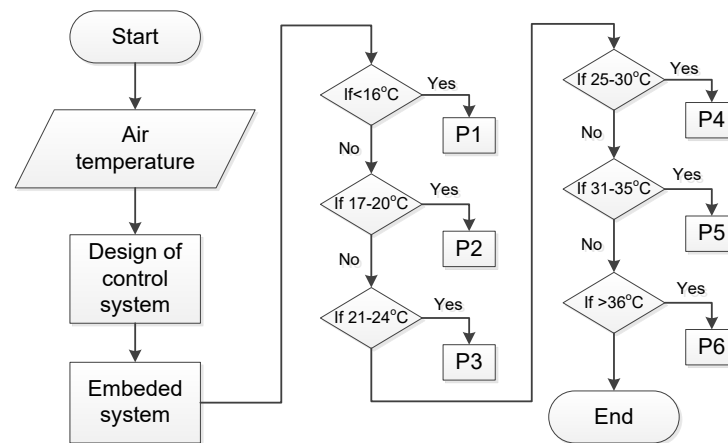
Fig. 5: Logic rule of temperature control system.

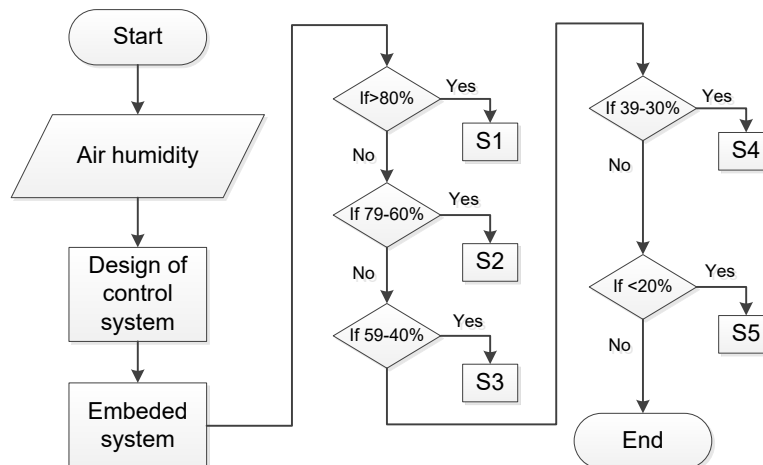Fig. 6: Logic rule of humidity control system.

The cabin temperature is set at 25 to 30 °C, where the programming statement turns on evaporator fan to medium speed position, condenser, and expansion valve are in position 2 (P2). Furthermore, a cabin temperature of 31 to 35 °C requires the statement program to turn on the evaporator fan to high speed, while the condenser fan and expansion valve are

in position 3 (P3). In addition, cabin temperatures above 36 °C require the statement program to turn on a maximum high evaporator fan, while the condenser and expansion valve are in position 4 (P4). Table 2 shows the various temperature control system statements. The condenser fan, compressor and magnetic coupling are connected in one line, so that if the magnetic coupling is on, condenser fan, the compressor will start. Likewise, if the magnetic coupling turns off, the condenser fan, the compressor will shut off.

Table 2: Statement of the air temperature control system

No	Position	Functioning system
1.	P1	• Heater on • Evaporator fan off • Compressor off
2.	P2	• Heater on • Evaporator fan on (min. low speed) • Compressor on
3.	P3	• Heater off • Evaporator fan on (low speed) • Compressor on
4.	P4	• Heater off • Evaporator fan on (medium speed) • Compressor on
5.	P5	• Heater off • Evaporator fan on (hight speed) • Compressor on
6.	P6	• Heater off • Evaporator fan on (max. high speed) • Compressor on

The humidity control system algorithm works with the following conditions. If the humidity in cabin space is more than 80%, the statement program is set to turn on the air conditioning system which aims to remove moisture in cabin space. If the air reads very dry (below 39%), water spray is activated to increase humidity. Meanwhile, if the humidity reads at 40 to 60%, the sprinkler and heater are turned off. Table 3 shows the humidity control system statements and algorithms.

Table 3: Statement of the air humidity control system

No	Position	Functioning system
1.	S1	Heater on
2.	S2	Heater on
3.	S3	-
4.	S4	Sprayer in position 1
5.	S5	Sprayer in position 2

Air temperature and humidity were measured in the cabin space, the lowest and highest values observed were 17 °C and 31 °C, respectively. Meanwhile, the lowest and highest humidity data were obtained in the range of 20% and 84%. Data is collected at 380 meters above sea level. Temperature, air velocity, and humidity data were collected using a digital thermometer, airflow meter and humidity meter, respectively.

3. RESULTS AND DISCUSSION

3.1 Wiring Diagram of Developed Prototype

Integrated control system for cabin room comfort has interconnected parts. The circuit which includes input, controller, actuator, output and feedback is characterized by a sequential working system. The LM 35 sensor is a temperature sensitive device that is known to produce analog signals. Therefore, changes in temperature of simulation room can be detected based on modification of the resistance. The DHT11 sensor is able to detect ambient air humidity by measuring amount of water vapor in simulation room. Figure 7 shows the wiring diagram made.
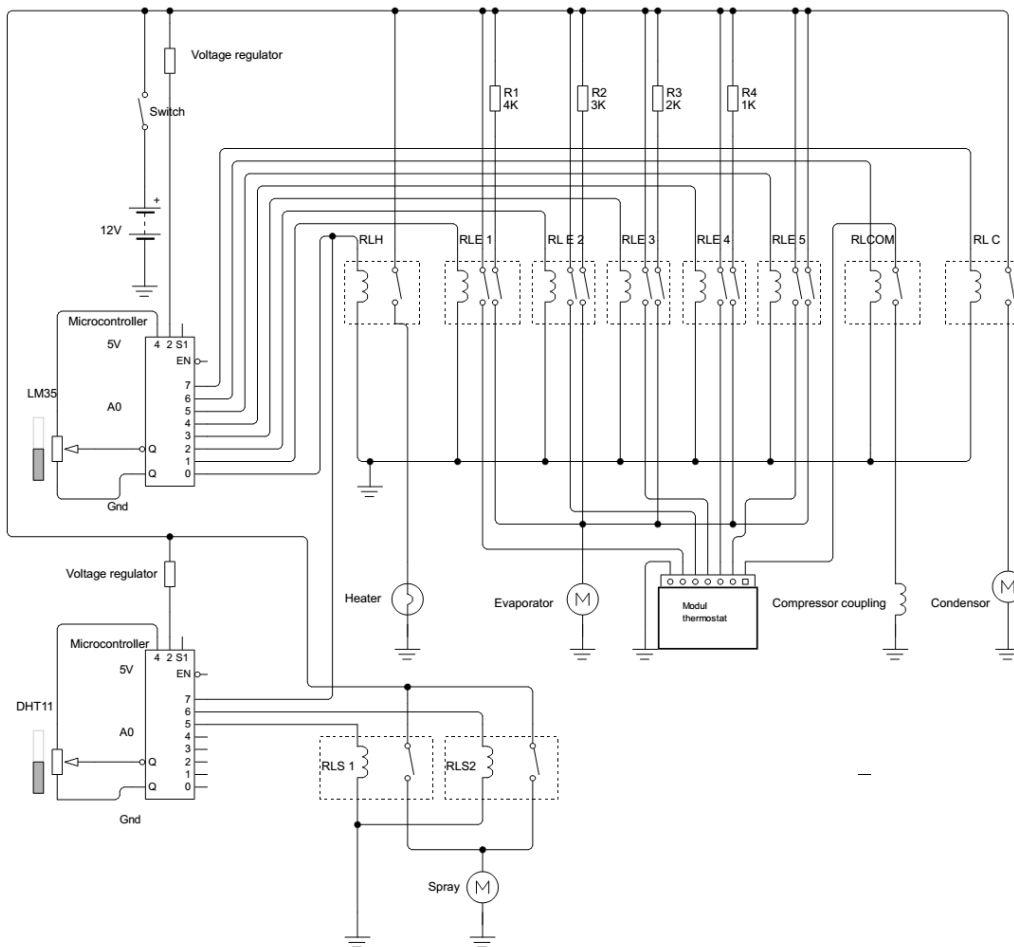
Fig. 7: Wiring diagram of the controller system.

3.2 Air Speed, Temperature, and Humidity Measurement

The automatic integration control system for room comfort was set at 22 °C, based on the effective comfort for humans [19], while the simulation room temperature was obtained from 31 °C. The temperature at the 21st minute has reached a precise setting, and period of decline is affected by thermal load. Furthermore, airspeed is modified based on temperature previously achieved, as 7.8 m/s produced by evaporator fan is generated at 31°C. Based on the evaluation, an automatic decline to 7 m/s was reported at 30°C, and 6.5 m/s was achieved after reaching 22 °C. The controller system subsequently maintains temperature in the range of 21 to 23 °C, and the results in Fig. 8 show comparison between automatic and manual techniques.
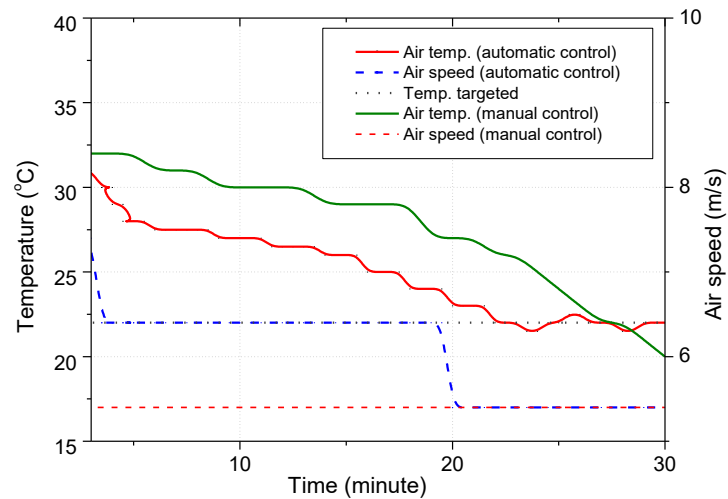
Fig. 8: Temperature and airspeed at the highest temperature position.

Manually controlled air temperatures have several conditions, and 5.5 m/s is used as speed position of evaporator fan. Furthermore, a decline in temperature requires a longer time compared to an automatic control system, as only 18 °C is reached within 30 minutes. This condition possibly occurs due to the presence of constant evaporator fan speed, which does not increase automatically, hence the need to achieve the addition of automatic comfort temperature. In addition, it was not possible for the manual control system to reach an effective position for humans (22 °C) in the 30th minute.

Data were collected at 17 °C, and under this condition, the controller turns on the heater. This subsequently generates heat in the simulation enviroment, while the airspeed assists in spreading the warm air emitted. Furthermore, 20 °C was reached on the 20th minute, and then the control system turns off the heater, subsequently circulating the heat in order to maintain 22 °C. Also, the system works to achieve an effective temperature for humans, and Fig. 9 shows the simulation environment characteristics with the heater. The manually controlled systems require a speed of 5.5 m/s and only 18 °C is reached at the 30th minute. The temperature increase process tends to be slower because the manual controls are not integrated with the heater system. The performance characteristics of the temperature control system are successful in working in the range of 21 °C to 23 °C which is closer to human thermal comfort (effective temperature setting).
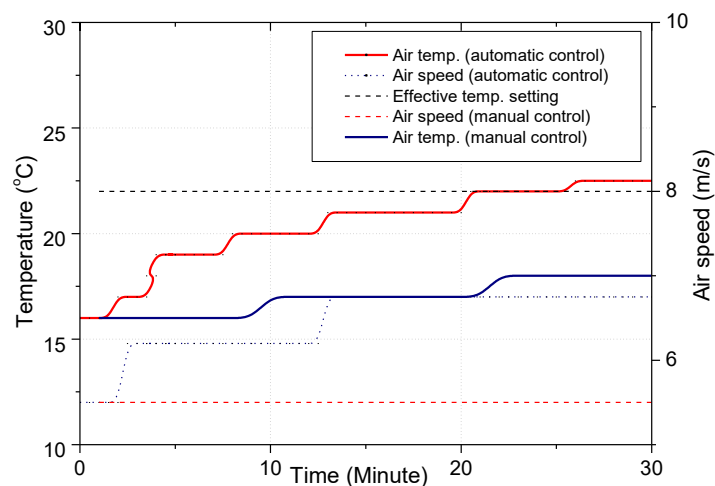

Fig. 9: Temperature and airspeed at the lowest temperature position.

Air humidity data is obtained from simulation chamber at the highest condition of 90%, characterized by relatively large (wet) water vapor content. Furthermore, the automatic control system turns on the heater to 60% position and aimed at achieving the simulation room dry out. The heated air with water vapor content is further removed from the room with a removal system, while the humidity decreases. Meanwhile, the automatic system has the ability to maintain the humidity conditions at 40% to 60%. Figure 10 shows the control system characteristics. The regulation data for air humidity in a manual system is obtained at around 90%, in order to turn on the heater. However, a slight decline was observed at 89% on the 30th minute, resulting from the opened ventilation.
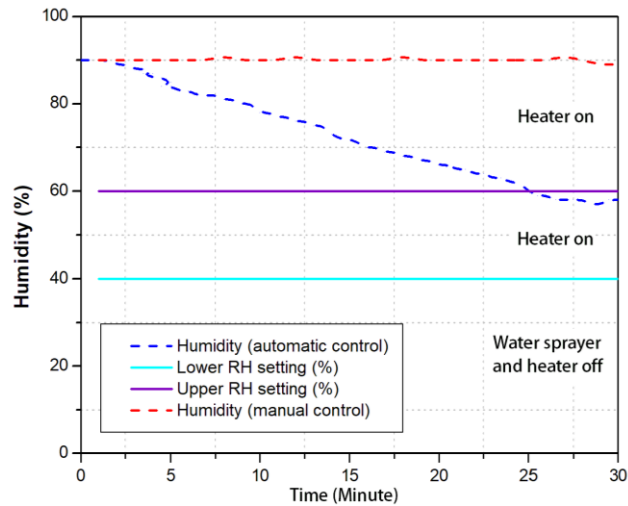
Fig. 10: Air humidity at the highest position.

The air humidity is obtained at the lowest position (dry) in simulation room, using a humidity tester. Therefore, the speed of achieving this condition is increased by exposing the environment to an initial draining process. This involves the removal of hot air, and new data is collected after reaching the least position (dry). The automatic control systems operated is then commenced at the initial lowest humidity level of 20%, where the water sprayer is turned on, and consequently emitting moist mist. Therefore, the humidity slowly increases to 40%, where the sprayer is turned off. This controller system maintains ideal humidity conditions between 40% to 60%, and Fig. 11 shows test results from the lowest humidity position.
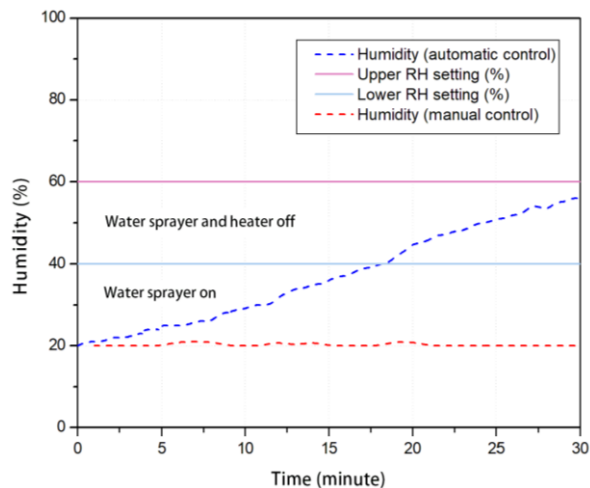
Fig. 11: Air humidity at the lowest position.

Furthermore, the air humidity in a manual system is obtained data at 20% because of the inability to turn on the water sprayer. Hence, there is a high difference between this application and an automatic system with the capacity to reduce and maintain effective humidity for humans. The script programming of the temperature control system is shown in **Appendix 1**.

4. CONCLUSION

Comprehensive conclusion was made based on the test results, which include:

- In the aspect of room temperature, the control system data retrieved was in the highest position (hot), and the automatic control system was able to reduce the room temperature from 31 ℃ to range from 21 °C to 23 °C in 21 minutes. This prototype works according to settings in effective temperature area to attain human comfort. However, the manual controllers only reach 27 °C in 21 minute, hence longer time is required to cool the room, and it is also difficult to achieve optimal temperatures for passengers. Room control systems are tested from the lowest temperature position (cold), where automatic unit turns on heater in the simulation room. Therefore, 17 °C is raised to the settings in range of 21 °C to 23 °C, and the speed temperature fluctuation is influenced by room volume and heater/AC control capacity. Furthermore, effective temperatures are not reached in manual control systems because of the inability to warm up the room.

- Based on the data retrieved, the humidity control system was at the highest position (wet) at 90%. Therefore, the automatic unit turns on the heater system to promote air vapor dryness and subsequent removal from the simulation room. This unit reduces humidity to a range of 40% to 60% (effective humidity for human comfort). Meanwhile, the manual system is unable to cause a decline to the effective value for passengers due to the non-integration with the heater and sprayer.

- Based on the data retrieved, humidity control system was in the least position (dry), working at 20%. Furthermore, automatic unit turns on water sprayer, subsequently leading to higher humidity up to the range of 40% to 60%. Also, it is able to work according to the setting of humans effective comfort, both in terms of temperature and humidity regulation. However, this condition is not attainable by the manual controllers. This is a model study, and the automatic system created shows better work capacity than the manual, hence greater potential for application in the cabin rooms of real vehicles. The fluctuation rate of temperature and humidity is set based on the regulation capacity of the heater, air conditioner, and room volume.

REFERENCES

[1] Kristanto D, Leephakpreeda T. (2017) Sensitivity analysis of energy conversion for effective energy consumption, thermal comfort, and air quality within car cabin. Energy Procedia, 138: 552-557. https://doi.org/10.1016/j.egypro.2017.10.158

[2] Danca P, Nastase I, Bode F, Croitoru C, Dogeanu A, Meslem A. (2019) Evaluation of the thermal comfort for its occupants inside a vehicle during summer. IOP Conference Series: Materials Science and Engineering, 595(1). https://doi.org/10.1088/1757-899X/595/1/012027

[3] Setiyo M, Widodo N, Purnomo BC, Munahar S, Rahmawan MA. (2019) Harvesting cooling effect on LPG-fueled vehicles for mini cooler : A lab-scale investigation. Indonesian Journal of Science & Technology, 4(1): 39-47. https://doi.org/10.17509/ijost.v4i1.12834

[4]   Ravindra K, Agarwal N, Mor S. (2020) Assessment of thermal comfort parameters in various car models and mitigation strategies for extreme heat-health risks in the tropical climate. Journal of Environmental Management, 267: 110655. https://doi.org/10.1016/j.jenvman.2020.110655

[5]   Zhou X, Lai D, Chen, Q. (2019) Experimental investigation of thermal comfort in a passenger car under driving conditions. Building and Environment, 149: 109-119. https://doi.org/10.1016/j.buildenv.2018.12.022

[6]   Shahzad S, Brennan J, Theodossopoulos D, Hughes B, Calautit JK. (2016) The accuracy of thermal comfort zone, ASHRAE Standard 55-2013. CIBSE Technical Symposium. http://hdl.handle.net/10545/620577

[7]   Zhai Y, Zhang Y, Zhang H, Pasut W, Arens E. (2015) Human comfort and perceived air quality in warm and humid environments with ceiling fans. Building and Environment, 90: 178-185. https://doi.org/10.1016/j.buildenv.2015.04.003

[8]   Toftum J, Anette SJ, Fanger PO. (1998) Upper limits for indoor air humidity to avoid uncomfortably humid skin. Energy and Buildings, 28: 1-13. https://doi.org/10.1016/S0378-7788(97)00017-0

[9]   Javadinejad S, Dara R, Jafary F. (2020) Potential impact of climate change on temperature and humidity related human health effects during extreme condition. Safety in Extreme Environments, 2: 189-195. https://doi.org/10.1007/s42797-020-00021-x

[10] Gładyszewska-Fiedoruk K, Teleszewski TJ. (2020) Modeling of humidity in passenger cars equipped with mechanical ventilation. Energies, 13(11). https://doi.org/10.3390/en13112987

[11] Watson P, Whale A, Mears SA, Reyner LA, Maughan RJ. (2015) Mild hypohydration increases the frequency of driver errors during a prolonged, monotonous driving task. Physiology and Behavior, 147: 313-318. https://doi.org/10.1016/j.physbeh.2015.04.028

[12] Afzal A, Saleel CA, Badruddin IA, Khan TMY, Kamangar S, Mallick Z, Samuel OD, Soudagar MEM. (2020) Human thermal comfort in passenger vehicles using an organic phase change material– an experimental investigation, neural network modelling, and optimization. Building and Environment, 180: 107012. https://doi.org/10.1016/j.buildenv.2020.107012

[13] Li CL, Zhang X, Chung SL. (2012) Temperature and humidity control inside an automobile during heating period. Journal of the Chinese Institute of Engineers, Transactions of the Chinese Institute of Engineers, Series A, 35(6): 641-654. https://doi.org/10.1080/02533839.2012.701853

[14] Khatoon S, Kim MH. (2020) Thermal comfort in the passenger compartment using a 3-D numerical analysis and comparison with Fanger's comfort models. Energies, 13(3). https://doi.org/10.3390/en13030690

[15] Purnomo BC, Setiawan IC, Nugroho HA. (2020) Study on cooling system for parked cars using mini air cooler and exhaust fan. Automotive Experiences, 3(2): 81-88. https://doi.org/10.31603/ae.v3i2.3801

[16] Wang Y, Gao Q, Zhang T, Wang G, Jiang Z, Li Y. (2017) Advances in integrated vehicle thermal management and numerical simulation. Energies, 10(10). https://doi.org/10.3390/en10101636

[17] Brusey J, Hintea D, Gaura E, Beloe N. (2018) Reinforcement learning-based thermal comfort control for vehicle cabins. Mechatronics, 50: 413-421. https://doi.org/10.1016/j.mechatronics.2017.04.010

[18] Warey A, Kaushik S, Khalighi B, Cruse M, Venkatesan G. (2020) Data-driven prediction of vehicle cabin thermal comfort: using machine learning and high-fidelity simulation results. International Journal of Heat and Mass Transfer, 148: 119083. https://doi.org/10.1016/j.ijheatmasstransfer.2019.119083

[19] Buonocore C, De Vecchi R, Scalco V, Lamberts R. (2020) Thermal preference and comfort assessment in air-conditioned and naturally-ventilated university classrooms under hot and humid conditions in Brazil. Energy and Buildings, 211: 109783. https://doi.org/10.1016/j.enbuild.2020.109783

Appendix 1: Script Programming

```
const int TemperatureLM35 = A0;
float temperature, data;
const int relay1 = 2 ;
const int relay2 = 3 ;
const int relay3 = 4 ;
const int relay4 = 5 ;
const int relay5 = 6 ;
const int relay6 = 7 ;

void setup() {
 Serial.begin(9600);
pinMode(TemperatureLM35, INPUT);
pinMode(relay1, OUTPUT);
pinMode(relay2, OUTPUT);
pinMode(relay3, OUTPUT);
pinMode(relay4, OUTPUT);
pinMode(relay5, OUTPUT);
pinMode(relay6, OUTPUT);
}
void loop() {
 data = analogRead (TemperatureLM35);
 temperature = data / 2.0408;
 Serial.print("temperature: ");
 Serial.print(temperature);
 Serial.println();
 delay(1000);
 if (temperature <= 16 ) //heater on
{
 digitalWrite(relay1, HIGH);
 digitalWrite(relay2, LOW);
 digitalWrite(relay3, LOW);
 digitalWrite(relay4, LOW);
 digitalWrite(relay5, LOW);
 digitalWrite(relay6, LOW);
}
 else if ( temperature <= 20 )// very low speed
{
 digitalWrite(relay1, HIGH);
 digitalWrite(relay2, HIGH);
 digitalWrite(relay3, LOW);
 digitalWrite(relay4, LOW);
 digitalWrite(relay5, LOW);
 digitalWrite(relay6, LOW);
}
 else if( temperature <= 24)// low speed
{
 digitalWrite(relay1, LOW);
 digitalWrite(relay2, LOW);
 digitalWrite(relay3, HIGH);
 digitalWrite(relay4, LOW);
 digitalWrite(relay5, LOW);
 digitalWrite(relay6, LOW);
}
 else if( temperature <= 30)// medium speed
{
 digitalWrite(relay1, LOW);
 digitalWrite(relay2, LOW);
 digitalWrite(relay3, LOW);
```

```
      digitalWrite(relay4, HIGH);
      digitalWrite(relay5, LOW);
      digitalWrite(relay6, LOW);
      }
     else if (  temperature <= 35)// high speed
     {
      digitalWrite(relay1, LOW);
      digitalWrite(relay2, LOW);
      digitalWrite(relay3, LOW);
      digitalWrite(relay4, LOW);
      digitalWrite(relay5, HIGH);
      digitalWrite(relay6, LOW);
      }
     else if (  temperature >= 36)// very high speed
     {
      digitalWrite(relay1, LOW);
      digitalWrite(relay2, LOW);
      digitalWrite(relay3, LOW);
      digitalWrite(relay4, LOW);
      digitalWrite(relay5, LOW);
      digitalWrite(relay6, HIGH);
     }
     }
```

Meanwhile, the script embedded in the humidity control system is shown as follows =

```
#include <dht.h>
#define sensor A0
dht DHT;
int relay1= 2;
int relay2= 3;
int relay3= 4;
void setup(){
Serial.begin(9600);
delay(500);
pinMode(sensor, INPUT);
pinMode(relay1, OUTPUT);
pinMode(relay2, OUTPUT);
pinMode(relay3, OUTPUT);
}
void loop(){
DHT.read11(sensor);
Serial.print("air humidity = ");
Serial.print(DHT.humidity);
Serial.println("% ");
delay (1000);
int sen = DHT.humidity;
if ( sen <= 20.00){
    digitalWrite(relay1, HIGH);
    digitalWrite(relay2, LOW);
    digitalWrite(relay3, LOW);
}
if ( sen <= 40.00){
    digitalWrite(relay1, HIGH);
    delay(500);
    digitalWrite(relay2, LOW);
    digitalWrite(relay3, LOW);
else if ( sen <= 60.00){
    digitalWrite(relay1, LOW);
    digitalWrite(relay2, LOW);
    digitalWrite(relay3, LOW);
```

```
    }
else if ( sen <= 80.00){
      digitalWrite(relay1, LOW);
      digitalWrite(relay2, LOW);
      digitalWrite(relay3, HIGH);
      delay(500);
   }
else if ( sen <= 100.00){
      digitalWrite(relay1, LOW);
      digitalWrite(relay2, LOW);
      digitalWrite(relay3, HIGH);
}
}
```

Fábregas et al.

COMPUTATIONAL FLUID DYNAMICS MODELING OF MICROCHANNELS COOLING FOR ELECTRONIC MICRODEVICES

JONATHAN FÁBREGAS [1], HENRY SANTAMARÍA[1], EDGARDO BUELVAS[1], SAUL PÉREZ[1], CARLOS DÍAZ[1], JAVIER CARPINTERO[2], RICARDO MENDOZA[3] AND JENNIFER VILLA[2*]

[1]*Faculty of Engineering, Universidad Autónoma del Caribe, Colombia*
[2]*Department of Civil and Environmental, Universidad De La Costa, Calle 58 #55-66, 080002 Barranquilla, Atlántico, Colombia*
[2]*Energy Department, Universidad De La Costa, Calle 58 #55-66, 080002 Barranquilla, Atlántico, Colombia*

*Corresponding author: jvilla27@cuc.edu.co

ABSTRACT: A simulation of the cooling of electronic devices was carried out by means of microchannels, using water as a coolant to dissipate the heat generated from a computer processor, and thus stabilize its optimum operating temperature. For the development of this study, computational fluid mechanics modeling was established in order to determine the temperature profiles, pressure profiles, and velocity behavior of the working fluid in the microchannel. In the results of the study, the operating temperatures of the computer processor were obtained, in the ranges of 303 K to 307 K, with fluid velocities in the microchannels of 5 m/s, a pressure drop of 633.7 kPa, and a factor of safety of the design of the microchannel of 15. From the results, the improvement of the heat transfer in a cooling system of electronic devices was evidenced when using a coolant as a working fluid compared to the cooling by forced air flow traditional.

ABSTRAK: Simulasi penyejukan alatan elektronik telah dibina menggunakan saluran mikro, di samping air sebagai agen penyejuk bagi menghilangkan haba yang terhasil dari pemproses komputer, dan penstabil pada suhu operasi optimum. Kajian ini mengenai model komputasi mekanik bendalir bagi menentukan profil suhu, profil tekanan, dan halaju perubahan bendalir dalam saluran mikro. Dapatan kajian menunjukkan suhu operasi pemproses komputer adalah pada julat suhu 303 K sehingga 307 K, dengan halaju bendalir dalam saluran mikro adalah pada kelajuan 5 m/s, penurunan tekanan sebanyak 633.7 kPa, dan faktor keselamatan 15 bagi reka bentuk saluran mikro. Ini menunjukkan terdapat kenaikan pemindahan haba bagi sistem penyejukan alatan elektronik ini, terutama apabila cecair digunakan sebagai penyejuk haba berbanding kaedah tradisi iaitu dengan mengguna pakai aliran udara sebagai agen penyejuk.

KEYWORDS: *computational fluids dynamics; microchannels; processor; cooling*

1. INTRODUCTION

At present, there is a growing demand for greater performance in electronic devices and for reliability in the level of heat rejection, which make it necessary to create alternatives for the removal of heat and which in turn are much more efficient. Therefore, some alternatives have been presented to solve this problem by developing research using

microchannels (MC). Belhardj et al. [1] used MC with a phase change fluid to improve heat transfer in the cooling of processors.

Chen and Ding [2] analyzed the performance of cooling devices using MC with working fluids of water and nanofluids. Their results showed adequate behavior with the two proposed alternatives. Moreover, Chiu et al. [3] studied the effect of the MC geometry and the pressure used in the heat transfer. It was found that a higher pressure drop improved the heat transfer coefficient. Bosi et al. [4] designed a series of MC modules with different channel separation configurations to study the cooling phenomenon of a silicon pixel detector system. In addition, Brinda et al. [5], in their study, propose a series of MC in a stepped form with a rectangular cross-section to increase the area of the walls, which decreases the thermal resistance and increases the heat transfer coefficient.

Naqiuddin et al. [6] carried out a study applying the technology of MC for the cooling of electronic chips, adapting the principles of straight channels by a segmented method. Modeling was developed for this research by computational fluid dynamics (CFD) and the statistical method of Taguchi-gray to optimize the system according to the required specifications. In other studies, Zhang et al. [7] worked in MC using the effect of the model k-e turbulent in three types of cross-section for the MC. They used circular, trapezoidal, and rectangular sections, comparing the results obtained in terms of heat transfer and mechanics of the fluid, establishing the best design in terms of performance.

Naqiuddin et al. [8] conducted a study on the recent technological advances in electronic systems that use MC systems. In their study, they emphasized the importance of geometry, fluid mechanics, fluid type, phase change, and the applications of the same to improve heat dissipation. Kirsch and Thole [9] evaluated the behavior of MC developed by additive metal fabrication methods with simulated profiles through computational tools, comparing the effect on the performance of the device in the tests performed, highlighting the influence of the roughness present on the surfaces of the elements manufactured with respect to the change of the shape of the profiles.

Yue et al. [10] developed a study by CFD modeling of the segment of a steam turbine separated by MC varying the filling ratio of the refrigerant, finding the optimum operating percentages, and establishing a method to simplify the experiments. A more complete review of the main applications that use CFD for Physical phenomena modeling associated with heat transfer and fluid movement can be found in studies by Hnaien et al. [11] where they compared several turbulence models using computational mechanics to simulate the interaction of parallel jets, highlighting better predictions in the results when using the standard k - ε model.

Mohammed [12] reviewed literature focusing on the use of CM and nanofluids in both experimental and numerical designs, showing in his findings the improvement of heat transfer from devices because of increasing pressure drop. Mohd and Parashram N. [13] in their study used numerical techniques to predict the behavior of the dimensionless Nusselt number, through CFD simulations where the turbulence model SST Gamma-theta has greater precision in convergence. Aqilah et al. [14] performed a mesh effect study on CFD simulations of the aerodynamic profile in an airfoil, indicating the importance of mesh quality when comparing results with experimental studies. Drăgan [15] conducted a performance study of a centrifuge compressor using CFD software to simulate fluid behavior and heat transfer in equipment with optimized design under different operating conditions.

Thome [16] conducted a review study of the effect of boiling in MC devices, for CFD simulations and experiments with two-phase flows, and evaluated the behavior of heat transfer in MC when boiling. Talimi et al. [17] conducted a review on numerical simulation research in small channels in which the hydrodynamic and heat transfer characteristics in non-boiling gas-liquid and liquid-liquid slug flows were studied for circular and non-circular channels. Bagheri-Esfe and Manshadi [18] developed a code for CFD simulations estimating the behavior of flow fields to design a wind tunnel.

Azizi et al. [19] studied gas-solid heat transfer in risers using two-fluid CFD modeling to evaluate the effect of bed angle and particle feed velocity. Villegas et al. [20] used a coupling of computational tools, applying CFD to represent the friction-stir welding phenomenon. Culun et al. [21] developed a synergistic analysis in CFD of heat transfer of impinging multi jets, evaluating parameters such as the geometry of the jet holes, their arrangement, the density of the jets through spanwise and streamwise directions, and the type of confinement. Elsamni et al. [22] used CFD to study the characteristics of laminar flow in a semi-circular duct and the effect of the Reynolds number on the hydrodynamic development length and the friction factor, and subsequently compared them with straight and curved ducts.

Thus, computational modeling through CFD software of the design of the device with MC system starts from the advances of the computational technology of last generation processors, which require a heat removal system that satisfies the conditions for its performance over maximum efficiency. Traditional propeller heatsinks have been in the market for many decades obtaining a good performance in their operation, but as the technology of the processors increases, the system must meet their maximum operation demands. MC technology has had a great impact on cooling processes with good results. Based on these studies and technologies, the design and modeling of a device that satisfies the conditions of the last generation processor is generated.

In this study, a cooling system of an electronic device is evaluated, using water as the working fluid in a MC system, considering the heat transfer and the physical modeling involved in this case, in order to compare the operating temperature of the device with traditional forced airflow cooling. Finally, the safety factor of the MC design is verified in the numerical analysis.

2. MATERIALS AND METHOD

The development and application of phenomena associated with the behavior of CM technology are described by its formulation of mathematical models, as explained below, considering that the modeling equations were made with the use of ANSYS® software.

It begins with a description of the physical phenomena that govern the system. Similarly, the boundary conditions for heat conduction and the thermodynamic relationship of the working fluid with convection heat transfer are exposed. The external and internal working fluids were studied through the logarithmic mean temperature difference to establish the change of temperature in the exchange device system. From the description of the heat transfer model, the variables involved in the process are established to use a computational tool where these values will be entered. Previously, a CAD (Computer-Aided Design) model was developed. Then, an ANSYS CFX tool was used to evaluate the energy, continuity, moment, and turbulence models to obtain the results.

2.1 Physical Modeling

The heat transfer phenomenon to which the MC cooling device is subjected, together with the working fluid and heat dissipation in the computer processor, requires a mathematical model to describe its behavior. Therefore, the following numerical formulations are established. Heat input from processor to MC device is:

$$\frac{\dot{Q}_{CPU}}{A_{s,CPU}} = -k_d \frac{\partial T(0,t)}{\partial y} \tag{1}$$

where k_d is the thermal conductivity of the solid material with which the device MC was designed, $\dot{Q}_{CPU}$ is the heat generated by the processor, $A_{s,CPU}$ is the surface area of contact between the processor and the device MC. Consequently, the liquid used for cooling inside the MC is water, and the heat transfer rate of the coolant without phase change is described with equations (2-3):

$$\dot{Q}_{H2O} = C_{pH2O}\dot{m}_{H2O}(T_{out,H2O} - T_{in,H2O}) = h_{mc}A_{s,mc}(\Delta T_{\ln,mc}) \tag{2}$$

$$\Delta T_{\ln,mc} = \left| \frac{T_{in,H2O} - T_{out,H2O}}{\ln\left(\frac{T_{s,prom} - T_{out,H2O}}{T_{s,prom} - T_{in,H2O}}\right)} \right| \tag{3}$$

Assuming in the first stage of calculation the surface temperature of the MC as average temperature. Where $\dot{m}_{H2O}$ is the mass flow of the coolant (water) and C_{pH2O} is the specific heat, $T_{in,H2O}$ and $T_{out,H2O}$ are the coolant inlet and outlet temperatures in the MC, $T_{s,prom}$ is the average temperature on the surface of the MC, $\Delta T_{\ln,mc}$ is the average log temperature of the MC, h_{mc} is the coefficient of heat transfer by internal convection in the MC. For obtaining the coefficient of heat transfer by convection the number of Nusselt Nu is calculated by Dittus-Boelter equation (4).

For the turbulent regime:

$$Nu = \frac{h_{mc}D_d}{k_{H2O}} = 0.023\,\mathrm{Re}_D^{0.8}\,\mathrm{Pr}^n \tag{4}$$

For the laminar regime with constant heat flux, and the laminar regime with an average surface temperature of constant MC, given the dimensions of the MC, the Nusselt number is:

$$Nu_{\dot{q}} = 4.12; \quad Nu_{T_s} = 3,308; \quad f = 61.144/\mathrm{Re}_D \tag{5}$$

where k_{H2O} is the thermal conductivity of the coolant liquid (water), D_d is the hydraulic diameter before the test section at the entrance, f is the friction factor and the Reynolds number represented by D_d is calculated according to equations (6-7):

$$\mathrm{Re} = \frac{\vec{V}D_d}{v} \tag{6}$$

$$D_d = \frac{4A_c}{p} \tag{7}$$

where $\vec{V}$ represents the velocity of the coolant (water), v is the kinematic viscosity of the coolant (water), A_c is the area of the cross-section located before the test zone and p is the perimeter of this.

The heat generated around the MC device is represented by the equation (8):

$$-k_d \frac{\partial T(L,t)}{\partial y} = h_{2,\infty}\left[T(L,t) - T\infty\right] + \varepsilon\sigma\left[T(L,t)^4 - T\infty^4\right] \tag{8}$$

where $h_{2,\infty}$ is the coefficient of free heat transfer of the material of the device MC with the air environment of the surroundings, $T\infty$ is the environment air temperature of the surroundings, σ is the Stefan-Boltzmann coefficient for radiation, ε is the emissivity of the surface of the MC device. Figure 1 describes the system developed.
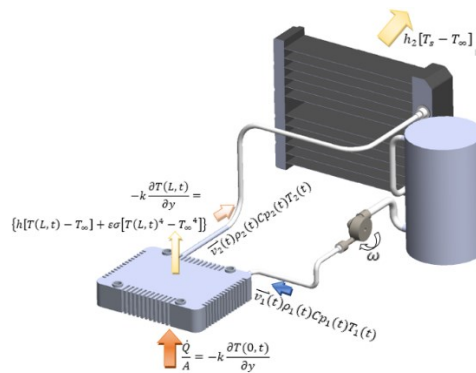
Fig. 1: Representation of the cooling system with the use of MC.

2.2 Computational Model

The design of the MC cooling device was generated because of the size specifications of the last generation processor studied. That is, a compact device made of commercial aluminum that consists of an internal fluid inlet of 3.8 mm in diameter, the constitution of the series of MC of height 0.9 mm and width 0.5 mm, a fluid outlet of 3.8 mm in diameter, as shown in Fig. 2.
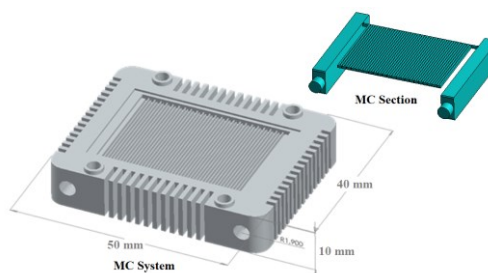
Fig. 2: Geometric representation of the cooling device by MC.

Figure 3 shows the volumetric meshing of the system in which the size of the elements is stipulated for a minimum of 0.015 mm and a maximum of 0.3 mm with a growth rate of 1.2, obtaining an element quality of 82 % indicating a good mesh, for a ratio of 369,995 nodes and 1,047,186 elements in the microchannel system. These meshing data are selected by performing different meshing independence tests according to a response variable, obtaining an error percentage of 0.6%.

The input boundary condition is assigned by the velocity variables and the ambient temperature of 298.15 K of the water domain, the velocity is calculated by the flow and the transverse area of the input.

The boundary condition of the MC cooling device domain presents a set of variables in the initial state, the initial temperature of the medium at 298.15 K, free convection of the medium with the aluminum material at 25 W/m²K. The processor generates a heat flux corresponding to its maximum operation consumption on the surface or base of the MC cooling device and this corresponds to 22,849 W/m² by equation (1).
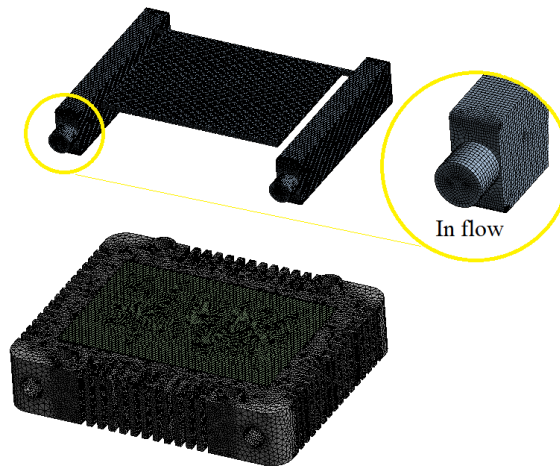

Fig. 3: Volumetric mesh of the microchannel section.

Therefore, the models applied to the system consist of the movement of the working fluid and the heat transfer between the contact interfaces and the environment, for which, the computational models of momentum conservation, energy conservation, and turbulence models for fluid movement are shown in equations (9) to (12).

Momentum conservation:

$$\frac{\partial}{\partial t}(\rho \vec{v}) + \nabla(\rho \vec{v}\vec{v}) = -\nabla p + \nabla\left[\mu\left(\nabla \vec{v} + \nabla \vec{v}^T\right)\right] + \rho \vec{g} + \vec{F} \tag{9}$$

where ρ is the density of the fluid, μ is the dynamic viscosity, p is the pressure, is the dynamic viscosity of the fluid, $\vec{v}$ is the velocity of the fluid.

$$\frac{\partial}{\partial t}(\rho \vec{v}) + \nabla(\rho E) + \nabla \vec{v}(\rho E + p) = \nabla p\left(k_{eff}\nabla T\right) + S_h \tag{10}$$

The equation (10) represents the energy conservation of the system, where the variable k_{eff} is the coefficient of effective thermal conductivity, and S_h represents the energy of the potential chemical system.

Turbulence model *k-ε*:

$$\frac{\partial}{\partial t}(\rho k) + \frac{\partial}{\partial x_i}(\rho k u_j) = \frac{\partial}{\partial x_i}\left[\left(\mu + \frac{\mu_i}{\partial_k}\right)\frac{\partial k}{\partial x_i}\right] + G_k + G_b - \rho\varepsilon - Y_M + S_k \tag{11}$$

$$\frac{\partial}{\partial t}(\rho\varepsilon) + \frac{\partial}{\partial x_j}(\rho k u_j) = \frac{\partial}{\partial x_j}\left[\left(\mu + \frac{\mu_i}{\partial_z}\right)\frac{\partial s}{\partial_j}\right] + \rho C_1 S_\varepsilon - \rho C_2 \frac{\varepsilon^2}{k + \sqrt{v\varepsilon}} + C_{1z}\frac{\varepsilon}{k}C_{3z}G_b + S_z \tag{12}$$

where G_k represents the turbulence generation of the kinetic energy due to the average velocity gradient, Y_M represents the contribution of the incompressible turbulence of fluctuating expansion to the general dissipation rate, and G_b is the generation of turbulence due to the floating kinetic energy. Due to defined boundary conditions and interface domains, a convergence criterion of 1E-04 is established to start the CFD software solver. Table 1 presents the boundary conditions applied to the computational model with the process conditions.

Table 1: Boundary conditions

Conditions	Value
Initial temperature	298.15 K
Heat Flux	22.849 kW/m^2
Pump's rotational Speed	100 – 2000 rpm
External heat transfer coefficient of the microchannel	25 W/m^{2}K
External environment Temperature	298.15 K
Inlet and outlet pipe area	11.341 mm^2
The cross-sectional area of the microchannel	**1.45**m^2

3. RESULTS AND DISCUSSION

The transfer models that govern the design of the MC system were indicated in the modeling of the device. The design was generated from two aluminum materials for the MC device with water as the cooling liquid. The MC cooling device was generated based on the size specifications of the studied computer processor, that is, a compact device using MC in series, the boundary conditions assigned by the variables of velocity and ambient temperature of the water domain, and the limit conditions of the MC cooling device presenting a set of variables in an initial state such as ambient temperature. After the CFD software solution process was complete, the temperature, pressure, and velocity profiles were rendered for analysis purposes. The reading of results was presented in two specific areas, the interior of the MC and the contact surface of the processor-cooling device in planes, therefore, the results of the study carried out are shown in Fig. 4 and 5.
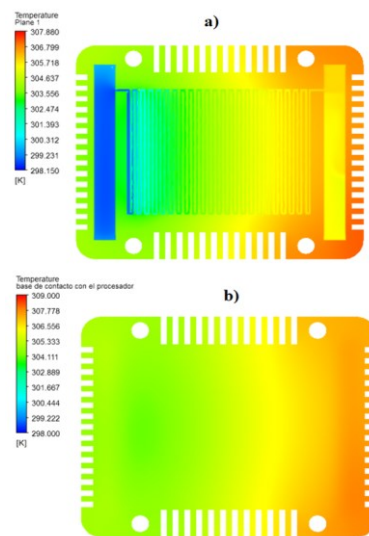

Fig. 4: Temperatures profiles: a) Region of MC, b) Region of processor-cooling device contact.

Figure 4 shows the distribution by contours of the temperature in the device and inside the MC, from which it can be noted that the coolant reached a working temperature of approximately 306 K, while the solid-body reached a temperature of 307.5 K and a minimum temperature of 304 K located in the inlet zone of the coolant to the system. These results of MC temperature profiles were compared with those proposed by Naqiuddin et al. [6], Moradikazerouni et al. [23], and Abdollahi et al. [24]. It was observed that the temperature differences were greater by up to 5 K according to the simulation conditions demonstrating that the operating principle of liquid cooling is adequate to maintain the working conditions of the electronic element, meaning the processor.
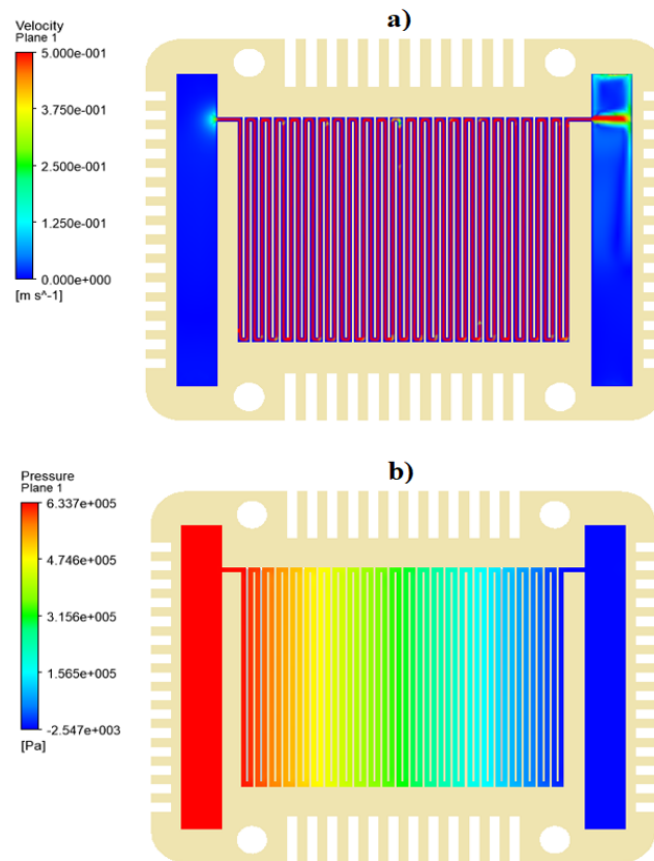
Fig. 5: Profiles in the MC region: a) Speed of the cooling fluid, b) Pressure in the cooling fluid.

In Fig. 5, the velocity and pressure profiles corresponding to the working fluid inside the MC are observed, from which it can be seen that for the flow rate established when using equation (9), the operating pressure at the beginning of the conduit is 633.7 kPa and the speed reached by the liquid in the MC is 0.5 m/s. This relationship shows that increasing the fluid velocities requires a greater pressure range so that the flow parameters remain at the working condition that is required by the processor in terms of temperature. This velocity result is within the range of results obtained by Chiu et al. [3] on hydraulic simulations in the CFDs of microchannels used as heatsinks.

When graphing, there is a line along the length of the device, these represent the temperature curves in two regions, which appear as a result of the system temperature is stabilized from 299 K to 306.4 K together with the MC and the temperature in the region of contact of the device with the processor from 304.5 K to 307.4 K, in the range of the optimum operating temperature of the processor as seen in Fig. 6.
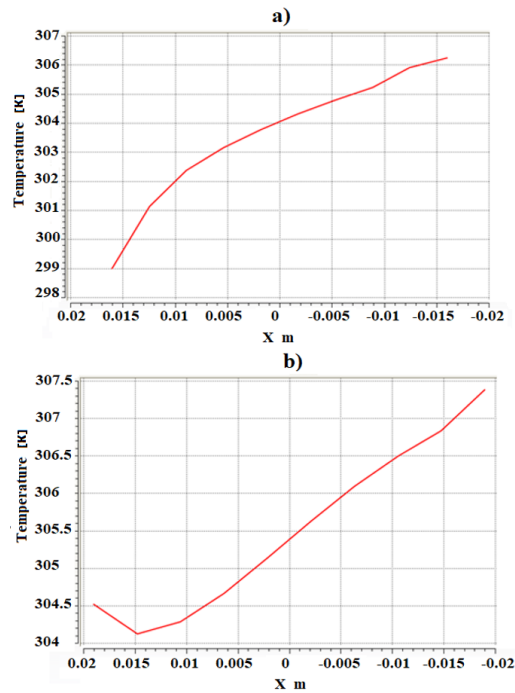
Fig. 6: Temperature curves: a) Region of MC, b) Region of contact processor-cooling device.

The analysis of the behavior of the stabilized temperature in the computer processor was carried out, varying the range of angular velocity from the water pumping system to the MC device, thus obtaining characteristic curves that allowed choosing the best range of speeds to model. Figure 7 shows the graphs of the temperature profile reached in the computer processor, for each point of variation of the angular velocity in the pumping system. It is observed that the angular velocity ranges between 500 rpm and 1000 rpm do not represent a significant variation in the temperature obtained in the computer processor, so this range of velocity is a good option to model the process.
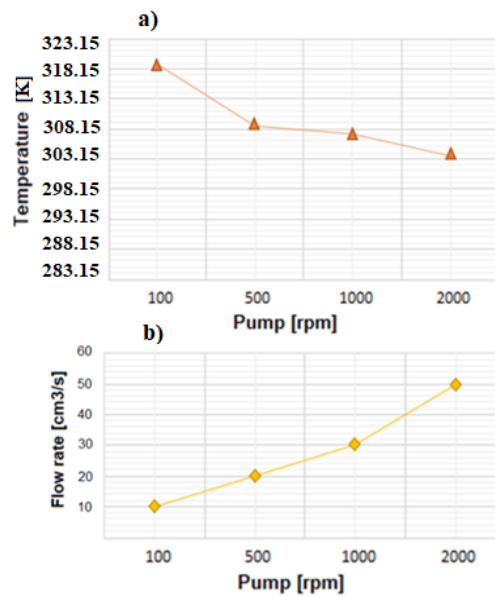
Fig. 7: Temperature & flow rates curves: a) Region of Processor, b) Region of contact processor-cooling device.

Once the fluid dynamic behavior of the working liquid inside the MC system has been evaluated, a multiphysics coupling is made in the simulation software, by importing the pressures reached inside the MC system by the working fluid, in order to analyze in a structural mechanics tool, the stresses caused by this pressure on the walls of the MC. Figure 8 shows the pressure vectors transferred to the structural mechanics' tool.
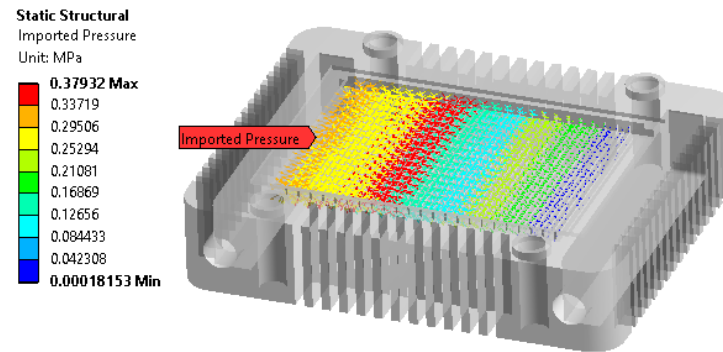
Fig. 8: Pressure imported from CFD tool to structural mechanics' tool.

Upon obtaining the results of the temperature and pressure profiles the coupling between computational tools was performed to determine the effect caused by the pressures reached by the working fluid and the stress it causes on the MC surfaces. The magnitude of the stresses applied to the MC surfaces was obtained using commercial aluminum as the device material, in addition to estimating the safety factor to evaluate the feasibility of manufacturing a physical design under these working conditions. These results are shown in Fig. 9.
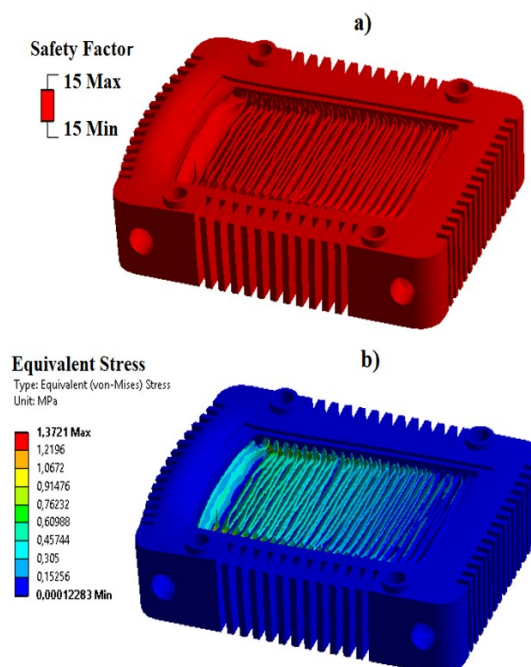
Fig. 9: Design contours: a) Security factor, b) Von Mises stress.

Figure 9 can be analyzed to reveal the maximum applied stress for the pressure conditions generated for the cooling of the electronic processor device. The maximum

applied stress is 1.38 MPa with a safety factor of 15 granting design reliability for the use of a Wide field of pressures used for cooling electronic devices.

Sreehari and Sharma [25] carried out research about the thermal performance in MC using water as the working fluid. The effect of three types of surface engraving that were modeled were compared (rectangular coil, U-curvature coil, and V-shaped coil) and subjected to computational and experimental study. These microchannel systems have a rectangular cross-section with dimensions of 0.6 mm x 0.3 mm using heat flux of 10 kW/m^2, 20 kW/m^2, and 30 kW/m^2. The results have shown an acceptable deviation between the experimental and numerical results with a maximum value of 11%. The rectangular coil behaved similarly to the device analyzed in the present investigation.

4. CONCLUSION

The main motivation for carrying out this study was the fact that the usual working temperatures of a CPU range between 328.15 K and 343.15 K when using the traditional dissipation system for air ventilation, which affects the performance of the device, causing forced labor. On this basis, the following conclusions are drawn when liquid cooling is used in a microchannel-type device.

The main result is that the variables analyzed in the study such as fin geometry and MC distribution influence the heat transfer less than the flow rate used. For low flow rates, the temperature tends to exceed the normal operating range of the system, which implies that the design of the device must have the corresponding mechanical properties for the pressure range in the MC, as well as the supply hoses and the pumping device.

The results of the simulation of the system were analyzed and it was observed that the behavior of the MC cooling device, when the processor is at its maximum use in operations, maintains an optimum working temperature in an average range of 307 K. It should be noted that the value depends on the conditions of fluid entry, such as the flow rate.

It is concluded that at a lower flow rate than the one used in the fluid, the behavior of the temperature exceeds the range of 313 K, which is still suitable for optimal operation for the studied processor which establishes a limit of operation at 333 K and critical state at more than 373 K. The design of the device is suitable for its operation since it has a safety factor of 15 for optimal process conditions using commercial aluminum material, which is a light material and good conductor.

The mesh size was evaluated with respect to the temperature reached by the contact surface with the computer processor. varying the number of elements in the mesh from a default value of 320,775 to 1,047,186, obtaining an error percentage between samples of 0.6%, which is an acceptable value for the reliability of the simulation.

This study consisted of analysis using computational tools to simulate the explained phenomenon. Validations were carried out with works published by various authors applying similar simulation techniques. The experimental validation of the design will be carried out in future studies.

REFERENCES

[1] Belhardj S, Mimouni S, Saidane A, Benzohra M. (2003) Using microchannels to cool microprocessors: A transmission-line-matrix study. Microelectronics Journal, 34(4): 247–253. https://doi.org/10.1016/S0026-2692(03)00004-1

[2] Chen CH, Ding CY. (2011) Study on the thermal behavior and cooling performance of a nanofluid-cooled microchannel heat sink. International Journal of Thermal Sciences, 50(3): 378–384. https://doi.org/10.1016/j.ijthermalsci.2010.04.020

[3] Chiu HC, Jang JH, Yeh HW, Wu MS. (2011) The heat transfer characteristics of liquid cooling heatsink containing microchannels. International Journal of Heat and Mass Transfer, 54(1–3): 34–42. https://doi.org/10.1016/j.ijheatmasstransfer.2010.09.066

[4] Bosi F, Balestri G, Ceccanti M, Mammini P, Massa M, Petragnani G, Ragonesi A, Soldani A. (2011) Light prototype support using micro-channel technology as high efficiency system for silicon pixel detector cooling. Nuclear Instruments and Methods in Physics Research, Section A: Accelerators, Spectrometers, Detectors and Associated Equipment, 650(1): 213–217. https://doi.org/10.1016/j.nima.2010.12.187

[5] Brinda R, Joseph Daniel R, Sumangala K. (2012) Ladder shape micro channels employed high performance micro cooling system for ULSI. International Journal of Heat and Mass Transfer, 55(13–14):3 400–3411. https://doi.org/10.1016/j.ijheatmasstransfer.2012.03.044

[6] Naqiuddin NH, Saw LH, Yew MC, Yusof F, Poon HM, Cai Z, Thiam HS. (2018) Numerical investigation for optimizing segmented micro-channel heat sink by Taguchi-Grey method. Applied Energy, 222: 437–450. https://doi.org/10.1016/j.apenergy.2018.03.186

[7] Zhang Y, Wang S, Ding P. (2017) Effects of channel shape on the cooling performance of hybrid micro-channel and slot-jet module. International Journal of Heat and Mass Transfer, 113: 295–309. https://doi.org/10.1016/j.ijheatmasstransfer.2017.05.092

[8] Naqiuddin NH, Saw LH, Yew MC, Yusof F, Ng TC, Yew MK. (2018) Overview of micro-channel design for high heat flux application. Renewable and Sustainable Energy Reviews, 82: 901–914. https://doi.org/10.1016/j.rser.2017.09.110

[9] Kirsch KL, Thole KA. (2018) Isolating the effects of surface roughness versus wall shape in numerically optimized, additively manufactured micro cooling channels. Experimental Thermal and Fluid Science, 98: 227–238. https://doi.org/10.1016/j.expthermflusci.2018.05.030

[10] Yue C, Zhang Q, Zhai Z, Ling L. (2018) CFD simulation on the heat transfer and flow characteristics of a microchannel separate heat pipe under different filling ratios. Applied Thermal Engineering, 139: 25–34. https://doi.org/10.1016/j.applthermaleng.2018.01.011

[11] Hnaien N, Marzouk KS, Ben HA, Jayb J. (2016) Numerical Study of Interaction of Two Plane Parallel Jets. International Journal of Engineering, 29(10): 1421–1430. https://doi.org/10.5829/idosi.ije.2016.29.10a.13

[12] Mohammed HA, Bhaskaran G, Shuaib NH, Saidur R. (2011) Heat transfer and fluid flow characteristics in microchannels heat exchanger using nanofluids: A review. Renewable and Sustainable Energy Reviews, 15(3): 1502–1512. https://doi.org/10.1016/j.rser.2010.11.031

[13] Mohd Umair S, Parashram Gulhane N. (2016) On numerical investigation of non-dimensional constant representing the occurrence of secondary peaks in the Nusselt distribution curves. International Journal of Engineering, Transactions A: Basics, 29(10):1 431–1440. https://doi.org/10.5829/idosi.ije.2016.29.10a.00

[14] Aqilah F, Islam M, Juretic F, Guerrero J, Wood D, Nasir Ani F. (2018) Study of mesh quality improvement for. IIUM Engineering Journal, 19(2): 203–212. https://doi.org/https://doi.org/10.31436/iiumej.v19i2.905

[15] Drăgan V. (2017) Centrifugal compressor efficiency calculation with heat transfer. IIUM Engineering Journal, 18(2): 225–237.

[16] Thome JR. (2004) Boiling in microchannels: A review of experiment and theory. International Journal of Heat and Fluid Flow, 25(2): 128–139. https://doi.org/10.1016/j.ijheatfluidflow.2003.11.005

[17] Talimi V, Muzychka YS, Kocabiyik S. (2012) A review on numerical studies of slug flow hydrodynamics and heat transfer in microtubes and microchannels. International Journal of Multiphase Flow, 39: 88–104. https://doi.org/10.1016/j.ijmultiphaseflow.2011.10.005

[18] Bagheri-Esfe H, Manshadi MD. (2018) A low-cost numerical simulation of a supersonic wind-tunnel design. International Journal of Engineering, Transactions A: Basics, 31(1): 128–135. https://doi.org/10.5829/ije.2018.31.01a.18

[19] Azizi K, Keshavarz Moraveji M. (2017) Computational fluid dynamic- two fluid model study of gas-solid heat transfer in a riser with various inclination angles. International Journal of

Engineering, Transactions A: Basics, 30(4): 464–472. https://doi.org/10.5829/idosi.ije.2017.30.04a.02

[20] Villegas JF, Guarín AM, Unfried-Silgado J. (2019) A Coupled Rigid-viscoplastic Numerical Modeling for Evaluating Effects of Shoulder Geometry on Friction Stir-welded Aluminum Alloys. International Journal of Engineering, Transactions B: Applications, 32(2): 184–191. https://doi.org/10.5829/ije.2019.32.02b.17

[21] Culun P, Celik N, Pihtili K. (2018) Effects of design parameters on a multi jet impinging heat transfer. Alexandria Engineering Journal, 57(4): 4255–4266. https://doi.org/10.1016/j.aej.2018.01.022

[22] Elsamni OA, Abbasy AA, El-Masry OA. (2019) Developing laminar flow in curved semi-circular ducts. Alexandria Engineering Journal, 58(1): 1–8. https://doi.org/10.1016/j.aej.2018.03.013

[23] Moradikazerouni A, Afrand M, Alsarraf J, Mahian O, Wongwises S, Tran MD. (2019) Comparison of the effect of five different entrance channel shapes of a micro-channel heat sink in forced convection with application to cooling a supercomputer circuit board. Applied Thermal Engineering, 150: 1078–1089. https://doi.org/10.1016/j.applthermaleng.2019.01.051

[24] Abdollahi A, Mohammed HA, Vanaki SM, Osia A, Golbahar Haghighi MR. (2017) Fluid flow and heat transfer of nanofluids in microchannel heat sink with V-type inlet/outlet arrangement. Alexandria Engineering Journal, 56(1): 161–170. https://doi.org/10.1016/j.aej.2016.09.019

[25] Sreehari D, Sharma AK. (2019) On thermal performance of serpentine silicon microchannels. International Journal of Thermal Sciences, 146: 1-14. https://doi.org/10.1016/j.ijthermalsci.2019.106067

COMPARATIVE STUDY ON DEGRADATION OF POLYLACTIC ACID/ *SYZYGIUM AROMATICUM* COMPOSITES AGEING IN OUTDOOR ENVIRONMENT AND SOIL BURIAL

SALINA BUDIN*, NORMARIAH CHE MAIDEEN, KOAY MEI HYIE, HAMID YUSSOF AND HALIM GHAFAR

School of Mechanical Engineering, College of Engineering, Universiti Teknologi MARA, Cawangan Pulau Pinang, Jalan Permatang Pauh, 13500 Penang, Malaysia

*Corresponding author: salinabudin@uitm.edu.my

ABSTRACT: Major environmental problems resulting from non-degradable components of plastic wastes have awakened great attention to bioplastic as an alternative material. Among various bioplastic materials, polylactic acid (PLA) is recognised as a promising material especially as a food packaging material. The development of PLA composites using various fillers has extensively been in focus in order to preserve the high quality, safety, and extended shelf-life of packed food. Among the interesting fillers is *Syzygium aromaticum* (SA). SA, also known as clove, has biological activities such as antibacterial, antifungal, insecticidal, and antioxidant properties. This work investigated the effects of SA filler on the degradations of virgin PLA (VPLA) and recycled PLA (RPLA). The VPLA/SA composites and RPLA/SA composites were prepared using the solvent casting method. The content of SA filler varied in the range of 0 to 20 wt%. The composites were aged in outdoor environment and soil burial. The results revealed that the degradation rate was increased with the increase of SA filler in both ageing environments. After 10 weeks of ageing in the outdoor environment, the weight loss of VPLA/SA composites and RPLA/SA composites containing 20 wt% of SA were 7.7% and 12.8% respectively. Whereas in soil burial, the weight loss of VPLA/SA composites and RPLA/SA composites with similar SA content were 25.6% and 38.3% respectively. The degradation rate was observed to be more rapid in the soil burial as compared to the outdoor environment. Comparably, RPLA and RPLA/SA composites experienced higher degradation rates than VPLA and VPLA/SA composites. The degradation rate was consistent with scanning electron microscope (SEM) images which observed the formation of holes, cavities, cleavages, and grooves on the surfaces of the samples. Thermogravimetric analysis (TGA) results on aged samples showed that VPLA/SA composites and RPLA/SA composites that had aged in soil burial decomposed at lower temperatures. The shortening of degradation time of the VPLA/SA composites and RPLA/SA composites could increase their potential to be used as food packaging materials.

ABSTRAK: Masalah utama terhadap alam sekitar yang disebabkan oleh sisa plastik yang sukar terurai, telah menarik perhatian terhadap bioplastik sebagai bahan alternatif. Di antara pelbagai jenis bahan bioplastik sedia ada, asid polilaktik(PLA) dilihat sebagai bahan yang paling sesuai terutamanya sebagai bahan pembungkusan makanan. Perkembangan di dalam penghasilan komposit asid polilaktik yang ditambah dengan pelbagai bahan pengisi telah menjadi fokus terutamanya bagi tujuan meningkatkan kualiti, kesegaran dan jangka hayat makanan. Salah satu pengisi yang mendapat perhatian adalah *Syzygium aromaticum* (SA). SA yang juga dikenali sebagai bunga cengkeh mempunyai aktiviti biologi, seperti sifat antibakteria, antijamur, racun serangga dan antioksidan yang tinggi. Didalam kajian

ini, siasatan terhadap kesan penambahan SA terhadap penguraian PLA asal (VPLA) dan PLA kitar semula (VPLA). Komposit VPLA/SA dan komposit RPLA/SA disediakan dengan menggunakan kaedah pelarutan pelarut. Kandungan pengisi SA adalah didalam julat 0 – 20% mengikut berat. Komposit tersebut dibiarkan menua didalam persekitaran luaran dan didalam tanah. Keputusan kajian mendapati bahawa kadar penguraian semakin meningkat dengan penambahan peratus berat bahan pengisi SA setelah melalui penuaan didalam kedua-dua persekitaran. Setelah penuaan selama10 minggu di dalam persekiran luaran, pengurang berat komposit VPLA/SA dan komposit RPLA/SA yang mengandungi 20 wt% SA adalah 7.7% dan 12.8%. Manakala bagi penuaan didalam tanah, pengurangan berat komposit VPLA/SA dan komposit RPLA/SA dengan kandungan SA yang sama masing-masing adalah 25.6% dan 38.3%. Kadar penguraian diperhatikan lebih cepat bagi penuan didalam tanah dibandingkan dengan penuaan didalam persekitaran luaran. Disamping itu, RPLA dan komposit RPLA/SA mengalami kadar penguraian yang lebih tinggi berbanding VPLA dan komposit VPLA/SA. Kadar penguraian adalah konsisten dengan imej yang dihasilkan oleh imbasan mikroskop elektron (SEM) dimana dapat dilihat pembentukan lubang, rongga, pembelahan dan alur di permukaan sampel. Hasil analisis termogravimetri (TGA) terhadap sampel yang telah dituakan menunjukkan bahawa komposit VPLA/SA dan komposit RPLA/SA yang melalui penuaan didalam tanah terurai pada suhu yang lebih rendah. Tempoh penguraian komposit VPLA/SA dan komposit RPLA/SA yang lebih pendek ini meningkatkan potensi penggunaannya komposit ini sebagai bahan pembungkusan makanan.

1. INTRODUCTION

Huge employment of plastic materials in various fields is derived from its excellent properties such as its light weight, flexibility, strength, transparency, permeability, and cost-effectiveness [1]. Approximately 50% of plastics are used for single-use disposable applications, such as packaging, agricultural films, and disposable consumer items [2]. These have led to the continuous generation of bulk plastic wastes that have ended with environmental and marine issues. It has been reported that at least 180 kinds of marine organisms have been detected consuming plastics by mistake ranging from whales to planktons [3]. Most commercial plastics are non-biodegradable, highly resistant to microbial attacks, and require a longer time to degrade, which will be approximately around 10 to 1000 years. The issue related to plastic waste management and its disposal is seen to be the main inspiration for the commercialisation of bioplastics. Bioplastics are plastics materials produced from renewable biomass sources, such as vegetable fats and oils, corn starch, straw, woodchips, sawdust, and recycled food waste. Various bioplastic materials are available such as polyhydroxy-alkanoates (PHA) and poly-3-hydroxybutyrate (PHB). Among these, polylactic acid (PLA) is the most popular bioplastic which has higher potential in replacing fossil-based commercial plastic. PLA is biobased and easily compostable with a relatively higher production produced by fermentation from renewable substrates such as sugar, starch, sugarcane, corn, beets, rice, and carbohydrates from other crops [4,5]. As a bioplastic material, PLA completely decomposes to CO_2 and H_2O as final degradation products without contributing any harmful effects to the environment. Moreover, it was reported that PLA will take at least 2 years to be fully degraded under normal circumstances [3].

Both the chemical and physical properties of PLA influence the mechanisms of biodegradation. The surface area, hydrophilic or hydrophobic properties, chemical structure, molecular weight, glass transition temperature, melting temperature, modulus of elasticity, crystallinity, and crystal structure of polymers play important roles in the biodegradation

processes [6]. Degradation of PLA is primarily due to the hydrolysis of the ester linkages which occurs more or less randomly along the backbone of the polymer. In the presence of water, the hydrolysis takes place via a diffusion reaction mechanism whereby water penetrates the polymer matrix and simultaneously converts the long polymer chain to low molecular weight, water soluble oligomers, and finally the given monomer [7]. It is noteworthy that under UV irradiation and light exposure, the hydrolysis of the PLA molecular chain is accomplished through photocleavage, photolysis, and photooxidation [8]. Photolysis leads to chain scission especially in the C–O bonds of the PLA ester backbone structure through the absorption of a photon while photocleavage takes place at the ester group and ethylidene group next to the ester oxygen in the PLA structure leading to chain cleavage and the formation of C=C double bonds and carboxylic acid –OH stretching. Photooxidation of PLA results in the formation of hydroperoxide derivative and its subsequent degradation into carboxylic acid and diketone end groups [9]. The presence of moisture in the environment would further promote the hydrolysis degradation of PLA.

PLA has been recognised by the United States Food and Drug Administration (FDA) as a safe material for food packaging [10]. However, brittleness, low heat distortion temperature, and poor antioxidant, antibacterial, and barrier properties have only limited its application [11]. In order to have high quality, safe packaging and extend the shelf-life of packed food, the packaging material must be able to reduce or retard the growth of microorganisms and inhibit the process of lipid oxidation [12]. The addition of antibacterial and antioxidant agents in PLA substrate is one of the rational solutions. Moreover, the addition of filler in PLA substrate would also accelerate the degradation and decomposition of the PLA. A higher degradation rate would assist in accelerating PLA waste degradation, especially for single-use products. Several efforts have been devoted to the modifications of PLA by incorporating various fillers in order to improve those properties. Many studies on fillers reacted as antioxidant, antimicrobial, antibacterial, and degradation accelerator agents have been conducted with fillers such as chitosan, cinnamaldehyde, *Syzygium aromaticum* (clove), *Melissa officinalis L.* (lemon balm), *Salvia officinalis* (sage), zinc oxide (ZnO), titanium oxide (TiO), magnesium oxide (MgO) and calcium carbonate [13-17].

Besides that, past research has been investigated globally in order to improve the desirable properties for food packaging applications. Zhang et al. [18] synthesised PLA/cinnamaldehyde (CA) films. The findings proved that the morphology, crystallinity, oxygen resistance, water resistance, and tensile strength properties were improved. The antibacterial activity against *Escherichia coli* and *Monocytogenes* was 100%. Similar results were also published by Cui et al. [19]. On the other hand, Ahmed et al. [11] developed PLA/ PEG/PCL films loaded with ZnO and SA/clove essential oil (CEO). The results showed that the reinforcement of ZnO and CEO were significant in the mechanical properties and structural and barrier properties of the films. Meanwhile, Chen et al. [12] investigated the effects of polyvinyl alcohol (PVA) film with an addition of clove oil (CO). It was concluded that the incorporation of CO in PVA films had demonstrated effective antimicrobial and antioxidant activities. However, the mechanical properties, oxygen barrier properties, and thermal stability of the films were reduced.

Techawinyutham et al. [20] also reported on the improvement of tensile properties and antibacterial activity with the addition of capsicum oleoresin impregnated porous silica (SiCO). The authors have remarked that the tensile properties, thermal stability, and rheological properties were reduced when the films underwent ageing in accelerated weathering for 520 hours. However, the aged samples showed good antimicrobial activity against bacteria. In other research done by Varsavas and Kaynak [21], the mechanical properties of neat PLA and PLA/glass fibre composite (PLA/GF) under outdoor conditions

were evaluated. The samples were exposed to accelerated weathering conditions of both UV-irradiation and moisture cycles. The authors observed that the decreased in mechanical properties of neat PLA was more significant as compared to PLA/GF composite. After 400 hours of ageing, the reduction in the tensile strength of the neat PLA specimen was as much as 92%, while the reduction for the PLA/GF specimen was only 34%.

In other works, Fathima et al. [22] have developed PLA/chitosan films to evaluate the antimicrobial activity of the films against *E. coli* and *Listeria monocytogenes*. The results revealed that incorporation of chitosan in PLA was capable of producing packaging films with good mechanical, barrier, and antimicrobial properties. On the other hand, Hadidi et al. [23] reported that PLA composites with chitosan nanoparticles encapsulated with clove essential oil exhibited higher antioxidant activity as compared to unencapsulated chitosan nanoparticles. Similar results were supported by Han et al. [24], which observed that there was a significant improvement in the antibacterial activity of the films against *E-coli*. The authors also reported on the degradation rate of PLA/chitosan films ageing in buffer solutions at 0.01 M, pH 7.4 and 37 °C for 12 weeks. The degradation rate increased as the amount of chitosan increased. The weight loss of PLA/CS films was expected to reach up to nearly 45% after 3 months. Another research done by Vasile et al. [25] examined the soil burial degradation behaviour of PLA/tributyl o-acetyl citrate/chitosan (PLA/ATBC/CS) bio-composites. The results proved that there was a small loss in the samples' weight after 150 days buried in the soil. However, significant changes were reported on mechanical, thermal, and surface properties. The presence of CS increased the hydrophilicity of bio-composite surfaces and favoured the interaction with moisture, hence promoted an attack by microorganisms.

Wang et al. [26] developed PLA nanocomposite films combined with CNC-ZnO. The authors reported that the addition of CNC-ZnO in the PLA matrix improved the crystallisation ability, interaction between nanofiller and matrix, UV-shielding performance, and degradation ability. It was reported that after 110 days buried in soil, the weight loss of pure PLA and PLA/25% CNC-ZnO were 9% and 28%, respectively. Similar trends were reported by Rajesh et al. [27]. The authors reported that there was 1.26% of weight loss for neat PLA after 90 days buried in soil and 15.2% of weight loss after the PLA had been loaded with 25% of sisal fibre. In a separate study, Lv et al. [28] looked into the degradation behaviour of PLA that was blended with starch and wood flours under soil burial. The outcomes proved that the increase of starch in the PLA matrix improved the degradation rate. Comparable results were remarked by Zuo et al. [29] whereby a significant increment in weight loss was observed after adding starch to the PLA matrix.

Therefore, this research aims to study the effects of SA filler on the degradation of virgin-PLA (VPLA) and recycled-PLA (RPLA) ageing in outdoor environment and soil burial. Excellent biological properties including antioxidant, antimicrobial, antiseptic, pesticide, analgesic, and anticarcinogenic activities have positioned SA as a potential filler in PLA for various applications such as in food, sanitary, biomedical, pharmaceutical, active packaging, and cosmetics industries [23]. Although many studies have been reported on the performance of SA as antioxidant and antimicrobial agents, limited outcomes on the degradations of PLA/SA composites have been published. Thus, it is essential to investigate the degradation behaviours of PLA/SA composites under the outdoor environment and soil burial that are the common plastic waste disposal environments. The weight loss, surface morphology, and thermal stability of PLA/SA composites after 10 weeks of ageing are examined thoroughly in this study.

2. METHODOLOGY

2.1 Material

VPLA pellets were purchased from a local supplier (Vistec Technology Services) in an injection moulding grade, 3251D Natureworks Ingeo™ (China). The pellets were cylindrical, with an average length and diameter of 3 mm. On the contrary, RPLA was retrieved from the 1st cycle of injection moulding wastes. The wastes were mostly collected from runners and crushed using a grinding machine. The recycled ground materials were in angular shape with an average size of less than 4 mm. The SA powder was purchased from a local hypermarket (Mydin Hypermarket). The size of the powder was in the range of 100 to 200 μm. The size of the powder is measured using Energy Dispersive X-Ray Analyzer (EDX).

2.2 Sample Preparation

PLA/SA composites were prepared through the solvent casting method at various composition contents of PLA and SA fillers. Five different combinations of blends were prepared for both virgin and recycled PLA/SA composites. The list of the composition of the samples that were prepared is summarized in Table 1. The amount of SA filler varied in the range of 0 wt% to 20 wt% in 5 wt% increments. The PLA resin was pre-conditioned in a drying oven at 70 °C for 12 hours to reduce the moisture content prior to use. PLA resin was then dissolved in dichloromethane (DCM). After being completely dissolved, SA filler was added to the solution. In order to obtain a homogenous PLA/SA blend, the mixture was continuously stirred using a magnetic stirrer for 30 minutes. The mixture was cast onto a glass plate and dried at room temperature for 24 hours. After drying the PLA/SA composites, the substrates were peeled off. The thickness of the PLA/SA composites substrates was in the range of 0.5 to 0.9 mm and was cut into 25 x 60 mm sizes. For each composition, six samples were prepared.

Table 1: Sample composition

Sample composition	VPLA		RPLA	
	VPLA (wt%)	SA (wt%)	RPLA (wt%)	SA (wt%)
1	100	0	100	0
2	95	5	95	5
3	90	10	90	10
4	85	15	85	15
5	80	20	80	20

2.3 Ageing Condition

The degradation of VPLA/SA composites and RPLA/SA composites was performed in outdoor environment and soil burial. Under the outdoor environment ageing, the samples were placed on the roof in order to attain optimum exposure. The geographic parameters of the test site were at the latitude of 5.4°N, longitude of 100.4° E, and altitude of 10 m. The temperature and humidity were monitored weekly within the range of 24 °C to 35 °C and 47% to 84%, respectively. The average normal sun irradiation was 298.9 W/m^2 [30].

For soil burial ageing, the samples were buried in organic soil that was placed in a plastic container with a depth of 2 inches from the soil surface. The pH and the humidity of the soil were 6.8 ± 0.5 and 60 ± 10%, respectively. The average soil temperature was 28.5

± 1.0 °C. The soil was regularly watered with tap water to ensure the humidity of the soil was consistent.

The ageing took place for 10 weeks. The weight of the samples was measured before and after ageing using an analytical balance. After 10 weeks of ageing in the outdoor environment, the samples were subjected to a drying process in a hot oven at a temperature of 70 °C for 3 to 4 hours before the final weight was measured. For samples ageing in soil burial, the samples were dug and rinsed with tap water in order to remove adherent soil. The samples were then dried in a hot oven at a temperature of 70 °C for 24 hours prior to final weight measurement. A longer drying time was required for samples ageing in soil burial due to excessive water content in the samples. The percentage of weight loss for each sample was calculated using Eq. (1).

$$\% \text{ weight loss} = (w_f\text{-}w_i)/w_i \text{ X } 100\% \tag{1}$$

where w_i is the weight of samples before ageing, and w_f is the weight of samples after ageing.

2.4 Surface Morphology

The surface morphology of the PLA/SA composites after ageing was observed using a Hitachi TM3030 scanning electron microscope (SEM) at a constant accelerated voltage of 15 kV. The images were captured under a magnification of 100X.

2.5 Thermogravimetric Analysis

The thermal stability of PLA/SA composites was analysed using TA instrument, SDT-Q600 thermogravimetric analysis (TGA). The samples were heated from 30° C to 600 °C at a heating rate of 10 °C/min in a nitrogen environment. The flow rate of nitrogen gas was set at 20 ml/min. Initial degradation temperature, T_i and maximum degradation temperature, T_{max} (which corresponded to the weight loss) were measured from the thermogram. T_i, is the temperature where the weight loss is started to gradually decline, whereas T_{max} is the temperature where the maximum weight loss occurred.

3. RESULTS AND DISCUSSION

3.1 Weight loss

The percentage of weight loss after ageing in outdoor environment and soil burial is summarized in Table 2. The data shows the percentage of weight loss is increased with the increment of wt% of SA filler. Figure 1 represents the plots of weight loss of VPLA/SA composites and RPLA/SA composites at various contents of SA filler after 10 weeks of ageing in outdoor environment and soil burial.

In both ageing environments (outdoor environments and soil burial) it was interesting to observe that the degradation rates of VPLA/SA composites were faster than the 100 wt% VPLA. A similar trend was noted for RPLA/SA composites, which revealed a higher degradation rate compared with the degradation rate of 100 wt% RPLA. The weight loss for 100 wt% VPLA after ageing in outdoor environment and soil burial were 3% and 13.2% whereas for 100 wt% RPLA after ageing in outdoor environment and soil burial were 3.4% and 14.5%. After being incorporated with 20 wt% of SA filler, the weight loss for VPLA/SA composites after ageing in outdoor environment and soil burial had increased to 7.7% and 25.6% respectively.

Table 2: Weight loss after ageing in outdoor environment and soil burial

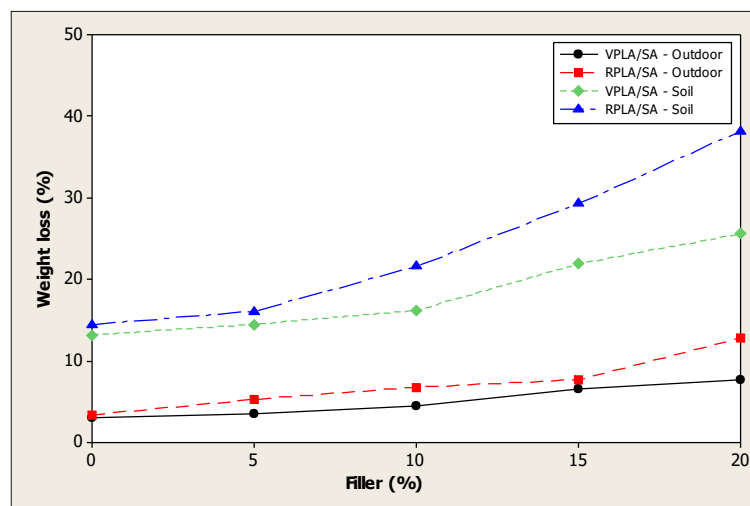| Sample	Composition	Weight loss (%)	
		Outdoor environment	Soil burial
1	100 wt% VPLA	3.0	13.2
2	95 wt% VPLA + 5 wt% SA	3.5	14.5
3	90 wt% VPLA + 10 wt% SA	4.5	16.2
4	85 wt% VPLA + 15 wt% SA	6.5	21.9
5	80 wt% VPLA + 20 wt% SA	7.7	25.6
6	100 wt% RPLA	3.4	14.5
5	95 wt% RPLA + 5 wt% SA	5.3	16.1
8	90 wt% RPLA + 10 wt% SA	6.8	21.6
9	85 wt% RPLA + 15 wt% SA	7.7	29.3
10	80 wt% RPLA + 20 wt% SA	12.8	38.2

Fig 1: Plots of SA filler content versus weight loss.

While for RPLA/SA composites with 20 wt% of SA filler, the weight loss after ageing in outdoor environment and soil burial had increased to 12.8% and 38.2%, respectively. The lowest weight loss exhibited in 100 wt% VPLA and 100 wt% RPLA was due to its low hygroscopic activity that was attributed to a slower rate of hydrolysis at lower temperatures and to the low degradation capacity of PLA microorganisms in composting [31]. When fillers were added to the PLA matrix, the interface between filler particles and matrix served as a leading path for the water molecules to penetrate the samples while simultaneously breaking the long polymer chain to low molecular weight. As the content of the filler increased, the interface surface was also increased and consequently accelerated the polymer chain scission and degradation process.

The results were noteworthy as they revealed that the degradation rates were more rapid in the soil burial as compared in the outdoor environment. The excessive volume of water in the soil introduced higher water diffusion into the composites, which consequently promoted active hydrolysis degradation of the composites. The presence of microorganisms in the soil would additionally enhance the degradation process of the composites. In contrast, when PLA/SA composites were exposed to the outdoor environment, it was known that UV irradiation, heat, and moisture from the atmosphere during ageing process had led to the deterioration in the polymer molecular chain via chain scission reactions through

photolysis and hydrolysis degradations. The photodegradation and moisture penetration started at the exposed surface followed by propagation through the interior body.

It was also noticeable that the weight loss for RPLA/SA composites was higher as compared with VPLA/SA composites. It was well known that due to shear forces and thermal impact encountered during the processing, RPLA exhibited a shorter molecular chain with lower molecular weight [32]. The chain scissions during the processing were reported by Chavez-Montes et al. [33], in which the authors observed around 30% to 40% of reductions in average molecular weight for virgin PLA after undergoing the single stage of injection moulding. The smaller molecular weight would intensively accelerate the degradation process upon ageing in outdoor environment and soil burial.

Table 3: Comparison of weight loss on various PLA composites

No	Ageing environment	Composition	Weight Loss (%)	References
1	Soil Burial - 110 days	PLA	9	[26]
		PLA/15% CNC-ZnO	28	
2	Soil Burial - 90 days	PLA	1.26	[27]
		PLA/25% sisal fiber	15.2	
3	Soil Burial - 105 days	PLA <1%	<1	[28]
		PLA/9% starch/21%wood floor	6	
		PLA/15%starch/15%wood floor	9	
		PLA/21%starch/9%wood floor	12	
4	Soil Burial - 120 days	PLA	0.102	[29]
		PLA/starch	27.11	
5	Soil Burial - 18 days	PLA	18.1	[34]
		PLA/coir fiber	22.6	
6	Outdoor environment - 10 weeks (70 days)	100 wt% VPLA	3	**Present work**
		VPLA/20 wt% SA	7.7	
		100 wt% RPLA	3.4	
		RPLA/20 wt%SA	12.8	
7	Soil Burial - 10 weeks (70 days)	100 wt% VPLA	13.2	**Present work**
		VPLA/20 wt% SA	25.6	
		100 wt% RPLA	14.5	
		RPLA/20 wt%SA	38.2	

The comparison between degradation of various PLA composites from previous works and present works is listed in Table 3. There was not much information related to weight loss in the outdoor environment that was currently available. Similarly, the degradation of RPLA and RPLA composites was also rarely reported. In general, the findings from this work were consistent with the previous findings. The dissimilar percentage in mechanical properties reduction could be explained through the divergent variations in soil conditions such as temperature, humidity, and pH of the soil. The types of microorganisms in the soil also highly affected the degradation rate. The shorter degradation time of the PLA/SA composites obtained from this study have increased its potential to be used as food packaging material.

3.2 Surface Morphology

The surface morphology was examined using SEM. Before ageing, the surfaces of the VPLA/SA composites and RPLA/SA composites were smooth. The SA fillers were evenly dispersed in the PLA matrix. After 10 weeks of ageing in outdoor weathering and soil burial, the surfaces were observed to be eroded with multiple formations of voids, cavities, cleavages, and grooves. It was also noted that the aged samples were more brittle and easily broken. These might be due to the recrystallisation of PLA/SA composites during ageing process.

The comparison of the surface morphology of VPLA/SA composites after ageing in outdoor environment and soil burial is shown in Fig. 2. As demonstrated in Fig. 2a and 2b, in both environments, VPLA did not show any significant macroscopic alternations on the surfaces as the surfaces were still compact and tight with the presence of minimum voids. This was due to its poor hydrophilic characteristic which had hindered the penetration of water [35]. The number of voids on soil burial samples was more discernible as compared to samples that aged in the outdoor environment.

When 5 wt% of SA fillers were added into the VPLA matrix, the number of voids increased and the size of the voids was enlarged (as seen in Fig. 2c and 2d). As the amount of SA fillers increased to 20 wt%, the surfaces of VPLA/SA composites were seriously eroded with multiple formations of cavities, cleavages, and grooves as illustrated in Fig. 2g and 2h. The observations on the surface morphologies were consistent with the weight loss findings.

A similar pattern was observed on RPLA/SA composites. As shown in Fig. 3a and 3b, after the ageing processes in outdoor environment and soil burial, numerous voids were present. The presence of SA fillers in the composites had accelerated the formations of voids and cavities. With the increase of SA fillers, the damages on surface morphologies were gradually expanded. As shown in Fig. 3c until 3h, the number and size of voids and cavities were increased with increasing of wt% of SA fillers. The presence of voids and cavities indicated that the composites have degraded, and these explained the reductions in weight. Similarly, it was seen that the formations of voids and cavities were more significant on the samples that aged through soil burial as compared to the samples that aged under outdoor environment. In the soil burial degradation, the composites were subjected to hydrolysis degradation under the conditions of water and microorganisms while in the outdoor environment, degradation was induced through UV irradiation, photo-thermal factors, and moisture. The degradations from these resources produced ruptures in the molecular chain, reduced the interfacial adhesion between fillers and PLA matrix, and finally led to the disintegration and fragmentation of the composites.

3.3 Thermogravimetric analysis (TGA)

Thermal stabilities of VPLA/SA composites and RPLA/SA composites after ageing were evaluated through thermogravimetric analysis (TGA). The TGA curves for VPLA/SA composites and RPLA/SA composites are shown in Fig. 4. The curves clearly indicate that the composites had undergone a normal single-step thermal degradation process.
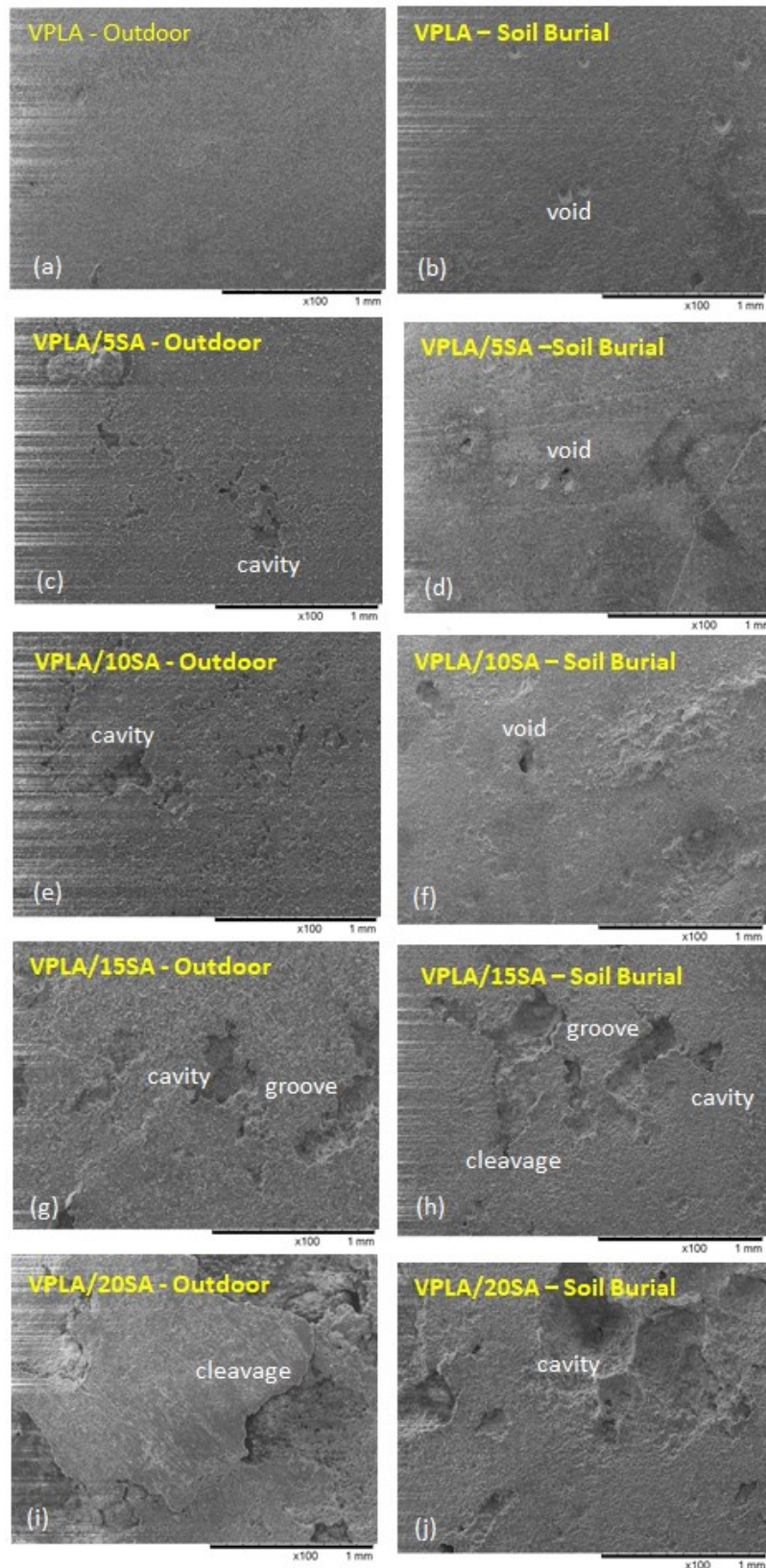
Fig. 2: Surface Morphologies of VPLA/SA composites with varying SA filler composition after 10 weeks of ageing in outdoor environment and soil burial (a-b) 0 wt%, (c-d) 5 wt%, (e-f) 10 wt%, (g-h) 15 wt%, (i-j) 20 wt% .
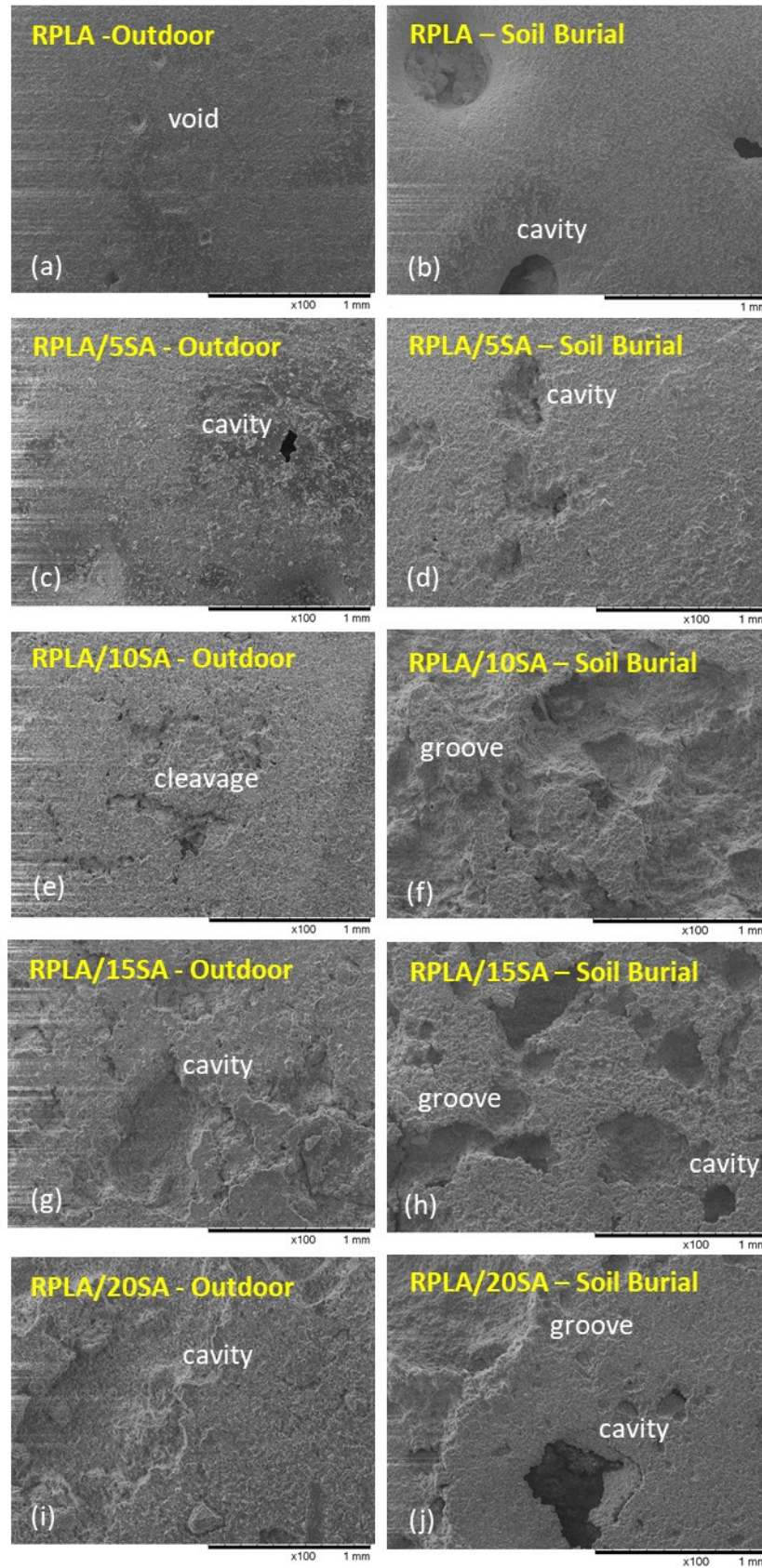
Fig. 3: Surface Morphologies of RPLA/SA composites with varying SA filler composition after 10 weeks of ageing in outdoor environment and soil burial (a-b) 0 wt%, (c-d) 5 wt%, (e-f) 10 wt%, (g-h) 15 wt%, (i-j) 20 wt%.
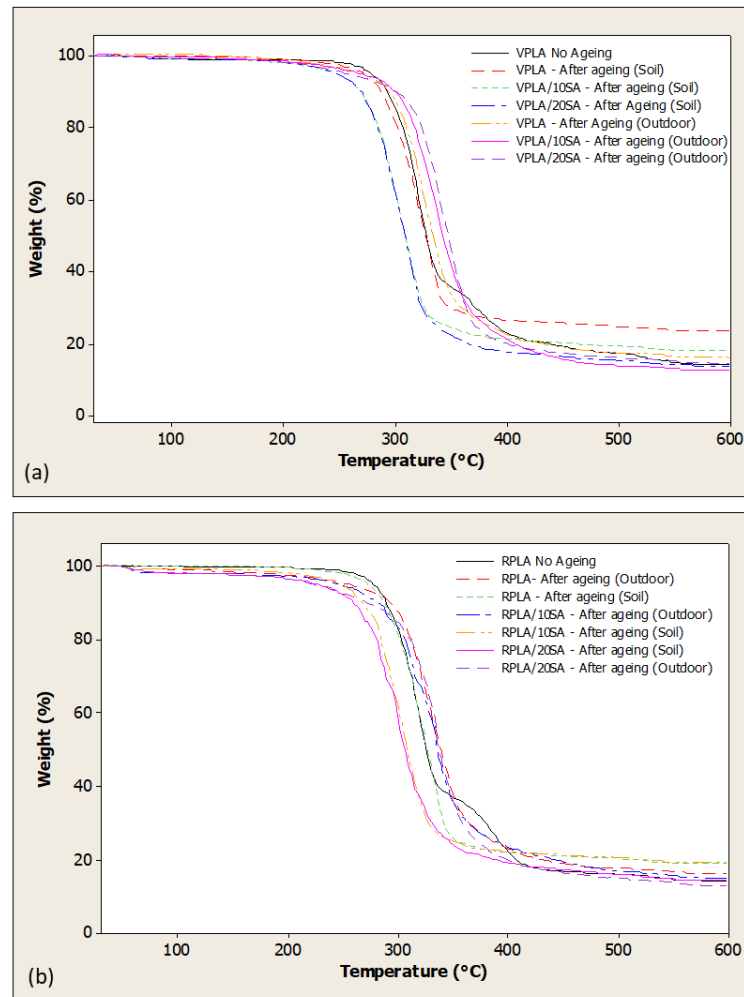
Fig. 4: Thermogravimetric curves of (a) VPLA/SA composites and (b) RPLA/SA composites.

Table 4 summarized the initial degradation temperature (T_i) and maximum degradation temperature (T_{max}) for VPLA/SA composites and RPLA/SA composites with the addition of 10 wt% and 20 wt% SA fillers after ageing in outdoor environment and soil burial. T_i and T_{max} for VPLA and RPLA before ageing were also included. Before ageing, the thermal degradations for VPLA and RPLA started around 290 °C. A slight decrease in the initial degradation temperature for RPLA was seen. The observation was reasonable since RPLA experienced molecular weight reduction during reprocessing which naturally affected the onset of degradation temperatures. After ageing in outdoor environment, the initial degradation temperatures for VPLA, RPLA, and its composites were increased. An increase in T_i had become more recognizable with the increment of wt% of SA fillers. An increase in the degradation temperature was probably due to the increased crystallinity during photolysis and photodegradation. As noted by Lv et al. [28], during the degradation process, the crystallinity of the PLA composites was increased at the initial stages and decreased as degradation progressed. A similar observation was reported by Zuo et al. [29]. It was expected that the T_i would be decreased with the extension of ageing time and the degradation rate would be rapidly augmented.

Table 4: The initial and maximum degradation temperatures of (a) VPLA/SA composites and (b) RPLA/SA composites

Composition	T_i (°C)	T_{max} (°C)	Composition	T_i (°C)	T_{max} (°C)
VPLA No Ageing	291	356	RPLA No Ageing	286	355
VPLA – After ageing (Outdoor)	295	359	RPLA – After ageing (Outdoor)	296	370
VPLA – After ageing (Soil)	288	347	RPLA – After ageing (Soil)	291	348
VPLA/10SA – After ageing (Outdoor)	302	371	RPLA/10SA – After ageing (Outdoor)	287	372
VPLA/10SA-After ageing (Soil)	270	335	RPLA/10SA – After Ageing (Soil)	270	335
VPLA/20SA – After ageing (Outdoor)	313	370	RPLA/20SA – After ageing (Outdoor)	299	368
VPLA/20SA – After ageing (Soil)	270	335	RPLA/20SA – After ageing (Soil)	263	340

In contrast, the T_i decreased after ageing through soil burial. The decrease in the T_i was more significant with the addition of SA fillers in the PLA/SA composites. The results indicated that PLA/SA composites started and completely decomposed earlier when buried in soil. Elevated diffusion of water molecules accelerated the polymer chain scission. The addition of hydrophilic SA fillers caused a large amount of water molecules to penetrate the composites and provided a boost to the hydrolysis degradation process. Additionally, the presence of microorganisms in soil promoted the enzymatic degradation of the composites [36]. The extensive polymer chain scission during the degradation in soil burial consequently decreased the thermal stabilities of the PLA/SA composites.

4. CONCLUSIONS

This paper reported on the biodegradations of VPLA/SA composites and RPLA/SA composites upon ageing in outdoor environment and soil burial. SA was employed and added as a filler in VPLA matrix and RPLA matrix in the range of 0 to 20 wt%. The results revealed that the degradations of PLA in outdoor environment and soil burial increased when SA filler was incorporated in the PLA matrix. The weight loss for 100 wt% VPLA and 100 wt% RPLA after 10 weeks of ageing in the outdoor environment were very low, at approximately 3% and 3.4%, respectively. When SA filler was added to the PLA matrix, the weight loss was proportionally increased. The maximum weight loss was observed in PLA/SA composites with 20 wt% of SA filler. The weight loss for VPLA/SA composites was 7.7% while the weight loss for RPLA/SA composites was 12.8%. In comparison, after 10 weeks of ageing in soil burial, the weight loss for 100 wt% VPLA and 100 wt% RPLA were 13.2% and 14.5% respectively. Similarly, when PLA was incorporated with SA filler, the degradation rate was found to be rapidly increased. The weight loss for VPLA/20 wt% SA was 25.6% whereas the weight loss for RPLA/20 wt% SA was 38.2%.

In outdoor environment, UV irradiation, light, and heat resources from the sun, the hydrolysis degradation on the molecular chains were accomplished through photocleavage, photolysis, and photooxidation. In contrast, soil burial degradation occurred through the hydrolysis of water molecules on the ester group along the backbone of the polymer chain and enzymatic degradation produced by microorganisms in the soil. The findings proved that the degradation rate of soil burial is higher as compared with photolysis degradion in outdoor environment.

In conclusion, it can also be concluded that the RPLA/SA composites exhibited higher degradation rates than VPLA/SA composites. Due to the shear forces and thermal impact encountered during the processing, VPLA exhibited shorter molecular chain with lower molecular weight which consequently catalysed the degradation process to take place. The shortening of the degradation time of the PLA/SA composites may provide a bright potential as an essential alternative for packaging materials.

ACKNOWLEDGEMENT

REFERENCES

[1] Ingrao C, Tricase C, Cholewa-Wójcik A, Kawecka A, Rana R, Siracusa V. (2017) Polylactic acid trays for fresh-food packaging: A carbon footprint assessment. Science of the Total Environment, 537:385–398.

[2] Hopewell J, Dvorak R, Kosior E. (2009) Plastics recycling: challenges and opportunities. Philosophical Transactions of the Royal Society B, 364:2115-26. https://doi.org/10.1098/rstb.2008.0311

[3] Wan L, Li C, Sun C, Zhou S, Zhang Y. (2019) Conceiving a feasible degradation model of polylactic acid-based composites through hydrolysis study to polylactic acid/wood flour/polymethyl methacrylate. Composite Science and Technology 181:107675. https://doi.org/10.1016/j.compscitech.2019.06.002

[4] Farah S, Anderson DG, Langer R. (2016) Physical and mechanical properties of PLA, and their functions in widespread applications — A comprehensive review. Advanced Drug Delivery Reviews, 107:367–392. https://doi.org/10.1016/j.addr.2016.06.012

[5] Silva D, Kaduri M, Poley M, Adir O, Krinsky N, Shainsky-Roitman J, Schroedera A. (2018) Biocompatibility, biodegradation and excretion of polylactic acid (PLA) in medical implants and theranostic systems. Chemical Engineering Journal, 340:9–14. https://doi.org/10.1016/j.cej.2018.01.010

[6] Tokiwa Y, Calabia CP, Ugwu CU, Aiba S. (2009) Biodegradability of plastics. International Journal of Molecular Sciencee, 10:3722-3742. doi:10.3390/ijms10093722

[7] Porfyris A, Vasilakos S, Zotiadis C, Papaspyrides C, Moser K, Vander Schueren L, Buyle G, Pavlidou S, Vouyiouka S. (2018) Accelerated ageing and hydrolytic stabilization of poly(lactic acid) (PLA) under humidity and temperature conditioning. Polymer Testing 68:315-332. https://doi.org/10.1016/j.polymertesting.2018.04.018

[8] Kaynak C, Sarı B. (2016) Accelerated weathering performance of polylactide and its montmorillonite nanocomposite. Applied Clay Science 121:86–94. https://doi.org/10.1016/j.clay.2015.12.025

[9] Bocchini S, Frache A. (2013) Comparative study of filler influence on polylactide photooxidation. Express Polymer Letters, 7:431–442. DOI: 10.3144/expresspolymlett.2013.40

[10] Risyon NP, Othman SH, Kadir Basha R, Talib RA. (2020) Characterization of polylactic acid/halloysite nanotubes bionanocomposite films for food packaging. Food Packaging and Shelf Life, 23:100450.

[11] Ahmed J, Mulla M, Jacob H, Luciano G, Bini TB, Almusallam A. (2019) Polylactide/poly(Ɛ-caproplactone)/zin oxide/clove essential oil composite antimicrobial films for scrambled egg packaging. Food Packaging and Shelf Life, 21:100355. https://doi.org/10.1016/j.fpsl.2019.100355

[12] Chen C, Xu Z, Ma Y, Liu J, Zhang Q, Tang Z, Fu K, Yang F, Xie J. (2018) Properties, vapour-phase antimicrobial and antioxidant activities of active poly(vinyl alcohol) packaging films incorporated with clove oil. Food Control, 88:105-112. https://doi.org/10.1016/j.foodcont.2017.12.039

[13] Gavril GL, Wrona M, Bertella A, Świeca M, Râpă M, Salafranca J, Nerín C. (2019) Influence of medicinal and aromatic plants into risk assessment of a new bioactive packaging based on polylactic acid (PLA). Food and Chemical Toxicology, 132:110662. https://doi.org/10.1016/j.fct.2019.110662

[14] Sivakanthan S, Rajendran S, Gamage A, Madhujith T, Mani S. (2020) Antioxidant and antimicrobial applications of biopolymers: A review. Food Research International, 126:109327. https://doi.org/10.1016/j.foodres.2020.109327

[15] Rehman A, Jafari SM, Aadil RM, Assadpour E, Randhawa MA, Mahmood S. (2020) Development of active food packaging via incorporation of biopolymeric nanocarriers containing essential oils. Trends in Food Science & Technology, 101:106–121. https://doi.org/10.1016/j.tifs.2020.05.001

[16] Hamad K, Kaseem M, Deri F. (2010) Rheological and mechanical properties of poly(lactic acid)/polystyrene polymer blend. Polymer Bulletin 65:509–519. DOI 10.1007/s00289-010-0354-2

[17] Murariu M, Dubois P. (2016) PLA composites: From production to properties. Advanced Drug Delivery Reviews, 107:17–46. http://dx.doi.org/10.1016/j.addr.2016.04.003

[18] Zhang L, Huang C, Xu Y, Huang H, Zhoa H, Wang J, Wang S. (2020) Synthesis and characterization of antibacterial polylactic acid film incorporated with cinnamaldehyde inclusions for fruit packaging. International Journal of Biological Macromolecules, 164:4547-4555. http://doi.org/10.1016/j.ijbiomac.2020.09.065

[19] Cui R, Jiang K, Yuan M, Cao J, Li L, Tang Z, Qin Y. (2020) Antimicrobial film based on polylactic acid and carbon nanotube for controlled cinnamaldehyde release. Journal of Materials Research and Technology, 9(5):10130-10138. https://doi.org/10.1016/j.jmrt.2020.07.016

[20] Techawinyutham L, Siengchin S, Dangtungee R, Parameswaranpillai J. (2019) Influence of accelerated weathering on the thermo-mechanical, antibacterial, and rheological properties of polylactic acid incorporated with porous silica-containing varying amount of capsicum oleoresin. Composites Part B, 175:107108. https://doi.org/10.1016/j.compositesb.2019.107108

[21] Varsavas SD, Kaynak C. (2018) Weathering degradation performance of PLA and its glass fiber reinforced composite. Material Today Communications, 15:344-353. https://doi.org/10.1016/j.mtcomm.2017.11.008

[22] Fathima PE, Panda SK, Ashraf PM, Varghese TO, Bindu J. (2018) Polylactic acid/chitosan films for packaging of Indian white prawn (*Fenneropenaeus indicus*). International Journal of Biological Macromolecules, 117:1002-1010. https://doi.org/10.1016/j.ijbiomac.2018.05.214

[23] Hadidi M, Pouramin S, Adinepour F, Haghani S, Japari SM. (2020) Chitosan nanoparticles loaded with clove essential oil: Characterization, antioxidant and antibacterial activities. Carbohydrate Polymers, 236:116075. https://doi.org/10.1016/j.carbpol.2020.116075

[24] Han W, Ren J, Xuan H, Ge L. (2018) Controllable degradation rates, antibacterial, free-standing and highly transparent films based on polylactic acid and chitosan. Colloids and Surfaces A 541:128–136. https://doi.org/10.1016/j.colsurfa.2018.01.022

[25] Vasile C, Pamfil D, Râpă M, Darie-Niţă RN, Mitelut AC, Popa EE, Popescu PA, Draghici MC, Popa ME. (2018) Study of the soil burial degradation of some PLA/CS biocomposites, Composites Part B 142:251–262. https://doi.org/10.1016/j.compositesb.2018.01.026

[26] Wang YY, Yu HY, Yang L, Abdalkarim SYH, Chen WL. (2019) Enhancing long-term biodegradability and UV-shielding performances of transparent polylactic acid nanocomposite films by adding cellulose nanocrystal-zinc oxide hybrids. International Journal of Biological Macromolecules, 141:893–905. https://doi.org/10.1016/j.ijbiomac.2019.09.062

[27] Rajesh G, Prasad AVR, Gupta AVSSKS. (2019) Soil degradation characteristics of short sisal/PLA composites. Materials Today: Proceedings 18:1–7. https://doi.org/10.1016/j.matpr.2019.06.270

[28] Lv S, Zhang Y, Gu J, Tan H. (2017) Biodegradation behaviour and modelling of soil burial effect on degradation rate of PLA blended with starch and wood flour. Colloids and Surfaces B: Biointerfaces, 159:800-808. https://doi.org/10.1016/j.colsurfb.2017.08.056

[29] Zuo YF, Gu J, Qiao Z, Tan H, Cao J, Zhang Y. (2015) Effects of dry method esterification of starch on the degradation characteristics of starch/polylactic acid composites. International Journal of Biological Macromolecules, 72:391-402. https://doi.org/10.1016/j.ijbiomac.2014.08.038

[30] Mohammad ST, Al-Kayiem HH, Aurybi MA, Khlief AK. (2020) Measurement of global and direct normal solar energy radiation in Seri Iskandar and comparison with other cities of Malaysia. Case Studies in Thermal Engineering, 18:100591. https://doi.org/10.1016/j.csite.2020.100591

[31] Salazar-Sánchez MR, Campo-Erazo SD, Villada-Castillo HS, Solanilla-Duque JF. (2019) Structural changes of cassava starch and polylactic acid films submitted to biodegradation process. International Journal of Biological Macromolecules, 129:442–447. https://doi.org/10.1016/j.ijbiomac.2019.01.187

[32] Zhao P, Rao C, Gu F, Sharmin N, Fu J. (2018) Close-looped recycling of polylactic acid used in 3D printing: An experimental investigation and life cycle assessment. Journal of Cleaner Production, 197:1046-1055. https://doi.org/10.1016/j.jclepro.2018.06.275

[33] Chavez-Montes WM, Gonzalez-Sanchez G, Lopez-Martinez EI, Lira-Gomez P, Ballinas-Casarrubias L, Flores-Gallardo S. (2015) Effect of artificial weathering on PLA/Nanocomposite molecular weight distribution. Polymers 7:760-776. https://doi.org/10.3390/polym7040760

[34] Dong Y, Ghataura A, Takagi H, Haroosh HJ, Nakagaito AN, Lau KT. (2014) Polylactic acid (PLA) biocomposites reinforced with coir fibres: Evaluation of mechanical performance and multifunctional properties. Composites: Part A, 63:76–84. http://dx.doi.org/10.1016/j.compositesa.2014.04.003

[35] Qi Y, Ma HL, Du ZH, Yang B, Wu J, Wang R, Zhang ZQ. (2019) Hydrophilic and antibacterial modification of poly(lactic acid) films by γ-ray irradiation. ACS Omega, 4:21439−21445. http://pubs.acs.org/journal/acsodf

[36] Bahl S, Dolma J, Singh JJ, Sehgal S (2021). Biodegradation of plastics: A state of the art review. Materials Today: Proceedings 39:31–34. https://doi.org/10.1016/j.matpr.2020.06.096

NUMERICAL MODELLING OF BIRD STRIKE ON A ROTATING ENGINE BLADES BASED ON VARIATIONS OF POROSITY DENSITY

**SHARIS-SHAZZALI SHAHIMI[1], NUR AZAM ABDULLAH[1*],
MEFTAH HRAIRI[1], AMEEN TOPA[2,3] AND AHMAD FARIS ISMAIL[1]**

[1]*Structural Mechanics and Dynamics Research Group, Department of Mechanical Engineering,
International Islamic University Malaysia,
Jalan Gombak, 53100 Kuala Lumpur, Malaysia*
[2]*Insitute of Transportation Infrastructure, Universiti Teknologi PETRONAS,
Seri Iskandar, 32610, Malaysia*
[3]*Faculty of Ocean Engineering Technology and Informatics, Universiti Malaysia Terengganu,
Kuala Terengganu, 21300, Malaysia*

*Corresponding author: azam@iium.edu.my

ABSTRACT: A numerical investigation is conducted on a rotating engine blade subjected to a bird strike impact. The bird strike is numerically modelled as a cylindrical gelatine with hemispherical ends to simulate impact on a rotating engine blade. Numerical modelling of a rotating engine blade has shown that bird strikes can severely damage an engine blade, especially as the engine blade rotates, as the rotation causes initial stresses on the root of the engine blade. This paper presents a numerical modelling of the engine blades subjected to bird strike with porosity implemented on the engine blades to investigate further damage assessment due to this porosity effect. As porosity influences the decibel levels on a propeller blade or engine blade, the damage due to bird strikes can investigate the compromise this effect has on the structural integrity of the engine blades. This paper utilizes a bird strike simulation through an LS-Dyna Pre-post software. The numerical constitutive relations are keyed into the keyword manager where the bird's SPH density, a 10 ms simulation time, and bird velocity of 100 m/s are all set. The blade rotates counter-clockwise at 200 rad/s with a tetrahedron mesh. The porous regions or voids along the blade are featured as 5 mm diameter voids, each spaced 5 mm apart. The bird is modelled as an Elastic-Plastic-Hydrodynamic material model to analyze the bird's fluid behavior through a polynomial equation of state. To simulate the fluid structure interaction, the blade is modelled with Johnson-Cook Material model parameters of aluminium where the damage of the impact can be observed. The observations presented are compared to previous study of a bird strike impact on non-porous engine blades.

ABSTRAK: Penyelidikan berangka telah dijalankan ke atas bilah enjin berputar tertakluk kepada impak pelanggaran burung. Pelanggaran burung tersebut telah dimodelkan secara berangka sebagai silinder gelatin dengan hujungnya berbentuk hemisfera demi mensimulasikan impaknya ke atas bilah enjin yang berputar. Pemodelan berangka bilah-bilah enjin yang berputar tersebut menunjukkan bahawa pelanggaran burung mampu menyebabkan kerosakan teruk terhadap bilah enjin terutamanya apabila bilah enjin sedang berputar oleh sebab putaran menghasilkan tekanan asal di pangkal bilah enjin. Kajian ini mengetengahkan pemodelan berangka ke atas bilah-bilah enjin tertakluk kepada pelanggaran burung terhadap bilah-bilah enjin yg mempunyai keliangan demi menyelidik dan menilai kerosakan kesan daripada keliangan tersebut. Keliangan juga mempengaruhi tahap-tahap desibel ke atas bilah kipas ataupun bilah enjin, kerosakan hasil serangan

burung boleh menterjemah tahap ketahanan struktur integriti bagi bilah-bilah enjin tersebut. Penyelidikan ini menggua pakai perisian "LS-Dyna Pre-post" untuk simulasi pelanggaran burung. Hubungan konstitutif berangka telah dimasukkan sebagai kata kunci di mana ketumpatan SPH burung, masa simulasi 10ms, dan halaju burung ditetapkan kepada 100 m/s. Bilah tersebut berputar pada 200 rad/s arah lawan jam dengan jejaring tetrahedron. Kawasan berliang atau kosong di sepanjang bilah ditetapkan diameternya kepada 5 mm, dan dijarakkan 5 mm di antara satu sama lain. Burung pula dimodelkan sebagai material "Elastic-Plastic-Hydrodynamic" untuk mengkaji sifat bendalir burung melalui persamaan polinomial. Demi mensimulasi interaksi struktur bendalir, bilah tersebut dimodelkan sebagai parameter aluminium material "Johnson Cook" di mana kerosakan daripada impak tersebut dapat diteliti. Penelitian-penelitian tersebut dibandingkan dengan kajian terdahulu ke atas serangan burung terhadap bilah-bilah enjin tidak berliang.

KEYWORDS: *bird strike; rotating engine blades; porosity; SPH; structural damage*

1. INTRODUCTION

Bird strikes are one of the most dangerous phenomena threatening aircraft in aviation today. As bird strikes can cause severe damage to an aircraft, especially during take-off and landing, numerous attempts must be made to ensure aircraft are structurally robust, strong, and able to withstand high speed impacts. These birds can strike at any part of the aircraft such as the wings, parts of the fuselage, the windscreen, and the engine. Research and experimentations are important to predict and analyze these bird strike impacts as bird strikes have become more frequent in recent times [1]. Many aircraft, civilian and military, have been destroyed or damaged by bird strikes; increasing aircraft expenses and lives lost due to these dangerous strikes, calling for a need to make aircraft parts more robust.

Although birds can strike at any part of the aircraft, the engine is the most dangerous part the bird can impact. If the engines are damaged, this can cause the pilot to lose control of the aircraft, prompting the pilot to attempt an emergency landing. As such, the aircraft must have sufficient power to land safely in the event of bird impact. In the specific event of bird impact to the engine, bird strikes will most probably damage the engine, causing the aircraft to crash land and destroy the aircraft, losing many lives. It is essential to predict and assess these bird strikes on the engine turbine blades during flight.

Bird strikes were already tested through experimentation during the early 80s. The earliest experimental tests were conducted by Wilbeck [2]. The basis of the experimental procedures was conducted through Liu et al. [3] on flat plates and Guan et al. [4] with fan rotor blades. In these experiments, the bird was modelled as a fluid structure and the design of the bird changed over the years from a spherical model, to cylindrical model, and into the hemispherical-ended cylinder that is the most frequent model in use today. The bird's mass density is modelled as a gelatin structured bird that can be fired onto the aircraft part, thus analyzing the damage of the aircraft part.

Numerical simulations have since been more in favor as compared to experimentation. Throughout the years, experimentation has become expensive by damaging aircraft parts during testing, and repeated use of gelatin synthetic birds is unsanitary. However, Wilbeck's experiment basis has since been discussed, referred, and verified by other researchers today. The discussions of these impacts to engine blades state that the bird transfers its momentum to the engine blades due to the oscillations of the blade's rotation [2]. Wilbeck analyzed these oscillations and blade response to accurately predict the impact loads of the synthetic

birds. With these impact loads, comparisons can be made with several different types of aircraft parts impacted by bird strikes.

2. BIRD STRIKE ENGINE BLADE STRUCTURAL INTEGRITY

Many numerical simulations have been conducted and expanded pertaining to the structural integrity and materials of aircraft structures [5]. These works discuss the damage and cracking of several aircraft wing boxes. Bird strikes must be considered in these research analyses as part of the impact loads that can cause these damage threats to the aircraft structural integrity, especially to the aircraft engine's blades, as mentioned. There is a gap in the research pertaining to the structural damage on engine blades where the engine blade's rotational oscillations are involved. Most of the research on bird strikes have shown the blade as static where there is in fact blade rotation. There is currently a gap in analysis and numerical modelling in which bird strike impacts the blades as dynamic rotations. A numerical analysis conducted by Shahimi et al. [8] and Vignjevic et al. [9] has shown that centrifugal forces due to rotation contribute to the loads and stresses experienced by the engine blades as they rotate. Both these analyses assess the damage of a numerically modelled engine blade subjected to bird strike impact. Even after impact, the stresses persist and affect the structural integrity of the blade.

Research on aviation has also expanded to include porosity in the wings and blade structure [10], pertaining the need to further expand the scope of bird strike impact on these types of configurations. Porosity on aircraft wings and blades have an adverse effect on these aircraft parts in that it can weaken the structural integrity of those mentioned parts due to the holes punctured on the surface of the wing or blade. The trade-off here would be to analyze the damage if such a configuration were to be established on the aircraft parts versus the advantages that porosity offers. The aerodynamics of a porous wing were presented as variations in lift coefficient, drag coefficient, and lift versus drag as a function of porosity. These aerodynamic factors had the adverse effect that porosity on the wing structure shows close agreement with the behavior of the lift coefficient slope and a similar trend in the performance of the lift slope [10]. However, these aerodynamic changes due to porosity, while good, must be analyzed with the structural compromise that might happen in a bird strike event.

Similarly, methods of reducing noise on aircraft propeller blades were presented where an experimental investigation on the effect of a 'butterfly acoustical skin' on the acoustic performance of two-bladed propellers with a rotational speed [11]. The paper discusses different micro and nanostructures of porous scales, applying it fully to the skin surface of a two-bladed propeller. The experiment's measurements of noise frequency on the porous surface skin are significant, where even a small diameter hole of around 0.5mm to 1.25mm can reduce the wave drag and large side forces and redistribute the pressure on the outer surface by establishing communication between high- and low-pressure regions in the holes on the surface of the blade. The studies show that noise reduction of as much as 4 dB for a rotating propeller with a 'butterfly acoustical skin' with a porous region compared to a hollow region with 2 dB [11]. This is a good step into more silent propellers in aviation but as with the mentioned aerodynamics of a wing, this has an adverse effect on the structural integrity of the blade structure in the event of a bird strike.

Based on all these analyses and observations, this paper assesses the damage of a porous engine blade subjected to a bird strike impact. The numerical simulation was conducted with an LS-Dyna prepost software to visualize a rotational porous engine blade impacted by an SPH bird model with mass and density parameters [12]. This numerical analysis method

was validated through a study of parametric engine blades by Vignjevic et al. [9]. The engine blade structure was modelled with 5 mm diameter holes punctured on the leading edge of the blades and a Johnson-Cook failure model constant was implemented through the LS-Dyna keyword manager.

3. BIRD MODEL

3.1 Bird Geometry and SPH

In bird strike analysis, establishing the method, geometry and bird model is an essential part of the numerical analysis. The Smoothed Particle Hydrodynamics (SPH) method is the most common and widely used in numerical simulations for any bird strike cases. Various approaches and other methods were presented and compared to be referred in a single study to differentiate the approaches to bird strike modelling [13].

The Lagrangian Method and the Rigid Bird Model are presented. The method presents the bird model as a geometry mesh with distinctive shapes, whether spherical, cylindrical, or cylindrical with hemispherical ends. However, a cylinder with hemispherical ends does more closely resemble an artificial bird. This model can establish a better bird pressure history in real time with more accuracy during testing. The Lagrangian and Bird Rigid Body method, however, shows that during the impact of the bird, the meshes move together and are not treated as individual particles. As the bird impacts the aircraft, large indentations on the aircraft part would show damage at the point of splatter impact with the bird, concentrating the splatter to a single point, rather than to a more diverse splatter that a real bird would produce.

This is the advantage that the SPH method can present, where each individual particle of the mesh distortions carries the mass, velocity and material law assigned to each particle. As the splatter occurs, a more diverse spread is shown beyond the point of impact, where each particle would then impact other parts of the aircraft, damaging the parts and accurately predicting the analysis. Figure 1 presents the SPH model of the bird used in this numerical analysis.
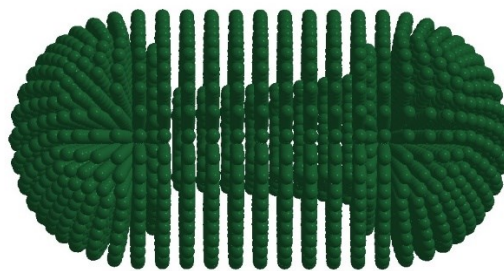

Fig. 1: Bird model SPH. Length to radius ratio equal to two.

3.2 Bird Parameters and Material Model

The bird parameters are first established as density and diameter of the hemisphere as a function of the bird's mass. The equations are revised by Banerjee et al. [14] as the Johnson Cook failure constants are also established together further in the paper. The equations of density and diameter of the bird model are presented below:

$$\rho = -0.063(log_{10} m) + 1.148 \tag{1}$$

Based on these two relationships, with a density $\rho = 950 \, kg/m^3$ is obtained to determine the mass, m to be 1.145 kg. The volume of the bird model is then determined as:

$$V = \frac{m}{\rho} = 1.205.10^{-3} \ m^3 \tag{2}$$

$$V = \frac{5\pi D^3}{12} \rightarrow D = 0.097 \ m \tag{3}$$

Referring to Eq. (2), the volume is then used to calculate the diameter and length of the bird model as 0.097m and 0.194m, respectively, as the length to radius ratio is equal to two.

Establishing the material of the bird would often depend on the internal organs of the bird, as would depend on different bird sizes or species. In numerical modelling, the bird's flesh, blood, and bones must be modelled as close to a real bird's innards as possible, where gelatin has been established as one of the materials used in simulating bird strikes. Real birds were launched from pressure nozzles to strike aircraft parts during early experimentations but this practice has since died down due to it being unsanitary as well as inhumane. Having to reuse or replace each bird during testing was not practical.

In Wilbeck's experiments, observations show that an important factor in bird strikes are the fact that birds can be considered as a fluid during high velocity impacts. Hence the use of SPH model would align with this factor as the splatter would spread the organs further. As such, Dar et al. [12] proposed the use of Elastic-Plastic-Hydrodynamic (EPH) material model to analyze the bird behavior through a polynomial equation of state. This is implemented through the LS-Dyna keyword manager in this paper.

The pressure-density relationship equation of state for the bird is expressed as an isotropic and non-viscous model, allowing the model to be used as a large strain during deformation and be defined with the yield stress and tangent modulus of the engine blade material. The pressure P is shown below:

$$P = C_0 + C_1\mu + C_2\mu^2 + C_3\mu^3 + (C_4 + C_5\mu + C_6\mu^2)E \tag{4}$$

The internal energy, E and the seven polynomial coefficients, C_i are the basis of the polynomial equation of state and can be determined to model birds accurately. The relative density, μ is expressed as the ratio of the instantaneous density ρ to initial density ρ_0 in Eq. (5):

$$\mu = \left(\frac{\rho}{\rho_0}\right) - 1 \tag{5}$$

As the bird is considered a fluid, Banerjee et al. states the coefficients C_4, C_5, C_6 are set to zero to match the behaviour of water. The equilibrium conditions would also mean that C_0 is set to zero. Therefore, the physical properties of the bird are presented below in Table 1.

Table 1: Bird physical properties [12]

Density [kg/m³]	Shear Modulus [GPa]	Yield Stress [MPa]	C_1	C_2	C_3
950	2	0.02	2.1×10^9	6.2	10.1

4. POROUS ENGINE BLADE

4.1 Blade Material Model

A Johnson-Cook material model is implemented in this paper as the material model of the engine blades. The damage assessed in this paper with a porous engine blade can be compared to the numerical computational bird strike by Shahimi et al. [8], it can be observed how a porous blade would compromise the structural integrity of the engine blade during

bird strikes. High impact velocity would cause high elastic and inelastic strains, where there would be an impact load interaction between the bird and the engine blade. The Johnson-Cook material is expressed with this high elastic and inelastic strain, thereby accurately simulating the bird strike computationally. The relation is expressed as follows:

$$\sigma_{eq} = \left[A + B\varepsilon_p^n\right]\left[1 + cln(\dot{\varepsilon}^*)\right]\left[1 - T^{*m}\right] \tag{6}$$

The equivalent stress, σ_{eq} is expressed as a function of plastic strain ε, strain rate $\dot{\varepsilon}$ and temperature, T. The function's constants are expressed in Table 2 by determining the constants of yield stress A, strain hardening parameter B, strain hardening exponent n, strain rate sensitivity parameter c, and temperature exponent m for the material properties of aluminium. The material properties are implemented together with the equation of state as discussed previously in the bird model.

Table 2: Johnson-Cook failure model constants for aluminium [14]

Yield Stress [MPa]	Strain hardening parameter [MPa]	Strain hardening exponent	Temperature exponent	D_1	D_2	D_3	D_4	D_5
167	590	0.551	0.859	0.0261	0.263	-0.349	0.247	16.8

4.2 Porous Blade Mesh and Assembly

Porosity is defined as the ratio of void volume to the total volume or can also be the ratio of void area to the total area. The term porosity is defined as a section where there are tiny 'voids' that are littered on the surface area, that can be either regional or distributed. A regional porosity is more concentrated such as the leading edge of a wing airfoil section whereas distributed porosity would cover the whole cross-sectional area. As such, the relationship is defined as:

$$Porosity\ (P) = \frac{void\ volume}{total\ volume} \tag{7}$$

This porosity value can be increased depending on how many voids are covered throughout the whole cross-sectional area. The blade model is meshed as a hexahedron element to accurately observe the computational bird strike and is shown in Fig. 2(a). Figure 2(b) shows the area of 620209.73 mm^2 with an arc length of 1099.71 mm at the leading edge where the porous holes are located along the arc. The porosity of the blade is featured as 5 mm diameter voids each spaced 5 mm apart. With around 103 holes distributed at the leading edge along the curvature, the porosity is determined with Eq. (7) to be $P = 0.32\%$ of the whole blade.

The blade assembly consists of 18 blades: equally spaced 20° around the hub. Computationally, the bird interacts with the leading edge, slicing the bird slightly before striking the whole of its weight onto the blade leading edge that causes high deformation.

5. COMPUTATIONAL RESULTS

5.1 Computational Simulation

LS-Dyna prepost software was used to computationally mesh and simulate the bird strike impact onto a porous engine blade. The initial velocity of the bird is set to v = 120 m/s from the basis of Wilbeck's experiment. The engine blades were set to ω = 200 rad/s angular rotation to simulate a take-off and landing scenario set by Vingjevic et al. [9]. Much

of the computational framework has been established through the keyword manager, where each of the bird model coefficients and blade material Johnson-Cook failure constants were implemented. The numerical framework established by Vingjevic et al. [9] provided much of the initial bird velocity, initial rotation of the engine blades and the implementation of a damage model.
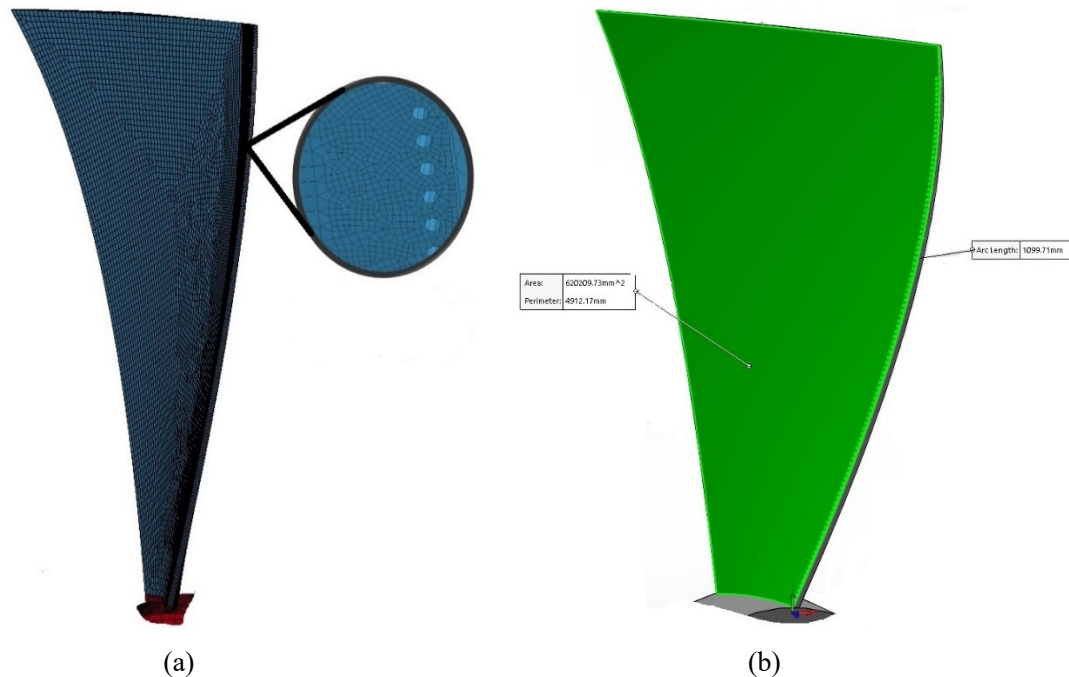

<div align="center">(a)   (b)</div>

Fig. 2: (a) Blade mesh assembly, (b) Blade geometry.

This paper studies closely the methodology and numerical framework established by Vingjevic. Vinjevic's failure model was analyzed as a Grüneisen parameter, this paper utilizes the keyword manager of LS-Dyna in conjunction with the numerical methods done by Vingjevic et al. [9]. It is shown that initial stresses appear at the blade's root due to the engine's rotation creating centrifugal forces. The stresses caused by these centrifugal forces can contribute to the load deformation once impact occurs. The termination time was set to 10 ms to allow observation of the bird impact into the subsequent blade after the initial impact. The simulation results are presented in Fig. 5 (a), (b), (c), (d), (e), and (f) where the impact loads are shown at 2 ms, 3 ms, 4 ms, 5 ms, 6 ms, and 7 ms respectively. The numerical analysis is presented as impact loads of Von-Mises effective stress. It is observed in Fig. 5 that as the bird impacts the blade, high stress occurs and bends the leading edge of the engine blade, thus causing deformation.

5.2 Computational Approach Validation

The computational method presented for this work is validated through a parametric study of bird strikes on engine blades done by Vingjevic et al. [9]. The research performed by Vingjevic et al. [9] utilised a Grüneisen parameter done through LS-Dyna Keyword manager and the polynomial equations of state of the bird model. The studies show that there are fringe levels and initial stresses (v-M) due to centrifugal forces. Figure 4 shows the resultant displacement (mm) or deformations caused by the bird strike impact along the leading edge and located at the porous regions. The trend here indicates that the bending forces and centrifugal force are consistent at the leading edge despite different modelling

parameters. The displacement shown at the leading edge has proven that the method used here can be utilized to the same effect.
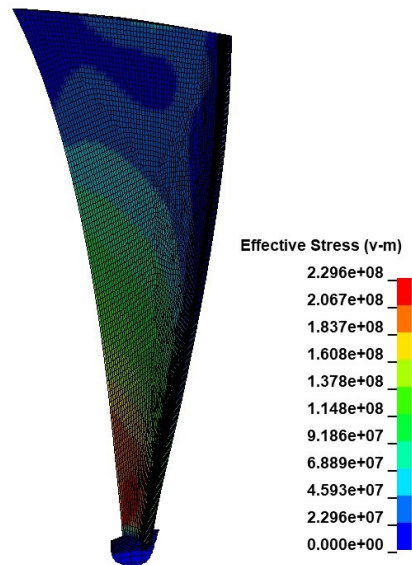

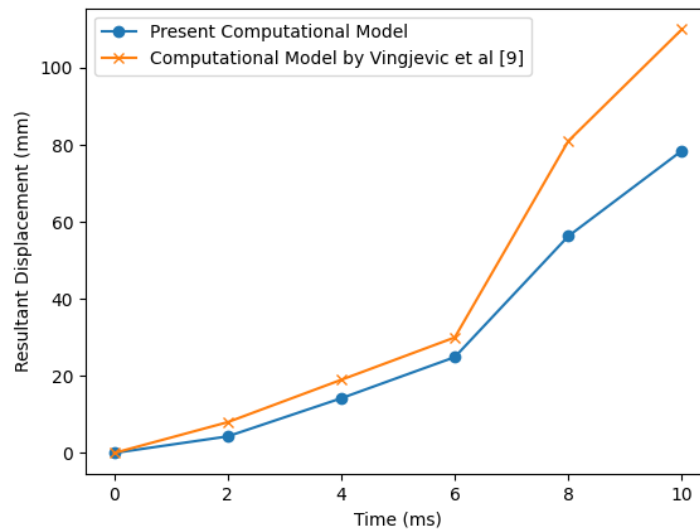Fig. 3: Initial stresses occur at the root due to centrifugal forces.

Fig. 4: Numerical validation through resultant displacement of present work with the computational result by Vingjenic et al. [9] based at the leading-edge.

5.3 Computational Results

The blade mesh geometry does flow well with the impact of the bird during computation. Despite the porous regions being more exposed to heavy impact, this allows the structure to be more visualized in many other aspects of the study. Effective stress here would be consistent with the validated procedures and show the behavior of the fluid flow structure interaction between the bird and the blade. The effective mean stress thus relates to the equivalent stress from the Johnson-Cook relationship that was defined. It is now

observed that a bird strike event can be computationally composed through the implemented method.
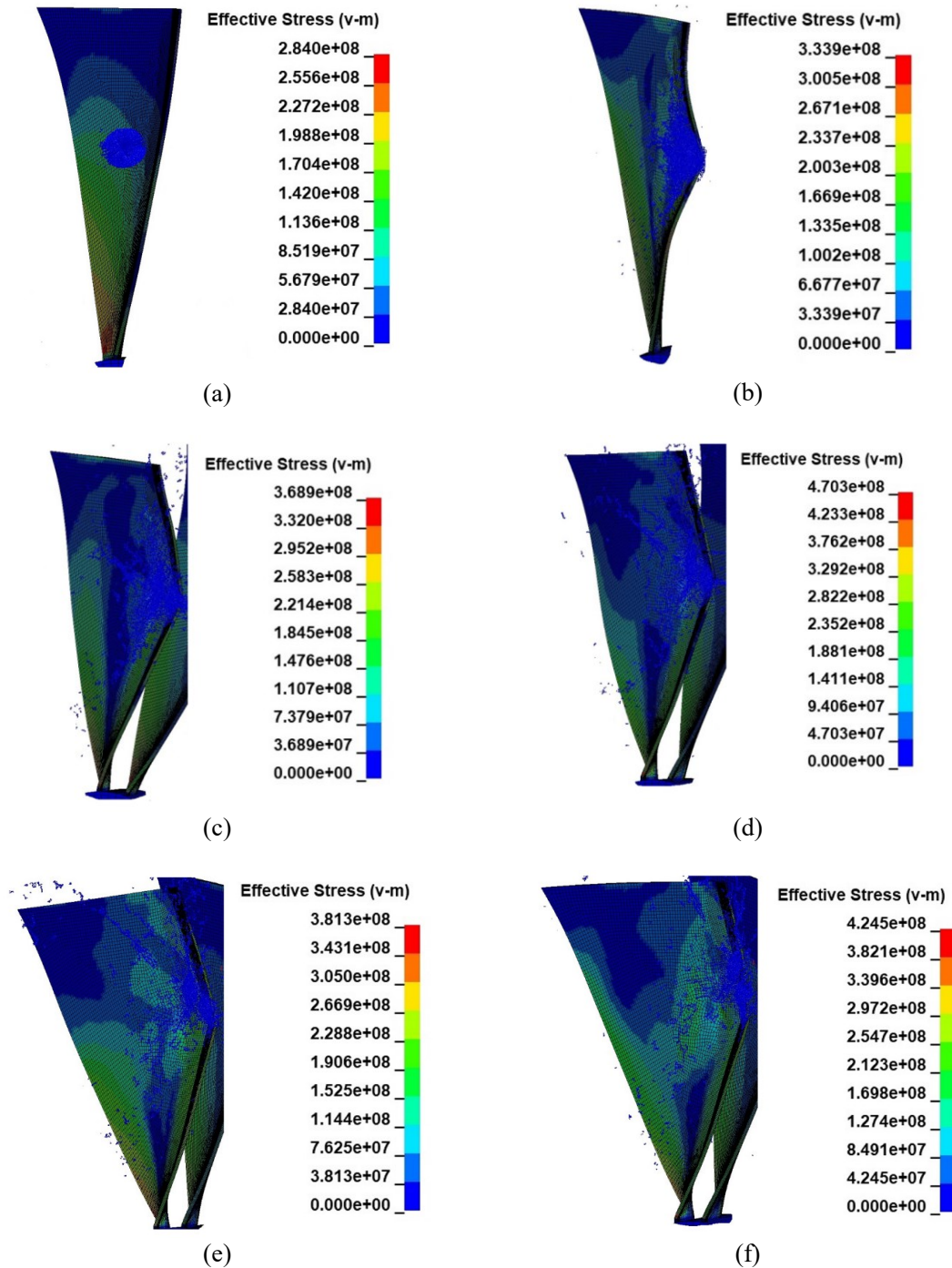

Fig. 5: V-M stresses (kPa) at time intervals (a) 2 ms, (b) 3 ms, (c) 4 ms, (d) 5 ms, (e) 6 ms, and (f) 7 ms.

When the bird interacts with the blade structure, the bird behaves as a fluid body, the SPH particles move individually, impacting and spreading the splatter throughout the whole surface of the blade. It is observed here that the impact point at the leading edge shows significant damage at the root and the leading edge where the voids are located. The impact at 2 ms in Fig. 5(a) is the initial condition just before impact where the bird travels at 120 m/s at the blade rotating at 200 rad/s. At 3 ms in Fig. 5(b), the bird smashes into the leading

edge, causing high deformation, and damaging the blade completely, bending the root at 339 MPa. Part of the bird splatter then moves on to the subsequent blade and also damages part of that blade with the stresses increasing for each subsequent time frame as shown in Fig. 5 (c), (d), (e), and (f).

5.4 Effect of Porosity

This paper investigates the effect of porosity implemented on the leading edge of a rotating engine blade. The effect of porosity compromises the structural integrity of the engine blade, causing higher deformation. Referring to Fig. 6(a) shows the porous blade while Fig. 6(b) shows a normal engine blade. The deformation of both the engine blades are slight while focusing on the blue region where the deformation of the model with small holes has slightly more deflection in z direction (0.1349 meters) while the model with no hole's deflection is only 0.1127 meters. Due to the holes disturbing the flow of the bird particles, the SPH particles become lodged into porous regions, interrupting the flow of impact as compared to the normal engine blade as shown in Fig. 5 (c), (d), (e), and (f).
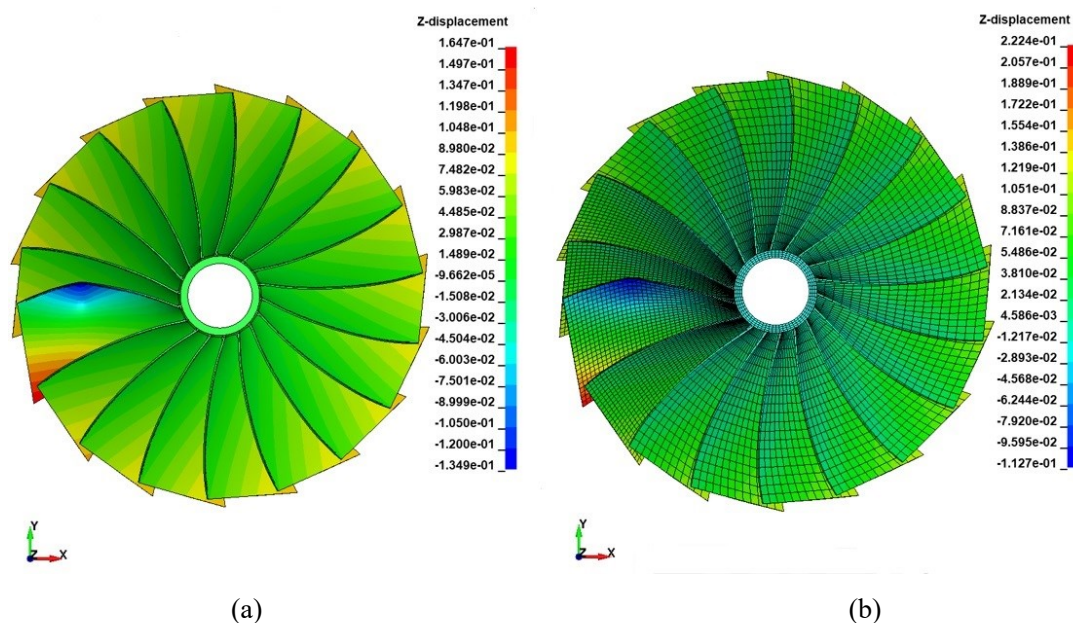

Fig. 6: z-displacement of jet engine blade after bird strike.

This comparison can be further analyzed by the energy absorbed by the jet engine blades. Referring to Fig. 7, the energy absorbed by both blade types see a slight drop after the initial impact as all the weight of the bird is concentrated at a that one point of impact. At 2 ms, when the bird has impacted the blade, the energy absorbed by both blades; porous and non-porous appear to be similar, since the bird has only impacted the smooth part of both blades, however, as soon as the SPH particles spread, it is more prevalent on the porous blade, the particles are lodged in the porous region and the voids absorb the energy of the impact, thus creating a higher change in absorbed energy for the porous blade at 4 ms. At 6 ms, the SPH particles have mainly swept off for the non-porous blade, as the flow of particles are much smoother, but for the porous blade, the jump in energy shows that the lodged particles observe a high increase in energy. After, 8 ms, most of the particles have spread around each blade, stabilizing the energy absorbed for the non-porous but increasing much more for the porous region.
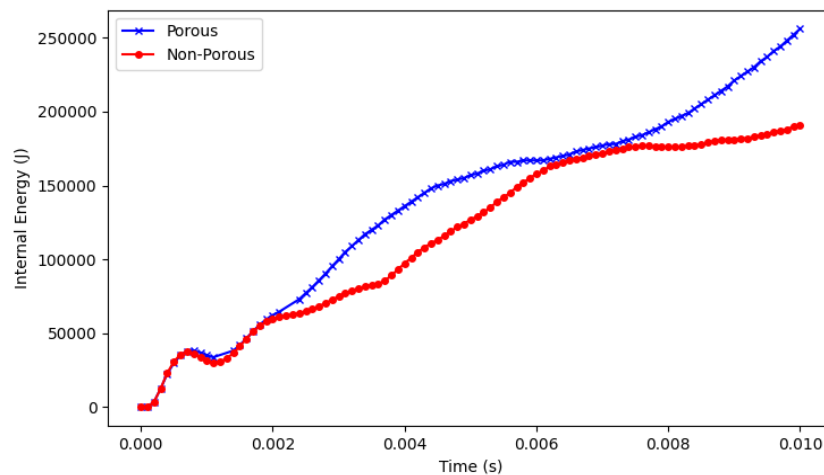
Fig. 7: Internal energy (J) vs Time (s) for porous and non-porous blade.

6. CONCLUSION

This paper analyses the damage of a numerically modelled porous engine blade subjected to bird strike. The bird is modelled as a hemispherical SPH particle model to accurately splatter the rotating engine blades at 120 m/s. The computational result for the porous blade observes a high impact damage at the porous region where the SPH particles spread and lodge within the voids of the porous, creating a high energy absorption compared to a non-porous engine blade for as much as 38.6 kJ or 39.63% increase at 4ms. Even the non-porous blade has stabilized by the end of 10ms, whereby the porous blade sees an increase in the energy absorbed, damage is prevalent enough for as much as 65 kJ or 34.03%. Bird strikes are indeed shown to be dangerous even for a normal engine blade used today. The compromise to the structural integrity of the engine blade is significant if a porous engine blade were to be implemented. As the energy absorbed is higher, the impact reaction toward the engine turbine can cause a very dangerous scenario in the event of a bird strike accident.

In terms of energy absorbed, since even though the voids contain no mass, the SPH particles are still lodged within the voids by the impact energy transferred by the bird momentum from the initial velocity onto the engine blades. The entire strength of the structure however has been reduced, the porosity on the leading edge is minuscule in that it would not really reduce the strength of the structure but since the bird struck directly at that area, the damage is still significant and the energy absorbed is still increased. Where there are voids located in the structure, the vibrational energy is still considered even though there is no mass to absorb the energy [11].

ACKNOWLEDGEMENT

REFERENCES

[1] Thorpe J. (2012) 100 years of fatalities and destroyed civil aircraft due to bird strikes. 30th Meeting of the International Bird Strike Committee, 1-36.

[2]   Wilbeck JS, Rand JL. (1981) The development of a substitute bird model. J. Engineering for Gas Turbines and Power, 103(4):725-730.

[3]   Liu J, Li Y, Gao X. (2014) Bird strike on a flat plate: Experiments and numerical simulations. Int. J. Impact Engineering, 70:21-37.

[4]   Guan Y, Zhao Z, Chen W, Gao D. (2008) Foreign objecct damage to fan rotor blades of aeroengine part II: Numerical simulation of bird impact. Chinese J. Aeronautics, 21(4):328-334.

[5]   Abdullah NA, Akbar M, Wirawan N, Curiel-Sosa JL. (2019) Structural integrity assessment on cracked composites interaction with aeroelastic constraint by means of XFEM. Composite Structures, 229.

[6]   Wirawan N, Abdullah NA, Akbar, Curiel-Sosa JL. (2018) Analysis on cracked commuter aircraft wing under dynamic cruise load by means of XFEM. J. Physics: Conference Series, 1106(1).

[7]   Ahmad MIM, Curiel-Sosa JL, Akbar M, Abdullah NA. (2018) Numerical inspection based on quasi-static analysis using Rousselier damage model for aluminium wingbox aircraft structure. J. Physics: Conference Series, 1106(1).

[8]   Shahimi SS, Abdullah NA, Hrairi M, Ahmad MIM. (2021) Numerical investigation on the damage of whirling engine blades subjected to bird strike impact. J Aeronautics, Astronautics and Aviation, 53(2):193-200.

[9]   Vignjevic R, Orlowski M, De Vuyst T, Campbell JC. (2013) A parametric study of bird strike on engine blades. Int. J. Impact Engineering, 60:44-57.

[10] Aldheeb M, Asrar W, Sulaeman E, Omar AA. (2018) Aerodynamics of porous airfoils and wings. Acta Mechanica, 229(9):3915-3933.

[11] Kovalev IS. (2019) Buttefly acoustical skin – new method of reducing aero acoustical noise for a quiet propeller. J. Engineering Mechanics and Machinery, 4(1):1-28.

[12] Dar UA, Awais M, Mian HH, Sheikh MZ. (2019) The effect of representative bird model and its impact direction on crashworthiness of aircraft windshield and canopy structure. Proceedings of the Institution of Mechanical Engineers, Part G: J. Aerospace Engineering, 233(14):5150-5163.

[13] Riccio A, Cristiano R, Saputo S. (2016) A brief introduction to the bird strike numerical simulation. American J. Engineering and Applied Sciences, 9(4):946-950.

[14] Banerjee A, Dhar S, Acharyya S, Datta D, Nayak N. (2015) Determination of Johnson Cook material and failure model constants and numerical modelling of Charpy impact test of armour steel. Materials Science and Engineering, 640:200-209.

OPTIMAL PIEZOELECTRIC SHUNT DAMPER USING ENHANCED SYNTHETIC INDUCTOR: SIMULATION AND EXPERIMENTAL VALIDATION

MUHAMMAD NAZRI SUHAIMI, AZNI NABELA WAHID[*]**,
NOR HIDAYATI DIYANA NORDIN AND KHAIRUL AFFENDY MD NOR**

*Smart Structure System & Control Lab (S3CRL), Mechatronics Engineering Department,
International Islamic University Malaysia,
Jalan Gombak, 53100 Kuala Lumpur, Malaysia*

[*]*Corresponding author: azni@iium.edu.my*

ABSTRACT: Piezoelectric material has the ability to convert mechanical energy to electrical energy and vice versa, making it suitable for use as an actuator and sensor. When used as a controller in sensor mode, the piezoelectric transducer is connected to an external electrical circuit where the converted electrical energy will be dissipated through Joule heat; also known as piezoelectric shunt damper (PSD). In this work, a PSD is used to dampen the first resonance of a cantilever beam by connecting its terminal to an *RL* shunt circuit configured in series. The optimal resistance and inductance values for maximum energy dissipation are determined by matching the parameters to the first resonant frequency of the cantilever beam, where $R = 78.28$ kΩ and $L = 2.9$ kH are found to be the optimal values. To realize the large inductance value, a synthetic inductor is utilized and here, the design is enhanced by introducing a polarized capacitor to avoid impedance mismatch. The mathematical modelling of a cantilever beam attached with a PSD is derived and simulated where 70% vibration reduction is seen in COMSOL. From experimental study, the vibration reduction obtained when using the piezoelectric shunt circuit with enhanced synthetic inductor is found to be 67.4% at 15.2 Hz. Results from this study can be used to improve PSD design for structural vibration control at targeted resonance with obvious peaks.

ABSTRAK: Material piezoelektrik mempunyai keupayaan mengubah tenaga mekanikal kepada tenaga elektrik dan sebaliknya, di mana ia sesuai digunakan sebagai penggerak dan pengesan. Apabila digunakan sebagai alat kawalan dalam mod pengesan, piezoelektrik disambung kepada litar elektrik luaran di mana tenaga elektrik yang ditukarkan akan dibebaskan sebagai haba Joule; turut dikenali sebagai peredam alihan piezoelektrik (PSD). Kajian ini menggunakan PSD sebagai peredam resonan pertama pada palang kantilever dengan menyambungkan terminal kepada litar peredam *RL* bersiri. Rintangan optimal dan nilai aruhan bagi tenaga maksimum yang dibebaskan terhasil dengan membuat padanan parameter pada frekuensi resonan pertama palang kantilever, di mana $R = 78.28$ kΩ dan $L = 2.9$ kH adalah nilai optimum. Bagi merealisasikan nilai aruhan besar, peraruh buatan telah digunakan dan di sini, rekaan ini ditambah baik dengan memperkenalkan peraruh polaris bagi mengelak ketidakpadanan impedans. Model matematik palang kantilever yang bersambung pada PSD telah diterbit dan disimulasi, di mana 70% getaran berkurang pada COMSOL. Hasil dapatan eksperimen ini menunjukkan pengurangan getaran yang terhasil menggunakan litar peredam piezoelektrik bersama peraruh buatan menghasilkan 67.4% pada 15.2 Hz. Hasil dapatan kajian ini dapat digunakan bagi membaiki rekaan PSD berstruktur kawalan getaran iaitu pada resonan tumpuan di puncak ketara.

1. INTRODUCTION

In applications for vibration control, a piezoelectric patch can be perfectly bonded to a vibrating mechanical structure to supply equal and opposite force to its host structure (active control) or dissipate the mechanical energy via joule heat (passive control). In the latter case, whenever the host structure vibrates, an electrical charge will accumulate in the piezoelectric material and this energy can be dissipated as Joule heat if the patch terminal is connected to an external shunt circuit matched to the mechanical resonance of its host structure; also known as piezoelectric shunt damping. This results in vibration suppression equivalent to a tuned mass damper in a mechanical system.

The concept of electromechanical damping using a piezoelectric shunt damper was introduced by Hagood Von Flotow in 1991 [1] and ever since, there have been various studies conducted due to its potential and versatility in various applications requiring suppression; for example in aircraft [2], marine [3] or railway vehicles [4], and many more. For maximum energy dissipation to occur, the shunt circuit needs to be tuned to the targeted resonant frequency of the host structure, and the simplest form of circuit available uses resistor-inductor (*RL*) components, equivalent to mass-springs in mechanical systems. The electrical impedance of the shunt circuit matched with the mechanical resonance typically will have a significantly large inductance value. To realize this, a synthetic inductor circuit is introduced using op-amps. Although this method has been proven to be successful [5-9], there are areas of improvement that can be made in terms of its efficiency. One of the problems that arise is the large internal resistance developed in the synthetic inductor circuit to generate the huge inductance. As a result, the resistance developed usually exceeds the optimum resistance value required to suppress the matched vibration mode, thereby creating a mismatch in the circuit impedance. To alleviate this, the concept of enhanced shunt circuit will be applied, where an additional capacitor will be added in parallel to the shunt circuit [10,11].

In this work, a resonant-type piezoelectric shunt damper on a cantilever beam will be studied and the optimal shunt circuit will be constructed. In section 2, the mathematical model of a cantilever beam attached with a PSD in series configuration is presented. The optimal values of resistance, *R* and inductance, *L* for the shunt circuit is also derived and shown. Following that, simulation studies are carried out in section 3 to show the performance of the PSD in suppressing the first resonant by using COMSOL Multiphysics software. Since the value of inductance, *L* will be large, an enhanced synthetic inductor method will be adopted and shown in section 4 where experimental study is also carried out to validate the findings.

2. MATHEMATICAL MODELLING

2.1 Modelling of the Piezoelectric Shunt Damper System

The piezoelectic constitutive equation can be written as follows [12]:

$$\begin{Bmatrix} T \\ D \end{Bmatrix} = \begin{bmatrix} c^E & -e \\ e^t & \varepsilon^S \end{bmatrix} \begin{Bmatrix} S \\ E \end{Bmatrix} \tag{1}$$

where *T* is a stress vector, *D* is an electric displacement vector, *S* is a strain vector, *E* is an electric field vector, c^E is an elasticity stiffness matrix evaluated at constant electric field, *e* is a piezoelectric stress matrix, ε^S is a dielectric matrix evaluated at a constant mechanical

strain, t is a matrix transpose. The coupled cantilever beam-piezoelectric equation can be derived after applying Hamilton's principle to obtain the following electromechanical system [13,14]:

$$\begin{bmatrix} M & 0 \\ 0 & 0 \end{bmatrix} \begin{Bmatrix} \ddot{w} \\ \ddot{v} \end{Bmatrix} + \begin{bmatrix} C & 0 \\ 0 & 0 \end{bmatrix} \begin{Bmatrix} \dot{w} \\ \dot{v} \end{Bmatrix} + \begin{bmatrix} K & \Theta \\ \Theta^t & -C_P \end{bmatrix} \begin{Bmatrix} w \\ v \end{Bmatrix} = \begin{Bmatrix} F \\ q \end{Bmatrix} \tag{2}$$

where $[M]$ is a global mass matrix, $[C]$ is a global damping matrix, $[K]$ is a global stiffness matrix, $[C_P]$ is an inherent piezoelectric capacitance matrix, $[\Theta]$ is an electromechanical coupling matrix of the host structure and piezoelectric material, $\{F\}$ is an applied mechanical force vector, $\{q\}$ is an electric charge vector, $\{w\}$ is a generalized mechanical coordinate and $\{v\}$ is a generalized electrical coordinate. The shunt damping voltage can be represented by the current-voltage relationship in the Laplace domain when the piezo patch is shunted by an impedance, as illustrated in Fig. 1.
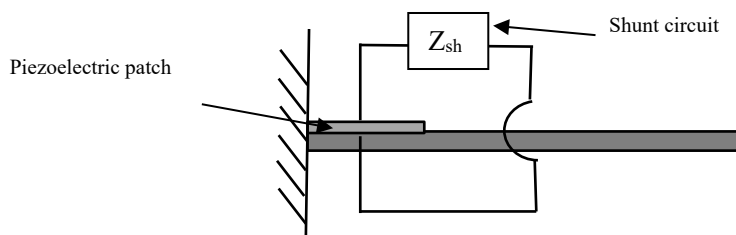

Fig. 1: Illustration of a cantilever beam attached with piezoelectric shunt damper (PSD).

$$V_{sh}(s) = Z_{sh}(s) . I_{sh}(s) \tag{3}$$

where $V_{sh}(s)$ is the voltage across the impedance; $I_{sh}(s)$ is the current flowing through the shunt circuit; Z_{sh} is the shunt impedance and s is a Laplace operator. Differentiating electric potential, q in Eq. (2) and substituting into Eq. (3), the following is obtained:

$$\begin{aligned} V_{sh}(s) = Z_{sh}(s) . \dot{q}(s) = Z_{sh}(s) . ([\Theta]^t \{w\}s \\ - [C_P] V_{sh}(s)s) \end{aligned} \tag{4}$$

Rearranging Eq. (4),

$$V_{sh}(s) = \frac{Z_{sh}(s) [\Theta]^t \{w\} s}{1 + Z_{sh}(s) [C_p] s} \tag{5}$$

Finally, substituting Eq. (5) into Eq. (2), the total equation of motion for a cantilever beam attached with a piezoelectric patch connected to a shunt circuit is obtained as follows:

$$[M]\{\ddot{w}\} + (Z_{total}[\Theta][\Theta]^t)\{\dot{w}\} + [K]\{w\} = \{F\} \tag{6}$$

The term Z_{total} is the total electrical impedance of the shunt circuit where:

$$Z_{total} = \frac{Z_{sh}}{1 + Z_{sh}[C_p]s} \tag{7}$$

If the electrical impedance for the shunt circuit is in series configuration, Z_{sh}^s, it can be written as,

$$Z_{sh}^s = L_s^* s + R_s^* \tag{8}$$

where L_s^* and R_s^* are the optimal inductance and resistance, respectively. Both can be written as follows [7]:

$$L_s^* = \frac{1}{C_P^S(\omega_s \delta_s^*)^2} \; ; \quad R_s^* = \frac{r_s^*}{\omega_s C_P^S} \tag{9}$$

where C_P^S is the piezo capacitance at constant strain, $C_P^S = C_P^T(1 - k_{31}^2)$, and C_P^T is the piezo capacitance at constant stress,

$$C_P^T = \frac{K_3^T \times \varepsilon_o \times A_P}{t_p} \tag{10}$$

All the terms in Eq. (10) are dependent on the type of piezoelectric patch used where $K_3^T, \varepsilon_o, A_P$ and t_p are the relative dielectric constant, relative permittivity of free space, area of the patch, and thickness of the patch, respectively. The terms δ_s^* and r_s^* in Eq. (9) are the optimal tuning ratio and optimal damping ratio for series configuration, which are dependent on the piezo electromechanical coupling coefficient for a transverse mode 31, k_{31}:

$$\delta_s^* = \sqrt{1 + k_{31}^2} \; ; \quad r_s^* = \sqrt{2}\frac{k_{31}}{1 + k_{31}^2} \tag{11}$$

The coefficient k_{31} describes the conversion of energy by the piezo element from electrical to mechanical and vice versa. It can be derived in several ways; one of them is using resonant frequency change with respect to the electric boundary conditions,

$$k_{31} = \sqrt{(\omega_o^2 - \omega_s^2)/\omega_s^2} \tag{12}$$

where ω_o and ω_s are natural frequencies of the beam when the piezoelectric patch is in open circuit and short circuit condition, respectively. In this work, these values will be obtained experimentally, which will be discussed in Section 4. For this work, the electromechanical coupling value for this specific piezoelectic patch is found to be $k_{31} = 0.196$.

The total electrical impedance in series, Z_{total}^S as shown in Eq. (6) can be re-written as,

$$Z_{total}^S = \frac{L_s^* s + R_s^*}{L_s^* C_p s^2 + R_s^* C_p s + 1} \tag{13}$$

The values found for the optimal parameters, as discussed above, are tabulated in Table 1.

The optimal resistance and inductance in Table 1 make up the electrical impedance of the series shunt circuit in order to dissipate the mechanical energy of the host structure at first resonant frequency. These values will be constructed using physical RL components where evidently, the resistance value can be realized by using off-the-shelf resistors, however this is not the case for the inductor. Since inductor value typically ranges from 1 μH to 20 H, an enhanced synthetic inductor will be implemented to acquire inductance in the range of kH.

Table 1: Values of optimal tuning and damping ratio and optimal resistance and inductance calculated using Eqs. (9) and (11)

	Series shunt circuit
Optimal tuning ratio, δ^*	1.0197
Optimal damping ratio, r^*	0.2715
Optimal resistor, R^*, Ω	78.28×10^3
Optimal inductor, L^*, H	2902.9

3. SIMULATION STUDIES

For simulation study, a stainless-steel cantilever beam with dimensions of 280 mm x 40 mm x 2 mm is used. A PZT-5A piezoelectric patch with 50 mm x 20 mm x 0.38 mm dimension is attached at the fixed end of the beam. The terminal of the piezoelectric patch is connected to an optimal *RL* circuit in series configuration as found in Table 1. The damping performance of the PSD will be investigated where the difference between the displacement of the beam at its first resonant frequency, without damping and with damping is compared. For this, the circuit is made open so there will be no current passing through i.e. the shunt damping circuit is not connected and is hereby considered as a no-damping condition. And when the circuit is made closed, current can pass through the shunt damping circuit and this is when damping condition exists.
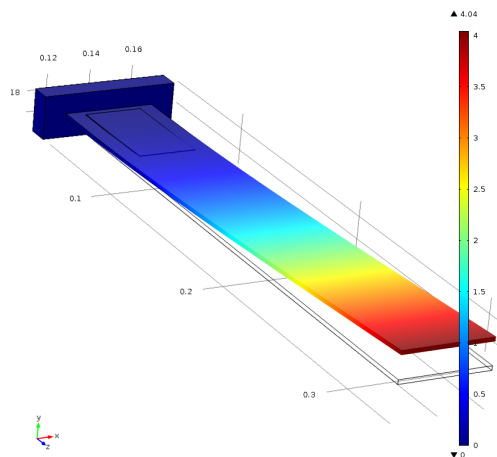

Fig. 2: Cantilever beam attached with piezoelectric patch at its fixed end modelled in COMSOL.
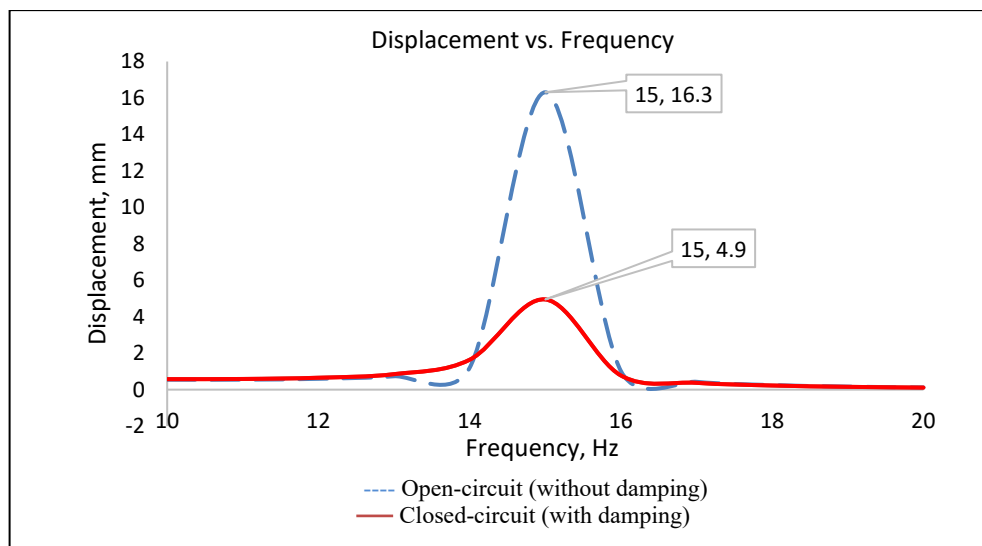

Fig. 3: Comparison of the beam displacement amplitude at first resonance (blue-dashed: open circuit, red-solid: closed-circuit) using COMSOL.

Figure 3 shows the response of the beam-PSD system simulated via COMSOL where the terminal of the piezoelectric is set as 'floating potential' and 'terminal' for open and close circuit condition, respectively. A series *RL* circuit following the values found in Table 1 is connected to the terminal as the optimal shunt circuit. The displacement of the cantilever beam is plotted at a frequency range that covers its first resonant frequency. The responses

when PSD is in open circuit (without damping) and closed circuit (with damping) conditions are plotted and compared to see the PSD damping performance. From the figure, the difference between the displacement peak i.e. vibration reduction is recorded to be 70% in COMSOL.

4. OPTIMAL SHUNT CIRCUIT CONSTRUCTION

4.1 Equation of Input Impedance for Synthetic Inductor

To realize the significantly large value of inductance, a synthetic inductor is constructed utilizing two op-amps, three resistors, and a capacitor with some voltage being supplied to the op-amps. To calculate the input impedance of the synthetic inductor, a few conditions must be stated. First, the op-amp is assumed to be ideal, so that the input impedance of the amplifier is infinitely high. This caused the current at input terminal to be zero. Secondly, the voltage gain is infinitely high, therefore the voltage across input terminal is zero while output voltage remained finite [9].

$$Z_{in} = j\omega \frac{R_1 R_3 R_5 C_4}{R_2} \tag{14}$$

From Eq. (14), it is shown that the circuit has the same characteristics as an ideal inductor. Rearranging Eq. (14),

$$L = \frac{R_1 R_3 R_5 C_4}{R_2} \tag{15}$$

Essentially, the desired inductance can be changed by changing the value of R_2 accordingly. The optimal inductance, L value for maximum energy dissipation was found earlier to be 2902.9 H. Following Eq. (14), the resistance values for resistors R_1, R_3, and R_5 are chosen to be 97.4 kΩ, 101.1 kΩ and 95 kΩ, respectively and achieved using potentiometers. For C_4, a 1 μF capacitor is used. Therefore, the value of R_2 needs to be 322, 260 Ω to achieve the desired optimal inductance, L.

4.3 Enhanced Shunt Circuit Implementation

Although physically doable, one of the problems that arise is the large internal resistance developed in the synthetic inductor circuit to generate the huge inductance. From this, the developed resistance exceeds the optimum resistance value required to suppress the matched vibration mode, therefore creating a mismatch in the circuit impedance. Utilizing the concept of enhanced shunt circuit [10,11], an additional capacitor will be added in parallel to the shunt circuit to increase the capacitance of the piezoelectric patch. In this case, a 4.7 mF capacitor (i.e. polarized capacitor) is connected in parallel to 55 nF piezoelectric, creating an equivalent capacitor of, $C_{eq} = C_{piezo} + C_{capacitor}$.

The schematic of the shunt circuit to be constructed is shown in Fig. 4 using the values obtained in Table 1. From Fig. 4, the shunt circuit consists of a resistor in series with a synthetic inductor, connected in parallel with a 4.7 mF polarized capacitor and the piezoelectric patch, where the patch can be modelled as a capacitor having an inherent capacitance of 55 nF. Figure 5 shows the physical implementation of the shunt circuit.
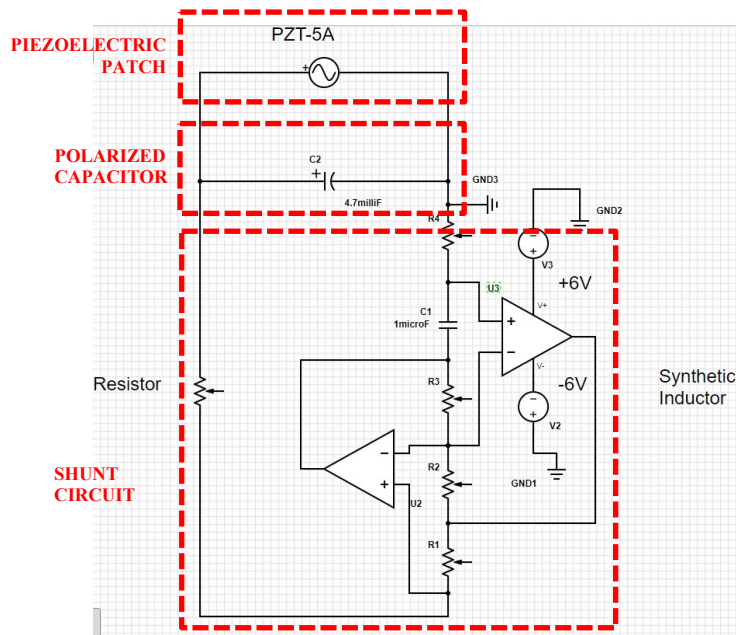
Fig. 4: Schematic of the piezo patch attached with optimal *RL* shunt circuit
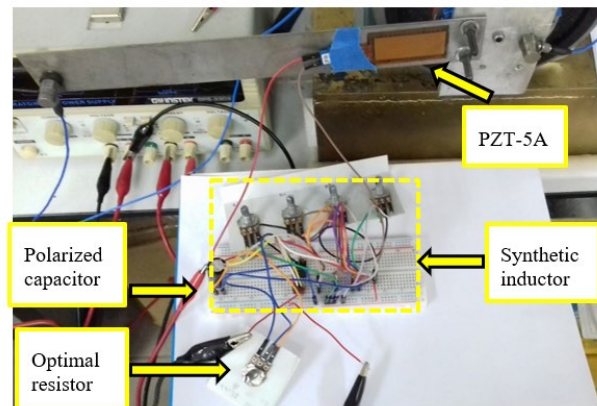in series utilizing a synthetic inductor.

Fig. 5: Experimental setup of the piezo patch attached with optimal *RL* shunt circuit
in series utilizing a synthetic inductor.

5. EXPERIMENTAL STUDIES

The complete setup of the experiment is shown in Fig. 6. Here, a piezoelectric patch is bonded on the surface of cantilever beam using a thin layer of epoxy adhesive. The position of the patch is near the fixed end of the beam as this is where the largest stress and strain is generated when it deflects. In this study, the piezoelectric patch used is QuickPack model QP10N made from PZT-5A (3195HD material type). The dimensions of the beam and piezoelectric patch used are shown in Table 2. The end of the beam is clamped to an ET-139 electrodynamic shaker with two accelerometers mounted at the free end and at the clamped end of the beam to measure the output and input to the system, respectively. The piezoelectric terminals are connected to the optimal shunt circuit as constructed in Section 3.
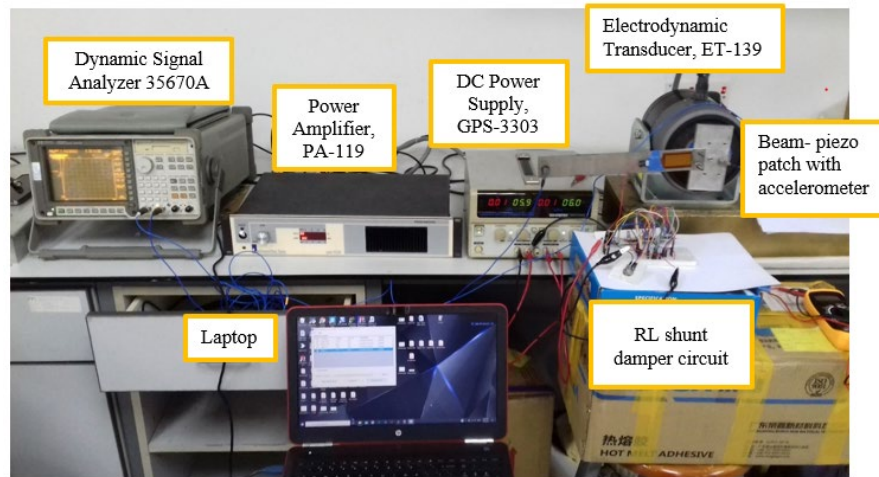
Fig. 6: The complete experimental setup for vibration control using optimal piezoelectric shunt damper.

Table 2: The dimensions of beam and piezoelectric patch used in experiment

	Length, m	Width, m	Thickness, m	Material
Beam	0.28	0.04	0.002	Stainless steel
Piezoelectric patch	0.04597	0.02057	0.000381	PZT-5A (3195HD)

5.1 Determining Short Circuit Natural Frequency, ω_s and Open Circuit Natural Frequency, ω_o

The purpose of determining short circuit natural frequency, ω_s and open circuit natural frequency, ω_o is to determine the electromechanical coupling, k_{31} of the piezoelectric patch, as stated in Eq. (12). Here, the open circuit natural frequency is obtained when the beam-PSD system is excited at its first natural frequency where the terminal is left open; while for short circuit natural frequency, the piezoelectric terminal is put in short circuit condition by connecting a wire through both terminals. Figure 7 shows the frequencies obtained for each case.
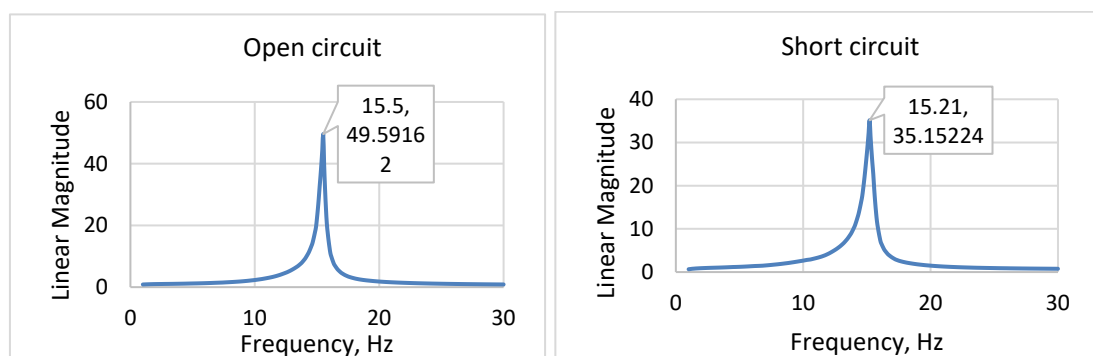

Fig. 7: Natural frequency in open-circuit (left) and short-circuit (right) condition, ω_o = 15.50 Hz and ω_s = 15.21Hz, respectively.

From these values, it is determined that electromechanical coupling value for this specific piezoelectric patch to be k_{31} = 0.196 which will be used throughout the work.

5.2 Vibration Control of Cantilever Beam with Optimal PSD

The performance of the piezoelectric shunt damper system is to be validated. The terminal of the piezoelectric patch is now connected to the optimal shunt circuit constructed as discussed in Section 4. For implementation of the synthetic inductor, a DC power supply is required to supply voltage to the LM358P op-amps. The experiment is performed by supplying sine-wave input to the beam-PSD system through the electromagnetic shaker, capturing the first resonance of the beam. The response of the beam is collected when the piezoelectric terminal is in open-circuit condition (without damping) and when the terminal is connected to the optimal shunt circuit (with damping), respectively.
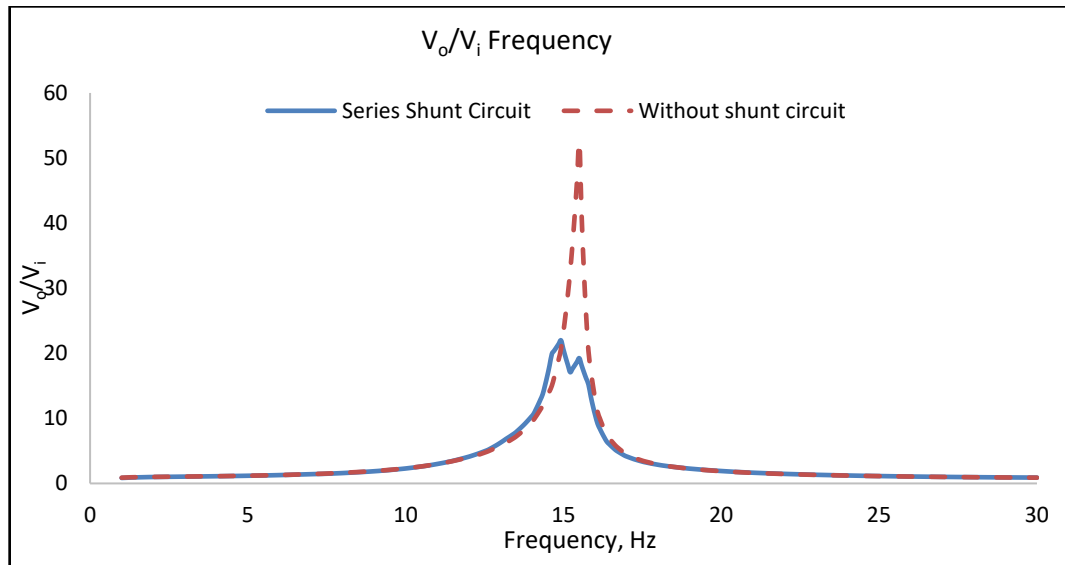

Fig. 8: Experimental result on the vibration response of the beam-PSD with damping (blue-solid) and without damping (red-dashed).

Figure 8 shows the vibration response of the cantilever beam at its first resonant frequency denoted by the ratio of output and input voltages (V_o/V_i) from the accelerometer located at the beam tip (output from the system) and at the beam clamp (input to the system), respectively. Two measurements are taken, i.e. in open-circuit and closed-circuit condition, and the data is plotted on the same graph for comparison. Reduction of vibration can be seen at the first resonant peak, calculated to be 67.4%. The comparison of the PSD performance from simulation and experiment is shown in Table 3. It can be concluded that the constructed enhanced optimal shunt circuit manages to dissipate energy from its host structure successfully, and therefore validated the results from simulation studies conducted.

Table 3: The performance of the vibration reduction using optimum *RL* values.

Technique	1st nat. freq.	Amplitude at 1st nat. freq.	Vibration reduction percentage, %
Simulation (COMSOL)	15 Hz	16.3 mm (disp.) – no damping 4.9 mm (disp.) – with damping	70
Experiment	15.2Hz	52.4 (V_o/V_i) - no damping 17.1 (V_o/V_i) - with damping	67.4

6. CONCLUSION

In this work, a piezoelectric shunt damper with enhanced synthetic inductor is used to damp the first resonance of a cantilever beam, which is shown both in simulation and via experiment. The optimal resistance and inductance values for the shunt circuit are found to be R = 78.28 kΩ and L = 2.9 kH, respectively. Due to the significantly large value of inductance required, a synthetic inductor is utilized and enhanced by introducing a polarized capacitor attached in parallel to the synthetic inductor to avoid impedance mismatch. Finally, the series shunt circuit is tested and it is found that the vibration reduction achieved is 67.4% experimentally which agrees with the simulation study.

ACKNOWLEDGEMENT

REFERENCES

[1] Hagood NW, von Flotow A. (1991) Damping of structural vibrations with piezoelectric materials and passive electrical networks. Journal of sound and vibration, 146(2): 243-268.

[2] Chatziathanasiou, G., Chrysohoidis, N., Kostas, G., & Saravanos, D. A. (2021). Semi-Active Vibration Control of Aircraft Structures. In *AIAA Scitech 2021 Forum* (p. 1736).

[3] Pernod, L., Lossouarn, B., Astolfi, J. A., & Deü, J. F. (2021). Vibration damping of marine lifting surfaces with resonant piezoelectric shunts. *Journal of Sound and Vibration*, *496*, 115921.

[4] Yun, Y. S., Kim, J. C., Noh, H. M., & Kim, M. S. (2021). Reduction in High-Frequency Wheel Noise/Vibration of Railway Vehicles Using Piezoelectric Shunt. *International Journal of Precision Engineering and Manufacturing - Green Technology*, *8*(3), 981–995.

[5] Mohammadi A. (2017) Passive vibration control of a cantilever beam using shunted piezoelectric element. 5th RSI Int. Conf. Robot. Mechatronics, no. IcRoM, pp. 389–393.

[6] Park, C. H. (2003). Dynamics modelling of beams with shunted piezoelectric elements. *Journal of Sound and Vibration*.

[7] Jeon, J. Y. (2009). Passive vibration damping enhancement of piezoelectric shunt damping system using optimization approach. *Journal of Mechanical Science and Technology*.

[8] Lossouarn, B., Aucejo, M., Deü, J. F., & Multon, B. (2017). Design of inductors with high inductance values for resonant piezoelectric damping. *Sensors and Actuators A: Physical*, *259*, 68-76.

[9] Mayer, D., Linz, C., & Krajenski, V. (2015). Synthetic inductor for passive damping of structural vibrations. In *7th ECCOMAS Thematic Conference on Smart Structures and Materials. SMART*.

[10] Park CH, Inman DJ. (2003), Enhanced piezoelectric shunt design. Shock Vib., 10(2):127–133.

[11] Fleming, A. J., Behrens, S., & Moheimani, S. O. R. (2003). Reducing the inductance requirements of piezoelectric shunt damping systems. *Smart Materials and Structures*.

[12] American and Standard. (1998) IEEE Standard on Piezoelectricity: An American National Standard. ANSI/IEEE Std 176-1987

[13] Wahid AN. Muthalif AG, Nor KA. (2016) Investigating negative capacitance shunt circuit for broadband vibration damping and utilizing ACO for optimization. Int. J. Circuits Electron, 1: 168-173.

[14] Marakakis, K., Tairidis, G. K., Koutsianitis, P., & Stavroulakis, G. E. (2019). Shunt piezoelectric systems for noise and vibration control: A review. In *Frontiers in Built Environment*.

MAXIMIZING OUTPUT VOLTAGE OF A PIEZOELECTRIC ENERGY HARVESTER VIA BEAM DEFLECTION METHOD FOR LOW-FREQUENCY INPUTS

MOHAMAD SAFIDDIN MOHD TAHIR, NOOR HAZRIN HANY MOHAMAD HANIF[*]
AND AZNI NABELA WAHID

Department of Mechatronics Engineering, International Islamic University Malaysia, Jalan Gombak, 53100 Kuala Lumpur, Malaysia

[*]*Corresponding author: noorhazrin@iium.edu.my*

ABSTRACT: In micro-scale energy harvesting, piezoelectric (PZT) energy harvesters can adequately convert kinetic energy from ambient vibration to electrical energy. However, due to the random motion and frequency of human motion, the piezoelectric beam cannot efficiently harvest energy from ambient sources. This research highlights the ability of piezoelectric energy harvester constructed using a PZT-5H cantilever beam to generate voltage at any input frequency from human motion. An eccentric mass is used to convert the linear motion of human movement to angular motion. Then, using a magnetic plucking technique, the piezoelectric beam is deflected to its maximum possible deflection each time the eccentric mass oscillates past the beam, ensuring the highest stress is induced and hence the highest current is generated. For testing works, the frequency of oscillation of the eccentric mass is controlled using an Arduino Uno microcontroller. In this work, it is found that when given any input frequencies, the energy harvester produced a consistent AC voltage peak around 5.8 Vac. On the other hand, the DC voltage produced varies with respect to the input frequency due to the number of times the peak AC signal is generated. The highest DC voltage produced in this work is 3.7 Vdc, at 5 Hz, which is within the frequency range of human motion. This research demonstrated that energy can still be effectively harvested at any given low-frequency input, in the condition that the piezoelectric beam is being deflected at its maximum.

ABSTRAK: Piezoelektrik dapat mengubah tenaga kinetik daripada getaran persekitaran kepada tenaga elektrik melalui penjanaan tenaga berskala mikro. Namun, PZT tidak dapat menjana tenaga dengan berkesan dari sumber persekitaran kerana pergerakan dan kekerapan pergerakan manusia adalah rawak. Kajian ini adalah mengenai keupayaan penuai tenaga piezoelektrik menggunakan bilah kantilever PZT-5H bagi menjana voltan pada sebarang frekuensi menerusi gerakan manusia. Jisim eksentrik digunakan bagi menukar gerakan linear manusia kepada gerakan putaran. Kemudian, teknik penjanaan piezoelektrik secara magnetik digunakan bagi memesongkan bilah piezoelektrik ke tahap maksimum. Bagi memastikan tenaga tertinggi dihasilkan, jisim eksentrik perlu berayun melepasi bilah PZT. Ayunan frekuensi jisim eksentrik ini dikawal melalui kawalan mikro Arduino Uno. Dapatan kajian menunjukkan bagi setiap frekuensi input, PZT ini dapat menghasilkan voltan AC yang konsisten, iaitu sekitar 5.8 Vac. Namun, voltan DC maksimum yang terhasil adalah berbeza-beza bagi setiap frekuensi input, iaitu berdasarkan bilangan kekerapan maksimum isyarat AC yang terhasil. Voltan DC tertinggi ialah 3.7 Vdc, pada 5 Hz, iaitu pada kadar frekuensi gerakan manusia. Ini menunjukkan bahawa tenaga masih dapat dihasilkan secara berkesan pada frekuensi rendah, dengan syarat bilah piezoelektrik terpesong pada tahap maksimum.

1. INTRODUCTION

The miniaturization of electronics components such as sensors has been rapidly developed for wearable and portable devices. These sensors have a variety of uses on the human body, including heart monitoring sensors, glucose level sensors, blood pressure and oxygenation sensors, and medication administration systems [1]. The sensors' diminutive size enables them to be comfortably fastened to a human body part. Additionally, the size reduction resulted in a reduction in power usage. By and large, most electronic gadgets use a conventional battery that has a finite life and requires replacement. This increases the attractiveness of alternatives to batteries as a power source. Batteries are the single largest source of electronic waste on a global scale. These conventional batteries contain hazardous elements that can be lethal to human health and the environment if not disposed of correctly [2].

One viable solution is to build self-powered gadgets capable of generating their own electricity, a process commonly known as energy harvesting. Energy harvesting can be used to harvest energy from a variety of sources, such as vibration, wind, sound, and human motion [3-5]. Numerous studies have been conducted on energy harvesting from human motion, which is the conversion of kinetic (vibration) energy to electrical energy. Motion from human limbs can be exploited as an input to the energy harvester, which will be used as a power supply to the wearable device. Human motion typically has a vibration frequency of between 0.1 to 25 Hz [6], which is quite low in comparison to the resonance frequency of the numerous varieties of piezoelectric materials.

Piezoelectric energy harvesters can have high output voltage from vibration as compared to other conversion mechanisms such as electromagnetic and electrostatic energy harvesters [7]. Additionally, it has been demonstrated that PZT-5H can generate a greater voltage than polyvinylidene difluoride (PVDF), aluminum nitride (AIN), and barium sodium niobate ($Ba_2NaNb_5O_{15}$) [2]. Traditionally, the piezoelectric energy harvester is designed as a linear resonator and only works effectively within a narrow bandwidth of frequency. The range of frequency bandwidth was around 5 Hz. For example, a PZT-5H beam has an optimum frequency range between 48 Hz and 53 Hz, while a PVDF beam has an effective frequency range between 250 Hz to 255 Hz [8-10]. Outside of a specified frequency range, the effectiveness of energy harvesting decreases tremendously.

Numerous solutions have been proposed to address the issue. One of the approaches is the plucking technique. Regardless of the frequency of the input, the energy harvester will always operate at its most efficient state. This technique is capable of matching the low frequency of human motion, such as an arm swinging forwards and backwards in a walking motion, which occurs at approximately 0.9 Hz [11], or running motion which occurs at 1.9 Hz [12]. This plucking technique can be categorized into two types: contact or non-contact. Contact methods, also known as impact types, have been demonstrated by Gu and Livermore [13]. The piezoelectric was struck by plucking it with another beam with a low resonance frequency.

On the other hand, non-contact types use a magnet to pluck the piezoelectric beam, such as in a knee joint harvester [14]. This energy harvester is worn on the knee. By using the motion of the knee while walking or running, the piezoelectric cantilever beams are plucked by the magnets and generate up to 3.3 V of electricity. Other research using the same mechanical plucking include impulse excited energy harvester for human body excitation

[6] and design and simulation of bistable piezoceramic cantilever for energy harvesting from slow swinging movement [15].

Although the piezoelectric energy harvester can convert kinetic energy to electrical energy, it could not properly harvest energy from ambient sources due to the unpredictable motion and periodicity of human movements. Thus, this paper will highlight the capability of the proposed beam deflection method in addressing the limitation. In this method, by utilizing magnetic force, the piezoelectric beam in the energy harvester device can be bent to its maximum deflection regardless of the input frequencies. The relationship between maximum deflection and applied voltage will be demonstrated by simulation. The findings will be further validated with a prototype to investigate the amount of energy harvested at various frequencies of motion.

2. RESEARCH METHOD

2.1 System Design

The principle of using a piezoelectric bimorph beam for energy harvesting based on magnetic plucking motion is demonstrated in this paper. Figure 1 shows an assembly of an eccentric mass that was used to convert linear motion into rotational motion. This configuration made it suitable for the piezoelectric beam to be magnetically plucked due to excitation by low frequency or random human motion. The piezoelectric beam used for this research is the PZT-5H piezoelectric bimorph beam with a dimension of 40 mm x 10 mm x 0.5 mm. The magnet used is a Neodymium magnet with a diameter of 12 mm and height of 3 mm. This piezoelectric beam consists of a layer of copper sandwiched between two layers of lead zirconate titanate (PZT).

The PZT-5H beam was chosen because it has demonstrated a higher capability for voltage generation than other piezoelectric materials such as polyvinylidene difluoride (PVDF), aluminum nitride (AIN), and barium sodium niobate ($Ba_2NaNb_5O_{15}$) [16-19]. Additionally, according to Table 1, PZT-5H has the greatest piezoelectric strain coefficient, d_{33} value, indicating that it can generate a comparatively greater charge under normal stress applied due to transverse vibration. The parameters of the piezoelectric energy harvester assembly are listed in Table 2.

Table 1: Comparison of strain coefficients, d_{33} for different types of piezoelectric materials

Material	d_{33} (m/V)
PZT-5H	600×10^{-12}
PVDF	30×10^{-12}
AIN	5.1×10^{-12}
Barium sodium niobate	319×10^{-12}

Table 2: Parameters of the piezoelectric energy harvester assembly

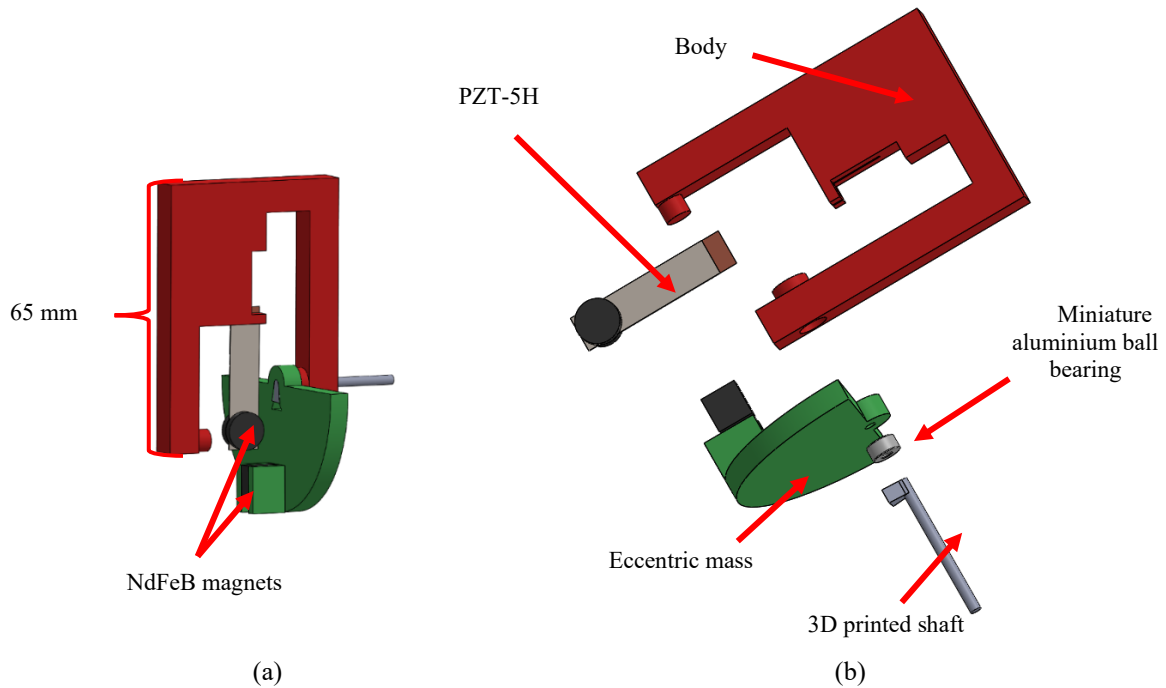| Material	Length/Mass
Diameter eccentric mass	80 mm
Circular magnet at the tip of the beam (proof mass)	12 mm (diameter), 3 mm (height)
Mass of the magnet at the tip of the beam (proof mass)	4.64 g
Rectangular magnet to bend the beam	10 mm x 10 mm x 3 mm
Piezoelectric beam	40 mm x 10 mm x 0.5 mm

Fig. 1: (a) The design of the piezoelectric energy harvester utilizing beam deflection method,
(b) Exploded view of the design.

Referring to Fig. 1, the design consists of an 80-mm diameter fabricated eccentric mass (green) with 65-mm length body (red), a PZT-5H piezoelectric bimorph beam, 6-mm diameter of neodymium (NdFeB) magnets, 10-mm length of rectangular NdFeB magnets and a miniature aluminum ball bearing with 8 mm outer diameter and 3 mm inner diameter. The circular neodymium magnet is mounted at the tips of the piezoelectric beam and the rectangular neodymium magnet is placed at the end of the eccentric mass, as shown in Fig. 1.

Due to the identical polarity of the magnets at the piezoelectric beam tip and eccentric mass, the piezoelectric beam will bend when the eccentric mass rotates, causing the magnets to push against one another. As the magnets move away from each other, stress is induced in the piezoelectric beam and output voltage is generated. The distance between the two magnets can be adjusted to ensure that the PZT-5H piezoelectric beam always bends at its 2 mm deflection. According to the product datasheet [20], the maximum deflection of the PZT-5H was 2 mm.

$$Ymax = -\frac{Fl^3}{3EI}$$

(1)

The cantilever beam formula, Eq. (1), was used to calculate the magnetic forces required to deflect the beam at 2mm. The term Y_{max} is maximum deflection, F is force, l is length of the beam, E refers to modulus elasticity of the beam and I refers to moment of inertia. From the calculation, the required force was 0.0344 N. Before each experiment began, the deflection was also measured using a Vernier scale. This is referred to as the mechanical plucking technique. It is well suited to human motion, which is predominantly random and low in frequency. It is capable of converting low-frequency movements into higher-frequency vibrations.

2.2 Simulation Study Using MATLAB Software

When a piezoelectric material experiences mechanical strain, some amount of voltage is generated at its terminal (known as sensor mode), and if a voltage is applied to the piezoelectric material, this will cause it to deform (actuator mode). Here, a simulation study was carried out to investigate the relationship between the deflection produced by the piezoelectric cantilever beam with the amount of voltage applied to the beam. The amount of voltage applied to the PZT beam in this study is made equal to the voltage generated when it vibrates at its resonance in sensor mode. MATLAB software was used to conduct the simulation.

The equations used in this paper have been discussed [21]. The typical constitutive equations for piezoelectric material are:

$$\{S\} = [s^E]\{T\} + [d]^T\{E\} \tag{2}$$

$$\{D\} = [d]\{T\} + [\varepsilon^T]\{E\} \tag{3}$$

In Eq. (2) and (3), constant *{S}* refers to the deformation vector, *{D}* is the electric displacement vector, *{E}* is the electric field vector, *[ε]* is the dielectric constant matrix, *[s]* and *[d]* are the elasticity and piezoelectric constant matrices whereas *{T}* refers to the stress vector. Based on the constitutive equations above, the state space equations are derived.

$$\begin{Bmatrix} S_{11} \\ S_{22} \\ S_{33} \\ S_{23} \\ S_{13} \\ S_{12} \end{Bmatrix} = \underbrace{\begin{bmatrix} s_{11} & s_{12} & s_{13} & 0 & 0 & 0 \\ s_{12} & s_{22} & s_{23} & 0 & 0 & 0 \\ s_{13} & s_{23} & s_{33} & 0 & 0 & 0 \\ 0 & 0 & 0 & s_{44} & 0 & 0 \\ 0 & 0 & 0 & 0 & s_{55} & 0 \\ 0 & 0 & 0 & 0 & 0 & s_{66} \end{bmatrix}}_{\text{Coupling}} \begin{Bmatrix} T_{11} \\ T_{22} \\ T_{33} \\ T_{23} \\ T_{13} \\ T_{12} \end{Bmatrix} + \underbrace{\begin{bmatrix} 0 & 0 & d_{31} \\ 0 & 0 & d_{32} \\ 0 & 0 & d_{33} \\ 0 & d_{24} & 0 \\ d_{15} & 0 & 0 \\ 0 & 0 & 0 \end{bmatrix}}_{\text{Permitivity}} \begin{Bmatrix} E_1 \\ E_2 \\ E_3 \end{Bmatrix} \tag{4}$$

Piezoelectric coupling matrices have a few non-zero elements due to the crystal symmetries as shown in Eq. (4), and the design of the sensing and actuation device is dictated by the available coupling modes. There are two state-space formulas which are for actuation and sensing mode. However, the actuation mode state-space formula is only used because only the actuation mode will be simulated. The piezoelectric material that will be used is PZT-5H. Therefore, PZT coupling matrices are shown below.

$$[d]_{PZT} = \begin{bmatrix} 0 & 0 & 0 & 0 & d_{15} & 0 \\ 0 & 0 & 0 & d_{15} & 0 & 0 \\ d_{31} & d_{31} & d_{33} & 0 & 0 & 0 \end{bmatrix} \tag{5}$$

In this simulation, the electric field will be applied perpendicularly to the poling direction, resulting in transverse displacement, as shown in Fig. 5. In order to obtain the bending action, thin PZT materials are bonded on the structure. The geometrical arrangement causes d_{31} to dominate the design, and the useful direction of expansion is normal to that of the electric field. By solving Eq. (3) and (4), a deflection for the bimorph PZT can be found based on Eq. (6) [21].

$$Deflection = -\frac{3}{2}\frac{d_{33}\varnothing}{h^2}L^2 \tag{6}$$

In Eq. (6), d_{33} refers to the piezoelectric strain coefficient at the z-axis direction, $\emptyset$ denotes the electrical potential, h and L are the height and length of the piezoelectric beam, respectively. The design of the piezoelectric beam is illustrated in Fig. 2. Here, the beam material used is PZT-5H in bimorph configuration.
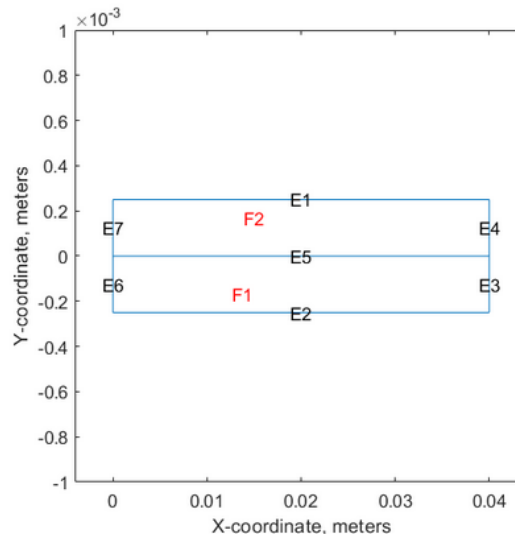

Fig. 2: Piezoelectric beam with a dimension of 40 mm x 10 mm x 0.5 mm.

Based on Fig. 2, *E1, E2,* and *E5* are the length of the PZT-5H beam, which is 40 mm, *E7, E6, E4,* and *E3* are the height of the beam, which is 5 mm. The PZT-5H is a bimorph beam, therefore, the total height is 10 mm. Table 3 shows the parameters that are set in the MATLAB software based on the selected PZT-5H beam according to the datasheet [20].

Table 3: Parameters of PZT-5H piezoelectric beam

Parameter	Value
Elastic modulus	7.2×10^{10} N/m^2
Poisson ratio	0.31
Shear modulus	4.6×10^{10} N/m^2
Piezoelectric constant, d_{31}	-270×10^{-12} m/v
Piezoelectric constant, d_{33}	600×10^{-12} m/v
Maximum deflection	2 mm

The amount of voltage that needs to be applied to the beam (actuator mode) in this study is determined via experiment by investigating the maximum voltage produced when the PZT beam vibrates at its resonant frequency (in sensor mode). In accordance with prior work [22], a digital signal analyzer (DSA HP-35670A) was used to provide base excitation to the same piezo cantilever beam over a frequency sweep from 0 Hz until 100 Hz. The result of this study is shown in Fig. 3. At its resonant frequency of 18.33 Hz, the PZT beam produced 4.55 V with a proof mass of 2.3 g and 4.01 V without proof mass. Although the resonant frequency was within the range of frequency of human motion (1 Hz - 25 Hz)[23], it is observed that the frequency bandwidth was quite narrow. This means that the PZT beam can only efficiently harvest energy at 18.33 Hz but will tremendously degrade when there is a slight change in the frequency of vibration. From this study, the voltage 4.55 V will be

taken as input to the simulation study, as shown in Fig. 2. The result will be discussed in a later section.
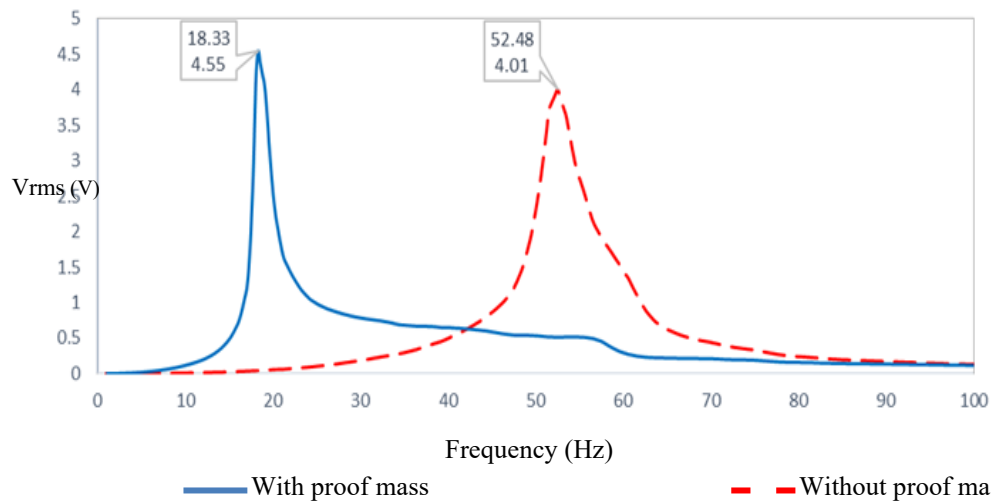

Fig. 3: Frequency sweep of PZT-5H piezoelectric beam. The peaks show the resonant frequencies of the beam with and without proof mass [22].

2.3 Measurement of Output Voltage from Beam Deflection

An experimental setup for the whole assembly of the fabricated energy harvester in measuring the output voltage is shown in Fig. 4. The apparatus for the experiment includes an Arduino Uno microcontroller to control the servo motor, a servo motor to oscillate the eccentric mass and imitate the average frequency of a human hand swinging forward and backward while walking and running, and a data acquisition board (National Instruments cDAQ-9171) to acquire the output signals from the piezoelectric beam to send to a computer with LabView software. The fabricated prototype was held using a tripod stand.
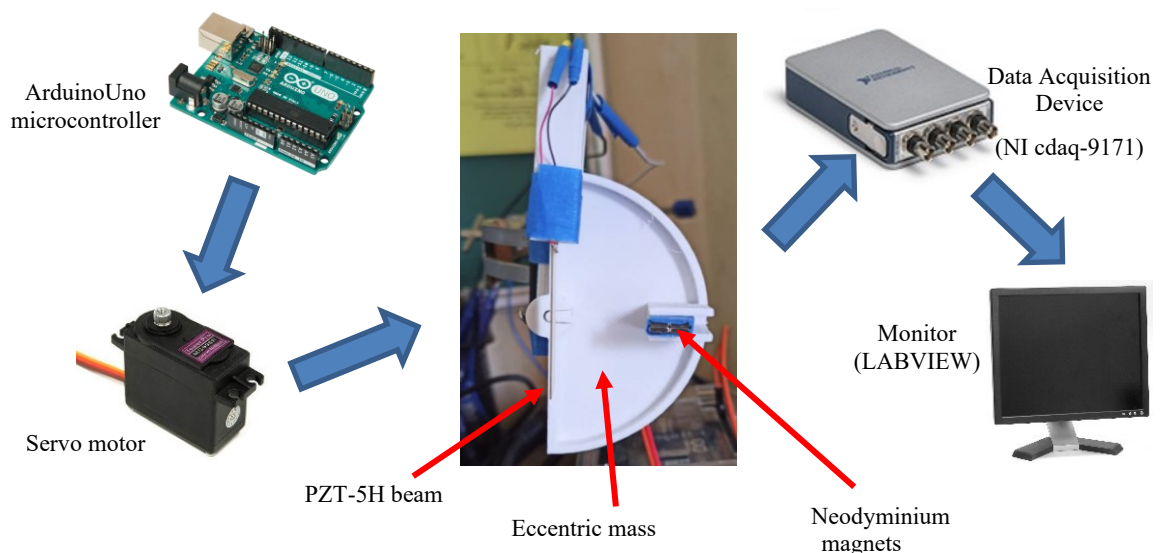

Fig. 4: Experimental setup.

The Arduino Uno was programmed to oscillate the servo motor at specific frequencies (0.9 Hz (walking) [11] and 2 Hz (running) [12]) to show that the peak AC voltage will

always be the same, regardless of the input frequencies. Additionally, four more frequencies (1.5 Hz, 2.5 Hz, 3.0 Hz, and 5 Hz) were also tested to observe the capability of the proposed design at other frequencies, as shown in Table 4. The frequency of oscillation for the eccentric mass was measured using a tachometer during the experiment.

Table 4: Frequency of the human limb motion when walking, running, and randomly pick frequencies

Test	Frequency of arm swing forward and backward (Hz)
Walk	0.9
Run	2.0
Test 1	1.5
Test 2	2.5
Test 3	3.0
Test 4	5

3. RESULTS AND ANALYSIS

3.1 MATLAB Software Simulation Results

The simulation research results stated in Section 2.2 will be discussed in this section. At the resonant frequency, the beam vibrates vigorously, resulting in greater deflection than at other frequencies, allowing for more voltage generation. To verify this, identical voltage is applied to the PZT beam and its resulting deflection is recorded. According to Fig. 3 (shown in the preceding section), the voltage generated when it vibrates at its initial resonance frequency is 4.55 V. Figures 5(a) and 5(b) illustrate the initial condition of the beam before any voltage is applied, during which no deflection occurs. When 4.55 V is supplied, the tip of the beam deflects 1.56 mm in the y-direction as seen in Fig. 5(c) and 5(d).

According to this investigation, the tip deflection of the beam generated by applying 4.55 V to its terminal is 1.56 mm, but the maximum deflection specified in the datasheet is 2 mm (Table 3), a difference of almost 22%. The following section will show experiments conducted to demonstrate that by ensuring the piezo beam deflects maximally via the plucking approach, the same maximum output voltage, Vac, can be generated regardless of the frequency.

3.2 Voltage Output from Beam Deflection

Figure 6(a) illustrates the AC output voltage measured by the data acquisition device as the energy harvester device is swung back and forth at a 0.9 Hz input frequency. This motion is meant to mimic the frequency of hand gestures made by an average healthy human when walking. Magnetic repulsion occurs when the magnets on the beam have the same polarity as the eccentric mass, deflecting or bending the beam. The piezoelectric beam is pushed and operated to its maximum deflection of 2 mm before the magnet is pulled away from the tip mass and the repulsion force is released. Within a brief period of time, the beam will vibrate and dampen, bringing the magnets closer together once more.

A similar experiment was repeated at a frequency of 2 Hz, which is the average frequency of healthy human motion while running. Similarly, the peak voltage was produced when the piezoelectric beam was actuated, as shown in Fig. 6(b). As shown in the graph, the highest output voltage produced was nearly identical, at 5.9 Vac. However, the frequency of the peak voltage produced in Fig. 6(b) was greater than in Fig. 6(a). This is because the eccentric mass oscillates at a higher frequency.
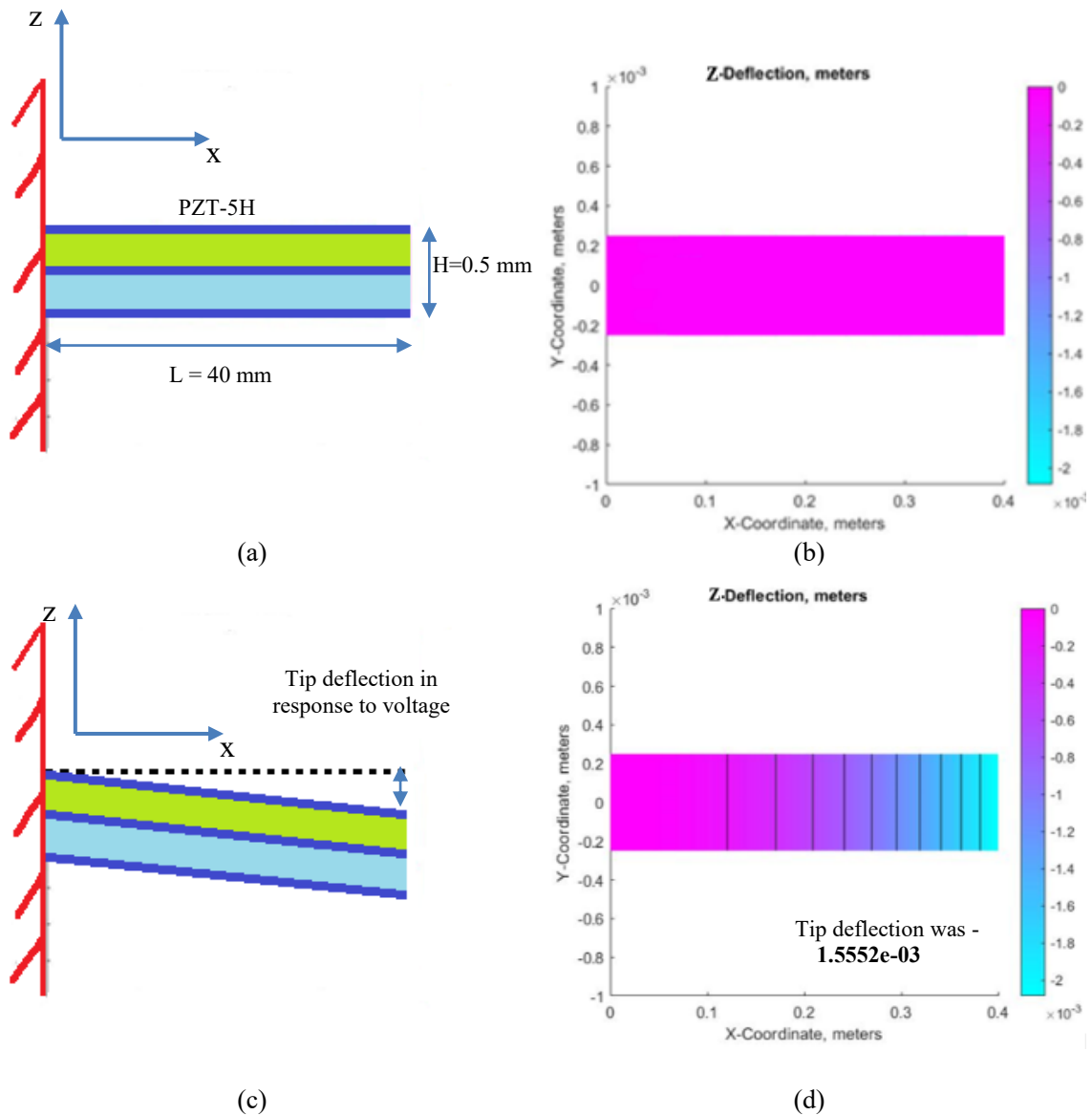
(a)

(b)

(c)

(d)

Fig. 5: (a) Initial shape of PZT-5H beam, (b) Deflection of PZT-5H beam in the z-direction during initial condition, (c) Shape of PZT-5H beam after a deflection in response to voltage, (d) Deflection of PZT-5H beam in the z-direction in response to voltage.

As illustrated in Fig. 6, when the plucking approach is used in the experiment, the peak output voltage does not significantly alter at the different excitation frequencies. This is because the piezoelectric beam always bends at its maximum deflection at the same amount of force every time the eccentric mass's magnet passes beneath it, resulting in the highest peak output AC voltage. However, the frequency of peak voltage is varied because the eccentric mass's frequency varies with the tested frequencies of motion. Figure 7 demonstrates that even when the frequency is altered up to 5 Hz, the output AC voltage remains constant.

It can be observed from Fig. 7 that the peak voltages for all four different frequencies vary between 5.76 Vpeak (at 3 Hz) to 5.88 Vpeak at 2.5 Hz i.e. 2% difference. The distance between the two magnets is adjusted continuously to maintain the deflection of the piezo beam such that it will be at its maximum value i.e. 2 mm.

(a)   (b)
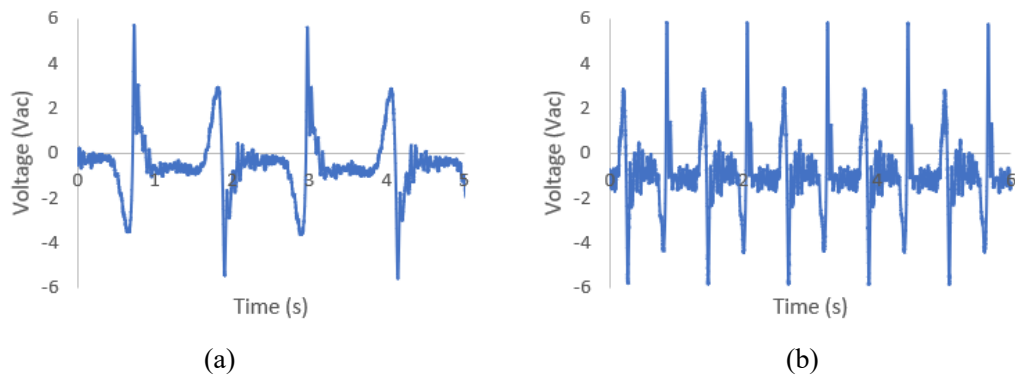
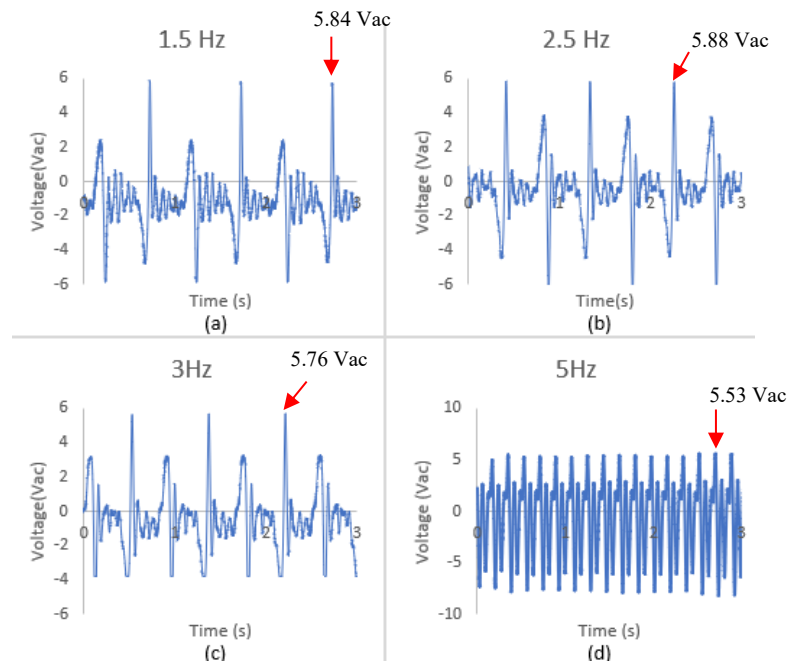Fig. 6: Output voltage (a) during 0.9 Hz frequency excitation, (b) during 2 Hz frequency excitation.

Fig. 7: Result for different tests for frequency (a) 1.5 Hz (b) 2.5 Hz (c) 3 Hz (d) 5 Hz.

3.3 Signal Rectification

The AC signals of the generated voltage for all frequencies were converted to DC signals using the same full bridge rectifier circuit in the previous works [22], shown in Fig. 8. The rectified signals from the full bridge rectifier circuit were then stored inside a 100 μF capacitor.

For each frequency, the experiment was conducted for 5 minutes to allow the DC voltage to stabilize and reach steady state. During the initial stages, the DC voltage will continue to rise [24]. Figure 9 shows that the voltage is the highest, 3.7 Vdc, when the energy harvester is excited by a 5 Hz frequency of motion. This is because its alternating current voltage has a higher peak value than others. As the frequency of the signal rises, the DC voltage stored inside the capacitor increases proportionately. Although the walking frequency of 0.9 Hz is the lowest due to the lower peak voltage in the AC Voltage, it can still generate an average of 1.5 Vdc over a 5-minute period, which is sufficient to drive low-powered electronic equipment.
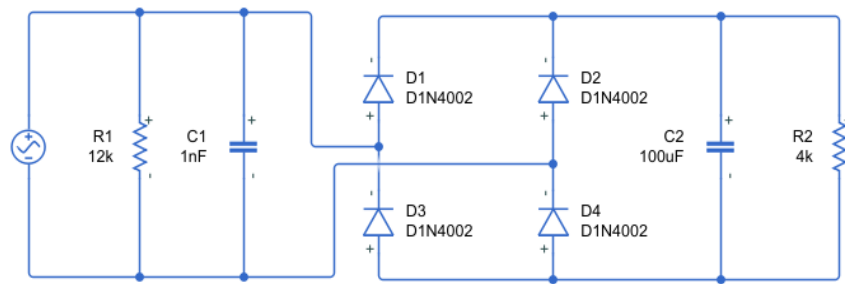
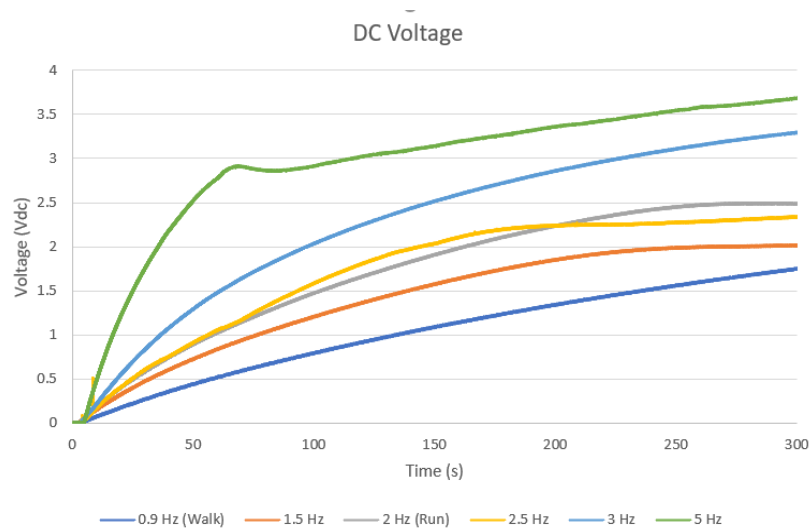Fig. 8: Full-bridge rectifier circuit for the assembly [22].

Fig. 9: Rectified voltage of the energy harvester at different frequencies.

The generated voltage is summarized in Table 5 for various frequency settings both before and after rectification. As can be seen, the average AC output voltage across all frequencies is 5.77 V. However, the rectified signals changed in response to the amount of frequency excited by the harvester. A higher DC voltage is generated when the excitation frequency is increased, and vice versa. This is proven in another work; a 5 V output was produced by a PZT-5H piezoelectric beam under 50 microstrain loading, which is the ultimate strain limit, over 50 MΩ load resistance [25].

Table 5: Summary of the generated voltage

Frequency (Hz)	Voltage peak of AC voltage (V)	DC Voltage (V)
0.9 (Walking)	5.70	1.6
2.0 (Running)	5.90	2.5
1.5	5.84	2.0
2.5	5.88	2.3
3.0	5.76	3.3
5	5.53	3.7

4. CONCLUSION

When subjected to input frequencies ranging from 0.9 Hz to 5 Hz, the fabricated energy harvester device consistently produced peak AC output voltages of 5.5 – 5.8 Vac. This implies that the PZT beam always deflects in the same direction when the magnet on the eccentric mass passes below the PZT beam's tip. The results of the studies demonstrate the

benefits of the suggested energy harvester for wearable devices using a magnetic plucking approach. As the eccentric mass in the proposed design can convert any directions of motion, it is less reliant on one-directional motion thus making it ideal for human applications with varying and random motion.

In the future, the efficiency of AC to DC conversion can be improved by employing alternative rectifiers such as voltage doubler rectifiers and synchronized switch harvesting on inductor rectifiers [26]. Apart from that, the size can be enhanced by making it more compact, allowing the gadget to be worn comfortably.

ACKNOWLEDGEMENT

REFERENCES

[1] Pillatsch P, Yeatman EM, Holmes AS. (2013) A wearable piezoelectric rotational energy harvester. In Proceedings of IEEE Internatinal Conference Body Sensor Networks: 6-9 May 2013; Cambridge, pp 1-6.

[2] Huda A, Noor Hazrin Hany MH, Aliza Aini MR. (2019) Magnetically plucked piezoelectric energy harvester via hybrid kinetic motion. IIUM Engineering Journal, 20(1): 245-257. doi: 10.31436/iiumej.v20i1.981.

[3] Fan PMY, Wong OY, Chung MJ, Su TY, Zhang X, Chen PH. (2015) Energy harvesting techniques: energy sources, power management and conversion. In Proceedings of European Conference on Circuit Theory and Design: 24-26 August 2015; Trondeim, pp 1-6.

[4] Nguyen S, Amirtharajah R. (2018) A hybrid RF and vibration energy harvester for wearable devices. In proceedings of IEEE Applied Power Electronics Conference and Exposition: 4-8 March 2018; San Antonio, pp. 1060–1064.

[5] Sang Y, Huang X, Liu H, Jin P. (2012) A vibration-based hybrid energy harvester for wireless sensor systems. IEEE Tranactions on Magnetics, 48(11): 4495-4498. doi: 10.1109/TMAG.2012.2201452.

[6] Pillatsch P, Yeatman EM, Holmes AS. (2012) A scalable piezoelectric impulse excited energy harvester for human body excitation. Smart Materials and Structures, 21(11): 1-9. doi: 10.1088/0964-1726/21/11/115018.

[7] Mohd Fauzi AR, Kok SL, Noraini MA, R. Affendi, Khairul Azha AA. (2013) Hybrid vibration energy harvester based on piezoelectric and electromagnetic transduction mechanism. In Proceedings of the IEEE Conference Clean Energy Technology: 18-20 November 2013; Langkawi, pp 1–5.

[8] Fan K, Tan Q, Liu H, Zhu Y, Wang W, Zhang D. (2018) Hybrid piezoelectric-electromagnetic energy harvester for scavenging energy from low-frequency excitations. Smart Materials and Structures, 27(8): 1-28. doi: 10.1088/1361-665X/aaae92.

[9] Anton SR, Sodano HA. (2007) A review of power harvesting using piezoelectric materials (2003-2006). Smart Materials and Structures, 16(3): R1-R21. doi: 10.1088/0964-1726/16/3/R01.

[10] Haitao L, Weiyang Q, Chunbo L, Wangzheng D, Zhiyong Z. (2015) Dynamics and coherence resonance of tri-stable energy harvesting system. Smart Materials and Structures, 25(1):1-10. doi: 10.1088/0964-1726/25/1/015001.

[11] Quantification of Arm Swing during Walking in Healthy Adults and Parkinson ' s Disease Patients : and Validation [https://www.ncbi.nlm.nih.gov/pmc/articles/PMC5685089/].

[12] Is the Relationship Between Stride Length, Frequency and Velocity Influenced by Running on a Treadmill or Overground ? [https://www.ncbi.nlm.nih.gov/pmc/articles/PMC5685089/].

[13] Gu L, Livermore C. (2011) Impact-driven, frequency up-converting coupled vibration energy harvesting device for low frequency operation. Smart Materials and Structures, 20(4):1-10. doi:

10.1088/0964-1726/20/4/045004.

[14] Pozzi M. (2016) Magnetic plucking of piezoelectric bimorphs for a wearable energy harvester. Smart Materials and Structures, 25(4):1-12. doi: 10.1088/0964-1726/25/4/045008.

[15] Rubes O, Hadas Z. (2018) Design and simulation of bistable piezoceramic cantilever for energy harvesting from slow swinging movement. In Proceedings of IEEE 18th International Conference Power Electronics and Motion Control: 26-30 August 2018; Budapest, pp 1-6.

[16] Noor Hazrin Hany MH, Ahmad Jazlan M, Huda A, Mas Ehsan R. (2018) Rotational piezoelectric energy harvester for wearable devices. Cogent Engineering, 5(1): 1-11. doi: 10.1080/23311916.2018.1430497.

[17] Cheng X, Wu J, Lou X, Wang X. (2014) Achieving both giant d_{33} and high T_C in patassium-sodium niobate ternary system. ACS Applied Materials and Interfaces, 6(2): 1-7. doi: 10.1021/am404793e

[18] Tian W, Ling Z, Yu W, Shi J. (2018) A review of MEMS scale piezoelectric energy harvester. Applied Sciences, 8(4): 1-20. doi: 10.3390/app8040645.

[19] Gao S, Ao H, Jiang H. (2019) Properties and performance of general piezoelectric materials on a novel cantilevered energy harvester. In Proceedings of 7th Annual International Conference on Materials Science and Engineering: 19-20 April 2019; Hubei, pp 1-8.

[20] Steminc Steriner & Martins Inc [https://www.steminc.com/PZT/en/piezo-ceramic-bimorph-40x10x05mm-2-khz].

[21] V. Piefort (2001) Finite element modelling of piezoelectric active structures. PhD thesis. Universit´e Libre de Bruxelles, Faculty of Applied Sciences.

[22] Mohamad Safiddin MT, Noor Hazrin Hany MH, Muhammad Hafizuddin CK. (2021) Performance measurement of piezoelectric energy harvester with permanent magnet assembly for wearable devices. In Proceedings of IEEE International Instrumentation and Measurement Technology Conference: 17-20 May 2021; Glasgow, pp 1–5.

[23] Von Büren T, Mitcheson PD, Green TC, Yeatman EM, Holmes AS, Tröster G. (2006) Optimization of inertial micropower generators for human walking motion. IEEE Sensors Journal, 6(1): 28-38. doi: 10.1109/JSEN.2005.853595.

[24] Muhammad Aiman ZA, Noor Hazrin Hany MH, and Mohamad Safiddin MT. (2021) Energy storage system for dual energy harvester for wearable or portable devices. In Proceedings of 8th International Conference Computer and Communication Engineering: 22-23 June 2021; Kuala Lumpur, pp 135-139.

[25] M. Rhimi. (2013) Power management and damage assessment techniques for self-powered sensing based on piezoelectric. PhD Dissertation. University of Michigan, Civil Engineering Department.

[26] Vishnu Sidharthan P, Bhasker MU, Korla S, Chandrasekhar MS. (2018) Energy harvesting of synchronized switch harvesting on inductor. In Proceedings of International Conference Recent Innovations in Electrical Electronics and Communication Engineering: 27-28 July 2018; Bhubaneswar, pp 2282-2887.